ICCC 2023 - Guidelines for citation and reuse

Please cite the conference proceedings as following:
Thailand Concrete Association, Ed. *Further Reduction of CO2 -Emissions and Circularity in the Cement and Concrete Industry, 16th International Congress on the Chemistry of Cement 2023 - ICCC2023* (Bangkok 18.-22.09.2023). Bangkok, 2023. Available at: https://www.iccc-online.org/archive/

Please cite individual papers as following:
Author. Title. In: Thailand Concrete Association, Ed. *Further Reduction of CO2 -Emissions and Circularity in the Cement and Concrete Industry, 16th International Congress on the Chemistry of Cement 2023 - ICCC2023* (Bangkok 18.-22.09.2023). Bangkok, 2023. Available at: https://www.iccc-online.org/archive/

Organized by

TCA
สมาคมคอนกรีตแห่งประเทศไทย
Thailand Concrete Association

THE 16TH INTERNATIONAL CONGRESS ON THE CHEMISTRY OF CEMENT
ICCC 2023
BANGKOK THAILAND

CONGRESS PROCEEDING VOLUME V

Further reduction of CO_2-emission and circularity in the cement and concrete industry

SEPTEMBER 18-22, 2023

CENTARA GRAND & BANGKOK CONVENTION CENTRE @CENTRALWORLD

Co-Sponsor by

aci American Concrete Institute Always advancing

SEADMA

gcca

ASTM INTERNATIONAL

Contact infomation :
Email: iccc2023.tca@gmail.com
Website : https://www.iccc2023.org/

PREFACE

The International Congress on the Chemistry of Cement (ICCC) is the renowned global platform that summarizes the state of the art of cement chemistry as well as major trends in cement application. Since the first International Congress on the Chemistry of Cement started in London in 1918, it has provided a strong and fruitful link between the academic world and the cement industry. It has always stimulated scientific exchanges and discussions between researchers, students, and those who have already gained working experience in many fields of chemistry relevant to cement production and its use in concrete and mortar. The ICCC is the venue to present cement and environmental development together with meeting worldwide and renowned experts from all over the world who come to present their works at the congress.

This proceeding collects the papers submitted to the 16th International Congress on the Chemistry of Cement (ICCC 2023), which was held in Bangkok, Thailand between September 18-22, 2023, and organized by Thailand Concrete Association on the theme of "further reduction of CO2-emission and circularity in the cement and concrete industry". The ICCC 2023 attracted more than 565 papers and more than 800 delegates and students from 49 countries.

The scientific program covers the topics of the newest and the most important research and development describing the new dimensions in clinker production, advances in hydration chemistry, enhancing clinker substitution and supplementary cementitious materials, advances in characterization methods and modelling, new low carbon cement and carbonatable binders, new findings in admixture & rheology, new technology for quality concrete, durability & reactive transport, sustainability, circular economy, waste processing and recycling, and standardization of cement and concrete.

The Organizing Committee and the Scientific Committee believe that our participants will be most satisfied with the congress and will gain the knowledge to improve their professional works in the future.

Prof.Thanakorn Pheeraphan
Chairman of the Organizing Committee

Prof.Somnuk Tangtermsirikul
Chairman of the Scientific Committee

Steering Committee Members

The Steering Committee is comprised of 26 members.

1. Prof. Dr. Mark G. Alexander, University of Cape Town, South Africa
2. Prof. Dr. Alexandra Bertron, INSA Toulouse, France
3. Prof. Dr. Shashank Bishnoi; Indian Institute of Technology Delhi, India
4. Prof. Dr. Leon Black, University of Leeds, United Kingdom
5. Dr. Cesar Constantino; Titan America LLC, USA
6. Jesper Sand Damtoft, Aalborg Portland A/S, Denmark
7. Prof. Dr. Jan Deja; Stowarzyszenie Producentów Cementu – PCA, Poland
8. Dr. Wolfgang Dienemann, HeidelbergCement AG, Germany
9. Daniel Duque, Cementos Argos S.A., Columbia
10. Ing. Jan Gemrich, Czech Cement Association, Czech Republic
11. Prof. Dr. Frederik Paul Glasser, University of Aberdeen, Scotland
12. Prof. Dr. R. Doug Hooton, University of Toronto, Canada
13. Prof. Dr. Vanderley M. John, Escola Politécnica da USP, Brasil
14. Prof. Dr. Kimberly Kurtis, Georgia Institute of Technology, USA
15. Christophe Levy, Lafarge Holcim Innovation Center (Chairman), France
16. Prof. Dr. Ippei Maruyama, Nagoya University Furocho, Japan
17. Dr. Bibekananda Mohapatra, Director General of the National Council for Cement and Building Materials, India
18. Dr. Marta Palacios, Instituto Eduardo Torroja, Spain
19. Prof. Dr. Angel Palomo, Instituto Eduardo Torroja, Spain
20. Prof. Dr. Thanakorn Pheeraphan, Thailand Concrete Association (Deputy-Chairman), Thailand
21. Prof. Dr. Martin Schneider, VDZ e.V., Research Institute, Germany
22. Prof. Dr. Karen Scrivener, École Polytechnique Fédérale de Lausanne – EPFL, Switzerland
23. Prof. Dr. Caijun Shi, Hunan University, China
24. Prof. Dr. Sui Tongbo, Sinoma International Engineering Co., Ltd., China
25. Prof. Dr. Jannie S. J. Van Deventer, Zeobond Pty Ltd, Australia
26. Dr. Kazuo Yamada, National Institute for Environmental Studies, Japan

Dr. Joerg Rickert, VDZ (Permanent Secretariat of ICCC), Germany - (Without the right to vote)

Organizing Committee Members

Advisory committee members

1. Dr. Wonchalerm Chalodhorn, Siam City Cement Co. Ltd.
2. Prof.Dr. Chai Jaturapitakkul, King Mongkut's University of Technology Thonburi
3. Prof.Dr. Parinya Jindaprasert, KhonKaen University
4. Mr. Ferdinand Leopolder, The South East Asia Drymix Mortar Association SEADMA,
5. Assoc.Prof.Dr. Pichai Nimityongskul , 1st President of Thailand Concrete Association
6. Mr. Chakporn Oonjitt, Construction Institute of Thailand
7. Mr. Wanchai Phanomchai, Thai Industrial Standards Institute
8. Mr. Chana Poomee, Thai Cement Manufacturers Association
9. Dr. Phirun Saiyasitpanich, Office of Natural Resources and Environmental Policy and Planning
10. Mr. Manasit Sarigaphuti, The Siam Cement Group Public Company Limited
11. Assoc.Prof. Anek Siripanichgorn, Engineering Institute of Thailand
12. Prof.Dr. Boonchai Stitmannaithum, Chulalongkorn University
13. Prof.Dr. Piti Sukontasukkul, King Mongkut's University of Technology North Bangkok
14. Mr. Sumate Surabotsopon, Italian-Thai Development Public Company Limited
15. Prof.Dr. Somnuk Tantermsirikul, Sirindhorn International Institute of Technology
16. Dr. Saranyu Viriyavejakul, Neighboring Countries Economic Development Cooperation Agencies
17. Prof.Dr. Pennung Warnitchai, Asian Institute of Technology
18. Mr. Boonyanit Wongrukmit, Electricity Generating Authority of Thailand

Organizing Committee members

1. Prof.Dr. Thanakorn Pheeraphan, Thailand Concrete Association and NavamindaKasatriyadhiraj Royal Air Force Academy (Chairman)
2. Asst.Prof. Dr. Chuchai Sujivorakul, King Mongkut's University of Technology Thonburi (Deputy Chairman)
3. Mr. Boonrawd Kuptitanhi, The Concrete Products and Aggregate Co., Ltd. (Treasurer)
4. Asst.Prof.Dr. Nattapong Magaratat , King Mongkut's University of Technology North Bangkok (Secretariat)
5. Dr. Praveen Chompreda, K.C.S. & ASSOCIATES. Co., Ltd.
6. Assoc.Prof.Dr. Phongthorn Julphunthong, Naresuan University
7. Miss Sunkamol Khongsawatvorakul, Saint-Gobain Thailand.
8. Mr. Sumet Kiatmetha, Hilti (Thailand) Ltd.
9. Gp.Capt. Nuth Limsuwan, Office of Civil Engineering Royal Thai Armed Forces.
10. Dr. Nontapat Nimityongskul, Asia Cement Public Company Limited.
11. Assoc.Prof. Panuwat Joykad, Srinakharinwirote University
12. Dr. Yut Panitanwong, Concrete Product and Aggregate Co.,Ltd.
13. Mr. Suwatchai Puwapattanachat, SIKA (Thailand) Ltd.
14. Mr. Narin Sayanwisuttikam, KAO Industrial (Thailand) Co., Ltd.
15. Dr. Kritsada Sisomphon, The Siam Cement Group Public Company Limited.
16. Mr. Chalermwut Snguanyat, The Siam Cement Group Public Company Limited.
17. Mr. Pakorn Sutthiwaree, Siam City Cement Public Company Limited.
18. Assoc.Prof.Dr. Weerachart Tangchirapat, King Mongkut's University of Technology Thonburi
19. Asst. Prof. Dr. WarangkanaSaengsoy, Construction and Maintenance Technology Research Center, SIIT
20. Prof.Dr. Wanchai Yodsudjai, Kasetsart University

Scientific Committee Members

1. Prof.Mark Alexander, South Africa
2. Prof.Carmen Andrade, Spain
3. Prof.Sergio Angulo, Brazil
4. Dr.Mohsen Ben Haha, Germany
5. Prof.Susan Bernal Lopez, UK
6. Prof.Alexandra Bertron, France
7. Prof.Shashank Bishnoi, India
8. Prof.Maria Blanco, Spain
9. Prof.Jeff Bullard, USA
10. Prof.Maria Alba Cincotto, Brazil
11. Prof.Jan Deja, Poland
12. Prof.Donguk Choi, South Korea
13. Prof.Josee Duchesne, Canada
14. Mr.Wilmar Echeverri, Colombia
15. Prof.Ivan Escalante, Mexico
16. Dr.Duncan Herfort, Denmark
17. Prof.Bruno Huet, France
18. Prof.Jason Ideker, USA
19. Prof.Edgardo Irassar, Argentinia
20. Prof.Zhengwu Jiang, China
21. Prof.Maria Juenger, USA
22. Dr.Marios Katsiotis, Greece
23. Prof.Shiho Kawashima, USA
24. Prof.Paula Kirchheim, Brazil
25. Prof.Jiaping Liu, China
26. Mr.Federico Lopez, Mexico
27. Prof.Barbara Lothenbach, Switzerland
28. Prof.Horst Ludwig, Germany
29. Prof.Ippei Maruyama, Japan
30. Prof.Thomas Matschei, Germany
31. Mr.Mike McDonald, South Africa
32. Dr.Sean Monkman, Canada
33. Prof.Paulo Monteiro, USA
34. Mr.Carlos Orozco, Colombia
35. Dr.Marta Palacios, Spain
36. Prof.Martin Palou, Slovakia
37. Dr.César Pedrajas, Spain
38. Prof.Rafael Pileggi, Brazil
39. Prof.Kedsarin Pimraksa, Thailand
40. Prof.John Provis, UK
41. Prof.Francisca Puertas, Spain

Scientific Committee Members

42.Prof.Jueshi Qian, China
43.Prof.Aleksandra Radlinska, USA
44.Dr.Nailia Rakhimova, Russia
45.Prof.Matteo Romano, Italy
46.Prof.Nicolas Roussel, France
47.Dr.Kwesi Sagoe-Crentsil, Australia
48.Prof.Manu Sanathanam, India
49.Prof.Miguel Sanjuán, Spain
50.Prof.Caijun Shi, China
51.Dr.Denise Silva, USA
52.Prof.Somnuk Tangtermsirikul, Thailand (Chairman)
53.Dr.Theodor Staněk, CZ
54.Prof.Arezki Tagnit-Hamou, Canada
55.Mr.Antonio Telesca, Italy
56.Dr.Paul Tennis, USA
57.Prof.Michael Thomas, Canada
58.Prof.Jorge Tobon, Canada
59.Prof.Sandro Torres, Brazil
60.Prof.Matthieu Vandamme, France
61.Dr.Yury Villagrán Zaccardi, Argentina
62.Prof.Fazhou Wang, China
63.Prof.Zhang Wensheng, China
64.Prof.Claire White, USA
65.Dr.Frank Winnefeld, Switzerland
66.Dr.Hong Wong, UK
67.Dr.Kazuo Yamada, Japan
68.Prof.Cheng Yu, China
69.Prof.Doug Hooton, Canada
70.Peter Kruspan, Switzerland

Contents

	Topics	Page
	Preface	i
	Committees	
	- Steering Committee Members	ii
	- Organizing Committee Members	iii
	- Scientific Committee Members	v
	Papers	
PB0001	Prediction of Total Bond Order Density of Cement Crystals using Fermionic Hubbard Model and Bloch and Fermi Surface	1
PC0070	Accelerating mechanism of calcium additives on alkali activated cementitious material	5
PC0077	The Influence of Aluminum Uptake on the Mechanical Properties of Calcium Silicate Hydrate	9
PD0002	The Effects of Supplementary Cementitious Materials on the Hydration Kinetics of G-Oil Cement	13
PD0018	Industrial Deployment of Calcined Clays Cements	17
PD0021	Simulation of sulfate attack on carbonated Portland cement-blast furnace slag binary cement	21
PD0023	Mineralogical analysis of BOF slag with different grinding characteristics	25
PD0049	Use of machine learning for predicting phase assemblages of supplementary cementitious materials-blended cements	29
PD0052	Restraining strength retrogression of silica-cement at high temperature above 200 ℃ using flint clay and graphite	33
PD0063	A Particle Packing Approach for Eco-efficient Ultra High-Performance Concrete (E-UHPC)	38
PD0068	Effect of chloride salts on cement hydration: influence of the cation part II	42
PD0079	Impact of curing time on carbonation of low-clinker binders	46
PD0133	Quantitative microstructure analysis of SCM-blended cementitious materials through deep learning-based computer vision methods	50
PD0134	Effect of steam curing on the hydration of limestone calcined clay cements (LC3) with low kaolinite content	54

Contents

	Topics	Page
	Papers	
PE0010	A comparative study of tribometer rotor configurations and analytical methods for concrete pumping pressure prediction	58
PE0036	Comparison of superabsorbent polymer characterization by filtration test in water and cementitious filtrate	62
PE0052	Atomic Scale Insight of Hydration Temperature Rise Inhibitors (TRI) Affecting Calcium Activity via AIMD	66
PE0057	Multi-scale model for characterizing thermal conductivity of cement-based materials with nano inclusions	70
PE0063	Multi-phase and Multi-ion Modelling of Electric Current, Electric Potential and Species Transport in Reinforced Concrete During Active corrosion Process Applied to Optimization of a Patching Repair Process	74
PF0040	Improved tensile performance of strain-hardening geopolymer composites using treated CBA and polyethylene fiber	79
PF0049	Effect of CO_2 curing on bonding strength and microstructure in the interfacial transition zone	83
PF0062	Incorporation of construction and demolition waste (CDW) in fiber cement submitted to the accelerated carbonation process	87
PF0095	Effect of Low Temperature Calcination on Pozzolanic Activity of Volcanic Powder	91
PF0099	Comparative Study of Mechanical Properties of Limestone Calcined Clay Cement, Ordinary Portland Cement, and Pozzolana Portland Cement	95
PF0104	Suitable solvent extraction method selection and gel structure evolution for alkali activated slag (AAS) pastes at early age	99
PF0133	Case Studies on the Large-Scale use of Low-Carbon Belitic Calcium Sulfoaluminate (BCSA) concrete	103
PF0139	High-efficient Solidification and Stabilization by Low Carbon Supersulfated Cement	107

Contents

	Topics	Page
	Papers	
PF0145	Comparison of set retarders in CSA and blended CSA/OPC systems	111
PF0146	CO_2 mineralization in the limestone calcined clay cement	115
PF0151	Influence of slaked lime on hydration kinetics of Portland cement	119
PG0002	Effect of alkanolamines in kaolinitic calcined clays pozzolanic reactivity	123
PG0011	Influence of raw and mechanically activated shale on rheological properties of cement based binder	127
PG0025	Changes in Rheology and Tensile Properties of UHPC with Silica Fume Content	131
PG0039	Understanding the effect of slag particle size, shape, and morphology on the flow characteristics of Portland cement – blast furnace slag blends	135
PG0050	Sacrificial agents for clayey aggregates. An understanding of mortar and concrete scale	139
PG0051	Effect of the use of different dispersing molecules on the rheological properties and kinetic hydration of Portland cement pastes	143
PG0053	Pore structure of polymer-modified dry mix tile adhesive mortars	147
PG0057	Aluminum sulfate-based accelerators: rheological implications for 3D-printed concretes	151
PG0065	Effects of different types of shrinkage reducing agents on shrinkage properties of mortars incorporating slag or silica fume	155
PG0067	On the impact of sulphate source on admixtures in limestone calcined clay cements	159
PG0071	A study on the adsorption and dispersion capability of PCEs with different structures on cement containing montmorillonite	163
PG0072	Preparation and performance of EPEG-type PCE and its application in ultra-high performance concrete	167

Contents

	Topics	Page
	Papers	
PG0074	Development of ultra-fine SAP powder for lower-shrinkage and higher-strength cement pastes made with ultra-low water-to-binder ratio	171
PH0019	New trend line of compressive strength and unit volume weight of cement composites: Lightweight and high-strength at the same time	175
PH0023	Strength Development Prediction and Mixture Optimization of Concrete Used in the Three Gorges Dam	179
PH0025	Design of High-Performance Concrete (HPC) using calcined clay as supplementary cementitious materials	183
PI0027	Influence of negative temperature hardening on hydration and pore structure evolution of Portland cement paste	187
PI0072	Resistance of portland-dolomite cement to thaumasite sulfate attack	192
PI0083	Contribution of the thermochemical conversion kinetics to predict the mass transfer of hydraulic binders panels submitted to fire	196
PI0098	Surface effect on chloride diffusion in calcium silicate hydrate	200
PJ0017	Increasing circularity and material efficiency using ore sand in concrete - A Brazilian case study	204
PJ0080	Effect of Mix Proportion as W/C and Amount of GGBS Contents on CO_2 Adsorption	209
PJ0114	Formation of closed pore structure porous glass-ceramics for thermal insulation	213
PJ0116	Carbonation effects on mechanical performance and microstructure of LWAs produced with hydrated cement paste powder	217
PK0002	Cement types and seawater exposure in Europe – implications for infrastructure and its integration into marine habitats	222
PK0005	A micromechanical modelling approach to study the effect of shape of hydrates on creep properties of cement pastes	226

The 16th International Congress on the Chemistry of Cement 2023 (ICCC2023)
"Further Reduction of CO_2 -Emissions and Circularity in the Cement and Concrete Industry"
September 18–22, 2023, Bangkok, Thailand

Prediction of Total Bond Order Density of Cement Crystals using Fermionic Hubbard Model and Bloch and Fermi Surface

Natt Makul

Department of Civil Engineering Technology, Faculty of Industrial Technology, Phranakhon Rajabhat University, 9 Changwattana Road, Bangkhen, Bangkok 10220, Thailand
Email: natt@pnru.ac.th

ABSTRACT

This work used quantum physics to predict how cement crystals' internal cohesiveness will evolve. At low temperatures, the electron-electron interactions of cement-based materials' internal cohesiveness may be more accurately predicted with the assistance of the Hubbard model. This model should make research on the bosonic version of the Hubbard model and the fermionic version possible. The total bond order density, or TBOD, is a quantum mechanical metric used to characterize C-S-H crystals. For a better understanding of cement crystal cohesiveness, this measurement considers geometric components and interatomic interactions. The orthogonalized linear combination of atomic orbitals (OLCAO) approach will be used to determine the source of internal cohesion in C-S-H crystals by comparing the bond order of an atom pair to the bond length of the pair. This study should contribute to the information on the internal cohesiveness of cement-based crystals and provide practical approaches to reinforce calcium-silicate-hydrate crystals in addition to contributing to the body of knowledge on cement-based crystals.

KEYWORDS: *Calcium-Silicate-Hydrate; Quantum-physical theory; Hubbard model; Total bond order density (TBOD); OLCAO*

1. Introduction

Portland cement consists of four distinct clinker phases: alite (Al_3SiO_5), belite (Ca_2SiO_4), ferrite (Al_xFe_{2-x}), and tri-calcium aluminate ($Ca_2(Al_xFe_{2-y})\ O_5$) ($Ca_3Al_2O_6$). C-S-H with varied compositions is the principal hydrate product responsible for cement-based concrete's strength, calculated as an average of the Ca/Si percentage and water content. The C-S-H phase with a large fraction of Ca/Si forms during the hydration of pure cement, as reported by Kunther et al. (2015).

Colloidal materials and systems commonly display net interactions between surfaces with the same electrical charge. The DLVO theory was first proposed by Derjaguin, Landau, Verwey, and Overbeek. In order to investigate the interactions between ions in space and their changing behavior, the theory depended on the mean-field approximation. This allowed the theory to capture some of the scenarios that were presented. However, it is generally agreed that the DLVO theory does not apply to cement hydration products such as C-S-H. This is because the ions that make up cement hydration products are of a multivalent nature (Ca^{2+}), and they can only be found on charged surfaces with a surface density of approximately 3 to 5 e/nm^2 in the hardened C-S-H phase. Given this information, the DLVO hypothesis cannot predict how the internal cohesiveness of cement crystals changes over time.

Molecular simulation of the extended Hubbard model for internal cohesion and direct measurement, on the other hand, has provided strong arguments on how to determine the surface forces supported with hydrated calcium ions, which are essential in the compressive strength of concrete. This is the case because the extended Hubbard model predicts that it is anticipated that this model will both facilitate research into the bosonic version of the Fermionic Hubbard model and promote research into the latter. In addition, the research will analyze the cohesiveness of cement-based crystals by classifying C-S-H crystals based on an ideal quantum mechanical metric known as total bond order density (TBOD)

(Kunther et al., 2015). In order to give a more in-depth understanding of the cohesiveness of cement-based crystals, this metric will take into account the influence of geometric parameters and interatomic interactions. In this particular scenario, the first-principles OLCAO approach will be used to compare the bond order (BO) in an atom pair and the bond length to discover the source of the internal cohesiveness in the C-S-H crystals. It is anticipated that this will give vital hints about modifying the cement's internal cohesiveness at the nano- and meso-structure levels. It is anticipated that the results of this research will significantly contribute to the expanding body of literature on the internal cohesion of cement-based crystals and will also provide valuable strategies for increasing the robustness of cement in the face of silicate and hydrate. This paper presents the data using an expanded Hubbard model adjusted for crystal polymerization. The data from crystalline phases may assist in understanding experimental spectroscopic results, leading to accurate models of the C-S-H phase in Portland cement.

2. Internal cohesion of cement crystals

Nineteen well-documented cement crystals are classified based on the increasing order of Ca/Si ratio into four groups (Zang et al., 2012). The first group includes anhydrous cement (a.1 (Belites) and a.2 (Alite)), and the groups b.x through d.x are C-S-H crystals (Mills et al., 2009) as shown in Table 1.

Table 1. Chemical characteristic of (a) Clinkers/Hydroxide phases, (b) Nesosubsilicates, (c) Sorosilicates and (d) Inosilicates (Zang et al., 2012).

Mineral Name		Chemical formulas	Ca/Si
(a) Anhydrous cement			
	a.1	Belites ($2(CaO)\ SiO_2$)	2.00
	a.2	Alite ($3(CaO)\ SiO_2$)	3.00
(b) Nesosubsilicates			
	b.1	Afwillite ($Ca_3(SiO_3OH)_2{\cdot}2H_2O$)	1.50
	b.2	α-C_2SH $Ca_2(HSiO_4)(OH)$	2.00
	b.3	Dellaite ($Ca_6(Si_2O_7)(SiO_4)(OH)_2$)	2.00
	b.4	Ca Chondrodites ($Ca_5[SiO_4]_2(OH)_2$)	2.50
Remark: Sorosilicate structures feature solitary (Q0) and finite (Q2) tetrahedra linked by 6- or 8-fold Ca atoms. Silicate tetrahedra pair each polymerization phase's (Qn) Si. Group d has the highest polymerization compared to C-S-H (Dharmawardhana et al. (2014).			

Mineral Name		Chemical formulas	Ca/Si
(c) Sorosilicate			
	c.1	Rosenhahnites $Ca_3Si_3O_8(OH)_2$	1.00
	c.2	Suolunites $Ca_2[Si_2O_5(OH)_2]H_2O$	1.00
	c.3	Kilchoanites $Ca_6(SiO_4)(Si_3O_{10})$	1.50
	c.4	Killalaites $Ca_{6.4}(H_{O.6}Si_2O_7)_2(OH)_2$	1.60
	c.5	Jaffeites $Ca_6[Si_2O_7](OH)_6$	3.00
(d) Inosilicates			
	d.1	Nekoite $Ca_3Si_6O_{15}{\cdot}7H_2O$	0.50
	d.2	T11 Å $Ca_4Si_6O_{15}(OH)_2{\cdot}5H_2O$	0.67
	d.3	T14Å $Ca_5Si_6O_{16}(OH)_2{\cdot}7H_2O$	0.83
	d.4	T9 Å $Ca_5Si_6O_{17}5H_2O$	0.83
	d.5	Wollastonites $Ca_3Si_3O_9$	1.00
	d.6	Xonotlites $Ca_6Si_6O_{17}(OH)_2$	1.00
	d.7	Foshagites $Ca_4(Si_3O_9)(OH)_2$	1.33
	d.8	Jennites $Ca_9Si_6O_{18}(OH)_6{\cdot}8H_2O$	1.50

3. Hubbard model, Bloch and Fermi surface of C-S-H

In this case, using the Hubbard model, the interaction between electrons in the crystals will involve a series of fractional filling factors. A quantum mechanics representation of the Hubbard model is presented in Eq. (1), considering the site repulsion (i) and nearest neighbor repulsion (j). Electron interactions in a 2-dimensional lattice crystal are summated using i and j to cover all pairs of nearest-neighbors sites; t represents the magnitude of *NN* interaction; U represents crystal interaction onsite.

$$H = -t\sum_{i,j} b_i^{+} b_j + \sum_{i,j} n_i U_{i,j} n_j - \mu \tag{1}$$

A general form of the Hamiltonian H, can be expressed as a product of $|\varphi> = \sum_{e,p} |e>_{e,i} * |p>_{pk}$, where e and p represent electronic interaction and the bosonic state of the crystal. This truncated bosonic version of the infinite crystal takes one electron for each crystal. In this case, we argue that the change of the internal cohesion of a crystal where another crystal is already present does not necessarily change the scenario of the interacting electrons qualitatively. In order to overcome this challenge, we considered a scenario where two electrons spin in the opposite direction. The

electrons were also restricted to one phonon operator identical $b_i^+|1_t>=|1_t>$; $b_i^+|0_t>=|1_t>$; $b_i|1_t>=|0_t>$; and $b_i|0_t>0$ where 1(0) represents a change in the internal cohesion of a cement crystal. To establish the effect of a pair electron interaction in the crystal, the study computed the electron-electron density correlation using the function $C(i-j)=<\varphi_0|n_i n_j|\varphi_0>$.

Bloch's theorem presents the one-dimensional symmetry of an infinite crystal through the absence of the aggregate electric current at an equilibrium state (Watanabe, 2022). Yamamoto (2015) applied Bloch's theorem to generic systems to gauge particles in symmetry to understand the chiral transport concept. The study investigates the fermionic and bosonic versions of the Hubbard model to determine changing internal cohesion in a lattice. From the findings, the study demonstrated the adoption of the theorem to a non-equilibrium state, which is similar to the integral quantum Hall effect. For the case of cement crystals, this concept remains valid as long as there are no topological variations in the internal cohesion subject to periodical conditions, as illustrated in $|\varphi(x)|^2 = |\varphi(x+a)|^2$. In case a crystal changes by '*a*' as illustrated in $\varphi(x+a)=C.\varphi(x)$, there should be no difference in the internal cohesion with the magnitude of C is equal to 1.0. This main feature of Bloch's theorem remains valid as the fermion interaction of the crystals considers the bosonic excitations perturbatively (Zhang & Zubkov, 2019). Using a periodic boundary condition, research assumes that an infinite crystal can transverse the entire lattice and return to its initial position. However, the empirical literature has not elaborated on the different forms that can be assumed by *C ()*. Suppose *s = 0, 1, 2, ..., N*, one of the forms assumed by $C\ is\ e^{i2\pi\frac{s}{n}}$, with no clear indication of the crystal momentum. Thus, the weak version of Bloch's theorem is underpinned by the notion that the total current vanishes in any system, provided that smooth modification of its gapped charged fermions and periodical boundary conditions do not change (Zhang & Zubkov, 2019).

4. Results and discussion

This section presents internal cohesion data for cement crystals. The research compared TBOD and C/S to investigate cement crystal internal cohesiveness. TBOD and C/S ratio are inversely related in Fig. 1. The identical C/S ratio crystals (≈ 1.7 of cement gel is chosen from the mean of Belites (a.1) and Alite (a.2)) have different TBOD values. TBOD does not affect four significant categories of cement crystal internal cohesion. Comparing the four groups, group c had the most C/S and TBOD. Group d had a limited cement crystal dispersion near hydrated cement in C/S compared to TBOD. Based on TBOD, cement crystals may be categorized as high, medium, or low. Due to their high C/S ratios, cement crystals a.1, b.4, and c.5 have a lower TBOD than b.1, c.1, c.2, d.1, d.2, and d.4 (group d). Group d's middle TBOD range contains the remaining cement crystals. The blending of Strunz groups and a poor link between TBOD and C/S ratio imply deteriorating internal cohesiveness in C-S-H structures. Interlayer hydroxyl, water, and HBs lowered cement's internal cohesiveness with reduced Qn chains in group d crystals. Variations in the silicate chain from one group to another alter the internal cohesiveness of C-S-H crystals.

This research also assessed the role of bonding order in cementing crystal internal cohesion using total bond order density (TBOD). No uniform rule for crystal bonding was found; however, several tendencies were detected. TBOD of cement crystals showed many features of its internal cohesion: (1) how bonding contributed to stiffness; (2) the dispersion of each bond type in the C-S-H phase; and (3) the vital importance of precise crystal structure. The standard criteria for distinguishing C-S-H crystals and their internal cohesiveness explained variances. Total bond order density (TBOD) was used to assess cement crystals' internal cohesion and strength using the extended Hubbard model, fermions, and Bloch's theorem.

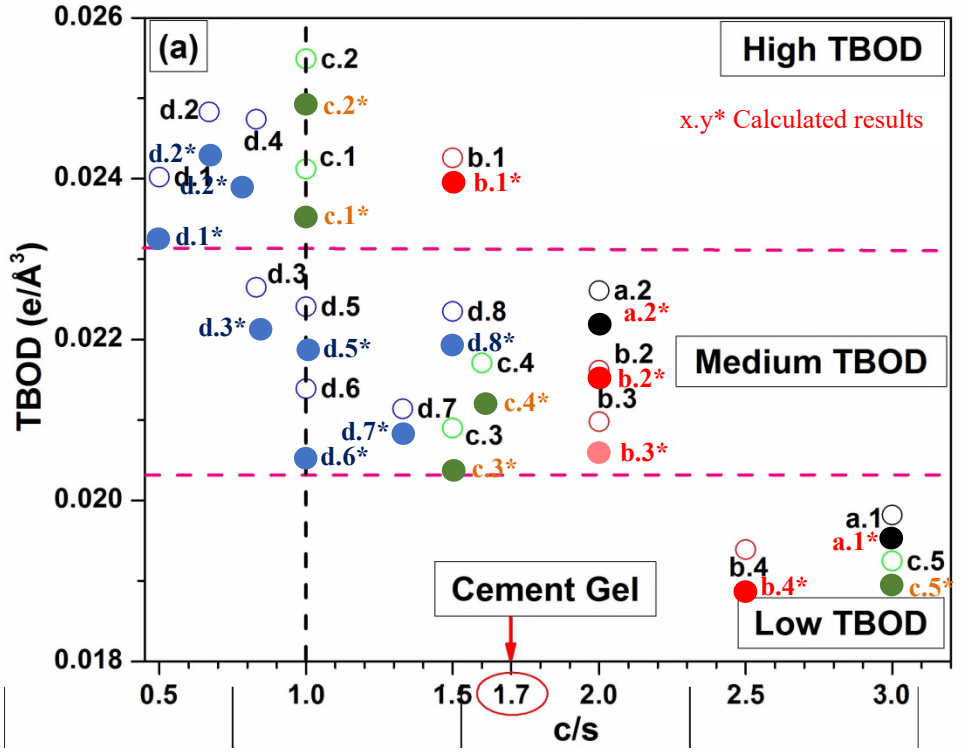

Fig. 1: The relationship between TBOD and the C/S ratio of cement-based crystals (Dharmawardhana, Misra, and Ching (2014))

5. Conclusion

Bloch and Fermi surfaces, and the TBOD to evaluate the changing internal cohesion of cement-based crystals. This method approximates crystal transition using geometric variables and interatomic interactions. TBOD evaluated the internal cohesiveness of several cement crystal classifications. There is no direct association between changing cement crystal cohesiveness and calculated TBOD. Using the fermi and Bloch spectral functions on 19 anhydrous and C-S-H crystals, affiliate (b.1) had the most internal cohesion.

Acknowledgements

This project is funded by National Research Council of Thailand (NRCT) and Phranakhon Rajabhat University (No. N42A660379).

References

Derjaguin, B. V., N. V. Churaev, and V. M. Muller. "The Derjaguin—Landau—Verwey—Overbeek (DLVO) theory of stability of lyophobic colloids." *Surface Forces*. Springer, Boston, MA, 1987. 293-310.

Dharmawardhana, C. C., Anil Misra, and Wai-Yim Ching. "Quantum mechanical metric for internal cohesion in cement crystals." *Scientific reports* 4.1 (2014): 1-8.

Kunther, Wolfgang, Barbara Lothenbach, and Jørgen Skibsted. "Influence of the Ca/Si ratio of the C–S–H phase on the interaction with sulfate ions and its impact on the ettringite crystallization pressure." *Cement and concrete research* 69 (2015): 37-49.

Watanabe, Haruki. "Bloch theorem in the presence of an additional conserved charge." *Physical Review Research* 4.1 (2022): 013043.

Yamamoto, Naoki. "Generalized Bloch theorem and chiral transport phenomena." *Physical Review D* 92.8 (2015): 085011.

Zhang, L., Lin, Z., Li, Z. "The Structure of Silicate Ions in C-S-H Discussed from Chemical Composition." *Advances in Cement Research* (2012):24, 263-281.

Accelerating mechanism of calcium additives on alkali activated cementitious material

Feng Wu, Hui Li, Huimei Zhu

（College of Material Science and Engineering, Xi'an University of Architecture and Technology，Xi'an, 710055）

Abstract: In this paper, the alkali activated cementitious materials (AAMs) were prepared with coal gasification residue as raw material and NaOH as alkali activator, different calcium materials were added to AAMs, the effects of different calcium additives on the mechanical properties and micro morphology of AAMs were compared, the accelerating mechanism of different calcium additives was discussed. The results shows that the different calcium additives presents different mechanisums of enhacing the strength and optimizing microstructure obviously. $Ca(OH)_2$ provides non-uniform surface and easier to generate C-S-H gel with high Si / Ca ratio, and the strength of AAMs was obviously improved. PC (ordinary portland cement) needs to be hydrated to generate $Ca(OH)_2$ and then participate in the C-S-H gels formation reaction, the acceleration effect was poor. The C-S-H gel and C-A-S-H gel production of AAMs can be promoted with the addition of 5% $Ca(OH)_2$. The crystallization degree and microstructure of hydration products can obviously enhance, and the pore structure and distribution are optimized, the effect of the accelerated agent is more obvious.

Keywords: *AAMs, calcium additives, accelerating effect, mechanical properties, microstructure.*

Introduction

AAMs is a new type of binder that replaces cement with environmentally friendly materials. It is a product of the reaction between aluminum silicate and alkali activator, and has a three-dimensional network structure. The most common precursors of AAMs are fly ash (FA), ground blast furnace slag (GGBFS) and metakaolin, a by-product of traditional industry. CGR should be a pozzolanic active mineral (I. Yoshitaka. 2012). Domestic scholars have shown that CGR has volcanic ash activity and has a good contribution to the flow ability and strength of cement-based materials (S. Fang, et al., 2020). Coal gasification residue should have a certain pozzolanic activity, which can be used as the precursor of AAMs. However, such studies are rarely reported. The type of hydration products of AAMs has a great relationship with the calcium content in the raw materials, the amount of calcium element in the raw material affects the type of hydration product. On the basis of previous studies, this paper focuses on the influence of adding different calcareous materials to alkali activated coal gasification slag based cementitious materials on their strength development and hydration product types.

1 Experiment

1.1 Raw material

The CGR chemical composition is shown in Table 1, and its mineral composition is shown in Figure 1. It can be seen that the coal gasification slag is mainly rich in SiO_2, Al_2O_3, Fe_2O_3 and CaO, with the total content of more than 80%. It should has potential cementitious activity, which can be used as raw materials for AAMs. The carbon content of CGR used is 1.52%, with a specific surface area of 320 m^2/kg and a density of 2.72 g/cm^3. The alkali activator used in the experiment is analytically pure sodium hydroxide. The calcium additives used are cement and calcium hydroxide. The cement is made by mixing

95% clinker with 5% gypsum (with a CaO content of 60%), with a specific surface area of 330 m^2/kg and a density of 3.27 g/cm^3; Calcium hydroxide is analytically pure.

Table 1 The composition of CGR / wt%

Oxide	SiO_2	Al_2O_3	CaO	Fe_2O_3	MgO	Na_2O	K_2O	P_2O_5	SO_3	Other	LOI
Content	48.75	20.05	10.69	9.67	2.84	1.65	2.11	0.17	0.56	1.88	1.52

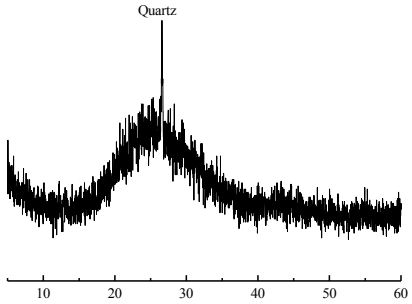

Fig.1 Mineral composition of CGR

1.2 Sample preparation and testing methods

Preparation of AAMs: Weigh 5% sodium hydroxide and dissolve it in water to prepare an alkali solution. Add 95% solid sample to the alkali solution and stir evenly to obtain a slurry. Pour it into 3 cm × 3 cm ×5cm trial mold, it is compacted and smoothed, and steam cured at 80 ℃ for 24 hours before demolding. It is then transferred to a standard curing box for curing until the specified age, and its compressive strength is tested. Crush the sample and soak it in alcohol to terminate hydration. Mineral composition analysis was conducted using a D/Max 2200 X-ray diffractometer (XRD). The molecular structure was analyzed by PerkinElmer Spectrum Two Fourier transform infrared spectrometer (FTIR). Observe the microstructure of hydration products using JSM 5900 scanning electron microscopy (SEM).

2. Test Results and Discussion

2.1 Macromechanical properties

Table 2 Mix ratio of PC and $Ca(OH)_2$ in AAMs

Type	CGS / wt%	NaOH / wt%	PC / wt%	$Ca(OH)_2$ /wt%	W/C	Curing temperature/℃
NH	95	5%		—	0.4	80 (24h)
NH-PC	95	5%	10%	—	0.4	80 (24h)
NH-CH	95	5%	—	5%	0.4	80 (24h)

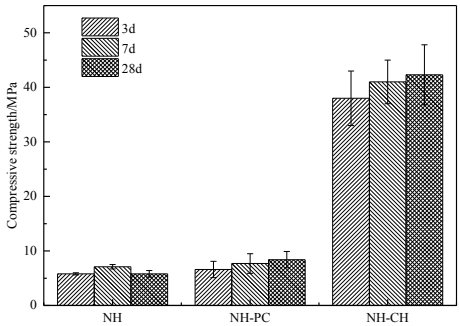

Fig.2 Effect of different calcium additives on compressive strength of AAMs

Table 2 shows the proportion of different calcium raw materials added to AAMs. It can be seen that

when the AAMs hardens to 28 days, its compressive strength decreases to a certain extent compared to 7 days, and there is a phenomenon of strength shrinkage. The addition of PC and $Ca(OH)_2$ into AAMs has a significant difference in their macroscopic mechanical properties. $Ca(OH)_2$ has a strong promoting and enhancing effect on coagulation. $Ca(OH)_2$ can significantly increase the compressive strength of the sample at 3 days, 7 days, and 28 days, with an increase of 555%, 432%, and 629%. The effect of PC on the strength development of the sample is similar to that of $Ca(OH)_2$, but the reinforcement effect of PC is relatively weak. The addition of $Ca(OH)_2$ and PC can counteract the phenomenon of later strength shrinkage of AAMs.

2.2 Mineral Phase Analysis (XRD)

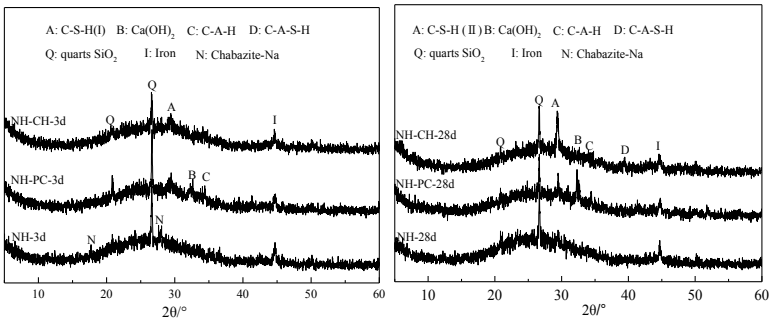

(a. 3 days) (b. 28 days)

Fig.3 XRD patterns of AAMs after adding calcium at age of 3 days and 28 days

Figure 3 shows the XRD patterns of AAMs hardened with PC and $Ca(OH)_2$ slurry for 3 days and 28 days. When 10% PC was added, the hydration products showed obvious C-S-H (I) characteristic peaks. Compared with NH system; When 5% $Ca(OH)_2$ was added, a more obvious C-S-H characteristic peak appeared, and the amorphous hump in CGR became smoother, indicating that more active Si and Al were dissolved to participate in the reaction. It is reported that normally, cement hydration should form C-S-H (II) with a high Ca/Si ratio. Since the PC content in this test is only 10% (CaO content is 60%), another type of gel with low Ca/Si ratio has been formed (Tang, Z., et al., 2019). The characteristic peaks of C-S-H and C-A-S-H can be found in XRD, but the characteristic peaks of N-A-S-H cannot be identified, we will discuss the effect of adding different calcium materials on the formation of rules of C-A-S-H and N-A-S-H in AAMs by FTIR.

2.3 Fourier transform infrared analysis (FTIR)

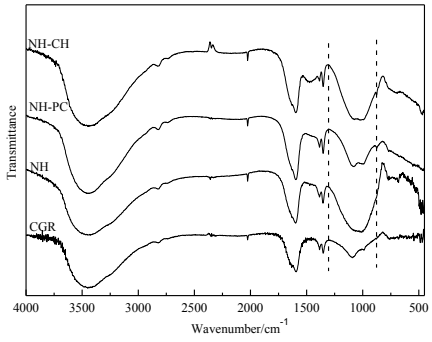

Fig.4 FTIR spectra of hydration products of AAMs after adding calcium

Figure 4 shows the 28 days FTIR spectrum of AAMs calcium doped hardening. After the addition of PC and $Ca(OH)_2$, there is an obvious Si-O-Si contraction vibration peak between 1200 and 900 cm^{-1}, in which 980~1000 cm^{-1} and 1050~1100 cm^{-1} respectively correspond to the absorption bands of hydrated

C-A-S-H and N-A-S-H. The strength and width of the expansion vibration spectrum in the range of 1200 cm^{-1}~900 cm^{-1} vary depending on the calcium source added, It can also be confirmed that hydration reaction occurred after calcium was added into AAMs, and at the same time, the formation of C-A-S-H reduced the content of N-A-S-H, and the strength of cementitious materials was greatly improved. Adding calcareous additives to the N-A-S-H gel can not only modify the aggregation morphology of the N-A-S-H gel, but also promote the formation and aggregation of the C-S-H gel and the C-A-S-H gel.

2.4 Microstructure (SEM)

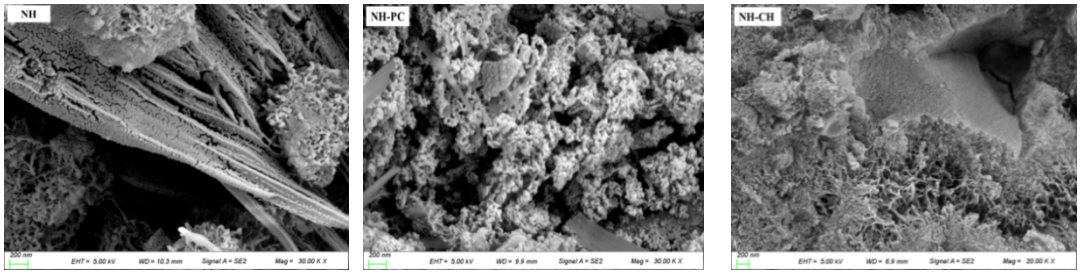

(a) (b) (c)

Fig.5 SEM of samples hardened for 28 days after adding calcium (30000×)

Figure 5 shows the microstructure of the sample hardened for 28 days after adding different calcium raw materials at a magnification of 30000 times. In the NH system, the surface of CGR is eroded and becomes a large number of cracks and flocculent or granular hydration products, which are concentrated on the surface of CGR. When 10% PC was added to NH system, the erosion of CGR was intensified, the surface zeolite phase was densely distributed, the network structure of hydration products was relatively compact, and the interface gap between unreacted particles and hydration products was large; When 5% $Ca(OH)_2$ is added to the NH system, the CGR particles basically all participate in the reaction, and the generated hydration products are fibrous at the reaction interface, which is conducive to interface bonding, and the hydration products form an interpenetrating network structure, which is more compact. It can be seen that $Ca(OH)_2$ is more conducive to the polymerization reaction of Ca^{2+} with active Si and Al.

3 Conclusion

$Ca(OH)_2$ has a significant promoting effect on the cementitious material. PC needs to be hydrated to generate $Ca(OH)_2$, which increases the alkali concentration of the reaction environment and releases Ca^{2+} to participate in the reaction. But $Ca(OH)_2$ can be directly dissolved in water and react with active Si and Al released from CGR to form C-S-H gel with low Ca/Si ratio. The addition of $Ca(OH)_2$ in AAMs promoted the formation of C-S-H gel and C-A-S-H gel, while the content of N-A-S-H gel decreased, the microstructure of cementitious materials became more compact, the pore structure and pore distribution were optimized, and the accelerating effect was more obvious.

Acknowledgement

Financial supports from National Natural Science Foundation of China (51828201).

References

I. Yoshitaka. (2012) “Utilization of coal gasification slag collected from IGCC as fine aggregate for concrete”, in: Proceedings of the EUROCOALASH 2012 Conference, Thessaloniki, Greece, p. 1.

S. Fang, E.S.S. Lam, B. Li, et al. (2020) “Effect of alkali contents, moduli and curing time on engineering properties of alkali activated slag”, Construct. Build. Mater, 249: 118799.

Tang, Z., Li, W.G., Hua, Y., et al. (2019) “Review on designs and properties of multifunctional alkali-activated materials (AAMs)”, Constr. Build. Mater, 200:474–489.

The 16th International Congress on the Chemistry of Cement 2023 (ICCC2023)
"Further Reduction of CO_2 -Emissions and Circularity in the Cement and Concrete Industry"
September 18–22, 2023, Bangkok, Thailand

The Influence of Aluminum Uptake on the Mechanical Properties of Calcium Silicate Hydrate

Z. Zhang[1*], G. Geng[2]

[1] *National University of Singapore, Singapore*
Email: zhangzhe@u.nus.edu

ABSTRACT

Supplementary cementitious materials (SCMs) are widely used in cement-based materials, which reduces the amount of cement usage and provides a solution to reduce the amount of CO_2 emitted in construction industries. In addition, it can enhance final strength and durability of concrete. However, the mechanism of this enhancement is unclear. Having a better understanding of the mechanism is helpful for mix design improvement. Incorporating SCMs in cement-based materials often modifies cement paste by incorporating aluminum to calcium silicate hydrate (C-S-H). Previous research explains how aluminum modifies the nanostructure of C-S-H. In molecular scale, Al takes up a bridge position on silica chains, elongates the main silicate chain length, and can even form cross-linking structure among interlayers of C-A-S-H. How these structure changes influence mechanical properties are still unclear. In this research, hydrothermally synthesized C-A-S-H powders were used to study the effect of aluminum on the multi-scale mechanical properties with a series of methods including Superficial Rockwell hardness and Vickers hardness. Among the mechanical properties in different length scales, a relationship between chemical composition especially Al/Si ratio and strength would be built and explained in detail.

KEYWORDS: *C-A-S-H, Mechanical Properties, Aluminum, Multi-scale*

1. Introduction

Incorporation of supplementary cementitious materials (SCMs) in cement-based materials alters the pore network and composition of the primary hydration product, calcium (-aluminate)-silicate-hydrate (C(-A)-S-H) (Güneyisi et al (2012) and Duan et al (2013)). While numerous studies have investigated the impact of chemical composition, particularly the Ca/Si ratio, on the multiscale mechanical properties of C-S-H, few have focused on the influence of aluminum uptake. A few experiments suggest that the presence of Q_3(Al) in the C(-A)-S-H interlayer is a critical factor affecting the micromechanical properties.
Geng et al (2017) confirmed that the incorporation of aluminum increases the crystallinity of C-(A-)S-H, particularly along the c-axis, as observed through Rietveld refinement. Cross-linking induced by aluminum was observed in C-A-S-H synthesized at 80 °C, resulting in a similar basal spacing of 11 Å to tobermorite increasing the overall bulk modulus. Hunnicutt et al (2016) demonstrated that the increased mean coordination number (MCL) and crosslinking of C-A-S-H contribute to a lower viscous response compared to C-S-H.
In order to accurately analyze the influence of aluminum uptake on the strength of C-A-S-H, well-controlled porosity, and chemical composition of samples is needed (Zhang et al (2022)).
In this study, we attempt to generate a C-A-S-H pellet from C-A-S-H powders produced by hydrothermal reaction. Through this practice, we aim to investigate the effect of chemical conditions on the strength of compacted C-A-S-H pellets. Hardness in different length scales were measured to study the influence of controlled Al/Si, porosity and water content on mechanical properties.

2. Materials and methods

2.1 Materials

C-A-S-H powders were synthesized by mixing silica fume (99.09% SiO_2), calcium oxide, and monocalciumaluminate (synthesized from $CaCO_3$ and Al_2O_3) and deionized water. The synthesis involved an initial bulk Ca/(Si+Al) of 1.1 and a water-to-solid ratio of 20. One set of samples utilized KOH solution instead of deionized water to investigate pH effects. Further sample details are provided in Table 1.

Table 1 Sample information

Sample	CASH_1	CASH_2	CASH_3	CASH_4	CASH_5
Al/Si ratio	0	0.05	0.1	0.2	0.2
KOH (mol/L)	0	0	0	0	0.5

The mixtures were stored in high density polyethylene bottles at 80 °C for 2 months to accelerate the reaction (Myers et al., 2015). Afterward, the products underwent vacuum filtration and isopropanol washing using 0.45 μm filter papers in an N_2-filled glovebox to prevent carbonation. The filtered C-A-S-H was then stored in a vacuum oven (up to 0.1 MPa) at 40 ℃ for 15 days. Each of the four C-S-H powders were divided into two groups and transferred to desiccators with RH of 8% and 100% respectively.
Subsequently, the powder was compressed at 500 MPa, 1000 MPa, and 2000 MPa using a hydraulic press to create dense C-S-H pellets for further investigations.

2.2 Methods

The microscale morphology of the C-A-S-H powders was imaged using a Hitachi Regulus 8230 field emission scanning electron microscope (FE-SEM) in secondary electron mode with an accelerating voltage of 5 kV. The major crystalline phases were identified using a Shimadzu diffractometer (LabX XRD-6000) with a Cu-Kα 2θ range of 5°-45°, a scan rate of 1.5°/min, and operating parameters of 40 kV and 30 mA.
The hardness test is advantageous for evaluating the mechanical properties of materials independently of initial defects such as voids or cracks, providing a reliable measure of bulk strength. For macro hardness testing, Superficial Rockwell hardness was employed, while Vickers hardness (HMV SHIMADZU) was chosen for micro hardness assessment.

3. Results

3.1 Morphology of C-A-S-H powders

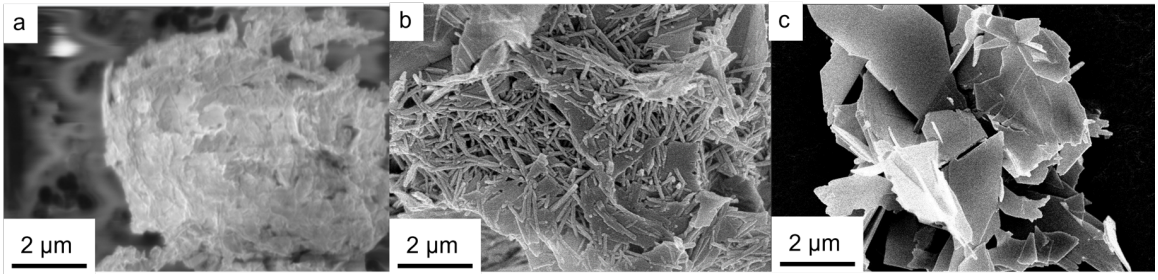

Figure 1 Morphology of C-A-S-H powders of (a) CASH_1 (b) CASH_4 and (c) CASH_5

Figure 1 demonstrates that C-S-H powders exhibit a foil-like shape, while the inclusion of aluminum leads to the formation of needle-like structures in C-A-S-H. Higher pH values result in the transformation

of needle-like structures into plate-like shapes, enhancing the crystallinity of C-A-S-H. This is corroborated by the XRD findings presented in Figure 2, where the intensity of the 002 peak is notably strengthened when aluminum is incorporated, particularly under higher pH conditions.

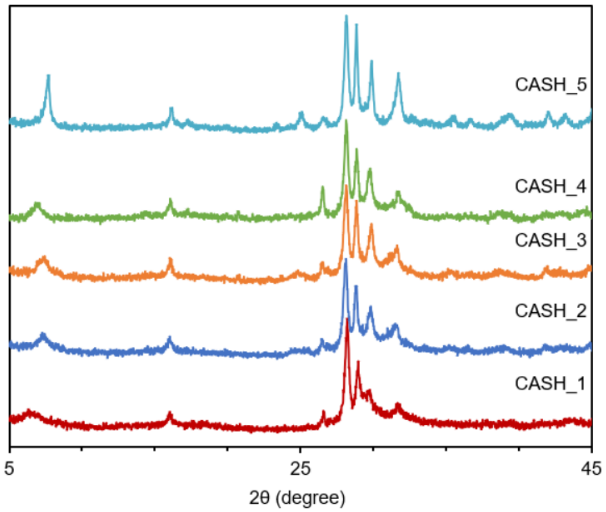

Figure 2 XRD reuslts of C-A-S-H powders

3.2 Hardness of C-A-S-H monoliths

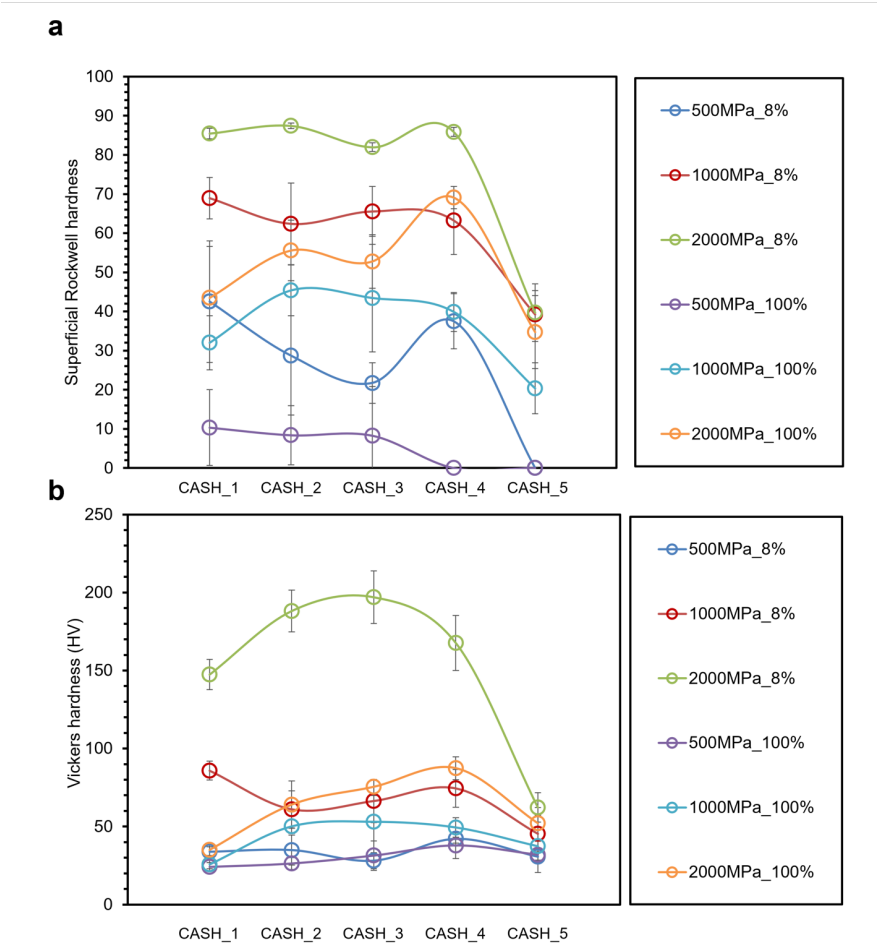

Figure 3 (a)Superficial Rockwell hardness and (b) Vickers hardness of C-A-S-H monoliths

Two length scales of hardness were employed to assess the impact of aluminum incorporation on the mechanical properties of C-S-H. Figure 3 illustrates that increasing the compacting pressure from 500 MPa to 2000 MPa results in a noticeable enhancement of both macro and micro hardness in all samples. Additionally, a higher water content leads to a decrease in macro and micro hardness. The changing pattern of macro hardness among different samples is similar to that of micro hardness. Notably, a higher pH value has a significant detrimental effect on hardness when comparing the hardness of CASH_4 and CASH_5.

Regarding the influence of Al/Si ratio, the micro hardness of samples cured under 100% RH conditions increases as the Al/Si ratio increases. However, for samples cured under 8% RH conditions, only the micro hardness of samples made at 2000 MPa (with the least porosity) exhibits an increasing trend with increasing Al/Si ratio. Samples made at 500 MPa and 1000 MPa show a slight decreasing trend. The regulation of macro hardness follows a similar pattern, albeit with some exceptions due to the formation of larger-scale cracks.

4. Conclusions

In conclusion, this paper investigates the impact of aluminum uptake in C-S-H on morphology and mechanical properties. The study examines multiscale mechanical responses and C-S-H particle shapes based on initial chemical conditions (Al/Si ratio and moisture content). The findings reveal that aluminum uptake enhances the crystallinity of C-S-H, as does a higher pH value. However, a higher pH value reduces the hardness of C-A-S-H. The strengthening effect of aluminum uptake on hardness is particularly evident in higher water content or lower porosity. The underlying reasons for these influences warrant further exploration. This paper offers a new direction for understanding the effects of surface chemistry on the mechanical properties of C-A-S-H, which could guide the design of cement with improved performance.

Acknowledgements

This research is funded by the MOE Tier 1 project in Singapore under WBS A-0009288-01-00.

References

Güneyisi, E. et al. (2012) “Strength, permeability and shrinkage cracking of silica fume and metakaolin concretes”, *Construction and Building Materials*, 34: 120–130

Duan, P. et al. (2013) “Effects of metakaolin, silica fume and slag on pore structure, interfacial transition zone and compressive strength of concrete”, *Construction and Building Materials*, 44 :1–6

Geng, G. et al. (2017) “Aluminum-induced dreierketten chain cross-links increase the mechanical properties of nanocrystalline calcium aluminosilicate hydrate”, *Scientific Reports*, 7(1): 44032

Hunnicutt, W.A., Mondal, P. and Struble, L.J. (2016) “Effect of Aluminum Substitution in C-S-H on Viscoelastic Properties: Stress Relaxation Nanoindentation”, *1st International Conference on Grand Challenges in Construction Materials*

Zhang, Z. et al. (2022) “Endowing strength to calcium silicate hydrate (C-S-H) powder by high pressure mechanical compaction”, *Cement and Concrete Research*, 159:106858

Myers, R.J. et al. (2015) “Effect of temperature and aluminium on calcium (alumino)silicate hydrate chemistry under equilibrium conditions”, *Cement and Concrete Research*, 68: 83–93

The 16th International Congress on the Chemistry of Cement 2023 (ICCC2023)
"Further Reduction of CO_2 -Emissions and Circularity in the Cement and Concrete Industry"
September 18–22, 2023, Bangkok, Thailand

The Effects of Supplementary Cementitious Materials on the Hydration Kinetics of G-Oil Cement

M. T. Palou[1, 2*], R. Novotný[3], E. Kuzielová[1,2], M. Žemlička[1], J. Čepčianska[1], J. Podhorská[1]
[1]*Institute of Construction and Architecture, Slovak Academy of Sciences, Dúbravská cesta 9, SK–845 03 Bratislava, Slovak Republic*
[2]*Faculty of Chemical and Food Technology, Slovak University of Technology Radlinského 9, SK–812 37 Bratislava, Slovak Republic*
[3]*Materials Research Centre, Faculty of Chemistry, Brno University of Technology Purkyňova 118, CZ–612 00 Brno, Czech Republic*
[*] martin.palou@savba.sk

ABSTRACT

The present study was undertaken to study the kinetics of the hydration reaction of G-Oil Well Cement and its blends by conduction calorimeter and thermogravimetric analysis. The coupling effect of temperature (25, 40, 50, 60, 80 °C) and material composition (100, 95, 90, 85, 80, 75, 70, 65 %) with different substitution levels by blast slag furnace, metakaolin, and limestone were analyzed on the light of hydration products and activation energy of different reactions. The apparent activation energies calculated from the hydration peaks characterizing the different reactions decrease with the increase in the substitution levels, but that of the second peaks (33.31 to 31.95 kJ°mol^{-1}) is higher than that of the former (31.33 to 27.88 kJ ° mol^{-1}) at the same level of substitution. Thermogravimetric analysis of the samples after calorimetric measurement shows that the main hydration products are C-S-H, C-A-S-H, CH, and calcium carbonate. Their quantity depends on the composition of the material and the temperatures.

KEYWORDS: *G-oil well cement, material composition, hydration, temperature, thermal analysis, kinetics*

1. Introduction

G-Oil Cement (GOWC) is a specific class of binders used mainly as zonal isolation materials during oil well cementing operations. Indeed, the cement slurry, primarily prepared at normal temperatures, is pumped through the steel casing to the bottom of the well and then up through the annulus between the casing and the surrounding rock (De Andrade and Sangesland (2016). The temperatures and vapor pressures increase with the well depth making cement slurry hydrating under different conditions, including hydrothermal ones. From the chemical point of view, C-S-H, ettringite, and CH are formed when the temperature does not exceed 110 °C. At different equilibrium temperature/pressure phases, C-S-H gradually changes its structure from semi-crystalline to crystalline one while ettringite is decomposed. The transformation of the C-S-H to α-C_2SH phase at a temperature exceeding 150 °C leads to the beginning of strength deterioration due to the change in pore structure (Jupe et (2006)). These changes continue with increasing temperature/pressure causing the transformation of a-C_2SH to $C_6S_5H_3$. Some products like $C_5S_2H_2$ and scawtite ($C_7S_6CH_2$,) to some extent are also formed (Kuzielová eet al.(2019)). Therefore, Supplementary Cementitious Materials (Blast furnace slag, silica fume, metakaolin, fly ash) are added, concomitantly or individually, to the commercial Oil-well cements to prevent this high-temperature transformation (Palou et al. (2014)). The main objective of the present work is to study the effect of Supplementary Cementitious Materials and temperatures on hydration heat and kinetics of G-Oil cement via conduction calorimeter and

thermal analysis to determine its suitability for developing heavyweight structure for application in the underground depository.

2. Experimental

The Class G-Oil Well Cement used in this study was manufactured by Dyckerhoff GmbH Hauptverwaltung, Germany. Granulated blast furnace slag (Kotouč Štramberk, spol. s r.o., Czech Republic); metakaolin (metakaolin L05 Mefisto from České lupkové závody, a.s., Czech Republic); and finely ground limestone (Calmit, spol. s.r.o., Slovakia) were used as Supplementary Cementitious Materials. Their oxide composition, surface area, and related mineralogical were reported by (Palou et al. (2014)).

2.1. Material composition

Table 1 shows the mix proportions of GOWC and Supplementary Cementitious Materials (Blast Furnace Slag-BFS, Metakaolin-MK, and finely ground limestone –LS). The replacement levels of GOWC by combining 3 SCMs were 0%, 5%, 10%, 15%, 20%, 25%, 30%, and 35% by mass, respectively.

Table 1 Mix composition of blends (wt. %).

	GOWC	BFS	Metakaolin	Limestone
GOWC100	100	0	0	0
GOWC95	95	5	0	0
GOWC90	90	10	0	0
GOWC85	85	10	5	0
GOWC80	80	10	5	5
GOWC75	75	15	5	5
GOWC70	70	15	5	10
GOWC65	65	15	5	15

The study of cement hydration kinetics in the temperature range of 25°C to 80°C was conducted using the conduction isothermal calorimeter to record the heat flow and determine the heat of G-oil well cement and its composites. By way of illustration, 5 coupled figures of heat flow and heat of hydration curves are presented to illustrate the influence of the material composition, to demonstrate the influence of different temperatures on each sample, and to calculate the „apparent activation energy. “

The hydration products of the samples after calorimetric measurement were analyzed by TGA/DSC technique (TGA/DSC-1, STARe software 9.30, Mettler Toledo). After having stopped hydration, 10.00 (± 0.03) mg of finely ground samples were heated in the open platinum crucibles until 1000 °C at the heating rate of 10 °C min^{-1} under an N_2 atmosphere.

3. Results and Discussion

3.1. Assessment of hydration of GOWC and its blends by conduction calorimetry

The heat flow and cumulated hydration heat during the first 48 h hydration of GOWC and its blends at different temperatures are depicted in Figs. 1. In general, three main exothermic peaks with four main stages (dissolution, induction, acceleration, and deceleration) can be observed at the curves of the hydration heat flow of all samples.

The first observed peak after the induction period is due to the hydration of C_3S, resulting from the nucleation and crystallization of C-S-H and CH. In addition, the second peak observed in the deceleration period is attributed to the second exothermic reaction related to C_3A (formation of ettringite after depletion of the protective layer or decomposition of AFt into AFm). Moreover, Fig. 1 (60°C and 90°C) of heat flow illustrates a phase of acceleration due to the alkali-activated reactions or the formation of monocarboaluminate $Ca_4Al_2(CO_3)(OH)_{12}.H_2O$ and hemicarboaluminate $Ca_4Al_2(CO_3)_{0.5}(OH)_{13}1.5H_2O$ due to the presence of limestone. Also, it can be observed that the total released hydration heat of blended

cements is lower than the reference one. Though the decrease of cumulative heat is related to the content of GOWC in mixtures, the difference between the overall heat of hydration tends to disappear with increasing hydration temperatures and converge towards the value of 325 j°g^{-1}. This fact could confirm that the alkali-activation reactions are more temperature-sensitive than the hydration of the reference GOWC.

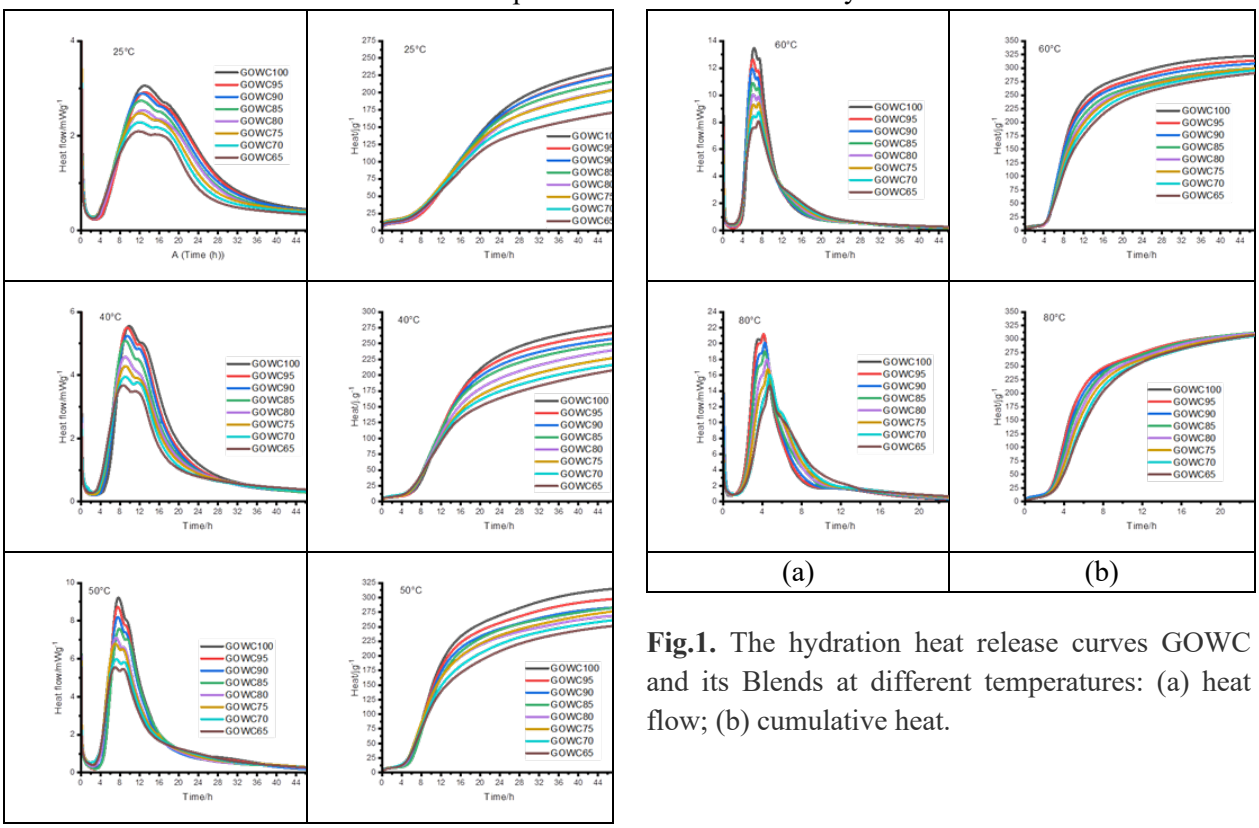

Fig.1. The hydration heat release curves GOWC and its Blends at different temperatures: (a) heat flow; (b) cumulative heat.

3.2. Apparent activation energy

Apparent activation energy using Arrhenius (Eq.1) general rule was calculated for each reaction represented by peaks at the curve of heat flow of hydration based on five different temperatures.

$$k(T) = Aexp\left(-\frac{E_a}{RT}\right) \quad (1)$$

where k is the temperature-sensitive rate or rate constant, A is a pre-exponential constant sometimes called the attempt frequency, and R is the ideal gas constant (8.314 J/(mol°K^{-1}); T is the absolute temperature (K); E_a is the activation energy (J°mol^{-1}).

Table 2 Values of E_a for each peak and samples

	Pre-exponential factor	First peak	Pre-exponential factor	Second peak
	A	E_a (kJ°mol^{-1})	A	E_a (kJ°mol^{-1})
GOWC100	13.79	31.33	14.46	33.31
GOWC95	13.74	31.29	14.47	33.40
GOWC90	13.36	30.41	14.18	32.72
GOWC85	12.86	29.25	14.02	32.46
GOWC80	12.81	29.35	14.04	32.70
GOWC75	12.34	28.25	13.73	31.99
GOWC70	12.24	28.22	13.66	31.98
GOWC65	12.03	27.88	13.57	31.95

The values of E_a (kJ°mol^{-1}) are reported in Table 2. They decrease with the degree of substitution, but the E_a of the second peak is higher than that of the first one. It indicates a relatively strong barrier to overcome for the second reaction of C_3A. Indeed, the formation of ettringite after the induction period requires the rearrangement of the gel structure surrounding the original minerals into crystal one before the penetration of water and dissolved ions to activate the reaction. Moreover, the presence of SCM-bearing aluminum compound (BFS, MK) contributes to the formation of ettringite and mainly under the temperature effects. Therefore, temperature becomes a key factor in increasing the second peak intensity.

3.3. Determination of hydration products by thermal analysis

The determination of hydration products is mainly based on the TG/DTG analysis at four temperature intervals. The dehydration of C–S–H, gypsum, and ettringite occurs at 100–140°C temperature, followed by thermal decomposition of C–A–S–H products at 140–420 °C, and then CH at 420–500 °C. 600–1000 °C corresponds to the decomposition of different carbonated calcium. Fig. 2 represents the effect of SCMs under two extreme temperatures (25 and 80 °C).

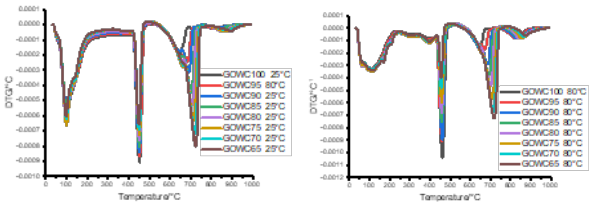

Fig. 2. Influence of material composition on DTG curves at 25°C and 80°C.

CH is released by the hydration of calcium silicate phases and consumed in the alkali-activated reaction and overall carbonation. The hydration products and their amount depend on material composition and curing temperatures. The formation of C–S–H is retarded at temperatures over 50°C, which supports the formation of C-A-S-H mainly in the presence of SCMs.

4. Conclusions

The conduction calorimeter assessing the hydration heat evolution at different temperatures has provided data for calculating the activation energy. Two main peaks, which intensities vary with material composition and temperature, represent the hydration reaction of the "silicate" and "aluminate" phases. Their apparent activation energy depends on material composition. The higher the substitution level, the lower the value of apparent activation energy. The 48-hour total heat evolved varies between 172 J°g^{-1} and 310 J°g^{-1}. Some blends can be considered as low heat cements for massive underground structures. The DTG figures provide a deep analysis of the decomposition and phase changes in the main cement hydrates in the temperature range of 0 to 1000°C. The hydration products are similar and stable at up to 80 °C at least.

Acknowledgments

This work was supported by the courtesy of APVV-19-0490, APVV-15-0631, Slovak Grant Agency VEGA No. 2/0032/21 and 2/0017/21, and the Czech Science Foundation No. GA19-16646S.

References

De Andrade, J. and Sangesland, S. (2016) "Cement Sheath Failure Mechanisms: Numerical Estimates to Design for Long-Term Well Integrity", *Journal of Petroleum Science and Engineering*, 147:682–698

Boháč, M., Palou M.T., Novotný, R., Másilko, J., Všianský, D., Staněk, T (2014) "Investigation on early hydration of ternary Portland cement–blast–furnace slag–metakaolin blends," Construction and Building Materials (2014):64;333–341

Jupe, A.C., Wilkinson, A.P., Luke, K., Gary, P. And Funkhouser, G.P. (2008) "Class H cement hydration at 180 °C and high pressure in the presence of added silica ". Cement and Concrete Research, 38(5):660-666.

Kuzielová, E., Žemlička, M., Másilko, J., Palou, M.T. (2019) "Development of G-oil well cement phase composition during long therm hydrothermal curing". *Geothermics*, 80:129-37.

Palou, M.T., Šoukal F., Boháč. M., Šiler. P., Ifka, T. and Živica, V. (2014) "Performance of G-Oil Well cement exposed to elevated hydrothermal curing conditions", *Journal of Thermal Analysis and Calorimetry*, 118(2):865–74.

The 16th International Congress on the Chemistry of Cement 2023 (ICCC2023)
"Further Reduction of CO_2 -Emissions and Circularity in the Cement and Concrete Industry"
September 18–22, 2023, Bangkok, Thailand

Industrial Deployment of Calcined Clays Cements.

Néstor Isaías Quintero Mora[1*]

[1] *CEMEX, Monterrey, Mexico*

Email: nestorisaias.quintero@cemex.com

ABSTRACT

Cement is one of the most used materials in the world, and its production is classified as an energy intensive process that accounts for approximately 4% to 6% of all anthropogenic CO_2 emissions in the world. For many years the cement industry has strived to reduce its CO_2 emissions by substituting cement clinker by Supplementary Cementitious Materials (SCMs). This substitution is a frequent practice in the cement industry, and it includes the use of materials classified as by-products that fit into the cement production process, thus supporting the circular economy scenarios.

CEMEX promotes the use of these type of materials to continue reducing its CO_2 footprint thus contributing towards a carbon neutral world. Currently 30% of Cemex's CO_2 emission reduction goal vs. the 1990 baseline has been achieved and by 2030 it is expected to reach around 47%, which is approximately equivalent to 430 kg CO_2/ton c.

The present efforts aim to explore and improve the experience of manufacturing new SCMs such as calcined clays, in which diverse types of clays are thermally treated. Calcined clays have allowed Cemex to continue reducing the overall CO_2 footprint while maintaining the properties and performance of the cements. Industrialization of this process is essential to properly activate the ~~calcined~~ clays, so that it can be incorporated into the cement production resulting in reduced CO_2 emissions and making Cemex one of the industry leaders in its use.

KEYWORDS: *Calcined Clays, low carbon cements, CO_2 footprint.*

1. Introduction

Some clay minerals are potential candidates to be transformed into new supplementary cementitious materials or SCMs. They can partially replace Portland cement, and consequently enhance strength, improve durability, and reduce the CO2 emissions (Samet et al. 2007) associated with cement production.

In recent years, there has been a growing trend in thermal activation of clays due to their low cost and availability in many countries and as well because some clays achieve pozzolanic properties when thermally activated.

The pozzolanic activity is a result of a thermal activation of kaolinite and some other compounds present in the clays.

There is a distinct difference between metakaolin and other pozzolanic materials, such as fly ash and silica fume in the fact that metakaolin is a primary product obtained during a controlled process, while fly ash and silica fume are secondary products of other industrial processes.

As kaolinite is heated, the temperature leads to a loss of chemical water and consequently a phase transformation from kaolinite to an amorphous phase with high reaction ability, called metakaolin.

However, it has been found other compounds achieving good activation at different temperatures.

Temperature, heating rate and time significantly influence producing thermally activated materials in a reactive state, which would be between 600° and 800°C. If temperature is too high inert crystalline phases will be formed.

The main characteristic of the produced calcined clay is its pozzolanic activity or its ability to react with calcium hydroxide (Thomas, 2013) to obtain compounds with cementitious properties.

This reaction forms additional cementitious CSH gel, together with crystalline products, which include calcium aluminate hydrate and alumina-silicate hydrates.

And finally, similar cementitious materials such as slag represent about 5%-10% of the amount of cement, which unlikely options to increase (Scrivener, 2018)

2. Objective

The main objective is to deploy the use of calcined clays at industrial scale using existing assets, and as well assuring that the material will maintain the characteristics evaluated at laboratory scale. For this purpose, a set of laboratory testing has been defined using different clay materials from selected location in Middle East, South America, and Central America. Finding the clay activation temperature is crucial, but as well to replicate the temperature control at a large-scale system is on e of the hardest topics to achieve.

3. Laboratory tests

Finding the right temperature and materials is crucial, therefore, to ensure full clay activation, we tested it at temperatures ranging from 500°C to 950°C.

Several tested materials reached close to 100% Activity Index. The Activity Index is measured by comparing the strength of a reference Ordinary Portland Cement (OPC/CEM I), versus a blended cement containing 70% OPC and 30% of a pozzolanic material, in this case calcined clay.

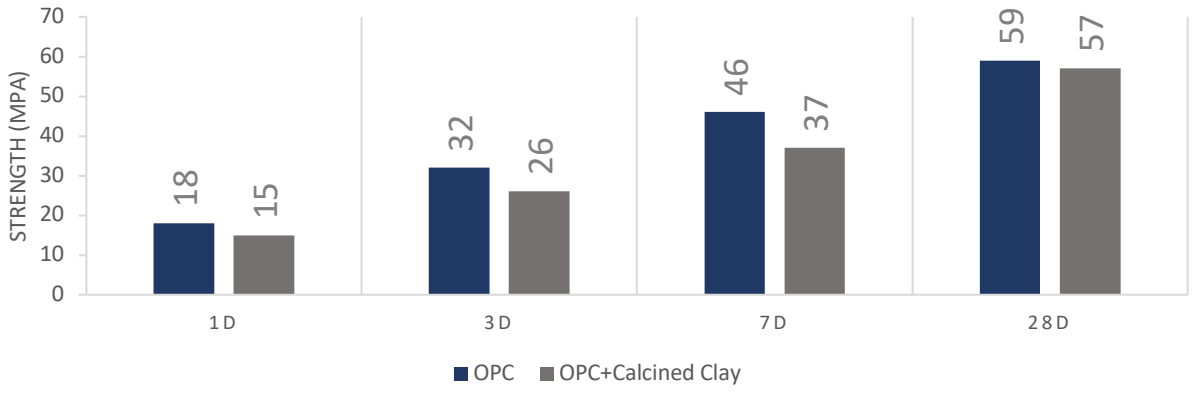

Fig. 1: Cement performance introducing calcined clays materials.

In table 1, some examples are shown of clays evaluated across Cemex and as can be seen, in many cases Kaolinite its main constituent. Traditionally research has found out that Kaolinite provides the reactivity to the calcined clay, however in other cases clays are a mixture of different compounds that can be activated as well such as illite containing materials, among others.

As shown in table 1, it is possible to have low kaolinite content and a high activity index, the most important factor is finding the right activation temperature.

Another important expect to observe is that the temperature for activation differs from one to another.

Table 1. Activity Index vs. Kaolinite content.

Compound	**Site 1**	**Site 2**	**Site 3**	**Site 4**	**Site 5**
Kaolinite	78%	4%	65%	-	9%
Activity Index (AI)	110%	90%	90%	99%	88%

4. Industrialization

After testing at laboratory scale, a first Industrialization test was held in a location in the Middle east, where three different materials were tested: kaolin, clay and a mixture of clay and feldspar.

Testing Kaolin resulted in higher fuel consumption, higher CaO, and higher Loss of Ignition than expected. Concluding that the Kaolin pile was contaminated with limestone.

For the combination of clays, the strength result was not as high as what was obtained in the laboratory testing, but still was in a good range of 95%- 98% pozzolanic activity at 28 days, compared to 110% at laboratory scale.

For the second industrial test in South America, the main goal of was to enhance the existing pozzolanic activity at a temperature close to 800°C, reduce the cement clinker factor with replacement of the activated clays thus reducing CO_2 emission levels and to establish the main parameters and control variables to guarantee optimal results for clay activation in industrial tests.

This test was successful due to the ability to accomplish good stability at nominal kiln conditions and good quality of calcined clays. The plant was also able to successfully identify the new main control variables while also reducing fuel consumption.

As for the third set of trials in Central America plant, the goal was to produce an activated clay with pozzolanic activity by a calcination process in one of the wet kilns.

The main challenge was to evaporate the excess water and achieve the required temperatures for thermal activation of the clay

Table 2. Operating conditions optimization.

Description\ Plant	**Middle East**	**Central America**	**South America**
Materials	Kaolinite, mix of Clays + local Clay	Clay from the plant	Clay from the Plant
Kiln arrangement	Double preheater string with double calciner and bypass system	Wet kiln	Single string without calciner
Clay activation	In rotary kiln	In rotary kiln	In rotary kiln
Cooler	Grate	Grate	Rotary
Adaptations	• Material crushed	• Kiln speed decreased	• Material crushed
	• Dosing line to the kiln inlet	• Cooler grates and fans adjusted in case of dust production	• Preheater not used

	• Preheater not used	• Control of new process parameters vs temperature and expected AI	• Dosing line adapted to feed clay to the kiln inlet
	• Kiln speed decreased & Cooler fans adjusted	• No color control	• Control of new process parameters vs temperature and expected AI
	• No color control		• No color control

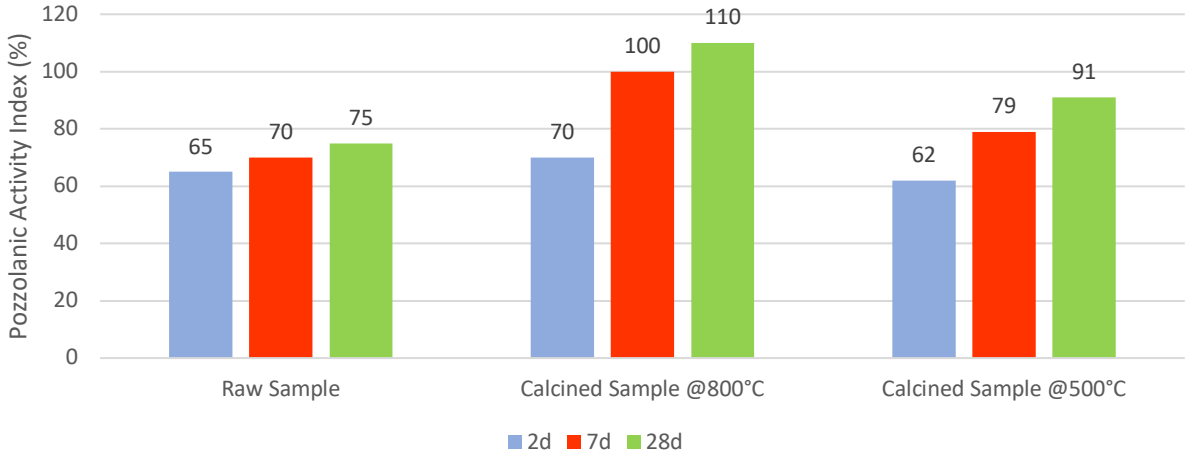

Fig. 2 Pozzolanic Activity Index of raw clay and calcined at different temperatures.

5. Conclusions

Operational conditions and temperature control are the key parameters, since it can drastically affect the quality of the material produced. As shown in Figure 2, the calcined sample that only reached 500°C, resulted in a significant loss of quality.

The quality of the calcined clay obtained at an industrial level is critical to make it suitable to replace the clinker content in cement production.

Calcined clay's ability to reduce cement's clinker factor can be a key element in Cemex's decarbonization strategy and goals.

6. References

[1] Samet B., Mnif, T., Chaabouni M. (2007). Use of a kaolinitic clay as a pozzolanic material for cements: Formulation of blended cement. *Cement and Concrete Composites*, 29(10) 741-749.

[2] Thomas, M., Jewell, R., & Jones, R. (2017). Coal fly ash as a pozzolan. *Coal Combustion Products*, pp 121-154.

[3] Scrivener, K., Martirena, F., Bishnoi, S. & Maity, S. (2018). Calcined clay limestone cements (LC3). *Cement and Concrete Research*, 114, pp 49-56

Simulation of sulfate attack on carbonated Portland cement-blast furnace slag binary cement

N.S. Melaku[1*], and S. Park[2]

[1] *Pukyong National University, Busan, South Korea*
Email: naspknu@pukyong.ac.kr
[2] *Pukyong National University, Busan, South Korea*
Email: solmoi.park@pknu.ac.kr

ABSTRACT

Carbonation of cement paste results in numerous physiochemical changes that have a detrimental impact on the concrete structure, such as pH reduction which causes corrosion of reinforcement bars. Sulfate attack on cement paste results in the formation of phases that leads to development of expansive cracks. Both of these are natural occurrences that can cause a premature failure of a concrete structure. This study aims to describe and compare the effects of exposure of a carbonated Portland cement-blast furnace slag blend to various sulfate solutions. Thermodynamic modeling was used as a predictive method to determine the resulting phase assemblage of the binary blend system. The binary mix was exposed to Na_2SO_4 or $MgSO_4$ solutions. Various discrete levels of carbonation were simulated with sulfate solution up to 10^4 ml / 100g of binder. As the extent of carbonation increased, the hydration products destabilized and formed amorphous aluminosilicate, calcite and gypsum prior to the additions of sulfate solutions. On the other hand, exposure to different levels of sodium solutions resulted in the precipitation of various phases depending on the extent of carbonation. The pH level was observed to reduce as C-S-H starts to destabilize either due to carbonation or exposure to a higher level of sodium solutions.

KEYWORDS: *Portland cement, Blast furnace slag, Sulfate attack,* and C*arbonation*

1. Introduction

Concrete structures are often exposed to environmental conditions that can cause durability issues, with sulfate attack being a prime example. The sulfate ions react with C_3A and portlandite from the Portland cement to form ettringite and gypsum, leading to the expansion and degradation of the concrete. The type of cement used, the type of sulfate involved, the concentration of sulfate, and the quality of the concrete are some of the major factors that can influence the impact of sulfate attack. Additionally, studies have shown that a lower water-to-cement ratio reduces porosity and limits the transportation of sulfate ions in the concrete, thereby improving the sulfate resistance of concrete structures, (Omar (2002)).

To improve the sulfate resistance of cement and cementitious materials, researchers have explored the use of supplementary cementitious materials such as fly ash, silica fume, and blast furnace slag. These materials contribute to the development of resistance by reducing the expansion of cement in sulfate attack. However, the effectiveness of blast furnace slag depends on its Al_2O_3 content, with higher content resulting in reduced resistance to expansion (Higgins (2003)).

Another environmental condition that causes durability issues is the exposure of concrete structures to CO_2. When cement structures are exposed to CO_2, the hydrated phases carbonate leading to shrinkage, cracking, and corrosion of reinforcement bars in the concrete (Reddy, Melaku and Park (2022)). Sulfate attack and carbonation are common durability issues. However, there have been only a limited number of studies that have investigated the combined effect of sulfate attack and carbonation of cement and cementitious materials. As such, further investigations are required to better understand their impact. This research aims to explain the

microstructural phase changes that occur when a carbonated PC-slag blend is exposed to $MgSO_4$ and Na_2SO_4 solutions.

2. Methods

Thermodynamic analysis was conducted using Gibbs free energy minimization software GEM-Selektor v.3.7. CEMDATA 18 database was selected, with an extended Debye-Hueckel equation for the aqueous electrolyte model. KOH was chosen as the background electrolyte, with common ion size and short-range interaction parameters of 3.67 Å and 0.123 kg/mol, respectively.
The compositions of ASTM Type I cement and BFS used in the simulation are listed in Table 1. BFS was introduced as a 10% replacement with a water-to-cement ratio of 0.6. A hydration period of one year was assumed and Parrot and Killoh's hydration model was used to determine the degree of reactivity of PC for such a date. For slag, the degree of reactivity was obtained from separate thermodynamic modeling (Degefa, Yang and Park (2023)). To simulate carbonation, CO_2 was added at discrete levels of 0, 1, 5, 10, 20 and 30g per 100g binder. Sulfate solutions of $MgSO_4$ and Na_2SO_4 were used in the simulation keeping the concentration of the sulfates as 10%. The sulfate solution was increased from 0 to 10,000 g per 100g of binder to simulate extreme conditions.

Table 1: Compositions of PC and BFS

PC	C_3S	C_2S	C_3A	C_4AF	$CaSO_4$	Other phases				
	55	19	10	7	4.2	4.8				
BFS	CaO	SiO_2	Al_2O_3	SO_3	MgO	K_2O	Fe_2O_3	Na_2O	TiO_2	LOI*
	47.49	30.59	13.19	3.15	3.01	0.54	0.51	0.1	0.69	0.66

3. Results and discussions

Prior to sulfate attacks and the addition of CO_2, the hydration products of Portland cement are C-S-H, portlandite, monosulfate and hydrogarnet. when Portland cement comes in contact with $MgSO_4$, the hydrated phases become destabilized and lead to the precipitation of new phases. As shown in **Figure *1***, in the presence of extra sulfate provided by $MgSO_4$, monosulfate is converted into ettringite and hydrotalcite, while portlandite produces brucite and gypsum. Ettringite possesses a higher density, making it beneficial for reducing the porosity of concrete (Schmidt, Lothenbach, Romer, Neuenschwander, Scrivener (2009)). However, its expansion can also bring negative effects. Similarly, gypsum has an expansive behavior that can result in concrete deterioration. As the amount of ettringite and gypsum increases, the concrete expands to a point where it causes cracking and fracture (Santhanam, Cohen and Olek (2002)). This results in a reduction of the strength of the concrete. Further sulfate attack causes ettringite to destabilize into hydrotalcite and gypsum. Finally, the sulfate attacks C-S-H and replaces the calcium, forming magnesium silicate hydrate (M-S-H) which has no binding property. Its continuous formation leads to a loss of cohesiveness of the concrete, ultimately resulting in a reduction of strength. Upon destabilization of C-S-H, the pH level starts to decline.

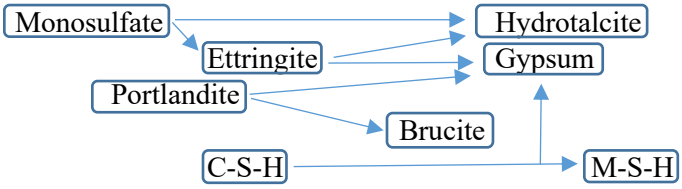

Figure 1: Illustrations of phase changes due to MgSO4 attack on PC

Adding 1g of CO_2 /100g binder causes monosulfate to transform into hemicarbonate and monocarbonate, which later forms ettringite and calcite when $MgSO_4$ is added. The remaining hydrated phases at this stage follow the same pattern as in the case of no carbonation. As the carbonation degree reaches 5 g/100g binder, calcite becomes a carbonation product before the destabilization of monosulfate from $MgSO_4$ reactions. With the addition of $MgSO_4$, calcite forms gypsum and magnesite. Further carbonation reduces the quantity of portlandite while increasing the quantity of calcite. The reduction of portlandite however brings an undesirable effect on the concrete. As portlandite reduces, the pH level also declines resulting in the disappearance of a protective oxide layer around the reinforcement bars in concrete structures. This exposes the reinforcement bars to corrosion (Revert, Weerdt, Hornbostel and Geiker (2018)). Carbonation level of 20 g/100g binder results in the complete carbonation of portlandite and thus the absence of brucite from the final list of phases due to $MgSO_4$ attack. Portlandite acts as a buffering agent preventing the carbonation of C-S-H. when portlandite vanishes, CO_2 starts to react with C-S-H and form calcite. After carbonation level of 20 g/ 100g, the quantity of C-S-H reduces even before the addition of $MgSO_4$ resulting in a lesser sulfate requirement for its destabilization. As a result, the joint occurrence of carbonation and sulfate attack can be considered to have the worst impact than the impact of individual conditions. As the carbonation level reaches 30 g/100g binder, amorphous aluminosilicate becomes a carbonation product while monocarbonate completely carbonates. Carbonation also affects the pH level as it reduces the quantity of C-S-H. The higher the carbonation level, the lower pH gets.

In PC-slag blended cement, C-A-S-H, portlandite, monosulfate, ettringite and hydrogarnet are the hydration products. The addition of slag results in the formation of C-A-S-H instead of C-S-H due to the higher availability of aluminum and silica, which create favorable conditions for the formation of C-A-S-H. However, the quantity of C-A-S-H that formed is less than C-S-H from PC due to the reduction of PC clinkers when slag is added. A lesser quantity of C-A-S-H implies lower resistance to carbonation and sulfate attacks. Ettringite forms as a hydration product in 10% slag replacement which increases in quantity with the addition of sulfate. The sulfate attack from $MgSO_4$ tends to lead to the same phases at 10 % replacement as it did in 0 % replacement but with a lesser requirement of sulfates to cause destabilization.

The sulfate attack from Na_2SO_4 results in the formation of gypsum, ettringite, hydrogarnet and C-S-H as final products (**Figure *2***). The quantity of gypsum formed here is much less than the one observed in $MgSO_4$ attacks and ettringite and C-S-H are more stable in these conditions. Portlandite also requires more quantities of sulfate solution to destabilize from Na_2SO_4 attack. This results in the requirement of even higher quantities of sulfate to destabilize C-S-H. Additionally, the total volume of the mixture after Na_2SO_4 attack is about one-third of the volume in $MgSO_4$ attack. Lesser volume implies that the expansion from the Na_2SO_4 attack is not as big as it is in $MgSO_4$ attack which leads to fewer cracks and less exposure of reinforcement bars. The reduction of pH is also much less in Na_2SO_4 attack, contributing to better resistance against corrosion of reinforcement bars. Overall Portland cement has better resistance capabilities against $NaSO_4$ attack than $MgSO_4$ attack.

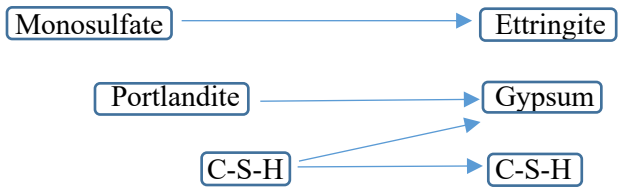

Figure 2: Illustrations of phase changes due to Na_2SO_4 attack on PC

Carbonation amplifies the effect of sulfate attacks. As the level of carbonation increases, the hydration phases start to destabilize even before the addition of sulfate. The quantity of C-S-H and portlandite reduces, leading to lower resistance capacity against sulfate attacks. At higher carbonation levels (20 g/100g binder), gypsum no longer forms from Na_2SO_4 attack due to the complete carbonation of portlandite. Further carbonation and addition of sulfate result in the reduction of ettringite and C-S-H quantities. The use of slag at zero or lower carbonation levels has little impact on the results of Na_2SO_4 attack. However, the 10 % slag replacement results

in a reduction of the resistance abilities of cement when exposed to carbonation and Na_2SO_4 attack. At higher carbonation levels, gypsum becomes more stable in lower sulfate attack levels, while ettringite forms from gypsum and C-A-S-H at higher sulfate attack levels before transforming back to gypsum.

4. Conclusion

The thermodynamic modeling results for a PC-slag blended cement exposed to carbonation and sulfate attacks after one-year hydration is summarized as follows.

1. C-S-H, portlandite, monosulfate and hydrogarnet are hydration products of PC. Addition of slag results in the formation of C-A-S-H instead of C-S-H due to the presence of higher quantities of aluminum and silica in slag.
2. 10 % slag replacement results in the reduction of the resistive capabilities of cement against sulfate attack.
3. Carbonation accelerates the effects of sulfate attack.
4. $MgSO_4$ attack is more severe than Na_2SO_4 attack. It converts C-S-H into a non-binding M-S-H phase resulting in a reduction of strength.

Acknowledgments

This work was supported by the National Research Foundation of Korea (NRF) grant funded by the Korean government (MSIT) (NRF-2021R1A4A3033128 and 2022R1C1C1007498).

References

Omar, S.B.A. (2002) “Attack on plain and blended cements exposed to aggressive sulfate environments”, Cement & Concrete Compositions, 24: 305-316

Higgins, D.D. (2003) “Increased sulfate resistance of ggbs concrete in the presence of carbonate”, Cement & Concrete Compositions, 25: 913-919

Reddy, K.C., Melaku, N.S. and Park, S. (2022) “Thermodynamic Modeling Study of Carbonation of Portland Cement”, materials, 15(14), 5060

Degefa, A.B., Yang, B., Park, S. (2023) “Predicting the degree of reaction of supplementary cementitious materials in hydrated Portland cement”, Submitted.

Schmidt, T., Lothenbach, B., Romer, M., Neuenschwander, J. and Scrivner, K. (2009) “Physical and microstructural aspects of sulfate attack on ordinary and limestone blended Portland cements”, cement and concrete Research, 39: 1111-1121

Santhanam, M., Cohen, M.D. and Olek, J. (2002) “Mechanisim of sulfate attack: A fresh look – Part 1; Summary of experimental results”, Cement and Concrete Research, 32: 915-921

Revert, A.B., Weerdt, D.K., Hornbostel, K. and Geiker, M.R. (2018) “Carbonation-induced corrosion: Investigation of the corrosion”, Construction and Building Materials, 162: 847-856

The 16th International Congress on the Chemistry of Cement 2023 (ICCC2023)
"Further Reduction of CO_2 -Emissions and Circularity in the Cement and Concrete Industry"
September 18–22, 2023, Bangkok, Thailand

Mineralogical analysis of BOF slag with different grinding characteristics

Seohyun Kim[1], and Juhyuk Moon[2,*]

[1] *Department of Civil and Environmental Engineering, Seoul National University, Seoul 08826, Republic of Korea*

Email: ksh0128706@snu.ac.kr

[2] *Department of Civil and Environmental Engineering / Institute of Construction and Environmental Engineering, Seoul National University, Seoul 08826, Republic of Korea*

Email: juhyukmoon@snu.ac.kr

ABSTRACT

Although Basic Oxygen Furnace (BOF) slag contains cementitious mineral components such as C_2S, and brownmillerite (C_2F), it has not been largely utilized in cement or concrete industry due to its low grindability as well as low chemical compatibility with cement-based materials. This study investigates the mineralogical and chemical properties of BOF slag with different grindability of low and high grindability groups. Low grindability group is named as Hard Steel Slag (HSS), and high grindability group is named as Soft Steel Slag (SSS). By applying proper grinding time, similar particle size distributions of both groups could be achieved. Therefore, it can eliminate the physical effect (i.e., from identical particle size) so chemical effect can be fairly compared. The mineralogy of both samples was determined by repeating X-Ray Diffraction (XRD) for 10 times so that it can minimize the non-homogeneity of steel slag. Also, isothermal calorimetry test was used to measure chemical reactivity of both sample groups. The XRD result shows that HSS group contains a larger amount of C_2S, C_2F, RO phase. Amorphous phase and reactive phases such as C_2S, C_2F in HSS group resulted in higher cumulative heat than SSS group from isothermal calorimetry test.

KEYWORDS: *BOF slag, Grindability, X-ray diffraction, Calorimetry*

1. Introduction

Basic Oxygen Furnace (BOF) slag is an industrial by-product with low recycling rate, globally. About 15% by mass of steel making process output is steel slag. The BOF slag is composed of CaO (30–50%), SiO_2 (10–20%), Fe_2O_3 (20–40%), Al_2O_3 (1–7%), MgO (4–10%), MnO (0–4%), P_2O_5 (1–3%) and TiO_2 (0–2%), with a mineral assemblage of C_2S, C_3S, $C_2(A,F)$, RO phase (CaO–FeO–MgO–MnO solid solution, crystallized in wuestite structure), and free lime (CaO). Some steel slag contains kirschsteinite which has low alkalinity. Among them, C_2S and $C_2(A,F)$ have potential to react with water. The utilization of BOF slag in concrete is further limited due to the volume instability problems caused by the presense of free CaO and low hydraulic acitivity.

In this study, we investigated mineralogical and chemical analysis of BOF slag with different grinding efficiency. By the result of XRD analysis, C_2S, C_2F and RO phase are contained more in HSS than SSS due to their strong hardness. Especially C_2S and C_2F are reactive phases in steel slag. Therefore, by the isothermal calorimeter experiment, HSS showed higher cumulative heat release than SSS due to its higher amount of reactive phases.

2. Materials and methods

2.1 Materials

To control the particle size distribution of steel slag, a lab-scale micro ball mill device (McCrone micronizing, McCrone Scientific LTD., Leighton Road London, UK) and desktop ball mill were used. The grinding process is described in Fig. 1. SSS is obtained by grinding raw steel slag with desktop ball mill for 3 hours. HSS is obtained by grinding raw steel slag with desktop ball mill for 3 hours, seived over 1.18mm, and additional grinding with desktop ball mill for 10 hours

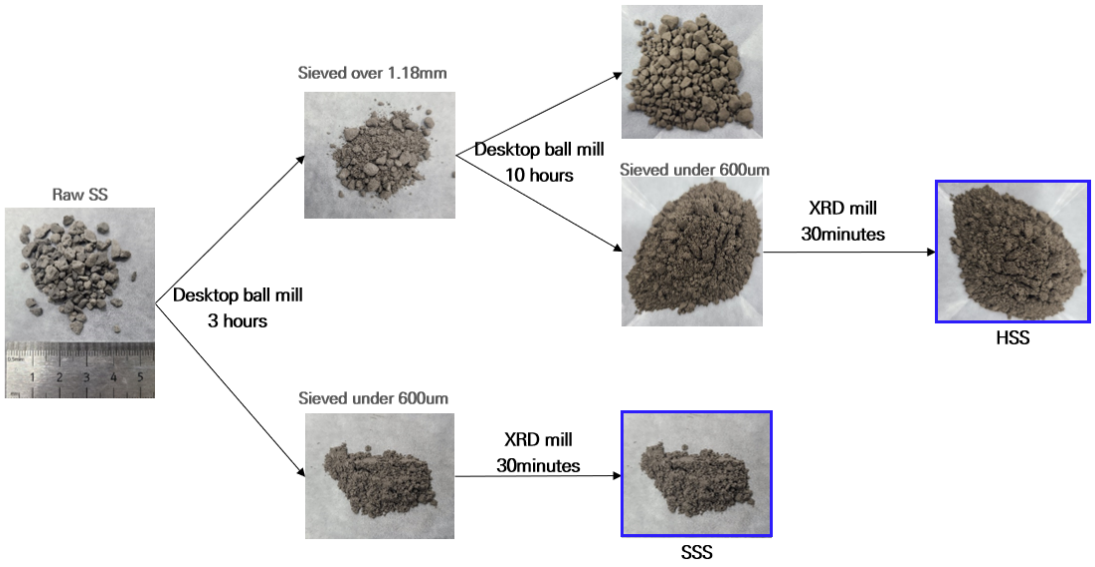

Fig. 1. The grinding process of SSS and HSS

Fig. 2 shows the particle size distribution of SSS and HSS after milling process. The similar particle size distributions were obtained in both groups.

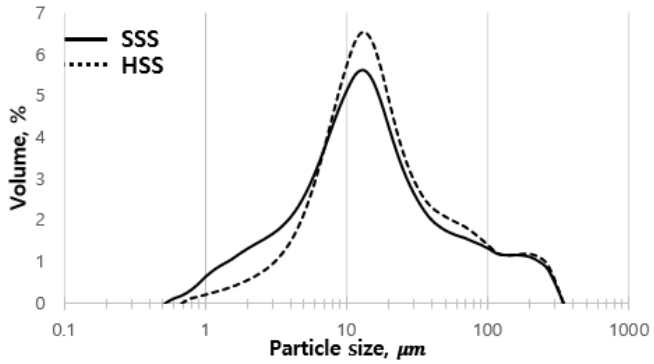

Fig. 2. The particle size distribution of SSS and HSS

Table. 1 shows the chemical composition determined by Energy Dispersive X-Ray Fluorescence (ED-XRF) analysis.

Table. 1. Chemical composition of SSS and HSS

SSS		HSS	
Oxide	**Content (wt%)**	**Oxide**	**Content (wt%)**
CaO	35.59	CaO	37.29
Fe_2O_3	33.82	Fe_2O_3	33.59
SiO_2	14.6	SiO_2	13.4
MgO	5.06	MgO	5.51
MnO	3.7	MnO	3.53
Al_2O_3	3.52	Al_2O_3	3.19
P_2O_5	1.99	P_2O_5	2.09
SO_3	0.33	SO_3	0.16
Cr_2O_3	0.29	Cr_2O_3	0.315
V_2O_5	0.21	V_2O_5	0.23

2.2 Methods

2.2.1 X-ray powder diffraction/Quantitative X-ray Diffraction

The degree of hydration and the phase development were analyzed through X-ray patterns measured from the X-ray diffractometer (D2 Phaser, Bruker Co. Ltd, Land Baden- Württemberg, Germany) equipped with Cu- Kα radiation (λ = 1.5418 Å) in the range of 2θ between 5˚ and 60˚.
For accurate quantitative XRD analysis, SSS and HSS were milled with micro ball mill for 30 minutes. Also, to minimize the non-homogeneity effect of steel slag, XRD measurement was conducted 10 times for each group.

2.2.2 Isothermal calorimetry

The hydration heat evolution and kinetics of SSS and HSS were analyzed through heat evolution measured from calorimeter (TAM Air, TA Instruments, New Castle, DE, USA). Cumulative heat flow was obtained in 40°C for 7 days.

3. Results

3.1 Quantitative X-ray Diffraction

Fig. 3 shows the mineralogical contents of SSS and HSS with 10 wt.% of internal standard(Rutile, TiO_2). HSS contains higher amount of C_2F, C_2S, RO phase, and amorphous phase than SSS. Especially, amorphous phase and reactive phases such as C_2F and C_2S are 5.9%, 2.9% and 4.8% more in HSS than in SSS respectively. Also, kirschsteinite which has low alkalinity is contained more in SSS than HSS. Other mineral contents such and portlandite, free lime, and so on are excluded due to their low amount (under 3 wt.%).

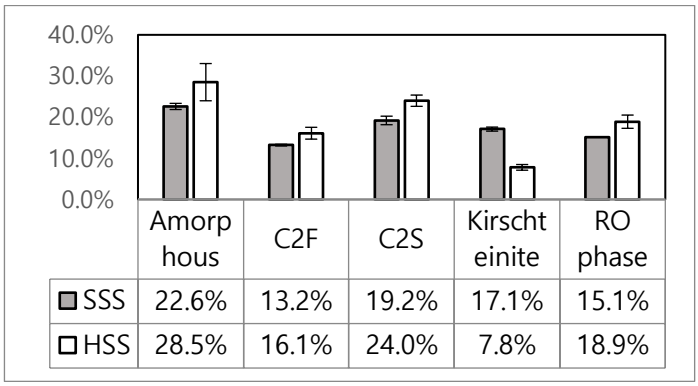

Fig. 3. QXRD results of SSS and HSS

3.2 Isothermal calorimetry

Fig. 4 shows the cumulative heat release of SSS and HSS. The cumulative heat of SSS is about 65 J/g, and that of HSS is about 90 J/g which is 38% higher than that of SSS. The higher cumulative heat of HSS is presumed to be due to higher amount of C_2S and C_2F and lower amount of kirschsteinite.

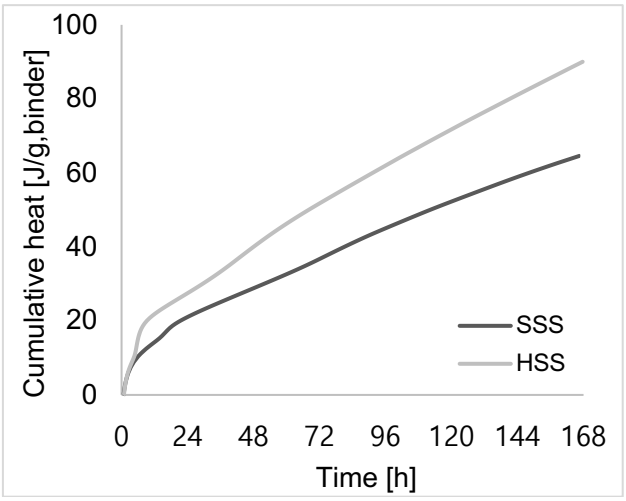

Fig. 4. Cumulative heat release of SSS and HSS

4. Conclusion

In this paper, the mineralogical and chemical analysis of steel slag sorted by different grinding efficiency were investigated. Soft Steel Slag powder is obtained by 3 hour grinding and Hard Steel Slag powder is obtained by 13 hour grinding.

i. According to quantitative X-ray diffraction result, Hard Steel Slag (HSS) contains larger amount of C_2F, C_2S, wuestite than Soft Steel Slag (SSS) and has lower amount of kirschsteinite. The reason is that C_2F, C_2S, and wuestite has strong hardness. Among them, C_2F and C_2S has potential to react with water.

ii. The cumulative heat of SSS for 7 days is 65 J/g and that of HSS is 90 J/g. This data correspond to the QXRD results in which HSS contains a larger amount of reactive phases such as C_2F, C_2S.

iii. Above results show that HSS is more reactive so that it is good to use as cementitious materials.

Acknowledgements

This work was supported by the Industrial Strategic technology development program-Development of manufacturing technology of hardened cement with carbonation curing (RS-2022-00155662, Development of manufacturing and application technology of 1,000 ton/year class hardened cement with carbonation curing) funded By the Ministry of Trade, industry & Energy (MOTIE, Korea).

References

A. van Zomeren, S.R. van der Laan, H.B.A. Kobesen, W.J.J. Huijgen, R.N.J. Comans. (2011), “Changes in mineralogical and leaching properties of converter steel slag resulting from accelerated carbonation at low CO2pressure,” Waste Manag., 31(11), pp. 2236-2244

D. Wang, J. Chang, and W. S. Ansari. (2019), “The effects of carbonation and hydration on the mineralogy and microstructure of basic oxygen furnace slag products,” *J. CO2 Util.*, vol. 34, pp. 87–98

The 16th International Congress on the Chemistry of Cement 2023 (ICCC2023)
"Further Reduction of CO_2 -Emissions and Circularity in the Cement and Concrete Industry"
September 18–22, 2023, Bangkok, Thailand

Use of machine learning for predicting phase assemblages of supplementary cementitious materials-blended cements

A.B. Degefa[1*], H.K. Yoon[2], J.Y. Bak[3] and S. Park[4]

[1] *Department of Civil Engineering, Pukyong National University, 45 Yongso-ro, Nam-gu, Busan 48513, Republic of Korea*

Email: aaronpknu@pukyong.ac.kr

[2] *Department of Artificial Intelligence, Sungkyunkwan University, 25-2 Sungkyunkwan-ro, Jongno-gu, Seoul, Republic of Korea*

Email: hkyoon95@g.skku.edu

[3] *Department of Artificial Intelligence, Sungkyunkwan University, 25-2 Sungkyunkwan-ro, Jongno-gu, Seoul, Republic of Korea*

Email: jy.bak@skku.edu

[4] *Department of Civil Engineering, Pukyong National University, 45 Yongso-ro, Nam-gu, Busan 48513, Republic of Korea*
Email: solmoi.park@pknu.ac.kr

ABSTRACT

The role of supplementary cementitious materials (SCMs) in reducing CO_2 emissions by lowering the clinker content is becoming invaluable. As such, developing a tool to predict the major properties of SCMs can be a significant step toward ensuring their effective use in hydrated Portland cement. In this research, the major hydration products of SCM-blended cements are predicted using artificial neural network (ANN) machine learning (ML) by employing different input data which are easily adaptable for a wide range of SCMs. The prediction results show that the model has a root mean squared logarithmic error of 0.6 on average. The model's applicability is tested for the current two most frequently utilized SCMs, namely fly ash and metakaolin by predicting the phase assemblages and investigating their correlations to oxide composition. The findings indicate that ML models can be utilized efficiently to predict phases of SCM-blended cements while also ensuring the better design of SCM addition.

KEYWORDS: *Portland cement; Machine learning; Supplementary cementitious materials; Phase assemblage*

1. Introduction

The cement industry frequently uses supplementary cementitious materials (SCMs) to mitigate significant carbon dioxide emissions caused by Portland cement (PC) production. These materials have been extensively researched and are considered a foundation for future projects. With a wealth of accumulated data available, machine learning can be utilized to predict multiple sets of SCM attributes.
The microstructural evolution of PC with SCMs involves a thorough investigation of the major stable phases formed during the hydration process. These include C-(A)-S-H, portlandite, monosulfate (monocarbonate), ettringite, hydrogarnet, hydrotalcite, and stratlingite. Accurately forecasting these phases would benefit the optimization of concrete mixture preparation and the prediction of hardened concrete characteristics. Various techniques have been utilized in predicting these phases, such as Nuclear magnetic resonance (NMR) spectroscopy, scanning electron microscopy/backscattered electron image analysis

coupled with energy dispersive spectroscopy (SEM-EDS/BSE-EDS), quantitative X-ray diffractometry (QXRD), and X-ray computed tomography (CT). Although the aforementioned techniques generally provide reliable results, they do have limitations. For instance, NMR has limited sensitivity, especially for isotopes with low natural abundance, and requires a certain level of expertise to execute experiments and interpret spectra accurately. Additionally, the presence of paramagnetic species, such as Fe in PC and fly ash, can alter the relaxation and chemical shift of adjacent nuclear spins, which can affect the characterization process (Walkley and Provis, 2019). SEM-EDS/BSE-EDS requires a large number of photos to obtain quantitative data and is heavily reliant on experience, which can lead to issues with grey value overlapping (Scrivener, 2004). QXRD may also encounter issues related to overlapping contributions from amorphous SCM products and C-S-H. Furthermore, due to the diversity of refining procedures and techniques used, reproducibility of findings between labs may be challenging (Soin et al., 2013). Lastly, CT's ability to deliver spatial resolution that provides equal grey scale values for distinct solid phases in the reconstructed image volume is limited (Deboodt et al., 2021).
Machine learning (ML) approaches can be employed to overcome challenges in identifying phases in hydrated SCM-blended cements. In this study, a machine learning model was developed to predict which solid phases of SCMs will form based on basic information about the materials. An artificial neural network (ANN)-based ML system was used due to its ability to generate reliable predictions from existing data. The findings of this study reveal that the predictions are strongly correlated with past experimental results and observations.

2. Methods

The data collected was made of 254 observations, 24 independent variables, and the hydrated PC-SCM phase outputs as a dependent variable. Inputs included oxide composition of PC and SCMs (SiO_2, Al_2O_3, Fe_2O_3, CaO, MgO, SO_3, Na_2O, and K_2O), the water-to-cement ratio ranging from 0.25-0.8, the proportion of binder materials (PC/SCM), curing temperature ranging from 10-50 ^{0}C, curing time ranging from 3-1000 days, particle size, surface area, specific gravity and the phase outputs.
In this study, a dataset was used to train and test an ANN ML algorithm. The dataset was randomly split into 80:20 training and test groups. The ANN had a basic three-layer structure with an input layer, a hidden layer, and an output layer. The input layer accepted numerous input characteristics, and the hidden layer utilized activation functions such as relu, abs, sigmoid, and softplus to introduce nonlinearity to the model and identify appropriate weights and biases. The best activation functions were found to be softplus and abs, and the dataset was divided into five parts for analysis, with the testset outcomes averaged across each partition. The study focused on the hydrated phase assemblage of PC-SCMs obtained from the ML predictions, and phase diagrams were constructed based on the SCMs' dominant oxide composition. Throughout the paper, the curing time and water-to-cement ratio were kept constant at 90 days and 0.4, respectively.

3. Results and discussion

3.1 Phase assemblage of hydrated PC with SCM

The effect of SCM replacement on the phase assemblage of hydrated cement for replacement values of 0,13,26,39,52, and 65 is described in this section. Figure 1 depicts the phase outputs of the model for metakaolin blended PC. The consumption of portlandite increases with metakaolin content. Up until 52% metakaolin substitution, the quantity of C-(A)-S-H formed rises; after that point, it starts to decline slightly; however, it still accounts for more than 50% of the available phases. Hydrogarnet stability decline towards cement and metakaolin-dominant compositions. Additionally, the greater alumina and silica concentration of metakaolin makes C-A-S-H formation easier in PC-metakaolin (Zhao and Khoshnazar, 2020). Monosulfate and hydrotalcite are found in small amounts and increase with metakaolin substitution. The concentration of ettringite is extremely low, at around less than 1%. Furthermore, the increase in metakaolin replacement results in more free water. Briki et al. (Briki et al., 2021) reported similar variations in phase assemblage for portlandite, monosulfate, and free water.

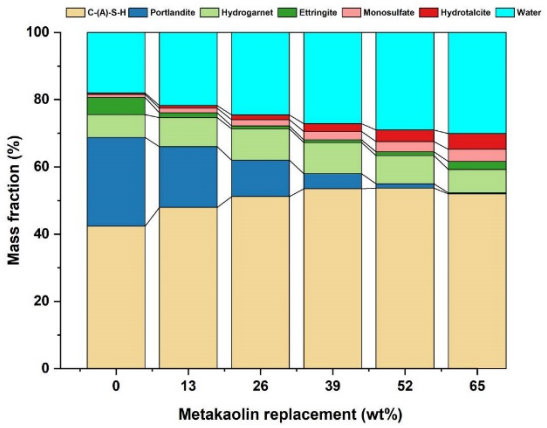

Figure 1 The effect of metakaolin replacement on the phase composition of hydrated PC at different concentrations

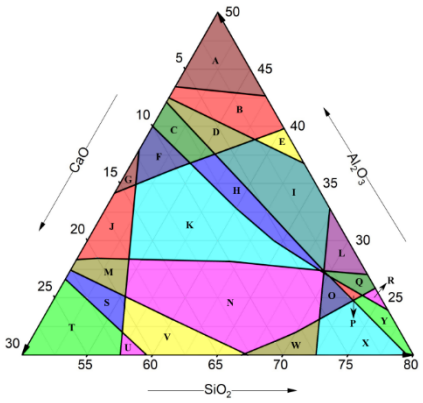

Figure 2 Phase assemblage output in $CaO\text{-}SiO_2\text{-}Al_2O_3$ composition for 25% fly ash replacement in hydrated PC

Table 1 Description of the regions shown in Figures 2. 'a' and 's' represent abundant and scarce solid phases, respectively.

Region	Predicted phase output					
	C-(A)-S-H	Portlandite	Ettringite	Monosulfate	Hydrogarnet	Hydrotalcite
A	s	s	s	-	a	s
B	s	s	s	-	-	s
C	s	s	s	-	-	-
D	-	s	s	-	-	s
E	-	s	-	-	-	s
F	-	-	s	-	-	-
G	-	-	s	s	-	-
H	-	s	-	-	-	-
I	-	s	-	-	-	s
J	-	-	-	s	-	-
K	-	-	-	-	-	-
L	-	s	-	a	-	s
M	-	-	-	s	s	-
N	-	-	-	-	s	-
O	-	-	-	a	s	-
P	-	-	-	a	s	s
Q	-	s	-	a	s	s
R	-	s	a	a	s	s
S	a	-	-	s	s	-
T	a	a	-	s	s	a
U	a	a	-	-	s	a
V	a	-	-	-	s	-
W	-	-	a	-	s	-
X	-	-	a	a	s	-
Y	-	-	a	a	s	s

3.2 Phase diagrams based on dominant oxide composition

This section describes the influence of the main oxide compositions on the phase formation of the PC-SCM hydrated system. To illustrate this, the ternary diagrams demonstrate the concentrations of solid phases for a 25% fly ash substitution in hydrated PC, based on the main oxides ($CaO\text{-}SiO_2\text{-}Al_2O_3$) in the PC-fly ash system. The major oxide ranges are established using the quantity of fly ash present in the PC-SCM combined environment, while the other oxides are kept constant. Once the ranges are determined, solid

phases that are abundant and scarce are designated as those that represent >75% and 25% of the difference between the maximum and lowest solid-phase masses, respectively, using the oxide composition range. Figure 2 depicts the CaO-SiO_2-Al_2O_3 ternary phase diagram for 25% fly ash substitution. The percentage ranges of the main oxides are $0 \leq CaO \leq 30$, $50 \leq SiO_2 \leq 80$, and $20 \leq Al_2O_3 \leq 50$. While it is reasonable to assume that SiO_2 composition has a major role in determining hydrated PC-fly ash phase stability, the explanations that follow focus on oxide composition variations occurring within the ranges specified. For example, CaO-dominated oxide composition indicates (CaO=30%, SiO2=50%, and Al2O3=20). The amount of C-(A)-S-H solid phase is largely determined by the concentration of CaO, with its formation being significantly promoted by higher CaO concentrations (Walkley et al., 2016). The highest concentrations of C-(A)-S-H solid phase can be expected to precipitate when $(CaO/(CaO+SiO_2+Al_2O_3) > 0.2)$. Portlandite and hydrotalcite also prefer CaO-dominated environments, remaining stable when $(CaO/(CaO+SiO_2+Al_2O_3) > 0.24)$. The consumption of Portlandite is highly facilitated for increased concentrations of Al_2O_3. Ettringite and monosulfate are stable in SiO_2-dominated compositions. However, ettringite becomes highly unstable in Al_2O_3-dominated compositions, while monosulfate becomes unstable in CaO-dominated compositions. Lastly, Al_2O_3-dominated compositions promote the formation of hydrogarnet.

4. Conclusions

The aim of this research was to create and analyze a model that can predict the primary phases of hydrated SCM-blended cements. The study examined the phase assemblage output and the impact of oxide composition on the development of these phases in hydrated PC-SCMs. The model's phase outputs demonstrate how the PC-SCM can be enhanced to produce the necessary phase output. Additionally, precise design of SCM additions can be achieved by calculating the stability fields of the primary phases in the hydrated PC-SCM system based on the oxide composition of the SCMs. In the case of PC-fly ash, for instance, C-(A)-S-H, portlandite, and hydrotalcite outputs were improved by adding extra amounts of CaO, while ettringite and monosulfate were enhanced by using additional amounts of SiO_2.

Acknowledgements

This work was supported by the National Research Foundation of Korea (NRF) grant funded by the Korea government (MSIT) (NRF-2021R1A4A3033128 and 2022R1C1C1007498).

References

Briki, Y., Avet, F., Zajac, M., Bowen, P., Haha, M. Ben, and Scrivener, K. (2021). Understanding of the factors slowing down metakaolin reaction in limestone calcined clay cement (LC3) at late ages: *Cement and Concrete Research*, Vol. 146, No. October 2020, p. 106477, DOI: 10.1016/j.cemconres.2021.106477.

Deboodt, T., Wildenschild, D., Ideker, J.H., and Burkan Isgor, O. (2021). Comparison of thresholding techniques for quantifying portland cement hydrates using synchrotron microtomography: *Construction and Building Materials*, Vol. 266, p. 121109, DOI: 10.1016/j.conbuildmat.2020.121109.

Scrivener, K.L. (2004). Backscattered electron imaging of cementitious microstructures: Understanding and quantification: *Cement and Concrete Composites*, Vol. 26, No. 8, pp. 935–945, DOI: 10.1016/j.cemconcomp.2004.02.029.

Soin, A. V., Catalan, L.J.J., and Kinrade, S.D. (2013). A combined QXRD/TG method to quantify the phase composition of hydrated Portland cements: *Cement and Concrete Research*, Vol. 48, pp. 17–24, DOI: 10.1016/j.cemconres.2013.02.007.

Walkley, B., and Provis, J.L. (2019). Solid-state nuclear magnetic resonance spectroscopy of cements: *Materials Today Advances*, Vol. 1, DOI: 10.1016/j.mtadv.2019.100007.

Walkley, B., San Nicolas, R., Sani, M.A., Rees, G.J., Hanna, J. V., van Deventer, J.S.J., and Provis, J.L. (2016). Phase evolution of C-(N)-A-S-H/N-A-S-H gel blends investigated via alkali-activation of synthetic calcium aluminosilicate precursors: *Cement and Concrete Research*, Vol. 89, pp. 120–135, DOI: 10.1016/j.cemconres.2016.08.010.

Zhao, D., and Khoshnazar, R. (2020). Microstructure of cement paste incorporating high volume of low-grade metakaolin: *Cement and Concrete Composites*, Vol. 106, DOI: 10.1016/j.cemconcomp.2019.103453.

The 16th International Congress on the Chemistry of Cement 2023 (ICCC2023)
"Further Reduction of CO_2 -Emissions and Circularity in the Cement and Concrete Industry"
September 18–22, 2023, Bangkok, Thailand

Restraining strength retrogression of silica-cement at high temperature above 200 ℃ using flint clay and graphite

H.T. Liu[1*], Z.R. Zhang[2], C.Q. Li[3], Y.J. Yu[4], F.Z. Q[5] and Y.C. Ke[6]

[1] *CNPC Engineering Technology R&D Company Limited, Beijing, China*
Email: liuhtdr@cnpc.com.cn
[2] *CNPC nano-Chemistry key laboratory, College of Science, China University of Petroleum, Beijing, China*
Email: zzr130618@163.com
[3] *Petro China Southwest Oil & Gasfield Company, Chengdu, China*
Email: lichengq@petrochina.com.cn
[4] *CNPC Engineering Technology R&D Company Limited, Beijing, China*
Email: yuyongjindri@cnpc.com.cn
[5] *CNPC Engineering Technology R&D Company Limited, Beijing, China*
Email: qfzh69dri@cnpc.com.cn
[6] *CNPC nano-Chemistry key laboratory, College of Science, China University of Petroleum, Beijing, China*
Email: key@cup.edu.cn

ABSTRACT

Strength retrogression phenomenon of silica-cement systems subjected to high pressure and high temperature above 200 ℃ is common, which is not conducive to the sealing integrity of cement ring and long-term exploitation of high-temperature oil and gas wells. In this paper, the effects of individual flint clay (FC), graphite and its hybrid combination on the silica-cement cured at 240 ℃ and 20.7 MPa for different ages were studied. The decline of controlled sample's compressive strength was obvious, ranging from 32.4 MPa at 2 days to 16.5 MPa at 28 days. Compared with the control, the compressive strength of FC2 cement and G3 cement increased by 182.4% and 187.9% at 28 days, respectively. High-temperature cement containing 15% FC and 2% graphite showed higher mechanical strength which is 52.8 MPa for 28 days than the FC2 or G3 cement. The mechanism is probably due to the high crystallinity hydration products formed via the volcanic ash reaction of FC, the fill effect and interface effect of graphite, and the synergy of the two forms a more stable and dense internal structure. To sum up, flint clay and graphite had excellent effects to increase the strength of silica-cement cured at 240 ℃, which provided a way to restrain strength retrogression of silica-cement at high temperature above 200 ℃.

KEYWORDS: *flint clay, graphite, mechanical behavior at high temperature, strength retrogression, oil well cement*

1. Introduction

With the development of oil and gas well exploration and, there are more and more.deep wells and super-deep wells. In high temperature cementing operation, serious problems such as cement strength retrogression and cement ring seal integrity failure occurred, which is extremely bad for production. It is found that adding silica sand can retard the strength decline of cement at high temperature ranged from 110 to 200 ℃ (Kanchanason et al (2019)). However, the strength of silica sand cement systems still decline severely at high temperature above 200 ℃, which is not conducive to the long-term exploitation of super high-temperature oil and gas wells. Therefore, it is particularly important to study the new high-temperature resistance strength decay material and the enhancement mechanism.

Flint clay is a kind of refractory clay, the main chemical composition are Al_2O_3 and SiO_2, the main mineral is kaolin. They can produce the volcanic ash effect with CH, significantly accelerate the hydration reaction. Graphite is a hexagonal lamella structure, with the characteristics of high temperature resistance, good toughness, and good chemical stability at room temperature (Liu et al (2021)). The unique properties of graphite-based materials prove to improve the properties of cemented nanocomposites (Le et al (2014)), so as to achieve higher or even super high mechanical and physical properties (Dimov et al (2018)). Relevant studies have found that metakaolin and graphite can inhibit the

decline of cement strength (Zhang and Yang (2020)). The current study has not fully solved the strength decline of cement under high temperature conditions, and the mechanism of resistance decline is not clear. In this paper, the effects of FC and graphite on compressive strength of SC cement were investigated. And microscopic morphology, pore structure changes and hydration products were studied. The research results have important reference value for cement slurry design of high-temperature and ultra-deep wells.

2 Materials and methods

2.1 Materials

The following raw materials were used: API class G oil well cement was obtained from Sichuan Jiahua Cement Factory (Leshan, China). Silica sands were got from Jingxi petroleum Engineering Co., Ltd. The study subject was 50% mass fraction sand-added class G oil well cement, which was used to prepare all samples. Flint clay was purchased from Shijiazhuang Yunwang Mineral Products Co., Ltd (Hebei, China). The chemical composition and physical properties are shown in Table 1. Graphite was obtained from Qingdao Yanhai Carbon Materials Co., Ltd (Shandong, China). Dispersing agent DRS-1S are made by the cementing research Institute of CNPC Engineering Technology Research Institute Co., LTD.

Table 1 Chemical Composition of FC

Chemical composition	Al_2O_3	Fe_2O_3	K_2O+Na_2O	TiO_2	Refractoriness/°C
content（wt%）	45~48	≤1.15	≤0.3	≤0.8	≥1770

2.2 Slurry sample preparation

Oil-well cement slurries were prepared and cured according to Chinese standard GB/T 19139-2012. Given the curing formulation of all samples in Table 2. The cement slurry was stored in standard curing molds at 240 ºC, 20.7 MPa, RH 95% for 2, 7 and 28 days.

Table 2 Mix compositions of different silica cement systems

Sample number	Cement(g)	silica sand	FC content(wt%)	Graphite content(wt%)	Dispersant(wt%)	Water(g)
SC	400	200	0	0	1.5	232
FC2	400	200	15	0	1.5	232
G3	400	200	0	2.0	1.5	232
FC2G3	400	200	15	2.0	1.5	232

2.3 Characterization

The universal pressure tester is used to test the compressive strength of the cube, and the average value is calculated. Using x-ray powder diffraction instrument (XRD, Bruker Corporation, D8 ADVANCE) (Cu target, K-alpha rays (λ = 0.154nm)), the scan range of 2θ is 5-90°, and the scan rate is 7°/min. The sample was broken with compressive specimen and ion sputtering metal film was coated on the surface of the cement was characterized via scanning electron microscopy (SEM, Hitachi SU8010, Japan), and the change of interface performance of the cement was evaluated. The pore structure of cement was tested with automatic mercury pressure aperture analyzer (AutoPore IV 9510, McMurray, USA).

3. Results and discussion

3.1 Compressive Strength

The compressive strength of SC, FC2, G3 and FC2G3 cement at 2, 7, and 28 days is shown in Fig. 1. The results showed that the compressive strength of FC2G3 cement increased significantly at 7 days curing ages, and did not decline at 28 days. At 240 ℃, the compressive strength of FC2 cement increased by 23.8%, 22.3% and 182.4%, respectively, compared with the SC cement. At 2, 7 and 28 days, the compressive strength of G3 cement has been increased 7.7%, 39.0% and 187.9, respectively, compared with SC cement. The compressive strength of FC2G3 cement is 52.4 MPa and 52.8 MPa at 7 and 28 days, increased by 23.9% and 13.3%, respectively, compared with FC2 cement. It shows that the addition of FC and graphite can improve the strength of cement, and the two play a synergistic role, which can effectively alleviate the decline of cement strength under high-temperature. In the following sections, we will study the crystalline phase components, micro-structure and pore structure changes, which can explain the mechanical results to some extent.

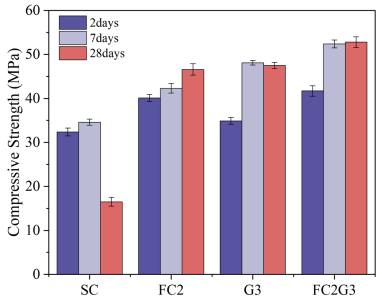

Fig. 1. Compressive strengths of SC, FC2, G3 and FC2G3 cement

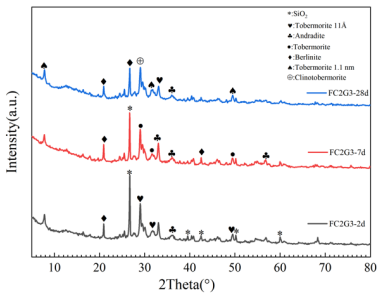

Fig. 2. Representative XRD profiles of FC2G3 cement at various curing age

3.2 XRD Analysis

In order to study the influence of flint clay and graphite on cement hydration products, XRD analysis of FC2G3 cement was performed. The representative XRD test results are shown in Fig. 2. The pattern shows that the main hydration products are tobermorite, andradite, tobermorite 1.1 nm and berlinite. Berlinite has good temperature resistance, which is conducive to the strength development of cement. And the qualitative analysis showed that the crystal form of the C-S-H changed, such as 2 days is tobermorite 11 Å ($Ca_5H_{10}O_{23}Si_6$), and 7 days becomes tobermorite ($Ca_{2.25}H_{3.5}O_{10}Si_3$), which has lower Ca/Si. At 28 days curing time, the characteristic peaks of tobermorite and clinomorite were identified, these hydrated phases have higher stability, and the strength of cement does not decline at high-temperature and long curing ages. Some studies (Bu and Du (2016)) have found that, tobermorite and andradite suppress the reduction in cement strength because they can fill the structure tightly and have high stiffness. The characteristic peak of CH is not observed, which is caused by the secondary hydration reaction.

3.3 Micro-structure Analysis

Fig. 3 shows the fracture surface morphology characteristics of SC(a), FC2(b), G3(c) and FC2G3(d) cement at 240 ℃, 28 days curing time. There are obvious micro-cracks, micro-gaps, lots of holes and aggregates (Fig. 3a). These agglomerates may be the hydration products with low crystallinity and poor stability produced by the hydration reaction. It is one of the important reasons for the decline of high-temperature cement strength. Fig. 3b appears tobermorite and needle-like xonotlite. Tobermorite has good temperature resistance and high strength, plays the role of filling in cement, so as to inhibit the strength decline of cement under high-temperature. Needle-like xonotlite can make the structure of cement denser. The denser structure and high stiffness are important factors hindering the reduction of cement strength (Bu and Du (2016)). Fig. 3c shows that graphite and cement matrix are strong bonding. The different layers of graphite are connected by van der Waals force, it will form cracks at the interface between the cement and graphite. Also, sliding between the graphite sheets to offset the strain force, resulting in stress relaxation of the crack tip. Graphite plays a physical filling role, and forms better adhesion with the cement matrix, which increases the roughness of the interface (Fig. 3d). Meanwhile, SiO_2 and Al_2O_3 have a secondary hydration reaction with CH, and form stable C_3S, C_2ASH_8 and C_4AH_{13}. The high stability of hydration products increases the strength of high-temperature cement and engenders the interface effect. This is consistent with the above mechanical properties and XRD results.

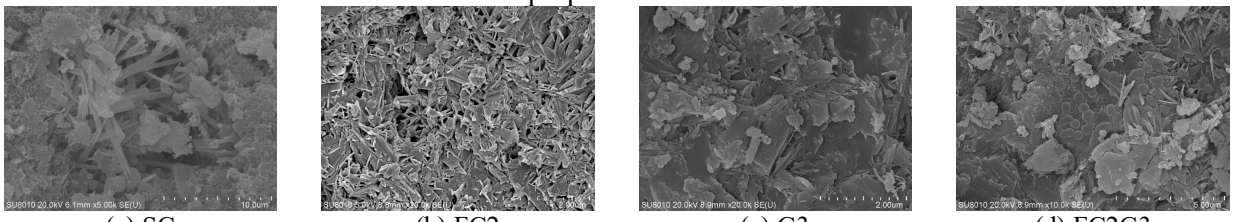

(a) SC (b) FC2 (c) G3 (d) FC2G3

Fig. 3. SEM images of silica cement systems at 28 days curing ages

3.4 MIP Analysis

Cement composites is a porous material with numerous air voids and capillary voids, which may be detrimental to the mechanical properties (Liu and Jin (2020)). MIP test method was used to characterize

the pore structure of cement. The porosity results of SC and FC2G3 cement was shown in Table 3. The total porosity of FC2G3 cement decreased 14.8%, compared to SC cement. The pore diameter of SC cement is mainly distributed in above 200 nm, accounting for 36.79%. The aperture of FC2G3 cement is mainly distributed in 20-50 nm, accounting for 30.01%. Compared with SC cement, the total porosity of FC2G3 cement changed from 42.76% to 36.43%, which reduced by 14.8%. This result may be the filling effect of graphite and FC, the synergistic effect of the two optimize the aperture distribution, make the pore structure get denser. This is one of the reasons to suppress the decline of high-temperature strength.

Table 3 Porosity and pore size distribution of SC and FC2G3 cement

Sample	Curing time	Total porosity/%	Distribution of pore size /%					
			>200nm	100-200nm	50-100nm	50-20nm	10-20nm	<10nm
SC	28d	42.76	36.79	23.95	18.43	14.65	5.03	1.15
FC2G3	28d	36.43	13.18	19.52	21.48	30.01	12.72	3.09

3.5 The mechanism to restrain strength retrogression of silica-cement at high temperature

Flint clay is a good quality kind of clay, the main components are Al_2O_3 and active SiO_2, which can react with the CH generated in the hydration process of cement, produce high-temperature resistant stable crystal phase, and inhibit the transition of tobermorite to xonotlite. FC mainly achieves the effect of high-temperature strength decline through volcanic ash reaction and pore filling effect. Graphite has a layered structure and rough surface. And the bond between graphite and the cement matrix is better. It manifested as the embedded form, fracturing through a similar fiber extraction effect to suppress the expansion of the cement crack. Because of its good compressibility, it can provide development space for hydration products in the hydration process, and optimize the crystalline phase structure of high temperature cement, improve the aperture distribution, micro-structure and density of cement effectively. In addition, there is Van der Waals force between graphite layers, and the combination force is weak, which make it have lubricity. This characteristic makes the graphite can slide in the cement matrix and offset the strain force, so as to reduce the production of cracks, which may be an important reason for its effective improvement of the mechanical strength of oil well cement under high-temperature.

4. Conclusion

1. The compressive strength decline of silica cement was obvious, ranging from 32.4 MPa at 2 days to 16.5 MPa at 28 days. Compared with SC cement, the compressive strength of cement increases by 23.8%, 22.3% and 182.4% cured at 2, 7, and 28 days with 15% FC, and increases by 7.8%, 39.0% and 187.9% with 2% graphite, respectively.
2. Flint clay plays a filling role and reduces the formation of micro-cracks. The hydration reaction of Al_2O_3 and SiO_2 in FC and Ca^{2+}, accelerates the hydration process of cement, promotes the formation of stable hydration phase. The graphite particles can produce mechanical binding force on the surface of the matrix, which is conducive to the interface and hindering the destruction of external force, thus inhibiting the strength decline of high temperature cement.
3. Flint clay and graphite had excellent and synergistic effects to increase the strength of silica-cements, which provided a way to restrain strength retrogression of silica-cement at high temperature above 200 ℃.

Acknowledgements

General Project of National Natural Science Fund (Approval No.51974339); The authors would like to acknowledge the co-financial support by CNPC Science and Technology Project (2021DJ4403).

References

Bu, Y., Du, J., Guo, S., Liu, H., & Huang, C. (2016). Properties of oil well cement with high dosage of metakaolin. CONSTRUCTION AND BUILDING MATERIALS, 112, 39-48.

Dimov, D., Amit, I., Gorrie, O., Barnes, M.D., Townsend, N.J., Neves, A.I.S., Withers, F., Russo, S., & Craciun, M.F. (2018). Ultrahigh Performance Nanoengineered Graphene-Concrete Composites for Multifunctional Applications. ADVANCED FUNCTIONAL MATERIALS, 28, 1705183.

Kanchanason, V., & Plank, J. (2019). Effect of calcium silicate hydrate – polycarboxylate ether (C-S-H–PCE) nanocomposite as accelerating admixture on early strength enhancement of slag and calcined clay blended cements. CEMENT AND CONCRETE RESEARCH, 119, 44-50.

Le, J., Du, H., & Pang, S.D. (2014). Use of 2D Graphene Nanoplatelets (GNP) in cement composites for structural health evaluation. Composites Part B: Engineering, 67, 555-563.

Liu, H., Jin, J., Yu, Y., Liu, H., Liu, S., Shen, J., Xia, X., & Ji, H. (2020). Influence of halloysite nanotube on hydration products and mechanical properties of oil well cement slurries with nano-silica. CONSTRUCTION AND BUILDING MATERIALS, 247, 118545.

Liu, L., Zhang, X., Xu, L., Zhang, H., & Liu, Z. (2021). Investigation on the piezoresistive response of carbon fiber-graphite modified asphalt mixtures. CONSTRUCTION AND BUILDING MATERIALS, 301, 124140.

Zhang, H., Yang, Y., Yu, W.Y., Li, L.K., & Zhang, X.G. (2020). "A Cementing Slurry Used in Alternating Ultra-High Temperatures." Drilling Fluid & Completion Fluid 37 (06): 771-776.

The 16th International Congress on the Chemistry of Cement 2023 (ICCC2023)
"Further Reduction of CO_2 -Emissions and Circularity in the Cement and Concrete Industry"
September 18–22, 2023, Bangkok, Thailand

A Particle Packing Approach for Eco-efficient Ultra High-Performance Concrete (E-UHPC)

B. Baten[1], H. Samouh[1], and N. Garg[1*]

[1] *Department of Civil and Environmental Engineering, University of Illinois at Urbana Champaign, Urbana, IL*
Email: bbaten2@illinois.edu, hsamouh@illinois.edu, nishantg@illinois.edu

ABSTRACT

Conventional design methods of Ultra-High-Performance Concrete (UHPC) usually involve high cement content (900-1100 kg/m^3) to enhance the mechanical and durability performance. However, the associated cost and environmental impact have limited its widespread usage. This study reports an efficient particle-packing approach in designing eco-efficient UHPC (E-UHPC) mixes with lower cement content while ensuring good rheological and mechanical properties. A total of five (5) UHPC mixes with different 'packing factors (PF)' (32.9 to 46.0) were designed by optimizing different commonly used supplementary cementitious materials (SCMs). The experimental results show that the packing factor strongly influences the workability (flow and yield stress), regardless of the binder types. Moreover, optimizing the packing factor resulted in a dense E-UHPC microstructure with open porosity of 3.67% at 28 days. The results also confirms that the packing factor govern the strength-porosity relationship of UHPC mixes with a higher strength development at PF:32.9. Furthermore, this study signifies that using packing factor and binder coefficient (BC) as design parameters can effectively allow cement replacement of >50% with adequate compressive strength ($f'_{c,28d}$: 118 MPa) and workability (flow: 230 mm). This implies an eco-efficient optimization method for designing low-cost E-UHPC (BC: 5.99 kg/m^3/MPa) with very low cement content (<50%) and thereby with significantly lower carbon footprint.

KEYWORDS: ***E-****UHPC, Packing factor, SCMs, Binder coefficient, Binder optimization.*

1. Introduction

The conventional design method of Ultra-High-Performance Concrete (UHPC) relies on a combination of very high cement content, low water-binder ratio, and high volume of steel fibers to ensure its enhanced mechanical properties and durability (Arora et al. (2018)). However, such elevated cement content increases the material's overall cost and carbon footprint. Hence, it is a significant incentive to replace cement with commonly used supplementary binders (SCMs) and fillers to make UHPC more sustainable and environmentally friendly (Huang et al. (2017)). As such, estimating the maximum cement replacement criteria and proportions is vital without compromising the mechanical and durability properties. This study used a packing model to investigate the extent of cement replacement with common SCMs while ensuring adequate packing, rheological and mechanical properties. With an inherently low w/b ratio, adequate packing of the microstructure plays a dominant role over the limited degree of hydration in governing the characteristic properties of UHPC. This concept was used to design five UHPC mixes with different replacement proportions of fly ash (≤ 35%), ground granulated blast furnace slag (≤20%), and silica fume (≤20%) to represent different ranges of packing density. The role of packing density on UHPC performance was investigated through fresh properties (flow and yield stress) and mechanical properties (porosity and compressive strength) at different ages. This study confirms that the packing model is more effective in optimizing the binder composition for a UHPC mix incorporating low cement content. Ensuring a microstructure with higher packing also exhibited enhanced flow and significantly higher compressive strength, even with lower cement requirements. This study also reveals that the 'binder coefficient' reflects an ideal evaluation tool of cement consumption in a UHPC function in terms of its performance. It was possible to reduce the cement consumption to one-third (5.99

kg/m^3/MPa) by enhancing the packing density through binder optimization. This design concept has significant potential in reducing the overall carbon footprint of UHPC mixes while maintaining its intended performance and making it applicable for sustainable construction practice.

2. Experimental Program

2.1 Materials

The binders used in this study include Type-I ordinary Portland cement (OPC), ultra-fine class-F fly ash (UFFA), slag (GGBS), and silica fume (SF). Masonry sand, sieved below 600 μm, was used as the fine aggregate. The particle size distribution (Fig. 1a) of each constituent was determined by using Laser Diffractometer to be used in the packing model. This study used an ultra-fine fly ash sample for a higher packing density. In addition, a polycarboxylate-based high-range water reducer (ADVA Cast 593) was used to reduce water demand and ensure adequate workability.

2.2 Mix Design based on Packing Model

In this study, five (5) UHPC mixes (M1-M5) were designed, with M1 being the control mix and Mix M2-M5 with varying replacement proportions of cement (up to 55%) with different SCM content (Table-1).

Table 1: Mix Details of UHPC Mix (M1-M5). The nomenclature represents the proportion in % of each constituent (represented by each letter) in the mix.

ID	Nomenclature	Mix Constituents (kg/m^3)						
		OPC	SF	UFFA	GGBS	Sand	Total Binder	S/B Ratio
M1	**C100**	1575	0	0	0	1325	1575	1
M2	**C70S5F10G15**	1103	55	131	221	1325	1509	1
M3	**C45S5F30G20**	709	55	392	295	1325	1450	1
M4	**C45S20F35**	788	244	508	0	1178	1539	0.8
M5	**C45S20F35**	709	220	457	0	1325	1386	1

A constant w/b ratio and HRWR dosage of 0.18 and 5% (wt. of binder), respectively, were used. Each mix's 'packing factor' was measured from the deviation between the ideal curve from Modified Anderson and Andreasen model (Yu et al. (2015)), using q=0.23, and the composite particle size distribution (Fig. 1a). Fig. 1b shows the variation of the packing factor with Mix M5 having the highest packing.

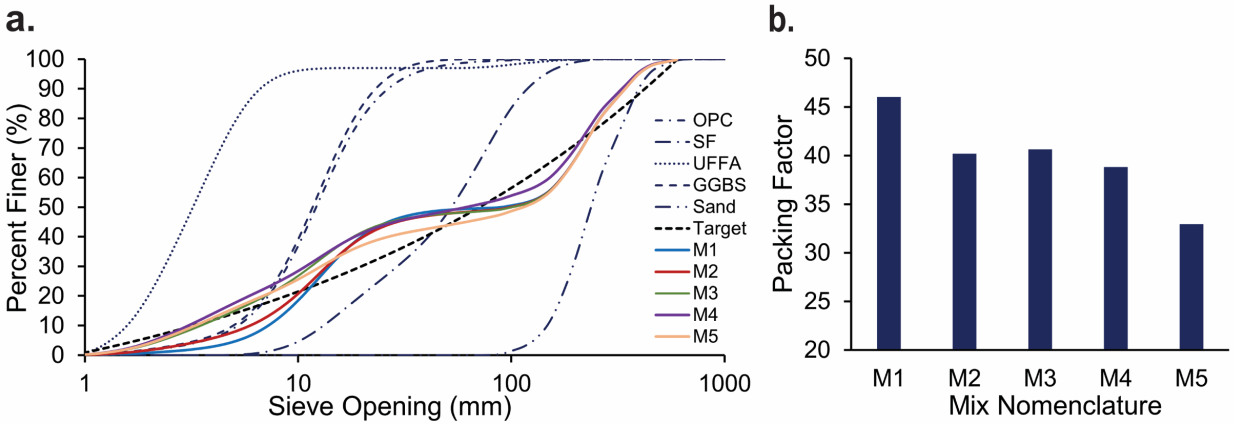

Figure 1. (a) Particle size distribution of the mix constituents used in designing the UHPC mixes. The composite particle size distribution of UHPC mixes, M1-M5, are represented in solid lines compared to the target curve from the Modified Anderson and Andreasen Model, (b) Packing factor of M1-M5 representing packing of the mixes.

3. Experimental Methods

The fresh properties of the UHPC mixes were measured through the modified flow test (ASTM C1611). The rheological properties (yield stress and plastic viscosity) were also evaluated using a TA DHR-3

Rheometer with a vane in cup geometry at 25±1 °C. A logarithmic shear sweep with a broad ramp-up phase of 0.1/s to 200/s was used to measure yield stress and viscosity accurately.
The compressive strength of 50 mm cube specimens was determined at different cured ages (3d, 7d, 14d, and 28d) following ASTM C109. The open porosity of the mixes was also determined at the same ages using AccuPyc 1330 Pycnometer at a constant pumping pressure (Kumar and Garg (2022)).

4. Results and Discussion

The stress-strain behavior, shown in Fig. 2a, reflects a significant influence of particle packing on the rheological behavior of UHPC mixes containing high SCM content.

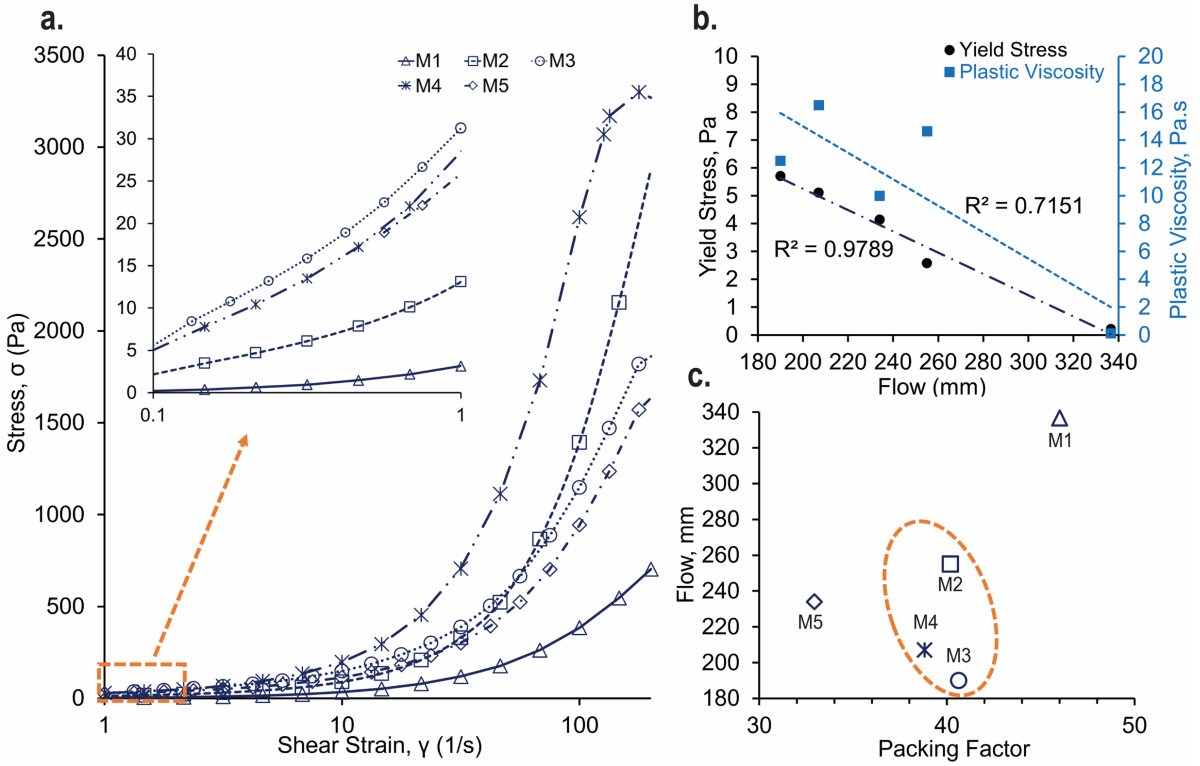

Figure 2. (a) Rheological behavior of the UHPC mixes for a logarithmic stress-strain sweep (0.1-200 s^{-1}) in a co-axial rheometer, (b) correlations developed between the flow and the rheological parameters (yield stress and plastic viscosity) and (c) role of packing density in influencing the rheological parameters of the mixes.

The presence of high SCM content increased the HRWR demand, resulting in much higher yield stress and flow than the control mix (M1). Meanwhile, M5 exhibits the highest packing (lowest packing factor), contributing to lower inter-particle voids and a higher amount of free water for enhancing flow despite much less cement content. This also explains a lower flow value and higher yield stress for Mix M4, which had similar mix composition but lower packing due to a lower s/b ratio of 0.8. While particle packing certainly governs the rheological behavior of UHPC mixes, HRWR demand should also be considered for an appropriate mix selection, as shown for Mix M2-M4 (marked zone) in Fig. 2c. Although M2 and M3 showed similar packing, however, the high UFFA content of M3 and higher HRWR demand resulted in lower flow spread and the highest yield stress. A similar trend was observed in all the rheological parameters, although flow values showed a better correlation (Fig. 2b) with the yield stress of any UHPC mix. This confirms that packing and HRWR dosage govern the inter-particle contact and friction, determining the water-film thickness required to initiate flow.
The effect of packing is more dominant on the mechanical behavior of UHPC mixes, as shown in Fig. 3. Although all the mixes showed a strong negative correlation between compressive strength and open porosity, however, it was found that the packing factor highly governs the relationship (Fig. 3a). Evidently, mix M5 showed the lowest porosity and the steepest slope along with a reducing slope with decreasing packing (lower PF value from left to right). This reflects that higher particle packing resulted in a refined microstructure and increased strength, even at an early age, and also contributed to higher

strength gain at later ages due to further pore refinement. Meanwhile, the control mix (M1) with lowest packing showed a broader change in porosity due to hydration. However, it still resulted in much lower strength ($f'_{c,28d}$: 77 MPa) compared to M5 ($f'_{c,28d}$: 118 MPa) with only 45% OPC content, as shown in Fig. 3b. This suggests that in UHPC mixes with low w/b ratio and degree of hydration, ensuring higher packing governs the mechanical properties and should be key in designing the mix. Most importantly, it offers an efficient approach to reducing the binder requirement and the associated environmental impact of UHPC. To justify the same, this study suggests evaluating the binder coefficient (amount of cement requirement per MPa strength) as a more appropriate parameter for comparing mix efficiency. With a reduced packing factor, the binder coefficient could be reduced by three folds (20.2 kg/m^3/MPa to 5.99 kg/m^3/MPa). Hence, considering the packing factor and binder coefficient as mix design criteria ensure low-cement UHPC with adequate performance.

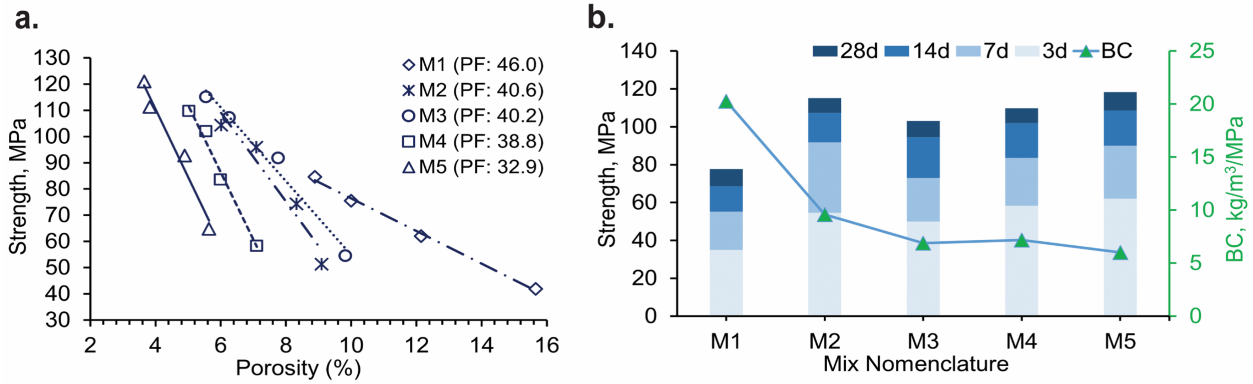

Figure 3. (a) Effect of packing factor on the strength-porosity relationship of the UHPC mixes (M1-M5) at different ages and (b) Compressive strength of the mixes at different ages as a function of the binder coefficient (BC)

5. Conclusions

This study demonstrated the significance of the packing factor in designing UHPC mixes with low binder content based on rheological and mechanical properties. Although the packing factor primarily governs the yield stress and flow of fresh UHPC mix, the amount of fines and HRWR dosage should also be considered while considering rheological criteria. Meanwhile, the packing factor has a more dominant effect in governing the strength-porosity development of UHPC mixes. This study also showed how ensuring a packed microstructure through a low packing factor can replace more than 50% cement without comprising strength (118 MPa) and rheology (flow: 230 mm). Moreover, optimizing the binder coefficient by ensuring a lower packing factor is a more effective approach to ensure an eco-efficient UHPC with low cement content and a significantly lower carbon footprint.

Acknowledgements

The authors acknowledge the support from the Illinois Center for Transportation (ICT) and Illinois Department of Transportation (IDOT) for funding the project (ICT R27-232)

References

Arora, A., Aguayo, M., Hansen, H., Castro, C., Federspiel, E., Mobasher, B. and Neithalath, N. (2018) "Microstructural packing-and rheology-based binder selection and characterization for Ultra-high-Performance Concrete (UHPC)", *Cement and Concrete Research*, 103: 179-190.

Huang, W., Kazemi-Kamyab, H., Sun, W. and Scrivener, K. (2017) "Effect of cement substitution by limestone on the hydration and microstructural development of ultra-high-performance concrete (UHPC)", *Cement and Concrete Composites*, 77: 86-101.

Kumar, V., and Garg, N. (2022) "The chemical and physical origin of incineration ash reactivity in cementitious systems", *Resources, Conservation and Recycling*, 177, 106009.

Yu, R., Spiesz, P. H. J. H. And Brouwers, H. J. H. (2015) "Development of an eco-friendly Ultra-High-Performance Concrete (UHPC) with efficient cement and mineral admixtures uses", *Cement and Concrete Composites*, 55: 383-394.

The 16th International Congress on the Chemistry of Cement 2023 (ICCC2023)
"Further Reduction of CO_2 -Emissions and Circularity in the Cement and Concrete Industry"
September 18–22, 2023, Bangkok, Thailand

Effect of chloride salts on cement hydration: influence of the cation - part II

P. Forni[1*]

[1] *Mapei S.p.A., Milan, Italy*

Email: p.forni@mapei.it

ABSTRACT

Chloride salts are used as cement hydration accelerators in mortar or concrete since decades. Their use in chemical activators formulations is even more important as clinker substitution is mandatory in the current scenario. Sodium and calcium chlorides are traditionally the most widespread, mainly due to their limited cost and vast availability. However, no thorough studies of the effect of the cation on the hydration kinetics and strength increase effect were carried out. The first part of the study (presented in 15th ICCC in Prague, 2019) concentrated on the comparison of the effect of different cations at the same level of chloride ion dosage. The second part concentrates on the comparison of the effect of different cations at the same level of cations equivalents. Dosage efficiency, heat of hydration, strength development profiles, setting times are some of the parameters to judge the effect of the addition. The study is performed on several Portland cements prepared in the laboratory with different clinkers, which are analysed for their chemistry and mineralogy.

KEYWORDS: *Cement, Chlorides, Hydration*

1. Introduction

In cement production, the use of chemical additives to lower manufacturing costs has become normal practice worldwide. These additives can be simple grinding aids (providing decreased energy costs for grinding) or hydration activators, able to influence the reaction of cement with water. In the latter case, higher potential for savings is given by the possibility to substitute clinker with secondary cementitious materials, as for example pozzolanas, blastfurnace slag, fly ash and limestone. The use of chloride salts (traditionally, sodium and calcium chloride), often coupled with alkanolamines (as for example triethanolamine), is well-known to impart grinding effect together with early strength enhancement of cement mortars. However, most of the scientific studies have regarded the effect on concrete and have been made at such high dosages of chemicals so to be insignificant for the grinding stage addition point of view (e.g. Rapp (1935), Dodson (1990)). Particular care has been given to the effect of chlorides on concrete reinforcement bars (e.g. MJ Kim et al (2016)). A few studies concentrated on proposed mechanisms (Ramachandran (1971)) and chloride migration (Wowra & Setzer (1997)), but again at very high dosages (in the order of magnitude of units of weight %).
Other studies have been carried out on the effect of chemical activators in cement at typical cement additive dosages, but they were not specifically focused on different sources of chlorides (e.g. Huang & Shen (2011), Huang et al (2010), Katsioti (2009)).
Basically though, no agreement exists on the actual mechanism of action of chlorides, apart from the common acceptance that it is a catalytic type of mechanism, due to the very low amounts of chemicals required and their absent/minimal consumption.
At this stage, it was not the purpose of this study to inquire further about these mechanisms. On the other hand, the focus has been to verify the effect of different forms of chlorides at the typical dosages used in the cement grinding stage. The first part of this work, presented at ICCC 2019 (Forni (2019)), offered the

conclusion that the well-known early strength effect of these chemicals is confirmed. However, at dosages typical of addition during the grinding stage, this seems to be limited to 24 hours, flattening out afterwards, even as early as 2 days. The cation plays a role in the mechanism, with calcium and sodium as the most effective on strength development and heat of hydration, but only calcium able to decrease initial setting time (however limited to 12 minutes on average).

2. Experimental

2.1 Materials

The following materials were selected for the investigation:

- eight Portland cement clinkers (coded C8831, C8606, C8792, C8718, C8440, C8593, C8747 and C8669)
- a natural calcium sulfate (in dihydrate – gypsum - form)

Criteria followed in choosing were to avoid any very particular material, trying to select a wide range of clinkers with "typical" characteristics, so to be closer to the field of application. Clinkers come from different geographical areas.

2.2 Preparation and analysis methods

Clinker and gypsum were ground together in a steel-ball laboratory mill for a standard time, in the w/w ratio of 95:5. Fineness of the finished cements so prepared is comparable to the one of commercial Ordinary Portland Cements (OPCs).
Finished cements were analyzed for their chemical composition by X-Ray fluorescence (XRF), and for their mineralogical composition by quantitative X-Ray diffraction with Rietveld method. Details on the equipment and method are available upon request.
Compressive strength was measured in mortar according to standard EN-196/1, so with fixed water/cement ratio of 0.5 and standard sand/cement ratio of 3:1. Siliceous sand was used according to the norm. For the determination of strengths in the presence of chemicals, the latter were added directly in the mixing water by weighing the appropriate amount of each.
Setting time determination was carried out in paste according to standard EN-196/3. Standard consistency was determined for each cement without chemical additions, and the water/cement ratio obtained was kept constant for all determinations with different chemicals on that specific cement. Again, chemicals were added directly in the mixing water by weighing the appropriate amount of each.

2.3 Chemical additions

On each cement, the following compositions were added (dosages refer to cement weight):
1. triethanolamine (TEA) 5% and sodium chloride 17%, in demineralised water, dosage 3000 ppm
2. triethanolamine (TEA) 5% and calcium chloride 16%, in demineralised water, dosage 3000 ppm
3. combination of 1. with 3000 ppm of 12% NaOH solution
4. combination of 2. with 330 ppm of powder $Ca(OH)_2$

The concentration of the different chloride salts is such to always have 10% chloride ion (w/w) in the solutions. Dosage was dictated by the average actual use of these chemicals in practical use.
Analytical grade of all chemicals was used.

3. Results

3.1 Analytical data

XRF results of the finished cements are reported in Table 1. Full analytical results of XRD-Rietveld are available upon request. Mineralogy of the clinkers is quite varied: total C_3S is generally >58-60%, with C_2S under 20%. This is in accordance with the good level of compressive strengths and reactivity found for all the cements. Total C_3A is generally within the range 4÷7%, with a few exceptions at higher values.

Some samples contain a significant amount of orthorhombic aluminate. C_4AF content is quite varied, ranging from 7 to 12%.

Table 1 – cement XRF results (% composition)

Cement code	Na_2O	MgO	Al_2O_3	SiO_2	SO_3	K_2O	CaO	Fe_2O_3	TiO_2	P_2O_5
C8440	0.47	1.20	3.52	21.00	3.55	0.58	65.29	4.72	0.26	0.12
C8593	0.17	2.27	5.12	20.61	3.22	0.72	64.97	2.86	0.30	0.17
C8747	0.21	2.50	5.03	19.25	4.58	0.54	63.65	3.39	0.44	0.08
C8669	0.18	1.01	5.28	23.09	2.64	0.55	64.10	2.79	0.24	0.18
C8718	0.20	1.32	5.02	20.73	3.27	0.72	64.55	3.51	0.30	0.27
C8792	0.25	2.21	5.34	19.60	2.92	0.79	64.14	3.80	0.32	0.18
C8606	0.24	1.32	4.95	20.00	3.21	0.80	65.13	3.43	0.27	0.07
C8831	0.15	0.89	5.40	20.60	2.88	0.39	65.63	3.12	0.24	0.15

3.2 Compressive strengths and setting time data

Compressive strengths values (at 1, 2 and 28 days, in MPa) and setting time data (IST, initial setting time, and FST, final setting time, in minutes) are reported in Table 2.

Table 2 – mortar strength data

	Average % strength increase vs blank			Average % setting time vs blank	
	1D	2D	28D	IST	FST
blank					
TEA + NaCl	10.1	9.6	-4.2	-3.8	-11.3
TEA + $CaCl_2$	9.5	7.7	-3.5	-4.2	-14.5
TEA + NaCl + NaOH	12.2	9.1	-5.3	-11.7	-23.4
TEA + $CaCl_2$ + $Ca(OH)_2$	7.6	6.5	-5.1	-5.5	-16.2
	Averaged strength value (MPa)			Averaged setting time value (mins)	
	R1	R2	R28	IST	FST
blank	20.4	29.2	55.1	124	178
TEA + NaCl	22.3	31.4	52.7	113	151
TEA + $CaCl_2$	22.0	30.8	53.1	113	150
TEA + NaCl + NaOH	22.4	31.2	52.2	104	134
TEA + $CaCl_2$ + $Ca(OH)_2$	21.9	30.5	52.2	110	146

All cements tested (with one exception, C8440) yielded significant strength increases at 1 and 2 days with all the formulations tested. Sodium chloride mixes gave very good average gains. At 2 days, the strength enhancing effect was somewhat less. Late strength tends to decrease. As for setting times, no significant differences were apparent between sodium or calcium chloride, with an average 10 minutes acceleration. The presence of additional alkali does not seem to give any additional advantage on strength development; for sodium, data show a stronger setting time acceleration in the presence of free NaOH.

4. Conclusions

As a continuation of the study presented in ICCC 2019, the purpose of the work was to assess the effect of changing cation in chloride-based activation of cement, and specifically at dosages typical of process grinding additives used industrially in cement manufacturing. To our knowledge, no such study exists or is divulged. The first step (2019) was focused on studying the difference between sodium, calcium, and potassium chloride activation. This further step regarded the simultaneous addition of sodium or calcium chloride with a corresponding strong alkali (sodium hydroxide or calcium hydroxide). This subject is quite interesting from the application point of view, since low-carbon cement require development of new chemical activators, and alkaline activation is one of the possible routes. Exploring the effect of strong alkali at the selected dosages can clarify the range of practical use of this approach.
The present study, while confirming the favourable effect of sodium and calcium chloride as early strength activators of cement, allowed to make clear that the simultaneous addition of free sodium or calcium hydroxide at dosages typical of grinding aid additions doesn't contribute significantly to strength development. Sodium hydroxide may accelerate setting time further to the effect of sodium chloride, but the extent of this is limited.

References

Dodson V (1990). Concrete Admixtures. Van Nostrand Reinhold. pp 84-86.

Forni P (2019). ICCC 2019 proceedings.

Huang H, Shen X, Zheng J (2010). Modeling, analysis of interaction effects of several chemical additives on the strength development of silicate cement. Construction and Building Materials, Volume 24, Issue 10, pp 1937-1943.

Huang H, Shen X (2011). Statistical study of cement additives with and without chloride on performance modification of Portland cement. Progress in Natural Science: Materials International, Volume 21, Issue 3, pp 246-253.

Katsioti M, Tsakiridis PE, Giannatos P, Tsibouki Z, Marinos J (2009). Characterization of various cement grinding aids and their impact on grindability and cement performance. Construction and Building Materials, Volume 23, Issue 5, pp 1954-1959.

Kim, MJ, Kim KB, Ann KY (2016). The Influence of C3A Content in Cement on the Chloride Transport. Advances in Materials Science and Engineering, Volume 2016, Article ID 5962821.

Rapp, P (1935). Effect of calcium chloride on Portland cements and concretes. Journal of Research of the National Bureau of Standards, Volume 14, pp 499-517.

Ramachandran VS (1971). Possible states of chloride in the hydration of tricalcium silicate in the presence of calcium chloride. Mat. Constr., Volume 4, Issue 1, pp 3-12.

Wowra O, Setzer MJ (1997). Sorption of chlorides on hydrated cements and C3S pastes. Frost resistance of concrete, E & FN Spon. pp 155-162.Leung, C.K.Y. and Cao, Q. (2010) "Development of Pseudo-ductile Permanent Formwork for Durable Concrete Structures", *RILEM Materials and Structures*, 43(7): 993-1007

The 16th International Congress on the Chemistry of Cement 2023 (ICCC2023)
"Further Reduction of CO_2 -Emissions and Circularity in the Cement and Concrete Industry"
September 18–22, 2023, Bangkok, Thailand

Impact of curing time on carbonation of low-clinker binders

E. L'Hôpital[1,a*], I. Outras[1,b], and K. Malaga[1,c]

[1] *Research Institute of Sweden, Borås, Sweden*
[a]*Email: emilie.lhopital@ri.se*
[b]*Email: ilias.outras@ri.se*
[c]*Email: katarina.malaga@ri.se*

ABSTRACT

The project studies low-clinker/high-supplementary cementitious materials (SCMs) systems exposed to early-age carbonation, starting within the first week of hydration. In practice, concrete starts its field exposure and carbonation at a very young age, i.e. just a few days old. As the binders are shifted towards a lower amount of clinker and a higher amount of SCMs (which increase the carbonation risk), the investigation of the impact of carbonation on the early-age microstructures becomes increasingly relevant. The goal of the study is to identify the negative impacts of early-age carbonation to achieve good concrete with low-clinker binders. The project will investigate the impact of carbonation on a young binder containing 40% of cement, 45% of slag, and 15% of limestone. Short curing times (3 and 7 days) were compared to the regular curing time (28 days). Two different relative humidity (75 and 98 % RH) were investigated to determine the effect of the environment on the carbonation rate. For each condition, the experiments were carried out in the presence of atmospheric CO_2 and compared to a reference experiment with CO_2 free atmosphere. After 60 days of exposure, the samples were investigated at the surface and powder by XRD and TGA. The carbonation is mainly located at the surface of the samples at 98% RH as ettringite and portlandite are not observed while powder samples show a similar amount of bound water, portlandite, and CO_3. At 75% RH, portlandite remains at the surface. However, the powder sample shows a decrease in the portlandite amount and a higher carbonation rate.

KEYWORDS: *low-clinker binders, short curing time, carbonation, supplementary cementitious material*

1. Introduction

The use of SCMs (supplementary cementitious materials) in cement and concrete is a common practice for decades. In recent years, the focus has shifted towards new binders, with combinations of SCM, new types of SCM, and higher clinker substitutions to help reach the climate goals towards carbon neutrality. Nowadays, numerous studies on carbonated binders were carried out on systems relatively well-hydrated cementitious systems, after 28 days (e.g. Shah 2018) but these results might not be representative of concrete which is exposed to ambient CO_2 after a few days. Since the removal of the concrete formwork may imply an early and drastic relative humidity (RH%) drop, the immature binder becomes exposed to a combination of drying and carbonation. Early carbonation disturbs hydration kinetics, phase assemblage, and porosity, leading to changes in transports and mechanical properties (e.g. Herterich 2017, Soja 2019). This study aims to identify the impact of carbonation and RH on the microstructure of a binder containing slag and limestone with a short curing time.

2. Material and method

A binder paste containing 40% Portland cement (CEM I 52.5 R from Cementa), 45% powder granulated blast furnace slag (Merit from Swecem), and 15 % limestone (Limus 25 from Nordkalk) was mixed with a water-to-binder ratio of 0.4. The paste was cast and cured at 20ºC for 3, 7, and 28 days in 50 ml sealed plastic cylindrical molds of a diameter of 37 mm and height of 45 mm. After curing, the cylinders were cut into slices with a thickness of 4 ± 1 mm. The samples were exposed to two different relative humidity

(RH) in the presence and absence of atmospheric CO_2. The exposure chambers were airtight containers with internal ventilation to homogenize the atmosphere. The RH was maintained with saturated salt solutions of sodium chloride and potassium sulfate to obtain 75% and 98% RH respectively. For the carbonated curing chambers, the ambient air was firstly equilibrated to the appropriate RH by bubbling through the corresponding saturated salt solution and then the air was injected with a pump into the chamber. The CO_2 free curing chamber was controlled with soda lime used as a CO_2 trap.

After 60 days of exposure in a controlled chamber, the hydration of the samples was stopped by isopropanol solvent exchange. The surface of the sample was analysed by XRD. The same sample was ground and called powder sample and analysed by XRD and TGA. X-ray diffraction (XRD) was carried out by a Rigaku Miniflex 600 with a CuK*a* source and a fast 1d solid-state detector with time delay integration. The X-ray tube worked at 40kV and 15mA. The Bragg-Brentano configuration included a fixed divergence slit of 1.25 ˚ and a Soller slit of 2.5˚. The sample powder was prepared by a front-loading method in a sample holder of 1 mm deep and 4 cm diameter. The sample was scanned between 3 and 73˚ (2θ) with an increasing step of 0.02 and a scanning speed of 1˚/min.

Thermogravimetric analyses were realized with a Mettler Toledo TGA/DSC 3+. The weight loss of the samples was recorded from 30°C to 1000°C with a heating rate of 10 K/min. The bounded water was quantified from the weight loss between 30°C to 500°C and the $CaCO_3$ between 500°C and 850°C. If the weight loss of calcite is observed around 680ºC, vaterite and aragonite are observed at earlier temperatures ranging around 500˚C, as shown by previous research (Vogler 2022). The different amounts of bound water (BW), portlandite (CH), and $CaCO_3$ are calculated as shown in equations 1, 2, and 3.

$$BW_{\text{measured, per 100g anhydrous}} = \frac{WL_{BW} * 100}{100 - WL_{BW}} \quad (1)$$

$$CH_{\text{measured, per 100g anhydrous}} = \frac{WL_{CH} * 100}{100 - WL_{BW}} x \frac{74\ (M_{CH})}{18\ (M_{water})} \quad (2)$$

$$CaCO_{3\ \text{measured}} = WL_{CaCO_3}\ x\ \frac{100}{44} \quad (3)$$

3. Results and discussion

The diffractograms of the sample's surface are shown in Figure 1. In the absence of CO_2, calcite is associated with the presence of limestone in the binder. In the presence of atmospheric CO_2, calcite and vaterite are observed at both RH, while aragonite is only observed at 75% RH. In addition to limestone, calcite is strongly associated with the carbonation of portlandite (Steiner 2020). At 98% RH, the portlandite is below the detection limit indicating that the portlandite was dissolved. At 75% RH, portlandite is detected in all the samples. It confirms the fact that the effect of carbonation on other hydrates can start before the complete consumption of portlandite. Vaterite and aragonite are associated with the carbonation of hydrates such as calcium silicate hydrate (C-S-H) and ettringite (Steiner 2020). Ettringite is dissolved and cannot be observed in the presence of CO_2, while it is present in CO_2 free atmosphere after 7 and 28 curing at 75% RH. Moreover, a small hump at 20.7º 2θ could be explained by a trace of gypsum that would agree with the carbonation of ettringite. At 98% RH, most of the ettringite is carbonated after 28 days of curing as only some traces are visible after carbonation while it is present in the CO_2-free sample.

The results of the powder samples are presented in Figure 2 and Table 1. In the absence of CO_2, no significant difference is observed between the samples. Similar hydrates, amount of bound water, portlandite, and $CaCO_3$ are observed. In the carbonated sample, calcite is observed at both RH but vaterite is observed as a trace, only at 98% RH. However, the TGA shows a similar amount of bound water, portlandite, and $CaCO_3$ at different curing times in the presence and absence of CO_2 meaning that the carbonation is relatively low. At 75% RH, when the curing time decreases from 28 days to 3 days, the bound water decreases by 39%, the amount of portlandite decreases by 51 % and the amount of $CaCO_3$ increases by 31%. The 7 days curing shows a great improvement towards carbonation as bound water and portlandite are reduced by 22% and 19% respectively, whereas $CaCO_3$ increases by 11%. The increase of $CaCO_3$ is linked to the dissolution of portlandite and ettringite; and the precipitation of calcite, vaterite,

and aragonite. In the powder samples, vaterite and aragonite are below the detection limit meaning that the presence is mainly at the surface of the sample.

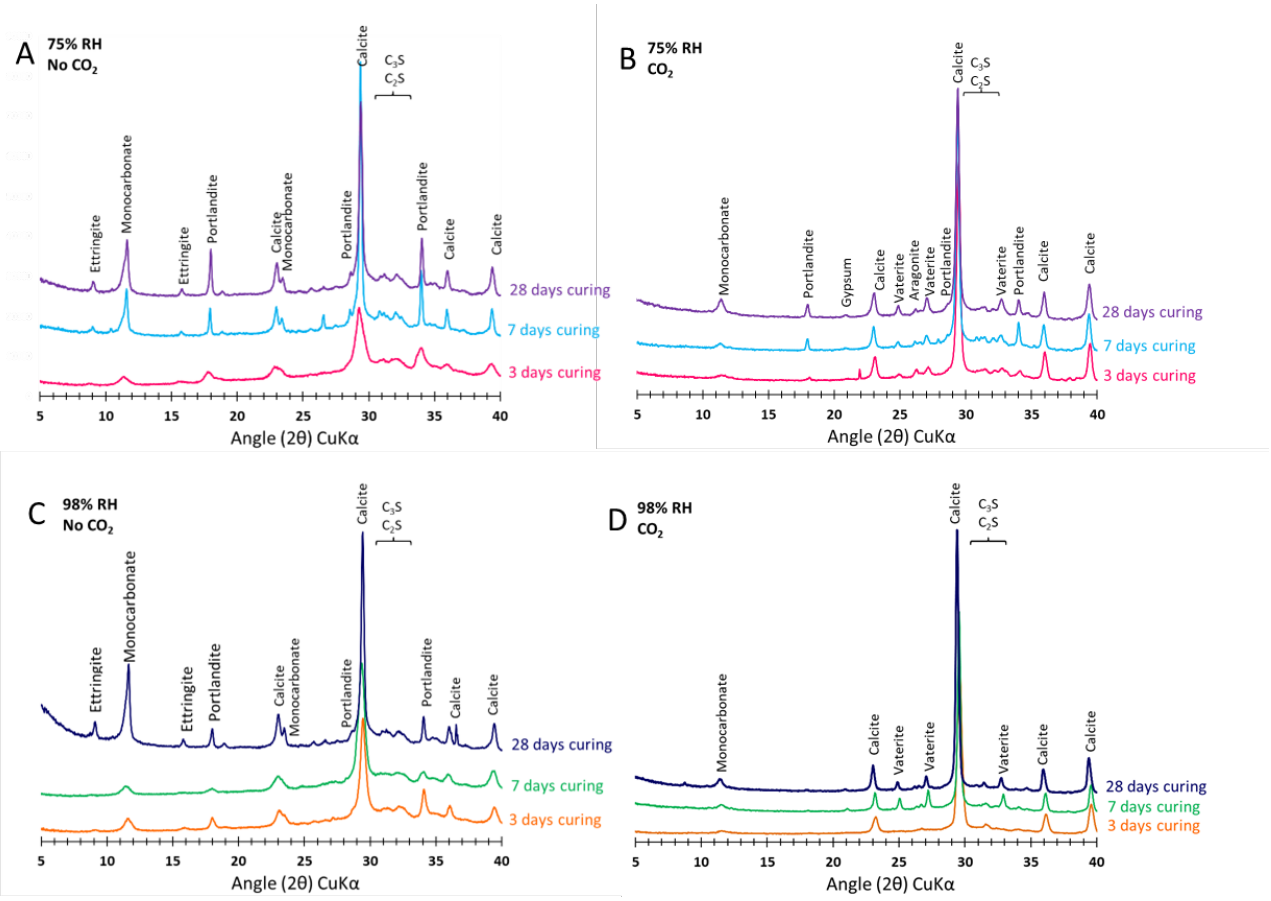

Figure 1: Diffractogram of the investigated samples on the surface cured for 3,7 and 28 days at 75%RH and no CO_2 (A), 75%RH and CO_2 (B), 98%RH and no CO_2 (C). 98%RH and CO_2 (D)

Table 1: Quantification in wt% of bound water (BW), portlandite (CH), and $CaCO_3$ realized by TGA.

RH (%)	Test age (Days)	Absence of CO_2			Presence of CO_2		
		BW	CH	$CaCO_3$	BW	CH	$CaCO_3$
75	3	16	7.8	19	9.4	3.1	31
	7	16	8.1	19	12	5.1	26
	28	17	7.8	18	15	6.4	23
98	3	17	7.5	18	15	5.8	23
	7	17	8.1	18	15	5.6	24
	28	18	9.0	17	16	5.6	22

4. Conclusions

At 98% RH, the sample surface is fully carbonated. However, a similar amount of bound water, portlandite, and $CaCO_3$ regardless of the curing time, meaning that the carbonation is rather low. At 75% RH, vaterite, aragonite, and a trace of gypsum are observed at the surface together with portlandite. It shows that carbonation of other hydrates such as C-S-H and ettringite can occur while portlandite is still present. Even if cement hydrates are observed at the surface, the amount of portlandite significantly drops whereas the amount of $CaCO_3$ increases in the powder sample with the reduction of the curing time meaning that the carbonation of the sample is higher than at 98%.

More investigation is needed on the short curing time of binders toward carbonation. This work is part of an ongoing study that investigates different binder systems containing slag, slag-limestone and fly ash-limestone mixes; and will be extended to slag-fly ash-limestone, calcinated clay-limestone, and bio ash binders. The carbonation will be studied for a longer time and also on mortar to determine the impact on compressive strength.

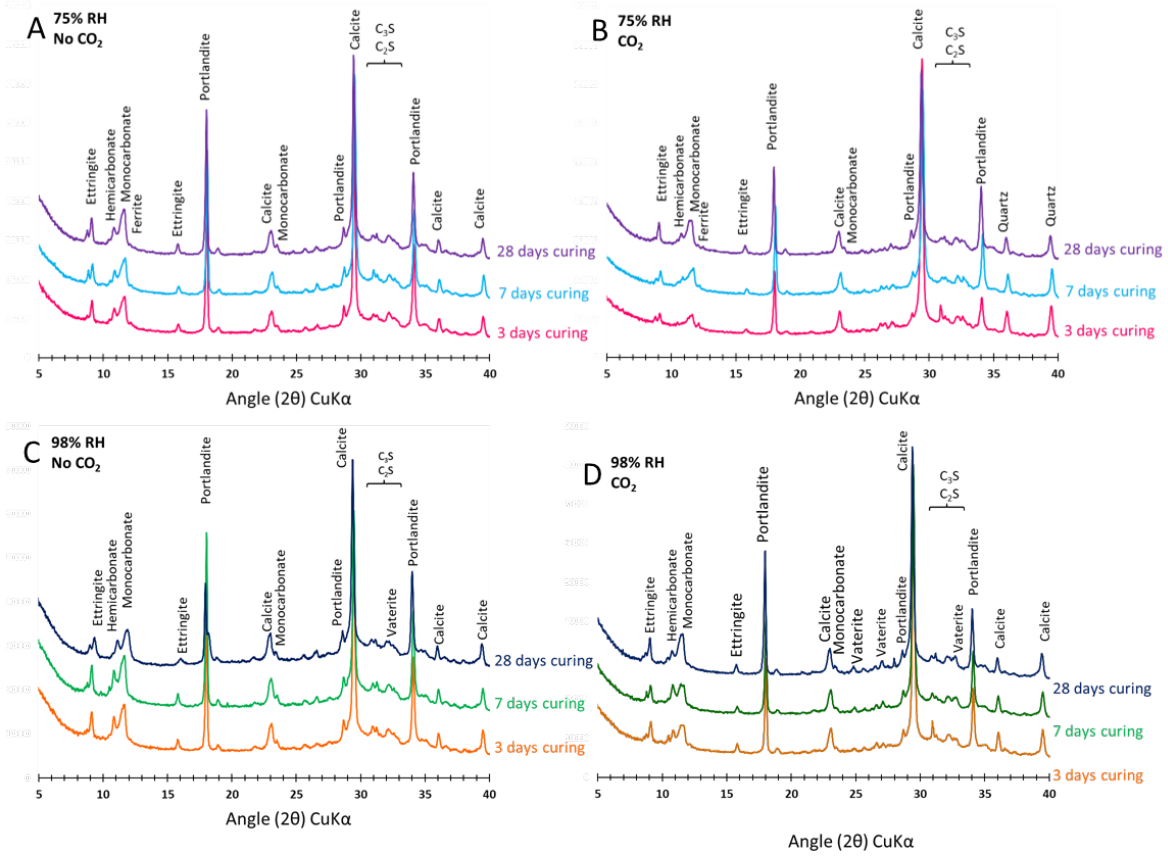

Figure 2: Diffractograms of powder samples cured for 3,7 and 28 days at 75%RH and no CO_2 (A), 75%RH and CO_2 (B), 98%RH and no CO_2 (C). 98%RH and CO_2 (D)

Acknowledgments

The project is co-funded by RISE and the Consortium for the Financing of Fundamental Concrete Research (consisting of Cementa, Thomas Betong, ABetong, Strängbetong, Betongindustri, and Swerock), which is warmly acknowledged here.

References

Herterich, J. (2017). Microstructure and phase assemblage of low-clinker cements during early stages of carbonation, *Doctoral dissertation*, University of Leeds.

Shah, V., Scrivener, K., Bhattacharjee, B., & Bishnoi, S. (2018). Changes in microstructure characteristics of cement paste on carbonation. *Cement and Concrete Research*, 109, 184-197.

Soja, W. (2019). Carbonation of low carbon binders, *Doctoral dissertation No.9400*. EPFL.

Steiner, S., Lothenbach, B., Proske, T., Borgschulte, A., & Winnefeld, F. (2020). Effect of relative humidity on the carbonation rate of portlandite, calcium silicate hydrates and ettringite. *Cement and Concrete Research*, 135, 106116.

Vogler N., Drabetzki P., Lindemann M., Kühne H.C. (2022). Description of the concrete carbonation process with adjusted depth-resolved thermogravimetric analysis. *Journal of Thermal Analysis and Calorimetry*, Vol. 147, pp. 6167-6180.

The 16th International Congress on the Chemistry of Cement 2023 (ICCC2023)
"Further Reduction of CO_2 -Emissions and Circularity in the Cement and Concrete Industry"
September 18–22, 2023, Bangkok, Thailand

Quantitative microstructure analysis of SCM-blended cementitious materials through deep learning-based computer vision methods

YAN Yu[1], GENG Guoqing[1*]

[1] *Department of Civil and Environmental Engineering, National University of Singapore, Singapore*
Email: yan_yu@nus.edu.sg, ceegg@nus.edu.sg

ABSTRACT

Supplementary cementitious materials (SCM) are increasingly used in concrete owing to the carbon footprint and economic reasons. The characterization of SCMs, for example the reaction degree and the distribution of hydration products, are essential to estimate the systems' properties. However, a reliable morphological study at microscale requires the analysis of large quantities of SEM-BSE images, which is impractical to be investigated by human eyes. Moreover, the chemical and mineralogical complexity of SCM phases makes the analysis rather qualitative. In this study, the microstructure of white cement paste with/without SCM (limestone, slag, quartz and metakaolin), has been investigated. We explore the application of multiple advanced deep learning-based image processing algorithms on the SCM-blended BSE images. Pixel-level semantic segmentation models based on U-Net architecture and ResNet backbone can robustly segment limestone, quartz and slag particles from complicated BSE images. Image enhancement methods including image denoising, super-resolution further help to optimize the image quality and improve the accuracy of phase assemblage. By automating the segmentation process and enhancing image quality, valuable insights into SCM phase microstructure and distribution within cement paste can be obtained, contributing to a better understanding of the properties and performance of SCM-based concrete systems.

KEYWORDS: *Supplementary cementitious materials, image processing, deep learning, segmentation*

1. Introduction

The scanning electron microscope (SEM) plays a crucial role in investigating the microstructure of modern concrete. The quantification of phase composition within the cement matrix is commonly achieved through the segmentation of BSE images using threshold methods based on grayscale values derived from the average atomic number of local areas (Scrivener 2004). However, determining fixed threshold values for image analysis proves impractical due to the substantial impact of sample preparation techniques and image acquisition parameters. Furthermore, conducting a thorough morphological analysis necessitates the examination of a considerable number of images, thereby increasing the time required for analysis. Nowadays, in the pursuit of greener, more cost-effective, and durable concrete, the utilization of supplementary cementitious materials (SCMs) has gained prominence. SCMs, in comparison to clinker minerals, exhibit relatively lower average atomic numbers (Snellings, Mertens, and Elsen 2012), resulting in the grey value distribution of SCM phases being closer to that of hydration products. Consequently, the segmentation of SCM particles and the corresponding hydration products present significant challenges in image analysis.

Recently, the advancement of deep learning, particularly computer vision technology, has revolutionized pixel-level microscopic image segmentation in materials science (Ge et al. 2020; Midtvedt et al. 2021). In this study, we investigate the potential of advanced deep learning-based image processing algorithms for segmenting complex BSE images of SCM-blended cement. Additionally, we explore the effectiveness of other deep learning-based image enhancement techniques, including denoising and super-resolution, to improve the accuracy of SCM particle segmentation in BSE images. By leveraging these cutting-edge

approaches, we aim to enhance the analysis and understanding of SCM-blended cement microstructures, paving the way for more accurate and efficient characterization of these materials.

2. Materials and methods

White Portland cement (manufactured by MAPEI) was used as the binding phase. The mineralogical composition measured by XRD are as follows: 54.6% C_3S, 28.9% C_2S, 1.2% C_3A, 0.7% C_4AF, 9.2% calcite, 4.6% gypsum. Four types of supplementary cementitious materials, namely limestone, metakaolin, quartz and slag, were used to prepare SCM-blended cement paste. A water-to-solid ratio of 0.45 was used to prepare all cement pastes. All experiments were carried out at 25 ± 2 °C.

Hitachi Regulus 8230 FE SEM was used to capture backscattered electron microscopic images of SCM-blended cement pastes. All the samples were studied at a voltage of 15 kV with a YAG detector. the magnification was set at 200 times. The image resolution was fixed at 5120 × 3840, with a 0.125 μm pixel resolution. In this study, we employed APEER by Zeiss (https://www.apeer.com) for manual annotation of the BSE images. Subsequently, the raw images and annotated masks were cropped and organized into 280 image pairs, each with a resolution of 256 × 256 pixels. To augment the dataset, various techniques such as image rotation, flipping, blurring, and noise addition were applied. The resulting dataset consisted of 7560 image pairs, which were used for training the networks. The training and validation images were split in a ratio of 9:1, ensuring robust model training and evaluation.

We used U-Net (Ronneberger, Fischer, and Brox 2015) as the architecture of semantic segmentation CNN model and replaced the encoder part with ResNet (He et al. 2016) using Segmentation Models (Iakubovskii 2019) (version 0.2.1). To compare the results, trainable Weka segmentation (TWS) (Arganda-Carreras et al. 2017) with a random forest classifier, a plugin from ImageJ, was also used to segment SCM particles from BSE images. ImageJ was also used for noise addition (standard deviation=15) and image resolution adjustment (bilinear interpolation) during denoise and super-resolution model training. A DnCNN model (Zhang et al. 2017) and a ESRGAN mode (Wang et al. 2018) were used to remove noise and enhance image resolution of BSE images. All the experiments in the present study were developed under Python 3.9.7, TensorFlow 2.9.1, CUDA 11.8 and performed on a workstation with a single graphics processing unit (Quadro RTX 4000).

3. Results and discussion

Figure 1 (a) to (c) provides an overview of the microstructure of SCM particles and illustrates the impact of SCM addition on the greyscale value of white cement paste. Cement particles exhibit distinctive characteristics that facilitate image segmentation, including a narrow distribution of greyscale values, a noticeable difference in greyscale values compared to adjacent phases, and being surrounded exclusively by inner C-S-H with a uniform greyscale distribution. Notably, characteristic peaks of anhydrous cement are discernible from the histogram. However, with the addition of SCMs, the transition between adjacent characteristic peaks becomes less prominent. From the perspective of single particle morphology, the transition from SCM particles to hydrated cement paste is less abrupt compared to cement particles, presenting as a weak-feature area spanning several pixels in width. Consequently, thresholding segmentation becomes disabled for SCM-blended systems. Metakaolin particles, due to their smaller size and orientation, exhibit minimal differences in greyscale values from the surrounding phases, posing difficulties even for experienced researchers to identify them visually. Therefore, relying solely on graphic information renders metakaolin segmentation unreliable.

Figure 1 (d) demonstrates the segmented outputs from the trained U-Net model with ResNet 101 backbone. Remarkably, an intersection over union (IOU) exceeding 0.9 can be easily achieved after 50 epochs of training. In most cases, limestone, quartz, and slag particles can be successfully segmented, even when they possess indistinct boundaries and exhibit similar greyscale distributions as the surrounding phases. Notably, all the BSE images of SCM-blended samples were raw images without adjustments to greyscale values and contrast. Deep learning models can reasonably segment SCM particles from a high-resolution 4k × 4k pixel BSE image within seconds. In comparison, traditional watershed segmentation (TWS) assists in approximating the location of larger particles, but it fails to provide satisfactory labeling for small particles and accurate boundaries for larger particles. As depicted in Figure 1 (e), TWS exhibits a relatively significant error of approximately 35%, whereas the utilization of deep learning models significantly

enhances accuracy to over 80%. Overall, the segmentation accuracy follows the order of limestone > quartz > slag. Notably, the segmentation error of deep learning models is highly sensitive to the edges of SCM particles and increases exponentially with every one percent increment in edge error.

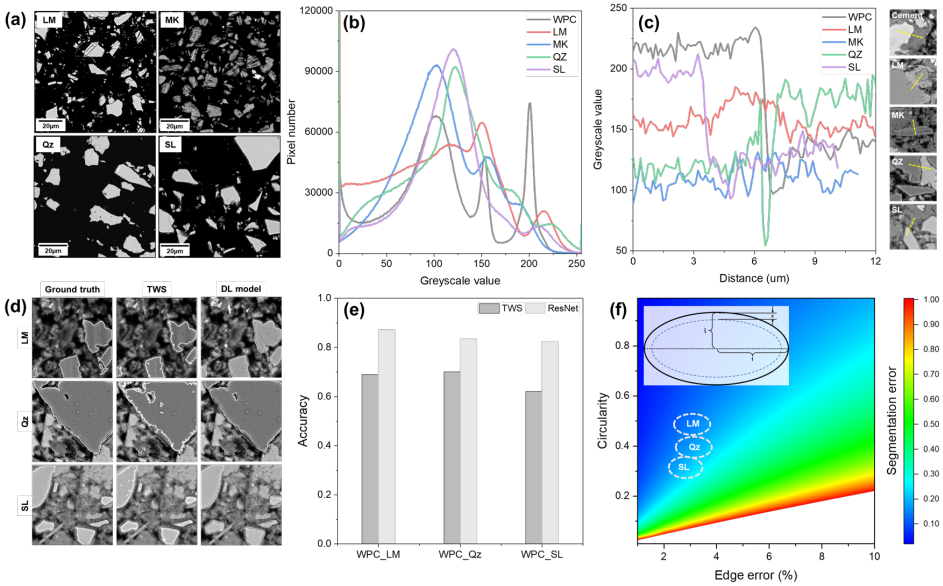

Figure 1 (a) BSE images of raw SCM particles. (b) Greyscale value distribution of WPC-blended paste with different SCMs. (c) Grey value change over the boundary of abovementioned particles in the cement paste. (d) Segmentation of limestone, quartz, and slag particles with TWS and deep learning model. (e) Segmentation accuracy compared to QXRD (limestone and quartz) and EDS mapping result (slag). (f) The effect of circularity and edge error on the accuracy of segmentation results.

In order to enhance the accuracy of segmentation, we implemented two additional models, namely the denoise model and the resolution enhancement model, to optimize the quality of the input image. Figure 2 illustrates the results obtained after denoising, where a more uniform greyscale value is observed within the SCM particles. The grayscale distribution diagram reveals distinct characteristic peaks atop the broader peaks of hydration products, predominantly portlandite and C-S-H. While the presence of these characteristic peaks does not simplify the problem to a mere threshold segmentation, the denoising process aids in enhancing the grayscale features of SCM particles and sharpening their edges.

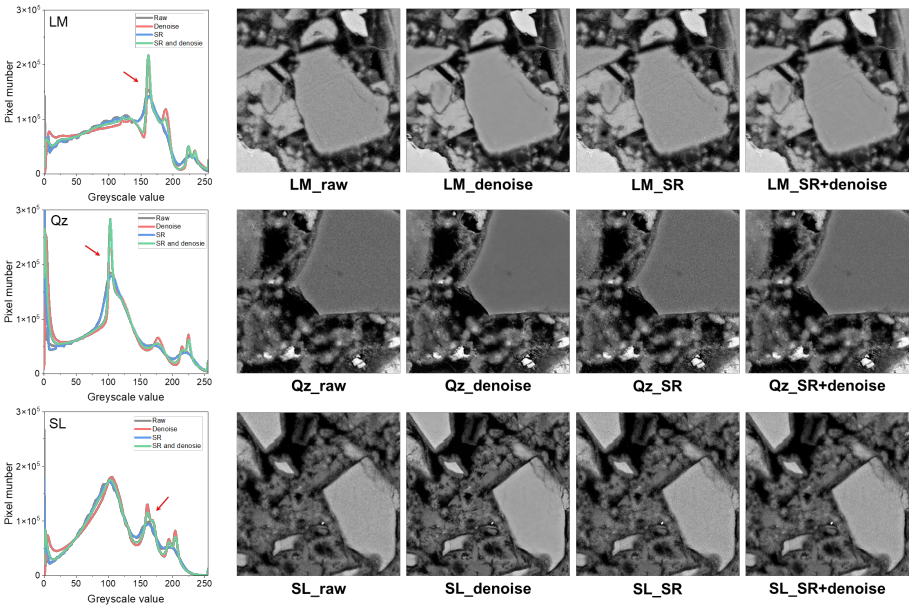

Figure 2 Example application of denoise and resolution enhancement models on BSE images of SCM particle.

On the other hand, the resolution enhancement has a limited impact on the greyscale value distribution of the BSE image. However, the output image consistently exhibits superior visual quality, displaying more realistic and natural textures on the edges of SCM particles when compared to the original image. Consequently, the transition between SCM particles and the background becomes more discontinuous, which proves advantageous for the semantic segmentation task. By combining image enhancement as a pre-processing step with deep learning-based semantic segmentation, we present a promising approach for effectively segmenting SCM particles from BSE images.

4. Conclusions

This study explored the potential application of deep leaning techniques in processing BSE image of complex SCM-blended cement paste, a task that cannot be effectively achieved through traditional thresholding methods. Four types of SCMs, including limestone, slag, quartz, metakaolin were analyzed. While metakaolin proved challenging to accurately segment based solely on graphical information, the remaining three SCMs exhibited robust segmentation with an accuracy of over 80% compared to QXRD. By employing denoise and resolution enhancement models, the grayscale features of SCM particles were enhanced, and the impact of edge errors on overall segmentation accuracy was reduced. These findings underscore the efficacy of deep learning techniques in improving the segmentation process of SCMs in complex cementitious materials, thereby highlighting their potential for advancing the field of cement research.

Acknowledgements

This research is funded by Singapore Minister of Education Tier 1 project under WBS A-0009288-01-00.

References

Arganda-Carreras, Ignacio, Verena Kaynig, Curtis Rueden, Kevin W Eliceiri, Johannes Schindelin, Albert Cardona, and H Sebastian Seung. 2017. “Trainable Weka Segmentation: A Machine Learning Tool for Microscopy Pixel Classification.” *Bioinformatics* 33 (15): 2424–26.

Ge, M., F. Su, Z. Zhao, and D. Su. 2020. “Deep Learning Analysis on Microscopic Imaging in Materials Science.” *Materials Today Nano* 11. https://doi.org/10.1016/j.mtnano.2020.100087.

He, Kaiming, Xiangyu Zhang, Shaoqing Ren, and Jian Sun. 2016. “Deep Residual Learning for Image Recognition.” In *Proceedings of the IEEE Conference on Computer Vision and Pattern Recognition*, 770–78. https://doi.org/10.1002/chin.200650130.

Iakubovskii, Pavel. 2019. “Segmentation Models Pytorch.” GitHub. 2019. https://github.com/qubvel/segmentation_models.pytorch.

Midtvedt, Benjamin, Saga Helgadottir, Aykut Argun, Jesús Pineda, Daniel Midtvedt, and Giovanni Volpe. 2021. “Quantitative Digital Microscopy with Deep Learning.” *Applied Physics Reviews* 8 (1). https://doi.org/10.1063/5.0034891.

Ronneberger, Olaf, Philipp Fischer, and Thomas Brox. 2015. “U-Net: Convolutional Networks for Biomedical Image Segmentation.” In *International Conference on Medical Image Computing and Computer-Assisted Intervention*, 234–41. Springer.

Scrivener, Karen L. 2004. “Backscattered Electron Imaging of Cementitious Microstructures: Understanding and Quantification.” *Cement and Concrete Composites* 26 (8): 935–45. https://doi.org/10.1016/j.cemconcomp.2004.02.029.

Snellings, Ruben, Gilles Mertens, and Jan Elsen. 2012. “Supplementary Cementitious Materials.” *Reviews in Mineralogy and Geochemistry* 74 (Blezard 2001): 211–78. https://doi.org/10.2138/rmg.2012.74.6.

Wang, Xintao, Ke Yu, Shixiang Wu, Jinjin Gu, and Yihao Liu. 2018. “ESRGAN: Enhanced Super-Resolution Generative Adversarial Networks.” *Proceedings of the European Conference on Computer Vision (ECCV) Workshops*, 1–16.

Zhang, Kai, Wangmeng Zuo, Yunjin Chen, Deyu Meng, and Lei Zhang. 2017. “Beyond a Gaussian Denoiser: Residual Learning of Deep CNN for Image Denoising.” *IEEE Transactions on Image Processing* 26 (7): 3142–55. https://doi.org/10.1109/TIP.2017.2662206.

The 16th International Congress on the Chemistry of Cement 2023 (ICCC2023)
"Further Reduction of CO_2 -Emissions and Circularity in the Cement and Concrete Industry"
September 18–22, 2023, Bangkok, Thailand

Effect of steam curing on the hydration of limestone calcined clay cements (LC^3) with low kaolinite content

Y. Hu[1] and G. Geng[1*]

[1] *Department of Civil and Environmental Engineering, National University of Singapore, 117576, Singapore*
Email: yc_hu@nus.edu.sg
**Email: ceegg@nus.edu.sg*

ABSTRACT

Limestone calcined clay cement (LC^3) is one of the promising blended cements with good performance (strength and durability) at a significantly low clinker content. However, early strength of LC^3 is usually lower than OPC concrete because of the reduced early stage cementing reaction. This study presents the influence of steam curing of 80 °C for 6h on the strength development and hydration of LC^3 containing low kaolinite content (less than 40%). Blends of different ratios of replacement level of clinker (30% and 50%) were employed at fixed w/c ratio. XRD were employed to detect the formation of hydration products to evaluate the degree of hydration. Results indicated that the early strength of steam curing samples of LC^3 would be higher than normal curing ones because of the acceleration of OPC hydration and pozzolanic reaction due to higher temperature. However further strength development of steam curing ones is not so significant from three days onwards. Detailed investigation on the hydration reveals that this issue is related to the slowing down of clinker hydration and conversion of ettringite and carboaluminate, which influence the pore structure and strength development significantly at later stage.

KEYWORDS: *LC^3, Steam curing, SCM, Hydration, Compressive Strength*

1. Introduction

Supplementary cementitious materials (SCM), like slag and fly ash, have been extensively studied and used to partially replace ordinary Portland cement (OPC). However, these materials are not always available in countries with limited industry scale, such as Singapore. Clay, abundant globally and generated as waste from excavation works before, has pozzolanic reactivity when its metakaolin (MK) component is activated at 700 °C (Fernandez, 2016). Moreover, limestone powder (LS) is commonly used as a filler to improve the performance of cementitious materials and (Scrivener et al.,2018) suggests that the calcite in limestone can interact with C_3A in clinker and metakaolin, forming stronger phases with better stability. This has led to the production of a new type of promising blended cement called limestone calcined clay cement (LC^3), which has significantly reduced clinker content and demonstrates good performance of strength and durability.

However, according to (Avet and Scrivener, 2018), the early strength of LC^3 is not satisfactory due to limited clinker hydration, which can be improved through steam curing. Steam curing (A.C. 517) is a method of heat curing with high moisture content that accelerates cement hydration. It leads to the rapid development of strength by increasing the rate of cement hydration through higher temperature and longer curing periods. Until now, the performance of cementitious materials blended with a combination of low-grade clays and LS under steam curing conditions is not well understood. Therefore, this study aims to leverage the high reactivity of LC^3 and its synergistic effect with limestone powder to achieve desirable early age mechanical properties.

2. Materials and methods

Marine clay samples from Singapore were excavated and treated as follows: oven-dried at 80°C for 48h, pre-milled in a ball miller at 300 rpm/min for 20 min. The kaolinite content of marine clays was found to be less than 20% after characterization. To address this, the marine clays were mixed with Kaolin clay (purchased from Kaolin SDN BHD, with a kaolinite content of 58%) using ball milling for 10 min, resulting in a mixture with a kaolinite content of 38% (determined by XRD/Rietveld). The mixture was then calcined at 700°C for two hours and cooled to room temperature. In addition, this study also used OPC (CEM I 52.5N), limestone, gypsum, and natural sands.

A mixture of calcined clay and limestone, in a weight ratio of 2:1 (Scrivener et al.,2018), substituted 50% and 30% of OPC (named LC^3_50 and LC^3_70 in this study). In accordance with Scrivener et al. (2018), a combination of calcined clay and limestone was used as a substitute for Ordinary Portland Cement (OPC) in the ratios of 2:1 by weight. This substitution resulted in two variants: LC^3_50, where 50% of OPC was replaced, and LC^3_70, where 30% of OPC was replaced. Gypsum was added at a 2% content to control flash setting, determined through preliminary calorimetry trials. Compressive strength of mortar was evaluated using 40 mm cube samples with a water:binder:sand weight ratio of 0.4:1:2.75, following ASTM C109 guidelines. Workability was enhanced by adjusting the superplasticizer (SP) content. After casting, half of the cubes were steam cured as depicted in Fig 1, after which all specimens were then placed in a fog room (30 °C, 100% RH) until testing ages of 1, 3, 7, and 28 days. Cement pastes with a w/c ratio of 0.4 were prepared for XRD tests. They were ground into powders to analyze the quantities of portlandite, ettringite, and AFm formed. To compensate for the presence of amorphous phases, the internal standard method employed 20 wt.% pure fluorites. Rietveld refinement was performed using the HighScore Plus v5.1 software.

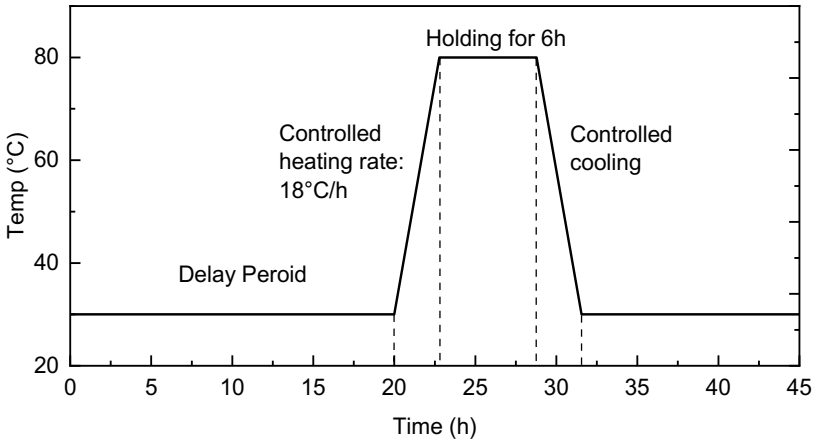

Fig. 1. Steam curing process in this study.

3. Results

3.1 Compressive Strength

The compressive strength variation of different mixes, both normal and steam curing, up to 28 days is depicted in Figure 2. The inclusion of clay and limestone as cement replacements led to a decrease in strength at early and late ages compared to the reference mix, regardless of the curing conditions. Notably, the effect of steam curing was significantly pronounced at 1 day for all three mixes, exhibiting a substantial strength improvement of over 30%. Particularly, LC^3_50 mix showed a remarkable doubling of strength in steam curing samples compared to those curing under normal conditions. However, this enhanced effect became relatively stable at day 3, in which only LC^3_50 showing a 27% improvement compared to the normal curing samples. Concurrently, the strength of steam curing specimens declined compared to the day 1 strength. There are two main factors contributing to this phenomenon. Firstly, the rapid evaporation of internal moisture due to high temperature hinders the ongoing hydration process. Secondly, elevated temperature stress induces the enlargement of pores in the outer layer and leads to the formation of cracks in the interfacial transition zone (Shi et al.,2021). As the curing period progressed beyond 3 days, the

strength of steam curing samples consistently remained lower than their counterparts subjected to normal curing. This effect persisted until the 28 days, where the strength began to rise again. At this stage, the compressive strengths of LC^3 samples approached those of the normal curing samples, while the strength of OPC was 23% lower than that of the normal curing samples. Meanwhile, in both curing conditions, the strength of LC^3 blends at 28 days are similar regardless of the replacement level.

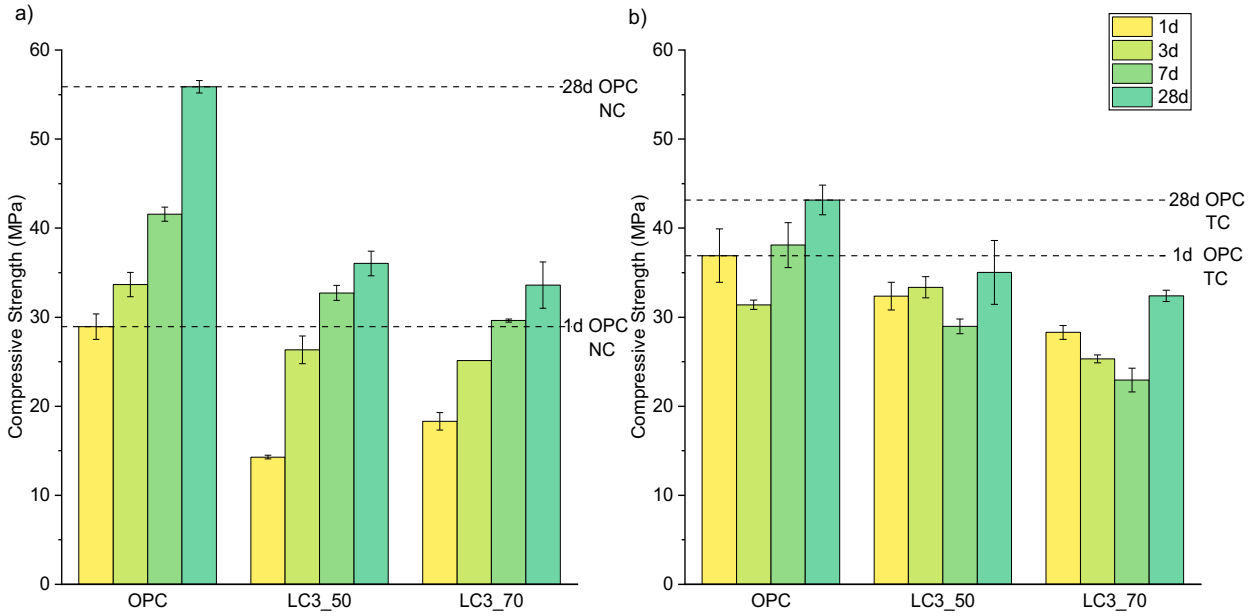

Fig. 2. Compressive Strength development of a) Normal Curing and b) Steam Curing samples.

3.2 Hydration Products

In Figure 3, the portlandite content in the pastes is shown from 3 days to 28 days, which reflecting clinker hydration and pozzolanic reaction to some extent. The reference mix consistently exhibits the highest portlandite content until 28 days, with a slower rate of increase between 3-7 days, similar to the trend in strength development. In LC^3 blends, the portlandite content initially increases from 3-7 days, indicating dormant clinker hydration, but decreases after 7 days as more metakaolin starts to form C-A-S-H in presence of more of generated portlandite until 28 days.

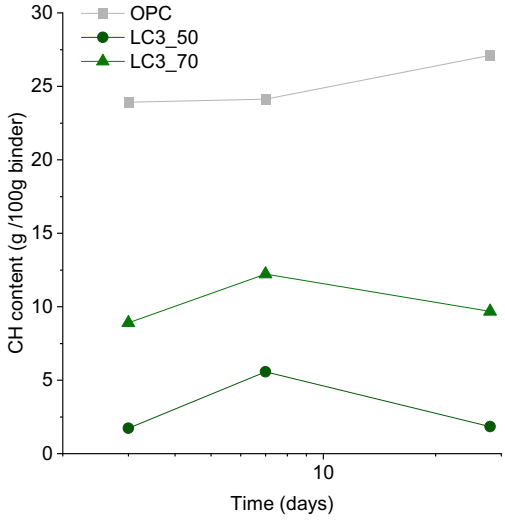

Fig. 3. Portlandite quantification by XRD as a function of time of steam-curing samples.

Figure 4(a), (b), and (c) present XRD plots of the paste samples at 3, 7, and 28 days, respectively. The presence of peaks corresponding to ettringite (AFt), monosulphate (Ms), hemicarboaluminate (Hc), and

monocarboaluminate (Mc) in the blended mixes indicates synergistic reactions between OPC, limestone, and metakaolin.

By comparing the intensity of four peaks, significant transformations of ettringite and CO_3-Afm to monosulphate can be observed over time. In OPC samples, the amount of ettringite and monosulphate increases gradually. In contrast, for LC^3 blends, ettringite and monosulphate coexist at low levels at 3 days. At 7 days, there is a higher content of ettringite and CO_3-AFm, while monosulphate disappears. Finally, at 28 days, the monosulphate content significantly increases while ettringite decreases and CO_3-AFm disappears. This indicates that steam treatment significantly destabilizes ettringite and CO_3-AFm, causing them to degrade rapidly into sulphate-AFm. This degradation process can result in delayed ettringite formation and subsequent volumetric expansion, which ultimately affects the development of strength.

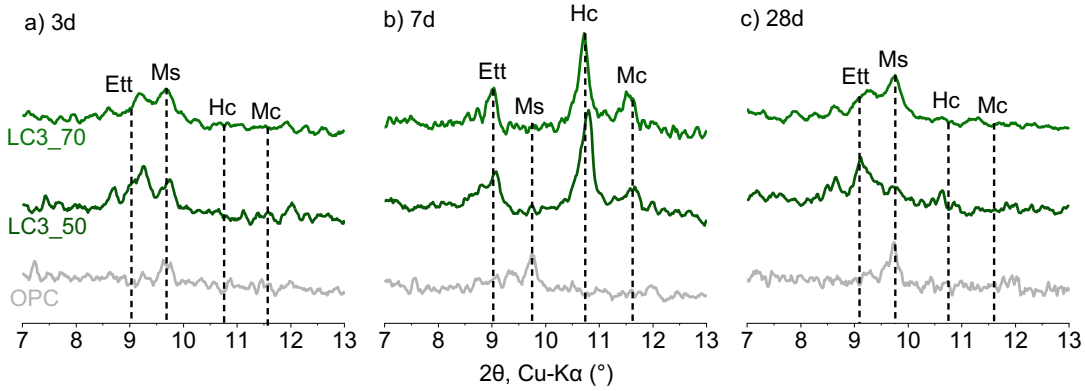

Fig. 4. XRD patterns at a)3 days, b) 7 days, and c) 28 days of hydration for steam-curing samples.

4. Conclusions

This study holds great significance as it provides evidence that steam curing at high temperatures effectively enhances the early stages strength (> 2 times of strength at 1 day for LC^3_50 samples using low-grade clays). However, it is important to note that as the curing period progressed, the positive impact of steam curing diminished, and in some cases, it even had a negative influence on the strength development.

Analyzing the hydration products provides valuable insights into the intricate relationship between hydration and strength development in OPC and LC^3 blends. Following the acceleration due to steam curing, the degree of hydration inhibits, impacting the overall hydration process. Additionally, there is a gradual transformation of ettringite and CO_3-Afm into monosulphate over long-term, resulting in less stable components in the bulk that affect the strength.

References

ACI Committee 517. (1992) "Accelerated Curing of Concrete at Atmospheric Pressure: State of the Art." American Concrete Institute.

Avet, F., and Scrivener, K., (2018) "Investigation of the calcined kaolinite content on the hydration of limestone calcined clay cement (LC^3)", *Cement and Concrete Research*, 107,124-135

Fernandez, R., Martirena, F., Scrivener, K.L., (2011) "The origin of the pozzolanic activity of calcined clay minerals: a comparison between kaolinite, illite and montmorillonite", *Cement and Concrete Research*, 41, 113-122

Scrivener, K., Martirena, F., Bishnoi, S., Maity, S., (2018) "Calcined clay limestone cements (LC^3)", *Cement and Concrete Research* ,114, 49-56

Shi, J.Y., Liu, B.J., Zhou, F., Shen, S., Guo, A., Xie, Y., (2021) "Effect of steam curing regimes on temperature and humidity gradient, permeability and microstructure of concrete", *Construction and Building Materials,* 281,122562

The 16th International Congress on the Chemistry of Cement 2023 (ICCC2023)
"Further Reduction of CO_2 -Emissions and Circularity in the Cement and Concrete Industry"
September 18–22, 2023, Bangkok, Thailand

A comparative study of tribometer rotor configurations and analytical methods for concrete pumping pressure prediction

Fumin Li[1, 2, 3, a], Qiang Yuan[4, b], Caijun Shi[1, 2, 3, c*]

[1]*College of Civil Engineering, Hunan University, Changsha 410082, China*

[2]*Key Laboratory for Green & Advanced Civil Engineering Materials and Application Technologies of Hunan Province, Changsha 410082, China*

[3]*International Innovation Center for Green & Advanced Civil Engineering Materials of Hunan Province, Changsha 410082, China*

[4]*School of Civil Engineering, National Engineering Research Center of High-Speed Railway Construction, Central South University, Changsha 410075, China*

[a]*lifumin@hnu.edu.cn*

[b]*yuanqiang@csu.edu.cn*

[c]*cshi@hnu.edu.cn*

ABSTRACT

Pumping of highly flowable concrete (HFC) is a vital construction technique. Tribometers have been designed to provide rheological data for pumpability assessments. Meanwhile, various analytical methods are claimed to have sound accuracy in predicting the pumping pressure loss for concrete. Naturally, curiosities are aroused in which combination of analytical method and measuring apparatus predicts pumpability result that better agrees with the actual flow behavior for highly flowable concrete. To examine this issue, a total of 60 HFC mixtures are pumped at constant flow rates in a 280-meter-long pipeline. Test results reveal that tribometer and rheometer with cone-shape rotor produce pressure prediction results that are almost 6 times more accurate than those with cylindrical-shape rotor. Both assuming constant rheological properties, Kaplan method is more accurate than Kwon method when using results by the cone-shape rotor, but less accurate when using results by the cylindrical-shape rotor.

KEYWORDS: *Highly flowable concrete (HFC); pumping pressure prediction; tribometer; pumpability*

1. Introduction

Sound pumping pressure loss prediction has been a crucial parameter to ensure the successful pumping of concrete. Among many prediction methods, Kaplan method and Kwon method are two commonly cited ones and both of them requires lubrication layer properties as inputs (Kaplan et al., 2005; Kwon et al., 2013b). On the one hand, the applicability and accuracy of both methods need to be studied and compared against a long-distance pumping setup, which has become increasingly popular in the construction industry. On the other hand, the answer to what kind of tribometer rotor configuration can provide reliable lubrication layer inputs for each method is also pending. Cone-shape rotor (Feys et al., 2014) and cylindrical-shape rotor (Ngo et al., 2010) are two common tribometer rotors. The latter was initially designed for traditional concrete. Therefore, it is important to compare the accuracy of each type of rotor against the nowadays widely used highly flowable concrete, which has different mixture composition and rheological characteristics comparing to the traditional concrete. Besides, it is also important to study the compatibility of each tribometer with different prediction method.

To answer questions above, this study conducted a horizontal pumping test with a 280-meter-long pipeline with 60 HFC mixtures. The pumping flow rate ranged from 4 to 16 L/s. Rheological testing results and comparisons between the measured pressure loss and calculated pressure losses by Kaplan and Kwon methods are presented and discussed.

2. Experimental program

2.1 Materials and mixture proportions

60 highly flowable concrete mixtures were used. Portland cement (P.O. 42.5) that meet the Chinese Standard GB 175-2007 were used. Class C fly ash (CFA), ground granulated blast furnace slag (GGBS), and silica fume were used as the supplementary materials. Well-graded siliceous river sand (0-4.75 mm with a fineness modulus of 2.8) and crushed limestone (5-20 mm) were employed as fine and coarse aggregates, respectively, to produce the concrete. The chemical and physical properties of the cementitious materials used in this study are listed in Table 1. A polycarboxylate high-range water-reducing agent (HRWRA), with a solid content of 19.3%, was used in the concrete mixtures with different strength grades. Mixture proportions are shown in Table 2.

Table 1 Chemical and physical properties of the binders

	P.O. 425	CFA	GGBS	Silica fume		P.O. 425	CFA	GGBS	Silica fume
Density, kg/m^3	3020	2170	2910	2210	Blaine fineness, m^2/kg	333	363	394	-
SiO_2, %	20.94	49.93	32.34	98.48					
Al_2O_3, %	5.09	21.53	14.05	-	SO_3, %	2.66	0.93	2.85	-
Fe_3O_4, %	3.48	3.97	0.4	-	LOI, %	4.08	5.18	0	-
CaO, %	60.53	15.46	40.16	-	C_3S, %	55.1	-	-	-
MgO, %	2.54	1.14	8.44	-	C_2S, %	11.94	-	-	-
K_2O, %	0.64	1.07	0.4	-	C_3A, %	2.08	-	-	-
Na_2O, %	0.06	0.2	0.39	-	C_4AF, %	10.81	-	-	-

Table 2 Concrete mixture design (kg/m^3)

Sample	Cement	CFA	GGBS	Silica fume	Water	w/cm Ratio	Sand	Aggregate	HRWRA
1	399.33	90.17	80.08	30.00	124.42	0.21	829.08	897.08	11.50
2	399.33	90.08	80.00	30.00	144.33	0.24	808.50	894.58	12.25
3	403.08	89.92	79.75	30.00	140.50	0.23	807.83	894.33	12.25
4	238.00	70.08	60.00	-	147.25	0.40	908.50	958.50	5.30
5	237.17	69.42	59.58	-	160.25	0.44	888.25	959.67	4.06
6	388.42	76.67	107.50	-	146.92	0.26	780.08	1142.33	6.97
7	237.17	110.42	69.58	-	183.00	0.44	928.42	878.58	6.49
8	422.67	95.33	82.92	30.00	141.25	0.22	767.00	998.83	13.87
9	400.67	89.50	79.42	30.00	138.92	0.23	780.17	928.67	12.60
10	408.33	93.33	79.75	30.00	160.25	0.26	736.25	971.67	12.09
11	400.17	90.42	79.83	30.00	138.50	0.23	706.75	998.75	12.14
12	400.67	90.50	79.58	30.00	129.67	0.22	780.83	928.08	12.00
13	353.92	67.58	96.58	-	133.00	0.26	700.50	1015.42	7.33

2.2 Experiment setups

A pipeline with length of 280 meters was used for the horizontal pumping campaign. The pipelines consist of straight pipes with radii of 125 mm and 150 mm and 90° bends with curvature radii of 0.5 meters and 1 meter. Pressure sensors with a capacity of 0-60 MPa and a measurement accuracy of 0.05% were used in each of the three pipelines. Pressure sensors were fixed on the pipe by placing them in the steel cylindrical supports welded on the pump pipe. After approximately 1.5 times the volume of the pipeline of concrete was discharged, pumped concrete was sampled at the tail of the pipeline (see Table 3).

Table 3 Flow rate of each mixture

Sample	**Q (L/s)**	**Sample**	**Q (L/s)**	**Sample**	**Q (L/s)**	**Sample**	**Q (L/s)**	**Sample**	**Q (L/s)**	**Sample**	**Q (L/s)**
1-1	4.46	**3-3**	9.37	**5-2**	8.74	**7-4**	13.51	**9-5**	12.26	**11-5**	12.94
1-2	8.35	**3-4**	12.12	**5-3**	9.63	**7-5**	15.74	**10-1**	3.22	**12-1**	2.73
1-3	13.19	**4-1**	5.80	**5-4**	14.04	**8-1**	3.40	**10-2**	5.16	**12-2**	4.97
2-1	4.69	**4-2**	7.01	**6-1**	4.39	**8-2**	5.89	**10-3**	7.08	**12-3**	8.88
2-2	5.82	**4-3**	9.12	**6-2**	6.93	**8-3**	8.51	**10-4**	8.82	**12-4**	11.07
2-3	8.27	**4-4**	11.83	**6-3**	8.31	**8-4**	12.45	**10-5**	10.82	**13-1**	3.80
2-4	8.50	**4-5**	13.28	**6-4**	9.01	**9-1**	3.80	**11-1**	3.14	**13-2**	5.17
2-5	10.98	**4-6**	17.00	**7-1**	4.31	**9-2**	5.31	**11-2**	6.17	**13-3**	7.62
3-1	3.29	**4-7**	18.20	**7-2**	6.71	**9-3**	7.64	**11-3**	8.91	**13-4**	8.87

3-2	7.72	**5-1**	5.50	**7-3**	10.57	**9-4**	10.41	**11-4**	11.25	**13-5**	11.05

Concrete bulk properties were tested by an ICAR concrete rheometer and lubrication layer properties were tested by two tribometers with different rotors. The testing sequence included a 30-s pre-shearing period at 0.5 rev/s, followed by the decrease of the rotational speed from 0.5 to 0.03 rev/s in six steps. The Bingham model (Tattersall & Banfill, 1983) parameters of mixtures were determined by Reiner-Riwlin equations to estimate the applied maximum shear rate during pumping. The cone-shape tribometer rotor has the same configuration as described by Feys et al. (2014), and the cylindrical-shape tribometer has the same configuration as described by Kwon et al. (2013). Lubrication layer properties were determined according to Feys et al. (2014) and Kwon et al. (2013).

3. Results and discussion

Two pumping pressure loss prediction methods were used. The first equation adopted is Kaplan method (Kaplan et al., 2005) and the second equation adopted is Kwon method (Kwon et al., 2013b).
Test results by two triometers are shown in Figure 1. For the yield stress of the lubrication layer (Figure 1-a), generally, tribometer with the cylindrical-shape rotor offered higher results, especially when the w/c ratio of the material is high. For the viscous constant of the lubrication layer (Figure 1-b), all results by the cylindrical-shape rotor are higher than those by the cone-shape rotor. The difference tend to be more pronounced when the material has low w/c ratio. Averagely, the yield stress and the viscous constant by the cylindrical-shape rotor is 4.63 and 4.30 times larger than that by the cone-shape rotor, respectively. The shape of rotor is indeed influential to rheological properties.

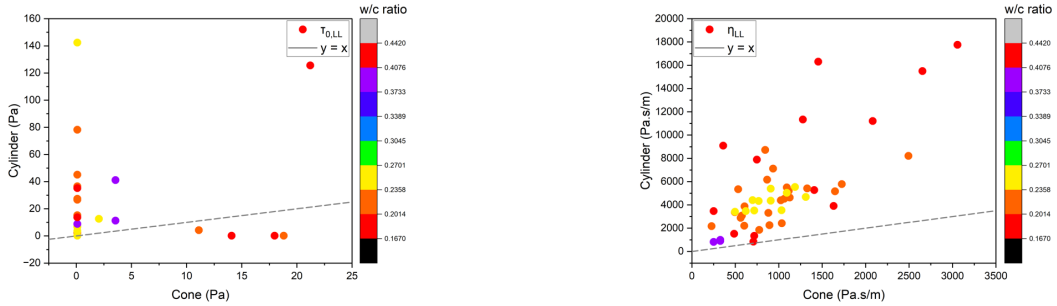

(a) yield stress (b) viscous constant

Figure 1 Comparison between the tested lubrication layer properties by the cone-shape tribometer (x-axis) and the cylindrical-shape tribometer (y-axis). Color of each point represents its corresponding w/c ratio.

Differences in the tested rhological property introduced large distinctions when predicting concrete pumping pressure loss (Figure 2). Using lubrication layer properties by cone-shape rotor tribometer, Kaplan method and Kwon method missed the actual pressure loss by 0.0092 MPa/m and 0.0278 MPa/m, respectively. Figure 2-a and 2-c show that although Kwon method has smaller error range, Kaplan method has higher accuracy rate. Similarly, using lubrication layer properties by cylindrical-shape rotor tribometer, Kaplan method and Kwon method missed the actual pressure loss by 0.0874 MPa/m and 0.0624 MPa/m, respectively. Therefore, the cylindrical rotor tribometer is more compatible with Kwon method, and the the cone-shape rotor tribometer is more compatible with Kaplan method. Overall, the combination of Kaplan method and cone-shaped tribometer has the highest accuracy among all four combinations. It is also worthnoting that in all four cases, higher pumping flow rate caused lower accuracy in pressure prediction. This could be a result due to the pumping-induced concrete property change (Li et al., 2022).

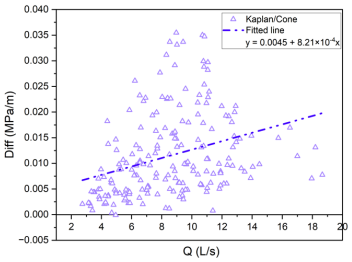

(a) Kaplan method and cone-shape rotor

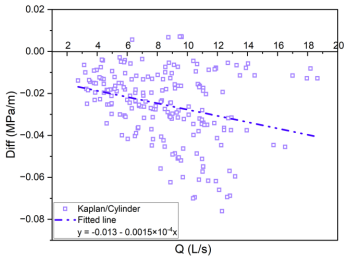

(b) Kaplan method and cylinder-shape rotor

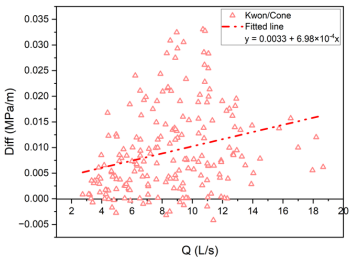

(c) Kwon method and cone-shape rotor

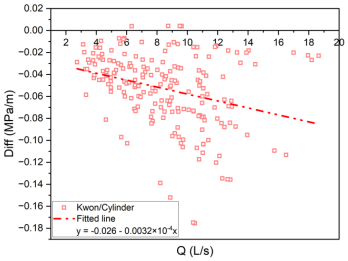

(d) Kwon method and cylinder-shape rotor

Figure 2 Difference between actual and calculated concrete pressure vs. the pumping flow rate

4. Conclusions

Concrete tribometer can assess properties of lubrication layer and the yield stress and viscous constant are two main parameters produced by tribometer. The shape of tribometer rotor has a profound influence on the measurement of parameters. The yield stress and the viscous constant by the cylindrical-shape rotor is averagely 4.63 and 4.30 times larger than that by the cone-shape rotor, respectively.

Two popular prediction methods are evaluated against the experimental result. Generally, Kaplan method is more accurate than Kwon method. The combination of Kaplan method and inputs by cone-shape tribometer rotor predicts the most accurate pressure loss, among all four combinations studied. Comparing to the cone-shape rotor, Kwon method is more compatible with cylinder-shape rotor, but Kaplan method is more compatible with cone-shape rotor comparing to the cylindrical-shape rotor.

Acknowledgements

The presented work was financially supported by the National Key R&D Program of China (2017YFB0310100) and the National Natural Science Foundation of China (51778629 and 51922109).

References

Feys, D., Khayat, K. H., Perez-Schell, A., & Khatib, R. (2014). Development of a tribometer to characterize lubrication layer properties of self-consolidating concrete. *Cement and Concrete Composites*, 54, 40–52.

Kaplan, D., de Larrard, F., & Sedran, T. (2005). Design of concrete pumping circuit. *ACI Materials Journal*, 102(2), 110–117.

Kwon, S. H., Park, C. K., Jeong, J. H., Jo, S. D., & Lee, S. H. (2013a). Prediction of concrete pumping: Part i-development of new tribometer for analysis of lubricating layer. *ACI Materials Journal*, 110(6), 647–655.

Kwon, S. H., Park, C. K., Jeong, J. H., Jo, S. D., & Lee, S. H. (2013b). Prediction of concrete pumping: Part II-analytical prediction and experimental verification. *ACI Materials Journal*, 110(6), 657–667.

Li, F., Shen, W., Yuan, Q., Hu, X., Li, Z., & Shi, C. (2022). An overview on the effect of pumping on concrete properties. *Cement and Concrete Composites*, 129(May), 104501.

Ngo, T. T., Kadri, E. H., Bennacer, R., & Cussigh, F. (2010). Use of tribometer to estimate interface friction and concrete boundary layer composition during the fluid concrete pumping. *Construction and Building Materials*, 24(7), 1253–1261.

Tattersall, H., & Banfill, G. (1983). *The rheology of fresh concrete*, Research report.

The 16th International Congress on the Chemistry of Cement 2023 (ICCC2023)
"Further Reduction of CO_2 -Emissions and Circularity in the Cement and Concrete Industry"
September 18–22, 2023, Bangkok, Thailand

Comparison of superabsorbent polymer characterization by filtration test in water and cementitious filtrate

L.F.M. Souza[1*], M.A.R.Fontes[2], and L.B.Agostinho[3]

[1] *Federal University of Uberlândia, Uberlândia, Brazil*
Email: luiza.f.souza@ufu.br
[2] *Federal University of Uberlândia, Uberlândia, Brazil*
Email: matheus.abdala@ufu.br
[3] *Federal University of Uberlândia, Uberlândia, Brazil*
Email: liviaborba@ufu.br

ABSTRACT

The use of internal curing (IC) has been a strategy to mitigate autogenous shrinkage in high performance concretes (HPC). Superabsorbent polymers (SAP) are one of these techniques, as they can retain water, and by osmotic pressure, release it during the cement hydration. They can reduce the autogenous shrinkage by reducing capillary pressure, as they replace the water in the matrix as it is consumed by the reaction. Therefore, reduce meniscus, reducing possible cracks. However, SAP desorption, leave voids in the concrete, potentially damaging its mechanical properties. Thus, the measuring and determination of SAP absorption and desorption behavior is necessary to be well implemented in cementitious materials. There are many tests for it, but not all of them are normalized, so, a detailed analysis of these tests is needed for a better researchers networking of data and standardization of the methods. This study has the objective to contribute to this, by comparing the methodology and results of the filtration test in two different liquids: tap water and cementitious filtrate. It was verified that the environment slightly interferes in the results. This fact shows that SAP mechanisms depends on the surroundings, in other words, the polymer is sensitive, so, your absorption and desorption can change in order to its atmosphere. Therefore, for an optimized concrete, mortar or paste design containing SAP, it is necessary the knowledge of how much their cement slurry will change its potential. Then, the right design for each situation will be determined, searching the maximization of the polymer potential and minimization of its disadvantages on the matrix.

KEYWORDS: *Superabsorbent polymer, autogenous shrinkage, internal curing, cementitious materials, supplementary cementitious materials.*

1. Introduction

High performance concretes (HPC) suffers from autogenous shrinkage due to their low water-cement ratio (w/c), addition of supplementary cementitious materials (SCM), and high cement consumption (Jensen and Hansen, 2001). This leads to self-desiccation and can affect the mechanical properties of these concretes. Internal curing by SAP is one strategy to mitigate these effects, so proper dosage depends on proper characterization of the polymer, including its sorptivity. This property can change depending on the composition and as well as the properties of the sorbed fluid (Snoeck *et al*., 2018). Therefore, three test methods were evaluated in this work: filtration test, mainly using RILEM TC 260-RSC (Snoeck *et al*., 2018). Some procedures were modified to simplify the method and evaluate its impact on the reliability of the results.

2. Methodology

The SAP used in this work is a covalently crosslinked acrylamide/acrylic acid polymer prepared by suspension polymerization with spherical particles, and average diameter of 100 μm. The amount of dry SAP for this test should also be determined in advance by a dummy test in the liquid to be used to ensure that there is sufficient liquid to be freely swollen by the polymer. This amount must be weighed to an

accuracy of 0.001 g. In this work, this amount was 0.050 g in 100 g of fluid analyzed in two ways: tap water and cement-based solution. The latter was prepared by a filtrate of cement slurry with a w/c of 5 (Mechtcherine *et al.*, 2018a). This solution aims to achieve a pH environment close to that of the cementitious materials. Two mixing methods have been used, in the literature for this purpose: 45 minutes of decantation (Wehbe and Ghahremaninezhad, 2017) and 24 hours of automatic stirring followed by filtration (Snoeck, Pel and De Belie, 2017)(Zhao, Jensen and Hasholt, 2020). Both were used in this study to compare their effects on SAP absorption. The dry polymers were then immersed in the liquids, and after 1, 5, 10, 30, 60 minutes, 3, and 24 hours, the entire solution was filtered and its mass weighed. Between these intervals, the beakers were sealed to prevent carbonation. Three samples were taken for each liquid. Equation (1) determines the SAP sorption (*SC*).

$$SC = \frac{m_{fluid} - m_{filtered}}{m_{SAP}} \quad (1)$$

The recommendation states that the filter paper should be saturated with the test liquid before filtration to avoid influencing the results. In this work are two groups of samples, one following this recommedation and another using a procedure similar to the tea bag test, as described in the same recommendation. The dry and wet masses of ten filter papers were recorded, and the average amount of absorbed water was used to exclude its influence on the results. Then, dry paper filters were used for the filtration experiments, and the results were adjusted according to the average amount of absorbed water on the previously obtained tissue. For comparison, a tea bag test was also performed, but only with tap water, according to the RILEM recommendation.

3. Results and Discussion

The filtration test in cement slurry showed that there is no difference between the two types of mixtures, as the two tests are very similar, being a complementary result to (Zhao, Jensen and Hasholt, 2020). Which compared the absorption evolution of SAP in cement slurry filtrate under different convection conditions and despite their differences, all measurements gave approximately the same 24-hour absorption capacity. In the present study, the obtained absorbance after 24 hours was the same for both methods namely 662 g/g. Figure 1(a) shows the comparison between the filtration tests with tap water and cement slurry filtrate, each with pre-wetted paper filters (wet filtration) and non-pre-wetted paper filters (dry filtration), and the tea bag test with tap water. First, the significant difference in results between dry and wet filtration in both tested liquids is noticeable, as shown in Figure 1(b). This invalidates the proposed procedure, which is different from the RILEM recommendation for the filtration test. In tap water, this difference increased with the time of the measurement, with a higher value of 119% after 24 hours of absorption. In cement slurry filtrate, this difference increased with time until 1-hour absorption (282%) and then decreased until 24-hour absorption.

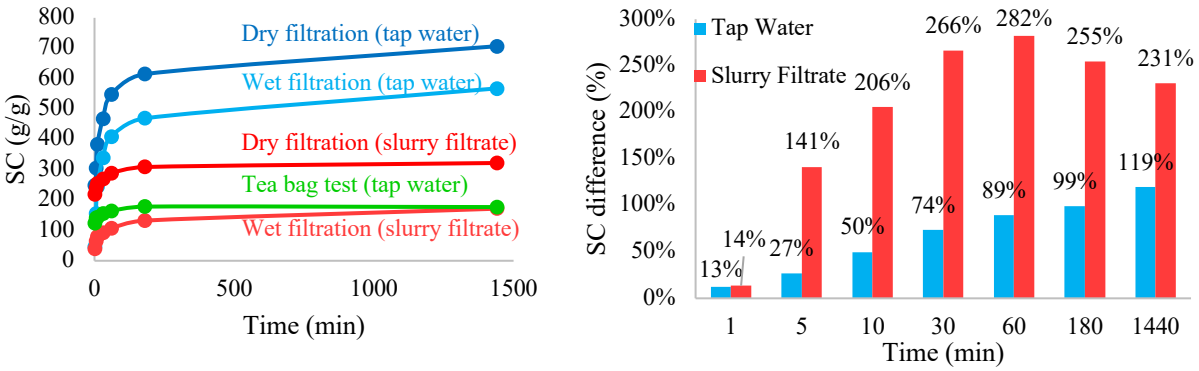

Figure 1 – (a) Comparison of SAP absorption in filtration test in tap water (blue lines), filtration test in cement slurry filtrate (red and pink lines) and tea bag test in tap water (green line), (b) Dry and wet filtration percentual different in SC values, in each measurement time

At 1 minute of liquid-polymer contact, the SAP absorption in cement slurry filtrate was 82% smaller than its value in tap water in both dry and wet filtration, as shown in Figure 2. Whereas in any other time, the difference between tap water and cement slurry filtrate absorption were higher in wet filtration. The higher difference between the two filtrations (wet and dry) was 38%, at 30-minute absorption. This difference between the two liquids decreases with time in both filtrations. From an absorption of 3 hours, it begins to stabilize, reaching values of 20% for dry filtration and 47% for wet filtration. This is different from the literature; Yuanliang *et al.* (2022) conducted filtration tests of cross-linked poly sodium acrylate SAP with deionized water and foam concrete pore solution and found a decrease in absorption in water to 80% on average after 24 hours, while this rate was 52% after 1 minute. Snoeck *et al.* (2016) also did this with demineralized water and cement filtrate in cross-linked potassium salt polyacrylate with average diameter of 475 μm, but only measured at a contact time of 5 minutes and a found an 80% decrease from water to cement filtrate liquid, which approximates to the wet filtration values of this work at the same time. Chidiac *et al.* (2021) used distilled water and cement slurry filtrate (w/c=10) for the filtration test in polyacrylate SAP with average diameter of 125 μm and came up with a decrease of 79%, close to the obtained values in wet filtration of this work, at 1 and 5-minute measurements.

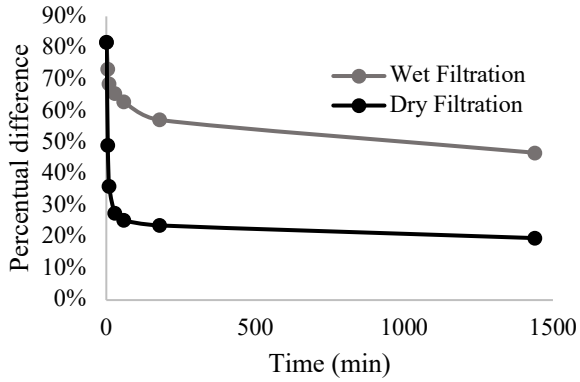

Figure 2 – Absorption in tap water and cement slurry filtrate percentual difference, in wet filtration (grey line) and dry filtration (black line)

In the tea bag test, an increase of 44% in the absorption of SAP is observed with water contact between 1 minute and 24 hours. Absorption measured in the filtration test with water increased by 47% for wet filtration and 186% for dry filtration between 1 minute and 24 hours. Comparing the values of the tea bag with the study of Mechtcherine *et al.* (2018) performed with cross-linked poly(acrylate-co-acrylamide) SAP with diameters above 200 μm in demineralized water, the absorption of SAP was in the range of 250-400 g/g, which is slightly different from the present work that reached a range of 120-200 g/g in tap water. Thus, it is clear that the substitution of the saturation of the paper filters with the test liquids by their previous weighing to estimate the water absorbed by them was not fully approved. The absorption SAP measured by the dry filtration test in both liquids showed much higher values compared to those reported in the literature. Zhong *et al.* (2019) tested different SAPs with different chemical structures in deionized water and cement slurry filtrate (w/c=5). They found absorption values between 200-400 g/g when water and SAP were in contact for 24 hours. While dry filtration in the present study gave a value of 707 g/g.

The SAP main driving force of swelling is osmotic pressure, which is proportional to the concentration of ions in the aqueous solution (Mechtcherine and Reinhardt, 2012). Tan and He (2022) have demonstrated that the absorption of SAP is higher in pure water than in tap water, because the latter has a higher ion concentration. Therefore, the values of this work in the filtration test in tap water were expected to be lower than those of Zhong *et al.* (2019), in deionized water. This was in the range of 150-400 g/g, which matches the range of wet filtration from this work (200-350 g/g) and does not match the values of dry filtration (250-710 g/g).The same discrepancy was observed in the slurry filtrate; while the cited work found values in a range of 5-25 g/g, the present study reached 568 g/g for dry filtration and 172 g/g for wet filtration in the 24-hour measurement. However, even if the values are consistent with the literature, a range of 5-20 g/g is also reported in the literature for use in concrete (Zhong *et al.*, 2021)(Palma e Silva *et al.*, 2022). Therefore, if no additional water is used, these methods are not so relevant.

3. Conclusions

The main conclusions found in this work can be summarized as follows:

(1) Using dry paper filters, even with the correction applied in this study, need to be more tested and explored to comprovate its efficienty on replacing the Recommendation procedure, by saturating them before the tests.
(2) In a cementitious filtrate, the absorption rate of SAP decreases. Even with the gap in the dry filtration test, this work could show this difference between the two liquids.
(3) The different methods to obtain the cement slurry did not seam to interfear at the absorption behaviour of the type of SAP used at this present work.
(4) Further reasearches with SAP need to be done to evaluate its sorption behaviour in concrete environment, to enable future optimizations of cementitious materials with SAP in their dosage.

References

Chidiac, S.E. *et al.* (2021) 'Efficiency measure of SAP as internal curing for cement using NMR & MRI', *Construction and Building Materials*, 278, p. 122365. Available at: https://doi.org/https://doi.org/10.1016/j.conbuildmat.2021.122365.

Jensen, O.M. and Hansen, P.F. (2001) 'Water-entrained cement-based materials: I. Principles and theoretical background', *Cement and Concrete Research*, 31(4), pp. 647–654. Available at: https://doi.org/https://doi.org/10.1016/S0008-8846(01)00463-X.

Mechtcherine, V. *et al.* (2018a) 'Testing superabsorbent polymer (SAP) sorption properties prior to implementation in concrete: results of a RILEM Round-Robin Test', *Materials and Structures/Materiaux et Constructions*, 51(1). Available at: https://doi.org/10.1617/s11527-018-1149-4.

Mechtcherine, V. *et al.* (2018b) 'Testing superabsorbent polymer (SAP) sorption properties prior to implementation in concrete: results of a RILEM Round-Robin Test', *Materials and Structures/Materiaux et Constructions*, 51(28). Available at: https://doi.org/10.1617/s11527-018-1149-4.

Mechtcherine, V. and Reinhardt, H.W. (2012) *Application of superabsorbent Polymers (SAP) in Concrete Construction*, *Springer*.

Palma e Silva, A.A. *et al.* (2022) 'Evaluation of mechanical properties and microstructure of high-performance mortars with superabsorbent polymers and metakaolin by means of X-ray computed microtomography', *Journal of Building Engineering*, 51(February). Available at: https://doi.org/10.1016/j.jobe.2022.104219.

Snoeck, D. *et al.* (2016) 'X-ray computed microtomography to study autogenous healing of cementitious materials promoted by superabsorbent polymers', *Cement and Concrete Composites*, 65, pp. 83–93. Available at: https://doi.org/https://doi.org/10.1016/j.cemconcomp.2015.10.016.

Snoeck, D., Pel, L. and De Belie, N. (2017) 'The water kinetics of superabsorbent polymers during cement hydration and internal curing visualized and studied by NMR', *Scientific Reports*, 7(1). Available at: https://doi.org/10.1038/s41598-017-10306-0.

Snoeck, D., Schröfl, C. and Mechtcherine, V. (2018a) 'Recommendation of RILEM TC 260-RSC: testing sorption by superabsorbent polymers (SAP) prior to implementation in cement-based materials', *Materials and Structures/Materiaux et Constructions*, 51(5). Available at: https://doi.org/10.1617/s11527-018-1242-8.

Snoeck, D., Schröfl, C. and Mechtcherine, V. (2018b) 'Recommendation of RILEM TC 260-RSC: testing sorption by superabsorbent polymers (SAP) prior to implementation in cement-based materials', *Materials and Structures/Materiaux et Constructions*, 51(116). Available at: https://doi.org/10.1617/s11527-018-1242-8.

Tan, Y., Chen, H. and He, R. (2022) 'Water distribution and transport-kinetics model in fresh cement-based mixtures containing superabsorbent polymers based on 1H low-field NMR', *Cement and Concrete Composites*, 127, p. 104396. Available at: https://doi.org/https://doi.org/10.1016/j.cemconcomp.2021.104396.

Wehbe, Y. and Ghahremaninezhad, A. (2017) 'Combined effect of shrinkage reducing admixtures (SRA) and superabsorbent polymers (SAP) on the autogenous shrinkage, hydration and properties of cementitious materials', *Construction and Building Materials*, 138, pp. 151–162. Available at: https://doi.org/https://doi.org/10.1016/j.conbuildmat.2016.12.206.

Yuanliang, X. *et al.* (2022) 'Effect of superabsorbent polymer on the foam-stability of foamed concrete', *Cement and Concrete Composites*, 127, p. 104398. Available at: https://doi.org/https://doi.org/10.1016/j.cemconcomp.2021.104398.

Zhao, S., Jensen, O.M. and Hasholt, M.T. (2020) 'Measuring absorption of superabsorbent polymers in cementitious environments', *Materials and Structures/Materiaux et Constructions*, 53(11). Available at: https://doi.org/10.1617/s11527-020-1442-x.

Zhong, P. *et al.* (2019) 'Internal curing with superabsorbent polymers of different chemical structures', *Cement and Concrete Research*, 123, p. 105789. Available at: https://doi.org/https://doi.org/10.1016/j.cemconres.2019.105789.

Zhong, P. *et al.* (2021) 'Mechanisms of internal curing water release from retentive and non-retentive superabsorbent polymers in cement paste', *Cement and Concrete Research*, 147, p. 106494. Available at: https://doi.org/https://doi.org/10.1016/j.cemconres.2021.106494.

The 16th International Congress on the Chemistry of Cement 2023 (ICCC2023)
"Further Reduction of CO_2 -Emissions and Circularity in the Cement and Concrete Industry"
September 18–22, 2023, Bangkok, Thailand

Atomic Scale Insight of Hydration Temperature Rise Inhibitors (TRI) Affecting Calcium Activity via AIMD

Jiale Huang[1,2,3*], Hegoi Manzano[2], Zhangli Hu[1,3], and Jiaping Liu[1,3]

1 School of Materials Science and Engineering, Southeast University, Nanjing, China
Email: jialehuang07@foxmail.com
2 Fisika saila, Euskal Herriko Unibertsitatea UPV/EHU, Sarriena Auzoa z/g, 48940 Leioa, Basque Country, Spain
3 State Key Laboratory of High Performance Civil Engineering Materials, Jiangsu Research Institute of Building Science Co., Nanjing, China

ABSTRACT

Thermal shrinkage and cracking are one of the main concerns for mass concrete. Small molecule sugar, known as hydration temperature rise inhibitors (TRI), can effectively control the hydration temperature of concrete. However, the atomic scale mechanism of TRI has not been clarified and the structural functioning relationship has not been established, which brings difficulties to the efficient application and targeted design of TRI. This study employs ab initio molecular dynamics simulations to investigate the complexation behavior of various small sugar molecules with calcium ions and to elucidate the underlying factors responsible for their differences. The aim is to explore the impact of such additives on the chemical reactivity of calcium ions. Our findings indicate that the charged characteristics of small sugar molecules play a crucial role in determining the complexation ability of calcium ions. Additionally, our analysis of Bader charges reveals that calcium ions interact with organic molecules through electron exchange, thereby disturbing their own reactivity. This may affect the 'dissolution-precipitation' equilibrium in the hydration process, leading to macroscopic perturbations such as delayed gelation or reduced heat of hydration. The present study sheds light on the atomic-level mechanism by which small sugar molecules affect the hydration environment and provides a basis for further research on molecular simulation and design theory for regulating early hydration.

KEYWORDS: *Hydration temperature rise inhibitors; atomic scale; ab initio molecular dynamics; chemical reactivity*

1. Introduction

In the construction of large infrastructure projects, the heat release problem caused by the hydration of large volume concrete can be difficult to mitigate. Unbalanced heat release can lead to the concentration of thermal stress, resulting in local thermal cracks in the concrete structure (Bullard et al., (2011); Scrivener et al., (2015)). In recent years, regulating cement hydration heat release has become an urgent problem for concrete engineers. Organic additives, such as hydration temperature rise inhibitors, are used as raw materials to assist in adjusting the reaction, known as the organic-inorganic composite reaction, to modify the hydration heat release (Yan et al., (2021), (2020)). The hydration of cement plays a crucial role in determining the microstructure of concrete. The reaction process is dependent on the balance between the dissolution and precipitation of cement minerals and the reaction environment (Mehta and Monteiro, (2017)). Understanding the impact of organic matter on the balance and reaction environment is crucial for controlling the cement hydration process. By doing so, it can be ensured that the process proceeds as required and achieves the desired outcome (Flatt and Houst, (2001); Marchon and Flatt, (2016)). The calcium ion is a pivotal factor in the equilibrium and reaction environment of cement hydration, as its reactivity can greatly influence the robustness of the hydration process. Therefore, understanding the behaviour of calcium ions during hydration is crucial for optimizing the performance and properties of cement-based materials (Lina et al., (2021)). Furthermore, the nano mechanisms by

which admixtures control the hydration process largely depend on phenomenological characterization. However, due to the limitations of current testing equipment resolution, it is a significant obstacle to gain a deeper understanding of the physical and chemical nature of control mechanisms and to develop admixture structures in reverse. In recent years, molecular dynamics simulation has played a fundamental role in providing necessary data for analytical models such as ion dissolution complexation, organic-inorganic interface interaction and structural design of chemical additives, but this accuracy depends on the choice of empirical force field (Manzano et al., (2015), (2011)). Ab initio Molecular Dynamics (AIMD) is a computational technique that employs quantum mechanics to investigate the characteristics of molecules and condensates. Through the analysis of electronic structure, Ab initio Molecular Dynamics (AIMD) offered valuable insights into the impact of external factors on the reactivity of chemical reactions, specifically regarding the ability to gain or lose electrons. In this work, AIMD was employed to explore the complexation differences and origins between calcium ions and various small molecule sugars, such as adsorption energy and electron transfer. Our particular emphasis was on elucidating the impact of electron transfer on the activity of calcium ions, thereby providing atomic-level insights into the modulation of hydration processes by chemical additives.

2. Methods

All calculations were performed within the framework of density functional theory (DFT) using the CP2K/QUICKSTEP package(Hutter et al., (2014); Kühne et al., (2020)). A mixed basis set consisting of Gaussian basis and plane waves (GPW) (Lippert et al., (1997)) was employed, with the Gaussian basis set using double-zeta valence plus polarization functions (DZVP) (VandeVondele and Hutter, (2007)) and the plane wave cutoff set to 350 Ry. Matrix diagonalization was employed to optimize the wave functions, with Fermi tail smearing aiding self-consistent field (SCF) convergence and the remaining core electrons represented by Goedecker-Teter-Hutter (GTH) pseudopotentials(Goedecker and Teter, (1996)). Initially, four small molecule sugars were placed in a cubic lattice with dimensions a=20 Å, b=20 Å, c=20 Å, and their geometries were optimized using the Broyden-Fletcher-Goldfarb-Shanno (BFGS) (Vandevondele et al., (2005)) minimizer to locate the positions of highest activity. Calcium ions were subsequently placed in the vicinity of the optimized positions, and the resulting complexes were subjected to geometry optimization. The ENERGY_FORCE function in the CP2K package was then utilized to analyze the electronic structure evolution of the small molecule sugars before and after complexation.

3. Results and discussion

Calcium atoms were placed at the positions of highest activity for four types of small molecule sugars, and AIMD was employed to investigate the complexation effects between the small molecule sugars and calcium ions. The adsorption energy results are presented in Table 1. As can be seen from the table 1, the adsorption energy of D-galactarate with calcium ions is much higher than that of the other three small molecule sugars, due to the higher activity of the ester functional group compared to the hydroxyl functional group. Additionally, D-galactarate is overall negatively charged, and in solution, calcium ions tend to complex with D-galactarate, possibly due to charge-driven effects. D-galactitol and α-D-glucopyranose are both hydroxyl-containing compounds with similar complexation abilities toward calcium ions. To investigate the possible role of charge in ion complexation, α-D-glucopyranose was selected and protonated, resulting in a decrease in adsorption energy from -0.2455 eV to -3.5384 eV. This suggests that charge plays a critical role in ion complexation, and therefore, it is particularly important to investigate the charge transfer between small molecule sugars and calcium ions.

Table 1 Adsorption energy of small molecule sugar and calcium ion

Type	D-galactarate	D-galactitol	α-D-Glucopyranose	Deprotonated α-D-Glucopyranose
E_{ads} (ev)	-6.4755	-0.2395	-0.2455	-3.5384

D-galactarate and D-galactitol were selected as the objects of study for charge transfer, since these two types of small molecule sugars exhibit the most significant difference in binding energy with calcium

ions. As shown in Table 2 and Fig 1, the Bader charge of calcium increased by 1.5639 |e| upon binding with D-galactarate, indicating the loss of 1.5639 |e| from calcium. In contrast, the result for D-galactitol showed a much smaller increase in the Bader charge of calcium, only 0.1754 |e|. Compared to D-galactarate, the binding of D-galactitol does not cause a significant change in the charge state of calcium, which may explain the poor condensation effect of D-galactitol due to its relatively weak influence on the hydration environment of calcium ions, such as the chemical state of calcium ions.

Table 2 Bader charge evolution of adsorption sites of small sugar and calcium ions

Sugar type	Atom	Bader Charge before composite	Bader Charge after composite
D-galactarate	Ca	0	1.5639
	O1	-1.5309	-1.817
	O2	-1.5677	-1.7748
	O3	-1.4336	-1.7096
D-galactitol	Ca	0	0.1754
	O1	-1.0029	-0.9984
	O2	-0.9706	-1.1057
	O3	-1.0596	-1.0548

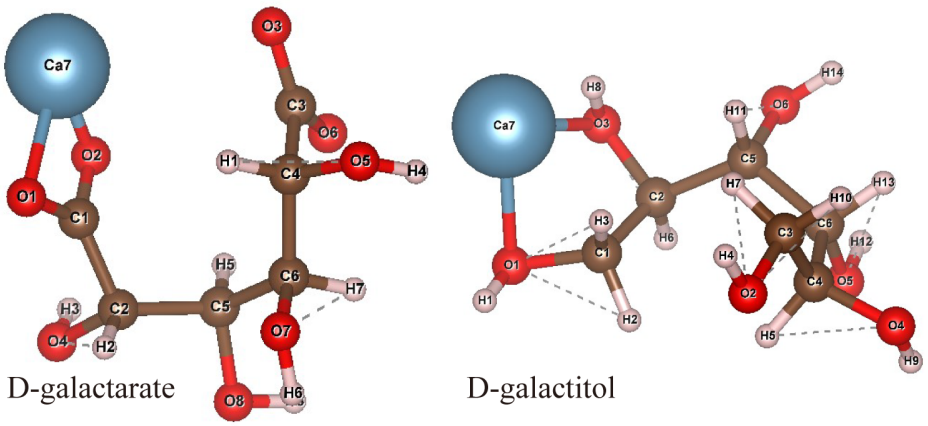

Fig 1 Structure diagram of small molecule sugar and calcium ion adsorption sites

4. Conclusion

In this study, we employed first-principles calculations to investigate the complexation behaviour of calcium ions with three small sugar molecules and the underlying factors for their differences. Our results indicate that the charged properties of α-D- Glucopyranose and its protonated form significantly affect the complexation ability of calcium ions. Furthermore, the Bader charge analysis results reveal that calcium ions interact with organic molecules through electron exchange, which disturbs the reactivity of the calcium ions themselves. This could potentially affect the "dissolution-precipitation" equilibrium in the hydration process, leading to disturbances in the macroscopic hydration processes such as slowing down of the hydration or decreasing the heat of hydration. Experimentally detecting the electron exchange phenomenon accompanying chemical reactions would be a formidable challenge. The first-principles provides an electron-scale perspective, laying a solid foundation for the design of future admixture.

Acknowledgements

The authors gratefully acknowledge the research supports provided by the National Natural Science Foundation of China (Grant No.:51738004), the scientific and techno-logical research and development plan of China railway corporation (Contract No.: 2017g006-b), the “Departamento de Educación, Política

Lingüística y Cultura del Gobierno Vasco" (Grant No. IT1458-22), the "Ministerio de Ciencia e Innovación" (TED2021-130860B-I00), and the Transnational Common Laboratory "LTC-Green Concrete". Jiale Huang gratefully acknowledges financial support from China Scholarship Council (CSC number: 202106090091). And the authors also greatly appreciate the State Key Laboratory of High-Performance Civil Engineering Materials for funding the research project and Beijng PARATERA Tech CO.,Ltd. For providing HPC resources that have contributed to the research results reported within this paper.

References

Bullard, J.W., Jennings, H.M., Livingston, R.A., Nonat, A., Scherer, G.W., Schweitzer, J.S., Scrivener, K.L., and Thomas, J.J., (2011). "Mechanisms of cement hydration." *Cement and Concrete Research*, 41, 1208–1223

Scrivener, K.L., Juilland, P., and Monteiro, P.J.M., (2015). "Advances in understanding hydration of Portland cement." *Cement and Concrete Research*, 78, 38–56

Yan, Y., Scrivener, K.L., Yu, C., Ouzia, A., and Liu, J., (2021). "Effect of a novel starch-based temperature rise inhibitor on cement hydration and microstructure development: The second peak study." *Cement and Concrete Research*, 141, 106325

Yan, Y., Ouzia, A., Yu, C., Liu, J., and Scrivener, K.L., (2020). "Effect of a novel starch-based temperature rise inhibitor on cement hydration and microstructure development." *Cement and Concrete Research*, 129, 105961

Mehta, P.K., and Monteiro, P.J.M., (2017). Concrete microstructure, properties and materials

Marchon, D., and Flatt, R.J., (2016). "Impact of chemical admixtures on cement hydration." *Science and Technology of Concrete Admixtures*, 279–304

Flatt, R.J., and Houst, Y.F., (2001). "A simplified view on chemical effects perturbing the action of superplasticizers." *Cement and Concrete Research*, 31, 1169–1176

Lina, B., Barbara, L., Alejandro, F.M., and Christophe, L., (2021). "Portlandite solubility and Ca2+ activity in presence of gluconate and hexitols." *Cement and Concrete Research*, 149, 106563

Manzano, H., Durgun, E., López-Arbeloa, I., and Grossman, J.C., (2015). "Insight on tricalcium silicate hydration and dissolution mechanism from molecular simulations." *ACS Applied Materials and Interfaces*, 7, 14726–14733

Manzano, H., Durgun, E., Abdolhosseine Qomi, M.J., Ulm, F.J., Pellenq, R.J.M., and Grossman, J.C., (2011). "Impact of chemical impurities on the crystalline cement clinker phases determined by atomistic simulations." *Crystal Growth and Design*, 11, 2964–2972

Kühne, T.D., Iannuzzi, M., Del Ben, M., Rybkin, V. V., Seewald, P., Stein, F., Laino, T., Khaliullin, R.Z., Schütt, O., Schiffmann, F., Golze, D., Wilhelm, J., Chulkov, S., Bani-Hashemian, M.H., Weber, V., Borštnik, U., Taillefumier, M., Jakobovits, A.S., Lazzaro, A., Pabst, H., Müller, T., Schade, R., Guidon, M., Andermatt, S., Holmberg, N., Schenter, G.K., Hehn, A., Bussy, A., Belleflamme, F., Tabacchi, G., Glöß, A., Lass, M., Bethune, I., Mundy, C.J., Plessl, C., Watkins, M., VandeVondele, J., Krack, M., and Hutter, J., (2020). "CP2K: An electronic structure and molecular dynamics software package -Quickstep: Efficient and accurate electronic structure calculations." *Journal of Chemical Physics*, 152

Hutter, J., Iannuzzi, M., Schiffmann, F., and Vandevondele, J., (2014). "Cp2k: Atomistic simulations of condensed matter systems." *Wiley Interdisciplinary Reviews: Computational Molecular Science*, 4, 15–25

Lippert, G., Hutter, J., and Parrinello, M., (1997). "A hybrid Gaussian and plane wave density functional scheme." *Molecular Physics*, 92, 477–488

VandeVondele, J., and Hutter, J., (2007). "Gaussian basis sets for accurate calculations on molecular systems in gas and condensed phases." *Journal of Chemical Physics*, 127

Goedecker, S., and Teter, M., (1996). "Separable dual-space Gaussian pseudopotentials." *Physical Review B - Condensed Matter and Materials Physics*, 54, 1703–1710

Vandevondele, J., Krack, M., Mohamed, F., Parrinello, M., Chassaing, T., and Hutter, J., (2005). "Quickstep: Fast and accurate density functional calculations using a mixed Gaussian and plane waves approach." *Computer Physics Communications*, 167, 103–128

The 16th International Congress on the Chemistry of Cement 2023 (ICCC2023)
"Further Reduction of CO_2 -Emissions and Circularity in the Cement and Concrete Industry"
September 18–22, 2023, Bangkok, Thailand

Multi-scale model for characterizing thermal conductivity of cement-based materials with nano inclusions

Jiahan Liu[1*]

[1] *Department of Civil Engineering, Shanghai Normal University, Shanghai, China*
Email: liujh@shnu.edu.cn

ABSTRACT

High carbon emissions generated by energy consumption has restricted the further coordinated development of construction industry seriously. Thermal conductivity is the most basic factor of researching energy consumption and developing energy-saving buildings. Hence, predicting the thermal properties of cement-based materials accurately is very important to quantify the thermal stresses in structures. This study aims to establish a multiscale model for the thermal conductivity of cement-based materials with considering the influence of interfacial thermal resistance and inclusion size. Nano-scale materials, such as carbon nanotube(CNT) with high thermal conductivity, has been widely used in developing heat storage concrete material. Hence, we focus on the effects of the thermal properties and microstructure of inclusions in nanoscale. The results showed that thermal properties of inclusions in nanoscale plays an important role on predicting the effective thermal conductivity of cement-based materials. The findings of this study help predict the thermal properties of old cement-based materials accurately and design new heat storage cement-based composites rationally.

KEYWORDS: *Energy consumption, Thermal conductivity, Cement-based materials, Multi-scale, Nano materials*

1. Introduction

Thermal properties of cement-based materials, the most extensively used materials in construction, are essentially important for energy consumption and developing energy-saving buildings. Predicting the thermal properties of cement-based materials accurately is essentially important to quantify the thermal stresses in structures and deepen the scientific understanding of thermally insulating effects of the materials for construction (Xiong et al.(2016)).

According to the recent research, there are some factors influencing the thermal conductivity, including type and volume fraction of aggregate, mineralogical character, water-to-cement ratio and saturation degree as well. Previous studies have proposed some experimental methods and calculation models of thermal conductivity. However, these methods are purely empirical and independent. Multi scale method is one of the most important theories in the study of heterogeneous materials. In microscale, cement-based composites can be treated as a porous inorganic material with microstructure, including C-S-H matrix, CH crystals, cement clinker and micro-meter porosity. Multi scale method is widely used in analysis of thermal and mechanical property of composite materials (Ji et al.(2014), Wei et al.(2013)).

Based on Eshelby equivalent inclusion principle and multi-scale nature of the microstructure of cement-based composites, this study attempted to employ micromechanical approach to evaluate the thermal properties of the composites using Mori-Tanaka homogenization method. A generalized multi-scale micromechanical model is developed to capture the thermal conductivity of the cement-based composites. Nano-scale materials, as carbon nanotube(CNT) which has high thermal conductivity, has been widely used in developing heat storage concrete material. The modelled results are comparable to the data from experimental measurement of cement-based materials with CNTs to verify the accuracy.

2. Micromechanical model of thermal conductivity

2.1 Multi-scale nature of cement-based materials

It is generally accepted that cement-based materials are typically multi-scale composite materials with extreme complexities in chemical components, and heterogeneities in physical properties and spatial distributions. By connecting the physical and chemical properties of each scale, a systematic understanding of the nature of materials will be established. Here the multi-scale microstructure of cement-based materials in four elementary levels is revisited; see Figure 1 (Constantinides et al. (2004), Jennings(2000), Sadat et al. (2018), Krakowiak et al. (2015)).

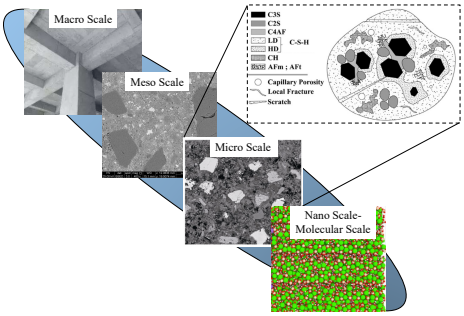

Figure 1 Four-level microstructure of cement-based composites

Level Ⅰ (10^{-8}-10^{-6}m): The presence of C-S-H is estimated at this scale, which is the hydration products of C_2S and C_3S. It is now established that C-S-H exists in two different forms, a low density (LD) and a high density (HD). The distinction of the two types is the difference of microstructure.
Level Ⅱ (10^{-6}-10^{-4}m): The C-S-H matrix with large CH crystals, cement clinker and micrometer porosity forms the cement paste. The cement clinker is including C_2S, C_3S, C_3A and C_4AF as well. The property of micrometer porosity is related to w/c.
Level Ⅲ (10^{-4}-10^{-2}m): This scale refers to mortar, which is a three phase composite material composed of cement pastes, sand particle inclusions, and an ITZ.
Level Ⅳ (10^{-2}-10^{-1}m): Concrete is considered as a three phase material composed of aggregates embedded in a mortar matrix and an ITZ in this scale.
Once the type, volume fraction and physical properties of the phases in a level are known, by using an appropriate homogenization method, the mechanical and thermal properties of the composite at a higher level can be calculated. In this way, a multi-scale model can be established to predict the physical properties of cement-based materials.

2.2 Thermal conductivity multi-scale model of composite materials

Mean-field theories present a consistent physical-mechanical framework to describe the behavior of composite materials with inhomogeneous structures. Based on the theories, the thermal properties of a material in a scale can be obtained by averaging the local phases in the subscale. The homogenized thermal conductivity at level i+1 is supposed to be $\boldsymbol{K}_{\text{hom}}(\boldsymbol{X})$, which is $\boldsymbol{K}_i(\boldsymbol{x})$ at level i. And $\boldsymbol{X}$, $\boldsymbol{x}$ are position vectors at level i+1 and level i, respectively. By spatially averaging the former identity, the homogenized thermal conductivity is expressed like:

$$\boldsymbol{K}_{\text{hom}}(\boldsymbol{X}) = \left\langle \boldsymbol{K}_i(\boldsymbol{x}) \cdot \boldsymbol{A}(\boldsymbol{x}) \right\rangle_V \tag{1}$$

V is the volume of representative volume element (RVE).

Based on mean-field theory, temperature gradients at levels i and i+1 can be assumed to be linearly related via a second order localization tensor at point x, $\boldsymbol{A}(\boldsymbol{x})$. Here the Mori-Tanaka method was used, so the localization tensor is expressed as:

$$\boldsymbol{A}_s = [\boldsymbol{I} + \boldsymbol{S}_s : (\boldsymbol{K}_{\text{M}}^{-1}\boldsymbol{R}\boldsymbol{K}_s\boldsymbol{R}^T - \boldsymbol{I})]^{-1} \left\langle [\boldsymbol{I} + \boldsymbol{S}_s : (\boldsymbol{K}_{\text{M}}^{-1}\boldsymbol{R}\boldsymbol{K}_s\boldsymbol{R}^T - \boldsymbol{I})]^{-1} \right\rangle_V^{-1} \tag{2}$$

Where $\boldsymbol{S}$ is an Eshelby tensor for the thermal conducting problem(Eshelby(1957)), $\boldsymbol{I}$ is the unit tensor, and $\boldsymbol{K}_M$, $\boldsymbol{K}_T$ are the thermal conductivity of the matrix and inclusion, respectively. The rotation matrix $\boldsymbol{R}$ is used to transform the local to global coordinate systems.
With the absence of preferential orientation for inclusions, the rotation matrix is reduced to $\boldsymbol{R} = \boldsymbol{I}$. Use the above equation in (2) (Qomi et al.(2015)):

$$\boldsymbol{A}_s = \boldsymbol{A}_s \boldsymbol{I} = \frac{3K_{\mathrm{M}}}{2K_{\mathrm{M}} + K_s} \tag{3}$$

We can obtain the generalized multi-scale micromechanical model:

$$K_{\mathrm{MT}} = \frac{f_{\mathrm{M}} K_{\mathrm{M}} + \sum_{s=1}^{n} f_s K_s A_s}{f_{\mathrm{M}} + \sum_{s=1}^{n} f_s A_s} \tag{4}$$

Where f_{M}, f_s are the volume fraction of the matrix and inclusion, respectively, n is the number of the inclusion phases, K_{M}, K_s are the thermal conductivity of the matrix and inclusion, respectively.

3. Application to cement-based materials with nano inclusions

In this paper, we choose carbon nanotube as nano inclusions of cement-based materials.The experimental data including the properties of nanotube and thermal conductivitis of composies are from Du et al. (2020), Li et al (2013).Based on the scale of nano inclusions, the nano materials can be assumed in level I or level II. Hence, we considered two situation to calculate the thermal conductivity of cement-based materials with nano inclusions.

The multi-scale model of cement paste is simplified to be a two-scale model from level I to level II. It need two times homogenization in the calculation of the thermal conductivity. The components and thermal conductivity of each solid phases need to be known. In the current work, the aluminate-related phases, such as C_3A and C_4AF, and their hydration products were regarded as C_3S and C-S-H to estimate the thermal conductivity of a cement paste due to the lack of data. The densities and thermal conductivities of C_2S, C_3S, CH, C-S-H, air and water are listed in Table 1 (Qomi et al.(2015), Farouki (1986)).

Table 1. Density and thermal conductivity of main phases in cement paste.

	Density (g/cm^3)	Thermal conductivity (W/m·K)	Sources
C_2S	3.55	3.45	Qomi et al. (Qomi et al.(2015))
C_3S	3.57	3.35	Qomi et al. (Qomi et al.(2015))
CH	2.25	1.32	Qomi et al. (Qomi et al.(2015))
C-S-H	2.40	0.98	Qomi et al. (Qomi et al.(2015))
Air		0.026	Farouki (Farouki.(1986))
Water	1	0.06	Farouki (Farouki.(1986))

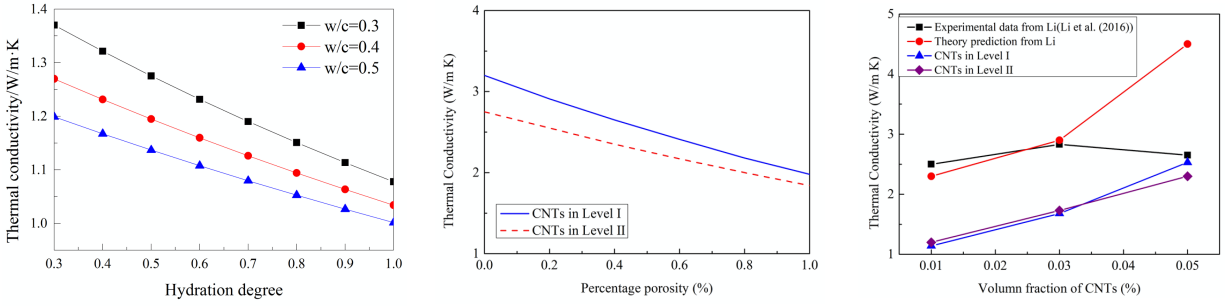

(a) (b) (c)

Figure 2 (a)Plots of predicted thermal conductivity of cement pastes against hydration degree;(b) Predicted thermal conductivity with different volume fraction of porosity percentage; (c) Comparation of predicted and experimental data of cement paste with CNTs

Figure 2(a) presents the predicted thermal conductivity of cement pastes with different w/c ratios against hydration degree. We focus that the thermal conductivity of cement paste decreases with increasing hydration degree. This is because the thermal conductivity values of CSH and CH are lower than those of clinker phases. Figure 2(b) and (c) presents the comparison of predicted and measured thermal conductivity in of a cement paste with carbon nanotube with w/c ratio of 0.4. Figure 2(b)shows the predicted thermal conductivity with different volume fraction of porosity percentage. We focus the

thermal conductivity decrease with increasing volume fraction of CNTs. This is because the thermal conductivity values of CNTs are much higher than other phases. Actually, CNT can decrease the porosity of cement-based materials significantly. Hence, the prediction of cement-based materials with nano inclusions in this paper consider the range of porosity percentage. Figure 2(c) shows the comparation of predicted and experimental data of cement paste with CNTs. It is found that the predicted values are in a good agreement with the experimental results with high CNT volume fraction.

4. Conclusions

Based on Eshelby equivalent inclusion principle and multi-scale nature of microstructure of cement-based composites, this study attempted to employ micromechanical approach to evaluate the thermal conductivity. Using Mori-Tanaka homogenization method, a generalized multi-scale micromechanical model is developed to capture the thermal conductivity of the cement-based composites. The modelled results are comparable to the experimental measurement of cement-based materials with CNTs. The following is research findings from the study.

1) The main factors influencing the thermal conductivity of cement-based materials are w/c, volume fraction of the phases and hydration degree. For composites with nano materials, the thermal properties and volume fraction of nano materials are also important for predicting the thermal conductivity.

2) It is verified that The CNT can decrease the porosity of cement-based materials, which will affect the thermal properties of the composites.

3) There are errors between the predicted and experimental values of thermal conductivity of cement-based materials. This is because the simplification of the spatial distribution and thermal property of pore water by utilizing the Eshelby equivalent inclusion principle and Mori-Tanaka homogenization method.

Acknowledgements

The authors acknowledge the National Natural Science Foundation of China (No. 5220080300 for JHL).

References

Xiong, M.X. and Liew, J.Y.R. (2016) “Mechanical behavior of ultra-high strength concrete at elevated temperatures and fire resistance of ultra-high strength concrete filled steel tubes”, *Materials and Design*, 104:414-427.

Ji, R., Zhang, Z., Liu, L. and Wang, X. (2014) “Development of the random simulation model for estimating the effective thermal conductivity of insulation materials”, *Building and Environment*, 80: 221-227.

Wei, S., Chen, Y., Zhang, Y. and Jones, MR. (2013) “Characterization and simulation of microstructure and thermal properties of foamed concrete”, *Construction and building materials*, 47: 1278-1291.

Constantinides, G. and Ulm, F.J. (2004) “The effect of two types of CSH on the elasticity of cement-based materials: Results from nanoindentation and micromechanical modeling”, *Cement & Concrete Research*, 34 (1): 67-80.

Jennings, H.M. (2000) “A model for the microstructure of calcium silicate hydrate in cement paste”, *Cement & Concrete Research*, 30 (1): 101-116.

Krakowiak, K.J., Thomas, J.J., Musso, S., James, S., Akono, A.T. and Ulm, F.J. (2015) “Nano-chemo-mechanical signature of conventional oil-well cement systems: Effects of elevated temperature and curing time”, *Cement & Concrete Research*, 67: 103-121.

Sadat, M.R., Muralidharan, K. and Zhang, L.Y. (2018) “Reactive molecular dynamics simulation of the mechanical behavior of sodium aluminosilicate geopolymer and calcium silicate hydrate composites”, *Computational Materials Science*, 150: 500-509.

Eshelby, J.D. (1957) “The determination of the elastic field of an ellipsoidal inclusion, and related problems”, *Proceedings of the Royal Society of London A: Mathematical, Physical and Engineering Sciences. The Royal Society*. 241(1226): 376-396.

Qomi, M.J.A., Ulm, F.J. and Pellenq, R.J.M. (2015) “Physical origins thermal properties of cement paste”, *Physical Review Applied*, 3(6): 064010.

Farouki, O.T. (1986) “Thermal properties of soils”.

Du, M., Jing, H., Gao, Y., Su, H. and Fang, H. (2020)“Carbon nanomaterials enhanced cement-based composites: advances and challenges”, *Nanotechnology Reviews*, 9(1):115-135.

Li, H., Zhang, Q. and Xiao, H. (2013) “Self-deicing road system with a CNFP high-efficiency thermal source and MWCNT/cement-based high-thermal conductive composites”, *Cold Regions Science & Technology*, 86(FEB.):22-35.

Multi-phase and Multi-ion Modelling of Electric Current, Electric Potential and Species Transport in Reinforced Concrete During Active corrosion Process Applied to Optimization of a Patching Repair Process

K. Szyszkiewicz-Warzecha

AGH University of Science and Technology, Faculty of Materials Science and Ceramics, Kraków, Poland
email: szyszkin@agh.edu.pl

ABSTRACT

Corrosion of the reinforcement bars in concrete constructions is one of the most important factor affecting their safety and useful lifetime. Due to the enormous scale of global usage of reinforced concrete, the problem of dealing with this degradative phenomenon is very important. Hence, the proper modelling of corrosion phenomena in reinforced concrete structures is crucial for the implementation of efficient corrosion control based on a good understanding of the underlying processes. A 3D corrosion model of reinforced concrete structures based on the Nernst–Planck flux for ionic species is presented and its application to cathodic protection with sacrificial anode (SACP) and patch repair aftereffects is demonstrated. Example of computing the optimal placement of the anode is included.

1. Introduction

During the service time of concrete structures, especially bridges, dams, roads, or parking garages, one repair technique is particularly frequently applied – the patch repair, where a part of defective or contaminated concrete cover of rebars is replaced with a fresh "patch". For example, if the contaminated concrete cover contains a high concentration of chlorides it is possible that the protective passive film on the rebar surface will break down, and in consequence the corrosion processes on the rebar surface will commence [1]. Hence, the patch is meant to reduce that risk by replacing the contaminated portion of concrete with fresh one which is free of chlorides. However, concerning the performance of repair it has been noted that recurring corrosion after patch repair is possible. To emend the effectiveness of repair, a sacrificial anode embedded into the concrete can be used. [2] The material of the anode is a less noble metal, such as zinc or magnesium, which corrodes more readily than the iron based rebar. However, the effectiveness of this method is not well understood and relatively little work on this topic is found in the literature. Relevant questions include the location and size of the anode and the influence of other ions on the electric current distributions. The main goal of this paper is to investigate the change of macrocell corrosion after patch repair. The study is based on a 3D model comprising electric potential, current density, flow of ions and heterogeneous redox reactions on the rebars surface. More specifically, the model involves transport of four components (O_2, Zn^{2+}, OH^-, Fe^{2+}), kinetics of electrode processes similar to the Butler–Volmer equation with concentration polarization. Numerical simulations based on this model evaluate the intensity of corrosion before and after repair and for various locations of the sacrificial anode. Additional, two cases are also considered: the cathodic protection with applied negative potential to the rebar (impressed current cathodic protection) and without applied potential. This approach is very helpful as experimental assessment for many possible cases of the patch and/or anode arrangements would be very costly, impractical or simply not feasible.

2. Description of the mathematical model

A schematic picture of a typical patch repair is shown in Figure 1. We assume that a central part (yellow block) is the patch which replaced a contaminated part around the cylindrical rebar. Moreover, the zinc

anode in the form of a small cylinder (pink color) is placed in the patch some distance away from the rebar. Two situations before repair are considered: (i) the middle (approx. one third length) of the rebar is in an active corrosion state and the rest surface is in a passive state; (ii) the middle of the rebar is in passive state and the rest surface is in an active state.

In dilute electrolytic solutions without convective flows, the flux of each dissolved species $(i = \mathrm{O_2}, \mathrm{Zn^{2+}}, \mathrm{OH^-}, \mathrm{Fe^{2+}})$ is given by [3]

$$\mathbf{J}_i = -D_i \nabla c_i - z_i u_i c_i \nabla \varphi \tag{1}$$

The flux $\mathbf{J}_i$ $(\mathrm{mol/m^2 \cdot s})$ of species i is a vector describing the direction of species movement and its intensity. The flux of species i expressed in equation (1) is composed of two parts: (i) diffusion term $(-D_i \nabla \varphi)$ and (ii) migration term $(-z_i u_i c_i \nabla \varphi)$. Here, $D_i\,(\mathrm{m^2/s})$ denotes its diffusion coefficient, $u_i\,(\mathrm{m^2/s \cdot V})$ denotes its mobility, c_i $(\mathrm{mol/m^3})$ gives its concentration, z_i is its charge number (for oxygen obviously $z_{\mathrm{O_2}} = 0$), and φ (V) is the electrostatic potential whose negative gradient, $-\nabla\varphi$, is the electric field density. We see that in dilute electrolytes the transport of each species is characterized by two transport parameters: diffusion coefficient (D_i) and mobility (u_i). But these two parameters are approximately related by the Einstein–Smoluchowski equation [3], $u_i = z_i(F/RT)D_i$, thus the flux expression is now simplified to

$$\mathbf{J}_i = -D_i(\nabla c_i + \tfrac{z_i F}{RT} c_i \nabla \varphi), \tag{2}$$

where: T is the temperature (K), F is Faraday's constant, and R is the universal gas constant.

Now a material balance for species i is

$$\frac{\partial c_i}{\partial t} = -\,\mathrm{div}\mathbf{J}_i + R_i, \tag{3}$$

with R_i $(\mathrm{mol/m^3 \cdot s})$ describing the homogeneous reaction in which species i is produced/consumed. The electric field could be in principle computed by using the Poisson equation, $\Delta\varphi = -\frac{F}{\varepsilon_r \varepsilon_0}\sum_i z_i c_i$, but it is almost impossible for larger domains (on the order of meters) as the numerical solution for Poisson equation with very small electrical imbalance would required the mesh with element size below 10^{-8} m. Hence, in the literature there are several approximations which replace the Poisson equation with some other equation. In this work the electroneutrality approximation will be used:

$$\sum_i z_i c_i = 0, \tag{4}$$

where the sum is over all ionic species.

Boundary conditions result from the assumed corrosion reactions [4]

$$\begin{aligned} &\textit{iron oxidation}: && \mathrm{Fe} \rightarrow \mathrm{Fe^{2+}} + 2e^- \\ &\textit{zinc oxidation}: && \mathrm{Zn} \rightarrow \mathrm{Zn^{2+}} + 2e^- \\ &\textit{oxygen reduction}: && \mathrm{O_2} + 2\mathrm{H_2O} + 4e^- \rightarrow 4\mathrm{OH^-} \end{aligned} \tag{5}$$

The Tafel equation which connects the electrode potential with the current density allows to define boundary condition for species Fe^{2+}, Zn^{2+}, O_2 and OH^-. Hence, we have the following equalities on the boundary:

$$\begin{aligned} &\text{active bar}: && -\boldsymbol{n}\cdot\mathbf{J}_{\mathrm{Fe^{2+}}} = \frac{1}{2F} i_{\mathrm{Fe}},\ -\boldsymbol{n}\cdot\mathbf{J}_{\mathrm{O_2}} = \frac{1}{4F} i_{\mathrm{O_2}},\ -\boldsymbol{n}\cdot\mathbf{J}_{\mathrm{OH^-}} = \frac{1}{F} i_{\mathrm{O_2}}, \\ &\text{passive bar}: && -\boldsymbol{n}\cdot\mathbf{J}_{\mathrm{O_2}} = \frac{1}{4F} i_{\mathrm{O_2}},\ -\boldsymbol{n}\cdot\mathbf{J}_{\mathrm{OH^-}} = \frac{1}{F} i_{\mathrm{O_2}}, \\ &\text{sacrificial anode}: && -\boldsymbol{n}\cdot\mathbf{J}_{\mathrm{Zn^{2+}}} = \frac{1}{2F} i_{\mathrm{Zn}},\ -\boldsymbol{n}\cdot\mathbf{J}_{\mathrm{O_2}} = \frac{1}{4F} i_{\mathrm{O_2}},\ -\boldsymbol{n}\cdot\mathbf{J}_{\mathrm{OH^-}} = \frac{1}{F} i_{\mathrm{O_2}}, \end{aligned} \tag{6}$$

where analytical form of the relation between current density through the electrode/electrolyte interface and the potential difference across this interface is:

$$\text{anodic Tafel eq}: \; i = i^0 \cdot e^{2.303(\varphi_s - \varphi - E_{eq})/b_a}, \quad \text{cathodic Tafel eq}: \; i = i^0 \cdot e^{-2.303(\varphi_s - \varphi - E_{eq})/b_c},$$
$$\text{cathodic Tafel with concentration polarization}: \; i = i^0 (c_i / c_{ref}) e^{-2.303(\varphi_s - \varphi - E_{eq})/b_c}, \tag{7}$$

where all relevant parameters: i^0 $(\mathrm{A/m^2})$ exchange current density, E_{eq} (V *vs. ref*) electrode reaction equilibrium potential (vs. reference electrode, usually SCE), Tafel coefficients b_a, b_c (V) are selected for the specific reaction and electrode.

Ther parts of the boundary system which are not covered by condition (5) and (6) will be assume as isolating boundary:

$$-\boldsymbol{n} \cdot \mathbf{J}_i = 0, \quad i = \mathrm{O_2}, \; \mathrm{Zn^{2+}}, \; \mathrm{OH^-}, \; \mathrm{Fe^{2+}}. \tag{8}$$

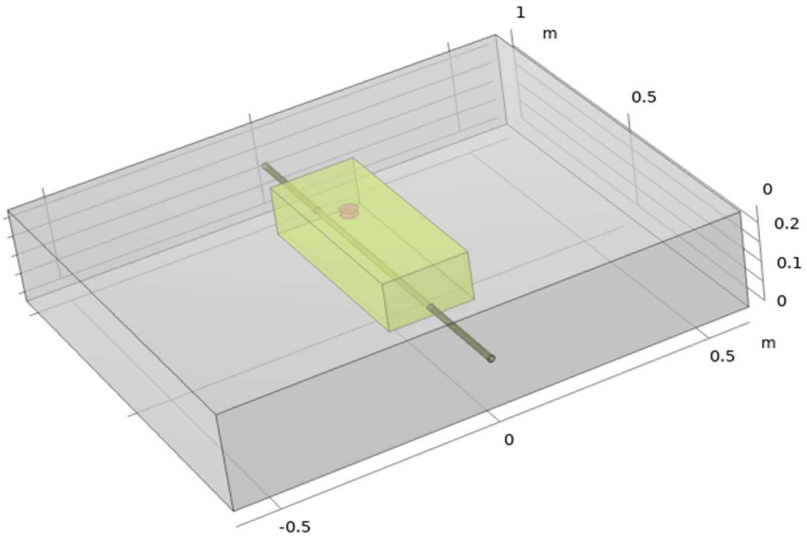

Figure 1. Geometry and arrangements of basic elements in patch repair considered in the work. Grey block represents a fragment of the concrete with embedded rebar (horizontal long dark-grey cylinder. Yellow block represents the part where contaminated concrete was replaced with a fresh one. Pink small cylinder represents the zinc anode.

3. Results of numerical simulations

A typical simulations consider the situation before and after repair. The model allows for computing all interesting quantities (concentrations and fluxes of all species, current density distributions, total current on the active bar etc.). For example, in the case of corroding rebar (Figure 1) the total corrosion current on the active part was calculated to be $1.87 \cdot 10^{-5}$ A before patch repair. After applying the patch repair as indicated in the picture and assuming that diffusion coefficients in the patch a reduced by one order as compared to values before repair we obtained the current value $6.51 \cdot 10^{-6}$ A which is almost ten times smaller. Moreover, the sensitivity analysis have shown that this value is not much effected by the diffusion coefficients in the patch, but rather on the presence of the SACP anode. Another type of simulations was related to the dependence of the corrosion current on the locations of the anode (SACP) and can be viewed as the search for its optimal position. For simplicity we performed only one dimensional optimization by changing the location of the SACP only in one direction. The results are presented in Figure 2, and from it we see that the plot is symmetric with respect to the middle position (as expected due to the symmetry of the model with respect to the plane perpendicular to the rebar axis), but more interestingly we see that better effectiveness is achieved not by placing the anode in the middle but near one of the edges of the patch.

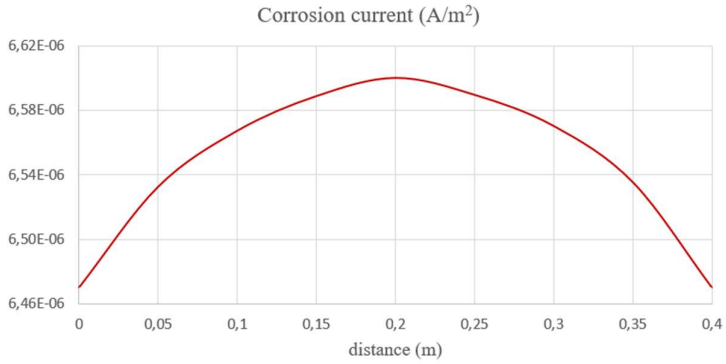

Figure 2. Corrosion current as a function of the location of SACP along the rebar. Distance = 0 corresponds to the initial position of SACP shown in Figure 1. Increasing values of distance correspond to moving the anode to the front.

We have also evaluated the impact of the active cathodic protection in the presented system. To this goal, the computations were performed with applied voltage $E_{app} = -0.7$ V (the rebar being negatively polarized relative to the SACP). Now the value of the corrosion current is changed dramatically, as from the anodic dissolution current it turns out to be the cathodic current with the value $I = -1.13 \cdot 10^{-4}$ A.

4. Conclusions

This study shows how a multi-species transport model with current and potential distribution can be applied to investigate cathodic protection and patch repair effects. It is more advanced than most of the treatments in the current literature which basically are simple electrical models based on Ohm's law ($\mathbf{i} = -\sigma \nabla \varphi$) with one bulk parameter (conductivity) [5]. Such models solve in fact a simple equation for the electric potential (Laplace's equation) with nonlinear boundary conditions (of the Tafel type). Some of these models do include very weak coupling with oxygen through the boundary conditions (concentration polarization), but still this is very simplistic. Currently, the models which are better description of reality should include the transport of all relevant species (ionic and neutral) where the current density is given by $\mathbf{i} = F \sum_i z_i \mathbf{J}_i$. Moreover, these models allow for realistic treatment of the surface reactions (such as shown in (5)) with each species having its own characteristic physical parameters (exchange current density, charge transfer coefficients, equilibrium potentials etc.). The main difficulty in this approach is the calculation of the electric potential. In theory, the Poisson equation could be used, but it is – for numerical reasons – not possible currently for larger domains (Poisson's equation has been successfully used in the domain of small sizes, for example the ion selective membranes or ionic channels in the biological membranes). Thus, in concrete construction (sizes on the order of meters) some approximation to replace the Poisson equation must be used There are two that are frequently used: the Laplace equation or the electroneutrality. We believe that the electroneutrality equation is a better approximation than the Laplace equation (which is very good for metal conductors) because the tests we have performed unequivocally show that when the Laplace equation is used with transport equations (2) and (3), a value of the charge density ($F \sum_i z_i c_i$) in the system assumes unreasonably larger values ($\sim 10^3$ C/dm^3) or higher which definitely can not exist in the macroscopic stable systems. This, often overlooked fact, leads us to promoting the use of electroneutrality condition (4) as the well justified approximation for computing the electric potential in the multi-ion transport systems.

References

[1] Zhang, B. *et al*. (2018) "Unmasking chloride attack on the passive film of metals", *Nat. Comm*. **9**, 2559.

[2] Lozinguez, E. *et al*. (2018) ”Contribution of Sacrificial anode in reinforced concrete patch repair: Results of numerical simulations”, *Constr. Build. Mat*. **178**, 405–417.
[3] Allen J. Bard, Larry R. Faulkner, ”Electrochemical Methods – Fundamentals and Applications”, Wiley, 2001, second edition.
[4] Muehlenkamp, E.B. et al. (2005) ”Effect of Moisture on the Spatial Uniformity of Cathodic Protection of Steel in Reinforced Concrete”, *Corrosion* **61**(6), 519–533.
[5] Cao, C. *et al*. (2013) ”Modelling of interaction between corrosion-induced concrete cover crack and steel corrosion rate”, *Corr. Sci*. **69**, 97–109.

The 16th International Congress on the Chemistry of Cement 2023 (ICCC2023)
"Further Reduction of CO_2 -Emissions and Circularity in the Cement and Concrete Industry"
September 18–22, 2023, Bangkok, Thailand

Improved tensile performance of strain-hardening geopolymer composites using treated CBA and polyethylene fiber

Suhawn Ju[1*], Minchang Kang[2], and Sukhoon Pyo[3]

[1] *Department of Urban and Environmental Engineering, Ulsan National Institute of Science and Technology (UNIST), 50 UNIST-gil, Ulju-gun, Ulsan 44919, Republic of Korea*
Email: gn00147@unist.ac.kr
[2] *Department of Urban and Environmental Engineering, Ulsan National Institute of Science and Technology (UNIST), 50 UNIST-gil, Ulju-gun, Ulsan 44919, Republic of Korea*
Email: cmway013@unist.ac.kr
[3] *Department of Urban and Environmental Engineering, Ulsan National Institute of Science and Technology (UNIST), 50 UNIST-gil, Ulju-gun, Ulsan 44919, Republic of Korea*
Email: shpyo@unist.ac.kr

ABSTRACT

In this study, a strain-hardening geopolymer composite (SHGC) based on ground granulated blast furnace slag (GGBFS) was developed by incorporating treated coal bottom ash (CBA) and polyethylene (PE) fiber. Treated CBA and PE fiber were used to improve the tensile performance and sustainability of SHGC, and CBA was treated using a solution-dissolving method based on a previous study. Through the solution-dissolving method, not only CBA was utilized as a silicate source for an alkaline solution, but also residue CBA was replaced with sand to mix a geopolymer composite. The morphological surface change after treating CBA was observed through SEM image analysis. SHGC was prepared by containing 2% PE fiber and replacing 100% of sand with treated CBA, and the mechanical performance of the SHGC was evaluated through compressive strength and direct tensile test. Using treated CBA enhanced the tensile behavior of SHGC compared to the sand series. In particular, it showed improvement not only in tensile strength but also in various indicators such as energy absorption capacity and strain-hardening capability.

KEYWORDS: *Strain-hardening geopolymer composites; Polyethylene fiber; Surface morphology; GGBFS; Coal bottom ash*

1. Introduction

Among the primary energy consumption, coal is the second major source occupying around 30% after oil, according to a report of world energy by British Petroleum (BP) ("BP Statistical Review of World Energy 2022, 71st edition," 2022). This use of coal-related energy has mass-produced coal bottom ash (CBA), which occupies about 20% of solid waste worldwide (Ban et al., 2022). The CBA, a by-product of coal-fired power plants, is difficult to recycle compared to the other coal ash types such as fly ash; therefore, most of CBA is buried in landfills. This study not only used CBA as a silicate source by dissolving in an alkali activator but also prepared a strain-hardening geopolymer composite (SHGC) using residual CBA as a fine aggregate after making the alkali activator.

2. Experiment

2.1 Materials

Ground granulated blast furnace slag (GGBFS), fly ash, CBA, and silica sand were used as binders, and an alkaline activator was prepared using sodium hydroxide solution, CBA, and silica fume.

2.2 Sample preparation

The alkaline activator was stirred at 75℃ for 24 hours using a magnetic stirrer after dissolving the CBA or silica fume in the sodium hydroxide solution. Table 1 summarizes the mix proportions and describes the sample names by CBA content. After mixing, the mixture was casted into molds and demolded after one day. After demolding, the samples were cured under sealed conditions at 80℃ for one day. A direct tensile test was performed to evaluate the tensile performance of the SHGC depending on the CBA content.

Table 1. Mix proportion of SHGC

Sample	Design parameter			Mix design (kg/m^3)								
				Precursor		Fine aggregate			Activator			
	CBA content	PE fiber 1)	SP Content 2)	GGBFS	fly ash	silica sand No.6	silica sand No.8	treated CBA	water	NaOH	SF	ion CBA
CBA0	0%	2%	4%	790.8	197.7	156.0	66.9	-	428.2	137.0	98.0	-
CBA25	25%	2%	6%	793.0	198.2	119.1	51.0	49.9	428.8	137.2	73.7	21.4
CBA50	50%	2%	6%	794.5	198.6	79.6	34.1	99.9	429.6	137.4	49.2	42.8
CBA75	75%	2%	6%	796.1	199.0	39.9	17.1	150.2	430.5	137.7	24.7	64.4
CBA100	100%	2%	6%	793.4	198.3	-	-	199.6	429.0	137.2	-	98.3

1) Volume fraction
2) Mass ratios of precursor weight

3. Result and discussions

3.1 Treated CBA

Figure 1 shows the amount of Si^{4+} extracted from CBA and SF in sodium hydroxide solution. When the same weight was used, the amount of Si^{4+} extracted from CBA was approximately 30% of that from SF. Additionally, the amount of Al^{3+} was analyzed but was not observed. Based on the ICP results, the calculated amount of Si^{4+} obtained when using CBA as a silicate source in the alkaline activator was determined, and the experimental mix design was finalized.

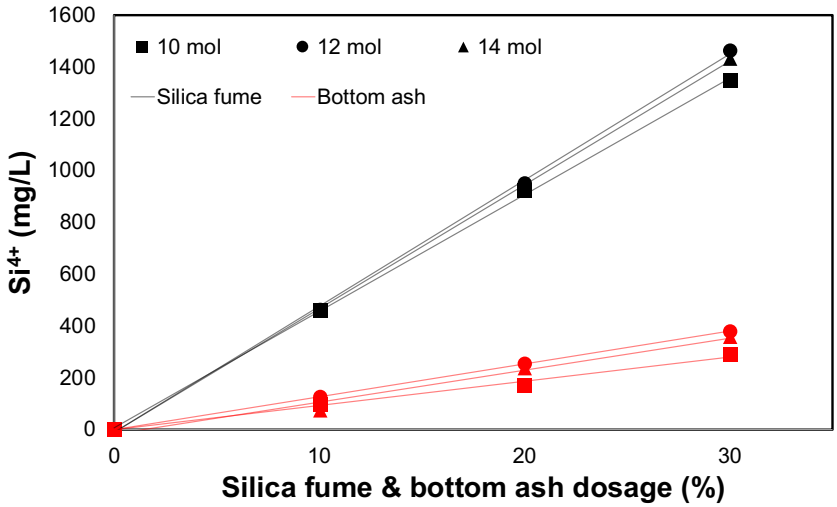

Figure 1. Amounts of Si^{4+} extracted from of CBA and SF in sodium hydroxide solution.

Figure 2 presents the XRD patterns of raw CBA and the residual CBA after preparing the alkaline activator. Raw CBA shows the crystal phase of mullite and quartz, as well as an amorphous phase. The amorphous phase is observed in a broad bump between 18-30°, and it can be observed that this broad bump decreases

in the residual CBA. This indicates that the amorphous phase of raw CBA was dissolved in the sodium hydroxide solution, resulting in the extraction of Si^{4+}.

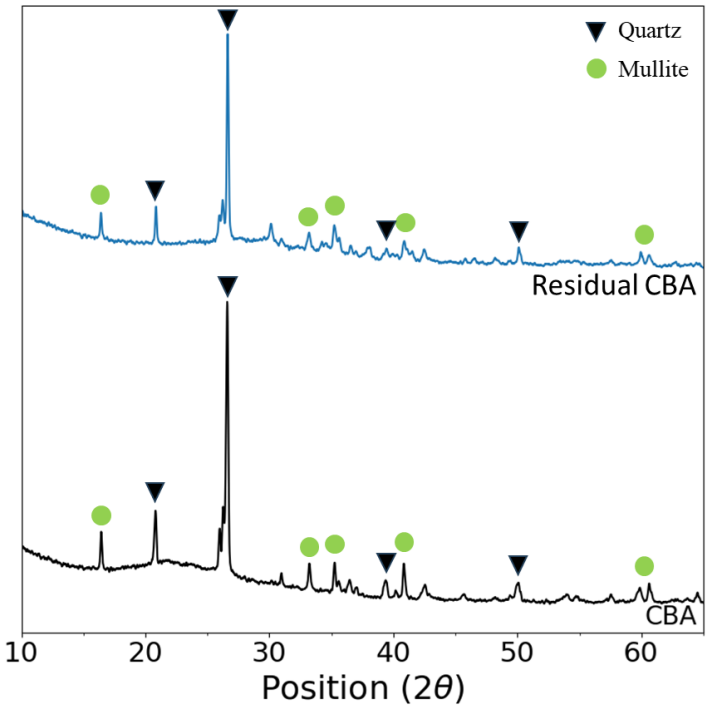

Figure 2. XRD patterns of raw CBA and residual CBA.

Figure 3 shows the surface changes of CBA after the preparation of the alkaline activator. It was observed that the surface of the CBA was rough after the silicate source of the amorphous phase in the raw CBA was extracted into the sodium hydroxide solution. It can be said that such a change in the surface of the CBA will have a positive effect on the tensile performance.

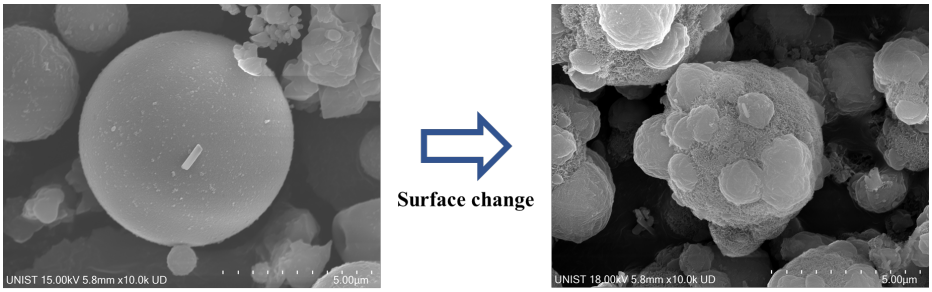

Figure 3. SEM images of the raw CBA and residual CBA.

3.2 Tensile performance

The results of the direct tensile test of SHGC by CBA content are illustrated in Figure 4. The CBA0 specimen, in which CBA was not incorporated, showed a comparable trend to previous research results (Yoo et al., 2022; Shaikh et al., 2018), and it was observed that the tensile performance improved with an increasing amount of CBA. This can be attributed to the rough surface of residual CBA, which has a positive impact on enhancing tensile performance.

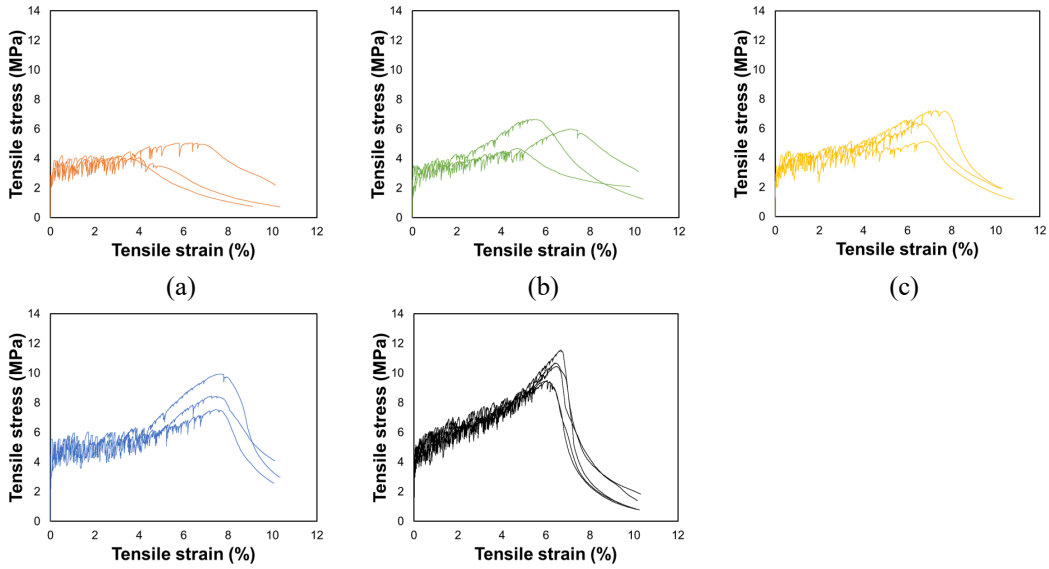

Figure 4. Tensile stress vs. strain curve according to CBA content: (a) CBA0, (b) CBA25, (c) CBA50, (d) CBA75, and (e) CBA100

4. Conclusions

This study employed the method of utilizing CBA as a silicate source developed in a previous study, while also utilizing the remaining bottom ash as fine aggregates to develop an eco-friendly SHGC. The results confirmed that as the amount of CBA increases, the tensile performance improves, thereby suggesting a novel sustainable method of utilizing CBA in SHGC.

Acknowledgements

This work was supported by the National Research Foundation of Korea (NRF) grant funded by the Korea government (MSIT) (No. 2021R1A4A1030867 and RS-2023-00212366).

References

BP Statistical Review of World Energy 2022, 71st edition, 2022. https://www.bp.com/en/global/corporate/energy-econ

Ban, C.C., Le Ping, K.K., Jia, L.J., Siddique, R., Tangchirapat, W., Bin Megat Johari, M.A., 2022. Coal bottom ash as constituent binder and aggregate replacement in cementitious and geopolymer composites: A review. J. Build. Eng. 104369. https://doi.org/10.1016/j.jobe.2022.104369

Shaikh, F.U.A., Fairchild, A., Zammar, R., 2018. Comparative strain and deflection hardening behaviour of polyethylene fibre reinforced ambient air and heat cured geopolymer composites. Constr. Build. Mater. 163, 890–900. https://doi.org/10.1016/j.conbuildmat.2017.12.175

Yoo, D.Y., Lee, S.K., You, I., Oh, T., Lee, Y., Zi, G., 2022. Development of strain-hardening geopolymer mortar based on liquid-crystal display (LCD) glass and blast furnace slag. Constr. Build. Mater. 331, 127334. https://doi.org/10.1016/j.conbuildmat.2022.127334

The 16th International Congress on the Chemistry of Cement 2023 (ICCC2023)
"Further Reduction of CO_2 -Emissions and Circularity in the Cement and Concrete Industry"
September 18–22, 2023, Bangkok, Thailand

Effect of CO_2 curing on bonding strength and microstructure in the interfacial transition zone

Y. Huang[1], X. Hu[1], and C.J. Shi[1*]

[1] *College of Civil Engineering, Hunan university, Changsha, 410082, China*
Email: yanhuang666@hnu.edu.cn
[1] *College of Civil Engineering, Hunan university, Changsha, 410082, China*
Email: xianghu @hnu.edu.cn
[1] *College of Civil Engineering, Hunan university, Changsha, 410082, China*
Email: cshi@hnu.edu.cn

ABSTRACT

The interfacial transition zone (ITZ) between aggregate and cement paste is a key factor for the performance and failure mechanism of concrete due to its high porosity and enrichment of the oriented calcium hydroxide ($Ca(OH)_2$) crystals, and CO_2 curing is a promising technique for consuming $Ca(OH)_2$ and forming calcium carbonate ($CaCO_3$) to reduce porosity and improve strength. However, the effect of CO_2 curing on the mechanical and microscopic properties of the ITZ is not clear. In this study, the effect of CO_2 curing on ITZ was investigated using splitting tensile bonding tests, X-ray diffraction (XRD) and backscattered electron imaging (SEM-BSE). In addition, the thickness of the ITZ was determined by the decreasing segment of porosity across the interface between the aggregate and cement paste. Results showed that the porosity and thickness of the ITZ were significantly reduced after CO_2 curing, and there were almost none of the $Ca(OH)_2$ crystal in the ITZ, which was replaced by a significant precipitation of $CaCO_3$. This indicated that the $CaCO_3$ crystals fill the pores and thus improve the bonding strength in the ITZ.

KEYWORDS: *CO_2 curing, interfacial transition zone, splitting tensile bonding strength, backscattered electron imaging*

1. Introduction

CO_2 is the main greenhouse gas blamed for global warming. Extensive studies have been conducted on strategies to mitigate CO_2 emissions, in which CO_2 curing techniques not only improving the performance of concrete, but also capturing and storing CO_2 (He et al,2016; Song et al, 2022). However, effects of CO_2 curing on the performance of the ITZ are critical and thorny problems, as the ITZ is generally considered to be the weakest link in concrete (Wang et al, 2020; Sun et al, 2020). Therefore, studying the effect of CO_2 curing on performance the ITZ will contribute to a further understanding of the influence of CO_2 curing on the properties of concrete.
This work aims to clarifies the bonding strength and microstructure of the ITZ based on the early accelerated CO_2 curing. The bonding strength of ITZ between cement paste and aggregate will be investigated by performing the splitting tensile strength test. The porosity distribution and chemical composition around the ITZs will be measured by the SEM and XRD.

2. Experimental program

2.1 Materials

The P.I 42.5 type Portland cement with a specific surface area of 356 m^2/kg was utilized in this work, and its chemical composition is shown in Table 1. The cube aggregates with 20 mm × 20 mm × 10 mm were

extracted from the limestone by cutting to test the bonding strength and microstructure properties of ITZ between the cement paste and aggregate.

Table 1 Chemical composition of Portland cement.

SiO_2	Al_2O_3	Fe_2O_3	CaO	MgO	SO_3	Na_2Oeq	f-CaO
20.78	5.08	3.29	63.46	2.30	2.15	0.56	0.80

2.2 Mix process

The water to cement ratio of 0.35 (mass basis) was used to study the bonding strength and microstructure of the ITZ. The mixing process of specimen was described as follows. Firstly, the cube aggregates were kept in water for more than 24 hours before casting to keep the surface moist. Before casting, they were removed and any excess water on the surfaces was dried by a damp cloth. Then, the aggregate was placed on one side of the mold and the fresh cement paste was filled into the other side, and the Fig. 1 showed the details of the specimen.

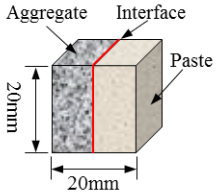

Fig. 1 A sketch of specimen with dimension details.

2.3 Curing regimes

After 8 h after casting, the molds were removed and divided into two batches. One batch was left in a room with 20 ± 2°C and 60% relative humidity for 4 h to make the specimens lose water for pre-condition. Then, the specimens were sealed on five sides, with hot paraffin coating and only one side of the paste exposed to ensure that CO_2 gas only diffused in one dimension. Next, the specimens were accelerated carbonated for two and a half days in a CO_2 chamber at a pressure of 0.2 MPa, a temperature of approximately 20°C and 60% RH. The other batch was cured in saturated lime water at 20°C for 3 d.

2.4 Samples preparation

To understand the effect of CO_2 curing on the chemical composition of the ITZ, the powders in the ITZ were collected for XRD analysis using a computer numerical controlled machine, which were ground to a finer powder and passed through a 45 μm sieve. And all finer powder samples were dried in a vacuum oven at 40 °C for 2 days.

To comprehend the effect of CO_2 curing on the microstructure of the ITZ, the small cube samples with 10 mm × 10 mm × 10 mm in the centre of the specimen was cut using a low-speed diamond saw-cutting system. After cutting, the samples were stored in the ethyl alcohol solution for 3 d to stop the hydration and then kept in the vacuum drying oven (40 ± 2 °C) for another 2 d. Then, the samples were vacuum-impregnated with a low viscosity and high permeability epoxy resin. Finally, the samples were ground and polished by an automatic grinding and polishing machine to ensure that the observation surface is smooth and flat for the SEM-BSE test.

2.5 Testing methods

The bonding strength of ITZ between cement paste and aggregate was measured by performing the splitting tensile test using microcomputer control electronic universal testing machine. A displacement-controlled load was applied at a rate of 0.05mm/min to ensure a quasi-static loading process.

The XRD analysis was performed using R-axis Spider X-ray diffraction and a Cu kα X-ray radiation source. The 2θ scanning range was 5° – 70°, the step size was 0.02°, and the speed was 2 °/min.

The BSE image analysis was tested by A field emission scanning electron microscope (SEM) equipment equipped with a backscattered electron (BSE) image detector to survey the porosity changes of ITZ at different curing regimes. At least 30 images of the ITZ for each sample were taken at 800× magnification

and the resolution were 2048 × 2176 pixels (pixel size of 0.131 μm). In order to characterize the performance of the ITZ along the distance from the aggregate surface, concentric expansion method was used to divide several successive strips of equal distance, so that each BSE image was delineated with 30 strips of 5 μm wide. The porosity of each strip was determined as the percentage of area of pores to total area of the strip (Xie et al, 2015).

3. Results and discussions

3.1 Bonding strength

Fig. 2 showed the splitting tensile bonding strength of different curing methods for 3d. It can be visually observed that the CO_2 curing significantly improved the bonding strength of the ITZ. The splitting tensile bonding strength of ITZ under saturated lime water curing was 1.06MPa, while the ITZ bonding strength subjected to CO_2 curing was 1.74 MPa, which was 64.1% higher than that of ITZ under saturated lime water curing. It indicated that CO_2 curing for 3 days can significantly improve the bonding strength of the ITZ.

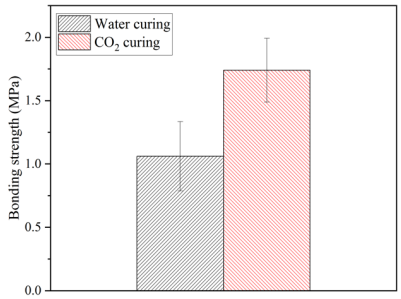

Fig. 2 Splitting tensile bonding strength of ITZ subjected to different curing methods

3.2 XRD analysis

Fig. 3 showed the XRD patterns of the ITZ with different curing methods. The results of the XRD pattern indicated that many diffraction peaks of $Ca(OH)_2$ were observed in water curing. However, after the CO_2 curing, these diffraction peaks disappeared and many new $CaCO_3$ diffraction peaks emerged. This showed that CO_2 curing can promote the convert of $Ca(OH)_2$ to $CaCO_3$, which filled the pores and cracks in ITZ and improved the performances of concrete. In addition, the C_2S and C_3S diffraction peaks of the cement clinker were evident in the water curing samples compared to the CO_2 curing samples. This indicated a more intense carbonation reaction and a higher degree of reaction (Lu et al, 2022). The Rietved method was used to quantify the content of each phase in the samples and the results were shown in Table 2. The results showed that the relative $CaCO_3$ content after CO_2 curing was approximately 61.6%, and the unhydrated cement clinker after CO_2 curing was approximately half of the water curing, indicating a higher degree of reaction to carbonation. This could be a possible evidence of the fast carbonation reaction kinetics and the formation of $CaCO_3$ prior to the formation of $Ca(OH)_2$ in the CO_2-cured samples (Tu et al, 2016).

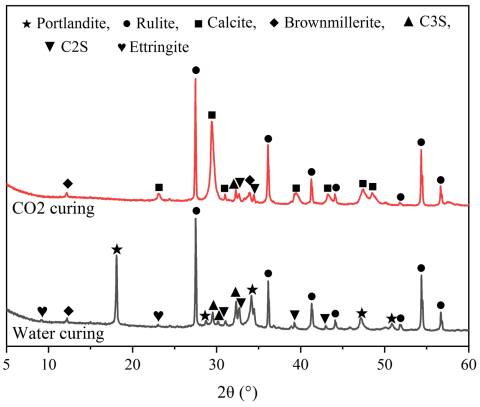

Fig. 3 XRD results of ITZ with different curing regimens

Table 2 Qualitative XRD results of ITZ

Sample	Portlandite	Calcite	Brownmillerite	C_3S	C_2S	Ettringite	Amorphous
Water curing	20.6	0	4.4	10.9	6.7	1	56.4
CO_2 curing	0	61.6	4.9	6.8	2.8	0	23.9

3.3 Microscopic characterization of ITZ

Fig. 4 gived the BSE results of the ITZ with different curing regimes, which showed that sample with CO_2 curing had lower porosity in the ITZ than those with water curing. In general, lower porosity of the ITZ suggestd stronger and more durable interface between cement paste and aggregates. In addition, as the distance from the aggregate surface increased, the porosity gradually decreased and eventually tended to a steady state in all sample. Therefore, many experts and scholars refer to the descending section as the ITZ (Xie et al, 2015). Based on Fig. 4, it can be concluded that the thickness of the ITZ of water curing was about 100 μm, while that of CO_2 curing was about 80 μm, a reduction of 20%, which demonstrated the effectiveness of CO_2 curing in reducing the thickness and porosity of the ITZ.

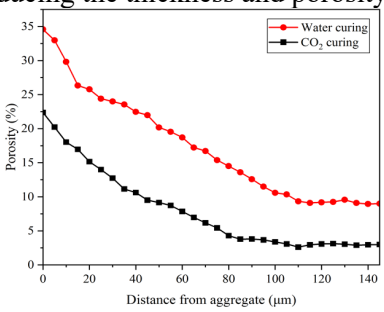

Fig.4 BSE results of the ITZ with different curing regimes.

4. Conclusions

The bonding strength and microscopic properties of the ITZ were investigated under different curing regimes. The experimental results showed that CO_2 curing improved significantly the bonding strength of the ITZ by 64.1% from1.06 MPa of water curing to 1.74MPa with CO_2 curing. In addition, based on the SEM-BSE results, the porosity of the ITZ subjected to CO_2 curing was substantially reduced, and the thickness of the ITZ was also decreased from around 100 μm to 80 μm. What's more, the product of the ITZ after water curing was mainly $Ca(OH)_2$ and the unhydrated cement clinker represented 22 % of the sample, whereas the product of the ITZ after CO_2 curing was mainly $CaCO_3$ crystals and the unreacted cement clinker accounted for only 14.5% of the sample and 65.9% of the clinker content with water curing. This is due to the more violent and the higher degree of carbonation reaction.

Reference

He, P.P., Shi, C.J., Tu, Z.J., et al. (2016) “Effect of further water curing on compressive strength and microstructure of CO_2 -cured concrete”, *Cement and Concrete Composites*, 72:80-88.

Lu, B., Drissi, S., Liu, J. H., et al. (2022) “Effect of temperature on CO_2 curing, compressive strength and microstructure of cement paste”, *Cement and Concrete Research*, 157: 106827.

Tu, Z. J., Guo, M. Z., Cai, S. P., et al. (2016) “Effects of limestone powder on CaCO3 precipitation in CO2 cured cement pastes”, Cement and Concrete Composites, 72: 9-16.

Song, B.X., Liu, S.H., Hu, X., et al. (2022) “Compressive strength, water and chloride transport properties of early CO_2-cured Portland cement-fly ash-slag ternary mortars”, *Cement and Concrete Composites*, 134: 104786.

Sun, D. D., Shi, H. S., Wu, K., et al. (2020) “Influence of aggregate surface treatment on corrosion resistance of cement composite under chloride attack”, *Construction and Building Materials*, 248: 118636.

Wang, X. Y., Dong, S. F., Ashour, A., et al. (2020) “Effect and mechanisms of nanomaterials on interface between aggregates and cement mortars”, *Construction and Building Materials*, 240: 117942.

Xie, Y. T., Corr, D. J., Jin, F., (2015) “Experimental study of the interfacial transition zone (ITZ) of model rock-filled concrete (RFC)”, *Cement and Concrete Composites*, 55: 223-231.

The 16th International Congress on the Chemistry of Cement 2023 (ICCC2023)
"Further Reduction of CO_2 -Emissions and Circularity in the Cement and Concrete Industry"
September 18–22, 2023, Bangkok, Thailand

Incorporation of construction and demolition waste (CDW) in fiber cement submitted to the accelerated carbonation process

D.O. Lima[1], R.H. Filomeno[2], M.R. Frías[3,*], and H. Savastano Junior[4]

[1] *University of São Paulo (USP), São Paulo, Brasil*
Email: Daniela.engcivil@usp.br
[2] *University of São Paulo (USP), São Paulo, Brasil*
Email: rafaelfilomeno@usp.br
[3] *Eduardo Torroja Institute for Construction Science (IETcc-CSIC), Madrid, Spain*
Email: mfrias@ietcc.csic.es
[4] *University of São Paulo (USP), São Paulo, Brasil*
Email: holmersj@usp.br

ABSTRACT

One of the main problems associated with the socioeconomic development of a country is the generation of construction and demolition waste (CDW), which represents between 30-50% of the total waste generated worldwide. The motivation of the present work is to develop materials with less cement utilization, and strategies for CO_2 sequestration. Thus, the work aimed to evaluate the application of the fine fraction of CDW (<63 μm) from waste concrete, to partially replace Portland cement (10% by mass) in the production of fiber cement composites submitted to the carbonation process in the early ages. The fiber cement pads were produced with 10% of bleached hardwood kraft pulp of eucalyptus by the slurry dewatering and pressing method and were analyzed before and after the accelerated carbonation curing. The accelerated carbonation took place in a laboratory chamber at 60°C, 5 bar of pressure, CO_2 saturation, and sample moisture of 60% for 24 h. The samples were evaluated for physic-mechanical and microstructural performance and X-ray diffraction. The carbonated samples presented an increase of approximately 60% in flexural strength compared with their non-carbonated counterparts. Although there is a tendency for carbonation to decrease the deformation capacity of fiber cement, the addition of CDW compensated for this embrittlement, providing an increase of 40% in specific energy, due to the better packing of the particles and optimizing the fiber interface. This behavior was confirmed through the microstructural assessment of the material, presenting a more compact and less porous matrix and fiber-matrix transition zone. In general, the substitution of 10% by mass of Portland cement by the fine fraction of CDW, contributes beneficially to the physic-mechanical performance of fiber cement, improving the effectiveness of the carbonation process.

KEYWORDS: *Construction and demolition waste; Eco-efficient cement; Fiber-cement; Accelerated carbonation.*

1. Introduction

Civil construction activities generate a large amount of waste, called construction and demolition waste (CDW). An alternative to minimize the impacts caused by this type of waste is to reuse it as a secondary raw material, such as aggregates, fillers, or eco-efficient pozzolana. Concerning the fine fraction of CDW (< 5 mm), studies have evaluated its viability as complementary cementitious materials for the production of eco-efficient cement (Frías et al, 2020; Monasterio et al, 2022). Concluding that depending on the origin, granulometry, chemical, and mineralogical composition, the recycled concrete fines generated during the production of recycled concrete aggregates can be used as filler or as supplementary cementitious materials (SCM), since the fine fractions can have cementitious properties, due to the presence of unhydrated cement grains in its composition (Frías et al, 2020; Moreno-Juez et al, 2021).

In this context, aiming at new applications for the use of CDW, the study evaluated the physic-mechanical and microstructural behavior of fiber cement reinforced with bleached eucalyptus cellulosic pulps, partially replacing Portland cement by recycled concrete fines (< 63 μm) subjected to thermal curing and the accelerated carbonation process, for the production of thin flat sheets without a structural function.

2. Materials and Methods

2.1 Materials

The composites were produced with type III Portland cement (ASTM C150); ground limestone, fixed in the formulation at 12.8% by mass; and bleached hardwood kraft pulp of eucalyptus (fixed at 10%, by mass), donated by Infibra (Brazil). The CDW was donated by the concrete recycling plant (Eco-X), Guarulhos - SP, Brazil. The material was previously dried in an oven at 60°C for 24 h. Then, it was sieved to obtain the fraction that passed through a 0.15 mm sieve. The fines were milled to fragment the particles at 63 μm. The materials presented D_{50} of 9.07 μm, 24.0 μm, and 16.4 μm, to the Portland cement, CDW, and limestone, respectively.

2.2 Methods

2.2.1 Production and curing of the fiber cement composites

The fiber cement pads (200 x 200 x 5) mm³ were produced by slurry dewatering and pressing method (Savastano et al, 2000). CDW was used to replace 10% of Portland cement, by mass. Initial curing was accomplished at a saturated condition (± 28 ºC) for 24 h. Then, thermal curing was used for the reference conditions and accelerated carbonation was used for the additional treatments. Thermal curing was controlled thermal bath chamber, with a relative humidity of ~ 90% at a temperature of 60 ºC (water vapor at 55 ºC), for 6 days. This process occurred in the formulations with CDW (CDW_TC) and without CDW (REF_TC). The accelerated carbonation was carried out after the initial 24 h of curing, the plates were placed in a laboratory chamber at 60ºC, under a pressure of 5 bar, CO_2 saturation (~100%), and sample moisture of 60% for 24 h, according to Filomeno et al (2020). This accelerated carbonation step used formulations with CDW (CDW_CO2) and without CDW (REF_CO2).

2.2.2 Characterization of fiber cement

X-ray diffraction (XRD) was determined operating at 40 kV and 30 mA, in a step of 0.02º per second and measurement interval between the Bragg angles (2θ) from 5º to 60º, with intensities recorded for 2º/min. Before the XRD analysis, the samples were previously ground and sieved (Filomeno et al, 2020).
The mechanical properties were obtained using a four-point bending test, following Tonoli et al (2007). Modulus of rupture (MOR), and specific energy (SE) were determined. The bulk density (BD), and apparent porosity were evaluated according to the procedures established by ASTM C 948-81. The results of the physic-mechanical analysis were treated statistically using the statistical software SAS 9.4 (Statistical Analysis System). The microstructural analysis was performed using scanning electron microscopy with backscattered electron image (SEM-BEI) to evaluate the fiber-matrix interface and the transition zone on the polished surface of the fiber cement.

3. Results and Discussion

3.1 X-Ray Diffraction (XRD)

The diffractograms (Fig. 1) show an increase in the intensity of calcite peaks after the carbonation process, due to the reaction that occurs between dissolved CO_2 and calcium hydroxide mainly, resulting in the dissolution of portlandite and precipitation of $CaCO_3$ (Hunnicutt et al, 2017). The accelerated carbonation process led to the disappearance of $Ca(OH)_2$ (broadband 2θ = 28.6º, 50.7º, and 54.3º), this

factor can provide greater durability of the vegetable fibers in the cementitious matrix. In composites with CDW, peaks related to quartz were identified, due to the aggregates in the original concrete.

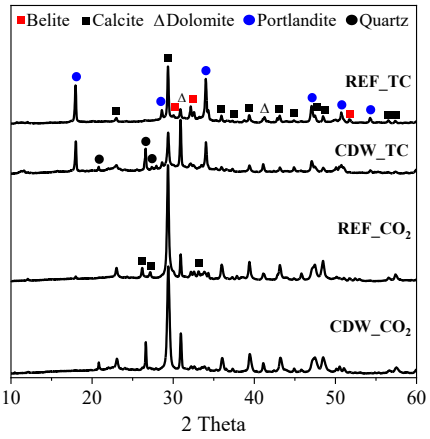

Fig. 1 – X-ray diffractograms of carbonated and non-carbonated fiber cement samples.

3.2 Physic-mechanical characterization

Fig. 2a shows the correlation of the modulus of rupture (MOR) versus specific energy (SE) of carbonated and non-carbonated fiber cement with 10% CDW. The CDW_TC composite presented physic-mechanical performance statistically equal to REF_TC. The MOR was 9.74 MPa (± 0.89a) and 8.68 MPa (± 0.91a), respectively. And SE of 5.49 (± 0.44a) and 3.69 (± 0.89a), demonstrating that with reduced levels of substitution, CDW does not impair the properties of the composite. The carbonated samples presented an approximately 60% increase in MOR compared to their non-carbonated counterparts. Furthermore, although there is a tendency for carbonatation to decrease the ability of energy absorption of the fiber cement, the addition of CDW compensated for this embrittlement, providing an increase of approximately 40% in the SE. This behavior is due to better particle packing and optimization of the fiber-matrix interface. Except for the MOR property, no statistically significant difference was observed for the other physic-mechanical properties of the carbonated samples. The bulk density (BD) results (Fig. 2b) confirm the better behavior of carbonated fiber cement, presenting a denser structure due to the reduction of apparent porosity, filled by the formation of $CaCO_3$.

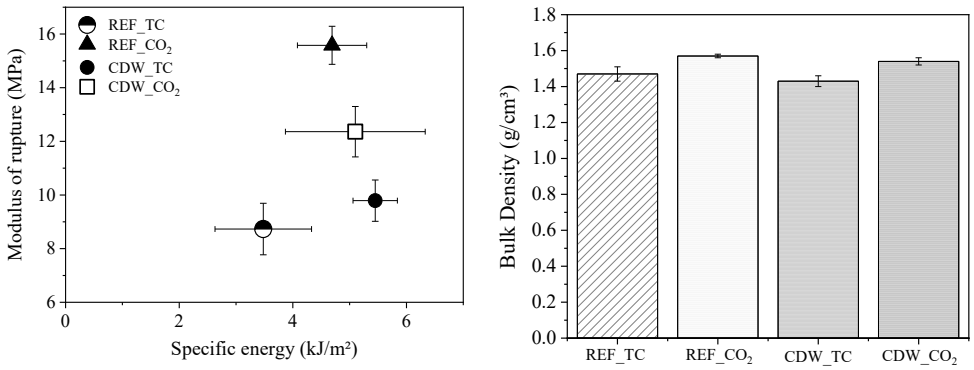

(a) (b)

Fig. 2 – Physic-mechanical properties: (a) MOR and SE, and (b) BD of fiber cement.

3.3 Scanning Electron Microscopy (SEM)

The micrographs of the composites are shown in Fig. 3. Arrow 1 indicates fiber contamination by calcium hydroxide. Arrow 2 represents the lack of adhesion between the fiber and the cementitious matrix. It is observed that the carbonation process improved the structure of the matrix, making it more compact, densified structure, and less porous matrix, improving the fiber-matrix transition zone, as indicated by arrow 3.

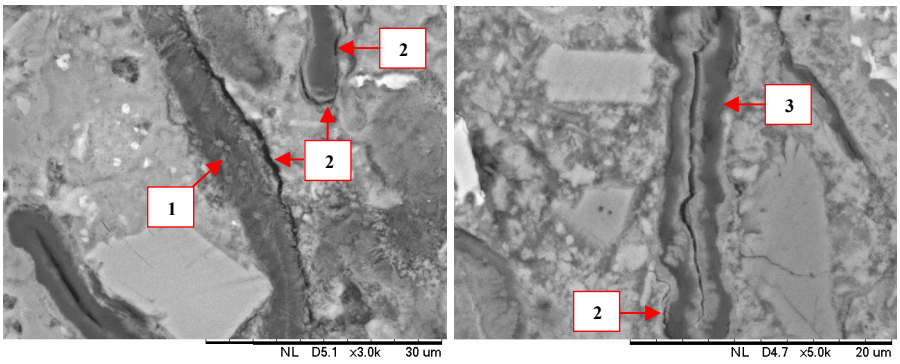

Fig. 3 - Fiber cement: (a) Sample without carbonation, and (b) sample with accelerated carbonation.

4. Conclusions

The use of CDW and accelerated carbonation presented efficient results to improve fiber cement performance with a high cellulose pulp content. Accelerated carbonation densified the cement matrix, refining the porosity and presenting an increase of 60% for the MOR compared to the non-carbonated counterpart. The use of CDW preserved the specific energy and bulk density of the fiber cement even after the accelerated carbonation process and did not present significant statistical differences for the other physic-mechanical properties. In general, the use of 10% CDW does not impair the physic-mechanical performance of the composites. The CDW compensated for the embrittlement, guaranteeing stability in the deformation of the fiber cement. The XRD analysis showed that the accelerated carbonation process led to the disappearance and reduction in the intensity of peaks referring to $Ca(OH)_2$, in addition to an increase in the $CaCO_3$ content.

Acknowledgments

The authors would like to thank the Fundação de Amparo à Pesquisa do Estado do Amazonas (FAPEAM) – POSGFE Scholarship – Notice nº 012/2021. This work was supported by Spain's Ministry of Science and Innovation, AEI, and eRDF (CIDECAR-PID2021-122390OB-C21). Also thanks to the Framework Collaboration Agreement between the IETcc-CSIC and the University of Sao Paulo (BDC20195702).

References

American Society for Testing and Materials. ASTM C 948-81: Standard test method for dry and wet bulk density, water absorption and apparent porosity of thin sections of glass-fiber reinforced concrete. ASTM International, West Conshohocken, PA, 2016.

Filomeno, R. H., Rodier, L. B., Ballesteros, J. E. M., Rossignolo, J. A., and Savastano, H. (2020) "Optimizing the modified atmosphere parameters in the carbonation process for improved fiber-cement performance", *Journal of Building Engineering*, 32: 101676

Frías, M., et al (2020) "Multi-Technique Characterization of a Fine Fraction of CDW and Assessment of Reactivity in a CDW/Lime System", *Minerals*, 10(7): 590.

Hunnicutt, W., Struble, L., and Mondal, P. (2017) "Effect of synthesis procedure on carbonation of calcium-silicate-hydrate", *Journal of the American Ceramic Society*, 100(8): 3736–3745.

Monasterio, M., Caneda-Martínez, L., Vegas, I., and Frías, M. (2022) "Progress in the influence of recycled construction and demolition mineral-based blends on the physical-mechanical behaviour of ternary cementitious matrices", *Construction and Building Materials*, 344: 128169.

Moreno-Juez, J., Vegas, I. J., Frías, M., Vigil de la Villa, R., and Guede-Vásquez, E. (2021) "Laboratory-scale study and semi-industrial validation of viability of inorganic CDW fine fractions as SCMs in blended cements", *Construction and Building Materials*, 271: 121823.

Savastano, H., Warden, P., and Coutts, R. S. (2000) "Brazilian waste fibres as reinforcement for cement-based composites", *Cement and Concrete Composites*, 22(5): 379–84.

Tonoli, G. H. D., Joaquim, A. P., Arsène, M.-A., Bilba, K., and Savastano, H. (2007) "Performance and durability of cement based composites reinforced with refined sisal pulp", *Materials and Manufacturing Processes*, 22(2): 149–156.

16th International Congress on the Chemistry of Cement
ICCC 2023
BANGKOK, THAILAND

Effect of Low Temperature Calcination on Pozzolanic Activity of Volcanic Powder

Fanyuan Mu[1,2], Zhengping Sun[1,2,3*], Chunsheng Wang[4] and Xing Yang[4]

[1] *Key Laboratory of Advanced Civil Engineering Materials of Ministry of Education, Tongji University, 201804 Shanghai, China*

Email: grtszhp@163.com
[2] *School of Materials Science and Engineering, Tongji University, 201804 Shanghai, China*

Email: grtszhp@163.com
[3] *Research Center of Intelligent Evaluation and Restoration Engineering Technology of Urban Pipe Network of Shanghai Water Bureau, Shanghai 201900, China*

Email: grtszhp@163.com
[4] *Xizang Wuyang Industry Co. Ltd., Lasa 85000, China*

Email: fymu@foxmail.com

ABSTRACT

The volcanic powder found in Tibet has a high crystal content, which results in low pozzolanic activity. In this paper, TG-DSC and XRD were used to explore the excitation effect of low temperature calcination (lower than 1000 ℃) on the pozzolanic activity of volcanic powder. The results showed that the appropriate calcination temperature and time can promote the transformation of crystals in the volcanic powder to amorphous form, and effectively improve its pozzolanic activity. The optimum calcination time is 1 hour. When the calcination time is less than 1 hour, the activity of the volcanic powder increases with the prolongation of the calcination time, and the activity of the volcanic powder does not change significantly after more than 1 hour. The activity of volcanic powder is highest when the calcination temperature is 800 ℃, and even decreases when the calcination temperature exceeds 800 ℃.

KEYWORDS: *volcanic powder, low temperature calcination, pozzolanic activity, amorphous*

1. Introduction

China is rich in volcanic rock resources, and a large amount of natural volcanic ash material is distributed in the southeast and southwest borders(Yuan et al, 2020). Due to the different formation history and conditions, the types of volcanic rocks and their volcanic ash activity are quite different(Fares et al, 2016). Among them, the volcanic powder in Tibet has a high crystal content with low pozzolanic activity, making it difficult to be used as an auxiliary gelling material in cement and concrete(Chen et al, 2001). Therefore, improving the pozzolanic activity of volcanic powder in Tibet is the focus of effectively utilizing volcanic powder in Tibet. In this study, volcanic powder was pretreated by low-temperature calcination to explore the effect of low-temperature calcination method on the physical and chemical properties of volcanic powder and its pozzolanic activity.

2. materials and test methods

The specific surface area of the raw materials used in the experiment is 450 cm^2/g. Its particle size distribution is shown in Fig. 1, Its chemical composition is shown in Table 1, and the XRD pattern is shown in Fig. 2.

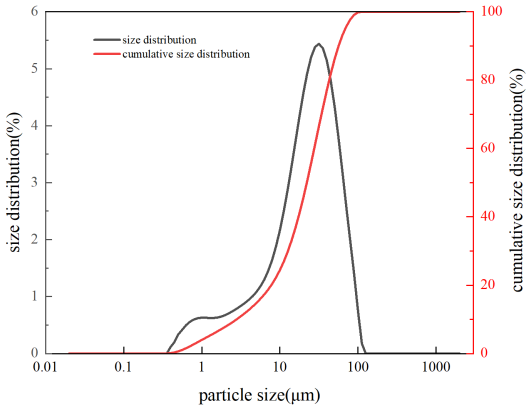

Fig. 1 Particle size distribution of volcanic powder

Table 1 Chemical composition of volcanic powder

mineral admixture	chemical components/%							
	SiO_2	Al_2O_3	Fe_2O_3	CaO	K_2O	Na_2O	MgO	SO_3
volcanic powder	55.87	17.51	9.12	6.99	3.98	2.53	2.01	/

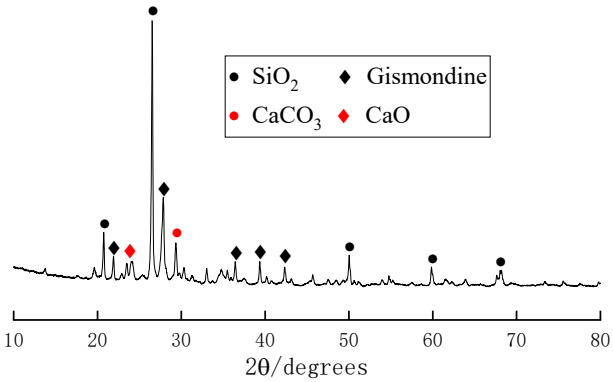

Fig. 2 XRD pattern of volcanic powder

The selected volcanic powder was calcined at different selected calcination temperatures for a certain time. The calcination was carried out in a muffle furnace with a heating rate of 20 °C/min and a cooling rate of 35 °C/min.
The content of volcanic powder in cement is 30%.

3. Results and discussion

The effect of volcanic powder at different calcination temperatures on the strength of the cement is shown in Fig. 3. When the calcination temperature does not exceed 600°C, the low-temperature calcination has no obvious effect on the activity of the volcanic powder. When the calcination temperature exceeds 600°C, the early strength of the cement will decrease with the increase of the calcination temperature, but 28-day strength will be significantly improved.

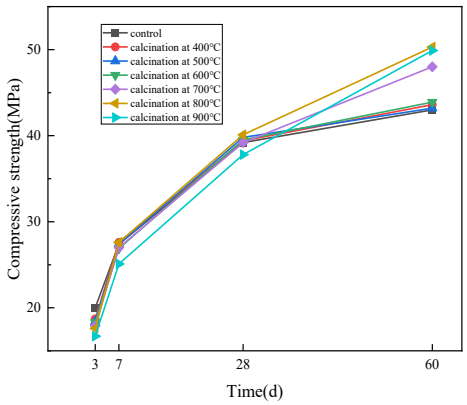

Fig. 3 Effect of volcanic powder at different calcination temperatures on the strength of cement

Two calcination temperatures of 500°C and 800°C were selected to explore the effect of calcination time of volcanic powder on the strength of the cementitious material system, and the results are shown in Fig. 4. The results show that when the calcination temperature is lower than 600°C, different calcination times have no significant effect on the activity of volcanic powder. When the calcination temperature exceeds 600°C, a shorter calcination time will lead to insufficient activation of the volcanic powder and lower strength in the later stage. A longer calcination time will reduce the early strength of cement, and the impact on the later strength is the same as that of calcination for 1 hour. Therefore, the best calcination time is one hour.

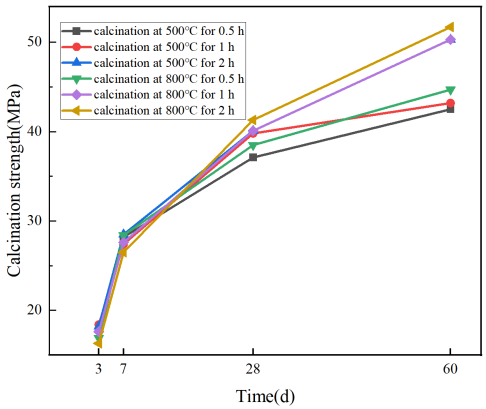

Fig. 4 Effect of volcanic powder at different calcination time on the strength of cement

Furthermore, from the TG-DSC curve of volcanic powder (Fig. 5), when the calcination temperature does not exceed 600 °C, the volcanic powder does not produce heat absorption or exotherm, and its crystal structure does not change. When the calcination temperature exceeds 600 °C, the volcanic powder begins to transform from crystal to glass, and the microstructure of the particles also changes. The lamellar structure of the volcanic powder particles disappears (Fig. 6), so the filling effect in the early stage of hydration is reduced, resulting in a certain degree of decline in the early strength of the gelled system. Due to the increase of the vitreous body, more volcanic powder participates in the hydration of the cement in the later stage of hydration, resulting in a significant increase in the strength of the later stage of the cement.

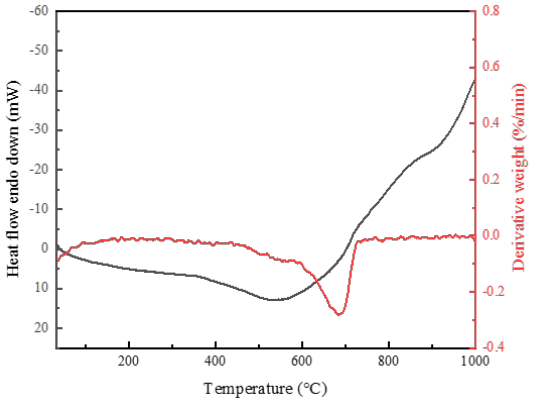

Fig. 5 TG-DSC curve of volcanic powder

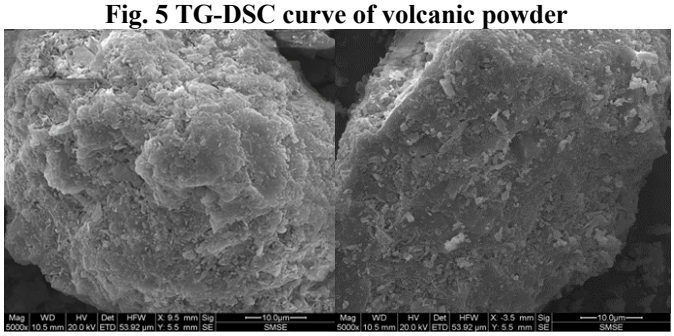

(a) Uncalcined volcanic powder; (b) 800°C calcined volcanic powder

Fig. 6 Effect of calcination on microstructure of volcanic powder particles

4. Conclusion

Based on the analysis of experimental data developed in the present study, following conclusions can be drawn:

1. Low-temperature calcination at an appropriate temperature can help improve the pozzolanic activity of volcanic powder. The optimal calcination temperature for volcanic powder is 800°C. When the calcination temperature is lower than 600°C, low-temperature calcination has no significant effect on the activity of volcanic powder. When the calcination temperature exceeds 800°C, the activity of volcanic powder has no significant change compared with 800°C, which is not conducive to the low-carbon and green development of cement.
2. The optimal calcination time is one hour. Short-term calcination cannot effectively improve the activity of volcanic powder, while long-term calcination reduces the early strength of cement but does not significantly increase the later strength.
3. Calcining at low temperature causes the crystals in the volcanic powder to transform into vitreous, which significantly increases the reactivity of the volcanic powder.

References

Yuan Q., Yang Z. & Shi C. et al. (2020). Fundamentals on Application of Natural Pozzolans in Cement-based Materials: a Review. *Bulletin of Chinese Ceramic Society*, *39*(8): 2379-2392.

Fares, G., Alhozaimy, A., Alawad, O. A., & Al-Negheimish, A. (2016). Evaluation of powdered scoria rocks from various volcanic lava fields as cementitious material. *Journal of Materials in Civil Engineering*, *28*(3), 04015139.

Chen Q. & Qian G. (2001). Feasibility of Using Tibet's Pozzolan as Mineral Admixture of Concrete. *Hydro-Science and Engineering*, (4), 22-26.

Comparative Study of Mechanical Properties of Limestone Calcined Clay Cement, Ordinary Portland Cement, and Pozzolana Portland Cement

Akash Mishra[1]*, Priyanshu Sinha[1], Amit Kumar[1] and Shashank Bishnoi[1]

[1]Department of Civil Engineering, Indian Institute of Technology Delhi, New Delhi, India

akdheeru@gmail.com, sinha.pkpk@gmail.com, iitd.amitkr@gmail.com, bishnoi@iitd.ac.in

Abstract

Carbon emissions from cement manufacturing are reduced by partially replacing cement clinkers with supplementary cementitious materials (SCM). In this study, Limestone calcined clay cement (LC^3) was prepared by blending 50% of OPC-43 grade with 50% Limestone calcined clay- LC^2 (63.3 % of calcined clay, 31.7% of limestone, and 5% of gypsum), Fly ash-based Pozzolana Portland Cement (PPC) and Ordinary Portland Cement (OPC) was used to compare the mechanical properties at the age of 7 & 28 days of curing for M-25 and M-50 grades of concrete. The specimens for the compressive strength test, flexure strength test, Modulus of elasticity test, and Bond test of concrete with reinforcement of 25mm diameter bars were prepared as per Indian standard codes. The results of the study showed that the LC^3 had higher compressive strength values at the age of 7 days, which is substantiated by flexure strength, modulus of elasticity, and pull-out strength values, whereas at the age of 28 days, LC^3, OPC, and PPC had similar strengths.

Keywords: *Limestone calcined clay cement, Fly ash-based pozzolana Portland Cement, Modulus of elasticity test, Bond test with reinforcement, Pull out strength.*

1. Introduction

OPC is the 2nd most consumed resource after water, and OPC is Manufactured by the process of calcination, where the heating of limestone and clay is done, which leads to the release of carbon dioxide into the atmosphere. The cement industry contributes 8% of worldwide artificial emissions of CO_2 gas, from which 50% is from the chemical process, 40% is from burning fuel, and 5-10% is emissions from electricity for plant machinery and transportation of raw materials (Rao AB, Rubin ES (2002)). With growing environmental demand for low-carbon emitting materials globally, the development of green construction materials is becoming significant in addressing the challenges of climate change. Limestone calcined clay cement (LC^3) is one such cement that has less environmental impact and excellent properties concerning strength and durability (Scrivener K. et al. 2018, Sharma M. 2021, F. Avet et al. 2019)

LC^3 is made by substituting cement clinker with limestone and calcined clay. It is expected to reduce the carbon emission of cement production by 30-40% (Berriel et al. 2016). In this experimental work, the mechanical performance of LC^3 concrete is evaluated and compared with the conventional OPC and PPC concrete.

2. Materials and methods

2.1 Materials

The three types of cement used were OPC- grade 43, PPC prepared by blending 70% of OPC 43 grade with 30 % class F fly ash, LC^3- Prepared by blending 50% of OPC 43 grade with 50% LC^2 containing 63.3 % of calcined clay, 31.7% of limestone, and 5% of gypsum. The aggregates used were crushed angular quartz stones of 20 mm and 10 mm nominal sizes, whereas the fine aggregate was river sand. The mix design of the concrete is listed in Table 1.

Table 1 Mix Design of Concrete as per IS 10262

Materials weight (kg) per m^3 of concrete	**OPC**		**PPC**		**LC^3**	
	M-25	M-50	M-25	M-50	M-25	M-50
Water Content	165.00	165.00	165.00	165.00	165.00	165.00
Cement Content	366.67	590.00	366.67	590.00	366.67	590.00
Fine Aggregate	638.45	523.87	623.19	501.49	627.41	507.67
Coarse Aggregate (10mm)	495.74	466.41	483.89	446.49	487.16	451.99
Coarse Aggregate (20mm)	743.60	699.62	725.84	669.73	730.74	677.99
Chemical Admixture	3.67	5.90	3.67	5.90	3.67	5.90

The specific gravity of cement was determined using Le Chatelier's flask as per IS 4031 Part-11, and the specific gravity of coarse and fine aggregates was determined as per IS 2386, as listed in Table 2.

Table 1 Specific Gravity of Materials

Material	OPC	PPC	LC^3	Coarse (20mm)	Coarse (10mm)	Sand
Sp. gravity	3.17	2.81	3.00	2.81	2.68	2.62

Coarse aggregates were well-graded, and fine aggregates conformed to zone II of IS 383. Malvern Mastersizer 3000E was used for determining the particle size of cement. Isopropyl alcohol was used as a dispersion medium. The particle size is mentioned in Table 3.

Table 2 Particle Sizes of different types of cement

D_x	**OPC**	**PPC**	**LC^3**
D_{10} (μm)	5.76	4.53	2.96
D_{50} (μm)	21.0	19.6	14.8
D_{90} (μm)	62.5	58.5	51.9

X-ray Fluorescence of different types of cement was done to determine the oxide composition of the cement, as mentioned in table 4.

Table 3 X-ray Fluorescence of different types of cement

Oxides Component	**OPC (%)**	**PPC (%)**	**LC^3 (%)**
SiO_2	20.69	35.22	29.70
Fe_2O_3	5.26	5.54	3.86
Al_2O_3	4.03	12.92	19.10
CaO	59.90	34.51	32.21
MgO	0.98	1.20	1.36
SO_3	2.53	2.86	2.74
Na_2O	0.09	0.42	0.48
K_2O	0.57	0.82	0.46
TiO_2	0.40	1.09	1.39
LOI	4.30	4.10	7.90

2.2 Methods

The materials were dry mixed for two minutes; water was mixed along with chemical admixtures to obtain a homogenous mixture. The specimens for compression, flexural strength, and modulus of elasticity tests were prepared as per IS 516, whereas the pull-out strength IS 2770 part 1 was followed to prepare the specimens. The specimens were demoulded after 24 hours of the casting. Then these specimens were cured in a water tank until the age of testing.

3. Results and Conclusions

3.1 Results

The results of the study are shown in Figure 1 (a, b, and c), and the following results have been obtained.

- The flexural strength of LC^3 M-25, at 7 days and 28 days, was found to be higher than PPC and OPC similar trend was observed for LC^3 M-50 concrete.
- The 7-day and 28-day pull-out strength of OPC-M-25 specimens was more than PPC and LC^3, and the strength of LC^3 was lower than PPC at 28 days. Whereas in the M-50 grade, the strength of PPC was highest, followed by LC^3 and OPC.
- The results of the compressive strength and modulus of elasticity (MOE) for both grades of concrete were found to be similar, where with the increase of compressive strength, the MOE value increases, and the highest compressive strength and MOE values were observed for LC^3 followed by OPC and PPC.

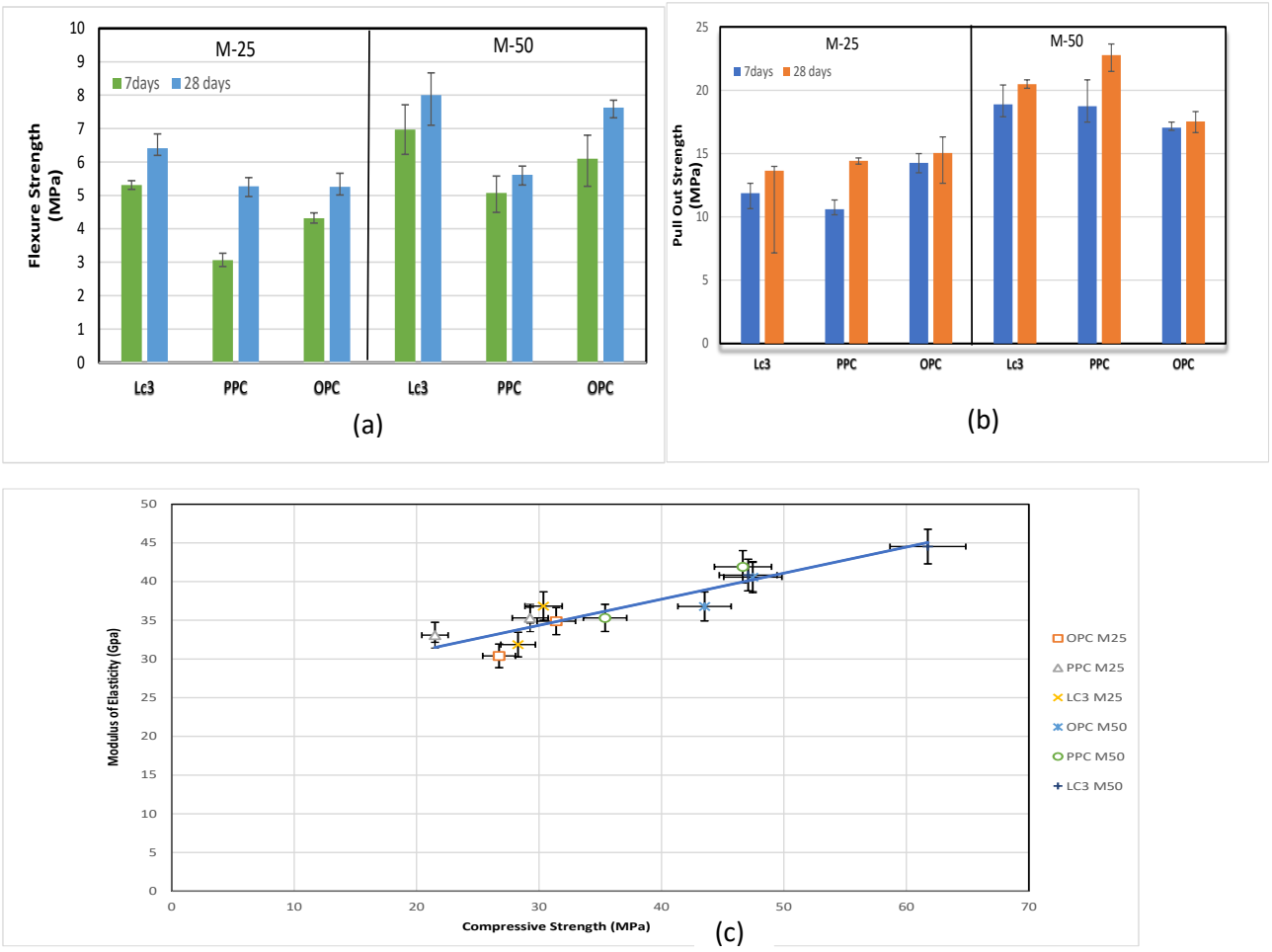

Figure 1 (a) Flexure Strength (b) Pull Out Strength (c) Modulus of Elasticity and Compressive Strength of the concrete samples at 7 and 28 days

4. Conclusions

From the results of the mechanical strengths of concrete specimens, as shown in the graph, it can be seen that LC^3 had similar strengths to OPC and PPC at 28 days, and the following conclusions were made from the study:

- The 7-day flexural and pull-out strength of the 25 mm steel bars and concrete were higher in LC^3 specimens for both grades of concrete than PPC and OPC, which signifies the high early strength of LC^3; this is because of the synergy reactions between the calcined clays, limestone and cement clinkers.
- The higher flexure, Modulus of elasticity, and compressive strength values of the LC^3 indicate that with similar mixture proportions, LC^3 binder has better strength evolution in concretes than OPC and PPC.
- The performance of LC^3 concrete in terms of mechanical parameters other than compressive strength is similar to OPC and PPC.

Acknowledgments

The authors acknowledge that this study is supported by of Swiss Development Cooperation (SDC), and Aalborg Cement is acknowledged for making the FutureCem technology available to us.

References

Avet, François, Lionel Sofia, and Karen Scrivener. 2019. "Concrete Performance of Limestone Calcined Clay Cement (LC3) Compared with Conventional Cements." *Advances in Civil Engineering Materials* 8(3).

Rao, Anand B., and Edward S. Rubin. 2002. "A Technical, Economic, and Environmental Assessment of Amine-Based CO2 Capture Technology for Power Plant Greenhouse Gas Control." *Environmental Science and Technology* 36(20):4467–75.

Sánchez Berriel, S., A. Favier, E. Rosa Domínguez, I. R. Sánchez MacHado, U. Heierli, K. Scrivener, F. Martirena Hernández, and G. Habert. 2016. "Assessing the Environmental and Economic Potential of Limestone Calcined Clay Cement in Cuba." *Journal of Cleaner Production* 124:361–69.

Scrivener, Karen, François Avet, Hamed Maraghechi, Franco Zunino, Julien Ston, Wilasinee Hanpongpun, and Aurélie Favier. 2018. "Impacting Factors and Properties of Limestone Calcined Clay Cements (LC3)." *Green Materials* 7(1):3–14.

Sharma, Meenakshi, Shashank Bishnoi, Fernando Martirena, and Karen Scrivener. 2021. "Limestone Calcined Clay Cement and Concrete: A State-of-the-Art Review." *Cement and Concrete Research*.

Indian Standards, Bureau *IS 10262 (2019) Concrete Mix Proportioning-Guidelines*.

Indian Standards, Bureau *IS 4031-11 (1988): Methods of Physical Tests for Hydraulic Cement, Part 11: Determination of Density.*

Indian Standards, Bureau *IS 2386-3 (1963): Methods of Test for Aggregates for Concrete, Part 3: Specific Gravity, Density, Voids, Absorption and Bulking.*

Indian Standards, Bureau *IS 383 (1970) Specification for Coarse and Fine Aggregates From Natural Sources For Concrete*.

Indian Standards, Bureau *IS 516 (1959): Method of Tests for Strength of Concrete*.

Indian Standards, Bureau *IS 2770-1 (1967): Methods of Testing Bond in Reinforced Concrete, Part 1: Pull-out Test*.

The 16th International Congress on the Chemistry of Cement 2023 (ICCC2023)
"Further Reduction of CO_2 -Emissions and Circularity in the Cement and Concrete Industry"
September 18–22, 2023, Bangkok, Thailand

Suitable solvent extraction method selection and gel structure evolution for alkali activated slag (AAS) pastes at early age

Dongdong Jiang [1], Zuhua Zhang [2], Caijun Shi [3*]

[1] *College of Civil Engineering, Hunan University, Changsha 410082, China*

Email: ddjiang@hnu.edu.cn
[2] *College of Civil Engineering, Hunan University, Changsha 410082, China*
Email: zuhuazhang@hnu.edu.cn
[3] *College of Civil Engineering, Hunan University, Changsha 410082, China*
Email: cshi@hnu.edu.cn

ABSTRACT

The selection of suitable solvent extraction method for early-age AAS samples is dependent on physical state of extra introduced silicate species, since that the liquid-state silica are inclined to react with ethanol. Before 1d of reaction time, some soluble silica from activator still exists in highly silicious AAS samples. Therefore combined solvent (water followed by ethanol) extraction is advised as the reliable method to halt reaction process and meanwhile effectively remove remanent soluble silica thus no affecting further structural characterization. Meanwhile this study also reports gel structure evolution at very early age on the basis of correct drying procedure. In general the polymerization degree of early gels increases with modulus at constant alkali dosage. In particularly some silica-rich gels are formed at final setting time in highly silicious samples. In addition the structure difference between AAS binders with varied modulus diminishes at 1d due to structural arrangement and higher degree of slag dissolution.

KEYWORDS: *AAS; modulus; solvent extraction; structure*

1. Introduction

It is commonly accepted that the reaction of slag grains in AAS is a solid-fluid reaction that follows a dissolution-precipitation-ion diffusion mechanism. In the first two reaction stages, pore solution composition determines the dissolution kinetics of slag and formation of reaction products if pore solution is saturated or oversaturated correspondingly. In the third reaction stages, the gel pores in the surrounding hydration products are the diffusion channels of ions.

It is reported that unreacted silicate species supplied by activator at early age may react with organic solvent and form high-polymerized products (Palacios et al (2021), Chen et al (2014)), when organic solvent extraction is applied to stop reaction processs. And combined extraction (solvent and combined water-solvent) was seen to reliably stop reaction without altering the reaction product (Palacios et al (2021)). However, there are no explicit recommendation for solvent extraction in respect of AAS samples with varied modulus.

The generation of "primary C-S-H" since initial setting time has been confirmed by SEM and NMR techniques (Palacios et al (2021)). It has also been reported that the exothermic peak representing precipitation of "primary C-S-H" is determined by the predominant silicate configuration in silicate solution (Jiang et al (2022).

Therefore, the paper is written aiming to (1) investigate whether drying treatment affect the nano/microstructure of AAS pastes with varied modulus; (2) if yes in the former purpose, determine the suitable drying process dependent on activator and relative timing points (3) elucidate the gels type of AAS samples especially high modulus ones. The obtained results will contribute to new sights regarding the mechanism of setting for AAS materials.

2. Materials and methods

2.1. Raw materials

Vitreous phases content in slag reach to 98.3% via Rietveld refinement method. The particle size distribution of slag determined by laser particle analyzer ranges from 1.4 μm to 148 μm, thereinto 16.11 μm is characterized as d50. Moreover the X-ray fluorescence technique is conducted to obtain chemical composition of slag, as shown in table 1, in which LOI is loss of ignition at 1000 °C. In addition, The ingredients used to manufacture activators consist of industrial-grade sodium hydroxide, raw waterglass with 64.16 wt% H_2O and SiO_2/Na_2O ratio of 3.3 and deionized water.

Table 1. Chemical compositions of blast furnace slag (by weight, %).

	CaO	SiO2	Al2O3	MgO	Fe2O3	Na2O	K2O	TiO2	SO3	LOI
wt%	38.81	33.81	14.78	7.09	0.36	0.26	0.44	0.52	2.49	1.40

2.2. Mixture design, sample preparation and treatment

Table 2 lists details of mixing proportion of AAS pastes, a constant water (deionized water and water from waterglass) to slag ratio of 0.35 is adopted to achieve satisfactory workability and almost no bleeding phenomenon. Meanwhile Alkaline activator is fabricated with Na_2O dosage of 6%, and three levels of silicate modulus of 0 (hydroxide activation system), 1 and 2 (silicate activation system). In respective of sample preparation process, the certain prepared activator is poured into mixing pot, followed by slag powders. Both of them are stirred at low speed for 120 s, subsequently a rest duration of 15s, then high speed for another 120s. Therein within the short test time of 15s, the slurry adhere to blade and wall should be scraped into pot. And all operations above are performed at ambient temperature of 20 ±1℃.

Table 2 mixture design of AAS pastes

Water /Slag	Slag (g)	Na_2O (wt%)	Modulus (Ms)	Deionized water (g)	NaOH (g)	waterglass (g)	Total water/ (slag+anhydrous activator)
0.35	100	6	0	35	7.74		0.33
			1	21.35	5.4	21.27	0.31
			2	7.7	3.05	42.55	0.30

Two kinds of drying methods are carried out in the text consisting of direct solvent extraction and combined solvent extraction, which are abbreviated hereafter as S and CS respectively. Two drying methods are described in detail as follows: In S method, 1g pastes are mixed with 100 ml ethanol. After a static placing time of 5 min, the liquid media is removed using vacuum-filtration. This procedure is repeated for three times Chen et al (2014). Then the filtered powders are immediately put into vacuum oven stabilized at 40℃ for two days for further characterization. In CS method, around 0.8 g of paste samples are firstly dispersed in 50 mL ultrapure water, then the suspensions are immediately centrifugated at a rate of 10000 r/min for 3min. This water extraction procedure above needs to be repeated until no detectable silicate species dissolves in liquid supernatant, which is verified through statement in Chen et al (2014). Subsequently ethanol extraction is performed as described in S method.

2.3. Experimental methods

FTIR method is applied to soluble residue after SAM method, 1 mg sample is ground together with 100 mg of IR-grade KBr. The resolution and scans set as 1 cm−1 and 64. Thereinto operational procedure of SAM chemical attack refers to (Yip et al (2005)).

3. Results and discussions

Figure 1 is depicted on the comparison between the direct ethanol extraction and combined solvent extraction for AAS samples with modulus ranging from 0 (sodium hydroxide solution) to 2. In the notations for the samples, CS and S indicate combined solvent extraction and direct ethanol extraction. It can be observed that both CS and S method can effectively remove water and halt reaction process, as indicated by H–O–H bending vibration of molecular H_2O around 1640cm^{-1}. And meanwhile CS treatment results in lower intensity of carbonates-related bonds in the range of 1400-1500cm^{-1}, which might be

ascribed to removed cations after water extraction. It can be observed that these two extraction ways cause no effect on sodium hydroxide activation system and direct solvent extraction results in higher polymerized species in silicate activated samples at 10min. Based on this, it can be inferred that there may exist abundant soluble silicate unites at 10min. Moreover at corresponding final setting the majority of soluble silicate unites introduced by activator are consumed and precipitate for samples with modulus no more than 2, since that almost same main peak position and spectra shape are present. But there is a nonnegligible upshift of main peaks for modulus of 2 treated with direct solvent exchange compared with combined exchange method at final setting point. And 1d are proved as reasonable time point for all samples beyond which direct solvent method can be utilized without affecting AAS binders.

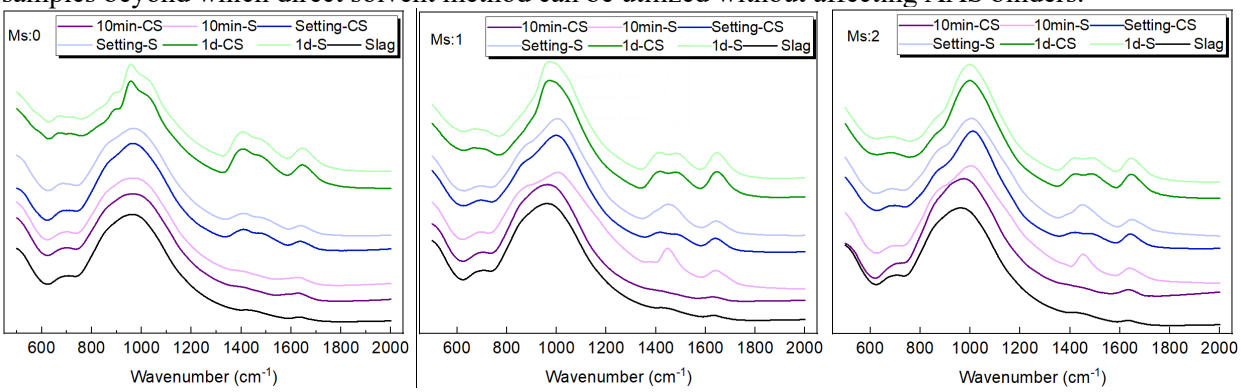

Figure 1. FTIR spectra of alkali activated slag pastes treated by two types of drying methods with alkali dosage of 6% and varied modulus. Thereinto CS and S indicate combined and direct solvent extraction respectively.

It is reported that the phases containing calcium dissolve in the salicylic acid/methanol (SAM) medium, whereas those with no calcium in their composition form an insoluble residue after the attack (García-Lodeiro et al (2009)). As shown in figure 2, regardless of modulus and investigation time, the characteristic profile of unreacted slag centering around 964 cm^{-1} can be obviously observed, which to some degree proves that SAM is a reliable method to dissolve reaction products of AAS binders. The peaks shape and position of all specimens at 10min are comparable with those of slag, indicating that phases susceptible to SAM treatment i.e. calcium-containing phases predominate at very early age such as 10min. The appearance of shoulders locating around 1058cm^{-1} and 1200cm^{-1}, frequency higher than the position of the band typical of C–S–H gels, are similar to the peaks characteristic of Q3 and Q4 silicon tetrahedra in silica gels (García-Lodeiro et al (2008)). This demonstrates that at final setting time, except for the C-(A-)S-H gels which dissolve in SAM process, a silica-rich gel with no or much little calcium in its composition may have been formed in AAS pastes activated with high modulus silicate activator. As reaction proceeds at 1d, the spectra of insoluble residue simply and the characteristic peaks prominent before are detected to decline even nearly disappear, probably because the phases assemblages are in dynamic equilibrium and calcium from slag dissolution is gradually incorporated.

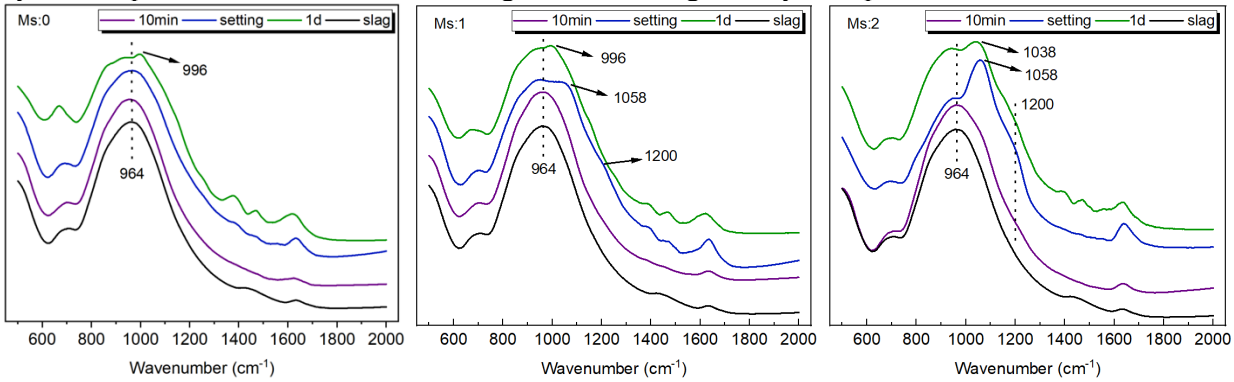

Figure 2. FTIR spectra of insoluble residue of AAS pastes after SAM attack with alkali dosage of 6% and varied modulus.

4. Conclusions

The combined extraction effectively removes soluble species and therefore provides a viable procedure to study structural changes excluding uncertainties. The modulus significantly affects timing point suitable for direct solvent exchange which is more convenient to carry on. 1d are proven to be the right point in time to utilize direct solvent extraction even for highly silicious specimens.

Besides typical C-(A-)S-H gels with main FTIR peak centering below 1000cm^{-1}, silica-rich gels are evidently formed at setting times especially in AAS pastes with modulus of 2, with characteristic band at 1058cm^{-1} and 1200cm^{-1}.

Acknowledgements

The authors are grateful of the financial support by the National Science Foundation of China projects U2001225 and 51878263.

References

Palacios, M., S. Gismera, M.M. Alonso, J.B. d'Espinose de Lacaillerie, B. Lothenbach, A. Favier, C. Brumaud, and F. Puertas. (2021) "Early reactivity of sodium silicate-activated slag pastes and its impact on rheological properties", Cement and Concrete Research, 140: 106302.

Chen, X., A. Meawad, and L. Struble. (2014) "Method to Stop Geopolymer Reaction", Journal of the American Ceramic Society, 97.

Jiang, D, C. Shi, and Z. Zhang. (2022) "Recent progress in understanding setting and hardening of alkali-activated slag (AAS) materials", Cement and Concrete Composites, 134: 104795.

Yip, C.K., G.C. Lukey, and J.S.J.V. Deventer. (2005) "The coexistence of geopolymeric gel and calcium silicate hydrate at the early stage of alkaline activation", Cement & Concrete Research, 35(9): 1688-1697.

García-Lodeiro. I, D.E. Macphee, A. Palomo and A. Fernández-Jiménez. (2009) "Effect of alkalis on fresh C–S–H gels. FTIR analysis", Cement and Concrete Research, 39(3): 147-153.

García-Lodeiro. I, A. Fernández-Jiménez, M. Teresa Blanco and Angel Palomo. (2008) "FTIR study of the sol–gel synthesis of cementitious gels: C–S–H and N–A–S–H", Journal of Sol-Gel Science and Technology, 45(1): 63-72.

Case Studies on the Large-Scale use of Low-Carbon Belitic Calcium Sulfoaluminate (BCSA) concrete

Theodore Hanein [1], Julian Calleros[2] and Eric P. Bescher[3*]

[1]*Department of Materials Science and Engineering, University of Sheffield, Sheffield, United Kingdom*

Email: t.hanein@sheffield.ac.uk

[2]*Grupo Cementos de Chihuahua, Chihuahua, Mexico*

Email: jcalleros@gcc.com

[3] *Department of Materials Science and Engineering, UCLA, Los Angeles, CA, USA*

[*]*Email:bescher@ucla.edu*

ABSTRACT

Belitic calcium sulfoaluminate (BCSA) cement has been successfully used for the rapid rehabilitation of large concrete infrastructure such as runway or highway pavements. Typically, such projects require specifying rapid-strength concretes because pavement must be returned to service within a few hours of closure. For these applications, the compressive strength of the concrete should be on the order of 40 MPa in 2-3 hours under penalty of large fines for delays. BCSA is an alternative cement that is not usually familiar to the construction workforce and its use generally requires close collaboration between the cement manufacturer, specifiers, general contractors, subcontractors, and academia. For example, *ad hoc* performance specifications, approvals, concrete mix designs, and delivery methods must be developed, and this can be complex. In this paper, we describe large-scale case studies involving the use of BCSA cement concrete.

KEYWORDS: *Belitic calcium sulfoaluminate concrete, BCSA, low carbon infrastructure*

1. Introduction

Belitic calcium sulfoaluminate (BCSA) was developed in the United States in the early 70s (Ost 1975) and is from the clinker family of cements. Alite, the carbon-intensive and early-strength-imparting phase in PC, is replaced in BCSA by ye'elimite $C_4A_3\bar{S}$. Ye'elimite is much less carbon-intensive, and more efficient at providing early-strength than alite. BCSA is one of many $C_4A_3\bar{S}$-containing binders (Bescher 2020) that can be used as a single cement, i.e. not requiring blending with PC. This makes it a uniquely attractive binder for its Global Warming Potential (GWP) which, is 0.673 kg-CO_2 eq/ton (CTS 2022). An important characteristic of BCSA is that is allowed concrete mixes to reach strengths of approximately 40 MPa (compressive) or 2.8 MPa flexural at pavement opening, in 4 hours [California Department of Transportation Standard Specifications, 2022].

Rapid strength is a crucial economic incentive because it catalyzes the use of the material on short-closure time projects. Finally, compared to other low-carbon cement technologies, BCSA is compatible with established concrete placement logistics developed for PC, such as the use of ready-mix plants, silos and the flexibility cast-in-place concrete. Although BCSA has been used as concrete pavement for over 40 years in the Americas, the practice has remained somewhat below radar. An objective of this article is to briefly discuss a few selected case studies of the use of BCSA on large-scale infrastructure projects. We briefly

cover the specifics of applications in North America, including examples of large projects on the Mexico City-Querétaro highway, large repair programs on the California highway system, and runway rehabilitation at the Seattle airport, and railroad rehabilitation repair. The performance of BCSA pavement in a wet climate was also assessed after 23 years in the field at the Seattle airport.

2. Case studies

2.1 BCSA concrete on highways

The Mexico City- Querétaro highway is the most heavily trafficked highway in Mexico, at 50,000 vehicles per day. A reinforced BCSA pavement system was designed for its rehabilitation. The objective of this project was to rehabilitate large sections of the highway, typically 250 m at a time in less than 12 hours. Combining the low shrinkage (Bescher 2021) of BCSA concrete with steel reinforcement also allowed an increase in joint spacing to 200 m, which is a notable increase in joint spacing over the typical 5-6 m joint spacing in PC-based pavement. Another key aspect of this project was the large haul distance from the batch plant to the site. Citric acid and shaved ice were used as means of controlling the set time of the mix. To accommodate variations in ambient temperatures, mix temperatures were kept between 24 and 32 °C, slab thickness was 22 to 24 cm and each truck was loaded with 6 m^3 of BCSA concrete. BCSA cement content was 470 kg/m^3 and curing of the slabs required 2 hours. Total volume of BCSA concrete placed on this project was 20,000 m^3 at a rate of 250 m^3 per day.

Figure 1- BCSA concrete placement on Mexico City- Queretaru highway.

BCSA concrete is part of a program of rehabilitation of concrete highways in California. Since 1997, approximately 250,000 tons of BCSA cement have been placed on California highways. The specifications are based on a flexural strength specification of 2.76 MPa at opening time of the pavement, in addition to strength at 7 days and other performance criteria. In many US States, the cement is specified as an ASTM C1600 “Rapid Hydraulic Cement”, and competes on that basis with other rapid-setting cements. Specifications in Europe or Asia are typically *ad hoc*.

2.2 BCSA concrete pavement on airports

Monterrey International Airport, Mexico

The project at Monterrey International Airport consisted of the replacement of fifteen 100 m taxilanes in the cargo area, consisting of 32 cm-thick slabs, placed at temperatures ranging from 38°C to 45°C. Specifications required a concrete achieving 48 MPa compressive in 6 hours. Haul time was 1.5 hours from the batch plant to the airport and the total volume delivered was 2,500 m^3 in 5 m^3 ready-mix trucks. Citric acid was used as a retarder, in combination with shaved ice. Citric acid concentration varied from 0.6 wt % (cement basis) at night to 1.2 wt% during the day, with 10% of the design water used as ice at night and up to 20% during the day. A total of 500 truckloads were used during the project. It was determined during the project that the concrete mix temperature should not exceed 23°C from the batch plant to the job site.

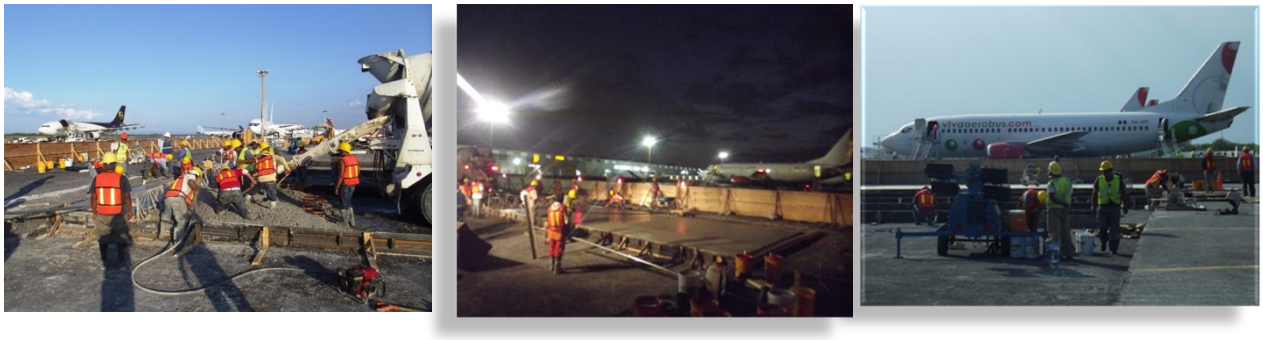

Figure 2- BCSA Concrete placement at the Monterrey International Airport, Mexico.

Seattle International Airport, United States

Approximately 30,000 m^3 of BCSA concrete have been placed at the Seattle Airport since 1997, in the overnight rehabilitation of the airport's concrete pavement (runway, taxilanes and aprons). Pavement performance after 23 years of service has been assessed. The flexural and compressive strengths of the BCSA concrete was found to have nearly doubled after 23 years in service (Deo, 2023). Concrete carbonation was measured at only 12.5 mm after 25 years. The pH of the hydrated BCSA paste was found to be 12.5 and no deleterious alkali-silica reaction was detected. BCSA was used at the Seattle airport to quadruple the size of concrete pavement and decrease the number of joints (McNerney 2021). Seattle airport remains the largest infrastructure project involving BCSA concrete at airports, but several airports in Asia-Pacific are using the cement: Melbourne Tullamarine, Sydney Hardord Smith and Lanyu in Taiwan, on which 1,200 tons of BCSA were used for runway rehabilitation.

2.3 BCSA concrete use on railroads

Mexico City-Veracruz tunnel

The 3.5 km El Mexicano tunnel on Pico de Orizaba, is the highest-altitude tunnel in Mexico. The railway track on which it is built links Mexico City to Veracruz on the Gulf of Mexico. The window of time for any repairs on the track is limited to 7 hours between train movements. BCSA concrete is currently being used for the rehabilitation of the track. During this short timeframe, a section of the track is removed, the base removed and BCSA concrete slab placed. The concrete is batched at a plant outside the tunnel and sent into the tunnel using two ready-mix trucks placed on a railroad platform. The specifications call for a compressive strength of 35 MPa at 3 hours, and 60 MPa at 28-days. Three hours after placement, a prefabricated concrete support element for the track is placed above the BCSA concrete, allowing installation of the new track and re-opening to traffic. The cement content of the concrete mix is 560 $kg.m^{-3}$ and uses basalt aggregate while the BCSA slab is 22 cm thick. w/c was maintained between 0.40 and 0.45. At 28°C, citric acid is used at a rate of 0.6 wt % (cement basis), varying by 0.1 wt% per degree of increase or decrease in temperature. If the temperature increases to 30°C, the citric acid content is increased to 0.8 wt%, or if the temperature decreases to 27°C, citric acid addition is reduced to 0.5 wt%. Therefore, the range of citric acid use is 0.3 wt% to 0.9 wt%. Approximately 3,500 m^3 of concrete (2,500 tons of BCSA cement) have been used on this project thus far.

Figure 3- BCSA concrete placed on the Pueblo-Veracruz railway tunnel, Mexico

3. Conclusions

Case studies demonstrate that BCSA concrete mixes have been successfully used on large infrastructure rehabilitation projects. These mixes have been developed for delivery of the low-carbon concrete using either volumetric or ready-mix trucks, allowing hauling times up to one hour or more if needed. These mix designs can be adjusted to achieve the specified strength over a wide range of ambient temperatures using citric acid and/or ice. We conclude that in favorable weather/moisture conditions and with appropriate combined focus on concrete mix design, logistics, specifications, contractor expertise, experience in the field demonstrates that BCSA cement concrete can be used for large infrastructure projects.

References

California Department of Transportation, Standard Specifications, 2022

CTS Environmental Product Declaration for Rapid Set Cement, https://www.ctscement.com/assets/doc/info/EPDlabel_RapidSet_Labeling_Sustainability_CTS_Cement.pdf.

Ost B. et al. (1975) "Very High Early Strength Cement", U.S. Patent 3,860,433.

Bescher, E., Kim, J. and Vallens, K. "Belitic calcium sulfoaluminate cement: Hydration chemistry, performance, and use in the United States" (2020) Tsement, November-December 2020.

Bescher, E., Kim, J. and McNerney M (2021) On the differences in Chemistry and Performance between Rapid Strength Concretes, Proceedings of the 12th ICCP (978-0-578-33418-9), December 31, 2021, 188–194,

Deo, O., Win, D., Bhuskute, N., Chung, D. de Ocampo, N. Bescher, E., Fast Setting, Low Carbon Infrastructure Rehabilitation Using Belitic Calcium Sulfoaluminate Concrete (2022), Concrete Solutions 2022, MATEC Web of Conferences 361, https://doi.org/10.1051/matecconf/202236100002.

Deo, O., Bhuskute, N.; Bescher, E. Naga Pavan Vaddey (2022), Belitic Calcium Sulfoaluminate Concrete Runway, Concrete International 45 (2), 27-31.

Hanein, T., Galvez-Martos, J.-L., Bannerman, M.N. (2018). Carbon footprint of calcium sulfoaluminate clinker production. J. Clean. Prod. 172, 2278–2287.

McNerney, M., Kim, J.; Paniagua, F., Paniagua, J. ; Chung, D; Morgan, M.; Deo, O, and Bescher, E., Drying Behavior of a Quadruple-Sized Belitic Calcium Sulfoaluminate Airfield Concrete Slab (2021) Proceedings of International Airfield and Highway Pavements Conference, June 8-10 2021.

The 16th International Congress on the Chemistry of Cement 2023 (ICCC2023)
"Further Reduction of CO_2 -Emissions and Circularity in the Cement and Concrete Industry"
September 18–22, 2023, Bangkok, Thailand

High-efficient Solidification and Stabilization by Low Carbon Supersulfated Cement

J.X. Ban [1,2], Jian-Xin Lu [2,3*], and C.S. Poon [2,3]

[1] *School of Water Resource and Environmental, Research Center of Environmental Science and Engineering, China University of Geosciences (Beijing), Beijing, China*
Email: jiaxing.ban@cugb.edu.cn
[2] *Department of Civil and Environmental Engineering, The Hong Kong Polytechnic University, Hung Hom, Kowloon, Hong Kong, China*
Email: jianxin.lu@polyu.edu.hk
[3] *Research Centre for Resources Engineering towards Carbon Neutrality, The Hong Kong Polytechnic University*
Email: cecspoon@polyu.edu.hk

ABSTRACT

This study developed a novel low-carbon supersulfated cement (SSC) mortar prepared with multiple types of solid waste, including phosphogypsum and cathode ray tube (CRT) panel glass for realizing carbon neutrality. In this present research, the mechanical (compressive strength) and durable (drying shrinkage) properties of the SSC system after incorporating the CRT glass aggregate is discussed. And the environmental impacts including toxic characteristic leaching procedure (TCLP) and carbon emission are clarified. A detailed stabilization mechanism for the heavy metals in the SSC system is proposed. The results show that the compressive strength witnesses a slight increase after replacing river sand with CRT glass. In terms of the drying shrinkage, it falls gradually with the addition of the CRT glass. Even when 100% CRT glass is used as aggregate, the leaching concentration of the heavy metals is still within the limit of the standard using the SW-846 Method 1311. Most of the heavy metals are trapped in the structure of the ettringite by replacing the place of the Al atom. Compared with ordinary Portlandite cement (OPC), the production of SSC can decrease 80% of carbon emissions resulting from incineration. In conclusion, the recycling of the waste CRT glass and waste phosphogypsum in the SSC system can not only obtain ideal mechanical and durable performance but also realize the stabilization of the heavy metals.

KEYWORDS: *Supersulfated cement; Pozzolanic reaction; CRT glass; Solidification and stabilization; Carbon emissions*

1. Introduction

Carbon dioxide emissions have been an urgent environmental problem across the world. The production of Ordinary Portland Cement (OPC) contributed to the major proportion of the carbon emissions in the construction industry (Cristelo et al., 2015). When producing one-ton clinker, there will be 0.8 tons of CO_2 released into the atmosphere (Turner and Collins, 2013). Besides, the energy-intensive manufacture of OPC can also emit hazardous gases such as NOx and SO_2 (Zhang et al., 2020). Therefore, it is urgent to look for a novel low-carbon cementitious material.

Super-sulfated cement (SSC) is a promising low-carbon cement prepared with sustainable raw materials without incineration, which includes gypsum and slag (Da Luz and Hooton, 2015). During the production procedure, there is no carbon emission, because it does not need any high-temperature clinkering process ,which could decrease by about 90% carbon emissions compared to OPC according to (Niu and Zhang, 2015). Due to its lower hydration heat and superior durability performance in terms of chemical resistance, it has the potential to be used as an alternative to OPC to some extent, (Juenger et al., 2011).

It is estimated that there is about 6 billion tons phosphogypsum generated around the world. And it still increases at a rate of 150 million tons/per year (Du et al., 2022), while only 15% of which is recycled (Silva et al., 2022). Besides, the hazardous waste cathode ray tubes (CRT) glass is gradually being replaced by liquid crystal displays and light-emitting resulting in much CRT glass abandoned in the world (Gao et al., 2022). If there is no appropriate treatment for the CRT glass, it would threaten the surrounding environment by heavy metals leaching (Elshkaki et al., 2005; Long et al., 2022).

Based on these solid waste, the present study recycle CRT glass as aggregate in replace of the river sand and use phosphogypsum to replace natural gypsum to conduct the mechanical and durable research.

2. Materials and Methods

2.1 Materials

The slag was collocted from a steel plant (Guangdong Shaoguan Steel Company Ltd.). The CRT glass (panel part) was collected from a waste electronic equipment recyclor. The phosphofypsum was recycled from a phosphoric acid production factory in Guizhou province (China).

2.2 Methods

The compressive strength of the SSC system mortar cubes (40 mm × 40 mm × 40 mm) was obtained using the compression machine at 3, 7, 28 d based on BS EN 12390-3. The loading speed was 0.6 MPa/s. After demolded, the mortar bars are first immersed in a water bath at 25 °C for 5 d. Hereafter, the lengths of the mortar bars are measured as the initial length. The length of the mortar bars from 0 d to 28 d are measured by using a length comparator (0.001 mm accuracy) according to ASTM C490. Then the TCLP test was conducted for exploring whether the recycled CRTGS can be applied to the SSC system in terms of environmental impact. Mortars after curing for 28d is smashed into small particles with the size of 9 mm. Then the particles are immersed in the glacial acetic acid with the pH of 2.88 ± 0.05 (EPA, 1992). The extract solution is set at a liquid-to-solid ratio of 20:1. The reactor is rotated at 30 rpm for 18 h. After tumbling, the supernatant was filtered through a 0.45 μm membrane filter and digested with concentrated nitric acid. The heavy metals in the leachate are determined by an inductively coupled plasma emission spectrometer (Spectro Blue).

3 Results and discussions

With the replacement of river sand by CRT glass, the crack propagation of the cement mortars was inhibited during the drying shrinkage period due to the irregular shape of the CRT glass (Fig. 1). The drying shrinkage was reduced with the increased content of the CRT sand (Fig. 2). The dense interfacial transition zone (ITZ) was found due to the pozzolanic reaction between the CRT glass and SSC matrix.

Simultaneously, during the pozzolanic reaction, the heavy metal ions in CRT glass were dissolved and released into the pore solution. These heavy metal ions reacted with sulfate ions dissolved in gypsum and precipitate as a form of insoluble sulfate substance around the aggregates and further improved ITZ. This can not only realize the bonding improvement between the aggregate and the paste, but also achieve a superior solidification and stabilization (S/S) effect for the heavy metals in the CRT glass (Fig. 3). The special reaction can not be observed in OPC-river sand based cementitious materials.

In addition, the larger amount of the ettringite crystals in the SSC also contributed to achieving S/S through the isomorphous replacement effects (Figs. 4 and 5) of the ettringite. The special cementitious products, dense ITZ, and high concentration of sulfate ions in the pore solution make it a promising construction material, which can be used for stabilizing hazardous wastes. The prepared SSC was able to reduce carbon emissions up to 80% compared to the OPC system (Fig. 6).

Overall, the joint use of low-carbon SSC and CRT glass can reduce carbon emissions by realizing the valorization of multiple types of solid wastes and achieve better solidification and stabilization, and durability performance.

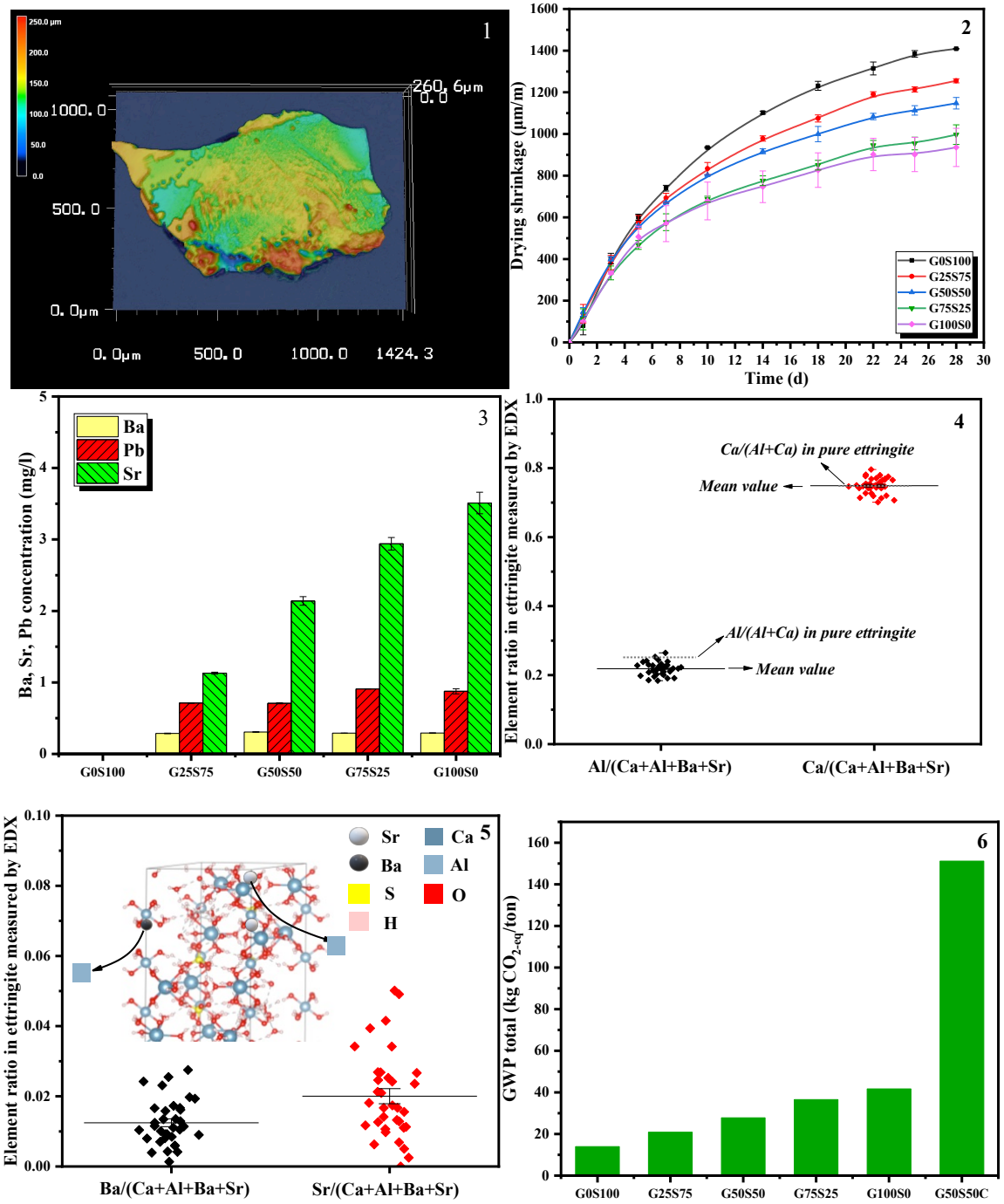

Fig. 1 3D microscope image of the CRT glass; **Fig. 2** Drying shrinkage of the SSC mortars with various CRT glass sand; **Fig. 3** TCLP test results after incorporating CRT glass; **Fig. 4** EDX statistical analysis (Al, Ca) on ettringite; **Fig. 5** EDX statistical analysis (Ba, Sr) on ettringite; **Fig. 6** GWP of SSC mortars with various CRT sand (/ton mortar)

Conclusions

The new low-carbon cementitious material provides a promising recycling approach for these two wastes. CRT glass in this cementitious system not only realizes the efficient immobilization of heavy metals but

also optimizes the SSC in terms of durable performance. This work can act as a reference to extend the application of hazardous CRT glass and phosphogypsum in engineering.

Acknowledgments

The authors would like to acknowledge the funding support from the General Research Fund from the Hong Kong Research Grants Council (Q80K) and Green Technology Fund (GTF202110180).

References

Cristelo, N., Miranda, T., Oliveira, D.V., Rosa, I., Soares, E., Coelho, P., Fernandes, L., 2015. Assessing the production of jet mix columns using alkali activated waste based on mechanical and financial performance and CO_2 (eq) emissions. J. Clean. Prod. 102, 447-460.

Da Luz, C.A., Hooton, R., 2015. Influence of curing temperature on the process of hydration of supersulfated cements at early age. Cem. Concr. Res. 77, 69-75.

Du, M., Wang, J., Dong, F., Wang, Z., Yang, F., Tan, H., Fu, K., Wang, W., 2022. The study on the effect of flotation purification on the performance of α-hemihydrate gypsum prepared from phosphogypsum. Sci. Rep. 12(1), 1-16.

Elshkaki, A., van der Voet, E., Timmermans, V., Van Holderbeke, M., 2005. Dynamic stock modelling: A method for the identification and estimation of future waste streams and emissions based on past production and product stock characteristics. Energy 30(8), 1353-1363.

EPA, U., 1992. Method 1311 Toxicity characteristic leaching procedure (TCLP). Agency EP, editor. Washington DC, USA1992.

Gao, X., Yao, X., Xie, R., Li, X., Cheng, J., Yang, T., 2022. Performance of fly ash-based geopolymer mortars with waste cathode ray tubes glass fine aggregate: A comparative study with cement mortars. Constr. Build. Mater. 344, 128243.

Juenger, M., Winnefeld, F., Provis, J.L., Ideker, J., 2011. Advances in alternative cementitious binders. Cem. Concr. Res. 41(12), 1232-1243.

Long, W.-J., Zhang, X., Xie, J., Kou, S., Luo, Q., Wei, J., Lin, C., Feng, G.-L., 2022. Recycling of waste cathode ray tube glass through fly ash-slag geopolymer mortar. Constr. Build. Mater. 322, 126454.

Niu, Q., Zhang, R., 2015. Experimental study on some properties of a low-carbon cement, 2015 3rd International Conference on Advances in Energy and Environmental Science. Atlantis Press, pp. 1440-1443.

Silva, L.F., Oliveira, M.L., Crissien, T.J., Santosh, M., Bolivar, J., Shao, L., Dotto, G.L., Gasparotto, J., Schindler, M., 2022. A review on the environmental impact of phosphogypsum and potential health impacts through the release of nanoparticles. Chemosphere 286, 131513.

Turner, L.K., Collins, F.G., 2013. Carbon dioxide equivalent (CO_2-e) emissions: A comparison between geopolymer and OPC cement concrete. Constr. Build. Mater. 43, 125-130.

Zhang, J., Ye, C., Tan, H., Liu, X., 2020. Potential application of Portland cement-sulfoaluminate cement system in precast concrete cured under ambient temperature. Constr. Build. Mater. 251, 118869.

The 16th International Congress on the Chemistry of Cement 2023 (ICCC2023)
"Further Reduction of CO_2 -Emissions and Circularity in the Cement and Concrete Industry"
September 18–22, 2023, Bangkok, Thailand

Comparison of set retarders in CSA and blended CSA/OPC systems

E. Kapeluszna[1*], I. Buchała[1,2], W. Szudek[1,3] and P. Szołdra[1,4]

[1] AGH University of Krakow, Faculty of Materials Science and Ceramics, Department of Building Materials Technology, Krakow, Poland

Email: ewak@agh.edu.pl

[2] Email:ilona.buchala1@gmail.com
[3] Email: szudek@agh.edu.pl
[4] Email: szoldra@agh.edu.pl

ABSTRACT

The aim of the presented work was to determine the influence of CSA on the properties of CSA/OPC blended binder. Moreover, the impact of four set retarders (citric acid, tartaric acid, sodium gluconate and borax) on the hydration and performance of such cement was investigated. DTA/TG and microcalorimetric analyses were carried out on cement pastes, followed by consistency, setting time and compressive strength measurements. DTA/TG method allowed for a qualitative and quantitative characterization of the phase composition of pastes after 24 hours of hydration. In the case of neat CSA, a correlation was found between the amount of water chemically bound in the samples and their compressive strength. All of the selected set retarders had a different effect on the hydration and properties of pure CSA, not only increasing its setting time but also affecting the amount of products formed during the hydration. In the case of CSA, the most efficient set retarders were sodium gluconate and borax while for the blended cement, the set-retarding effect was not observed.

KEYWORDS: *: calcium sulfoaluminate cement, hydration, set retarder, borax, sodium gluconate*

1. Introduction

In recent years, calcium sulfoaluminate cements (CSA) have attracted the attention of both scientists and cement industry. Compared to OPC, the reaction of CSA cements is much faster and a greater fraction of their hydration heat is generated within the first 12 h. The early-age hydration products include ettringite, monosulfate and amorphous aluminum hydroxide. Due to the fast reaction of CSA cements, the use of a retarder is often required in order to obtain a sufficient open time. Citric, tartaric and gluconic acids and their salts are powerful set retarders in calcium sulfoaluminate cements. Moreover, borax proved to be an effective CSA retarder by preventing (to a certain extent) the dissolution of ye'elimite and lowering the initial pH. However, little is known about their performance in binary CSA/OPC systems. Therefore, the goal of the presented study was to compare the effectiveness of various set retarders in pure CSA and blended CSA/OPC systems.

2. Experimental

2.1 Methods

Chemical composition of the materials used in the experiments was determined with a PANAnalytical WDXRF Axios Max spectrophotometer. Their phase composition was analyzed using a Philips PW 1050/70 diffractometer. Patterns were collected in the range of 5-65 °2θ, with a 0.05° 2θ step. The heat of hydration of cement pastes was measured at 25°C using a differential heat-conduction microcalorimeter. DTA/TG measurements were carried out in the temperature range of 25-1000°C using

a Netzsch STA 449F3 Jupiter thermoanalyzer in a synthetic air atmosphere. Grain size distribution was determined with a Malvern Mastersizer 2000 laser diffractometer. Consistency of mortars was investigated with a flow table according to PN-EN 1015-3. Setting time of cement pastes was measured according to PN-EN 196-3. The compressive strength of cement mortars was determined on 25 x 25 x 100 mm bar samples using a Controls Automax 5 hydraulic press.

2.2 Materials

Calcium sulfoaluminate cement (CSA) and ordinary Portland cement (OPC) were used in the investigations. Their chemical compositions are presented in Table 1. Their phase composition was examined by X-ray diffractometry. Fig. 1 shows the X-ray patterns of both types of cement.

Table 1. Chemical composition of cements.

Oxide		CaO	SiO_2	Al_2O_3	MgO	SO_3	Fe_2O_3	Na_2O	K_2O	Na_2O	Cl
Cement [%]	CSA	39.8	5.5	23.2	2.6	23.9	1.1	1.2	0.5	1.2	0.2
	OPC	64.7	18.7	4.6	1.7	4.7	3.7	0.4	0.4	0.4	0.1

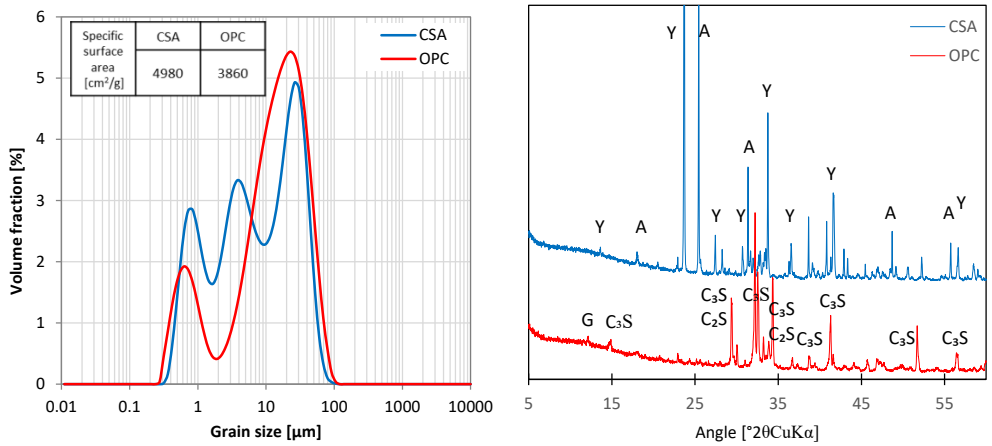

Fig 1. Grain size distribution and phase composition of CSA and OPC; C_3S-Alite, C_2S-Belite, Y-Ye'elimite, A-Anhydrite, G-Gypsum.

The effect of various set retarders (citric acid, tartaric acid, sodium gluconate and borax) on the properties of calcium sulfoaluminate cement (CSA100) and CSA/OPC blend (CSA20 - 80% of OPC and 20% of CSA) was investigated. For this purpose, heat evolution, consistency and compressive strength were examined as a function of time. Moreover, phase composition of CSA and OPC pastes with various set retarders was determined after 24 hours of hydration in order to compare the differences in the amount of the hydration products.

3. Results

The admixtures affect the kinetics of hydration (Fig 2). The analysis of the amount and rate of heat released during the reaction shows that sodium gluconate and borax most effectively prolonged the induction period and extended the setting time of CSA cement pastes, while the most effective set retarders of CSA20 were citric acid, borax and sodium gluconate. According to the literature, borax prevents the dissolution of ye'elimite, which was confirmed by the calorimetric analysis – the introduction of borax lead to the greatest extension of the induction period. The different shape of the calorimetric curves shows that the admixtures might have various action mechanisms. The presence of sulfates in CSA cement probably delayed the hydration of Portland clinker phases, resulting in a lower heat of hydration. All admixtures increased the setting time of CSA, as determined by Vicat apparatus (Table 2). At the same time, admixtures used in the amount of 0.2% did not effectively delay the setting of the blended binder. In its case, the rate of ettringite formation is very high; therefore, the effect of the admixtures may be decreased due to their incorporation into the structure of the hydration products.

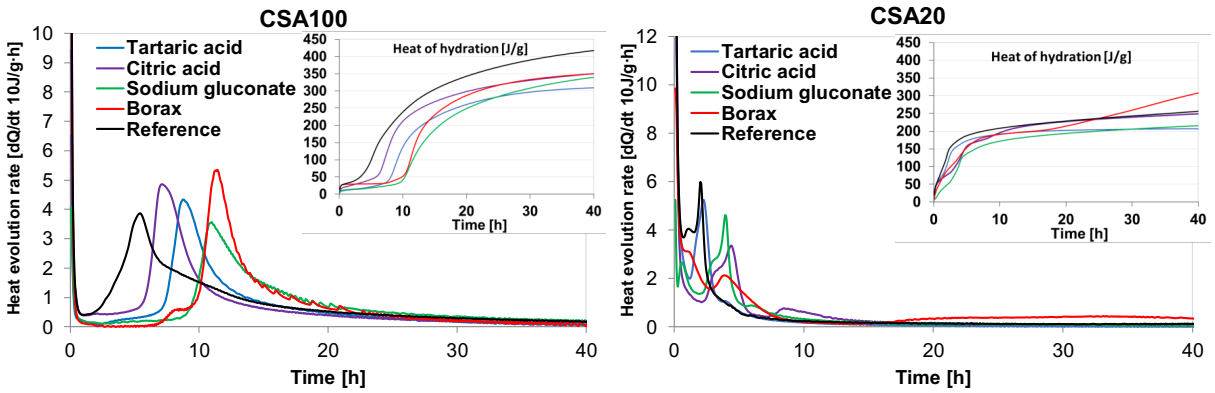

Fig 2. Heat of hydration of CSA and blended CSA/OPC pastes.

Table 2. Setting time determined by Vicat apparatus.

Setting time [min]	CSA100					CSA20				
	Ref	Citric acid	Sodium gluconate	Borax	Tartaric acid	Ref	Citric acid	Sodium gluconate	Borax	Tartaric acid
	105	154	228	360	230	30	38	32	28	31

In general, sodium gluconate and citric acid increased the consistency of mortars containing neat CSA cement, while borax and tartaric acid caused a decrease in their flow. On the other hand, in the case of CSA20 mortars, the consistency was increased by all of the admixtures except for borax (Fig. 3).

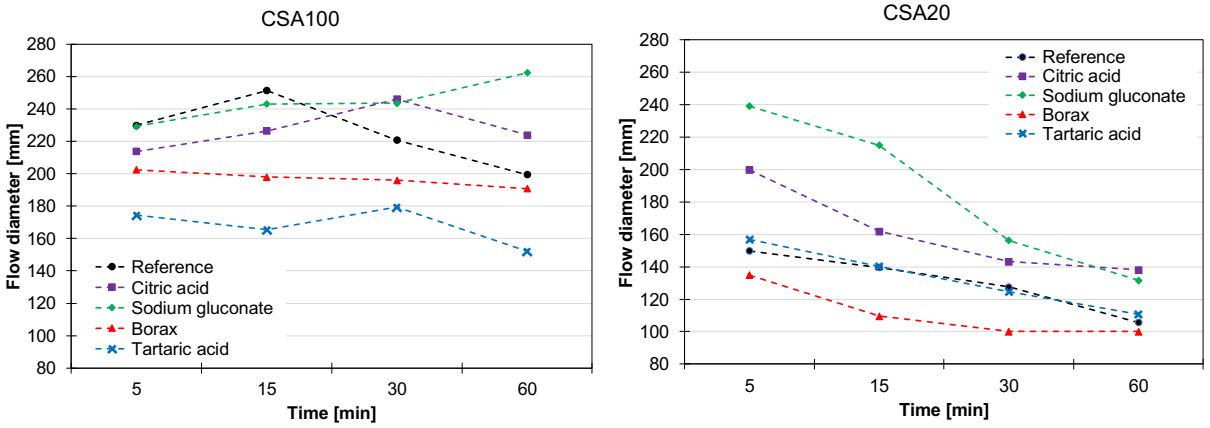

Fig 3. Consistency vs time of CSA and blended CSA/OPC mortars.

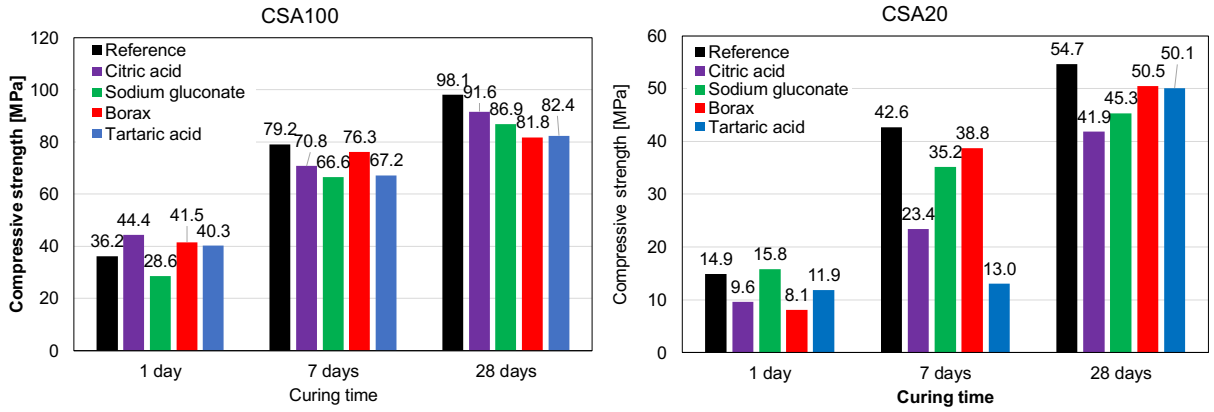

Fig 4. Compressive strengths of CSA and blended CSA/OPC mortars.

After 1 day of curing, citric acid, tartaric acid and borax increased the strength of CSA mortar by 11 to 23%, while sodium gluconate deteriorated its mechanical properties. Such outcome corresponds to the

results of the calorimetric measurements. After 7 and 28 days of curing, all admixtures caused a decrease in strength of the CSA100 mortars (Fig. 4). For blended cement, in general, a decrease in compressive strength was observed after the addition of all of the set retarders.
The differences in the compressive strength are related to the content and probably the morphology of ettringite, which was proven by the DTA/TG analysis. The increase in compressive strength after 1 day of curing may result from a different morphology of the ettringite formed and thus, a different contribution of chemically bound water. The amount of ettringite was the highest for CSA100 with the addition of citric acid (Fig 5). Tartaric acid probably affects the morphology of ettringite, which may result from the high affinity of tartrate ions towards aluminate phases and their incorporation into the forming hydration products. The DTA/TG results indicate that in the case of OPC with the addition of tartaric acid, after 24 hours, the amount of hydration products - AFt, C-S-H and $Ca(OH)_2$ was the lowest out of all admixtures.

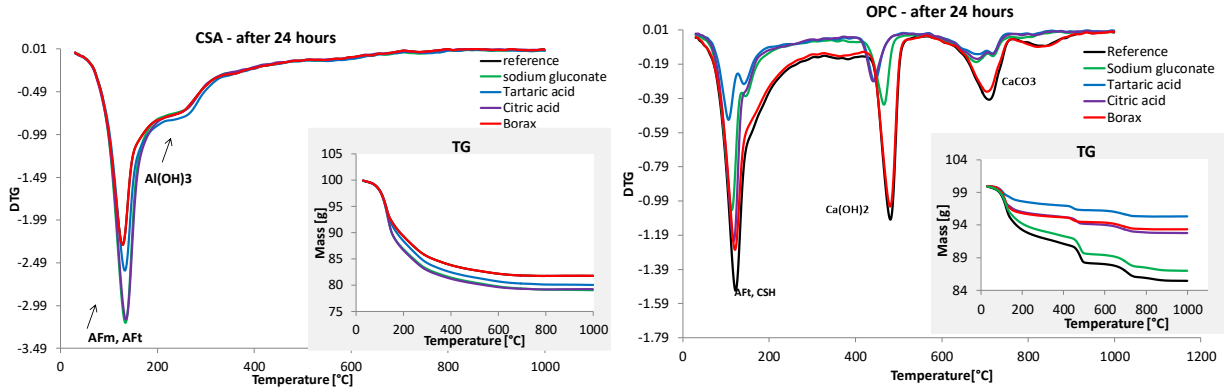

Fig 5. DTA curves of CSA and OPC pastes after 24 hour of hydration.

3. Conclusions

1. The addition of CSA to Portland cement significantly accelerates its early hydration and increases the amount of heat released after approx. 15 hours. However, the heat released after 40 hours is lower, most likely due to a delay in the hydration of Portland clinker phases resulting from the presence of sulfates.
2. In the case of CSA, the addition of borax results in the greatest extension of setting time and the most significant prolongation of the induction period. However, it leads to an increase in the compressive strength after 1 day and a decrease after 7 and 28 days of curing, compared to the reference sample.
3. Citric acid extended the setting time of CSA by approx. 50 minutes, making it the least effective among all tested admixtures. In the microcalorimetric curves of the samples containing citric acid, the shortest induction period was observed, compared to pastes with other admixtures.
4. The DTA/TG analysis showed that after 24 hours of hydration, the sample with citric acid contained a higher amount of ettringite, which explains the greatest increase in the strength of CSA100 mortars.
5. All admixtures influence the hydration of CSA/OPC blend, however, they are ineffective in retarding the setting of such binders.

Acknowledgements

This research was partially funded by the National Science Centre, Poland, project no. 2021/43/D/ST8/02603

References

Ben Haha, M., Winnefeld, F. and Pisch, A. (2019) "Advanced in understanding ye'elimite-rich cements", *Cement and Concrete Research*, 123(105778): 1-20

Bullerjahn, F., Zając, M., Skocek, J. and Ben Haha, M. (2019) "The role of boron during the early hydration of belite ye'elimite ferrite cements", *Construction and Building Materials*, 215: 252-263

El Khessaimi, Y., El Hafiane, Y. and Smith, A. (2020) "Effect of fineness and citric acid addition on the hydration of ye'elimite", *Construction and Building Materials*, 258(119686): 1-12

Zając M,, Skocek J., Bullerjahn F. and Ben Haha, M. (2016) "Effect of retarders on the early hydration of calcium-sulpho-aluminate (CSA) type cements", *Cement and Concrete Research*, 84: 62-75

The 16th International Congress on the Chemistry of Cement 2023 (ICCC2023)
"Further Reduction of CO_2 -Emissions and Circularity in the Cement and Concrete Industry"
September 18–22, 2023, Bangkok, Thailand

CO_2 mineralization in the limestone calcined clay cement

Q. Liu[1], S. Hu[2], Y.C. Hu[3], and G.Q. Geng[4*]

[1] *Department of Civil and Environmental Engineering, National University of Singapore, 117576, Singapore*
Email: liuqing@nus.edu.sg
[2] *Department of Civil and Environmental Engineering, National University of Singapore, 117576, Singapore*
Email: e0920941@u.nus.edu
[3] *Department of Civil and Environmental Engineering, National University of Singapore, 117576, Singapore*
Email: yc_hu@nus.edu.sg
4 Department of Civil and Environmental Engineering, National University of Singapore, 117576, Singapore
Email: ceegg@nus.edu.sg

ABSTRACT

In ready-mixed concrete plants, producing concrete inevitably generates waste cement paste which will pollute the environment if disposed of randomly. Herein, we carbonated the waste cement paste by aqueous carbonation to replace the limestone to develop a novel limestone calcined clay cement (LC^3). Carbonation not only reactivates the waste cement paste but also fixes the CO_2 in the cement matrix. The results showed that the waste cement paste could be carbonated quickly within 8.5 h with the formation of the carbonated products, mainly calcium carbonates and amorphous silica gel. By tuning the substitution ratio of carbonated waste cement paste, the compressive strength of LC^3 with carbonated waste cement paste is higher than the OPC and LC^3 due to the high activity and specific surface area of carbonated waste cement paste. The pore structure of LC^3 with carbonated waste cement paste was refined. Hopefully, our work may pave a new way to develop a novel LC^3 by replacing limestone with carbonated waste cement paste, accompanied by permanently realizing the sequestration of CO_2 in the cement matrix.

KEYWORDS: *Carbonation, Waste cement paste, LC^3, Mechanical strength*

1. Introduction

With the rapid development of the economy and society, concrete is extensively used to carry out infrastructure construction, leading to a huge demand for cement. It is well known that producing cement releases a large amount of CO_2, which abets global warming. Furthermore, the thriving concrete industry produces a mass of hardened cement and concrete waste, which is harmful to protecting the environment and achieving the sustainable development of society. Therefore, reusing hardened cement and concrete waste is becoming urgent.

The recycled coarse aggregate (RCA) can be extracted from the hardened concrete and was applied in concrete blocks and road construction (Zuo et al (2018) and Gupta et al (2018)). However, recycled concrete fines (RCF) have a rough surface texture, a high-water absorption ratio and inferior properties, restricting their application in new concrete. To expand the application of RCF, recently, researchers have focused on improving the properties of RCF by carbonation (Mehdizadeh et al (2021), Qin et al (2019) and Wu et al (2022)). Aqueous carbonation as an indirect method has been employed to improve the activity of RCF due to their high efficiency in producing calcium carbonate ($CaCO_3$) and amorphous silica gel (Zajac et al (2020) and Shen et al (2021)). The hydrated cement paste in RCF is eliminated via the leaching-carbonation process, where RCF is converted to $CaCO_3$ and silica-rich gel that can be used in concrete as supplementary cementitious materials.

LC^3 as a new cement has attracted a lot of attention from researchers due to its low carbon footprint and low cost. Clays with a kaolinite content of approximately 40% or above were calcined to prepare LC^3-50 which displayed a comparable compressive strength with the cement mortar for 7 days (Alujas et al (2015) and Avet et al (2016)). Although limestone is widely used in LC^3 due to its low price, high availability, and filling effect, its main component is $CaCO_3$ which has low activity, limiting the strength development of LC^3. To address this issue, here, the concrete slurry waste is carbonated by aqueous carbonation to produce $CaCO_3$ and amorphous silica gel to replace limestone.

In this study, we aim to fabricate a novel LC^3 whose limestone is replaced by carbonated products produced by carbonation of waste cement paste. The waste cement paste was carbonated first to obtain the carbonated products. The pH of the solution with waste cement paste was monitored during carbonation. X-ray diffraction (XRD) and thermogravimetric analysis (TGA) were used to characterize the carbonated waste cement paste. Finally, the compressive strength was measured to evaluate the effect of carbonated waste cement paste on the LC^3 mortar.

2. Materials and methods

2.1 Materials

Ordinary Portland cement (OPC) Type I is used to prepare LC^3. A combination of Singapore marine clay and kaolin is calcined at 800 °C to obtain the calcined clay. Limestone (98% $CaCO_3$ content) and gypsum with a purity of more than 99% were purchased from Singapore. The fine aggregate is river sand, and the fineness modulus is 2.4. The water-reducing (WR) agent is a high-performance polycarboxylate liquid water reducer with water reducing rate of 27%.

Cement pastes with a water-cement ratio of 0.4 were used to represent waste cement paste. After 21 days of standard curing, samples were taken out for drying, crushing, and ball milling, and finally obtained the waste cement waste powder with a diameter of less than 75μm. The component of LC^3 was listed in Table 1. The mix proportion was presented in Table 2. The WR agent was used to control the workability of the mortar. The preparation and curing of mortar specimens referred to the requirements of ASTM-C305. In this experiment, three kinds of mortars are prepared, namely OPC, LC^3 using limestone powder (LC^3), and LC^3 using carbonated waste cement paste (LC^3-waste).

Table 1 Components of LC^3

OPC	Calcined clay	Limestone or Waste cement slurry	Gypsum
70%	19%	9%	2%

Table 2 Mix proportion of mortar

LC^3 or Cement	Sand	Water	Water reducing agent
1	2.75	0.485	0.013

2.2 Methods

2.2.1 Carbonation test

The experiment was carried out using a self-made rapid carbonation device (in a liquid environment), as shown in Fig. 1. The raw material was waste cement paste powder with a particle size below 75 μm. The flow rate of carbon dioxide was 0.5 L/min, and the liquid-solid ratio was 2 with a mixing speed of 200 r/min. Samples were taken every 1 h from 0.5 h until 8.5 h. After carbonation, waste cement paste was taken out and dried to obtain carbonated waste cement paste powder for preparing LC^3.

Fig. 1 Carbonation of waste cement paste

2.3.2 XRD and TGA

After drying, the sample was ground into powder and mixed with 1-part CaF_2 in a mass ratio of 4:1. Finally, the D8 Advance X-ray Diffractometer was employed to characterize the phase composition quantitatively. The scanning angle was 5–60°, and the speed was 1°/ min. DTG-60H thermogravimetric

analyzer was conducted to study the thermal stability. The temperature range was from 30 °C to 950 °C at a rate of 20 °C/min.

2.3.3 Compressive strength test

The pressure testing machine was carried out to measure the compressive strength of cube specimens (40mm) according to ASTM-C109. The test loading rate was 144 kN/min. Three parallel specimens were tested to calculate the average value.

3. Rseults and discussion

3.1 Carbonation of waste cement paste

With the increase of carbonation time, the pH value of the cement slurry decreases continuously, showing a trend of rapid decline first and then slow decline (Fig. 2(a)). Through the test results of XRD and TGA, the time-history curves of calcium hydroxide ($Ca(OH)_2$) and $CaCO_3$ content can be calculated. The content of both $Ca(OH)_2$ and $CaCO_3$ increases rapidly in the first 4.5h and slows down in the next 4h.
After the 8.5h carbonation test, the content of $CaCO_3$ was calculated to be 55.97% in the carbonated waste paste by XRD (Fig. 2(c)), and that by TGA was calculated to be 59.42% (Fig. 2(d)). This indicates that the carbonation test can generate more than 55% $CaCO_3$ in the carbonated waste paste within 8.5h, which is because, under the high alkaline environment, the introduction of carbon dioxide rapidly converts the $Ca(OH)_2$ in the cement waste slurry to $CaCO_3$. However, as the carbonation time increases, the amount of $Ca(OH)_2$ decreases, resulting in a reduction in the conversion rate.

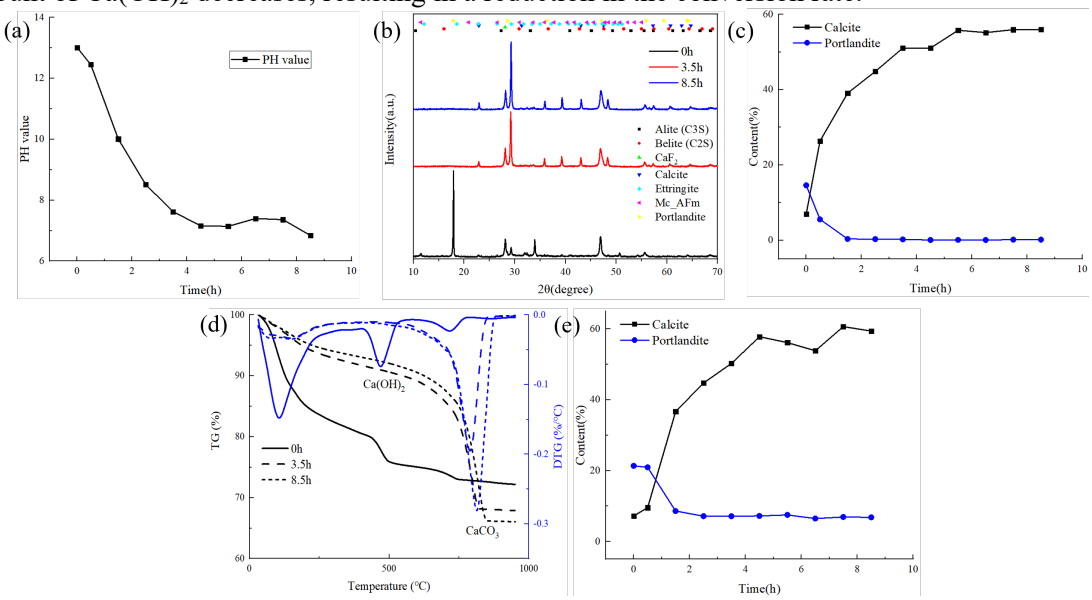

Fig. 2 Carbonation of waste cement paste. (a) pH of waste cement slurry after carbon dioxide injection. (b) XRD spectra; (c) Content of portlandite and calcite calculated from XRD; (d) TGA curves; (e) Content of portlandite and calcite calculated from TGA.

3.2 Compressive strength

Fig.3 depicts the compressive strength of mortars with different curing ages. The compressive strength of OPC is the highest at 3 days and 28 days among the three mixtures, whereas LC^3 shows the lowest compressive strength regardless of the curing age. LC^3-waste has a higher compressive strength than the counterpart of LC^3, indicating that carbonated waste cement paste promotes cement hydration. It is worth noting that the 7-day compressive strength of LC^3-waste is slightly higher than that of OPC, which may be due to the nucleation effect of calcium carbonate and the pozzolanic reaction of silica gel. The particle size of the limestone and the carbonated waste paste is at the same level, which means that the filling effect of the carbonated waste cement paste also contributes to the increased strength. The low compressive strength of LC^3-waste and LC^3 is attributed to their poor fluidity due to the presence of marine clay, which entraps some air bubbles in the matrix and thus deteriorates the compressive strength. The marine clay was found to increase the total porosity of cement mortar, resulting in a low mechanical strength (Dang et al (2020)). Moreover, the dilution effect reduces the compressive strength as well.

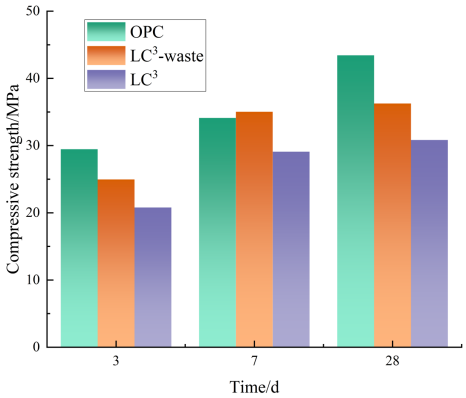

Fig. 3 Compressive strength of mortars with different curing ages. The dosage of WR is 1.3% for LC^3-waste and LC^3.

4. Conclusions

This work carbonated the waste cement paste by aqueous carbonation to produce carbonated products and amorphous silica gel and used the carbonated products to replace limestone to prepare LC^3. Through the self-made rapid carbonation device, more than 55% content of $CaCO_3$ can be generated within 8.5h. The compressive strength of LC^3-waste is slightly higher than the OPC and LC^3 at 7 days, while the 28-day strength of LC^3-waste and LC^3 is lower in comparison to the control mixture. Although the recycling of waste cement paste can be achieved by carbonation, the reduction in compressive strength of LC^3-waste is bad for the application of the carbonated waste cement paste. Therefore, it is essential to optimize the formula of LC^3 or use other chemical additives to increase the compressive strength and thus realize the application of this novel LC^3 in the construction industry.

References

Alujas, A., Fernández, R., Quintana, R., Scrivener, K.L. and Martirena, F. (2015) "Pozzolanic reactivity of low grade kaolinitic clays: Influence of calcination temperature and impact of calcination products on OPC hydration", *Applied Clay Science*, 108: 94-101

Avet, F., Snellings, R., Diaz, A.A., Haha, M.B. and Scrivener, K. (2016) "Development of a new rapid, relevant and reliable (R3) test method to evaluate the pozzolanic reactivity of calcined kaolinitic clays", *Cement and Concrete Research*, 85: 1-11

Dang, J., Du, H.J., and Pang, D.S. (2020) "Hydration, strength and microstructure evaluation of eco-friendly mortar containing waste marine clay", *Journal of Cleaner Production*, 272: 122784

Guo, Z., Tu, A., Chen, C. and Lehman, D.E. (2018) "Mechanical properties, durability, and life-cycle assessment of concrete building blocks incorporating recycled concrete aggregates", *Journal of Cleaner Production*, 199: 136-149

Gupta, N., Kluge, M., Chadik, P.A. and Townsend, T.G. (2018) "Recycled concrete aggregate as road base: Leaching constituents and neutralization by soil Interactions and dilution", *Waste Management*, 72: 354-361

Mehdizadeh, H., Jia, X., Mo, K.H. and Ling, T.C. (2021) "Effect of water-to-cement ratio induced hydration on the accelerated carbonation of cement pastes", *Environmental Pollution*, 280: 116914

Qin, L. and Gao, X. (2019) "Recycling of waste autoclaved aerated concrete powder in Portland cement by accelerated carbonation", *Waste Management*, 89: 254-264

Shen, P., Sun, Y., Liu, S., Jiang, Y., Zheng, H., Xuan, D., Lu J.X. and Poon, C.S. (2021) "Synthesis of amorphous nano-silica from recycled concrete fines by two-step wet carbonation", *Cement and Concrete Research*, 147: 106526

Wu, Y., Mehdizadeh, H., Mo, K.H. andLing, T.C. (2022) "High-temperature CO_2 for accelerating the carbonation of recycled concrete fines", Journal of Building Engineering, 52: 104526

Zajac, M., Skibsted, J., Skocek, J., Durdzinski, P., Bullerjahn, F. and Haha, M.B. (2020) "Phase assemblage and microstructure of cement paste subjected to enforced, wet carbonation", *Cement and Concrete Research*, 130: 105990

Zhang, J., Leung, C.K.Y. and Xu, S. (2010) "Evaluation of Fracture Parameters of Concrete from Bending Test using Inverse Analysis Approach", *RILEM Materials and Structures*, 43(6): 857-874

The 16th International Congress on the Chemistry of Cement 2023 (ICCC2023)
"Further Reduction of CO_2 -Emissions and Circularity in the Cement and Concrete Industry"
September 18–22, 2023, Bangkok, Thailand

Influence of slaked lime on hydration kinetics of Portland cement

Y. Zeng[1*], G.S. Munhoz[2], and G. Ye[3*]

[1] *Faculty of Civil Engineering and Geosciences, TU Delft, Delft, The Netherlands*
Email: Y.Zeng-4@tudelft.nl
[2] *Faculty of Civil Engineering and Geosciences, TU Delft, Delft, The Netherlands*
Email: G.daSilvaMunhoz-1@tudelft.nl
[3] *Faculty of Civil Engineering and Geosciences, TU Delft, Delft, The Netherlands*
Email: G.Ye@tudelft.nl

ABSTRACT

Due to the lower calcification temperature and better carbon sequestration performance, calcium lime binders are accepted as sustainable alternatives to conventional Portland cement in masonry structures. However, calcium lime binders mainly get hardened through long-term carbonation, and the strength development is slow. To overcome this drawback and ensure the mechanical performance at early ages, mixtures of slaked lime (i.e., $Ca(OH)_2$) and Portland cement are preferred in engineering practice. To investigate the hydration kinetics of lime-cement binders, especially to clarify the influence of lime-to-cement ratio (*l*/*c* ratio), calorimetry tests, X-ray diffraction (XRD) and thermogravimetric analyses (TGA) were carried out on binders with four different lime-to-cement ratios (*l*/*c*=0.0, 0.5, 1.0, and 2.0). Compared to pure cement paste, earlier occurrence of the main hydration peak (i.e., formation of C-S-H) and shorter induction period were observed in lime-cement binders, suggesting that the hydration is facilitated by additional slaked lime. The acceleration effect was further proved by quantitative analyses of XRD results and TGA, as the consumption rates of all four major phases (i.e., C_3S, C_2S, C_3A and C_4AF) increased with *l*/*c* ratio, and quicker transformation from Ettringite to AFm phases were observed in lime-cement binders. Further comparisons with inert SiO_2 fillers suggest that the acceleration effect is attributed to both physical and chemical influences, and detailed influence mechanisms will be investigated in future research.

KEYWORDS: *Slaked lime, Portland cement, hydration kinetics*

1. Introduction

Compared to Portland cement, calcium lime is calcined at lower temperatures, and the material itself could absorb CO_2 during the hardening process. Therefore, it is believed to be an ideal alternative to conventional cementitious materials in applications like plastering materials and joint materials between masonry blocks (Alvarez et al. 2021). However, one significant drawback of calcium lime binders is the poor early-age mechanical performance. Instead of gaining strength through hydration, calcium lime binders get hardened through carbonation, which may take months or even years. Therefore, in engineering practice, the mixture of calcium lime and conventional Portland cement is preferred to keep the balance between sustainability and mechanical properties (Gulbe et al. 2017).

Several previous studies have investigated the hydration process of lime-cement binders. For example, Cizer (2009) observed that the induction period could be greatly shortened by additional slaked lime. Fourmentin et al. (2015) observed similar results in their tests. However, neither of these investigations discussed the influence during the whole hydration process, and the detailed influence of slaked lime on cement hydration is still unclear.

Therefore, in this research, hydration process of four different lime-cement binders were investigated through the combined use of thermogravimetric analyses (TGA), X-ray diffraction (XRD) and

calorimetry. Based on these test results, hydration kinetics of lime-cement binders, as well as related influence mechanisms, will be discussed.

2. Materials and Methods

CEM I 42.5N cement from ENCI and CL-90S slaked lime from Lhoist were used in this research. Properties of these raw materials are summarized in Table 1.

Table 1 Raw material properties

Categories	Properties (Units)	Cement	Lime	Methods
Physical properties	Density (g/cm^3)	3.15	2.30	Pycnometer
	Specific surface area (m^2/g)	0.86	13.46	Nitrogen sorption (BET)
	Mean particle size D_{43} (μm)	29.41	15.56	Laser diffraction
Chemical composition	Alite C_3S (%)	62.90	N/A	XRD
	Belite C_2S (%)	10.26	N/A	XRD
	Alumina C_3A (%)	5.70	N/A	XRD
	Ferrite C_4AF (%)	10.37	N/A	XRD
	Portlandite CH (%)	N/A	96.30	XRD/TG
	Calcite CĈ (%)	N/A	3.70	XRD/TG
	Sulfates (%)	5.95	N/A	XRD

In order to investigate the influence of *l/c* ratio, three groups of lime-cement binders were considered in this research, and one group of pure cement paste was prepared for comparisons. Detailed mixture designs are presented in Table 2. It should be noted that, due to the large specific surface area of lime, a higher *w/b* ratio (0.8) was designed for all lime-cement binders to keep the consistency at a similar level.

Table 2 Mixture designs

Groups	Lime-to-cement (*l/c*) ratio	Water-to-binder (*w/b*) ratio
C100L0	0.0	0.6
C67L33	0.5	0.8
C50L50	1.0	
C33L67	2.0	

Following procedures recommended by Snellings et al. (2018), powder samples were collected after 6 hours, 1 day, 3 days, 7 days and 14 days for TGA and XRD. In the former test, around 30mg sample was heated to 1200℃ at a rate of 10K/min. In the latter analysis, 10% silicon powder was added as the internal standard, and the sample was scanned from 5° 2θ to 75° 2θ, with a stepwise of 0.02° 2θ.
Meanwhile, hydration heat release during the first 7 days (at 20℃) were measured through isothermal calorimetry. For comparisons, inert SiO_2 fillers with a similar specific surface area (11.94m^2/g) were also used to reflect the filler effect. All test results will be presented and discussed in the following section.

3.Results and Discussions

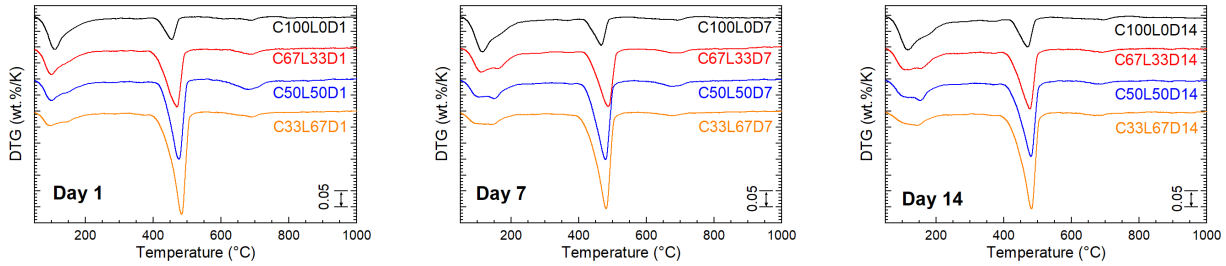

(a) Day 1 (b) Day 7 (c) Day 14

Figure 1 Representative DTG curves of hydration products

As shown in Figure 1, with the increase of lime content, the dehydration peak of $Ca(OH)_2$ at around 480℃ becomes more significant. Meanwhile, due to the inevitable existence of $CaCO_3$ in slaked lime (shown in Table 1), decarbonation peaks at around 700℃ were observed in lime-cement binders. However, after several days, these peaks become less obvious, indicating that $CaCO_3$ was consumed during the hydration process. As a result, calcium carboaluminate hydrate (C-A-Ĉ-H) was found in XRD tests (shown in Figure 2).

Regarding dehydration of other products, two peaks were observed between 50℃ and 300℃. The peak at around 100℃ appears right within the first day. This is mainly attributed to the rapid formation of ettringite and C-S-H. With the development of hydration, AFm phases are formed through continuous reactions between ettringite and cement clinkers. Therefore, the first peak gradually gets lower, and a new peak at around 170℃ grows with time. Other Afm phases, like C-A-Ĉ-H, should also contribute to the second peak, but their contributions should be marginal, as there is no obvious peak detected after 200℃. After 14 days, the second peak become dominant in lime-cement binders, while the first peak is still more obvious in pure cement paste. Therefore, it can be concluded that the additional slaked lime could facilitate the formation of AFm.

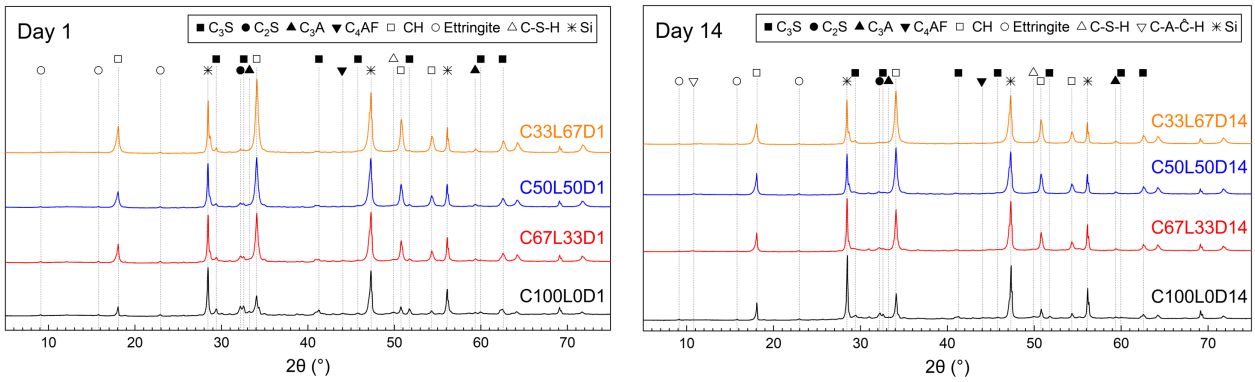

(a) Day 1 (b) Day 14

Figure 2 Typical XRD patterns of hydration products

Such acceleration effect could be better reflected through quantitative analyses of tests mentioned above. By calculating mass losses between 50℃ and 300℃, and normalizing them with cement proportion, it is obvious that the normalized mass loss increases with the lime content. Even though the mass loss cannot be clearly attributed to the dehydration of one single phase, this indicator can still prove that the total amount of hydration products is greater in groups with more slaked lime inside (shown in Figure 3a).

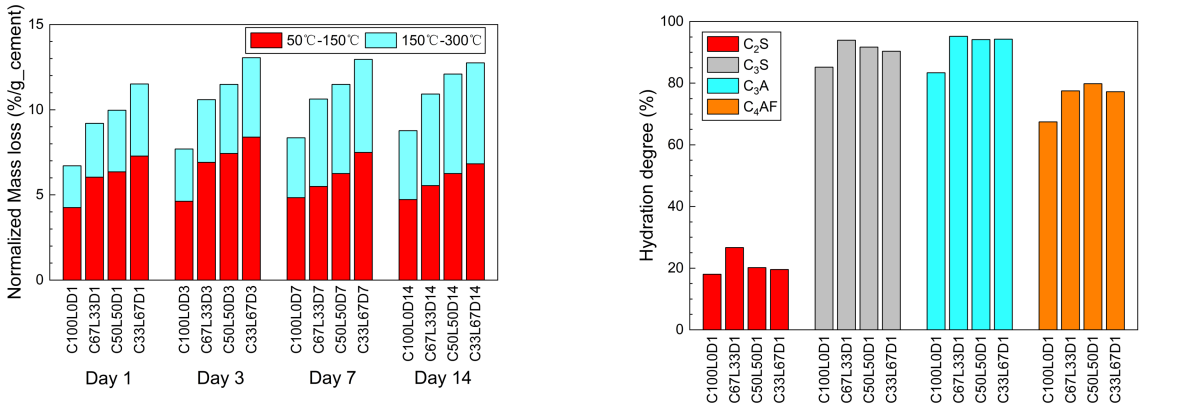

(a) Normalized mass losses observed in TGA (b) Hydration degrees of four major phases after 14 days

Figure 3 Quantitative analyses of TGA and XRD results

Through Rietveld refinements of XRD results, hydration degrees of four major hydraulic phases (i.e., C_3S, C_2S, C_3A, C_4AF) could be assessed (shown in Figure 3b). Despite the semi-quantitative nature of the analysis method, the accelerated hydration of all four phases is still obvious. However, the acceleration effect seems less relevant to the lime content, but vary significantly among different phases. For C_3S, C_3A and C_4AF, hydration degrees were increased by 8%-12%, while for C_2S, the increment is less obvious. A possible explanation to these phenomena is that the rapid hydration in early ages. Due to the growth of hydration products, further hydration reactions, especially the hydration of C_2S, could be greatly hindered, so the influence of slaked lime becomes less significant.

Several possible explanations to the acceleration effect have been proposed in previous investigations (e.g., Cizer 2009, Fourmentin et al. 2015), and among them the most reasonable one is the filler effect.

Due to the limited solubility of $Ca(OH)_2$, most of the slaked lime will not dissolve during the mixing process, and therefore could provide additional precipitation surface for hydration products. However, through comparisons with inert SiO_2 fillers (shown in Figure 4), it is clear that the induction period is significantly shorter in lime-cement binders, and the peak heat flow is also greater. Given that the surface area of inert SiO_2 fillers is similar to that of slaked lime particles, the decrease in the induction period should be more likely attributed to chemical effects, like higher affinity to hydration products and higher calcium concentration in pore solution systems. The detailed influence mechanism will be further investigated through ICP-OES tests and microscopy observations.

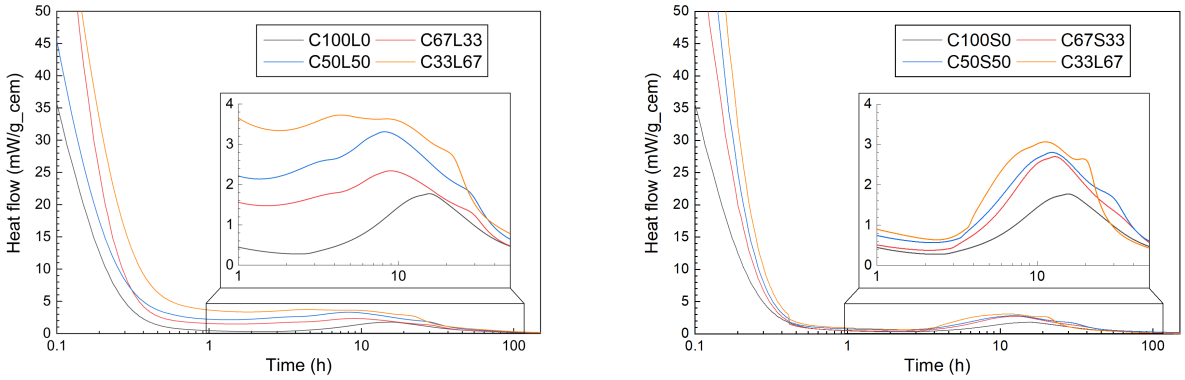

(a) Lime-cement binders (b) Cement pastes with SiO2 fillers

Figure 4 Heat release during the hydration process

4. Conclusions

In this research, hydration process of four typical lime-cement binders has been investigated, and related influence mechanisms have been briefly discussed. Within the scope of this research, the following conclusions could be drawn:

(1) The additional slaked lime could facilitate the formation of ettringite and C-S-H, as well as the formation of AFm.

(2) Hydration of all four hydraulic phases could be accelerated by slaked lime, but the acceleration effect is less significant on C_2S. This phenomenon may be related to the rapid formation of hydration products.

(3) The acceleration effect should be not only attributed to physical filler effect, but also related to chemical effects, which will be investigated in future research.

Acknowledgements

This project has received funding from the European Union's Horizon 2020 research and innovation programme under Marie Sklodowska-Curie project SUBLime [Grant Agreement no. 955986]

References

Alvarez, J., Veiga, R., Martinez-Ramirez, S., Secco, M., Faria, P., Maravelaki, P.N., Ramesh, M., Papayianni, I., and Valek, J. (2021) "RILEM TC 277-LHS report: a review on the mechanisms of setting and hardening of lime-based binding systems." *Materials and Structures*, 54, 63.

Cizer, O. (2009). "Competition between Carbonation and Hydration on the Hardening of Calcium Hydroxide and Calcium Silicate Binders." KU Leuven.

Fourmentin, M., Faure, P., Gauffinet, S., Peter, U., Lesueur, D., Daviller, D., Ovarlez, G., and Coussot, P. (2015). "Porous structure and mechanical strength of cement-lime pastes during setting." *Cement and Concrete Research*, 77, 1-8.

Gulbe, L., Vitina, I., and Setina, J. (2017). "The influence of cment on properties of lime mortars." *Procedia Engineering*, 172, 325-332.

Snellings, R., Chwast, J., Cizer, Ö., De Belie, N., Dhandapani, Y., Durdzinski, P., Elsen, J., Haufe, J., Hooton, D., Patapy, C., Santhanam, M., Scrivener, K., Snoeck, D., Steger, L., Tongbo, S., Vollpracht, A., Winnefeld, F., and Lothenbach, B. (2018). "RILEM TC-238 SCM recommendation on hydration stoppage by solvent exchange for the study of hydrate assemblages." *Materials and Structures*, 51(6), 172.

The 16th International Congress on the Chemistry of Cement 2023 (ICCC2023)
"Further Reduction of CO_2 -Emissions and Circularity in the Cement and Concrete Industry"
September 18–22, 2023, Bangkok, Thailand

Effect of alkanolamines in kaolinitic calcined clays pozzolanic reactivity

I. Koufany [1], I. Santacruz [1], M.D. Rodríguez-Ruiz [1], E.P. Bescher [2], M.A.G. Aranda [1] and A.G. De la Torre [1*]

[1] *Dpt. Química Inorgánica, Cristalografía y Mineralogía. Universidad de Málaga, Málaga, Spain.*

*Email: imane.k@uma.es; isantacruz@uma.es; mdrodriguez@uma.es; g_aranda@uma.es; mgd@uma.es**

[2] *CTS Cement Manufacturing Corp, 12442 Knott St, Garden Grove CA 92841, United States*

Email: ebescher@CTSCEMENT.com

ABSTRACT

Five kaolinitic clays with different amounts of kaolinite, ranging between ~70 wt% and ~30 wt%, have been studied to unravel the possible activation effect of alkanolamines on the aluminate fraction of calcined clays. This is of interest for enhancing the reactivity of LC^3 binders. These clays were calcinated at 860ºC for 4 h and ground to particle sizes of $D_{V,50}$ ~10 μm. Three alkanolamines were selected: triisopropanolamine (TIPA), triethanolamine (TEA) and methyldiethanolamine (MDEOA), added in two dosages, 0.025 and 0.050 wt% (by weight of calcined clay, *bwcc*). The role of alkanolamines as activators in calcined clays was assessed following the ASTM c1897 standard bases on R^3-tests. Concretely, first by measuring the heat evolved due to the pozzolanic reaction of the calcined clay and $Ca(OH)_2$ (i.e. R^3 mixture) by isothermal calorimetry at 40ºC during 7 days, and second, the bounded water by measuring the weight loss of R^3 mixture after heating them at 350ºC.This study concludes that there is no significant activation of the pozzolanic activity of kaolinitic calcined clays just by adding alkanolamines. However, a mild activation was observed, i.e., higher heat evolved up to 7 days, by adding 0.05 wt% *bwcc* of TIPA, TEA and MDEOA to a high kaolinite content disordered metakaolin with high specific surface area calcined clay.

KEYWORDS: *Alkanolamine activator, kaolinitic calcined clay, isothermal calorimetry.*

1. Introduction

The reduction of the clinker factor is the best current way to decrease the CO_2 footprint of cement industry. Calcined clays (containing more than 40 wt% of kaolinite) are being used in limestone calcined clays cements, LC^3, due to their inherent pozzolanic activity (Sharma et al., 2021). Moreover, due to the shortage of traditional supplementary cementitious materials (SCMs), calcined clays are promising alternatives (Yoon et al., 2022). These low clinker factor cements are considered as low CO_2 materials, with enhanced durability and long-term mechanical strengths. However, their main drawback is the poor early mechanical strengths, due to their slow hydration rate (Juenger et al., 2019). The use of chemical admixture to address this challenging is well spread, and recently, alkanolamines used as accelerators/activators of low CO_2 cements are attracting special attention (Dorn et al., 2022). Most of the studies agree that alkanolamines promotes the hydration of C_3A and C_4AF, also in LC^3 (Huang et al., 2021; Zunino and Scrivener, 2021). However, there is a gap in the knowledge of the effect of alkanolamine in the pozzolanic activity of the aluminate fraction of calcined clays. Here, the study of the effect on the pozzolanic activity of five different kaolinite content clays with three different alkanolamines, in two dosages is presented. The final goal was to determine the possible admixture activation of the kaolinitic calcined clays as a first step before moving to early-age low-carbon cement activation by the admixture usage.

2. Materials

Five Spanish raw clays (rc) were selected: rc1 (CVPM3B-2021, by Arcimusa, S.A., Zaragoza); rc2 (SY(A)-1-2021, by Comercial Silices y Caolines de Aragón S.L., Teruel); rc3 (F-35-2021, by Caolines de Vimianzo, S.A.U., A Coruña); rc4 (Kaolin-CN-2021, by Caobar S.A., Guadalajara); and rc5 (Kaolin-C-

2021, by Caobar S.A., Guadalajara). The five raw clays were dried at 105ºC for 2h in a furnace. The elemental compositions, determined by X-Ray Fluoresce (XRF), for all the raw clays are given in Table 1. The elemental composition of the calcined clays (see below) are also included in Table 1.

Table 1. Elemental compositions, determined by XRF, expressed as weight percentage of oxides (wt%) and loss on ignition (LOI) for the raw (rc#) and calcined at 800ºC(cc#) clays. Numbers in brackets: standard deviation.

	SiO_2	Al_2O_3	Fe_2O_3	CaO	MgO	SO_3	Na_2O	K_2O	TiO_2	P_2O_5	Other	LOI
rc1	50.3(4)	29.3(2)	6.8(2)	0.19(1)	0.27(3)	0.17(1)	-	0.28(2	1.89(2)	0.046(4)	0.16	10.5
cc1	*54.7(4)*	*33.5(2)*	*7.1(2)*	*0.54(4)*	*0.13(3)*	*0.20(1)*	-	*0.33(3*	*2.16(2)*	-	0.25	*1.1*
rc2	55.3(4)	29.3(2)	1.17(8)	0.23(1)	0.33(4)	0.23(1)	0.19(3	3.3(1)	0.49(1)	0.047(5)	0.5	9.3
cc2	*60.4(4)*	32.0(2)	1.34(8)	0.26(2)	0.35(4)	0.25(1)	0.18(3	3.6(2)	0.56(1)	0.044(5)	*0.04*	*1.0*
rc3	54.1(4)	30.2(2)	1.59(9)	0.022(2	0.33(4)	-	0.28(3	4.8(2)	0.20(1)	0.054(4)	0.69	16
cc3	58.9(4)	32.4(2)	1.79(9)	0.037(3	0.35(4)	0.020(4)	0.30(3	5.3(2)	0.231(4)	0.049(5)	*0.03*	*0.7*
rc4	72.6(3)	20.5(2)	0.23(2)	0.075(5	0.07(2)	-	-	1.1(1)	0.17(1)	0.029(4)	0.02	5.2
cc4	76.5(3)	20.5(2)	0.27(2)	0.104(8	0.080(2)	0.030(5)	-	1.4(1)	0.175(3)	0.019(5)	*0.00*	*1.0*
rc5	76.6(3)	14.8(2)	0.18(1)	0.061(4	0.08(2)	-	-	1.3(1)	0.14(1)	0.021(4)	*0.02*	*6.9*
cc5	81.4(3)	16.4(2)	0.21(2)	0.077(6	0.05(2)	0.013(5)	-	1.33(9	0.157(3)	0.019(5)	*0.01*	*0.3*

The dried clays were mixed with ~20.0 wt% α-Al_2O_3, as internal standard, to determine the full phase contents, including the amorphous and not quantified crystalline content, ACn, by analysing the powder patterns by the Rietveld method (De la Torre et al., 2001). The raw clays were activated in an industrial brick kiln at 860ºC for 4 hours and milled in a ball milling equipment up to particle sizes given in Table 2. Three alkanolamine from Sigma Aldrich were selected: triisopropanolamine (TIPA), triethanolamine (TEA) and methyldiethanolamine (MDEOA).

3. Methodologies: characterization techniques.

Table 2 gives the particle size distribution (PSD), BET specific surface area and density for the five calcined clays (cc), obtained as detailed elsewhere (Bernal et al., 2021). The PSD was computed using MIE-non-spherical methodology with a refractive index of 1.55 and an absorption index of 0.1 for cc1 and 0.01 for the remaining calcined clays.

Table 2. Textural properties and mass densities of the calcined clays.

	cc1	cc2	cc3	cc4	cc5
$D_{v,10}$ (µm)	0.87	2.79	2.14	2.47	2.69
$D_{v,50}$ (µm)	**8.4**	**11.8**	**11.8**	**12.0**	**12.3**
$D_{v,90}$ (µm)	41.4	58.9	51.6	47.0	47.8
BET (m^2/g)	27.3	10.0	7.6	4.0	3.2
ρ (g/cm^3)	2.71	2.63	2.63	2.63	2.61

Laboratory X-Ray Powder Diffraction (LXRPD) data of rc2 and rc3 with internal standard were collected on a D8 ADVANCE (Bruker AXS) and the mixtures with rc1, rc4 and rc5 on a X'PertPro (PANalytical) diffractometers. D8 ADVANCE and X'PertPro are equipped with Johansson monochromators to have strictly monochromatic, Mo-$K\alpha_1$ (λ=0.7093 Å) and Cu-$K\alpha_1$ (λ=1.54099 Å) radiations respectively. Rietveld quantitative phases analyses (RQPA) were performed using the GSAS suite of programs and the EXPGUI graphic interface. Thermogravimetric analysis (TGA) measurements for all the dried raw clays were performed in a SDT-Q600 analyser from TA instruments (New Castle, DE). The temperature was raised to 1000ºC at a heating rate of 10 ºC/min. The assessment of the role as activators of alkanolamines directly in calcined clays was performed following the ASTM c1897 (based on R^3-test). The R^3 mixture (calcined clay and alkaline solution) consisted on $Ca(OH)_2$/calcined clay=3.0, $CaCO_3$/calcined clay=0.50 and water/solid=1.20, as detailed in the standard. The alkanolamines were added in two dosages, 0.025 and 0.050 wt% *bwcc*. The R^3-mixtures were introduced in an eight channels Thermal Activity Monitor (TAM) isothermal calorimeter at 40ºC during 7 days using glass ampoules and water as reference. The heat evolved was normalized to the mass of calcined clay and reported from 75 minutes to 7 days. Moreover, the chemically bounded water (BW) was carried out by measuring the weight loss of the R^3 mixtures (30 g) at 7 days after thermal treatment from 40ºC to 350ºC in a furnace. The amount of bounded water is given by g/100g of calcined clay.

4. Results and discussion

4.1 Clays characterization.

The RQPA, including the ACn (amorphous and crystalline non-quantified) content, of the dried raw clays are given in Table 3. It is observed that all the clays contain kaolinite and quartz. Moreover, all, except rc1, contains microcline and muscovite. It is noted that the amorphous fraction may contains a fraction of kaolinite. Therefore, the reported values are minimum contents.

Table 3. RQPA, including the ACn, of the dried raw clays.

	Kaolinite	Muscovite	Fe_2O_3	Quartz	Anatase	Rutile	Microcline	Calcite	ACn
rc1	72.9	-	2.5	11.1	1.5	0.9	-	1.6	9.4
rc2	54.9	3.4	-	12.8	-	0.6	8.1	-	20.2
rc3	48.8	24.9	-	11.4	-	0.7	4.2	-	9.9
rc4	20.3	5.7	0.3	47.5	0.6	-	4.4	-	21.3
rc5	16.8	3.1	0.2	53.6	0.4	-	4.6	-	21.2

The content of kaolinite in the pristine clays have been assessed by four methodologies: i) RQPA including the ACn content, Table 3; ii) TGA of dried samples (Avet and Scrivener, 2018); iii) from the Al_2O_3 content by XRF, excluding the Al_2O_3 content within the other phases determined by RQPA; and iv) mineral intensity factor (MIF) (Schultz, 1964). The four values for each raw clay, and the final estimations are given in Table 4. The final contents are given as the average of the first three measurements. It seems that MIF approach consistently gives underestimated values.

Table 4. Kaolinite content (wt%) determined by different methodologies of the raw clays. Average of the four measurements and standard deviation are also included.

Kaolinite content (wt%)	rc1	rc2	rc3	rc4	rc5
TGA	76.3	55.3	50.8	44.7	36.1
RQPA	72.9	54.9	48.8	20.3	16.8
XRF	74.2	67.2	48.8	44.5	32.4
MIF	*61*	*53*	*27*	*24*	*17*
Final Kaolinite content	**74**	**59**	**49**	**37**	**29**

4.2 Effect of alkanolamine on pozzolanic activity of calcined clays.

Figures 1a and 1b show the heat evolved by all the R^3 mixtures up to 7 days.

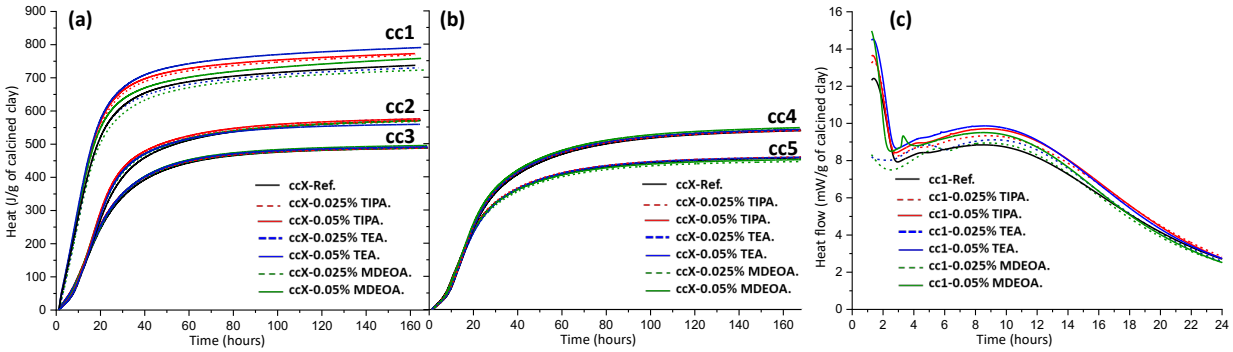

Figure 1. (a) and (b) Total heat curves for R^3 mixtures without and with alkanolamines up to 7 days. (c) Heat flow of cc1 without and with alkanolamines up to 24 hours.

As expected, cc1 evolves higher heat at any time, due to the highest content of kaolinite in the pristine clay, the lowest PSD and the highest BET surface area of the calcined clay. In addition, it has been recently published that this calcined clay presents a highly disorder metakaolin, with higher amounts of Al(V) (Bernal et al., 2022). The most relevant result here is that the additions of 0.025% and 0.05% *bwcc* of any alkanolamine have almost negligible effects on the heat evolved by all calcined clays, except for cc1 (Fig. 1a and 1b). For cc1, the addition of TIPA increased the total heat released at 7 days, from 737 J/g_{cc} to ~780 J/g_{cc}, for the two studied dosages. For TEA and MDEOA, the low dosage, 0.025 wt% *bwcc* decreased the total heat when compared to the reference cc1, while the addition of 0.05 wt% *bwcc* enhanced it. Figure 1c shows the heat flow up to 24 hours of cc1 without and with the selected alkanolamines. The first signal observed before ~3 h, is likely due to the dissolution of cc1 on the alkaline solution. On the one hand, it is observed that the addition of 0.025 wt% *bwcc* of TEA and MDEOA

slightly decreased these signals while TIPA enhanced it. On the other hand, these signals are more intense in R^3 mixtures with 0.05 wt% *bwcc* of the three alkanolamine, indicating an enhancement in the dissolution rate of the calcined clay components. The broad peak observed between 3 and 16 h is likely due to the reaction of cc1 components with the alkaline solution, to give C-A-S-H type products and possibly, calcium aluminate hydrates, AFm type (Avet et al., 2016). This signal is not significantly modified by the addition of alkanolamines. The bounded water obtained after 7 days for cc1-Ref, cc2-Ref, cc3-Ref, cc4-Ref and cc5-Ref are 12.1, 9.8, 9.4, 9.7 and 8.0 g/100 g dried R^3 mixture. The addition of the studied alkanolamines, in the employed dosages, has had a negligible impact on these values, showing that the formed hydrated products have not been modified nor in amount neither in type. For TIPA addition to cc1, the BW increased to 12.1 and 12.3 wt% for 0.025 and 0.05% dosages. We consider this variation within the variability of the measurements, and hence, an increase of BW could not be firmly established.

5. Conclusions

Alkanolamines, TIPA, TEA and MDEOA, do not enhance the pozzolanic activity of typical calcined clays. It has been observed a mild increase in the dissolution rate by the addition of 0.05 wt% *bwcc* of the three alkanolamines for the calcined clay with higher kaolinite content, highly disordered metakaolin, lower particle size and higher specific surface area. We speculate that this dosage of alkanolamine has enhanced the dissolution rate of the aluminate fraction of the metakaolin which is richer in Al(V). However, the nature and amount of the pozzolanic hydrated products is not modified since the bounded water remains constant with the addition of alkanolamines.

Acknowledgements

Research grant PID2020-114650RB-I00 (Spanish Ministry and ERDF) is gratefully acknowledged.

References

Avet, F., Scrivener, K.L. (2018). "Investigation of the calcined kaolinite content on the hydration of Limestone Calcined Clay Cement (LC^3)". Cem. Concr. Res. 107: 124–135.

Avet, F., Snellings, R., Alujas Diaz, A., Ben Haha, M., Scrivener, K.L. (2016) "Development of a new rapid, relevant and reliable (R3) test method to evaluate the pozzolanic reactivity of calcined kaolinitic clays" Cem. Concr. Res. 85: 1–11.

Bernal, I.M.R., Aranda, M.A.G., Santacruz, I., De la Torre, A.G., Cuesta, A. (2022) "Early-age reactivity of calcined kaolinitic clays in LC^3 cements: A multi technique study including pair distribution function analysis" J. Sustain. Cem. Mater. https://doi.org/10.1080/21650373.2022.2117248

Bernal, I.M.R., Shirani, S., Cuesta, A., Santacruz, I., Aranda, M.A.G. (2021) "Phase and microstructure evolutions in LC3 binders by multi-technique approach including synchrotron microtomography" Constr. Build. Mater. 300: 124054.

De la Torre, A.G., Bruque, S., Aranda, M.A.G. (2001) "Rietveld quantitative amorphous content analysis" J. Appl. Crystallogr. 34, 196–202.

Dorn, T., Blask, O., Stephan, D. (2022) "Acceleration of cement hydration – A review of the working mechanisms, effects on setting time, and compressive strength development of accelerating admixtures" Constr. Build. Mater. 323: 126554.

Huang, H., Li, X., Avet, F., Hanpongpun, W., Scrivener, K. (2021) "Strength-promoting mechanism of alkanolamines on limestone-calcined clay cement and the role of sulfate" Cem. Concr. Res. 147: 106527.

Juenger, M.C.G., Snellings, R., Bernal, S.A. (2019) "Supplementary cementitious materials: New sources, characterization, and performance insights" Cem. Concr. Res. 122: 257–273.

Sharma, M., Bishnoi, S., Martirena, F., Scrivener, K. (2021) "Limestone calcined clay cement and concrete: A state-of-the-art review" Cem. Concr. Res. 149: 106564.

Schultz, L.G. (1964) "Quantitative interpretation of mineralogical composition form X-ray and chemical data of the Pierre Shale". United States. Geological Survey, Professional Paper, 391-C, 31 pp.

Yoon, J., Jafari, K., Tokpatayeva, R., Peethamparan, S., Olek, J., Rajabipour, F. (2022) "Characterization and quantification of the pozzolanic reactivity of natural and non-conventional pozzolans" Cem. Concr. Compos. 133: 104708.

Zunino, F., Scrivener, K.L. (2021) "Assessing the effect of alkanolamine grinding aids in limestone calcined clay cements hydration" Constr. Build. Mater. 266: 121293.

The 16th International Congress on the Chemistry of Cement 2023 (ICCC2023)
"Further Reduction of CO_2 -Emissions and Circularity in the Cement and Concrete Industry"
September 18–22, 2023, Bangkok, Thailand

Influence of raw and mechanically activated shale on rheological properties of cement based binder

Thirumalini S[1] , Raghunathan Swaminathan[2], Shanmuga Priya T[1], Biju Karakkunnummal[2] Gayathri Chandran[1] and Aswathy Ajayan[1]

[1]School of Civil Engineering, Vellore Institute of Technology, Vellore, Tamil Nadu, India
thirumalini.selvaraj@vit.ac.in, shanmugapriya.t@vit.ac.in,
gayathri.chandran2022@vitstudent.ac.in, aswathyajayan.s2022@vitstudent.ac.in
[2]FLSmidth Private Limited, Chennai
RSW-IN@flsmidth.com, Biju.Karakkunnummal@flsmidth.com

ABSTRACT

The abundant availability of shale across the world and its pozzolanic and hydraulic properties make it a promising SCM. Two shales CRS and SRS were collected from two different locations to study about the rheological properties of the blended cement paste. Mini-slump test was performed for optimizing the amount of water and super plasticizer for different mixes. A polycarboxylic ether based super plasticizer was used as it can actively reduce the amount of water. The rheological properties of the blended cement paste with shale were investigated using Brookefield Rheometer at a constant shear rate of 5 to 150 s^{-1}. Cement was replaced with 30% raw and mechanically activated shale and the mechanical activation was carried out by grinding in a planetary ball mill of 200rpm. The cement paste with mechanically activated shale exhibited a lower yield stress than the raw shale which shows that less energy is required to make the material flow. Yield stress shows the amount of energy needed to de-flocculate the paste and make it flow. Mechanical activation has reduced the grain size of shale thus decreasing the energy for deflocculation hence reducing yield stress. Cement paste with mechanically activated shale showed better rheological behaviour compared to raw shale mixes.

KEYWORDS: *Shale, Mechanical Activation, Rheology, Yield Stress, Thixotropic behavior*

1. Introduction

Cement production is an energy intensive process as it emits carbon dioxide into the atmosphere. It accounts for 6 to 8% of anthropogenic CO_2 emissions because of its extensive production and consumption [1]. The de-carbonation of limestone during the clinkering process is responsible for about 60% of the CO_2 produced during the manufacturing of Portland cement. Supplementary cementitious materials are materials which exhibit pozzolanic and hydraulic properties and have capability to partially replace cement [2]. The use of SCMs in place of Portland cement has already become a widely researched area in recent years. Previously many studies have been carried out on the use of ground granulated blast furnace slag, fly ash, and metakaolin as SCMs [3-5]. Among these the most commonly used SCM across the world is fly ash. Studies have shown that the resources of above mentioned SCMs are becoming scarce and are located far from cement consumers[6]. This availability issues has led to the need to explore new and novel SCMs.

Clay shale is a less explored material which has physical and chemical properties that makes them a promising SCM[7]. Shale is the most common sedimentary rock, accounting for about 70% percent of the rock in the earth's crust. Based on how it settled inside its parent rock formations, each natural shale has a unique makeup. The Calcareous Shale comprises 20–35% CaCO3 (marls and shaly chalk, 35–65%), 70–85% amorphous silica, 25–35% Fe2O3, and 70–85% siliceous shale. India's clay shale resource availability is about 34.6 million tons from 2015 the total production of shale as follows; Himachal Pradesh contributing 46%, Karnataka 23%, Madhya Pradesh 14%, Maharashtra 11%, and the

remaining 6% percent contributed by Andhra Pradesh & Telangana. Many studies have shown that SCMs replacement upto 30% can improve microstructure and overall quality of cement based materials. Studies have shown that workability and rheological properties of cement paste can be positively impacted by the addition of cementitious materials [8-10]. Fineness of materials in cement paste can positively influence the rheological properties of cement paste by reducing the yield stress values [11]. When shear forces are applied and withdrawn, cement paste reacts in a thixotropic way; agglomerated cement particles will separate under stress, causing a reduction in viscosity, but rebuild over time once the stress is removed, leading to an increase in viscosity. The fresh state of concrete depends on this reversible feature, which has attracted a lot of attention in recent years[12].The main intention of carrying out this research as studies related to rheological behaviour of shale as SCM is very limited, how ever rheological behavioural study of shale gives idea on the viscoelastic flow behaviour of material as it is directly relaated to strength of material produced. In this study two shales, one calcium rich shale (CRS) and one silica rich shale (SRS) was collected from Kadapa region in Andhra Pradesh. CRS was collected from Dalmia cement plant in Kadapa and SRS was collected at a location far away from cement plant. The rheological properties of cement paste mixes with 30% shale will be studied. As mechanical activation proved to be an effective method in improving the efficiency of SCMs, a comparison of effect of raw and mechanically activated shale in rheology of cement paste will also be studied.

2. Materials and Methods

2.1 Materials

Ordinary Portland cement conforming to BIS specification IS:12269-1987 [13] was used. From the geological settlements of sedimentary rocks across India, two shales were identified. One CRS and SRS collected from Kadapa in Andhra Pradesh was used for the study. The chemical composition of materials used is specified in Table 1. Superplasticizer used for the study is Master Glenium SKY with relative density of 1.08 ± 0.02. Particle size, specific gravity and relative density of raw materials are shown in Table 2. As per ASTM C618 - 12a the selected shale samples has satisfied minimum 50 - 70% of primary oxides SiO_2+Fe_2O_3+ Al_2O_3.

Table 1. Chemical composition of raw materials

Materials	Major oxides (%)						
	SiO_2	Al_2O_3	Fe_2O_3	CaO	MgO	SO_3	Na_2O
Cement	15.67	5.21	1.25	64.21	0.78	2.67	0.23
Kadapa-Dalmiapuram Shale	47.31	11.43	6.81	14.35	1.80	0.37	0.57
Kadapa Shale	64.38	14.71	7.25	1.20	1.94	0.10	0.45

Table 2. Physical properties of raw materials

Materials	Type	Average Particle Size (µ)	Specific gravity (g/cc)	Relative Density
Cement	OPC	20.215	3.15	-
Kadapa Dalmiapuram	Raw	315.252	2.29	-
	Mechanically Activated	17.8	-	-
Kadapa	Raw	94.610	2.26	-
	Mechanically Activated	17.982	-	-
Master Glenium SKY 8233	-	-	-	1.08 ± 0.02

2.2 Methods

Raw shale and mechanically activated shale were used for making blended cement paste. Mechanical activation of CRS and SRS was carried out in a planetary ball mill of jar length 75mm and speed 200rpm with 30 zirconia balls of 10mm diameter for a time period of 120 minutes and 90 minutes respectively.
The flow behaviour of super plasticized cement paste with 30% shale has been studied using the mini-slump test created by Kantro [10]. A constant water cement ratio of 0.3 was used and super plasticizer dosage was optimized using mini slump test. The super plasticizer dosage was altered to get a flow of 12 to 13cm. AMTEK Brookfield rheometer (gap width =1 mm) coupled with Rheo 3000 software was used for the rheological experiments. For ensuring the homogeneity all the mixes were prepared without any lumps at a speed of 65 rpm for 2 minutes and placed in the rheometer plate within 60s. Shear rate was gradually increased first from 5 to 150 s^{-1} and then decreased to 5 s^{-1} in 120 load steps.

3. Results and Discussions

The flow curve was plotted using the shear stress and shear rate values obtained from the rheological studies. The values obtained were compared using Bingham model. Bingham model is the most commonly used and widely accepted model for studying the rheological behaviour of cement paste. The Bingham equation is

$$\tau - \tau_0 + \mu_p \dot{\gamma}$$

where τ, τ_0, μ_p and $\dot{\gamma}$ are considered as the shear stress, yield stress, plastic viscosity and shear rate respectively.

Fig 1 shows the shear stress vs shear rate graph of raw and mechanically activated CRS. The graph shows that when shear rate is increased the shear also increases this trend is observed due to the deflocculation of particles on the application of shear. From the graph the yield stress of mechanically activated shale is -3.92Pa and that of raw shale is -11.25Pa.As per Bingham model both raw and mechanically activated CRS showed a shear thickening behaviour with negative yield stress. Table 3 shows the flow parameters based on Bingham Model

The shear stress vs. shear rate graph of raw and mechanically activated SRS is shown in Fig.2. Since particles deflocculate when shear is applied, the graph demonstrates a trend whereby shear stress increases as shear rate increases. According to the graph, mechanically activated shale has a yield stress -17.56Pa and raw shale showed a yield stress of -38.21Pa. The negative yield stres shows that both raw and activated SRS shows a shear thickening behaviour.

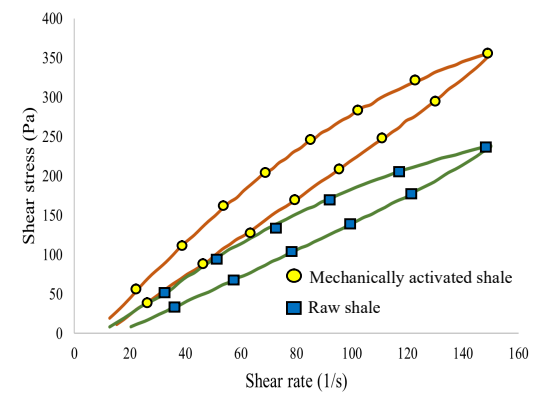

Fig. 1

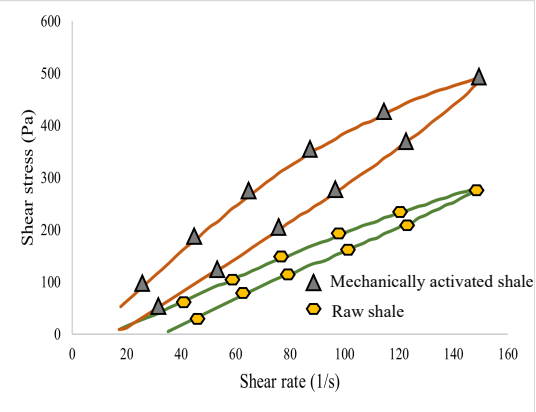

Fig. 2

Fig. 1 Shear stress vs shear rate graph of raw and mechanically activated CRS
Fig. 2 Shear stress vs shear rate graph of raw and mechanically activated SRS

Table 3 Flow parameters based on Bingham Model

Shale	Shale Type	Bingham Model	
		τ_0	μ_p
CRS	Raw	3.9287	2.474
	Mechanically Activated	11.253	1.696
SRS	Raw	38.212	2.136
	Mechanically Activated	17.561	3.453

CRS had a lesser yield stress when compared to SRS this can be due to better grinding effciency and lessser particle size. Silica rich shales have higher quartz content which makes it difficult to grind due to higher hardness of quartz mineral. Both the shales showed a thixotropic behaviour due to gradual break down of the agglomorates when shear stress applied and reduced gradually [8]. The results indicated that the mixes with mechanically activated shale samples exhibited a lower yield stress than the mixes with raw shale samples which shows that less energy is required to make the material flow.

4. Conclusions

Based on the experimental study the following conclusions were drawn

- Yield stress of mechanically activated CRS was less than that of raw due to lesser particle size and more workability.
- Yield stress of mechanically activated SRS was found to be less than that of raw due to the fineness of the activated shale.
- The rheological property of both mechanically activated shales was better than that of raw shales due to the structural break down and reduction in size.
- The results indicated that the mixes with mechanically activated shale exhibited a lower yield stress than the mixes with raw shale which shows that less energy is required to make the material flow.

References

1. M. Á. Sanjuán, C. Andrade, P. Mora, and A. Zaragoza, "Carbon Dioxide Uptake by Mortars and Concretes Made with Portuguese Cements," *Appl. Sci.*, vol. 10, no. 2, p. 646, 2020.
2. Lothenbach, B., Scrivener, K. and Hooton, R.D., 2011. Supplementary cementitious materials. *Cement and concrete research*, *41*(12), pp.1244-1256.
3. Shaji, N. and Tyrer, M., 2022. Review of fly-ash as a supplementary cementitious material.
4. Oner, A.D.N.A.N. and Akyuz, S., 2007. An experimental study on optimum usage of GGBS for the compressive strength of concrete. Cement and concrete composites, 29(6), pp.505-514.
5. Bakera, A.T. and Alexander, M.G., 2019. Use of metakaolin as supplementary cementitious material in concrete, with focus on durability properties. *RILEM Technical Letters*, *4*, pp.89-102.
6. K. Scrivener and A. Favier, "Calcined Clays for Sustainable Concrete," *RILEM Bookseries*, 2015:531–537.
7. Seraj, S., Cano, R., Ferron, R.P. and Juenger, M.C., 2015. Calcined shale as low cost supplementary cementitious material. In *Calcined Clays for Sustainable Concrete: Proceedings of the 1st International Conference on Calcined Clays for Sustainable Concrete* (pp. 531-537). Springer Netherlands.
8. Park, C.K., Noh, M.H. and Park, T.H., 2005. Rheological properties of cementitious materials containing mineral admixtures. *Cement and concrete research*, 35(5), pp.842-849.
9. A. Neaman, A. Singer, Rheological properties of aqueous suspensions of palygorskite, Soil Sci. Soc. Am. J. 64 (1) (2000) 427–436.
10. A. Gadkar, K.V. Subramaniam, An evaluation of yield and Maxwell fluid behaviors of fly ash suspensions in alkali-silicate solutions, Mater. Struct. 52 (6) (2019) 117.
11. Bentz,D.P., Ferraris, C.F., Galler, M.A., Hansen, A.S. and Guynn, J.M., 2012. Influence of particle size distributions on yield stress and viscosity of cement–fly ash pastes. *Cement and Concrete Research*, 42(2), pp.404-409.
12. R. Ferron, A. Gregori, Z. Sun, S.P. Shah, Rheological method to evaluate the thixotropy of cement pastes for SCC, ACI Materials Journal 104 (2) (2007) 242–250.
13. IS:12269-1987 Indian standard code ordinary portland cement, 53 grade — specification.

The 16th International Congress on the Chemistry of Cement 2023 (ICCC2023)
"Further Reduction of CO_2 -Emissions and Circularity in the Cement and Concrete Industry"
September 18–22, 2023, Bangkok, Thailand

Changes in Rheology and Tensile Properties of UHPC with Silica Fume Content

Zemei Wu [1, 2], Kamal H. Khayat [2]*, Caijun Shi [1]

[1] College of Civil Engineering, Hunan University, Changsha 410082, PR China, Email: wuzemei@hnu.edu.cn; cshi@hnu.edu.cn

[2] Department of Civil, Architectural and Environmental Engineering, Missouri University of Science and Technology, Rolla, Missouri, USA, Email: kkhayat@mst.edu

ABSTRACT
High silica fume content used in UHPC can increase viscosity and render agglomeration issue, leading to entrapped air bubbles and reduced mechamical properties related with fiber cluster issues. This study investigates the influecne of silica fume content, ranging from 0 to 25%, by mass of cementitious materials, on rheological and tensile properties of non-fibrous UHPC matrix and UHPC made with 2% micro-steel fibers. Mixtures containing cement and silica fume with targeted mini-slump flow of 280 ± 10 mm were prepared. Test results showed that the highest tensile properties was found on UHPC with 10% to 15% silica fume. The tensile strengths were increased by 65% - 85% in comparirion to the reference mixture without any silica fume. This was consistent with lower viscosity and more uniform fiber dispersion and orientation. The findings from the research highlight the importance of rheology associated with raw materials to modulate tensile properties of UHPC.

KEYWORDS: *Rheology, silica fume, tensile properties, UHPC*

1. Introduction

Properly designed ultra-high performance concrete (UHPC) can deliver high flowability with self-consolidation, high strength and toughness, superior durability, and self-healing ability (De Larrard and Sedran 1994). Silica fume is a critical component in producing UHPC, which plays a significant role in affecting its overall performance due to its high amorphous SiO_2 content and fine and spherical particle size. Previous investigations indicated that the typical silica fume content used in UHPC mixture is approximately 20% to 30%, by mass of cementitious materials (Russell and Graybeal 2013). Such substitution can result in low $Ca(OH)_2$ content and porosity, improved fiber-matrix bond, and enhanced compressive and flexural strengths of UHPC (Wu et al. 2016; Chan and Chu 2014). Lower silica fume content, ranging from 5% to 15%, can be also found in some published articles, given the material characteristics and mixture proportion (Arora et al. 2018).

Depending on silica fume content and other mixture design characteristics, silica fume produces a double-edged sword effect on the performance and cost-effectiveness of UHPC. Low silica fume content can reduce plastic viscosity with limited improvement in microstructure and performance of UHPC. High substitution content can ensure sufficient pozzolanic reaction and pore refinement, but can increase viscosity. It was observed that UHPC mixture prepared with high amount of cement and silica fume is very viscous (Wu et al. 2016). This can lead to the entrapment of air voids during mixing and casting and the risk of having non-uniform fiber dispersion, and eventually reduced mechanical properties (Wu et al. 2016; Arora et al. 2018; Meng and Khayat 2017). Therefore, developing UHPC with optimal silica fume

content and appropriate rheology can lead to denser microstructure and uniform fiber dispersion to benefit mechanical properties.
The main objective of this research is to evaluate the influence of silica fume content, varying from 0 - 25%, by mass of cementitious materials, on rheological and tensile properties of non-fibrous UHPC matrix and UHPC made with 2% micro-steel fibers. The slump flows of the tested mixtures were fixed at 280 ± 10 mm to ensure self-consolidation. The findings from the research highlight the importance of rheology associated with silica fume content to modulate tensile properties of UHPC.

2. Materials and mixture design

2.1 Raw Materials

The binder materials used in this study included ASTM C150 Type III Portland cement and silica fume (SF). The mean diameter and Brunauer-Emmet-Teller surface area of silica fume are about 0.15 μm and 18,200 m^2/kg, respectively. Well-graded river sand with size range of 0 - 4.75 mm and masonry sand with size in the range of 0 - 2 mm with specific gravities of 2.64 were used. Straight brass-coated steel fibers with a diameter of 0.2 mm and a length of 13 mm were used. They show tensile strength and elasticity modulus of 1.9 and 203 GPa, respectively. A polycarboxylate-based high-range water reducer (HRWR) with a solid mass content of 23% was incorporated.

2.2 Mixture proportion

Non-fibrous UHPC matrix and UHPC with 2% steel fibers were employed in this study. The mixtures had a fixed water-to-binder ratio (w/b) of 0.18 and a sand-to-binder ratio of 1.0. Five silica fume contents, varying from 0 to 25%, were employed. The HRWR dosage was adjusted to obtain a mini-slump flow of 280 ± 10 mm as measured with the mini-cone test without any jolting. The six UHPC mixtures incorporating 0, 5%, 10%, 15%, 20%, and 25% silica fume were designated as SF0-2, SF5-2, SF10-2, SF15-2, SF20-2, and SF25-2, respectively.

2.3 Specimen preparation

All mixtures were prepared using a Hobart mixer at room temperature. UHPC dog-bone specimens made with 2% steel fibers were cast from one end of the mold. The mixture was naturally flowed to the other end of the mold to ensure natural-oriented fibers without any intervention. All the specimens were cast and demolded and then cured in lime-saturated water at room temperature of 20 ± 2 °C and 95% relative humidity until testing age of 28 d.

3. Testing methods

3.1 Rheological Properties

A ConTech 5 coaxial cylinders rheometer was employed to determine yield stress and viscosity of the UHPC matrix and UHPC. Typically, the measurements began at 10 min after water addition with samples subjected to pre-shear at a rotational velocity of 0.50 rps for 35 s followed by seven steps of decreasing rotational velocities at a step duration of 5 s. The yield stress and linear term (viscosity) were determined through applying the modified Bingham model given the fact that the majority of the flow curves were non-linear.

3.2 Tensile behavior

Direct tensile testing was conducted using big dog-bone specimens measuring 25 mm in thickness and 526 mm in length with a narrow neck width and length of 50 and 175 mm, respectively. Load frame with a capacity of 250 kN was used to conduct the tensile tests at a displacement rate of 0.5 mm/min. Each end of the specimen was held by a fixture gripped on the load frame using a ball hinge connection. Extension

of the specimen was obtained from two linear variable differential transducer (LVDTs) attached to the frame over a gage length of 160 mm. Three specimens were averaged for each mixture.

4. Results and discussion

4.1 Rheological properties

Fig. 1 shows the yield stress and viscosity (linear term of the modified Bingham model) of the investigated mixtures. The yield stress, minimum stress to initiate the flow of the UHPC matrix, was ranged between 34 and 41 Pa at a fixed mini-slump flow of 280 ± 10 mm. The incorporation of 10% - 15% silica fume reduced the lower viscosity. Besides, the incorporation of steel fibers further increased the yield stress and viscosity to 70 - 80 Pa and 48 - 85 Pa.s, respectively. This is because the increased resistance to flow associated with interlocking effect between steel fibers and surrounding particles, thus increasing the viscosity of UHPC (Khayat and Roussel 2000).

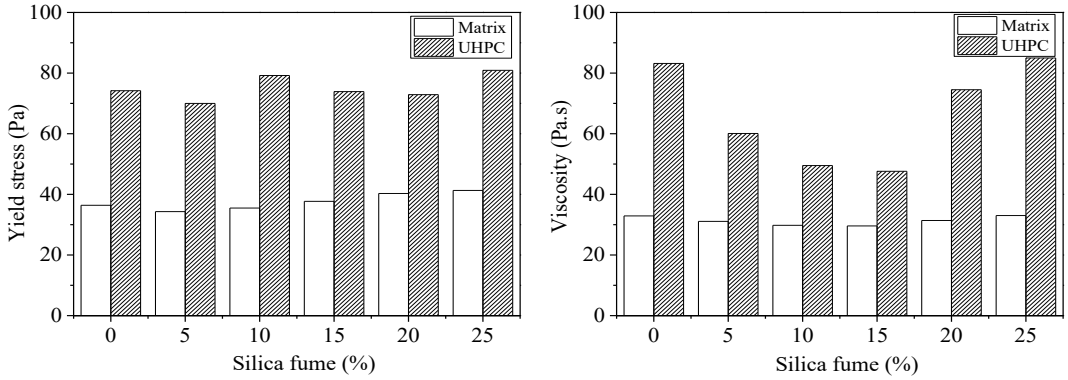

Figure 1. Change in rheological properties of UHPC matrix and UHPC with silica fume content: (a) yield stress; (b) viscosity.

4.2 Tensile behavior

Figure 2(a) illustrates the tensile load-extension relationships of UHPC mixtures made with different silica fume contents, and Figure 2(b) shows the calculated tensile strengths. The tested mixtures exhibited linear tensile load-extension behavior up to the peak load at a small extension of 0.01 mm, followed by gradually decreasing branch. With the increase of silica fume content up to 10%, the tensile strength increased before exhibiting some drop. The use of 10% - 15% silica fume enhanced the tensile strengths of the UHPC matrix and UHPC by 100% - 150% and 65% - 85%, respectively, compared to the reference mixtures. The tensile strength of the UHPC made with 25% silica fume was slightly greater (approximate 1 MPa) than that without any silica fume. This agrees well with the previous rheological results.

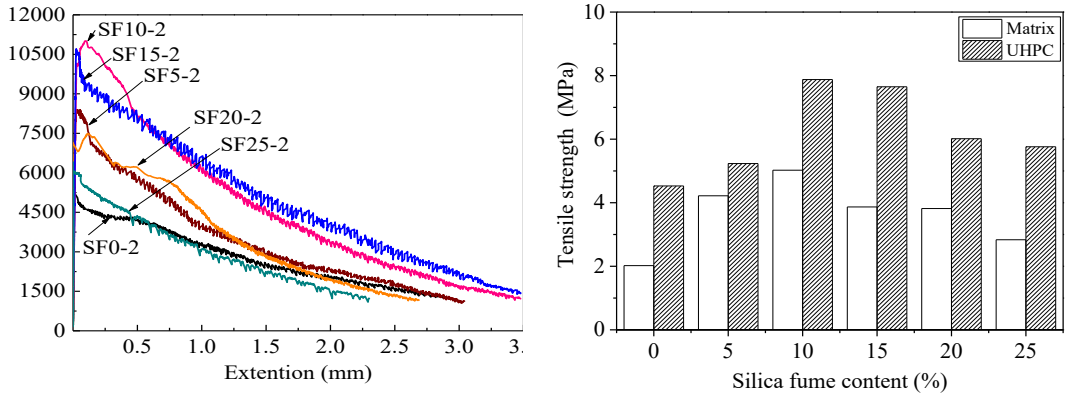

Figure 2. Tensile properties of UHPC: (a) load-extension relationships; (b) tensile strength.

5. Conclusions

The following conclusions can be drawn based on the results from this research:
(1) The HRWR demands for the non-fibrous matrix and UHPC at a fixed mini-slump flow decreased initially with the increase of silica fume content and then increased with further addition of silica fume. The HRWR demands were 2% to 3% and 4% to 8% for the matrix and UHPC, respectively. The incorporation of 10% - 15% silica fume resulted in lower viscosity in comparison with other mixtures.
(2) The optimal silica fume content for tensile properties of UHPC was found to be 10%-15%. Compared to the reference mixture, the tensile strengths of the optimized UHPC mixtures were enhanced by 65% - 85%. This is attributed to uniform fiber dispersion and orientation as confirmed by visual observation of the tensile cracking path during eperiment.

Acknowledgements

The authors gratefully acknowledge the financial support from the Ministry of Science and Technology of the People's Republic of China (No. 2022YFB3708700), the RE-CAST University Transportation Center (Tier - 1 UTC) at Missouri S&T under grant No. DTRT13-G-UTC45, and the National Science Foundation of China (Nos. 52008164).

References

Arora, A., Aguayo, M., Hansen, H., Castro, C., Federspiel, E., Mobasher, B., Neithalath, N. (2018). Microstructural packing-and rheology-based binder selection and characterization for Ultra-high Performance Concrete (UHPC). Cement and Concrete Research,103, 179 - 190.

Chan, Y. W., Chu, S. H. (2004). Effect of silica fume on steel fiber bond characteristics in reactive powder concrete. Cement and concrete research, 34(7), 1167 - 1172.

De Larrard, F., Sedran, T. (1994). Optimization of ultra-high-performance concrete by the use of a packing model. Cement and concrete research, 24(6), 997 - 1009.

Khayat, K. H., Roussel, Y. (2000). Testing and performance of fiber-reinforced, self-consolidating concrete. Materials and Structures, 33, 391 - 397.

Meng, W., Khayat, K. H. (2017). Improving flexural performance of ultra-high-performance concrete by rheology control of suspending mortar. Composites Part B: Engineering, 117, 26 - 34.

Russell, H. G., Graybeal, B. A., Russell, H. G. (2013). Ultra-high performance concrete: A state-of-the-art report for the bridge community (No. FHWA-HRT-13-060). United States. Federal Highway Administration. Office of Infrastructure Research and Development.

Wu, Z., Shi, C., Khayat, K. H. (2016). Influence of silica fume content on microstructure development and bond to steel fiber in ultra-high strength cement-based materials (UHSC). Cement and Concrete Composites, 71, 97-109.

The 16th International Congress on the Chemistry of Cement 2023 (ICCC2023)
"Further Reduction of CO_2 -Emissions and Circularity in the Cement and Concrete Industry"
September 18–22, 2023, Bangkok, Thailand

Understanding the Effect of Slag Particle Size, Shape, and Morphology on the Flow Characteristics of Portland Cement - Blast Furnace Slag Blends

A. Sjoberg[1]*, G. M. Cann[3]*, D. A. Geddes[1,2], J. L. Provis[2], B. Walkley[1]

[1] *Department of Chemical and Biological Engineering, University of Sheffield, United Kingdom*
Emails: amsjoberg1@sheffield.ac.uk, d.geddes@sheffield.ac.uk, b.walkley@sheffield.ac.uk
[2] *Department of Materials Science and Engineering, University of Sheffield, United Kingdom*
Email: j.provis@sheffield.ac.uk
[3] *National Nuclear Laboratory, Workington, United Kingdom*
Email: gavin.cann@uknnl.com

ABSTRACT

Where cementitious grouts are used to encapsulate intermediate level waste, supplementary cementitious materials (SCMs) such as ground granulated blast furnace slag (GGBS) are introduced in high quantities to Portland cement (PC). This blend can be used to produce high fluidity, low bleed grouts, with a suitable low heat evolution during the curing process. These formulations also have the benefit of enhancing longer-term physical properties such as strength, durability and reduced permeability, while GGBS as a by-product of iron production, provides the added benefit of reducing the grout embodied carbon.

Although GGBS is used widely on waste encapsulation plants, not all sources of civil construction industry grade GGBS produce grouts with the properties required for use in encapsulation grouts. The addition of superplasticiser admixtures may allow the use of otherwise unsuitable GGBS supplies in encapsulation grouts and may also improve the grout performance. However, there is little understanding of what physicochemical parameters of GGBS are critical to reliable performance in blended grouts when used in conjunction with superplasticisers.

The work reported here is an initial assessment of commercial GGBS sources produced via a variety of grinding techniques to provide baseline information on the GGBS properties which affect grout performance in non-superplasticised grouts. Different grinding technologies produce GGBS powders with different particle morphologies and thus, it is important to understand how morphology affects the fluidity and workability of a blended grout. An initial assessment of particle size, shape, and morphology of four GGBS is correlated with slump data. The overall aim of this research is to determine the resultant effect on grout flow characteristics and workability in order to establish a relationship between the physical characteristics of the grout and its performance as an encapsulant. This insight helps to reveal fundamental processes controlling dispersion, fluidity and workability of PC-GGBS grouts, providing better understanding of key parameters for robust specification which lays the foundations for further novel research surrounding the interactions between civil-grade GGBS and superplasticisers.

KEYWORDS: *Blended Portland Cement, Ground Granulated Blast Furnace Slag, Wasteforms, Flow Characteristics*

1. Introduction

Cementitious materials are used within the nuclear industry in the UK to encapsulate and immobilise intermediate level waste (ILW). The purpose of this is to produce a passive wasteform that is safe to handle, store and transport during the interim before the waste package (wasteform and container) is disposed of permanently in a geological disposal facility (GDF).

The encapsulation grout must satisfy certain properties and characteristics to ensure effective immobilisation; this paper will focus on the following:

- High fluidity to ensure the highest level of waste infiltration considering complex waste geometry.
- Low water-solids (w/s) ratio to ensure relatively low permeability in cured grout. This reduces the risk of shrinkage cracking of the grout. Low w/s also potentially minimises waste corrosion, gas generation

due to waste/grout interactions or radiolysis of water, and the chances of bleed during the formation of the wasteform.

- Relatively low heat evolution during hydration reaction (occurs between water and cement during curing process) to avoid high temperatures after grout pour. This also aids with minimising the likelihood of shrinkage cracking.
- Predictable characteristics to ensure consistent and reproducible performance, and minimise leaching of radionuclides.

To facilitate the above desired characteristics of the encapsulation grout, supplementary cementitious materials (SCMs), in this case ground granulated blast furnace slag (GGBS), are added to the Portland cement (PC). To minimise grout performance variability and enhance properties, strict parameters have traditionally been applied to all components of the grout, and therefore the nuclear industry has used bespoke powders meeting more stringent standards than those applied in civil construction (Angus et al., 2011). For example, variation of physical characteristics, such as shape and size, of the PC and GGBS particles on a microscale can drastically change characteristics such as fluidity, early strength and setting time (Reformat and Ludwig, 2014).

The cement industry is under increasing pressures to reduce greenhouse gas emissions associate with PC manufacture. (Angus et al., 2010). The resultant changes to the manufacturing process may alter the properties of the PC meaning that the powder may not meet the specifications required for encapsulation of nuclear materials. Similar considerations are true for GGBS. To address the challenge of security of supply, civil construction grade powders that meet British and European (BS EN) Standards are being considered.

This research aims to understand the physical properties of civil-grade GGBS and the effect on the workability of the blended grout. Specifically, this conference paper will focus on the effect of GGBS particle size, shape, and morphology on the flow characteristics of blended PC grouts for use as radioactive waste encapsulants. The outcomes of this preliminary research will provide the baseline data before further research to see if grout performance can be improved by the use of cement additives such as superplasticisers.

2. Mix Design

The performance of four different commercial sources of GGBS powder which were ground using varying grinding mechanisms were assessed (Table 1). These were blended with CEM I (also used as the Sellafield Ltd. standard), taken from a single source for all formulations. All formulations were prepared with a 50:50 (w/w %) GGBS/CEM I powder blend at 0.5 w/s. To respect supplier confidentiality, all sources of GGBS and CEM I have been anonymised.

Table 1: GGBS Grinding Mechanisms

GGBS Sample	Grinding Technology	Granulate Source
GGBS 1	High Pressure Grinding Roll (HPGR)	Blastfurnace on site
GGBS 2	Vertical Roller Mill (VRM)	Blastfurnace on site
GGBS 3	Ball Mill	Blastfurnace on site
GGBS 4	VRM or Ball Mill	Imported – multiple sources

2.1 Sample Preparation

Grouts were prepared in a room temperature laboratory. Grouts were mixed at 500 rpm for 10 minutes. Scanning Electron Microscope (SEM) stubs were prepared in sterile microchemistry laboratories and gold coated.

2.2 Method

Scanning electron microscopy (SEM) was undertaken using a Jeol JSM-6010LA. All images were taken at 15 kV accelerating voltage. Grout fluidity was measured using a standard mini-slump cone (top diameter: 19 mm, bottom diameter: 38 mm and height: 57 mm) procedure (for 3 repeats) where grout spread measurements were taken immediately after initial mixing at t_0. Particle size distribution (PSD) analysis was carried out using a Malvern Panalytical Mastersizer 3000 laser diffraction instrument.

3. Results and Discussion

Table 2: Mini Slump Data – Mean Diameter of Slumped Grout (D) in order of decreasing slump (Left to Right)

GGBS	GGBS 3	GGBS 4	GGBS 1	GGBS 2
Mean Slump (mm)	85.30	84.56	80.26	68.02

The mean slump data (Table 2) shows that GGBS 3, which was ground using a ball mill, had the largest slump and that GGBS 2, which was ground using a vertical roller mill, has the smaller slump.

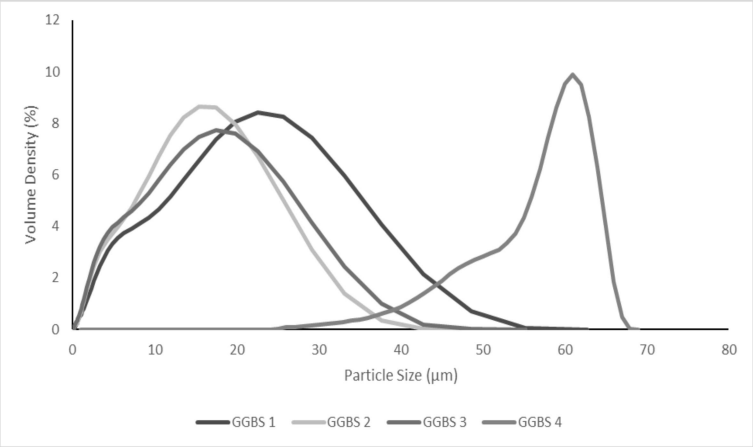

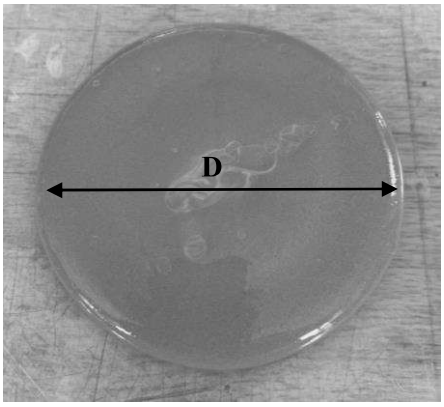

Left: Figure 1: A graph to show the PSD data for all GGBS samples. Right: Fig 2: Mini-Slump Test

It would be expected that the samples with a larger proportion of the smallest particles would have the smallest slump due to the larger surface area to volume ratio increasing water demand. When comparing the PSD data in Figure 1 to the mini-slump data, it can be seen that GGBS 1, 2 and 4 followed a trend of higher slump diameter for coarser PSDs, however GGBS 3 which gave the highest slump did not follow this trend suggesting there are other physiochemical properties influencing the flow characteritics.

GGBS 4 has PSD data of particular interest. The majority of the bulk of particles within GGBS 4 sample have a size of around double that of other samples, as shown by the strong peak at 61µm. Although this GGBS has the widest range of particle sizes, the majority of the particles are sized between 30 and 70 µm.

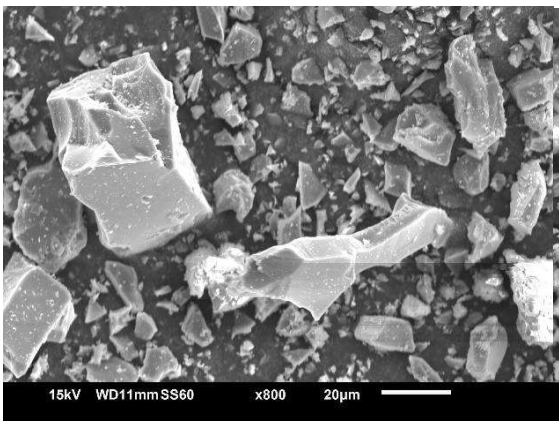

Figure 3: GGBS 1 (HPGR)

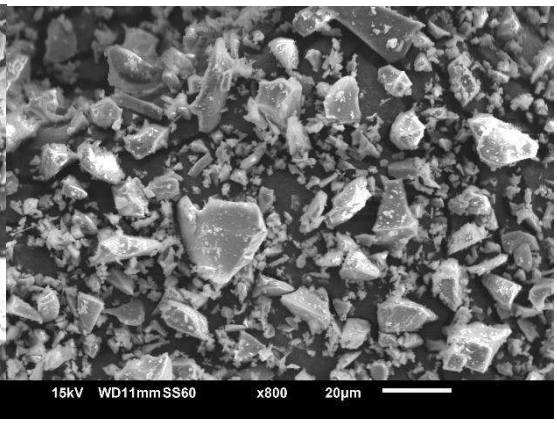

Figure 4: GGBS 2 (VRM)

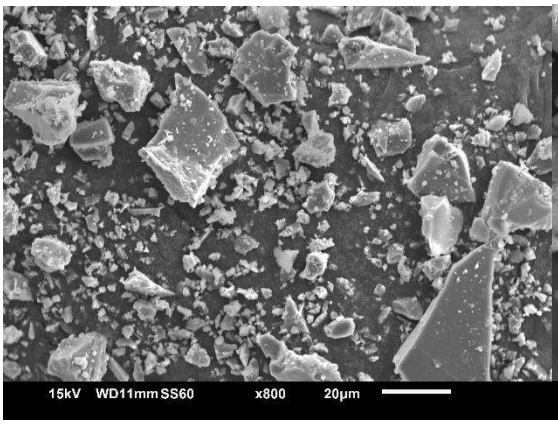

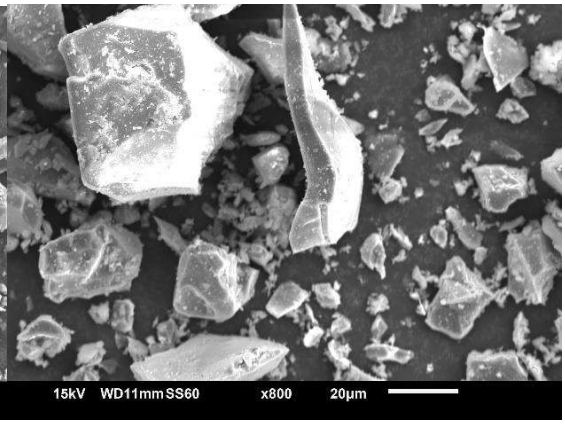

Figure 5: GGBS 3 (Ball Mill) Figure 6: GGBS 4 (VRM or Ball Mill)

The SEM output (Figure 3 to Figure 6) shows a variety of different particle morphology; all images show the samples at ×800 magnificaiton.

The particles in GGBS 1 are generally longer and thinner, whereas GGBS 2 exhibits smaller and more consistently sized particles. GGBS 3 has generally smaller and flatter particles with a few larger particles present. GGBS 4, however, exhibits lots of large particles, visibily much larger than all other samples. This qualititive analysis can be coherantly compared to the PSD data.

All samples are ground using different techniques and each sample's particle morphology varies considerably. This suggests that the grinding mechanism does influence the particle morphology.

5. Conclusions

- The grinding mechanism used to grind slag to GGBS influences the particle size and morphology.
- The particle size and morphology, influenced by the grinding mechanism, affects the flow characteristics of a grout.
- There are other physiochemical properties influencing the flow characteristics of a grout which cannot be identified from the scope of this paper.

6. Future Work

Chemical properties which could work in conjunction with physical properties to influence the flow characteristics of a blended PC grout will be investigated. Methods such as zeta potential analysis will be undertaken to investigate electrostatic interactions. Further analysis surrounding physical properties such as particle shape and surface area will be conducted to understand the trends identified in this paper. These findings can then be used to understand GGBS interactions with cement additives such as superplasticisers in blended grouts.

7. Acknowledgments

This research is funded by the Nuclear Decommissioning Authority (NDA) through an NDA PhD Bursary, and is jointly supervised by the Department of Chemical and Biological Engineering, The University of Sheffield, and the National Nuclear Laboratory. We are grateful to the Grantham Centre for Sustainable Futures for additional training and funding.

References

M. Angus, J. Borwick, G. Cann, M. Hayes, B. McLuckie and J. Jowsey, (2011) "The Specification of Cement Powders for Waste Encapsulation Processes at Sellafield Site," in Proceedings of Nuwcem 2011 Conference, Avignon, France, 2011.

Reformat, M. Ludwig H M (2014) "Influence of Different Grinding Devices on the Reactivity of Ground Granulated Blast Furnace Slag" published in the *Chemical & Engineering: Comminution and Classification Volume 37, Issue 5*. Weinheim, Germany. Pages 891-894.

Angus, M J. Godfrey, I H. Hayes, M. Foster, S. (2010). "Making Change in the Supply of Cement Powders for Radioactive Waste Encapsulation – Twenty Years of Operational Experience" in Proceedings of WM2010 Conference 2010, Phoenix, AZ.

The 16th International Congress on the Chemistry of Cement 2023 (ICCC2023)
"Further Reduction of CO_2 -Emissions and Circularity in the Cement and Concrete Industry"
September 18–22, 2023, Bangkok, Thailand

Sacrificial agents for clayey aggregates. An understanding of mortar and concrete scale

A.C. Gómez[1*], W.A. Echeverri[2], C.A. Orozco[3], C.P. Rodriguez[4]

[1] *Cementos Argos, Medellin, Colombia*
agomezgo@argos.com.co
[2] *Cementos Argos, Medellin, Colombia*
wecheverri@argos.com.co
[3] *Cementos Argos, Medellin, Colombia*
corozco@argos.com.co

[4]*Cementos Argos, Medellín, Colombia*
crodriguro@argos.com.co

ABSTRACT

Nowadays, clay on aggregates is one of many challenges facing the concrete industry due to the high affinity between the polycarboxylate superplasticizer (SP) technology that affects the concrete performance in the fresh and hardened state. The use of aggregates contaminated with clay is limited, so from a sustainability perspective, finding a solution that promotes its use and reaches the desired performance is a need. One of the solutions available to mitigate water demand and admixture dosage for cement dispersion is using sacrificial agents. Two types of commercial sacrificial agents were tested at mortar and concrete, identifying the potential adjustments for two types of clayey fractions in sands available for ready-mix production. First, XRD and TG for the sand (NS1) suggest kaolinite and illite clay presence (T-O type) on the fine sand fraction. At the same time, the second sand (NS2) was identified as smectite-type clay (T-O-T type).

For the equivalent mortar test following the ASTM C 1810 water reduction, and superplasticizer dosage optimization were tested at different dosages for clay mitigators, measuring the impact on workability, and mix aspect. One main finding of this study suggests that sacrificial agents could be as specific as the type of clayey fraction on the sand and could be limited based on sand availability. On the other hand, the amount of sacrificial agent required to keep water demand under control and SP dosage just for cement dispersion is higher (0.3 %-0.7 % w/w of sand proportion) despite the low amount of clayey fraction, which could impact around 30 % of the concrete cost and just a cement reduction about 6% of total cement content.

KEYWORDS: Polycarboxylate Superplasticizer, clay, aggregates, cement-based materials, sacrificial agent

1. Introduction

The use of superplasticizer admixtures in the production of concrete has enabled the development of products with high workability, as well as concretes with low water-cement ratio (a/c), self-compacting properties, and high-performance concretes with excellent durability performance (Ramachandran, 2002). Polycarboxylate technology changed the way of thinking about concrete production and defining new design strategies and new properties for concrete mixes. However, some authors such as Ng et al. (2012), Norwell et al. (2007), Muñoz et al. (2010), Ma et al. (2020), and Jardine et al. (2003) have noted that this type of technology responds poorly in the presence of clayey fractions in the binder or in the aggregate as impurities, which is associated with a high-water demand and a reduction in compressive strength, poor workability, and an increase in admixture dosage.

Based on these findings, tests were conducted on mortar and concrete to determine the advantages and disadvantages of two commercial sacrificial agents to identify the benefits-oriented to maintain concrete performance while using less cement content to lower CO_2 emissions.

2. Materials and methods

The cement type used in mortar and concrete reaches 45 MPa at 28 days. Two sources of sand samples were chosen for this study where one is an alluvial source (NS1), and the second sample is natural sand (NS2) from igneous rock. A second sample for the NS1 mine, CF-NS1 was examined to get a rejected material rich in clayey fractions that support the clay identification.

The XRF oxide components were evaluated using Axios Panalytical and the XRD patterns were assessed using Panalytical X'Pert PRO. The grading curves using the ASTM C 33 protocol. The specific gravity and absorption percentages were calculated using ASTM C 128. Two methods for methylene blue values: ASTM C 1777 for sand passing sieve # 4 and INV- 235-07 for the fine fraction, passing sieve 75 microns. Two commercial sacrificial agents M1 and M2 defined as Polyamine-based material were tested at different dosages in a mortar (ASTM C 1810) and concrete slump loss and compressive strength at 3 days, 7 days, and 28 days.

3. Results and discussion

The chemical composition of the cement, NS1 (Natural Sand 1), CF-NS1, and NS2 (Natural Sand 2) are in Table 1. The LOI for cement corresponds to a material with minimal limestone substitution and the addition of a reactive pozzolan to ensure early strength development.

Table 1. XRF data for cement, NS1, CF-NS1, NS2

	SiO_2	Al_2O_3	Fe_2O_3	MgO	CaO	Na_2O	K_2O	SO_3	LOI	XRD Identification**
Cement	22.77	5.04	3.3	2.39	59.05	0.01	0.39	2.76	4.08	N.M
NS1	69.1	13.5	4.1	2.7	4.3	2.3	0.84	0.1	2.3	Q ++, A ++, Cl-
CF-NS1	49.1	16.9	8.4	4.8	5.5	2.3	1.4	0.4	9.3	Q +, A +, (K, I; N) +
NS2	51.06	14.55	9.99	5.51	6.89	3.89	0.69	0.06	4.94	V ++, Cl-, ++, I,+Q+, An+

** Cl: chlorite, I: illite, K: kaolinite, N: nacrite, H: hornblende, Q: quartz, A: albite. Cl: chlorite, V: Vermiculite, An: Anorthite. N.M not measured

Figure 1a depicts two images of NS1(left) and NS2 (right); large particles and irregular shapes are distinguished in NS1, as quartz and high muscovite content can also be identified. The geology of the extraction zone for NS1 suggests that it is possible to find clay minerals such as kaolinite and illite identified on the XRD pattern.

N2 is specifically extracted from the felsic portion where minerals such as plagioclases, feldspar, hornblende, biotite, and possible chlorite and clays are found. XDR identification suggests low quartz and anorthite content, and the presence of vermiculite minerals, chlorite, and illite. Visually, NS2 has a higher proportion of fines but fewer high-shape aggregates than NS1. Grading curves for NS1 and NS2 that adhere to ASTM C 33 are depicted in Figure 1b.

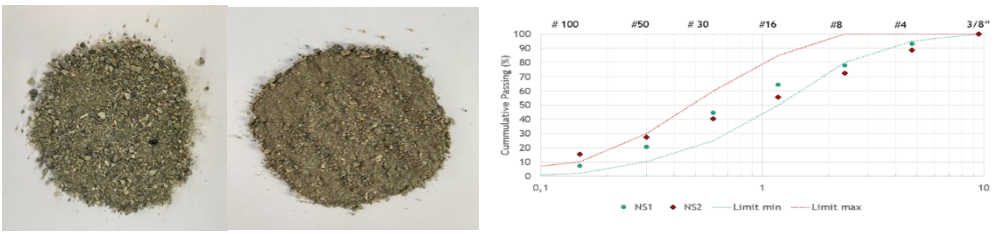

Figure 1. 1a. Images for NS1 (left) and NS2 (right).**1b**. Grading curves for NS1 and NS2.

Table 2 summarizes the basic characterization in accordance with ASTM C 128. The values for NS1 and NS2, which are related to specific gravity and absorption are normal for sand. It is worth noting that NS2 has a higher passing sieve # 200 than NS1 and MBV as well. Furthermore, CF-NS1 from the sand deposit for NS1 had the highest MBV for passing sieve # 200 and the lowest specific gravity, which could be attributed to the presence of clay.

Table 2. Basic aggregate characterization

	Specific Gravity	Absorption (%)	Passing Sieve # 200	MBV (g dye/g sample)	MBV-S200 (g dye/g sample)
NS1	2.63	1.64	3.79	1.46	3.56
NS2	2.67	1.26	6.40	2.57	7.63
CF-NS1	2.02	--	--	--	15.75

The corresponding mortar test is shown in Figure 2a. The test was performed with NS1 and the sacrificial agent M1 at dosages of 0.50%, 0.55%, and 0.60% (w/w of sand), while M2 was applied at doses of 0.40%, 0.50%, and 0.60% (w/w of sand). For the reference mixes the mini-slump retention was roughly 85% and all mixes using M1 got slump retention higher than the reference mix and 12% of water reduction. The same results were obtained for M2 with better slump retention than the reference mix and water reduction of about 25%.

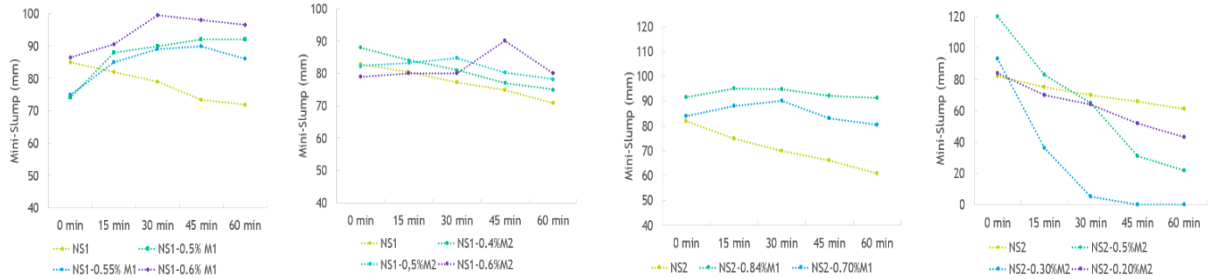

Figure 2. 2a. Slump Loss test for NS1with M1,M2 (Left). **2b**. NS2 with M1,M2 (Right)

Results for NS2 with M1 and M2 are shown in Figure 2b. M1 molecule had better mini-slump retention than the reference mix, with a water reduction of about 11%. M2 sacrificial agent exhibits a poor response at high and low dosages; due to 28% water reduction, this lack of water directly affects the slump loss of the system. Despite both commercial sacrificial agents being polyamine-based components, Ma et al., (2020) suggest that the molecular weight, the cationic molecule charge, and the clay present on the sand may all have an impact on the chemical and/or physical adsorption.

The dose sensitivity at the equivalent mortar test was used to conduct concrete studies for NS1 with M1 and M2, as well as NS2 with M1. Figure 3a and 3b summarizes the results with NS1 and M1 and M2. In Figure 3a at 0.5 (w/w sand) slump retention of 94% and a water reduction of 7%, the compressive strength increased by 24% after 28 days. Figure 3b, for M2 at 0.40% (w/w of sand) showed 33% strength improvement after 28 days and slump retention of 94% with 15% water reduction. When comparing M1 and M2 for the sand NS1, both sacrificial agents reduce water on their mixes and ensure slump retention: however, the amount of water that each sacrificial agent can reduce may be related to the amount of cement that can be reduced.

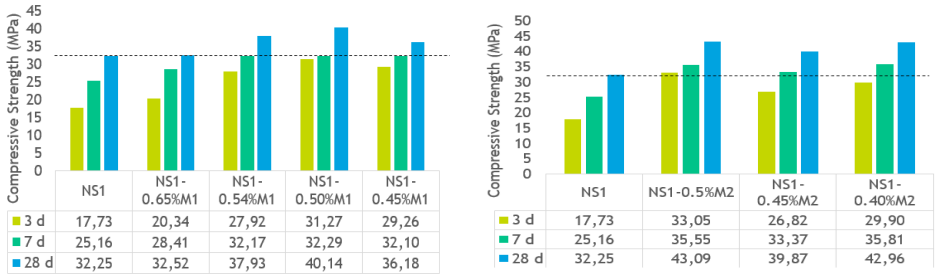

Figure 3. 3a Concrete test NS1- M1 sacrificial agent.3b. Concrete test NS1- M2 sacrificial agent.

NS2 To achieve better slump retention while reducing 15% of water content, using M1 was required from 0.50 %-1.0 % (w/w sand) and 33% strength gain after 28 days was obtained. M1 sacrificial agent could be effective in both grains of sand proposed in this study at different dosages that could be related to the amount of MBV of each sand and guarantee a potential cement adjustment while maintaining the same performance.

In addition, a cement reduction test for NS1 and M2 from 15 kg to 25 kg test and is shown in Figure 4. For all scenarios examined, the slump retention was higher than the reference mix. For 0.45% M2-15 kg and 0.45% M2-20 kg, the slump retention was 85% and 88% with a slight gain of strength after 28 days. For a reduction of 25 kg and 0.40%, the slump retention was 90% and 28 days strength improvement was 30% where the cement content was decreased by 25 kg.

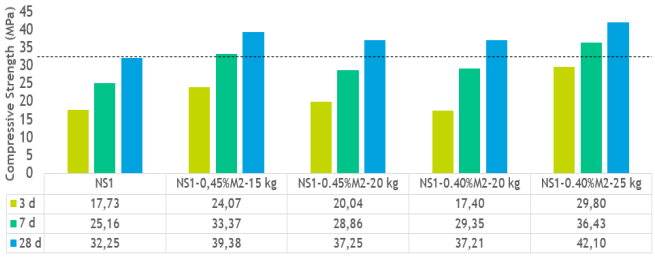

	NS1	NS1-0,45%M2-15 kg	NS1-0.45%M2-20 kg	NS1-0.40%M2-20 kg	NS1-0.40%M2-25 kg
3 d	17,73	24,07	20,04	17,40	29,80
7 d	25,16	33,37	28,86	29,35	36,43
28 d	32,25	39,38	37,25	37,21	42,10

Figure 4. Concrete test with cement reduction with M2.

More sustainable concretes could be produced by minimizing the additional water associated with the clayey fractions present on the aggregates, allowing a 6% reduction in CO_2 for each cubic meter produced or more depending on each scenario.

Conclusions

- Understanding how clayey fractions on aggregates affect concrete, particularly water demand to achieve the same slump that reduces the compressive strength, requiring more cement to ensure performance and emitting more CO_2 per cubic meter. By boosting cementitious efficiency and focusing on the aggregate fraction, the mix can be improved, requiring less cement to achieve the performance required.
- The chemistry behind the sacrificial agents could have a positive or negative effect based on the type of clayey fraction present on each sand, the molecular weight, the cationic molecule charge, and other parameters that need to be linked with the mineralogy of the clayey fraction, and understanding how other minerals, oxides may affect the dosage and effectiveness of the sacrificial agent.
- The heterogeneity of sand sources and the variability in sand extraction involves addressing additional tests and procedures to offer the data required to build trustworthy sacrificial agent molecules and avoid scenarios in which the solution fails.

Acknowledgments

To Cementos Argos R&D team to support and finance this study and use their expertise to find sustainable concretes through the company's drive toward the road to zero carbon.

References

ASTM C 33-Standard Specification for Concrete Aggregates. (2018)
ASTM C 128- Standard Test Method for Density, Relative Density (Specific Gravity), and Absorption of Fine Aggregate.
ASTM C 1777- Standard Test Method for Rapid Determination of the Methylene Blue Value for Fine Aggregate or Mineral Filler Using a Colorimeter.
ASTM C 1810- Standard Guide for Comparing Performance of Concrete-Making Materials Using Mortar Mixtures (2021)
INV E-235-07. Valor de azul de metileno en agregados finos.
Jardine, L., Koyata, H., Folliard, K., Chin Ou, C., Jachimowic, F., Chun, B., Jeknovarian, A. Hill, C. (2003). Admixture for optimizing the addition of EO/PO. USA, US 6,670,415 B2.
Ng, S., Plank, J. (2012). "Interaction mechanisms between Na montmorillonite clay and MPEG-based polycarboxylate superplasticizers". Cement and Concrete Research, 42(6), 847–854.
Ma, Y., Shi, C., Lei, L., Sha, S., Zhou, B., Liu, Y, Xiao, Y. (2020). Research progress on polycarboxylate based superplasticizers with tolerance to clays - A review. Construction and Building Materials, 255, 119386.
Muñoz, F., Tejedor, M., Isabel, M, Anderson, Marc, A., Cramer, S. (2010). Detection of Aggregate Clay Coatings and Impacts on Concrete. ACI Materials Journal, 107 (4), 387-395.
Norvell, K., Stewart. G, Juenger, M., Fowler, D. (2007). Influence of Clays and Clay-Sized Particles on Concrete Performance. Journal of Materials in Civil Engineering, 19 (12), 1053-1059.
Ramachandran, V.S., Paroli, M., Beaudoin, J., Delgado, A. (2002). Handbook of Thermal Analysis of Construction Materials. New York, USA, Noyes Publication.

The 16th International Congress on the Chemistry of Cement 2023 (ICCC2023)
"Further Reduction of CO_2 -Emissions and Circularity in the Cement and Concrete Industry"
September 18–22, 2023, Bangkok, Thailand

Effect of the use of different dispersing molecules on the rheological properties and kinetic hydration of Portland cement pastes

F.F. Danila[1*], A.C.R. Martho[2*], R.C.O. Romano[3*] and R.G.Pileggi [4*]

[1] *GCP Applied Technologies, Sorocaba, Brazil*
Email: danila.f.ferraz @gcpat.com
[2] *GCP Applied Technologies, Sorocaba, Brazil*
Email: ariane.martho@gcpat.com
[3]*University of São Paulo, São Paulo, Brazil*
Email: rcorjau@gmail.com
[4]*University of São Paulo, São Paulo, Brazil*
Email: rafael.pileggi@lme.pcc.usp.br

ABSTRACT
The use of water reducers to improve the rheological properties of concrete, in addition to dispersing cement particles, can modify the agglomeration potential of particles and the dissolution kinetics of the clinker phases during the early ages of hydration. In this work two molecules of admixtures based on sodium polycarboxylate were evaluated: the first, with higher dispersion efficiency was named as MR7525 and, the second, with lower dispersion efficiency and higher slump retention was named as MR2575. The study was carried out with the evaluation of cement pastes prepared with Portland cement type CPV, maintaining the constant water-to-cement ratio to evaluate the rheological properties, hydration kinetics and agglomeration. The results indicated differences in the rheological properties of the pastes with different admixtures (initial and depending on the time), facts that can directly impact the process of mixing, transport, application and hardening of the concretes.

Keywords: Portland cement, polycarboxylate, rheometry, Kantro's mini cone, chemical reaction.

1. Introduction

Several admixture technologies can be combined so that performance specifications are met, either from the use of polymers developed to obtain an adequate initial fluidity of the concrete for certain applications, to maintain the workability or even to extend the useful life of the component produced. The chemical affinity between the surface of the cement particle and the admixture is an important parameter for the adequate control of the dosage of the admixture, the specific surface area of the cement defines the dosage of admixture necessary to achieve the specified fluidity for each concrete and the maintenance of workability. The adsorption of the polycarboxylate molecules increases as the dosage of the admixture is increased, until the cement surface is completely covered, thus reaching the saturation or optimal dosage of the admixture. Different polymer structures result in different performances as water reducers or slump retention or to maintain stability. The length and amount of organic chains on the surface of the cement particle and the type, quantity and density of the side chains are responsible for the effectiveness of the steric stabilization of a polycarboxylate ether - PCE in cementitious suspensions, and define the adsorption of these polymers on the surface of the cement particle, in addition to the molecular weight of these admixtures (AÏTCIN et. al, 2016). To adapt admixtures with specific properties to match the requirements of each concrete. The use of rheological control methods can increase the precision of the analyses, since it allows the evaluation according to different shear conditions and the definition of the thixotropy profile, viscosity yield stress, rheological behaviour and consolidation kinetics over time (ROMANO, 2013). This work was carried out with the objective of evaluating the effect of the use of two polycarboxylate-based admixtures on the rheological properties of pastes formulated with Portland cement CP V, using different techniques to determine the ideal content of the admixtures at the initial moments of consolidation over time.

2. Material

A Portland cement type CPV was used , and two admixtures with complementary functions, developed especially for the study, named as MR 7525 and MR 2575. This identification was used to differentiate the amount of dose response polymer (which gives the materials greater initial fluidity), followed by the amount of slump retention polymer to maintain stability. Thus, in the first case, it is expected to obtain greater fluidity and little stability and in the second case, less fluidity and greater stability over time. The polycarboxylate admixtures used in this work are synthetic polymers that have a molecular structure with an organic backbone made of polyoxy-isoprene macromonomers (ethylene glycol), and grafted branches (or side chains) composed of poly-ethylene oxide, they are ester-linked to acrylic units, this conformation has caused polycarboxylate molecules to be often referred to as a "comb" structure. The X-ray fluorescence (XRF) is given in Table 1 (courtesy of the CTL Group), while the particle-size distribution is given in Figure 1 (Malvern Mastersizer 2000/2000E on "wet" samples, i.e. ethyl alcohol).

Property	%
L.O.I	3,90
SiO_2	19,3
CaO	58,9
MgO	3,50
Fe_2O_3	2,40
Al_2O_3	5,40
Mn_2O_3	0,18
TiO_2	0,25
SO_3	4,20
Na_2O	0,40
K_2O	0,88
Álcali eq.(in Na_2O) *	1,01

* $Na_2O + 0,658\ K_2O$

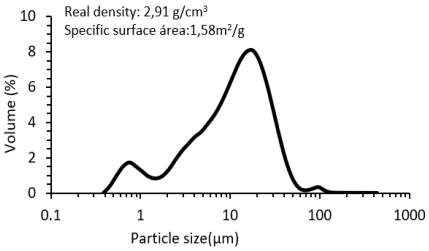

Table 1 and Figure 1: Chemical and physical results for cement CP V

3. Methods

A water-to-cement ratio (w/c) of 0.35 was used for all cement pastes, the pastes preparation, rotational and oscillatory rheometry, and calorimetry protocol was conducted using the same procedure described in described in Ferraz et al. 2020. In order to determine the admixture dosage, deflocculation curves were performed to find an optimum dosage. This resulted in the following dosages for each of the cement types.

4. Results and Discussion

The presentation of the results was divided into two stages, the first of which determined the ideal content of each admixture for the type of cement chosen, and the second evaluated the impact on consistency gain over time. With this strategy, it was intended to monitor the impact of the difference in admixtures in the stage of preparation and application of the cementitious component. Figure 2 shows the spreads (flow) of the pastes obtained from the Kantro cone test.

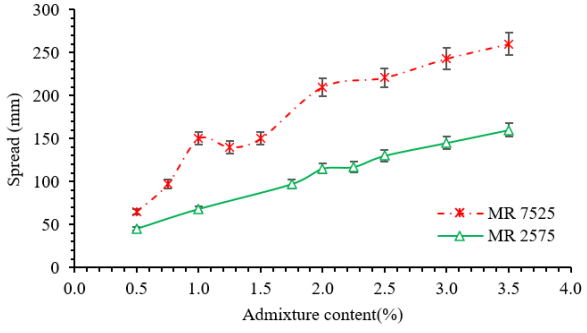

Figure 2: Spreading in the Kantro cone test, in the suspensions with the two admixtures

The higher the amount of DR polymer in the admix., the greater the spreading, following the initial expectation, based on the formulation of the admixtures, in addition, there is a correlation between the increase in the admixture content and the increase in spreading using Kantro mini-cone test. From the rotational rheometry tests it is possible to obtain more complete information about the characteristics of

the products under different application conditions. The results obtained are usually presented in the form of graphs of shear stress (or viscosity) vs. shear rate, as illustrated in a didactic way in Figure 9, making it possible to evaluate the rheological behavior profile of each composition. To determine the optimal admixture content, the results of yield stress, viscosity (apparent or plastic) and hysteresis area are used as a function of the content added in the composition (MONTEFUSCO et al. 2017). Based on these parameters, the graphs shown in Figure 3a indicate the variation in apparent viscosity, in b, flow stress and in c, hysteresis area of the pastes as a function of the variation in content and type of admixture.

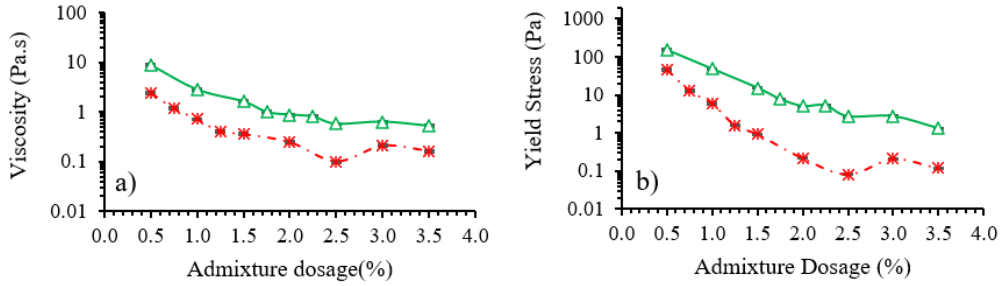

Figure 3: a) Evolution in apparent viscosity and b) yield stress

The choice of the optimized admixture content was made with the viscosity stabilization, but also considered the flow stress as close as possible to zero. The variation range of the admixture content was the same regardless of the type used, however the results of yield stress and viscosity were lower due to the increase in the amount of spreading polymer, converging with what was expected for the action of each admixture. Based on the results of rotational rheometry, it was possible to define that the optimized content of the admixtures was the same (2.5% by mass) and they were used to evaluate the stability over time, presented later. Even with the optimized content being the same for both admixtures, the apparent viscosity in the paste with the lowest amount of opening polymer (MR 2575) was an order of magnitude greater than in the paste with the highest amount of the same polymer. This fact was intensified with regard to the yield stress, the difference between them being two orders of magnitude, which indicates that the admixture acts more by altering the minimum stress necessary for the start of the flow than in the viscosity. In this work, it was possible to correlate the results of the rheological tests with the scattering obtained in the Kantro mini-cone method, as illustrated in Figure 4.

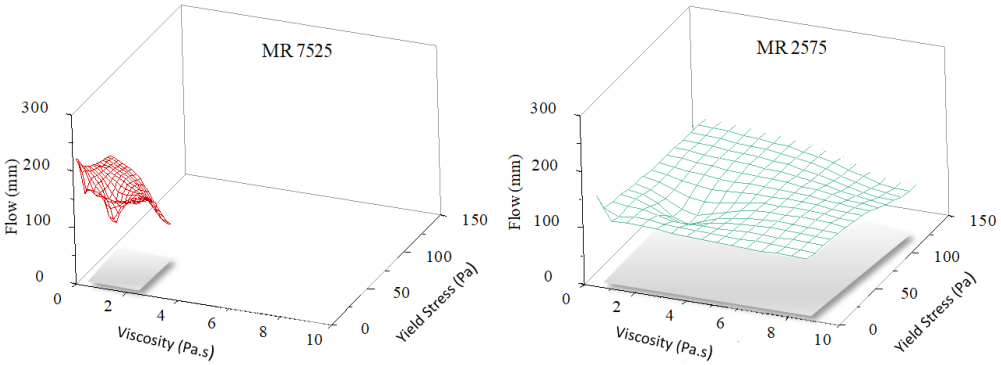

Figure 4: Surface analysis scattering x viscosity x yield stress

With the results presented so far, information is only available on the characteristics of the pastes in the first instants of cement hydration, since the tests were carried out 5 minutes after mixing. However, no information is available on stability over time.

For this, oscillatory rheometry tests were performed and the results are presented below. At this stage, the tests were carried out only for pastes with admixtures at ideal levels.

The results are shown in Figure 5 from the evolution of G' as a function of time after microstructural disruption (a), the particle reagglomeration rate (b) and the scattering measured from the Kantro mini-cone test along of time (c). Polymers intended for fluidity retention (slump-keeper) have slower

adsorption, modifying the fluidity of the system later, as observed for the MR2575 product. In addition, such polymers have greater affinity for the hydrates formed during the cement reaction and undergoing hydrolysis with the increase in the pH of the suspension. Thus, the combination of the two types of polymers in the same product made it possible to tailor an admixture for each desired property.

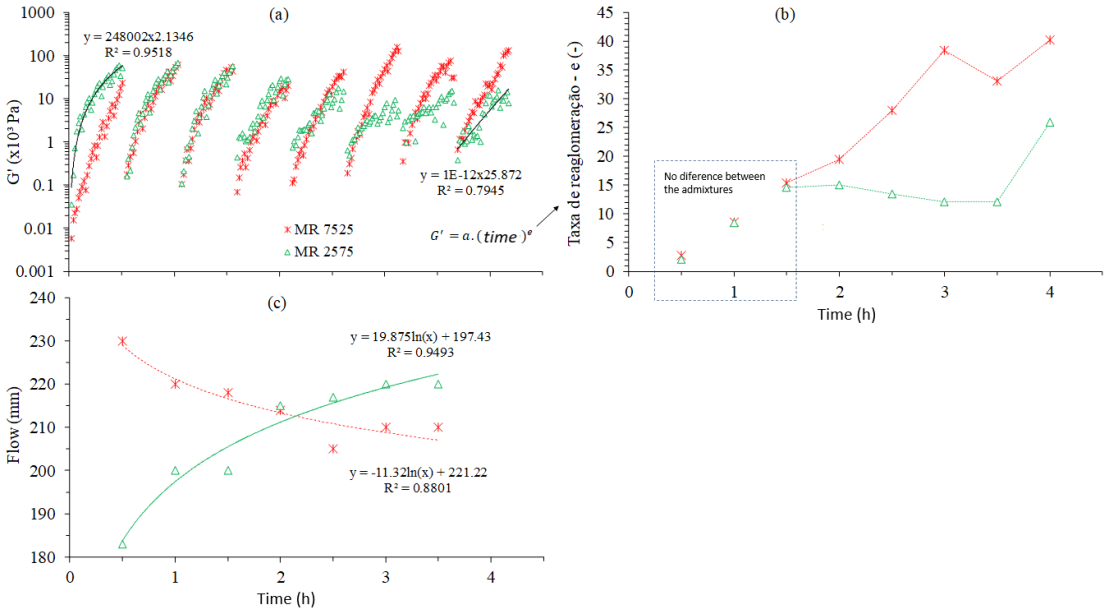

Figure 5: Evolution of G' in function of time after microstructural disruption (a), evolution of the particle reagglomeration rate (b) and scattering measured from the Kantro test along the time

5. Conclusion

The use of different polycarboxylate molecules, in synergy, showed different results regarding the initial dispersion efficiency of the cement particles and the maintenance of the open time.
In this way, it can be inferred that: a) both by rotational rheometry and from the spreading by the Kantro cone, it was possible to observe differences in the rheological behavior and fluidity, between the two admixtures in the pastes with the CPV cement; b) the greater amount of opening polymer resulted in lower values of yield strength and viscosity of the pastes, facilitating the quantified flow from mini-slump; c) from the results of rotational rheometry it was possible to define the ideal contents for each admixture in relation to the type of cement evaluated and d) correlating the scattering results with the rheological parameters, it was confirmed that the change in scattering was governed by both viscosity and yield stress (in this second case, a better correlation between the two techniques).

References

Aïtcin, P.-C.; and Flatt, R.; Science and Technology of Concrete Admixtures, Woodhead Publishing, 2015.
Berodier, E.; Gibson, L.R.; Burns, E.; Cheung, J.; Robust production of sustainable concrete through the use of admixtures and in-transit concrete management systems. Cement and Concrete Composites, Grand Challenges in Construction Materials 2016. v. 101, p. 52–66, 1 ago. 2019.
Ferraz, D; Martho, A.C.R.; Burns, E.G.; Romano, R.C.O.; and Pileggi, R.G.; "Effect of mixing procedure on the rheological properties and hydration kinetics of Portland cement paste," Rheology and Processing of Construction Materials, Mechtcherine, V.; Khayat, K.; Secrieru, E.; eds., 2020.
Romano, R. C. de O., Incorporação de ar em materiais cimentícios aplicados em construção civil. PhD thesis, University of São Paulo, 2013.
Montefusco, H., Maciel, M. H., Brasileiro, G.C.P., Mesquita, J.A.F.S, Evaluation of superplasticizer and particle size distribution of aggregates in the rheological properties of concretes; Conference: Congresso Brasileiro de Cerâmica, Gramado, Volume: 61, 2017.

The 16th International Congress on the Chemistry of Cement 2023 (ICCC2023)
"Further Reduction of CO_2 -Emissions and Circularity in the Cement and Concrete Industry"
September 18–22, 2023, Bangkok, Thailand

Pore structure of polymer-modified dry mix tile adhesive mortars

M. Kupiński[1*], Ł. Kotwica[2]

[1] *Henkel Polska Sp. z o.o., Stąporków, Poland*

Email: marcin.kupinski@henkel.com

[2] *AGH University of Science and Technology, Kraków, Poland*

Email: lkotwica@agh.edu.pl

ABSTRACT

Organic admixtures are used to alter the properties of cementitious mortars' properties. As they usually are or contain surfactants, a large number of air bubbles can be introduced, having a major impact on the mix performance in the fresh as well as in the hardened state. The air entraining and stabilization process can be influenced by a variety of factors, such as the pH of the pore solution, the presence of certain ions in the solution, surface charges on the grains of cement, or interference of different additives present in the mix. Thus, designing the pore structure and resulting properties of the mortar creates a significant technological challenge.
In this paper, we are focusing on the combined air-entraining action of methylcellulose and redispersible polymer powder (copolymer of vinyl acetate and ethylene) on the mortars based on Portland Cement (PC), and binary blend of Calcium Sulfoaluminate Cement (CSA) and Calcium Sulfate (C$).An attempt to determine the pore structure of fresh mix was made, using the Air Void Analyzer (AVA), yet it failed due to the gelation of cellulose ether in contact with the air-release liquid (glycerin) necessary in this technique. Instead, the porosity of the hardened mortars was quantified by image analysis of the high-resolution scans of the samples.
Significant differences in the introduced air pore size distribution were found, depending on the binder system used. The porosity of CSA-based mortars is finer than those of OPC-based mortars. Such materials also show a higher content of pores below 300 μm of equivalent diameter. The reasons behind such behavior remain unclear, which proves the high complexity of the topic.

KEYWORDS: *Cellulose ether, redispersable polymer powder, mortar, aeration, pore structure*

1. Introduction

The polymer modification of cementitious mortars is widely used in the dry mix industry. The most common additives are cellulose ethers (CE), providing beneficial rheological properties, the cohesion of the mortar, and water retention, resulting in a prolonged open time after application. These are often combined with redispersible polymer powders (RDP), increasing the adhesion strength to difficult substrates and the flexibility of the products. It is nearly impossible to formulate modern dry mix mortar without such additives, yet the presence of both dramatically alters the microstructure of the hardened product and has a pronounced effect on the mechanical parameters and durability.
As organic additives contain or are surfactants, a large amount of air is introduced during mortar mixing and is further stabilised into a hardened material. Details of the porosity formation over time of setting and hardening of Ordinary Portland Cement (OPC) pastes were investigated by Pourchez et al (2010). It was stated that the resulting aeration structure depends on the CE chemistry, acting mainly on the capillary pores range (around 500 nm) and air voids range (50 – 250 μm). The hypothesis was presented that both ranges impact the transport of water and permeability, hence the durability of hardened mortar is affected. The claim was supported by the earlier work of Malatrait (1992), which showed that CE stabilises the pore network consisting of large air voids connected by large capillaries (<1 μm). In contrast, Wyrzykowski et

al. (2014) found that the effect of CE on the Portland cement mortar matrix is negligible and only air voids > 10 μm can be varied with CE additions. The study referred to tile adhesive mortars and was limited to ethers of a specific degree of substitution of hydroxyl groups substitution degree (DS=1,87) without the presence of any redispersible polymer powder. Silva et al (2001) found the resulting pore structure of such mortars is a function of the interaction between cellulose ether and RDP. The especially strong impact of EVA (copolymer of vinyl acetate and ethylene) was noted at high dosages (up to 20%).

2. The aim of the study

Interestingly, little research has been found on the pore structure of polymer-modified mortars in binder systems other than OPC. However, the practice shows, that i.e. tile adhesive mortars formulated on: (OPC) solely, binary blend of Calcium Sulfoaluminate cement (CSA) and Calcium Sulfate (C$) or a ternary blend of PC, C$ and Calcium Aluminate Cement (CAC) vary in durability, especially in case of resistance against water immersion as well as following freezing and thawing cycles. The exemplary results are shown in Table 1.

Table 1. The adhesion strength of tile adhesive mortars after various storage conditions acc, to EN 12004.

Storage conditions	OPC - based	CSA - based
Adhesion after 28 days of ambient storage [N/mm^2]	2,1	2,3
Adhesion after water storage [N/mm^2]	1,4	0,6
Adhesion after freeze/thaw cycles [N/mm^2]	1,7	1,1

The presented study aims to verify whether differences in water and freeze/thaw resistance of tile adhesives based on various binders can be explained by differences in their pore structure.

3. Materials and methods

Two simple tile adhesive mortars were prepared. Organic additives amount and type: copolymer of vinyl acetate and ethylene (EVA) re-dispersible polymer powder (in the form of free flowing powder of MFFT = 1°C, bulk density = 520 kg/m^3 and ash content after heating up to 1000°C= 13%, protective colloid: polyvinyl alcohol (PVA)) and pure methylcellulose (Brookfield viscosity of 2% solution, RVT 20rpm = 40 000 mPas) – were kept the same for each mortar. The mineral binder content was always scaled to 40% - while its composition has been varied from pure portland cement (OPC) CEM I 52,5 R to a binary blend of Calcium Sulfoaluminate Clinker (CSA) and Calcium Sulfate (C$) in a proportion of 80: 20. The mix proportions and basic physical properties are given in Table 2.

Table 2. Compositions of the mortars tested.

	TA 1 (OPC)	TA 2 (CSA)
OPC CEM I 52.5 R [%]	40,0	
CSA clinker [%]		24,0
Calcium Aluminate Cement [%]		
Natural Anhydrite [%]		16,0
EVA polymer powder [%]	2,0	2,0
Methylcellulose [%]	0,5	0,5
Washed sand 0,1-0,5 mm [%]	55,5	57,5
Total [%]	**100,0**	**100,0**
Water [% of dry powder]	*25,0*	*25,0*
W/C [-]	*0,625*	*0,625*
Air content [%]	*26%*	*27%*
Density [kg/m^3]	*1540*	*1490*

All samples were prepared by blending 5 kg of material for 5 minutes in a powder mixer with a mixing speed of 340 rpm. The mortars were then mixed with water with a steel mixing paddle with a drill in 3 steps: 1 min of mixing, 3 min break, and 30 seconds of mixing to ensure sufficient maturation time for the dissolution of organic additives is provided.

The air content and density of the fresh mix were measured according to the PN-EN 1015-7:2000 (air pressure method). Then 40x40x160 mm mortar prisms were prepared according to PN-EN 196-1:2016-07. After 14 days of curing, the prisms were cut into slices with the precise low-speed diamond saw. Further preparatory work corresponds to the procedure described in PN-EN 480-11:2008. Polishing with fine sandpaper of two different gradations: #800 and #1000 was carefully performed with the use of a Struers LaboPol-20 polisher. Difficulties to do so were noted – due to the high porosity of the the samples and the weakening of mineral microstructure by the presence of polymer additives.

The cross sections obtained (6 samples of TA1 and 7 samples of TA2) were coloured with black marker and the air voids were filled with zinc paste. Such prepared samples were scanned with the office scanner (Epson Perfection V19) in the 9600 dpi resolution, given the smallest analysed pores (equivalent diameter of 15 µm) are covered by at least 25 pixels. The images were then analysed with ImageJ software and air void area distribution was collected. The surface area analysed was always between 900 and 1000 mm^2 (56-63% of the sample cross-sectional area).
An attempt to measure the size distribution of air voids in fresh mortar was made with the AVA 3000 apparatus (Germann Instruments).

4. Results

An attempt has been made to investigate the pore size distribution in mortars with the air-void analysis method. It was found that the mortar increases its consistency dramatically immediately after contact with the air-release liquid: glycerol. As this led to further miscibility problems and air entrapment in the sample, it was not possible to obtain reliable results. It is assumed that the gelation of methylcellulose occurred since glycerol decreases the gelation temperature. In the example, for the binary mixture of 0.5 glycerol volume ratio, the gelation point of methylcellulose decreases from 57°C to 37°C - Kuang et al. (2006). Given the 20 cm^3 of mortar was dissolved in 180 cm^3 of release liquid, the obtained glycerol volume ratio was >1000. In this conditions, further decrease of the gelation point of cellulose ether below room temperature is suspected.

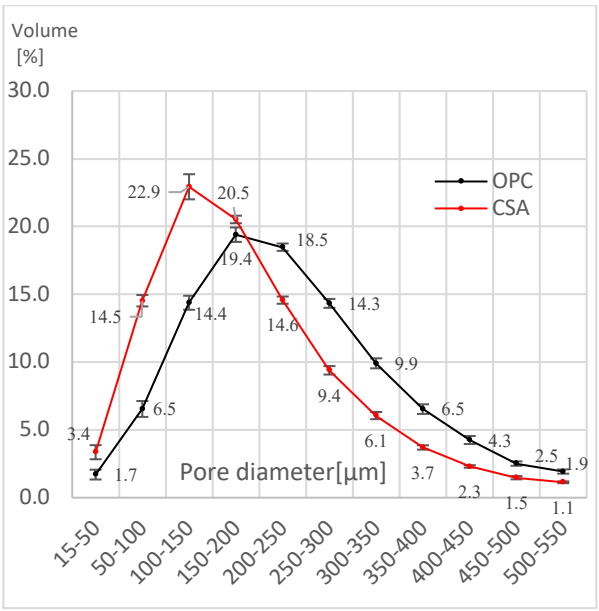

Figure 1. Pore size distributions as a function of pore size diameters. Error bars represent confidence intervals (α=0.05).

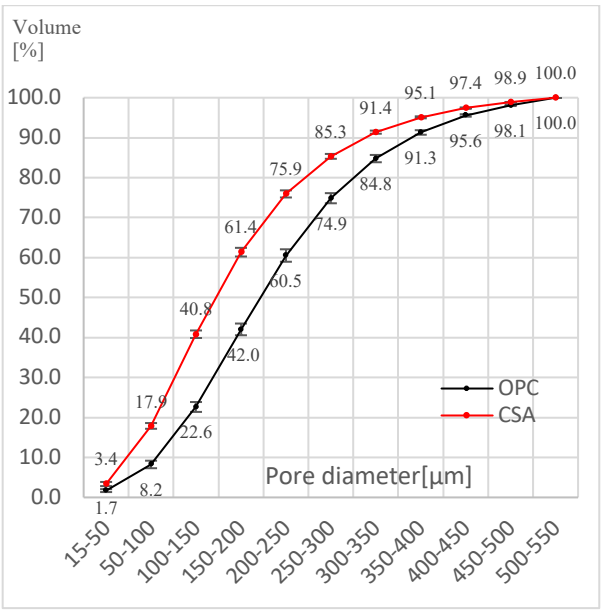

Figure 2. Cumulative distribution of pore volume. The error bars represent confidence intervals (α=0.05).

Figure 1. presents the results of the air void size distribution measured by polished cross-section image analysis. Significant differences were found depending on the binder system used. The porosity of mortars based on the CSA-C$ mixture is characterized by finer pores than the one based on OPC. The highest differences between samples are observed in the ranges of 50-100 µm (123% higher volume in TA2) and 100-150 µm (59% higher volume in TA2). The range of 100-150 µm of equivalent diameter also creates the largest volume of porosity in TA2: 22,9% whereas such a maximum in TA1: 19,4% places in the range of 150-200 µm of equivalent diameter. The observation finds its reflection in cumulative pore volume distribution (figure 2.). It is generally shifted towards smaller pores in TA2, where 85,2% of porosity has an equivalent diameter below 300 µm. For the sample TA1, the volume share of such pores is significantly smaller: 74,9%.

5. Discussion

As the results of the pore structure measurements by image analysis strongly depend on sample preparation, it is crucial to ensure the reproducibility of obtained results, especially given the difficulties encountered during the polishing of the mortar slices. Therefore, values of the confidence interval assuming the t-student distribution were calculated. For all data points, satisfactory accuracy was achieved proving the significance of the the measurements. The values of confidence intervals (α=0.05) are graphically represented in figures 1. and 2. as error bars.

The porosity of CSA-based mortar seems to favour a higher freeze/thaw resistance than OPC-based mortars due to the higher volume of smaller pores. This remains in contradiction with empirically obtained results, showing the decrease of adhesion strength after water immersion of 74% and 52% after freeze/thaw cycles compared to the storage under lab conditions, while for OPC-based mortars these are 33% and 19% respectively. Therefore, the reasons for these differences in the mechanism of adhesion strength drops remain unclear.

Jenni et al. (2006) investigated the decrease of the adhesion strength after water storage of OPC systems. The authors concluded that the polymer matrix coexisting with a mineral one is prone to water attack because of its water solubility. It was also proven that organic admixtures can migrate, segregate, and accumulate in certain parts of the microstructure - (De Gasparo et al. (2009) – which may lead to the presence of weak spots in the mortar body. Therefore, it is likely that the water transport mechanism plays an important role in shaping the durability of such systems, and it is advisable to follow up the presented study with the comparison of the capillary porosity of the investigated samples.

6. Conclusions

The aim of the study was to find whether differences in the distributions of pore sizes are responsible for differences in the resistance to water and freeze/thaw cycles of tile adhesive mortars based on different binders. Air void distributions were successfully measured by image analysis of polished mortars' cross sections. When CSA is used as a binder, significantly finer porosity is achieved and a higher volume (85,3%) of a pore diameter below 300 μm is observed compared to OPC-based mortar (74,9%). This suggests superior freeze/thaw resistance of CSA-based adhesive, which is in contradiction with empirical data. Thus, durability differences cannot be explained by the pore size distributions in the tested area (15-550 μm). New light could be shed on the topic if pores below 15 μm were analyzed.

Acknowledgements

The research presented in the paper was financed by Henkel's International Innovation Centre for Building Materials in Stąporków.

References

De Gasparo, A., Herwegh, M., Zurbriggen, R., Scrivener, K. (2009) "Quantitative distribution patterns of additives in self-leveling flooring compounds (underlayments) as function of application, formulation and climatic conditions", *Cement and Concrete Research, 39(4): 313-323.*

Jenni, A., Zurbriggen, R., Holzer, B. and Herwegh, M. (2006) "Changes in microstructures and physical properties of polymer-modified mortars during wet storage", *Cement and Concrete Research, 36(1): 79-90*

Kuang, Q., Cheng, G., Zhao, J. and Li, Y. (2006) "Thermogelation Hydrogels of Methylcellulose and Glycerol–Methylcellulose Systems", *Journal of Applied Polymer Science,* 100(5): 4120-4126

Malatrait, M. (1992) "Propriétés hydriques du mortier pour enduits de façades en relation avec sa structure poreuse, mise en oeuvre, durabilité" PhD thesis, *INP Toulouse University*

Pourchez, J. Ruot, B., Debayle, J., Pourchez, E. and Grosseau, P. (2010) "Some aspects of cellulose ethers influence on water transport and porous structure ofcement-based materials", *Cement and Concrete Research* 40: 242–252

Silva, D.A., John, V.M.,, Ribeiro, J.L.D and Roman, H.R. (2001) " Pore size distribution of hydrated cement pastes modified with polymers", *Cement and Concrete Research,* 31(8): 1177-1184

Wyrzykowski, M., Kiesewetter, R., Kaufmann, J., Baumann R.. and Lura, P. (2014) „Pore structure of mortars with cellulose ether additions – Mercury intrusion porosimetry study", *Cement & Concrete Composites,* 53: 25–34

The 16th International Congress on the Chemistry of Cement 2023 (ICCC2023)
"Further Reduction of CO_2 -Emissions and Circularity in the Cement and Concrete Industry"
September 18–22, 2023, Bangkok, Thailand

Aluminum sulfate-based accelerators: rheological implications for 3D-printed concretes

L. Caneda-Martínez [1,2*], E. Keita[1], H. Bessaies-Bey[1], M. Duc[1], B. González-Fonteboa[2], and N. Roussel[1]

[1] *Gustave Eiffel University, Champs sur Marne, France*

Email: E.K. : emmanuel.keita@univ-eiffel.fr; H.B-B.: hela.bessaies-bey@univ-eiffel.fr; M.D.: myriam.duc@univ-eiffel.fr; N.R.: nicolas.roussel@univ-eiffel.fr

[2] *Universidade de A Coruña, A Coruña, Spain*

Email: L.C-M.: laura.cmartinez@udc.es; B. G-F.: belen.gonzalez.fonteboa@udc.es

ABSTRACT

The implementation of digital fabrication in the concrete manufacturing industry, notably extrusion 3D printing, is emerging as a transformative and highly valuable tool for the construction sector. The main advantage of this method is the lack of need for formwork, which translates into greater design flexibility and optimization of materials and time, among other benefits. In the absence of formwork, however, the properties of concrete in the fresh state must be carefully tailored, as they must adapt to the rheological requirements of each stage of the process. In this context, accelerators play a central role. The utilization of alkali-free accelerators (based on aluminum sulfate solutions) has been conventionally relegated to shotcrete applications. However, increased interest in their use has arisen with the emergence of concrete 3D printing.

In this work, studies are conducted to relate the impact of the use of aluminum sulfate as an accelerator on the hydration reactions of cement and its subsequent effect on rheology. For this purpose, the evolution of the hydration reaction is evaluated by in-situ X-ray diffraction (XRD) on cement pastes. In parallel, the pastes rheology is assessed by penetration tests. XRD results allow for the monitoring of ettringite growth over time and the assessment of its impact on solid volume fraction. The results suggest that the evolution of the material rheological properties cannot be solely explained by the increase of the solid fraction caused by the precipitation of ettringite.

KEYWORDS: *concrete 3D printing, accelerators, aluminum sulfate, rheology, ettringite.*

1. Introduction

The digitization of concrete manufacturing has attracted increasing interest in recent times, especially in the field of concrete 3D printing by extrusion, as it promotes greater flexibility in construction and the creation of optimized designs. However, to be successfully printed, concrete must undergo a variety of processes involving demanding rheological requirements, particularly in the fresh state, which frequently implies the optimized use of admixtures. Among them, accelerators are instrumental in satisfying some of the requirements needed in 3D printing. Alkali-free accelerators, conventionally used in shotcrete applications, are one of the most demanded options in the sector. They are based on aluminum sulfate solutions, which are known to be highly effective in accelerating the hydration reactions of aluminates in cement. Even though alkali-free accelerators have been used for years, research related to their effects on the properties of concrete, particularly with respect to its rheology, is scarce.
This work aims to relate the effects of the acceleration of cement hydration caused by aluminum sulfate on the rheological properties of cement pastes. To this end, the study of the rheology of cement pastes by penetration tests is combined with the monitoring of the evolution of cement hydration by means of in-situ X-ray diffraction, focusing on its effect on the changes in the solid volume fraction of the pastes.

2. Materials and methods

A Portland cement type CEM I 52.5 N was used in this study. Its chemical composition is shown in Table 1. Mineralogically, the cement is composed by alite (65.3%), belite (14.1%), C_3A (8.1%), C_4AF (7.6%), basanite (3.2%), gypsum (0.4%) and others (1.3%). A commercial aluminum sulfate hydrate, supplied by Sigma Aldrich, was used as an accelerator.

Table 1. Elemental composition of the starting cement.

Oxide	CaO	SiO_2	Al_2O_3	Fe_2O_3	MgO	SO_3	MnO	Na_2O	K_2O	TiO_2	P_2O_5	LoI
%	65.17	20.3	4.86	2.8	0.95	2.01	0.11	0.22	0.89	0.24	0.31	1.48

In-situ X-ray diffraction (XRD) was performed on a D8 Advance diffractometer (Bruker AXS) equipped with a LynxEye detector and a cobalt anode, operated at 40 mA and 35kV. Scans were recorded from 8.5º 2θ to 49º 2θ, with a step size of 0.025º and 0.5 s/step. The reference paste (OPC) was prepared at a w/c of 0.35 by mixing the cement with water for one minute by hand. For the accelerated paste (1.5%Acc), 1.5% (by weight of cement) of aluminum sulfate was dissolved in the hydration water prior to the mixing. The pastes were placed in an airtight sample holder covered with kapton film to minimize water evaporation. The quantification of each phase was performed following the Rietveld method, using the software TOPAS v2.4 (Bruker). The G-factor method was applied by measuring a corundum sample of known crystallinity under the same conditions as the pastes (Jansen et al. 2011). In addition, the kapton film was measured by placing it on a single-crystal silicon sample holder, and it was later used as a model to fit the background of the diffractograms of the pastes.
The rheology of the pastes was indirectly assessed by penetration tests, using a VFG Mecmesin handheld force gauge and a 5 mm radius spherical probe. The cement pastes were mixed for one minute in a planetary mixer at 67 rpm, then placed in 4x4x16 cm^3 moulds and vibrated for 30 seconds. The maximum penetration force was measured at different hydration times.

3. Results and discussion

3.1. X-ray diffraction

Figure 1a compares the diffractograms obtained at the beginning of the hydration reaction for the reference (OPC) and the accelerated (1.5% Acc) pastes. Two significant changes with respect to the diffractogram of the anhydrous cement are observed. Firstly, the diffraction peaks corresponding to basanite are no longer detected, but an increase in the gypsum peaks is observed instead. This is consistent with the differences in solubility of both compounds, according to which an immediate dissolution of basanite upon contact with water is expected, leading to rapid precipitation of gypsum due to its low solubility. Secondly, the presence of peaks attributable to ettringite becomes manifest, evidencing the onset of hydration of the aluminate phases.

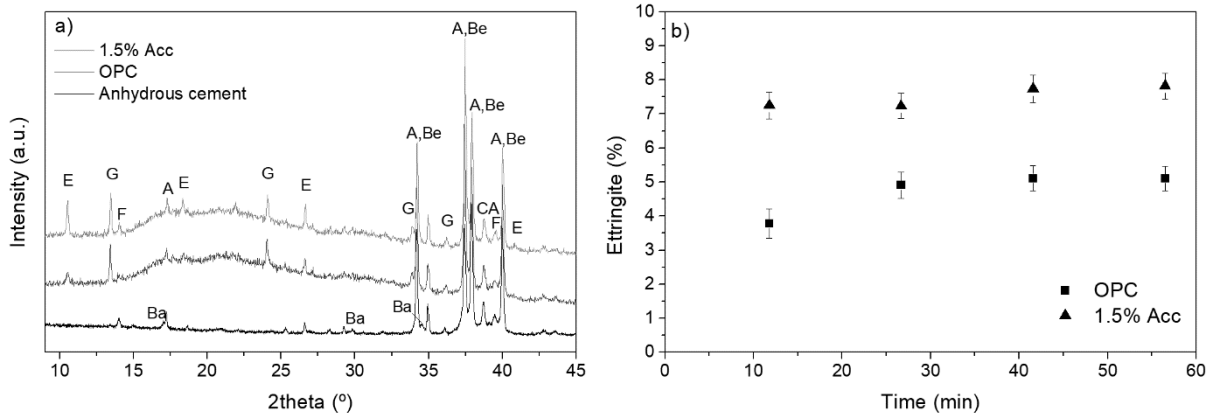

Figure 1. a) Initial diffractograms of the hydrated OPC and 1.5% Acc pastes and of the anhydrous cement (A: alite, Ba: basanite, Be: belite, CA: C_3A, E: ettringite, F: C_4AF, G: gypsum); b) Ettringite content over time.

The quantification of ettringite over the hydration time of the pastes is shown in Figure 1b. The results reveal that most of the ettringite precipitates in the first minutes of the reaction, although its content continues to increase slowly with time. The addition of the accelerator results in an increase in the initial ettringite formation of 80% with respect to the OPC paste, but this increase is reduced to approximately 50% in subsequent measurements.

3.2 Penetration tests and rheological analysis

The yield stress of the pastes was indirectly evaluated by penetration tests, as penetration forces are known to be directly correlated with the yield stress of cement pastes (Lootens et al. 2009). Figure 2 shows the evolution over time of the maximum forces of the Acc 1.5% paste relative to the initial maximum force of the OPC paste. The addition of the accelerator leads to an overall gain in the penetration force with respect to the OPC paste, resulting in an initial relative increase of approximately 5 times that of the OPC paste. This increase is further enhanced as hydration develops, following an approximately linear initial trend that tends towards stabilization after about 45 minutes. The explanation for this behavior could be found in the precipitation of ettringite, which consumes 32 molecules of water per mole of ettringite formed. This is typically associated with a rise in the solid volume fraction of the mix, and consequently with an increase in yield stress (Jakob et al. 2019). Such gain in the solid volume fraction has been verified by calculating the volume of the phases quantified by XRD, showing an increase of 6-8% in the 1.5%Acc paste with respect to the OPC paste (see Table 2).

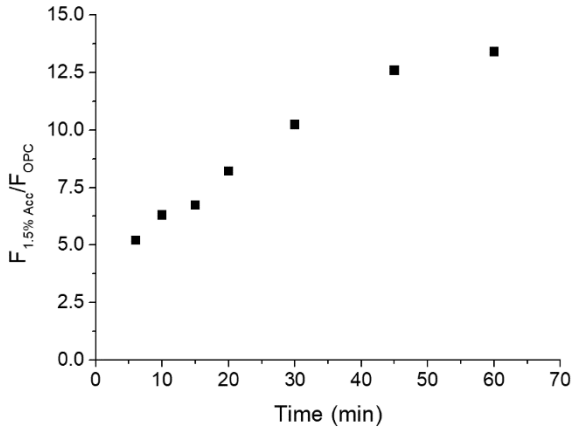

Figure 2. Relative maximum forces of paste Acc 1.5% with respect to the initial maximum force of paste OPC.

The relationship between yield stress and solid volume fraction (ϕ) can be described by the YODEL model (Flatt and Bowen 2006):

$$\tau_0 = \frac{m\,A_0 a^*}{d^2 H^2} \frac{\phi^2(\phi - \phi_{perc})}{\phi_m(\phi_m - \phi)} \quad (1)$$

Where m is a pre-factor associated to the particle size distribution, A_0 is the non-retarded Hamaker constant, d is the average particle diameter, a^* is the radius of curvature of the contact points, H is the surface separation distance at contact points, ϕ_{perc} is the percolation volume fraction and ϕ_m is the maximum packing fraction of the powder.

If we assume that the variation of yield stress in the system is dominated by the changes in solid volume, the YODEL model can be applied to calculate the relative increase in yield stress, based only on the variation of the solid volume fraction. For such calculation, it is assumed that ettringite precipitation does not have a significant effect on the interparticle forces, and therefore that the first term of equation 1 remains unaffected in the accelerated paste. In addition, the change in the maximum packing fraction is considered to be negligible in this hypothetical scenario. A value for ϕ_m of 0.66, measured on the OPC paste by centrifugation (Bessaies-Bey et al.), is considered for the calculations. The percolation volume fraction is assumed to be 0.37 (Perrot et al. 2012). The results in Table 2 show that the predicted relative increase in

yield stress resulting from the increase in solid volume fraction is considerably lower than the relative maximum forces assessed by penetration, despite the fact that both properties (yield stress and penetration force) are known to be proportional.

Table 2. Relative solid volume fraction, penetration force and yield stress of 1.5% Acc with respect to OPC.

	Time (min)			
	10	**30**	**45**	**60**
$\phi_{1.5\%Acc}/\phi_{OPC}$ (computed)	1.07	1.06	1.07	1.08
$F_{1.5\%Acc}/F_{OPC}$ (measured)	6.3	10.2	12.6	13.4
$\tau_{1.5\%Acc}/\tau_{OPC}$ (computed)	1.9	1.9	2.0	2.1

These findings suggest that ettringite precipitation has additional effects on the properties of the paste beyond the increase in solid volume. One possibility could be that the formation of ettringite affects the interparticle forces, and thus the initial term of the YODEL model. This phenomenon could occur, for example, if the ettringite crystals act as bridging agents between particles. Another option could be that the ettringite crystals impact the packing properties. This latter hypothesis would be supported by the characteristic needle-like shape of ettringite, as it is known that elongated particles tend to reduce the maximum packing fraction (Philipse 1996). Both aspects - the impact of ettringite formation on interparticle forces and on maximum packing fraction - are crucial for the understanding of the fresh properties of concrete and for the development of concrete 3D printing, and will be tackled in future works.

4. Conclusions

The addition of aluminum-sulfate accelerators promotes the precipitation of ettringite, which leads to an increase in solid volume fraction and in the yield stress of the cement paste, as evidenced by XRD measurements and penetration tests. However, this rise in yield stress, cannot be fully accounted for by the changes in the solid volume fraction, as other aspects such as variations in the interparticle forces or in the maximum packing fraction must also be taken into account.

Acknowledgements

Laura Caneda-Martínez gratefully acknowledges Xunta de Galicia for the funding of her postdoctoral fellowship (ED481B-2021-001).

References

Bessaies-Bey, Hela et al. “Packing Properties Assessement of Cement and Alternative Binders through Centrifugation: Artifacts and Protocol”, to be submitted.

Flatt, Robert J., and Paul Bowen. 2006. “Yodel: A Yield Stress Model for Suspensions.” *Journal of the American Ceramic Society* 89(4): 1244–56.

Jakob, Cordula et al. 2019. “Relating Ettringite Formation and Rheological Changes during the Initial Cement Hydration: A Comparative Study Applying XRD Analysis, Rheological Measurements and Modeling.” *Materials* 12(18).

Jansen, Daniel, Friedlinde Goetz-Neunhoeffer, Christopher Stabler, and Jürgen Neubauer. 2011. “A Remastered External Standard Method Applied to the Quantification of Early OPC Hydration.” *Cement and Concrete Research* 41(6): 602–8.

Lootens, D. et al. 2009. “Yield Stress during Setting of Cement Pastes from Penetration Tests.” *Cement and Concrete Research* 39(5): 401–8.

Perrot, A. et al. 2012. “Yield Stress and Bleeding of Fresh Cement Pastes.” *Cement and Concrete Research* 42(7): 937–44.

Philipse, Albert P. 1996. “The Random Contact Equation and Its Implications for (Colloidal) Rods in Packings, Suspensions, and Anisotropic Powders.” *Langmuir* 12(24): 5971–5971.

Flatt, Robert J., and Paul Bowen. 2006. “Yodel: A Yield Stress Model for Suspensions.” *Journal of the American Ceramic Society* 89(4): 1244–56.

The 16th International Congress on the Chemistry of Cement 2023 (ICCC2023)
"Further Reduction of CO_2 -Emissions and Circularity in the Cement and Concrete Industry"
September 18–22, 2023, Bangkok, Thailand

Effects of different types of shrinkage reducing agents on shrinkage properties of mortars incorporating slag or silica fume

B.B. Zhou[1], C.J. Shi[1*]

[1]Key Laboratory for Green & Advanced Civil Engineering Materials and Application Technology of Hunan Province, International Innovation Center for Green & Advanced Civil Engineering Materials of Hunan Province, Key Laboratory of Building Safety and Energy Efficiency of the Ministry of Education, College of Civil Engineering, Hunan University, Changsha, 410082, China
Email: beibeizhou@hnu.edu.cn
cshi@hnu.edu.cn

ABSTRACT

The effects of different types of shrinkage reducing agents (SRAs) on shrinkage of mortars containing slag or silica fume and their influence mechanisms on the shrinkage are not fully understood. This study aims to investigate the influences of small molecular-type and novel polymer-type SRAs on the shrinkage evolution of mortars incorporating ground granulated blast furnace slag (GGBFS) or silica fume (SF). The surface tension of pore solution and drying shrinkage of mortars containing GGBFS or SF were comprehensively investigated. The results indicated that the drying shrinkage of the GGBFS and SF cement mortars decreased with the increase of small molecular-type SRA dosage. Similarly, the addition of polymer-type SRA reduced the drying shrinkage of GGBFS and SF cement mortars, while the addition of 1% polymer-type SRA resulted in lower drying shrinkage than 2% polymer-type SRA. Compared to small molecular-type SRA, polymer-type SRA exhibited lower ability to decrease the drying shrinkage of the GGBFS and SF cement mortars.

KEYWORDS: *shrinkage reducing agent, drying shrinkage, mortar, slag, silica fume*

1. Introduction

Supplementary cementitious materials (SCMs) are widely used in concrete manufacturing by partially replacing cement to enhance the performance of cementitious materials and reduce carbon footprint (Juenger and Siddique (2015)). Some SCMs are industrial by-products such as ground granulated blast furnace slag (GGBFS) from pig iron industry and silica fume (SF) from ferrosilicon production (Lothenbach et al (2011)). The smaller grain size of GGBFS has been shown to increase autogenous and drying shrinkages compared to cement when used as a substitute for cement (Yalçınkaya and Yazıcı (2017)). SF exhibits higher pozzolanic activity and specific surface, compared to cement and GGBFS. It was found by Shen et al (2018) that SF increased the autogenous shrinkage due to the reduction of pore sizes and internal relative humidity (RH). Rao (2001) reported that the drying shrinkage of mortars containing higher SF content was observed to be 7-10 times higher than mortars without SF.
The shrinkage of mortar and concrete leads to deformation and cracking, which can affect the appearance of the building and even the safety of the structure. The application of shrinkage reducing agents (SRAs) is an effective technology for mitigating shrinkage cracking of cement-based materials. Zhang et al (2015) studied the effect of SRA (consisted of a hydrocarbon compound and a glycol ether system derivative) on the drying shrinkage of GGBFS mortar. The results showed that the addition of the SRA significantly reduced the drying shrinkage strains of ordinary Portland cement and low heat Portland cement mortars containing 45% GGBFS by total binder mass. However, the different dosages of SRA had an insignificant effect on the drying shrinkage of cement mortar with GGBFS. Folliard and Berke (1997) found that the drying shrinkages of normal concrete and SF concrete containing SRA at 28 d reduced by 28% and 52%, respectively, compared to the control concrete without SRA. Meanwhile, the drying shrinkage and cracks

of SF concrete with SRA reduced by 29% and 88% at 120 d, respectively. In spite of these efforts, the effect of different types of SRAs on the shrinkage of mortars containing GGBFS or SF and their influence mechanisms on the shrinkage are not fully understood. The complete understanding of these aspects is quite important for shrinkage control in concrete with GGBFS or SF.
The objective of this study is to clarify the influences of different types of SRAs with different dosage on the drying shrinkage evolutions of mortars incorporating different amount of GGBFS or SF. The surface tension and drying shrinkage measurements were performed.

2. Experimental

2.1 Raw materials

The cement used in this study was P·I 42.5 Portland cement conformed to Chinese Standard GB 8076-2008. The chemical compositions of cement, GGBFS and SF are presented in Table 1. The powder superplasticizer (SP) was used as an admixture. Diethylene-glycol monobutyl-ether (SRA-1) as a small molecule SRA was obtained from Shanghai Macklin Biochemical Co., Ltd (China). SRA-2 was a novel polymer-type shrinkage reducing agent and was obtained in laboratory.

Table 1 Chemical composition (%) of cement, GGBFS and SF.

Sample	CaO	SiO_2	Fe_2O_3	Al_2O_3	MgO	SO_3	Na_2O_{eq}	f-CaO	Loss	Cl^-
Cement	62.05	20.53	3.17	4.45	2.81	2.10	0.55	0.80	1.74	0.032
GGBFS	42.73	29.61	1.64	15.67	4.35	2.14	0.39	—	0.73	3.60
SF	1.84	95.38	0.61	—	0.26	—	0.16	—	1.84	2.48

2.2 Mix proportions

Table 2 summarizes the mixture proportions of mortars.

Table 2 Mix proportions of mortars.

Mix no.	Mix description	Binder (%)*			Water-to-binder ratio	Sand-to-binder ratio	SP (%)*	SRA-1 (%)*	SRA-2 (%)*
		Cement	GGBFS	SF					
M1	C	100	0	0	0.30	2	0.2	0	0
M2	10GGBFS	90	10	0	0.30	2	0.2	0	0
M3	20GGBFS	80	20	0	0.30	2	0.2	0	0
M4	10SF	90	0	10	0.30	2	0.3	0	0
M5	20SF	80	0	20	0.30	2	0.6	0	0
M6	C-1SRA-1	100	0	0	0.30	2	0.2	1	0
M7	C-2SRA-1	100	0	0	0.30	2	0.2	2	0
M8	10GGBFS-1SRA1	90	10	0	0.30	2	0.2	1	0
M9	10GGBFS-2SRA1	90	10	0	0.30	2	0.2	2	0
M10	20GGBFS-1SRA-1	80	20	0	0.30	2	0.2	1	0
M11	20GGBFS-2SRA-1	80	20	0	0.30	2	0.2	2	0
M12	10SF-1SRA-1	90	0	10	0.30	2	0.3	1	0
M13	10SF-2SRA-1	90	0	10	0.30	2	0.3	2	0
M14	20SF-1SRA-1	80	0	20	0.30	2	0.6	1	0
M15	20SF-2SRA-1	80	0	20	0.30	2	0.6	2	0
M16	C-1SRA-2	100	0	0	0.30	2	0.2	0	1
M17	C-2SRA-2	100	0	0	0.30	2	0.2	0	2
M18	10GGBFS-1SRA-2	90	10	0	0.30	2	0.2	0	1
M19	10GGBFS-2SRA-2	90	10	0	0.30	2	0.2	0	2
M20	20GGBFS-1SRA-2	80	20	0	0.30	2	0.2	0	1
M21	20GGBFS-2SRA-2	80	20	0	0.30	2	0.2	0	2
M22	10SF-1SRA-2	90	0	10	0.30	2	0.3	0	1
M23	10SF-2SRA-2	90	0	10	0.30	2	0.3	0	2
M24	20SF-1SRA-2	80	0	20	0.30	2	0.6	0	1
M25	20SF-2SRA-2	80	0	20	0.30	2	0.6	0	2

*by mass of total binder

2.3 Test methods

The surface tension was measured using a fully automatic surface tension meter (KINO A-601). Drying shrinkages of plain cement mortar and cement mortars containing GGBFS or SF in the absence and presence of SRAs were measured in accordance with JC/T603-2004.

3. Results and discussions

3.1 Surface tension

Effects of SRAs on surface tensions of supernatants of plain cement paste and GGBFS or SF cement pastes are illustrated in Fig. 1. In Fig. 1 (a), the surface tension decreased with the increase of SRA-1 content. The effects of SRA-1 on the surface tensions of supernatant solutions of plain cement paste and GGBFS or SF cement pastes were similar. The composition of SRA would lead to a difference in efficiency. As shown in Fig. 1 (b), the surface tensions of supernatant solutions of plain cement, 10% GGBFS, 20% GGBFS, 10% SF and 20% SF cement pastes significantly reduced by 31.47%, 31.96%, 32.26%, 29.92%, and 29.55%, respectively, due to the addition of 1% SRA-2. 2% SRA-2 exhibited a similar influence on the surface tension with 1% SRA-2. In presence of 2% SRA-2, the surface tensions of supernatant solutions of plain cement, 10% GGBFS, 20% GGBFS, 10% SF and 20% SF cement pastes were 48.783, 49.14, 49.3, 49.2, and 49.46 mN/m, respectively. The ability of decreasing surface tension of SRA-2 was higher than SRA-1.

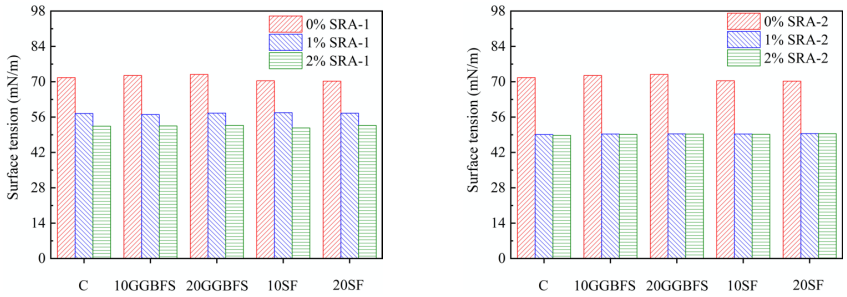

(a) SRA-1 **(b) SRA-2**

Fig. 1. Effects of SRAs on surface tensions of supernatants of cement pastes containing GGBFS or SF.

3.2 Drying shrinkage

The development of drying shrinkage of mortars containing GGBFS or SF in the absence and presence of different types of SRAs within 63 days is illustrated in Fig. 2. In Fig. 2 (a), 1% SRA-1 decreased the drying shrinkages of plain cement mortar, 10% GGBFS and 20% GGBFS cement mortars by 37.96%, 51.05%, and 59.95%, respectively, while 2% SRA-1 reduced their drying shrinkages by 57.74%, 64.34%, and 68.67%, respectively. In Fig. 2 (b), the addition of 1% SRA-1 decreased the drying shrinkages of 10% SF and 20% SF cement mortars by 61.65% and 54.03%, respectively, while 2% SRA-1 reduced their drying shrinkages by 68.45% and 61.41%, respectively. Fig. 2 (c) and (d) show the effects of SRA-2 on the drying shrinkage of all cement mortars. The drying shrinkages of all mortars in the addition of 1% SRA-2 were lower compared to 2% SRA-2. 1% SRA-2 decreased the drying shrinkages of plain cement mortar, 10% GGBFS and 20% GGBFS cement mortars by 48.90%, 41.86%, and 51.11%, respectively, while 2% SRA-2 reduced their drying shrinkages by 31.11%, 30.05%, and 29.44%, respectively. At the same time, the addition of 1% SRA-2 decreased the drying shrinkages of 10% SF and 20% SF cement mortars by 44.01% and 36.38%, respectively, while 2% SRA-2 reduced their drying shrinkages by 35.14% and 20.86%, respectively. The decreased drying shrinkage in the presence of SRA-1 and SRA-2 can be due to their reducing effect on the surface tension of pore solution, resulting in the reduction of capillary forces on the solid skeleton of the microstructure. Although the surface tension in the addition of SRA-2 was lower compared to SRA-1, the drying shrinkage of all cement mortars in the presence of SRA-2 was higher than SRA-1. This may be because that the drying shrinkage of cement-based materials is also related to their pore structure.

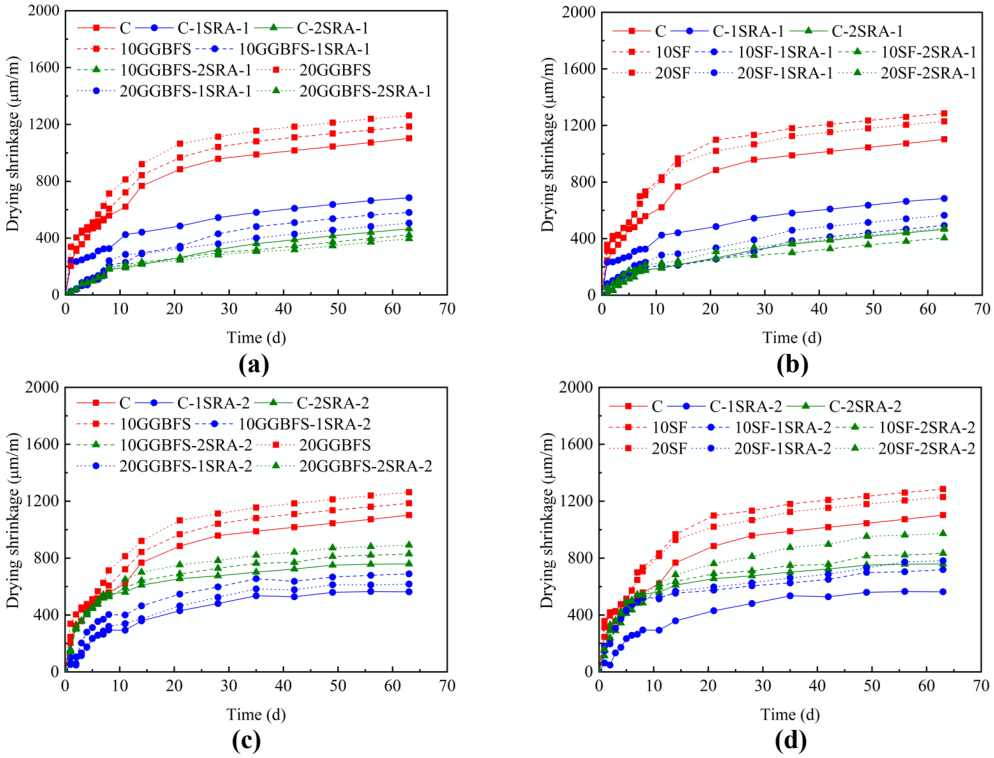

Fig. 2. Effects of SRAs on the drying shrinkages of mortars containing GGBFS or SF.

4. Conclusions

Based on results and discussions above, some conclusions can be obtained as follows:

(1) The surface tensions of supernatant solutions of GGBFS and SF cement pastes reduced with the increase of SRA-1 dosage. The ability of SRA-2 in reducing surface tension was higher than SRA-1.

(2) The drying shrinkage of GGBFS and SF cement mortars decreased with the increase of SRA-1 content. Similarly, it showed a reduction in the addition of SRA-2. However, it was lower in the addition of 1% SRA-2 compared to 2% SRA-2.

Acknowledgements

The authors gratefully acknowledge the financial supports from the Ministry of Science and Technology under Project No. 2018YFC0705400.

References

Folliard, K.J. and Berke, N.S. (1997) "Properties of high-performance concrete containing shrinkage-reducing admixture", *Cement and Concrete Research*, 27 (9): 1357-1364.

Juenger, M.C.G. and Siddique, R. (2015) "Recent advances in understanding the role of supplementary cementitious materials in concrete", *Cement and Concrete Research*, 78: 71-80.

Lothenbach, B., Scrivener, K. and Hooton, R.D. (2011) "Supplementary cementitious materials", *Cement and Concrete Research*, 41 (12): 1244-1256.

Rao, G.A. (2001) "Long-term drying shrinkage of mortar—Influence of silica fume and size of fine aggregate", *Cement and Concrete Research*, 31 (2): 171-175.

Shen, P., Lu, L., He, Y., Rao, M., Fu, Z., Wang, F. and Hu, S. (2018) "Experimental investigation on the autogenous shrinkage of steam cured ultra-high performance concrete", *Construction and Building Materials*, 162: 512-522.

Yalçınkaya, Ç. and Yazıcı, H. (2017) "Effects of ambient temperature and relative humidity on early-age shrinkage of UHPC with high-volume mineral admixtures", *Construction and Building Materials*, 144: 252-259.

Zhang, W., Hama, Y. and Na, S.H. (2015) "Drying shrinkage and microstructure characteristics of mortar incorporating ground granulated blast furnace slag and shrinkage reducing admixture", *Construction and Building Materials*, 93: 267-277.

The 16th International Congress on the Chemistry of Cement 2023 (ICCC2023)
"Further Reduction of CO_2 -Emissions and Circularity in the Cement and Concrete Industry"
September 18–22, 2023, Bangkok, Thailand

On the impact of sulphate source on admixtures in limestone calcined clay cements

S. Dhers[1*], B. Ecker[1], R. Guggenberger[1], B. Sachsenhauser[1], and P. Schwesig[1]

[1] Master Builders Solutions Deutschland GmbH, Dr-Albert-Frank-Strasse 32, 83308 Trostberg, Germany

Email: sebastien.dhers@mbcc-group.com

ABSTRACT

Calcined clays appear to be one of the most promising supplementary cementitious materials (SCMs) to reduce the CO_2 footprint of cement, in particular Limestone Calcined Clay Cement (LC^3). New and improved admixtures with tailored properties are necessary to ensure a broad implementation of LC^3 in the concrete industry. The high specific surface requires increased sulphation for these cements, which poses a challenge for admixtures. In this work, different LC^3 cements were prepared, by blending a CEM I (50 wt. %), two kaolinite based calcined clays (30 wt. %, specific surface area of 4.11 m^2/g or 27.79 m^2/g), limestone (15 wt. %) and two different sulphate sources (5 wt. %, gypsum or anhydrite). Two different superplasticizers, one conventional PCE-based slump retainer developed for ordinary concretes, and one new generation superplasticizer specifically suitable for LC^3 (labelled as SP1 and SP2, respectively) were used for this investigation carried out in concrete (Figure 1). This study highlights the robustness of a new generation of superplasticizers towards different calcined clays and sulphate sources, in respect to workability retention.

KEYWORDS: *Admixture, calcined clay, workability, sulphate, concrete*

1. Introduction

One of the most promising avenues to decarbonize the cement industry is lowering the clinker content of cement and to do so Supplementary Cementitious Materials (SCMs) are key (Scrivener et al., 2019). SCMs have been used in cement worldwide for many years, however traditional SCMs such as fly-ash and ground granulated blast furnace slag are waste by-products from CO_2 generating industries, whereas calcined clays have the advantage of both worldwide availability and lower CO_2 footprint (Hache et al., 2020). Calcined clays generally have a more demanding workability; admixtures and in particular superplasticizers are therefore essential to allow the widespread utilization of these new cements (Lei et al., 2020). In this work, two superplasticizers and two calcined clays have been used to investigate the impact of sulphate source on the workability.

2. Materials and methods

2.1 Materials

The two calcined clays used in this study are kaolin based calcined clays from Europe, with a metakaolin content respectively of 40% and 30% (as given by the provider) and a BET value of around 4.11 and 27.79 m^2/g, respectively, which are then abbreviated to reflect both these critical values: CC1-4 and CC2-28 (Table 1). The cement used in this study is an ordinary Portland cement CEM I 52.5 R, provided by

Schwenk GmbH. Particle size distribution and BET were measured for both calcined clay (Table 1), using Mastersizer 3000 (Malvern Panalytical) for PSD and a Nova 4000e (Quantachrom GmbH & Co. KG) for BET measurements done at 350°C. Two different superplasticizers provided by MBCC group were used in this study, SP1 and SP2, which are polymers with two different mechanisms for delayed action, based on acrylic acid and vinyl PEG monomers.

Table 1. Particle size and specific area of CEM I and calcined clays, and metakaolin content of calcined clays.

	d10	d50	d90	BET (m^2/g)	MK (%)
CEM I	0.89	7.77	26.50	1.49	-
CC1-4	1.12	9.84	34.33	4.11	40
CC2-28	1.66	12.76	51.09	27.79	30

2.2 Methods

Concrete mix designs: 380 kg/m^3 of total binder (including calcined clay and limestone) at w/b = 0,41 with a maximum aggregate size of 16 mm. As a descriptive example, LC^3-50 2:1 (2: 1 being the ratio of calcined clay to limestone) mix design have 190 kg/m^3 CEM I, 57 kg/m^3 limestone, 114 kg/m^3 calcined clay and 19 kg/m^3 of gypsum. The mixing sequence/time was as follow: 80 % water added up-front, consequently after 2 minutes the admixture in 20% water remaining is added to the mix, for a total mixing time 4 minutes (mixer: Pemat ZK 30, shear rate 60 rpm). Slump measurements: the procedure is analogous to DIN EN 12350-2, the DIN flow was adjusted to 60 cm. Compressive strength: the concrete mixes were each filled into concrete steel cubes (15/15/15 cm), and after 24h the hardened concrete cubes were demolded and stored at a temperature of 20 °C and relative humidity of 65%. The hardened concrete cubes were demolded and stored for 7 days at 20 °C in a water bath and further 21 days at 20 °C and relative humidity of 65% in a climate chamber. Compressive strength was measured at 1 day and 28 days adapted from DIN EN 12390-3.

3. Results and discussion

DIN flow measurements were reported in concrete to compare the dispersing performances of the two superplasticizers, namely SP1 and SP2, with an initial value target between 50 and 60 cm (Figure 1). Both superplasticizers are pure PCE-based polymers, using two different release mechanisms. Four different LC^3-50 systems have been tested, based on the combination of two calcined clays, low BET (CC1-4) and high BET (CC2-28) values, using two calcium sulphate sources, anhydrite and gypsum (Figure 1, shade of orange and red, respectively). To benchmark these LC^3 concretes, three different references were selected (Figure 1, shades of blue): pure CEM I, a CEM I and limestone reference in a 2.8:1 ratio (same amount of limestone as in the LC^3-50 mix design), and a CEM I and limestone reference in a 1:1 ratio (same amount of CEM I as in the LC^3-50 mix design). A low w/b ratio of 0.41, rather than higher such as 0.5, was selected to test the admixtures in a more challenging mix design.

SP1 shows fresh properties performances dependent on both the calcined clay and the sulphate source. Using anhydrite as a sulphate source, it is possible to reach a 2h open time using a 0.26% solid content of polymer to binder dosage for CC1-4, whereas the LC^3-50 mix containing CC2-28 reaches 1h30 open time with a higher dosage of 0.46%. When gypsum is used as the sulphate source, overall, a lower open time is obtained, whereas 1h30 is obtained using a dosage of 0.26% for CC1-4 and 1h with 0.52% dosage for CC2-28. When comparing the sulphate source, the workability of LC^3-50 mixes with both calcined clays is superior when using anhydrite versus gypsum. A possible explanation would be that the difference in

dissolution rate and solubility between gypsum and anhydrite affecting the competitive adsorption between the sulphates and the superplasticizer, which has a particularly bigger impact when calcined clays with higher surfaces are involved in the mix design (CC1-4 vs CC2-28). The influence of the calcined clay is clear and can be explained by a higher specific surface at a similar kaolin content: the BET value of the calcined clay alone appears to be a major factor influencing the workability of the entire concrete mix.

SP2 exhibits an impressive robustness with similar performances in all systems, both references and LC^3 mixes. The dependence on the sulphate source is not evidenced with this superplasticizer, as was the case for SP1, and 2 hours open time is reached with both calcined clays. Some refluidification is observed to different degrees for all systems, however it is important to note that this type of pure polymer is usually formulated to mitigate the observed refluidification – in this study both superplasticizers were used as pure polymer for direct comparison. The dosage needed is also higher compared to SP1, and when using CC2-28, two different dosages are needed depending on the sulphate source, 0.57% when anhydrite is used and 0.65% when gypsum is used, in line with the trends observed for SP1. This difference can likely be explained by the fact that a low BET calcined clay such as CC1-4 will have a smaller influence on the sulphate requirements than a higher BET calcined clay such as CC2-28 (Zunino et al., 2019).

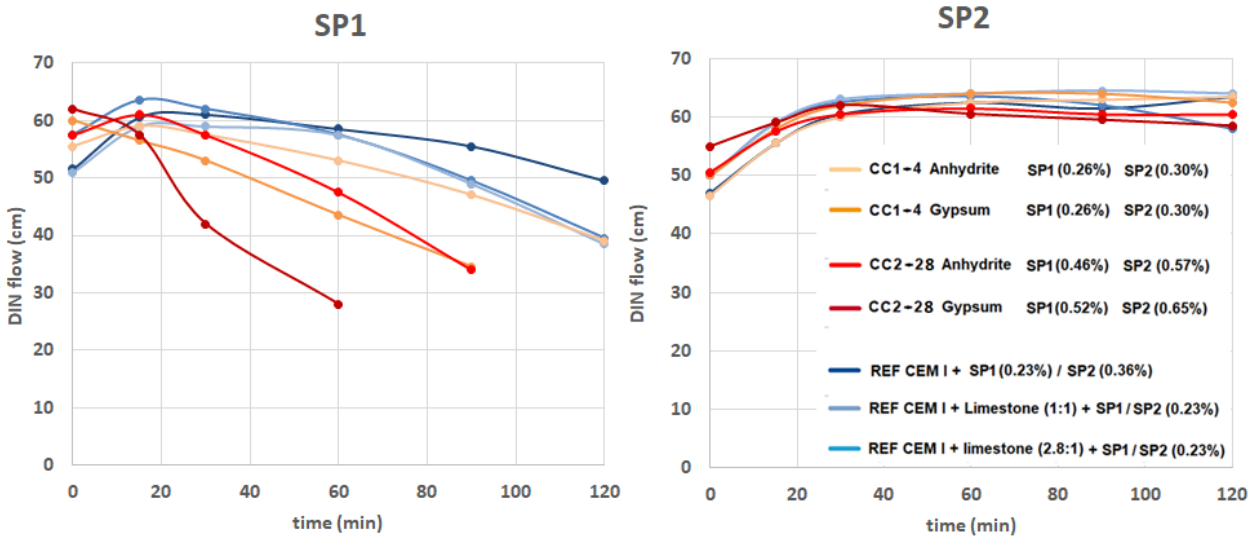

Figure 1. DIN flow values for concrete tests carried out at w/b = 0.41 in LC^3-50 mixes, using two calcined clays and two sulphate sources. Dosage (M.%bwoc active) for each superplasticizer shown in brackets in the legend.

Compressive strength values were measured at 1 and 28 days were measured for all systems (Figure 2). Interestingly, the type of admixtures has little impact on early strength for LC^3 mixes (Figure 2, 24h values) with SP2 showing slightly higher values than SP1. Overall, the compressive strength values at 1 day for LC^3 mixes are, as expected, significantly lower than the CEM I reference, as well as the reference with a 2.8:1 CEM I to limestone ratio. However, the 1:1 CEM I to limestone reference shows similar values as the LC^3-50 mixes, even slightly lower than the LC^3-50 mixes using SP2, evidencing that SP2 can have a beneficial effect on early strength, on top of offering a superior workability.

When discussing the late strength, the impact of the superplasticizer is more important (Figure 2, left vs right for 28 days). Compressive strength values for LC^3 mixes are roughly 10 MPa higher for SP2 than for SP1, which is quite a remarkable increase in late strength, around 15% for all 4 systems. References are also impacted by the superplasticizer but more importantly, using SP2 enables in these LC^3 systems to

reach the same late strength as a CEM I / limestone (2.8 : 1) blend, i.e. a lower CO_2 concrete using 190 kg/m^3 of CEM I instead of a concrete using 280 kg/m^3 of CEM I for the blend (Figure 2, right).

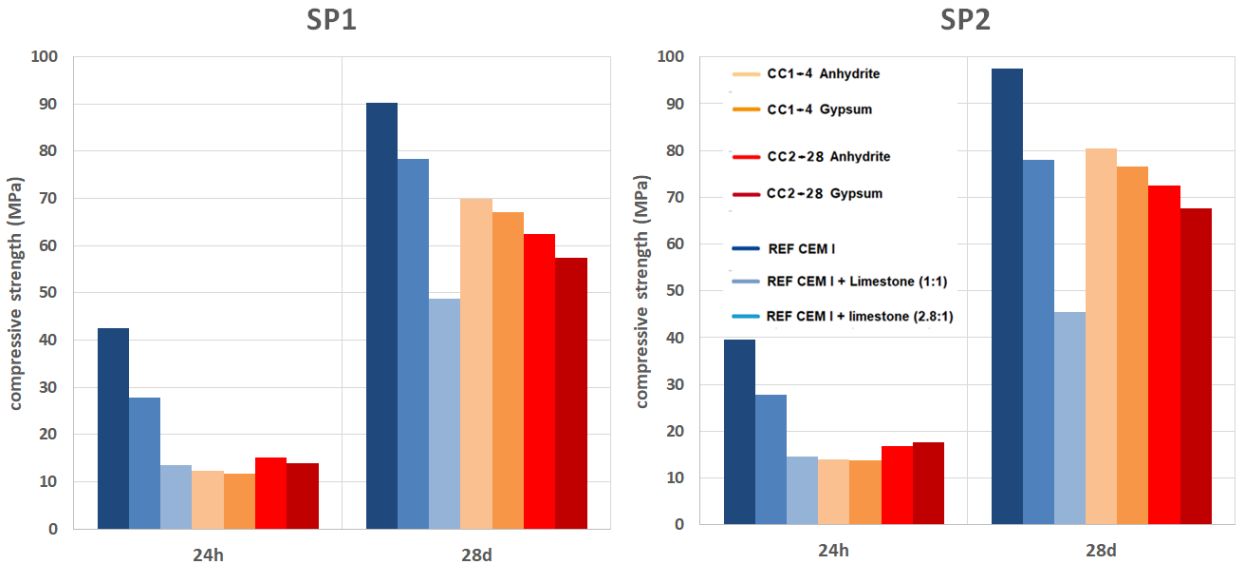

Figure 2. Compressive strength values at 24h and 28 days in concrete at w/b = 0.41 in LC^3-50 mixes, using two calcined clays and two sulphate sources.

4. Conclusion

In this work several LC^3-50 systems were tested for workability, as well as early and late strength, using low BET value (CC1-4) and high BET (CC2-28) calcined clays, and two sulphate sources, anhydrite and gypsum. SP1 showed good performances, with an interesting fresh properties performances dependence on both the calcined clay and the sulphate source. SP2 on the other hand exhibited an impressive robustness with similar performances in all LC^3 systems and references, in addition to an enhanced early and late strength enabling a substantial reduction of CO_2 content of the final concrete (190 vs 380 kg/m^3 CEM I).

Acknowledgements

This study was fully funded by MBCC Group.

References

Scrivener, K.; Avet, F.; Maraghechi, H.; Zunino, F.; Ston, J.; Hanpongpun, W.; Favier, A. (2019) "Impacting factors and properties of limestone calcined clay cements (LC3)"", *Green Materials*, 7: 3-14

Hache, E.; Simoën, M.; Seck, G. S.; Bonnet, C.; Jabberi, A.; Carcanague, S. (2020) "The impact of future power generation on cement demand: An international and regional assessment based on climate scenarios" *International Economics*, 163: 114-133

Lei, L.; Palacios, M.; Plank, J.; Jeknavorian, A. (2022) "Interaction between polycarboxylate superplasticizers and non-calcined clays and calcined clays: A review", *Cement and Concrete Research*, 154: 106717

Zunino, F.; Scrivener, K. (2019) "The influence of the filler effect on the sulfate requirement of blended cements", *Cement and Concrete Research*, 126: 105918

The 16th International Congress on the Chemistry of Cement 2023 (ICCC2023)
"Further Reduction of CO_2 -Emissions and Circularity in the Cement and Concrete Industry"
September 18–22, 2023, Bangkok, Thailand

A study on the adsorption and dispersion capability of PCEs with different structures on cement containing montmorillonite

Y. H. Ma[1] and C. J. Shi[2*]

[1] *College of Civil Engineering, Hunan University, Changsha, China*

Email: yhma@hnu.edu.cn

[2] *College of Civil Engineering, Hunan University, Changsha, China*

Email: cshi@hnu.edu.cn

ABSTRACT

Two conventional comb-like PCEs and a cross-linked PCE were synthesized in this paper. The rheological properties of paste containing different montmorillonite (MMT) contents in the presence of these PCEs were measured and the adsorption behaviors of these PCEs on MMT were investigated. Results show that compared to conventional PCE with carboxylate groups, the introduction of $-SO_3^-$ anchoring groups enhances the dispersion of PCE, and the paste with it exhibits lower yield stress and plastic viscosity. This is due to the lower adsorption of the PCE with $-SO_3^-$ groups on MMT and stronger dispersion to aggregated cement particles. In terms of PCE molecular structure, the cross-linked PCE has more arms that increase the intercalation efficiency on MMT, and the corresponding paste with it shows better workability.

KEYWORDS: *polycarboxylate ether superplasticizer, montmorillonite, adsorption, dispersion, intercalation*

1. Introduction

Polycarboxylate ether (PCE) superplasticizer has the advantage of a higher water reduction rate even at a lower dosage. However, it exhibits high sensitivity to clay (Lei and Plank 2014). Montmorillonite (MMT) is considered the most adverse mineral for the dispersion performance of PCE. The root cause for such strong inhibition in the dispersion power of PCE polymer is that PCE polymer is preferably adsorbed on clay contaminants, and is consumed by surface adsorption and intercalation (Ait-Akbour et al. 2015). This greatly decreases the workability of concrete and limits the application of PCE.

Compared to conventional PCE with carboxylate groups, the introduction of $-SO_3^-$ and $-PO_4^{2-}$ groups is beneficial to the enhancement of the dispersion capability of PCE due to their stronger attractive force (Qiu et al. 2011, Ran et al. 2016). However, there is no research on the effect of anchoring groups on the adsorption and dispersion capability of PCEs, and the interactions between PCEs with different anchors and MMT are unclear. The use of sacrificial agents and modification of PCE molecular structure are considered as the two approaches to enhance the tolerance of conventional PCE to MMT. However, these PCEs with special structures are synthesized by multi-steps, which increases the complexity and difficulty of the synthesis. The cross-linked polymer with much stronger steric hinderance benefits to disperse aggregated cement particles (Liu et al. 2014). Moreover, it can be prepared by a much simpler synthesis process than polymers with those novel structures. Thus, cross-linked PCEs are expected to decrease the negative effects of MMT on the flow of cement paste containing MMT.

This study synthesized two comb-like PCEs and a cross-linked PCE, and investigated their effects on the rheological properties of cement pastes without and with MMT. The interactions between PCEs and MMT were revealed. This paper provides enlightenment for further design and synthesis of PCE with stronger tolerance to MMT.

2. Materials and Methods

2.1 Materials

IPEG monomer (M_w = 2400 g/mol) purchased from Hunan CJS Building Materials Technology Co., Ltd, was used. Analytical grade acrylic acid (AA), sodium vinyl sulfate (Vs), trimethylolpropane trimethacrylate (TMPTA), ammonium persulfate (APS), mercaptopropionic acid (MPA), and sodium hydroxide (NaOH) were provided by Shanghai McLean Biochemical Technology Co., Ltd.
PO 42.5R Portland cement with a specific gravity of 3150 kg/m^3 and a specific surface area (Blaine) of 341 m^2/kg was supplied by China United Cement Group Co., Ltd. Clay was naturally Ca-MMT purchased from Xinyang penglai bentonite Co., Ltd (China).

2.2 Synthesis of PCEs

These PCEs were synthesized by free radical polymerization. Herein, comb-like PCEs with -COO^- and -SO_3^- groups, and the cross-linked PCE are named as CPCE, SPCE, and TPCE, respectively. The ratio of AA to IPEG is 3.5, and 0.5 mol AA was replaced by Vs to synthesize SPCE. The amount of the used cross-linker was 0.25% by the total mass of monomers.

2.3 Methods

Cement pastes with MMT replacements of 0%, 1%, 2%, and 3% by mass and PCE solutions were prepared, resulting in a water-to-powder ratio of 0.29. The mixed pastes were poured into the container immediately to measure the rheological properties on a rotational concentric rheometer (MCR 302, Anton Paar).
A mass of 1.5 g MMT was dissolved in 29 g synthetic pore solution with different concentrations of PCEs and then stirred using a magnetic stirrer. Then the suspension was centrifuged. The liquid was collected to measure the total organic carbon (TOC) content and the solid at the bottom of the centrifuge tube was collected and dried for X-ray diffraction (XRD) measurement.

3. Results and discussion

The H-B model was used to describe the rheological properties of pastes with the synthesized PCEs and the results are illustrated in Fig.1. Without MMT, the yield stress and plastic viscosity of cement pastes with these PCEs are in the same order of magnitude. However, they increase significantly with the incorporation of MMT, especially at high MMT contents, due to the adsorption of PCE on MMT. Compared to CPCE, the presence of SPCE decreases the rheological parameters of pastes, which indicates that SPCE shows better dispersion capability on the pastes containing MMT. The rheological properties of pastes are affected by PCE molecular structures. Paste with TPCE exhibits lower plastic viscosity than CPCE. This can be attributed to the stronger steric hinderance of TPCE with three arms and weaker interactions with MMT.

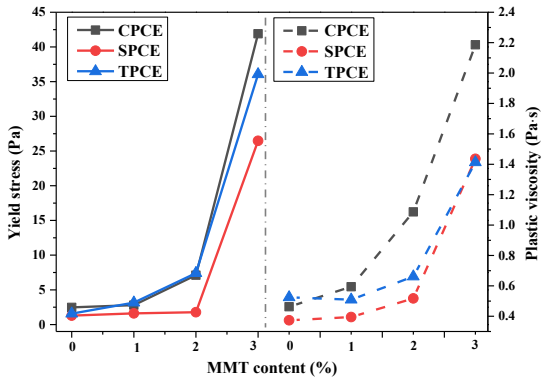

Fig.1 Rheological properties of pastes with these synthesized PCEs

The adsorption of the synthesized PCEs on MMT was measured and the result is shown in Fig.2. It can be seen that the adsorption amounts increase with the increased PCE concentrations. This is related to the physical and chemical adsorption of PCE molecules on MMT (Ma et al. 2020). It is well accepted that the lower adsorption of PCE on MMT results in its stronger tolerance to MMT (Lei et al. 2021). From Fig.2, SPCE shows lower adsorption on MMT than CPCE, which can explain the better rheological properties of paste with SPCE. However, TPCE has higher adsorption on MMT than that CPCE. This is related to their different molecular structures. Intercalation conformation of the side chains of PCE greatly depends on the molecular structure (Borralleras et al. 2020). Thus, it can be concluded that TPCE shows different intercalation modes than PCE with a comb-like structure.

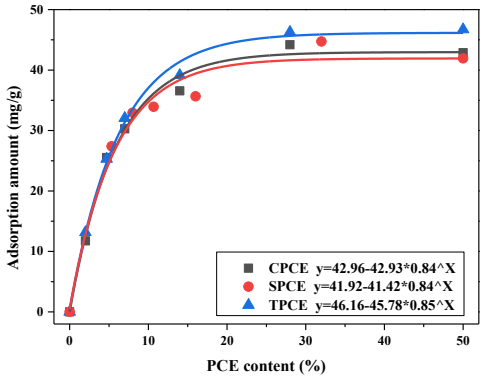

Fig.2 Adsorption of the synthesized PCEs on MMT

The XRD of MMT was conducted to investigate the intercalation behavior of CPCE and TPCE. According to the XRD pattern, the d-values of MMT are divided as 1.20 ± 0.05, 1.40 ± 0.05, and 1.70 ± 0.10 nm. The intercalation proportion of MMT was calculated and the result is shown in Fig.3. It can be seen that MMT has a lower intercalation proportion in the presence of TPCE, regardless of PCE concentrations. This indicates that the side chains of a single TPCE molecular can insert into multi-MMT particles, which enhances the intercalation efficiency and decreases the negative effects of MMT. Intercalation is the main hinderance to the dispersion of PCE (Ma et al. 2020, Lei et al. 2022). The less intercalation for TPCE contributes to its enhanced tolerance to MMT, which is in line with the results of the rheological properties of pastes.

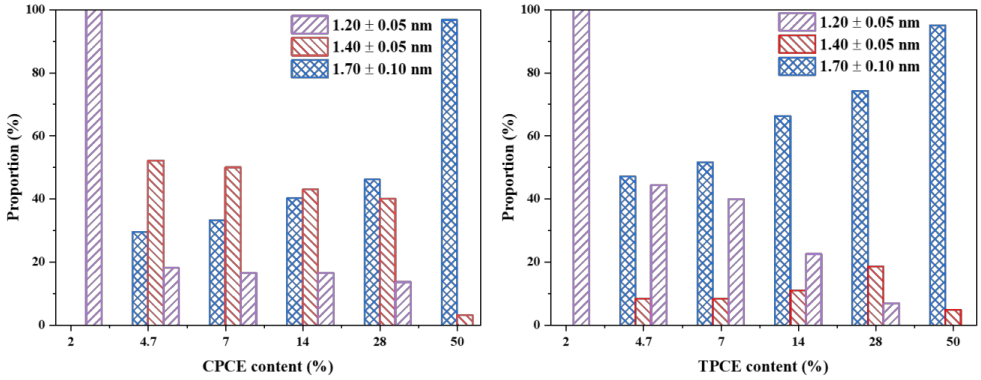

Fig.3 Intercalation proportion of MMT in the presence of CPCE and TPCE

4. Conclusions

This study synthesized two comb-like PCEs and a cross-linked PCE, and reported their effects on the rheological properties of cement pastes without and with MMT. Based on the analysis and discussion, the conclusions can be drawn.

(1) Regardless of MMT content, SPCE and TPCE show better dispersion capability than CPCE, as evidenced by the lower yield stress and plastic viscosity of pastes. This can be explained by their different interactions with MMT.

(2) SPCE has lower adsorption on MMT, which decreases the consumption of MMT to PCEs and enhances the dispersion capability of SPCE. Compared to comb-like PCEs, the less intercalation is attributed to the enhancement performance of TPCE on cement paste containing MMT.

Acknowledgements

The authors gratefully acknowledge the financial supports from the Ministry of Science and Technology under Project No. 2018YFC0705400.

References

Ait-Akbour, R., Boustingorry P. and Leroux, F. (2015) "Adsorption of Polycarboxylate Poly (ethylene glycol) (PCP) Esters on Montmorillonite (mmt): Effect of Exchangeable Cations (Na^{+}, Mg^{2+} and Ca^{2+}) and PCP Molecular Structure", *Journal of Colloid and Interface Science*, 437: 227-234

Borralleras, P., Segura, I. and Aranda, M. A. G. (2020) "Absorption Conformations in the Intercalation Process of Polycarboxylate Ether-based Superplasticizers into Montmorillonite Clay", *Construction and Building Materials*, 236: 116657

Lei, L., Palacios, M. and Plank, J. (2022) "Interaction Between Polycarboxylate Superplasticizers and Non-Calcined Clays and Calcined Clays: A Review", *Cement and Concrete Research*, 154: 106717

Lei, L. and J. Plank. (2014) "A Study on the Impact of Different Clay Minerals on the Dispersing Force of Conventional and Modified Vinyl Ether Based Polycarboxylate Superplasticizers", *Cement and Concrete Research*, 60: 1-10

Lei, L., Zhang, Y. and Li, R. (2021) "Specific Molecular Design of Polycarboxylate Polymers Exhibiting Optimal Compatibility with Clay Contaminants in Concrete", *Cement and Concrete Research*, 147:106504

Liu, H., Pang, H. and Ou, J. (2014) "Effect of Cross-Linked Polycarboxylate Type Superplasticizers on the Properties in Cementitious System", *Journal of Applied Polymer Science*, 131(19): 40856(40851-40858)

Ma, Y., Shi, C. and Lei, L. (2020) "Research Progress on Polycarboxylate Based Superplasticizers with Tolerance to Clays - A Review", *Construction and Building Materials*, 255: 119386

Qiu, X., Peng, X. and Yi, C. (2011) "Effect of Side Chains and Sulfonic Groups on the Performance of Polycarboxylate-type Superplasticizers in Concentrated Cement Suspensions", *Journal of Dispersion Science and Technology*, 32(2): 203-212.

Ran, Q., Ma, J. and Wang, T. (2016) "Synthesis, Characterization and Dispersion Properties of a series of Bis (phosphonic acid) amino-Terminated Polymers", *Colloid and Polymer Science*, 294(1): 189-198.

The 16th International Congress on the Chemistry of Cement 2023 (ICCC2023)
"Further Reduction of CO_2 -Emissions and Circularity in the Cement and Concrete Industry"
September 18–22, 2023, Bangkok, Thailand

Preparation and performance of EPEG-type PCE and its application in ultra-high performance concrete

Tong Xue[1]，Jie Bai[1*]，Wenying Xu[1]，Zuobao Song[2]，Ting Li[2]，Juan Li[3*]，Ruijun Gao[3]

[1] *China Building Materials Academy(CBMA), Beijing, China*
Email: xuetongcbma@163.com
[2] *CNBM Zhongyan Technology Co., Ltd., Beijing, China*
Email: zhongyankeji@chinasccm.com
[3] *Nonmetallic Excellence and Innovation Center for Building Materials, CBMA, Beijing, China*
Email: lijuan@cbma.com.cn

ABSTRACT: To improve the workability and mechanical properties of ultra-high performance concrete (UHPC), a novel EPEG-type ultra-high dispersion polycarboxylate superplasticizer (EPEG-type PCE) was developed by radical copolymerization reaction, and the effect of EPEG-type PCE on the workability, mechanical properties and durability of UHPC was investigated in this paper. The results show that the EPEG-type PCE can improve the workability and mechanical properties of UHPC at an appropriate dosage. However, there is a critical dosage for the effect of EPEG-type PCE on the early compressive strength and fluidity of UHPC, which is 1.5% (by mass of cement). The fluidity of UHPC does not improve any more when the dosage of EPEG-type PCE increases continuously after exceeding the critical point. The compressive strength decreases with the increase of EPEG-type PCE dosage when exceeding the critical point. The long-term drying shrinkage and electric flux of UHPC increased significantly with the increase of EPEG-type PCE dosage. The higher the dosage of EPEG-type PCE, the faster the increase of electric flux value of UHPC, and the worse the chloride ion penetration resistance of UHPC.

KEYWORDS: *UHPC, EPEG-type PCE, dosage, workability, compressive strength, shrinkage*

1. Introduction

UHPC is a kind of cement-based composite material born in the 1990s, which is characterized by extremely low water-binder ratio, dense accumulation of multiple fine particles and toughening with steel fiber[1]. It is widely used in strengthening and repairing bridges, building curtain walls, prefabricated buildings and other fields[2-4]. However, the shortcomings of UHPC are also very prominent. The workability of UHPC has become very poor due to the ultra-low water-binder ratio and ultra-high amount of cementitious materials, it is usually necessary to add a large amount of polycarboxylate superplasticizer (PCE) to improve its fluidity[5-6], and the role of superplasticizer becomes very critical. In this paper, a novel EPEG-type PCE with a high water reducing rate was synthesized, which successfully realized the ultra-high dispersion of cementitious particles under the condition of low water to binder ratio. The influence of EPEG-type PCE on the workability, mechanical properties and durability of UHPC was studied, and provide reference for the application of UHPC engineering.

2.Experiment

2.1 Materials

Ethylene glycol monovinyl polyethylene glycol ether (EPEG), self-developed; Acrylic acid (AA), hydrogen peroxide, ascorbic acid, and 3-mercaptopropanoic acid (3-MPA) purchased from Hongyan reagent factory of China.
Cement: PO 52.5, Tangshan Jidong Cement Co., LTD; Superfine mineral powder (SMP): 1250 mesh; Sand: quartz sand, 20~40 mesh and 40~80 mesh, Hebei; Silica fume (SF):,amorphous SiO_2 content is 95.8% and specific surface area greater than 20 m^2/g was purchased from Gansu Sanyuan Silicon Materials Co., Ltd; Steel fiber: copper-plated fiber with a diameter of 0.22 mm and a length of 13~15 mm. Polycarboxylate superplasticizer: EPEG-type PCE, solid content is 40%.

2.2 Synthesis of PCE

330 g EPEG, 3 g hydrogen peroxide and 210 g water were added to a four-necked flask with a stirring device. 60 g AA aqueous solution as A solution, and 103 g 3-MPA and ascorbic acid aqueous solution as B solution were dripped respectively into the flask at 20℃ for 1h. and then continued reaction at a constant temperature for 1h to obtain EPEG-type PCE.

2.3 UHPC mix design

The mix design of UHPC is shown in Table 1.

Table 1 Mix ratio of UHPC

Cement	SF	SMP	Sand 20~40 mesh	Sand 40~80 mesh	Steel fiber	Water
800	150	150	630	420	150	198

2.4 Test Methods

2.4.1 Structure characterization of EPEG-type PCE

Fourier transform infrared (FT-IR) measurements were performed by FT-IR spectrometer (TENSOR 27, BRUKER, Germany) and relative molecular mass was characterized by Gel Permeation Chromatography (GPC, BI-Molecular weight Analyzer, USA).

2.4.2 UHPC performance test

UHPC fluidity test: The test was carried out according to Chinese standard of GB/T 2419-2005 'Cement mortar fluidity determination method' without vibration.

Drying shrinkage and electric flux test of UHPC: refer to Chinese standard of GB/T 50082-2009 'Test method for long-term performance and durability of ordinary concrete'.

3.Results and discussion

3.1 Characterization of EPEG-type PCE

Fig.1 is the infrared spectrum of EPEG-type PCE. There is an obvious peak at 3442 cm^{-1}, indicating the stretching vibration absorption of -OH. A strong peak at 2889 cm^{-1} and multiple peaks suggest the stretching vibration absorption of alkyl saturated carbon (-CH_3, -CH_2, etc.). 1469 cm^{-1} is the stretching vibration absorption peak of saturated carbon C-H. 1243 cm^{-1} should be the stretching vibration absorption peak of C-O in the alcohol or ether structure, a strong absorption peak at 1109 cm^{-1} should be the stretching vibration absorption peak of -O- in the ether structure. The strong peak at 842 cm^{-1} should be the trans vibration absorption peak of enyne, and the out-of-plane bending vibration absorption peak of olefin C-H at 962 cm^{-1}. The above analysis results show that the polyether molecule includes the characteristic functional groups C=C, C-O, and -OH. According to the GPC data (Fig.2), the average molecular weight of the EPEG-type PCE is 36856 $g \cdot mol^{-1}$, the molecular weight distribution value (PDI) is 1.72, and the conversion rate is 96.34%.

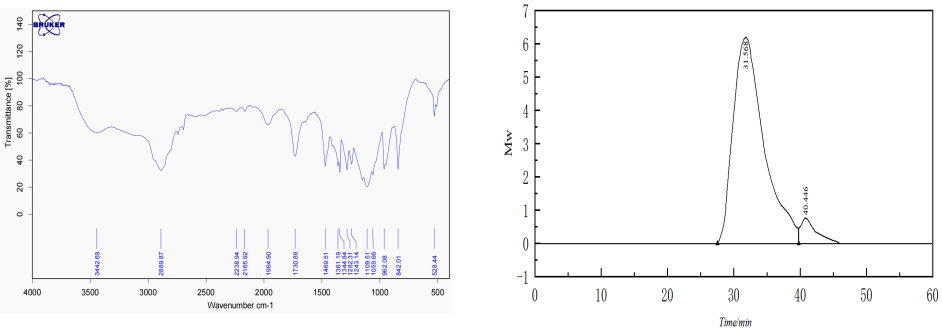

Fig.1 FT-IR of EPEG-type PCE

3.2 The effect of EPEG-type PCE dosage on the fluidity of UHPC

Table 2 shows the fluidity test results of UHPC with different EPEG-type PCE dosages. It can be seen from Table 2 that when the dosage of EPEG-type PCE is less than 1.5%, the amount of EPEG-type PCE

is positively correlated with the fluidity of UHPC. However, when the dosage of EPEG-type PCE is higher than 1.5%, this relationship is significantly changed. When the dosage of EPEG-type PCE is increased, the fluidity of the slurry remains stable and basically unchanged. Even when the dosage of EPEG-type PCE is very high, the fluidity tends to decrease slightly.

Table 2 Influence of dosage of EPEG-type PCE on fluidity of UHPC

PEC dosage %	0.5	1	1.5	2.0	2.5
Fluidity/mm	115	225	267	266	262

The dispersion mechanism of EPEG-type PCE on cement is the dual mechanism of adsorption, electrostatic repulsion and steric hindrance, which is dominated by steric hindrance, thus ensuring the good dispersion of EPEG-type PCE on cement particles. When the amount of water reducing agent exceeds the saturation point (Fig.3), the adsorption vacancies on the surface of cement particles are gradually occupied and saturated. At this time, the adsorption amount of EPEG-type PCE is almost no longer increased with the dosage of EPEG-type PCE, and the fluidity of paste is no longer increased as well. When the amount of water reducing agent is too high, the free molecules of EPEG-type PCE in the pore solution will crosslink with the molecules adsorbed on the surface of the rubber particles, thus reducing the slump flow of UHPC.

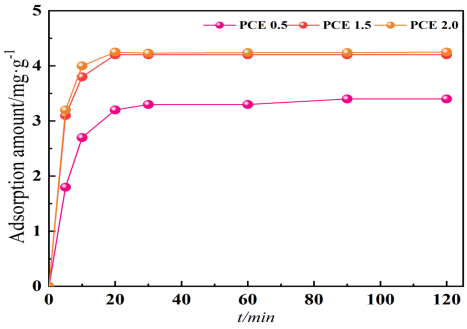

Fig.3 Adsorption capacity of EPEG-type PCE in binding material at different dosages

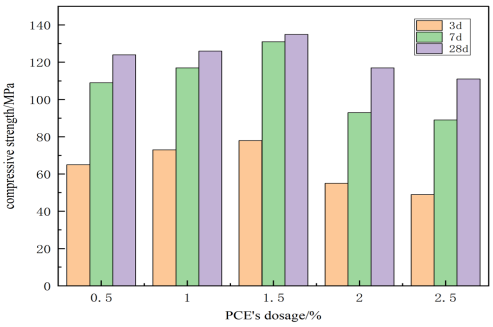

Fig.4 Compressive strength of UHPC with different dosage of EPEG-type PCE

3.3 Influence of dosage of EPEG-type PCE on compressive strength of UHPC

As shown in Fig.4. It can be seen that the dosage of EPEG-type PCE has a significant effect on the early strength of UHPC. Within a certain range, the early strength of concrete increases with EPEG-type PCE dosage, and the later strength develops steadily. When the dosage increased to 1.5%, the 3 d and 28 d compressive strength of UHPC increased to 78.6 MPa and 135.8 MPa respectively. While the water reduction dosage was 2.5%, the 3d and 28d compressive strength of UHPC decreased to 49.2 MPa and 111.9 MPa respectively. Before the saturated dosage point, the addition of EPEG-type PCE can release the flocculation water in the flocculation group of cement particles in the low water-binder ratio system and promote the hydration of cement particles. However, when the dosage of EPEG-type PCE exceeds the saturation point, EPEG-type PCE reacts with the free Ca^{2+} in the interstitial solution to form an unstable complex, which inhibits the hydration process and leads to the decrease of early strength. As the hydration process progresses, this unstable complex will decompose by itself, and hydration will continue normally.

3.4 Effect of EPEG-type PCE on durability of UHPC

3.4.1 Drying shrinkage

As shown in Table 3, The long-term drying shrinkage of UHPC increases significantly with higher PCE dosage, When the dosage of PCE increased from 1.0% to 1.5%, the drying shrinkage of UHPC increased by 9.4%. When the dosage of PCE increased to 2.0%, the drying shrinkage of UHPC reached 511×10^{-6}. The drying shrinkage of UHPC is due to the evaporation of water in the capillary pores and the gel. After the addition of PCE, the water in the system is relatively increased, and the size of the capillary pores is reduced. The greater the negative pressure generated due to the evaporation of water in the capillary pores, the more pronounced is the increase in negative pressure acting on the capillary pore wall, leading to enhanced drying shrinkage of UHPC[7].

Table 3 Drying shrinkage of UHPC with different EPEG-type PCE dosage

Age		Drying shrinkage/ $\times 10^{-6}$						
		1d	3d	7d	14d	28d	56d	90d
EPEG-type PCE dosage	1.0	93	154	276	331	402	431	443
	1.5	103	165	299	356	428	478	485
	2.0	132	209	324	376	444	501	511

3.4.2 Chloride penetration resistance

As Fig.5 shown, When EPEG-type PCE dosage is 1.0%, 1.5% and 2.0%, the electric flux values of UHPC are 100.3 C, 121.5 C and 145.7 C respectively. Compared to the electric flux at 1.0% dosage, it increases by 21.1% and 44.6% at dosage of 1.5% and 2% respectively, which indicates chloride ion penetration resistance decreases with the increase of dosage of EPEG-type PCE. This can be attributed to the low water to binder ratio, small porosity of hardened system, less internal interface defects and more active mineral admixtures in UHPC. The pozzolanic effect and secondary hydration reaction can effectively improve the pore structure of concrete.

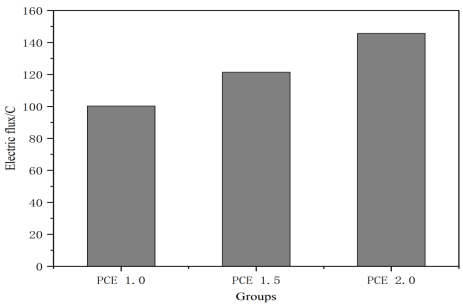

Fig.5 EPEG-type PCE on the electric flux of UHPC

4.Conclusions

A novel EPEG-type PCE was developed which can improve the workability and mechanical properties of UHPC at an appropriate dosage. When the dosage exceeds 1.5%, The slump of UHPC no longer increases with the increase of dosage of EPEG-type PCE and the compressive strength of UHPC gradually decreases. The drying shrinkage and electric flux of UHPC increase significantly with the increase of dosage of EPEG-type PCE, which indicates that the excessive addition of EPEG-type PCE will be detrimental to the durability of UHPC.

Acknowledgements

This study is sponsored by the program fund of NEXCEL, Non-Metallic Excellence and Innovation Center for Building Materials (Project No. 2022TDA3-1).

References

[1] Shi, C.J., Wu, Z., M, Xiao., J.F, et al. (2015) “review on ultra-high-performance concrete: Part I. Raw materials and mixture design”. Construction and Building Materials, (101): 741-751.

[2] Hao L W. (2013) “Preparation of polycarboxylic acid water-reducing agent for ultra-high strength RPC”, New Building Materials, (3): 27-28.

[3] Shao, Z.C, Guo, K.Y, Liu, S.W, et al. (2020) “Study on synthesis of high performance polycarboxylic acid water-reducing agent”. Chemical Industry and Engineering, 37(6): 30-37.

[4] Li F, Kong W Y, Luo J, et al. (2019) “Preparation and application of ultra-high performance concrete (UHPC)”, Concrete and Cement Products, (7): 26-29.

[5] Huang Z, Yang Y, Ran Q, et al. (2018) “Preparing hyperbranched polycarboxylate superplasticizers possessing excellent viscosity-reducing performance through in situ redox initialized polymerization method”. Cement and Concrete Composites, 93: 323-330.

[6] Shu X, Ran Q, Liu J, et al., (2016) “Tailoring the solution conformation of polycarboxylate superplasticizer toward the improvement of dispersing performance in cement paste”. Construction and Building Materials, 116: 289-298.

[7] TAM, C.M., TAM, V.W.Y., NG, K.M. (2012) “Assessing drying shrinkage and water permeability of reactive powder concrete produced in Hong Kong”. Construction and Building Materials, 26(1): 79-89.

The 16th International Congress on the Chemistry of Cement 2023 (ICCC2023)
"Further Reduction of CO_2 -Emissions and Circularity in the Cement and Concrete Industry"
September 18–22, 2023, Bangkok, Thailand

Development of ultra-fine SAP powder for lower-shrinkage and higher-strength cement pastes made with ultra-low water-to-binder ratio

Jianhui Liu[1,2,3*], Le Teng[4], Zheng Chen[1,2,3], and Caijun Shi[5]

[1] *Key Laboratory of Disaster Prevention and Structural Safety of China Ministry of Education, School of Civil Engineering and Architecture, Guangxi University, Nanning, PR China*
Email: liujianhui@gxu.edu.cn
[2] *State Key Laboratory of Featured Metal Materials and Life-cycle Safety for Composite Structures, Guangxi University, Nanning, PR China*
[3] *State Key Laboratory of Featured Metal Materials and Life-cycle Safety for Composite Structures, Guangxi University, Nanning, PR China*
[4] *School of Materials Science and Engineering, Southeast University, Nanjing, PR China*
[5] *Key Laboratory for Green & Advanced Civil Engineering Materials and Application Technology of Hunan Province, College of Civil Engineering, Hunan University, Changsha, PR China*

ABSTRACT

Superabsorbent polymer (SAP) as internal curing agent can effectively mitigate the autogenous shrinkage and promote cement hydration of ultra-high performance concrete (UHPC). However, it has a risk of impairing the mechanical performance of UHPC given the macro pores left. This study developed ultra-fine SAP powder aiming at securing the lower shrinkage and higher strength of UHPC. The influence of SAP powder on (average diameter (ds) of 5.78-60.85 μm) the water absorption/desorption characteristics, strength, shrinkage, and microstructure of cement paste with ultra-low water-to-binder ratio (w/b) was systematically studied. The results showed that the reduction of particle size of SAP can reduce the spacing distance of SAP in cement paste, which is beneficial for the internal curing, such as reducing the autogenous shrinkage, improving hydration of cement, and increasing the compressive strength.

KEYWORDS: *Autogenous shrinkage; Hydration; Internal curing; Microstructure; Superabsorbent polymer (SAP).*

1. Introduction

The objective of internal curing is to enable a higher internal relative humidity and a lower autogenous shrinkage in concrete by a subsequent release of water from pre-wetted lightweight aggregates (LWA) or superabsorbent polymers (SAP). The gradual release of internal curing water can also promote the hydration of cement. Compared to LWA, SAP can provide a more effective IC due to the higher water absorption.

The effectiveness of internal curing of SAP is related to the SAP chemical composition, content, and particle size. Zhong et al. found that the content of SAP is a factor that affects the internal curing of concrete. The internal curing efficiency or the reduced amplitude of autogenous shrinkage increased as the content of SAP increased. Besides, the size of SAP particles is a key factor on the internal curing efficiency for mitigating autogenous shrinkage. There is a controversy on the effect of particle size on the absorption capacity. The effect of SAP particle size on water adsorption and release characteristics can be influenced by other factors, such as the w/cm, which necessitates an in-depth study.

Because the moisture migration distance is reduced with the decrease of w/b given the dense microstructure. The particle size of conventional SAP currently studied ranges between 50 and 500 μm. The use of ultra-fine SAP can theoretically provide a larger internal curing zone compared to the conventional SAP because of larger specific surface area, which can enhance the cement hydration and reduce autogenous shrinkage of UHPC. However, the reduction of SAP particle size can influence the water adsorption and desorption characteristics, which might compromise the internal curing effect of SAP. Therefore, this study developed the ultra-fine SAP powder and characterized their water absorption and desorption capacity. The effect of

these ultra-fine SAP powder on the strength, shrinkage, and microstructure of paste phase of UHPC was investigated. The test results were used to determine the factors affecting the internal curing due to the variation of SAP particle size. A quantitative model that considers these factors was further established to understand the mechanism of SAP particle size on internal curing. The results of this paper aim to promote the application of using SAP to cure UHPC.

2. Raw materials、mixture proportion and experimental methods

2.1 Raw materials

The binder materials included P.I. 42.5 Portland cement and silica fume. A high-performance superplasticizer (SP) with a solid mass content of 23% was used in this study to enhance the workability (within 230±10 mm). The SAP powder used in this study was a cross-linked acrylamide/acrylic sodium copolymer, which is derived from manufacturers. The ratio of acrylamide and acrylic sodium is 0.3. The mean particle size of this commercially available SAP was 60.85 μm (noted as S0). Such SAP was ground into four sizes using an air pulverizer. The mean particle sizes of SAP powder were 45.46, 25.87, 11.55, and 5.78 μm, referring to S1, S2, S3, and S4, respectively.

2.2 Mixture proportion

The mixture proportions of cement paste are shown in Table 1.

Table 1 Mixture proportion of cement pastes with or without SAP powder

No.	Binder materials (%)		Total w/b	Additional w/b	SAP (%, by weight of binder)	SP (%, by weight of binder)
	Cement	Silica fume				
R0.18	80	20	0.18	0	0	2.0
R0.22	80	20	0.22	0	0	1.5
S0	80	20	0.22	0.04	0.3	2.0
S1	80	20	0.22	0.04	0.3	2.0
S2	80	20	0.22	0.04	0.3	2.0
S3	80	20	0.22	0.04	0.3	2.0
S4	80	20	0.22	0.04	0.3	2.0

2.3 Experimental methods

The test methods about ^{1}H nuclear magnetic resonance (NMR), Hydration heat, Autogenous shrinkage, Compressive strength, Hydration products and microstructure.

3. Results

3.1 Absorption/desorption properties of SAP

The T2 relaxation signals of cement paste was shown in Fig. 1. The intensity of the peak is presented using different colours. In order to quantify the water content of SAP powder at different time, the amount of water (α) absorbed/released by the unit weight of SAP over time was calculated according to the peak 2 intensity. In general, the water adsorption and desorption rates, as well as the maximum water absorption were shown to be influenced by the particle size of SAP powder. The bigger the particle is, the more pore fluid is absorbed into the cross-linked structure by its original mass.

3.2 Hydration heat

The SAP powder slowly released the water after reaching saturation point, thus promoting cement hydration., As hydration time increased, the heat flow rate of mixtures containing SAP powder was gradually greater than R0.22, which indirectly reflected the water release process of SAP powder.

On the other hand, it means that the increase in heat of hydration is not proportional to the decrease in SAP particle size. It is mainly because larger SAP particle had a lower absorption time and reduced the early-age hydration heat compared with smaller SAP. In addition, for cement-based materials with a certain

water-cement ratios (assuming the porosity is basically the same), there may be a threshold for the SAP particle size; if the particle size is below a certain value, the distribution of SAP particles can lead to a larger range of internal curing area, which is more beneficial for increasing hydration heat and this demonstrated that reduction SAP particle size promoted the early internal curing effect.

3.3 Autogenous shrinkage

Fig. 2 shows that the effect of particle size of SAP powder on autogenous shrinkage. The autogenous shrinkage of R0.18 and R0.22 mixtures were 2630 and 2011 με at 72h, respectively. This implies that the increase in w/b can reduce the autogenous shrinkage. The addition of SAP powder was more effective to reduce the autogenous shrinkage compared to the increase of w/b. This is because the water released form SAP powder can restrain the drop of relative humidity in cement paste.

3.4 Compressive strength

Figure 3 shows that the effect of w/b and particle size of SAP powder on the compressive strength at various ages. The addition of SAP powder and additional water led to a lower compressive strength compared to the reference UHPC made with w/b of 0.18. In fact, the use of conventional SAP can lead to 10-20% reduction in compressive strength of UHPC regardless of the internal curing effect of SAP. The lower decrease of compressive strength for UHPC made with finer SAP can be attributed to the smaller pores left after water desorption. With the increase of hydration age, the reducing amplitude of SAP group dropped because the enhanced cement hydration due to the internal curing effect of SAP compensated the influence of SAP pores on reducing the compressive strength. The influence of SAP particle sizes on compressive strength is mainly related to the spatial distribution and water absorption and release characteristics of SAP powder.

3.5 Hydration products

(1) TG and DTG analysis

The chemical bound water (CBW) and calcium hydroxide (CH) content were calculated. The CBW content increased with the increase of curing age and w/b. This was because the gradual release of water absorbed by SAP powder promoted the cement hydration. This also demonstrated that mixtures with a higher w/b exhibited a greater degree of cement hydration, which is consistent with the CBW content.And, the water absorbed by SAP powder gradually released to promote the hydration of cement, resulting in a higher content of CH. Such results were in an agreement with the variation of CBW content with SAP powder.

(2) 29Si NMR

The variation of 29Si NMR intensity of cement paste made with different particle sizes of SAP powder. The deconvolution results are shown in Table 4. The higher C and H values refers to greater degree of cement hydration and pozzolanic reaction of silica fume. The incorporation of SAP powder was also shown to increase the average C-S-H chain length, especially for the S2 and S3 SAP powder. Thus, it can be concluded that internal curing promotes the hydration of cement pastes, leading to the formation of long chain C-S-H, which is attributed to the continuing hydration of cement and increasing pozzolanic activity of silica fume.

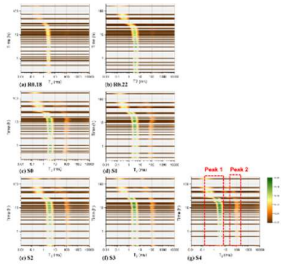

Fig. 1 T2 relaxation signal of cement paste containing with or without SAP powder

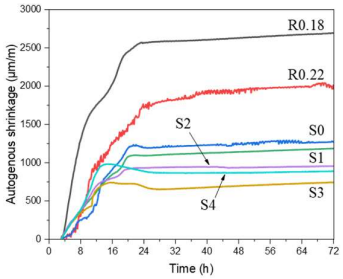

Fig. 2 Autogenous shrinkage of cement pastes with different particle sizes of SAP powder

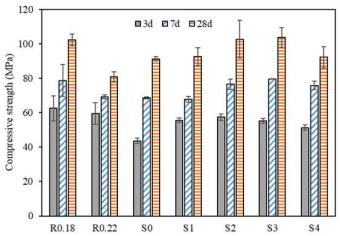

Fig. 3 Variation of compressive strength of cement pastes with different particles sizes of SAP powder

3. Conclusions

Based on the above experimental results and discussion, the following conclusions can be drawn: The maximum water absorption of reduced with decrease of SAP particle size; A linear relationship was found between the water absorption of SAP measured using 1H NMR and Tea bag method; The reduction of particle size of SAP decreased the spacing distance of SAP in cement paste, which benefits to the internal curing, and led to a reduction in autogenous shrinkage, improvement in cement hydration, and enhancement in compressive strength. The decrease of spacing distance between SAP particles and SAP water absorption led to a lower level of shrinkage when the total w/b was kept the same.

Acknowledgements

The authors gratefully acknowledge the financial supports of the science and technology innovation Program of Hunan Province (grant number 2020RC2034 and 2021JJ40079) and the National Natural Science Foundation of China (grant number 52208237).

References

L. Teng, A. Addai-Nimoh, K.H. Khayat. (2023) "Effect of lightweight sand and shrinkage reducing admixture on structural build-up and mechanical performance of UHPC", *Journal of Building Engineering*, 68 106144

Weina Meng and Kamal Khayat, C.K.Y. (2017) "Effects of saturated lightweight sand content on key characteristics of ultra-high-performance concrete", *Cement and Concrete Research*, 101: 46-54

L. Liu, Z. Fang, Z. Huang and Y. Wu. (2022) "Solving shrinkage problem of ultra-high-performance concrete by a combined use of expansive agent, super absorbent polymer, and shrinkage-reducing agent", *Composites Part B: Engineering*, 230(2): 105903

Liu JH, Shi CJ, Ma XW, Khayat KH, Zhang J and Wang DH. (2017) "An overview on the effect

of internal curing on shrinkage of high performance cement-based materials.", *Construction and Building Materials*, 146: 702-712

P. Zhong, Z. Hu, M. Griffa, M. Wyrzykowski, J. Liu and P. Lura. (2021) "Mechanisms of internal curing water release from retentive and non-retentive superabsorbent polymers in cement paste", *Cement and Concrete Research*, 14

J. Liu, N. Farzadnia, K.H. Khayat and C. Shi,. (2021) "Effects of SAP characteristics on internal curing of UHPC matrix", *Construction and Building Materials*, 280: 122530

J. Liu, X. Ma, and C. Shi, S . (2021) "Internal curing of blended cement pastes with ultra-low water-to-cement ratio: Absorption/desorption kinetics of superabsorbent polymer", *Journal of the American Ceramic Society*, 104: 3603-18

O.M. Jensen, and P.F. Hansen. (2002) "Water-entrained cement-based materials II. Experimental observations", *Cement and Concrete Research*, 32 : 973-978

J.H. Liu, N. Farzadnia, C.J. Shi and X.W. Ma. (2019) "Shrinkage and strength development of UHSC incorporating a hybrid system of SAP and SRA", *Cement and Concrete Composites*, 97: 175-89

K. Scrivener, R. Snellings, and B. Lothenbach. (2016) "A practical guide to microstructural analysis of cementitious materials", *Crc Press*

The 16th International Congress on the Chemistry of Cement 2023 (ICCC2023)
"Further Reduction of CO_2 -Emissions and Circularity in the Cement and Concrete Industry"
September 18–22, 2023, Bangkok, Thailand

New trend line of compressive strength and unit volume weight of cement composites: Lightweight and high-strength at the same time

Y. Jeong[1*], J.-I. Suh[2], J. H. Kim[3], Y. Cho[4], and S. Jung[5,] C.-W. Chung[6]

[1] *Construction Technology Research Center, Korea Conformity Laboratories (KCL), Seoul, Republic of Korea*

Email: yeonungjeong@kcl.re.kr

[2] *Construction Technology Research Center, Korea Conformity Laboratories (KCL), Seoul, Republic of Korea*

Email: rgtonesuh@kcl.re.kr

[3] *Construction Technology Research Center, Korea Conformity Laboratories (KCL), Seoul, Republic of Korea*

Email: kjhmole@kcl.re.kr

[4] *Construction Technology Research Center, Korea Conformity Laboratories (KCL), Seoul, Republic of Korea*

Email: young@kcl.re.kr

[5] *Construction Division, Korea Conformity Laboratories (KCL), Cheongju, Chungcheongbuk-do, Republic of Korea*

Email: jsh2593@kcl.re.kr

[6] *Department of Architectural Engineering, Pukyoung National University, Busan, Republic of Korea*

Email: cwchung@pknu.ac.kr

ABSTRACT

The relationship between compressive strength and unit volume weight of cement composites is an inverse relationship, indicating that, in general, high-strength composites have high unit volume weight and lightweight composites possess low compressive strength. This study aims to develop high-strength cement composites simultaneously with low-level unit volume weight and suggests mix designs for the composites with over 80 MPa of compressive strength and less than 1.6 g/cm^3 of unit volume weight at 28 days of curing age. The core constituents of the composites are ordinary Portland cement (OPC), silica fume, silica powder, artificial hollow microsphere, and lightweight fine aggregates, carbon nanotube suspension can be added for enhancing the compressive strength of the composites. The results indicate that compressive strength reaches 103 MPa with 1.53 g/cm^3 of hardened density at 28 days of curing age. The use of carbon nanotubes enhances early-age strength development without an increase in the hardened density of the composites.

KEYWORDS: *high-strength, lightweight, cement composite, hollow microsphere*

1. Introduction

The development of admixture technology has enabled the production of concrete with a water-to-cement ratio (w/c) of 0.2 or less, and concrete with a compressive strength of 150 MPa or more is known as ultra-high performance concrete (UHPC) (Zhu 2020). Cement, silica fume, quartz powder, quartz sand, superplastercizer, and steel fiber are typically used as the raw materials for UHPC (Shi 2015). A design method was proposed to maximize the internal packing of the particle size of the raw material used and reduce air gaps, which resulted in a high performance of 150 MPa or more (de Larrard 1994). To further enhance the mechanical performance of UHPC, high-temperature curing of up to 60 °C or 90 °C is

usually performed following curing, and rice husk ash, calcium carbonate powder, and nanomaterials are sometimes used as additional raw materials (Kang 2019a , Kang 2019b, Ghagari 2015).

On the other hand, the development of lightweight concrete by utilizing various lightweight materials is actively carried out. Concrete with a unit volume weight of 2,000 kg/m^3 or less is generally regarded as lightweight concrete (Yang 2013). A range of lightweight aggregates have been proposed for the production of lightweight concrete. Choi and Kim (2018) proposed using bottom ash and calcined artificial lightweight aggregate for lightweight concrete, while Kim et al., (2009) suggested the use of artificial lightweight aggregate derived from waste glass. Additionally, studies are being conducted to utilize materials such as palm oil shells as lightweight aggregates (Shafigh 2011).

It is commonly known that the strength and density of cement composites are inversely proportional. Lightweight concrete typically has a compressive strength of between 15 MPa and 40 MPa, and developing high strength is difficult. UHPC's density is known to be around 2.3 g/cm^3. Kılıç et al., (2003) reported that it was possible to produce a compressive strength of 43 MPa at 3 months of age at a unit volume weight of 1,944 kg/m^3 by using lightweight aggregate and admixture, but the strength level is still not enough to qualify as high-strength concrete. Furthermore, no substantial advances have been made in the development of lightweight high-strength concrete since then.

The objective of this study is to develop cement composites that are both lightweight and high-strength, by incorporating artificial microspheres and lightweight fine aggregate. The research presents the mixing conditions required to produce cement composites with specific properties, including a unit volume weight of 2,000 kg/m^3 at a compressive strength of 120 MPa, a unit volume weight of 1,800 kg/m^3 at a compressive strength of 100 MPa, and a unit volume weight of 1,600 kg/m^3 at a compressive strength of 80 Mpa.

2. Materials and Methodology

2.1 Materials

This study investigated the use of several materials in mix design of cement composites, including type I ordinary Portland cement (OPC), silica fume (SF), silica sand (SS), silica powder (SP), hollow microsphere (HMS), lightweight fine aggregate (LFA), and polycarboxylate superplasticizer (PCE). The LFA used in this study was a kind of expanded clay aggregate that was produced by Liapor GmbH & Co. KG in Deutschland. The SF and SP used in the study had smaller particle sizes than OPC, while HMS had a larger particle size. The unit weight of each material was 3,150 kg/m^3 for OPC, 2,200 kg/m^3 for SF, 2,650 kg/m^3 for SP, 2,648 kg/m^3 for SS, 600 kg/m^3 for HMS, and 1,770 kg/m^3 for LFA. The absorption rate of LFA was found to be 10 % at 3 days. These materials were mixed in various ratios to determine the optimal combination for lightweight and high-strength cement composites.

The mineral phase compositions of the raw materials were investigated using X-ray diffraction (XRD). The OPC used in this study was found to contain 51.0% C_3S, 32.7% β-C_2S, 9.0% C_4AF, 2.6% C_3A, 3.1% gypsum, and 1.7% anhydrite. The C_3A content of the OPC was slightly lower than that of typical Portland cement, but its light-weight consistency was consistent with the low Al_2O_3 content of the OPC. The SP was found to be composed of quartz (SiO_2) and a small amount of cristobalite (SiO^2), and SF was found to be amorphous containing a small amount of moissanite (SiC). The HMS was found to be composed of an amorphous phase containing no crystalline phase.

The solid content of the PCE used in this study was found to be 38.5%.

2.2 Mix Design and Curing Scheme

Three types of lightweight and high-strength cement composites were formulated according to the target compressive strength and unit weight, as outlined in Table 1. The target compressive strength for the first composite is 80 MPa with a unit weight of 1.6 g/cm^3, while for the second composite, it is 100 MPa with a unit weight of 1.8 g/cm^3. Finally, the third composite aims for a target compressive strength of 120 MPa at a unit weight of 2.0 g/cm^3.

The cement composite mixture described in Table 1 was cast into cylindrical specimens with dimensions of 10 cm in diameter and 20 cm in height. The specimens were then cured for 24 hours at a temperature

of 21°C and a relative humidity of 99%. After this initial curing period, the specimens were removed from their molds and placed in a chamber at a temperature of 90°C and a relative humidity of 99% for an additional 48 hours. Following this, the specimens were cured in a controlled environment at a constant temperature of 21°C and a relative humidity of 65% until the compressive strength measurements were taken.

Table 1. Mix design for lightweight and high-strength cement composites (unit: kg/m^3)

Label	Water	OPC	SF	SP	SS	HMS	LFA
1.6 // 80	212.5	739.1	110.9	208.0	0	211.0	111.0
1.8 // 100	212.5	739.1	110.9	208.0	255.0	152.0	115.0
2.0 // 120	195.5	739.13	110.87	208	513	101	125

3. Results

Figure 1 illustrates the compressive strength and unit weight results of the lightweight and high-strength cement composites developed in this study, in comparison to previous results of lightweight and high-strength concrete. The blue dots in Figure 1 indicate the results of this study. The results demonstrate a noticeable deviation to the left from the established trends of lightweight or high-strength concrete, suggesting that a cement composite can achieve both high strength and lightweight properties through appropriate mixing of HMS and LFA.

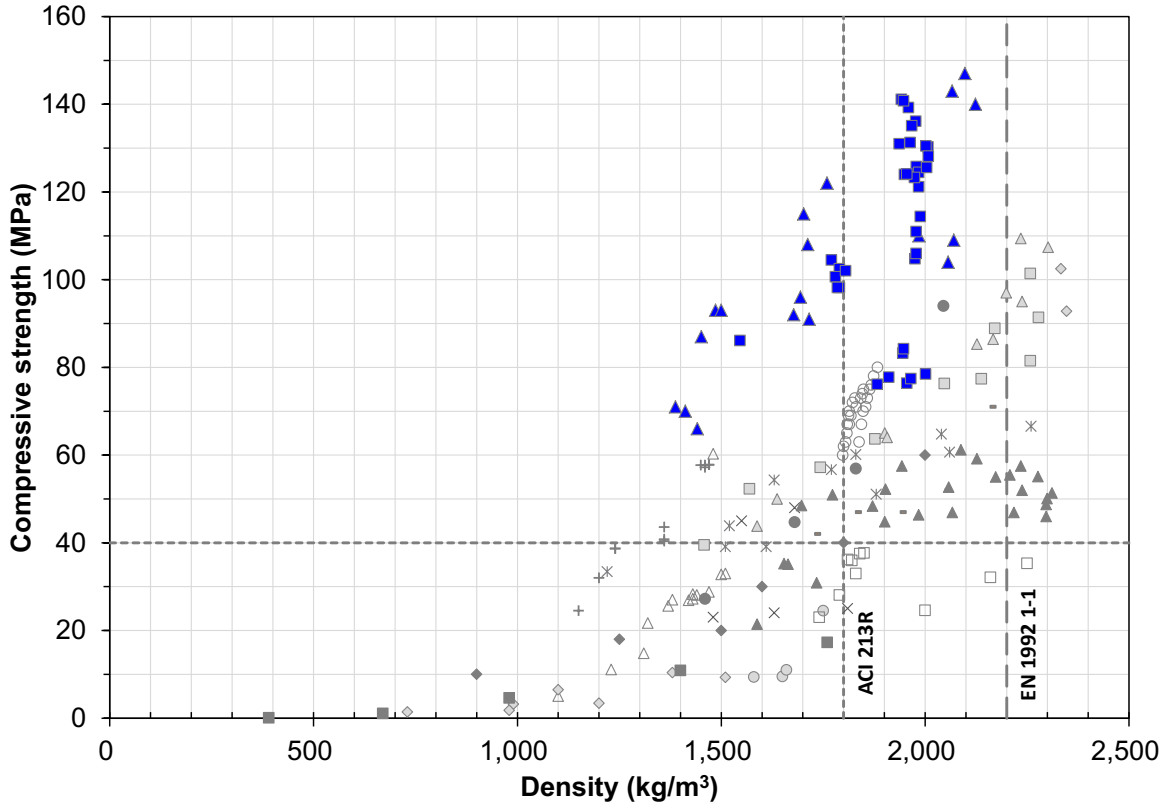

Figure 1. Results of compressive strength and density of hardened cement composites.

3. Conclusions

In this study, lightweight and high-strength cement composites were manufactured using hollow microspheres (HMS) and lightweight fine aggregate (LFA), and their compressive strength and density were investigated. The objective was to produce a lightweight and high-strength cement composite with compressive strengths of 80 MPa at a hardened density of 1.6 g/cm3, 100 MPa at a hardened density of 1.8 g/cm3, and 120 MPa at a hardened density of 2.0 g/cm3. As a result of the study, it was found that the proposed mixing conditions led to the target compressive strength being exceeded, even at a weight lower than the target density. The trend of compressive strength-density of the hardened body was clearly shifted to the left compared to previous research results, indicating that it is possible to manufacture a cement composite that is lighter and has excellent strength than previous results.

Overall, the results of this study suggest that incorporating HMS and LFA can effectively enhance the compressive strength of lightweight cement composites while also reducing their density. These findings have important implications for the development of sustainable construction materials that are both strong and lightweight.

Acknowledgements

This work is supported by the Korea Agency for Infrastructure Technology Advancement (KAIA) grant funded by the Ministry of Land, Infrastructure and Transport (RS-2020-KA156177).

References

Choi, H.-B. Kim, J.-M. (2018) “Fundamental properties of lightweight concrete with dry bottom ash as fine aggregate and burned artificial lightweight aggregate as coarse aggregate”, *Journal of Korean Recycled Construction Resources Institutute*, 6(4): 267-274

de Larrard, F. Sedran, T. (1994) “Optimization of ultra-high-performance concrete by the use of a packing model”, *Cement and Concrete Research*, 24(6): 997-1009

Ghagari, E. Costa, H. Júlio, E. (2015) “Critical review on eco-efficient ultra high performance concrete enhanced with nano-materials”, *Construction and Building Materials*, 101: 201-208

Kang, S.-H. Hong, S.-G. Moon, J (2019a) “The use of rice husk ash as reactive filler in ultra-high performance concrete”, *Cement and Concrete Research*, 115: 389-400.

Kang, S.-H. Jeong, Y. Tan, K.-H. Moon, J. (2019b) “High-volume use of limestone in ultra-high performance fiber-reinforced concrete for reducing cement content and autogenous shrinkage”, *Construction and Building Materials*, 213: 292-305

Kılıç, A. CAtiş, C. D. Yaşar, E. Özcan, F. (2003) “High-strength lightweight concrete made with scoria aggregate containing mineral admixtures”, *Cement and Concrete Research*, 33(10): 1595-1599

Kim, S.-S. Lee, J.-B. Nam, B.-R. Park, K.-P. (2009) “Performance evaluation of artificial lightweight aggregate mortar manufactured with waste glass”, *Journal of the Korea Concrete Institutute*, 21(2): 147-152

Shafigh, P. Jumaat, M. Z. Mahmud, H. (2011) “Oil palm shell as a lightweight aggregate for production high strength lightweight concrete”, *Construction and Building Materials*, 25(4): 1848-1853

Shi, C. Wu, Z. Xiao, J. Wang, D. Huang, Z. Fang, Z. (2015) “A review on ultra high performance concrete: Part I. Raw materials and mixture design”, *Construction and Building Materials*, 101: 741-751

Yang, K.-H. (2013) “Mix design of lightweight aggregate concrete and determination of targeted dry density of concrete”, *Journal of the Korea Institute of Building Construction*, 13(5): 491-497

Zhu, Y. Zhang, Y. Hussein, H. H. Chen, G. (2020) “Flexural strengthening of reinforced concrete beams or slabs using ultra-high performance concrete (UHPC): A state of the art review”, *Engineering Structures*, 205: 110035

The 16th International Congress on the Chemistry of Cement 2023 (ICCC2023)
"Further Reduction of CO_2 -Emissions and Circularity in the Cement and Concrete Industry"
September 18–22, 2023, Bangkok, Thailand

Strength Development Prediction and Mixture Optimization of Concrete Used in the Three Gorges Dam

X.H. Xu[1], Z.L. Hu[2], J.P. Liu[3*], W.W. Li[4]

[1] *School of Materials Science and Engineering, Southeast University, Nanjing, China*
Email: seumaturity@163.com
[2] *School of Materials Science and Engineering, Southeast University, Nanjing, China*
Email: zhanglihu@seu.edu.cn
[3] *School of Materials Science and Engineering, Southeast University, Nanjing, China*
Email: liujiaping@cnjsjk.cn
4 China Three Gorges Corporation, Beijing, China
Email: li_wenwei@ctg.com.cn

ABSTRACT

Machine learning (ML) based strength development prediction and mixture optimization of the massive concrete used in the Three Gorges Dam have benefits on efficiency and accuracy, providing guidance for mixture design employed in dam maintenance and other concrete constructions. This study established a relationship between material properties and strength development based on the compressive strength (CS) development data of concrete used in the main project of Three Gorges Dam with a time span of more than 20 years. A comprehensive determination method of the weight of strength influencing factors is proposed by combining models based on decision tree (DT) and statistical analysis. The water-to-cement ratio (W/C) and cement content are found to be the key feature parameters dominating the CS of the Three Gorges Dam concrete. For strength development prediction, the prediction efficiency of the commonly used ML regression model on concrete strength development are discussed. Meanwhile, this study presents a concrete mixture optimization method based on ML and multi-objective evolutionary algorithm (MOEA). NSGA-II and MOEA/D are used as the optimization model. By simultaneously optimizing multiple objectives (different development strength) with multiple variables (features), the Pareto fronts of the Three Gorges Dam concrete mixture optimization problem for strength development is successfully obtained.

KEYWORDS: *Strength development, Three Gorges Project, Machine learning, Multi-objective evolutionary algorithms, Mixture optimization*

1. Introduction

China is currently the country with the most high-arch dams under construction and in operation in the world, with the majority of dams using medium-heat and low-heat cement concrete (Fan et al (2017)). In previous mixture designs, low-heat cement concrete generally exhibited low early strength and high later strength growth, while medium-heat cement concrete exhibited high early strength but low later strength (Ji et al (2012)). To meet the requirements for high early strength during dam construction and high later strength for long-term loading, as well as to support the construction of the world's largest "clean energy corridor" in China, it is urgent to explore the laws of strength development and develop a mixture design that couples excellent early and later strength. However, traditional mixture design based on empirical methods suffer from problems such as large-scale experimentation, high economic costs, and significant environmental impact, leading to high carbon dioxide emissions and waste of precious resources. However, ML methods represent a new low-carbon path that can overcome the limitations of traditional empirical methods and predict the strength development of dam concrete and optimize mixture.
ML methods have been employed to identify crack behavior (Dai et al (2018)), predict deformation and monitor structural health (Kang et al (2020)), perform reliability analysis (Hariri-Ardebili and Pourkamali-

Anaraki (2018)) for concrete used in dams. In the field of using ML methods to predict concrete CS and optimize mixture, domestic and foreign scholars have conducted extensive research. ML methods for predicting CS include artificial neural network (ANN), support vector machine (SVM), DT, and others. These methods have achieved excellent prediction results for concrete materials such as ordinary concrete (Young et al (2019)) and high-performance concrete (Chou et al (2014)), etc. Research have been conducted using ML to evaluate the effects of industrial waste and curing methods on the strength development in geopolymer concrete (Ghosh and Ransinchung (2022)). Zhang et al. (Zhang et al (2020)) proposed a concrete mixture optimization method based on ML and metaheuristic algorithms, and successfully solved the bi-objective mix design optimization problem for high-performance concrete.
In this paper, for the strength development data of Three Gorges Dam concrete with a time span of more than 20 years, we analyzed the key features that affect the CS and predicted the strength development by using common ML. Furthermore, we employed a mixture optimization method based on ML and MOEA to obtain the Pareto front of mixture optimization for strength development.

2. Data and Methodology

2.1 Structured Data Sets

The structural data sets for predicting 7-day CS, 90-day CS and strength development were constructed. The data set for predicting strength development extracted the days of CS from the output targets with "day strength factor" as the input feature. The total sample size is 11,251, including 14 input features of mixtures and raw materials properties and one output target of CS without days label. The data sets of 7-day CS and 90-day CS retained 7 input features of optimizable continuous data, with total sample sizes of 1385 and 2814. 7-day CS and 90-day CS are used as output targets. For models based on ANN and SVM, the datasets should be normalized and (0,1) normalization was adopted in this study (Bishop and Nasrabadi (2006)).

2.2 ML Methods

2.2.1 Methods Used in Predicting Strength Development and CS

The Multilayer Perceptron Regression (MLPR), Random Forest Regression (RFR), and Epsilon-Support Vector Regression (SVR) were used to predict strength development and CS. For ML regression problems, R^2 and MSE are commonly used as evaluation criteria for model performance.

2.2.2 Methods Used in Feature Engineering (FE)

The regression method of eXtreme Gradient Boosting (XGBR) was used to evaluate the feature importance of influence strength development, and the influence of different normalization methods was considered.

2.3 MOEA Methods

In this study, MOEA adopted NSGA-II and MOEA/D. NSGA-II is a MOEA based on genetic algorithms and its main idea is to maintain population diversity and convergence by dividing the population into multiple different ranks and calculating the crowding distance of each individual, thereby effectively solving the Pareto front. MOEA/D is a popular MOEA, which determines the score of each solution on different objective functions by using the weight vectors, uses Tchebycheff decomposition formula to combine multiple objective functions into one function to optimize each subproblem, and finds the Pareto front by iteratively optimizing the subproblems and adjusting the weight vectors.

3. Results and Discussion

3.1 FE for Influence Strength Development

The three radar charts in Fig 1 show the feature importance of XGBR in the concrete strength development under different normalization methods. Combining all charts, it can be found that the weight values and ranking trends of each feature are basically consistent regardless of whether the dataset is normalized and which normalization method is used. From each chart, it can be seen that the W/C, cement content, and day strength factor have prominent feature weights. According to Pearson correlation analysis based on statistics, W/C, cement content, and day strength factor all have high correlation with CS in the data set for predicting strength development, which are -0.52122, 0.42381, and 0.34117.

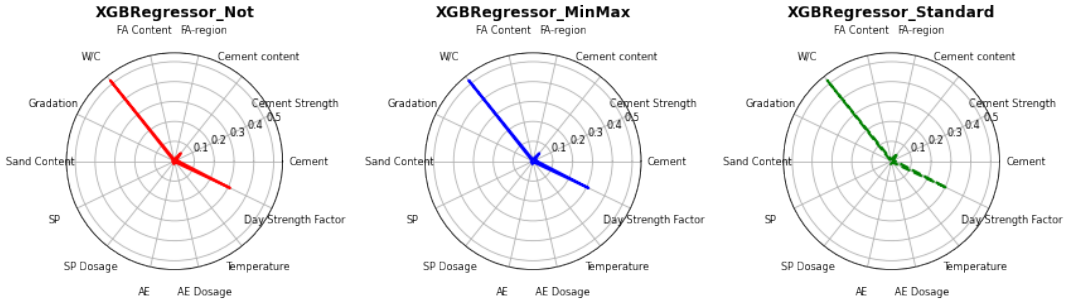

Fig 1. Feature importance of concrete strength development based on XGBR: Not normalized; (0,1) normalization; Z-score standardization

3.2 Strength Development Prediction

MLPR, SVR, and RFR were used to construct models for predicting the strength development. The performance of models was studied with default hyperparameters and hyperparameters optimized using GridSearchCV. Performance evaluation was based on 5-fold cross-validation. Fig 2 shows the comparison of the performance of various models on the training set. It can be found that the optimized RFR has the highest R^2 and the lowest MSE, which has relatively excellent fitting and bias. The hyperparameter is max_depth=13 and n_estimators=140. Fig 2 also shows the residual distribution of the optimized RFR on the training and testing sets. It can be observed that, except for a few outliers, the residual distributions are generally consistent, indicating the optimized RFR has a preferable predictive performance and robustness.

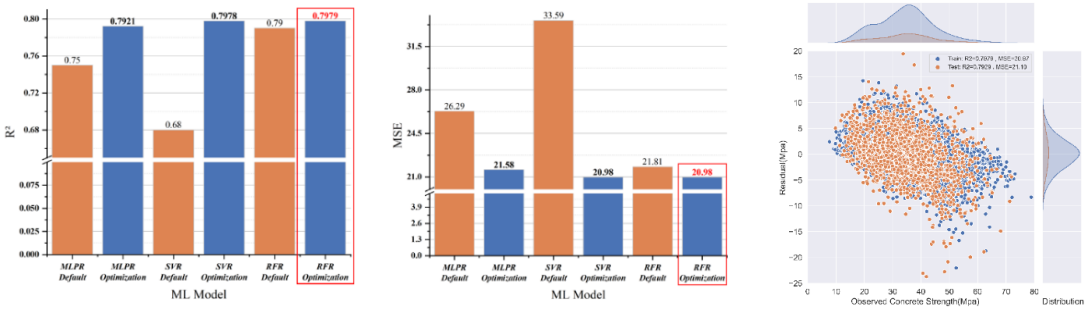

Fig 2. Comparison of performance on the training set among ML models and residual distribution of the optimized RFR model on the training and testing sets (For strength development prediction)

For the prediction of early and late CS, the optimized RFR also had the best performance on the training set compared to MLPR and SVR before and after optimization. The optimized RFR hyperparameters for 7-day CS and 90-day CS are max_depth=9 and 8, n_estimators=50 and 140, respectively. The predictive performance in the test set is also excellent. For 7-day CS and 90-day CS, R^2=0.7059 and 0.6361, MSE= 15.47 and 28.19. The optimized RFR can be used as the objective functions of multi-objective optimization.

3.3 Mixture Optimization for Strength Development

Based on the objective of maximizing both 7-day CS and 90-day CS as the goal, multi-objective optimization was performed using NSGA-II and MOEA/D. In this study, the population size of NSGA-II was 50, and other parameters were default values. MOEA/D was set to 50 reference directions, 15 neighbors, and a 70% probability of mating. The total iterations were 500 for both. The constraint conditions were set based on the datasets of 7-day and 90-day CS, and Table 1 shows the range constraints and ratio constraints.

Table 1. Range constraints and ratio constraints in multi-objective optimization

	Contents	Unit	Constraint value
Range constraints	Cement content	Kg/m^3	[70,450]
	Temperature	℃	[0,32]
	7-day CS	Mpa	[9.2,54]
	90-day CS	Mpa	[16.3,70.8]
Ratio constraints	W/C	/	[30,68] %
	Fly ash content	/	[0,98] %
	Sand content	/	[18,63] %
	Superplasticizer dosage	/	[0.3,2] %
	Air entrain admixture dosage	/	[0,7] %

Fig 3 shows the Pareto front of the optimized mixture for the Three Gorges Dam concrete and the actual engineering data. It can be seen that the two MOEA methods successfully and stably solved the Pareto front, and the Pareto solution set achieved preferable optimization of maximizing both the 7-day and 90-day CS.

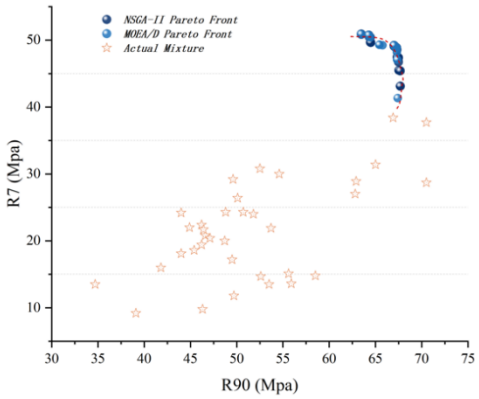

Fig 3. The Pareto front of optimized mixture based on 7-day CS and 90-day CS

4. Conclusions

This study mainly focused on FE, strength prediction, and mixture optimization for strength development. In terms of FE, based on the comprehensive evaluation method of influence factor weights, it was determined that normalization has little effect on the ranking of feature weights, and W/C and cement content are key factors affecting the CS. In terms of strength development prediction, the RFR with 13 max_depth and 140 n_estimators was found to have preferable predictive performance. In terms of mixture optimization, the Pareto front of the Three Gorges Dam concrete strength development optimization problem was successfully solved using NSGA-II and MOEA/D.

Acknowledgements

This work was financially supported by the Joint Program of National Natural Science Foundation of China (U2040222).

References

Fan, Q.X., Li, W.W. and Li, X.Y. (2017) "Key construction technologies of low heat Portland cement dam concrete", *Journal of Hydroelectric Engineering*, 36(4): 11-7

Ji, T., Ji, G. and Chen, G. (2012) "Influence of low-heat Portland cement on properties of dam concrete", *Journal of Hydroelectric Engineering*, 31(4): 207-10

Dai, B., Gu, C., Zhao, E., et al. (2018) "Improved online sequential extreme learning machine for identifying crack behavior in concrete dam", *Advances in Structural Engineering*, 22(2): 402-12

Kang, F., Liu, X. and Li, J. (2020) "Temperature effect modeling in structural health monitoring of concrete dams using kernel extreme learning machines", *Structural Health Monitoring*, 19(4): 987-1002

Hariri-Ardebili, M.A. and Pourkamali-Anaraki, F. (2018) "Support vector machine based reliability analysis of concrete dams", *Soil Dynamics and Earthquake Engineering*, 104: 276-95

Young, B.A., Hall, A., Pilon, L., et al. (2019) "Can the compressive strength of concrete be estimated from knowledge of the mixture proportions?: New insights from statistical analysis and machine learning methods", *Cement and Concrete Research*, 115: 379-88

Chou, J.S., Tsai, C.F., Pham, A.D., et al. (2014) "Machine learning in concrete strength simulations: Multi-nation data analytics", *Construction and Building materials*, 73: 771-80

Ghosh, A. and Ransinchung, G.D. (2022) "Application of machine learning algorithm to assess the efficacy of varying industrial wastes and curing methods on strength development of geopolymer concrete", *Construction and Building Materials*, 341

Zhang, J., Huang, Y., Wang, Y., et al. (2020) "Multi-objective optimization of concrete mixture proportions using machine learning and metaheuristic algorithms", *Construction and Building Materials*, 253

Bishop, C.M. and Nasrabadi, N.M. (2006) *Pattern recognition and machine learning*, Springer.

The 16th International Congress on the Chemistry of Cement 2023 (ICCC2023)
"Further Reduction of CO_2 -Emissions and Circularity in the Cement and Concrete Industry"
September 18–22, 2023, Bangkok, Thailand

Design of High-Performance Concrete (HPC) using calcined clay as supplementary cementitious materials

J. K. Das[1*], N. Manhas[2], S. Bishnoi[3], S. Bansal[4] and A. Shukla[5]

[1]*Department of Civil Engineering, Indian Institute of Technology Delhi, New Delhi, India*
Email: jk.das@iitg.ac.in
[2]*Department of Civil Engineering, Indian Institute of Technology Delhi, New Delhi, India*
Email: numairmanhas@yahoo.com
[3]*Department of Civil Engineering, Indian Institute of Technology Delhi, New Delhi, India*
Email: bishnoi@civil.iitd.ac.in
[4]*Department of Civil Engineering, Indian Institute of Technology Delhi, New Delhi, India*
Email: sahil.bansal@civil.iitd.ac.in
[5]*Department of Civil Engineering, Madhav Institute of Technology & Science, Gwalior, Madhya Pradesh, India*
Email: abhilash.shukla29@mitsgwalior.in

ABSTRACT
Ultra-High Performance Concrete (UHPC), incorporated with supplementary cementitious materials (SCMs), is a relatively new construction material with excellent mechanical and durability properties. The good pozzolanic characteristics and abundant availability of calcined clay make it an excellent SCM for UHPC. The present experimental work investigates the effect of different percentages of calcined clay replacement on the fresh properties and compressive strength of UHPC. In addition, the chloride penetration resistance of UHPC mixes in the presence of calcined clay were also determined. For this purpose, concrete mixes were prepared by replacing cement with calcined clay (metakaolin) at different replacement levels (i.e., 10%, 20%, and 30% by mass of cement). Control mixes were also prepared using silica fume as a partial replacement for cement. The obtained results indicated that in concrete substitution of silica fume by calcined clay led to a slight decrease in flow and compressive strength. Although the performance of calcined clay is slightly inferior compared to silica fume in the cement trials, it can be a promising SCM for the manufacture of High-Performance Concrete (HPC).

KEYWORDS: *UHPC, Silica fume, Metakaolin, Compressive strength, RCPT.*

1. Introduction

Ultra-High Performance Concrete (UHPC), is one of the most innovative concretes known for its exceptional strength, durability, and toughness, making it stand out among other concrete varieties. Typically, the amount of cement utilized in UHPC ranges from 800 to 1100 kg/m^3, which is approximately three times higher than that required in the manufacturing of conventional concrete (Wang et al., 2022). The higher use of cement in UHPC results in high carbon emissions and depletion of natural resources, thus limiting the widespread adoption of UHPC in the construction industry. Thus, there is a necessity to create an environmentally friendly UHPC to minimize the adverse environmental consequences.

In recent years numerous studies have been conducted to incorporate different types of SCMs into UHPC to reduce the consumption of cement, thereby reducing its cost and carbon footprint. Among the commonly used SCMs, silica fume is the most effective and widely used pozzolanic material in the production of UHPC due to its extreme fineness (high specific surface area) and high silica content, which results in a positive effect on concrete rheology and mechanical performance (Ahmad, 2017). However, the entire UHPC production industry cannot depend on silica fume as they are not available in abundant quantity. Therefore, it is imperative to explore the possibilities of alternative SCMs which can fulfil the increasing construction demand while being sustainable. In calcined clay, metakaolin which is prepared by heating kaolin clay under 800 ℃, holds high pozzolanic activity and can be a good alternative to silica fume in the production of UHPC (Mo et al., 2022). Tafraoui et al. (2009) found that under normal curing, the UHPC containing metakaolin showed equivalent or slightly lower compressive strength than those with silica fume, while in heat curing condition, metakaolin showed higher

compressive strength than silica fume. Further, the durability performance of UHPC containing metakaolin was equivalent to those UHPC containing silica fume (Tafraoui et al., 2009). Jiang et al. (2015) found that 10% metakaolin content in UHPC showed the best results in terms of compressive and flexural strengths of UHPC. Although numerous studies have been conducted on UHPC that incorporate metakaolin, but most of these investigations utilize metakaolin ranging from 5% to 25% of the cement mass (Jiang et al., 2015, Mo et al., 2022, Tafraoui et al., 2009). Only a few studies use higher percentage of metakaolin to produce UHPC (Amin et al., 2020). Therefore, there is a need to study the mechanical and durability performance of UHPC containing higher replacement levels of metakaolin. Keeping this in view, in the present experimental work, three different replacement levels of metakaolin i.e., 10%, 20%, and 30% by mass of cement were used in the production of UHPC. In addition, three UHPC mixes were also prepared using silica fume instead of metakaolin at the same replacement level. Flow and compressive strength tests were carried out to determine the fresh and mechanical properties of UHPC. In addition, Rapid Chloride Penetration Test (RCPT) was also carried out to evaluate the durability performance of UHPC.

2. Experimental work

2.1 Materials and mix proportion

The raw materials used to produce UHPC included 53-grade ordinary Portland cement, silica fume, metakaolin, quartz powder and quartz sand. The physical and chemical properties of Portland cement, silica fume and clays are presented in Table 1.

Table 1: Oxide composition and physical properties of binders

Oxide in weight %	SiO_2	Fe_2O_3	Al_2O_3	CaO	MgO	SO_3	Na_2O	K_2O	Loss on ignition	Median particle size (d50)	Specific gravity
OPC	19.18	6.37	4.49	62.34	1.33	2.53	0.15	0.51	1.32	16.9 µm	3.21
Silica fume	88.83	2.86	1.85	0.60	1.90	0.49	0.23	0.58	0.60	9.59 µm	2.22
Metakaolin	42.49	1.48	46.18	0.09	1.37	0.10	1.28	0.01	4.48	8.03 µm	2.53

Quartz powder (specific gravity 2.64) having median particle size (d50) of 35.4 µm and quartz sand (specific gravity 2.64) having size in the range of 1180 - 300 µm were used in the production of UHPC. A polycarboxylate base superplasticizer with a high solid content percentage was used to enhance the workability of UHPC. In total six UHPC mixes were prepared using three replacement levels (i.e., 10%, 20% and 30% by mass of cement) of silica fume and metakaolin. The details of mix design are presented in Table 2. It may be noted that the dosage of superplasticizer used for UHPC mixes containing silica fume was 1.5% by mass of binder and for UHPC mixes containing metakaolin was 2% by mass of binder.

Table 2: Details of UHPC mixes

Sl. No.	Abbreviation	w/b ratio	Cement (kg/m^3)	Silica fume (kg/m^3)	Metakaolin kg/m^3	Quartz sand (kg/m^3)	Quartz powder (kg/m^3)	Superplasticizer (kg/m^3)
1	UHPC10SF	0.22	931.52	93.15	0	996.97	175.94	15.37
2	UHPC20SF	0.22	839.94	167.99	0	996.97	175.94	15.12
3	UHPC30SF	0.22	764.76	229.43	0	996.97	175.94	14.91
4	UHPC10MK	0.22	940.22	0	94.02	996.97	175.94	20.68
5	UHPC20MK	0.22	854.19	0	170.84	996.97	175.94	20.50
6	UHPC30MK	0.22	782.59	0	234.78	996.97	175.94	20.35

2.2 Specimens fabrication and curing procedure

For each UHPC mix, cubes of size 100 mm for 7- and 28-days compressive strength and cylinders of size Ø100 × 200 mm for RCPT test were prepared. The cube and cylindrical moulds were filled with fresh UHPC in single layer without compaction and subsequently covered with plastic sheets to avoid water evaporation. The specimens were demoulded after 24 h and then subjected to hot water curing conditions for 3 days at a constant temperature of 60 ± 3º C (ASTM C1856/C1856M-17, 2017). Thereafter the specimens were moist cured at ambient temperature till the day of testing.

2.3 Test methods

2.3.1 Flow test
The workability of UHPC prepared in the present investigation was determined through flow test following the guidelines mentioned in ASTM C1856/C1856M (ASTM C1856/C1856M-17, 2017).

2.3.2 Compressive strength test
The compressive strength of each mix was determined by testing three cube specimens at two different ages, i.e., 7 and 28 days.

2.3.3 Rapid chloride penetration test
For RCPT test, Ø 100 mm × 50 mm concrete disks obtained from concrete cylinders (size Ø 100 mm × 200 mm) were used. The test setup for RCPT consisted of two cells where one cell was filled with 0.3 N NaOH solution and the other cell was filled with 3% NaCl solution. The disk was placed in between the cells and the cells were connected to a power supply of 60 V. The current was measured and recorded during a time period of 6 hrs, and the total charge passed through the specimen was calculated from the current and time.

3. Results and discussion

3.1 Flow test and Compressive strength
The results obtained from flow test for different UHPC mixes are shown in Fig. 1. The 7-and 28-day compressive strength of UHPC mixes prepared from different replacement level of silica fume and metakaolin are shown in Fig. 2.

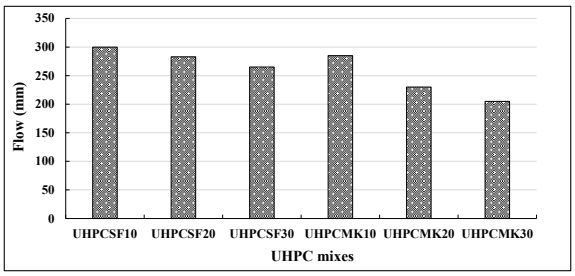

Fig. 1: Flow value for all UHPC mixes

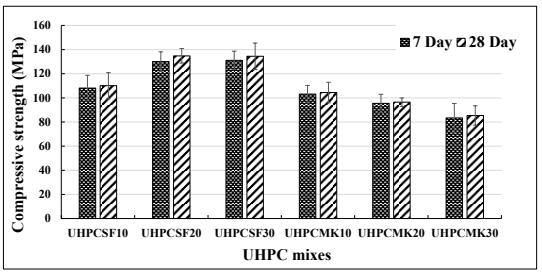

Fig. 2: 7- and 28-day compressive strength value for all UHPC mixes

From the flow value in Fig. 1, it is evident that the workability of UHPC mixes reduces with an increase in the replacement level of silica fume or metakaolin in UHPC mixes. This may be attributed to the very fine particle size of silica fume and metakaolin that adsorbed more water on its surface thereby increasing the water demand. Further, the UHPC mixes containing metakaolin showed slightly lower flow values as compared to those containing silica fume even though the UHPC mixes containing metakaolin were prepared with higher dosages of superplasticizer. The smaller particle size of metakaolin than silica fume may be the reason behind the lower workability of UHPC mixes containing metakaolin.

From Fig. 2, it is observed that the concrete mixes containing 10% silica fume and all those containing metakaolin showed compressive strength lower than 120MPa. According to ASTM C1856/C1856M-17 (2017), concrete having a compressive strength of at least 120 MPa can be classified as UHPC. Therefore, in the current research, it is more appropriate to refer to the concrete containing 10% silica fume and all those containing metakaolin as High-Performance Concrete (HPC), rather than Ultra High Performance Concrete (UHPC). The results of 7-and 28-day compressive strength showed that, in case of the mixes with silica fume the compressive strength increases with an increase in the silica fume content from 10% to 20% by mass of cement. Further increase in the silica fume content does not have significant influence on the compressive strength value as evident from Fig. 2. The increase in compressive strength with an increase in silica fume content (from 10% to 20% by mass of cement) may be attributed to the greater extent of pozzolanic reactions that results in the formation of more amount of C-S-H gel. The results in Fig. 2 suggested that by replacing 20% of the cement with silica fume in UHPC mixes, the maximum particle packing can be achieved. Further with an increase in the metakaolin replacement level, the

compressive strength decreases at both testing ages. This may be attributed to the fact that the hydration reaction has a greater influence at higher cement content in comparison to the packing effect and pozzolanic reaction in mixes containing a higher proportion of metakaolin. While comparing the effect of silica fume and metakaolin on compressive strength, it is observed that the mixes with silica fume showed higher compressive strength at both 7- and 28-day as compared to those containing metakaolin. The reason behind this may be the high reactivity of silica fume that causes the amorphous silica to react with hydration products, resulting in the formation of a denser microstructure (Ashraf et al., 2022). In addition, the larger surface area of metakaolin leads to more water absorption, which creates voids and gaps in the cementitious matrix (Ashraf et al., 2022). Further with increase in testing age the compressive strength of all UHPC mixes slightly increases.

3.2 Rapid Chloride Penetration test

The RCPT values in terms of total charge passed in coulombs for UHPC mixes containing 10%, 20% and 30% silica fume are 41.70, 11.04, and 6.38 coulombs respectively. Similarly, the RCPT values for UHPC mixes containing 10%, 20% and 30% metakaolin are 77.68, 39.74, and 19.7 coulombs respectively. The total charge passing through a concrete specimen can provide an indication of its ability to resist the penetration of chloride ions. The lower value of total charge passed indicated higher chloride penetration resistance of concrete. All the UHPC mixes showed total charge passed value lower than 100 coulomb indicating negligible chloride ion permeability in the UHPC mixes (ASTM C1202, 2012). This may be due to the denser microstructure of UHPC mixes that resist the ingress of chloride ions into the concrete.

4. Conclusions

Based on the results obtained from the present study the following conclusions were drawn.

- The concrete made with metakaolin can be classified as HPC rather than UHPC as the obtained compressive strength results are less than 120 MPa.
- The use of metakaolin as a partial substitute for silica fume in UHPC tends to decrease the workability and strength. This impact was more prominent when higher levels of metakaolin are used as a replacement.
- The compressive strength results indicated that the optimum proportion of silica fume for achieving maximum particle packing was 20%.
- The RCPT results showed negligible chloride ion permeability in all the UHPC mixes indicating the formation of denser microstructure in the presence of SCMs.

Acknowledgements

The authors wish to express their gratitude to the Border Roads Organisation, Government of India for funding the research work.

References

Ahmad, O. A. (2017) “Production of High-Performance Silica Fume Concrete”, *American Journal of Applied Sciences*, 14 (11): 1031-1038.

Amin, M., Tayeh, B. A., and Agwa, I. S. (2020) “Effect of using mineral admixtures and ceramic wastes as coarse aggregates on properties of ultrahigh-performance concrete”, *Journal of Cleaner Production*, 273:123073.

Ashraf, M., Iqbal, M. F., Rauf, M., Ashraf, M. U., Ulhaq, A., Muhammad, H., and Liu, Q. (2022) “Developing a sustainable concrete incorporating bentonite clay and silica fume: Mechanical and durability performance”, *Journal of Cleaner Production*, 337: 130315.

ASTM C1202 (2012) “Standard Test Method for Electrical Indication of Concrete’s Ability to Resist Chloride Ion Penetration” *ASTM International,* Pennsylvania, United States.

ASTM C1856/C1856M-17 (2017) “Standard Practice for Fabricating on Testing Specimens of UHPC”, *ASTM International,* Pennsylvania, United States.

Jiang, G., Rong, Z., and Sun, W. (2015), “Effects of metakaolin on mechanical properties, pore structure and hydration heat of mortars at 0.17 w/b ratio” *Construction and Building Materials*, 93: 564–572.

Mo, Z., Bai, L., and Fu, X. (2022), “Strength properties and hydration of ultra-high performance concrete incorporating calcined clay and limestone with steam curing regimes”, *Case Studies in Construction Materials,* 17: e011658.

Tafraoui, A., Escadeillas, G., Lebaili, S., and Vidal, T. (2009) “Metakaolin in the formulation of UHPC”, *Construction and Building Materials*, 23: 669–674.

Wang, F., Sun, X., Tao, Z., and Pan, Z, (2022) “Effect of silica fume on compressive strength of ultra-high-performance concrete made of calcium aluminate cement/fly ash based geopolymer” *Journal of Building Engineering*, 62:105398.

The 16th International Congress on the Chemistry of Cement 2023 (ICCC2023)
"Further Reduction of CO_2 -Emissions and Circularity in the Cement and Concrete Industry"
September 18–22, 2023, Bangkok, Thailand

Influence of negative temperature hardening on hydration and pore structure evolution of Portland cement paste

Shuai Bai[1*], Xinchun Guan[2]

[1] *School of Civil Engineering, Harbin Institute of Technology, Harbin, China*
Email: bai.shuai@outlook.com
[2] *School of Civil Engineering, Harbin Institute of Technology, Harbin, China*
Email: guanxch@hit.edu.cn

ABSTRACT

This paper investigated the hydration and pore structure evolution of negative temperature hardening cement paste, and the influence of negative temperature (-5 ℃) was highlighted. Thermogravimetric analysis (TGA) and mercury intrusion porosimetry (MIP) was used to gain information on hydration and pore structure. TG results show that negative temperature hardening severely inhibits the hydration reaction, resulting in a significant decrease in the hydration degree, C-S-H gel content and gel-space ratio. However, as the hydration age increases to 120 days, the hydration degree and gel-space ratio of negative temperature hardening cement paste can reach the positive temperature level, while the C-S-H gel content is still lower than the positive temperature level. MIP results indicated that negative temperature obviously delayed the development of pore structure and significantly increases total porosity and most probable pore diameter, indicating that negative temperature hardening seriously affects the compactness of pore structure.

KEYWORDS: *cement paste, negative temperature hardening, hydration, pore structure*

1. Introduction

Hardening temperature is known to affect the reactivity and hardened properties of cement-based materials adversely. Some literature [1,2,3] have provided experimental data to prove that hardening temperature plays a vital role in the development of strength. A decrease in hardening temperature can deaccelerate the strength development of cement-based materials [4,5,6,7].
Hydration progress is the key to affecting the macro strength of hardened cement pastes [8]. Previous studies [9,10,11] have shown the linear, cubic, or exponential relations between the compressive strength and hydration characteristic parameters.
Pore structure is also one of the key factors controlling the strength and durability of hardened cement pastes [12]. All types of pore and pore shapes control the mechanical properties, and the amount of interconnecting pores and the tortuosity of pores mainly affected the durability of concrete [13,14]. Large pores are considered to have more dominant effect on strength and durability, and gel pores mainly affect the shrinkage and creep [15,16].
Therefore, the aim of the present work was to study the hydration and pore structure evolution of negative temperature hardening cement paste. Thermogravimetric analysis (TGA) was used to gain information on hydration degree and hydrates. Mercury intrusion porosimetry (MIP) was used to obtain the pore structure information and pore size distribution, and the pore structure was analyzed with the help of the fractal model.

2. Experiment

2.1 Material and preparation

A commercially available ordinary Portland cement is used as a binder material and the physicochemical properties of the binder material are given in Tables 1. The water to cement ratio of 0.35 was used for all the cement pastes and the pastes were mixed according to ASTM C 305 standard [17]. After pre-curing for 24 h at room temperature, all the pastes were demolded and then cured at +20 ℃ and -5 ℃ for 3, 7, 14, 28, 56, and 120 days, respectively.

Table 1. Chemical and mineral composition of cement.

Chemical composition (wt%)	SiO_2	Al_2O_3	Fe_2O_3	CaO	MgO	f-CaO	Loss
	21.14	5.72	3.62	64.84	1.53	1.33	1.13
Mineral composition (wt%)	C_3S	C_2S	C_3A	C_4AF			
	54.30	19.66	9.04	11.00			

2.2 Methods

A thermogravimetric apparatus (TA Discovery SDT 650) was used to obtain the TG and DTG curves. The temperature range of TGA is from 30 ℃ to 800 ℃ at 10 ℃/min in a nitrogen atmosphere. TG samples were pulverized and then oven-dried at 60 ℃ for 72 h before testing.
The MIP technique (AutoPore IV 9500, USA) is used to measure the characteristic pore sizes and pore size distribution of cement-based materials. MIP samples were immersed in ethanol for 7 days to remove the free water inside pastes. After immersing, these samples are dried in an oven at about 60 ℃ for 72h before testing.

3. Results and discussions

3.1 Hydration degree and C-S-H gel content

According to the Refs. [18,19], hydration degree of cement paste is calculated by the chemically combined water content. Based on the thermogravimetric data, the calculated hydration degree of cement pastes cured at +20 ℃ and -5 ℃ is presented in Fig. 1. Before 28 days of hydration, the hydration degrees of negative temperature hardening cement pastes are much lower than those of positive temperature hardening cement pastes, indicating that the hydration reaction is seriously inhibited by negative temperature hardening. However, when the hydration age increases to 120 days, the hydration degree of negative temperature hardening cement pastes is similar to that that of positive temperature hardening cement pastes. It is indicated that the hydration degree of negative temperature hardening cement paste can reach the level of positive temperature hardening cement pastes by giving sufficient negative temperature hardening time.
Moreover, the mass loss between 100-250 °C was calculated to estimate the content of C-S-H gel with reference to the Refs. [20,21]. The C-S-H gel content of cement pastes cured at +20 ℃ and -5 ℃ is presented in Fig. 2. Unlike the hydration degree, the C-S-H gel content of negative temperature hardening cement pastes are always lower than those of positive temperature hardening cement pastes. As the hydration age increases, the gap of C-S-H gel content gradually shortens, but this gap still exists until 120 days of hydration.

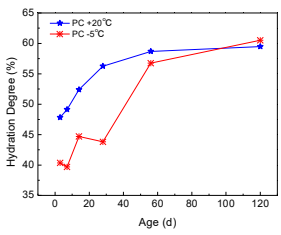

Fig. 1. Hydration degree

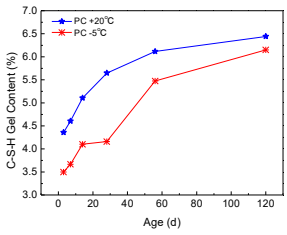

Fig. 2. C-S-H gel content

3.2 Pore size distribution

The pore size distribution curves measured by the MIP method are shown in Fig. 5 for cement pastes cured at +20 ℃ and -5 ℃. It can be seen intuitively that negative temperature hardening changes the pore size distribution of cement paste. The “Twin Peaks” is observed in positive temperature hardening cement pastes (Fig. 3a). The main peak located at 30-80 nm, and the secondary peak located at 80-200 nm. For negative temperature hardening cement pastes (Fig. 3b), the “Twin Peaks” disappeared and the single main peak located at the secondary peak position of positive temperature hardening cement paste, indicating that negative temperature hardening causes the main peak to move forward. The forward movement of the main peak also proves that negative temperature hardening can coarsen the pore diameter of cement matrix. In addition, the 120-day pore size distribution of negative temperature hardening cement pastes also appear in the form of “Twin Peaks”, which may be the result of sufficient negative temperature hardening time.

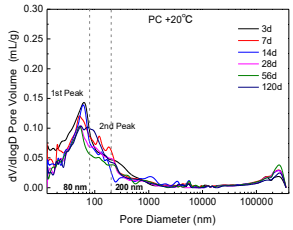

Fig. 3a. Positive temperature hardening

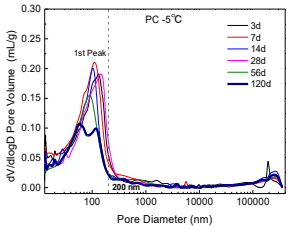

Fig. 3b. Negative temperature hardening

3.3 Characteristic parameters of pore structure

In Fig. 4a, the total porosity of negative temperature hardening cement paste is much higher than that of positive temperature hardening cement paste. In Fig.4b, the most probable pore diameter (corresponding to the peak position of pore size distribution) of negative temperature hardening cement paste is 1.5~2.0 times larger than that of positive temperature hardening cement paste. In Fig. 4c, the median pore diameter of negative temperature hardening cement paste is obviously higher than that of positive temperature hardening cement paste before 56 days. The median pore diameter represents the diameter value at 50% cumulative intrusion volume, which reflects the relative proportion of capillary pores in the overall pore size distribution [22]. This result indicates that negative temperature hardening increases the capillary pore fraction. In Fig. 4d, the threshold pore diameter of negative temperature hardening cement paste is slightly higher than that of positive temperature hardening cement paste. The above results show that negative temperature hardening can significantly increase the pore characteristic parameters, especially total porosity and most probable pore diameter, indicating that negative temperature hardening seriously affects the compactness of pore structure. Meanwhile, as the hydration age increases to 120 days, the pore characteristic parameters of negative temperature hardening cement pastes can approach the level of positive temperature hardening cement pastes.

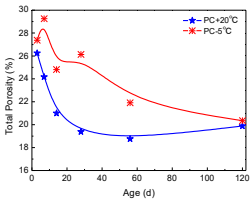

Fig. 4a. Total porosity

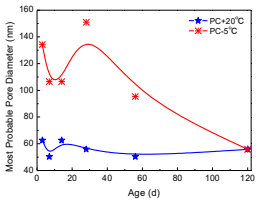

Fig. 4b. Most probable pore

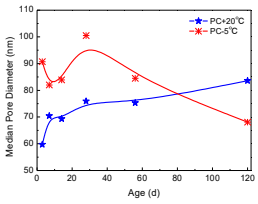

Fig. 4c. Median pore

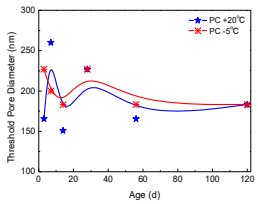

Fig. 4d. Threshold pore

4. Conclusions

Negative temperature hardening severely inhibits the hydration reaction, significantly decreasing in the hydration degree and C-S-H gel content. However, as the hydration age increases to 120 days, the hydration degree of negative temperature hardening cement paste can reach the positive temperature

level, while the C-S-H gel content is still lower than the positive temperature level. It is also indicated that the inhibition effect of negative temperature hardening on the hydration degree and hydration products is different.

Negative temperature hardening delays the development of pore structure and significantly increases total porosity and most probable pore diameter, which seriously affects the compactness of pore structure. Similar to the hydration degree, by giving sufficient negative temperature hardening time, the pore characteristic parameters of negative temperature hardening cement pastes can approach the level of positive temperature hardening.

References

[1] Kim, J. K. , Moon, Y. H. , & Eo, S. H. . (1998). Compressive strength development of concrete with different curing time and temperature. Cement and Concrete Research, 28(12), 1761-1773.

[2] Kjellsen, K. O. , & Detwiler, R. J. . (1993). Later-age strength prediction by a modified maturity model. Aci Materials Journal, 90(3), 220-227.

[3] Carino, N. J. . (1981). Temperature effects on the strength-maturity relation of mortar. Concrete.

[4] Hafiz, M. A. , Skibsted, J. , & Emmanuel Denarié. (2020). Influence of low curing temperatures on the tensile response of low clinker strain hardening uhpfrc under full restraint. Cement and Concrete Research, 128, 105940.

[5] Ulm FJ, Coussy O. . (1995). Modelling of thermo-chemo-mechanical couplings of concrete at early ages. ASCE J Eng Mech, 121(7), 785–94.

[6] Ulm FJ, Coussy O. . (1996). Strength growth as chemo-plastic hardening in early age concrete. ASCE J Eng Mech, 122(12), 1123–32.

[7] Cervera, M. , Faria, R. , Oliver, J. , & Prato, T. . (2002). Numerical modelling of concrete curing, regarding hydration and temperature phenomena. Computers & Structures, 80(18-19), 1511-1521.

[8] Pang, X., Sun, L., Chen, M., Xian, M., Cheng, G., Liu, Y., & Qin, J. (2022). Influence of curing temperature on the hydration and strength development of Class G Portland cement. Cement and Concrete Research, 156, 106776.

[9] Wang, X., & Lee, H. (2012). Evaluation of the mechanical properties of concrete considering the effects of temperature and aging. Construction and Building Materials, 29, 581-590.

[10] Park, K. B., Jee, N. Y., Yoon, I. S., & Lee, H. S. (2008). Prediction of temperature distribution in high-strength concrete using hydration model. ACI Materials Journal, 105(2), 180.

[11] Mehta, P. K., & Monteiro, P. J. (2014). Concrete: microstructure, properties, and materials. McGraw-Hill Education.

[12] Poon, C. S. , Wong, Y. L. , & Lam, L. . (1997). The influence of different curing conditions onthe pore structure and related properties of fly-ash cement pastes and mortars. Construction & Building Materials, 11(7/8), 383-393.

[13] Abbas, A. , Carcasses, M. , & Ollivier, J. P. . (1999). Gas permeability of concrete in relation to its degree of saturation. Materials & Structures, 32(215), 3-8.

[14] Kumar, R. , & Bhattacharjee, B. . (2003). Porosity, pore size distribution and in situ strength of concrete. Cement and Concrete Research, 33(1), 155-164.

[15] Bhattacharjee, R. K. . (2004). Assessment of permeation quality of concrete through mercury intrusion porosimetry. Cement and Concrete Research.

[16] Das, Bibhuti & Kondraivendhan, Ba. (2012). Implication of pore size distribution parameters on compressive strength, permeability and hydraulic diffusivity of concrete. Construction and Building Materials. 28. 382-386.

[17] ASTM C305-14. Standard practice for cmechanical mixing of hydraulic cement pastes and mortars of plastic consistency. Philadelphia: American Society for Testing and Materials; 2014.

[18] R. Yu, P. Spiesz, H. J. H. Brouwers, Effect of nano-silica on the hydration and microstructure development of ultra-high performance concrete (uhpc) with a low binder amount. Construction & Building Materials, 65(9), (2014), 140-150.

[19] L. Lam, Y. L. Wong, C. S. Poon, Degree of hydration and gel/space ratio of high-volume fly ash/cement systems. Cement & Concrete Research, 30(5), (2000), 747-756.

[20] M. Berra, F. Carassiti, T. Mangialardi, A. E. Paolini, M. Sebastiani, Effects of nanosilica addition on workability and compressive strength of portland cement pastes. Construction & Building Materials, 35(none), (2012), 666-675.

[21] C. Alonso, L. Fernandez, Dehydration and rehydration processes of cement paste exposed to high temperature environments. Journal of Materials Science, 39(9), (2004), 3015-3024.

[22] Zeng, Q. , Li, K. , Fen-Chong, T. , & Dangla, P. . (2012). Pore structure characterization of cement pastes blended with high-volu me fly-ash. Cement & Concrete Research, 42(1), 194-204.

The 16th International Congress on the Chemistry of Cement 2023 (ICCC2023)
"Further Reduction of CO_2 -Emissions and Circularity in the Cement and Concrete Industry"
September 18–22, 2023, Bangkok, Thailand

Resistance of portland-dolomite cement to thaumasite sulfate attack

Jiangtao Xu[1], Duyou Lu[1], and R.D. Hooton[2]

[1] *Nanjing Tech University, Nanjing, China*
Email: xujiangtao18@163.com

[2] *University of Toronto, Toronto, Canada*
Email: d.hooton@utoronto.ca

ABSTRACT

The use of dolomite, $CaMg(CO_3)_2$, to manufacture portland-dolomite cement (PDC) has recently attracted interest as a promising low-carbon cement alternative to portland-limestone cement. However, little is known about the potential for thaumasite sulfate attack in portland-dolomite cement. This study investigated the resistance to thaumasite sulfate attack of PDC with 0~30% dolomite powder exposed to 50g/L Na_2SO_4 solution at 23℃ and 5℃, and using portland-limestone cement (PLC) as a comparison. The expansion of mortar bars was measured periodically, and hydration products of cement pastes were examined using X-ray diffraction. The portland cement used had a C_3A = 10% and thus was not sulfate resistant, but results showed that the sulfate resistance of mortar stored at both 23℃ and 5℃ decreased significantly as dolomite and limestone additions increased. In contrast to limestone, dolomite exhibits a smaller adverse effect on sulfate resistance. When exposed to extremely high sulfate concentrations at low temperatures, PDC made with high C_3A cement is similarly vulnerable to thaumasite sulfate attack to PLC.

KEYWORDS: *thaumasite, sulfate attack, dolomite powder, expansion*

1. Introduction

Conventional sulfate attack proceeds as cement hydrate phases interact with external sulfates to form ettringite and gypsum, which can cause expansion and cracking of cementitious materials. Thaumasite sulfate attack (TSA) is a special form of sulfate attack with thaumasite ($CaSiO_3 \cdot CaCO_3 \cdot CaSO_4 \cdot 15H_2O$) as the deterioration product, that can destroy the C-S-H matrix and transform concrete into a white, non-cohesive mass without any binding properties, which is more severe than conventional sulfate attack. TSA has been reported in Norway, the United States, Canada, France, Germany, Austria, Denmark, and China since its discovery in the 1990s, attracting much attention from both academia and industry (Shi 2012). Thaumasite requires a source of calcium silicate, sulfate, carbonate and excess humidity. It has been shown that low temperature, magnesium sulfate exposure, high-C_3A content in cement, as well as the presence of carbonates may accelerate and promote thaumasite formation (Rahman 2014). The mechanism of thaumasite formation can be both direct and indirect. Thaumasite can be formed directly by a reaction between C-S-H, sulfate, carbonate and water or indirectly by an ettringite transformation due to the structural similarities of two compounds.

Portland-limestone cement (PLC) has been extensively used in building and construction due to its economic, environmental and technical benefits, such as low cost, reduced CO_2 emissions, improved workability, high early strength, and increased formation of hydrates of hemicarbonate and monocarbonate (Wang 2018). However, because PLC is susceptible to TSA, especially at cool temperatures, it is not recommended for sulfate exposure unless used together with sufficient levels of suitable supplementary cementitious materials (SCMs). As an internal source of carbonate, the limestone in PLC can dissolve CO_3^{2-} into cement pore solution and enhance the formation of thaumasite, increasing the risk of TSA (Hooton 2007, Ramezanianpour 2013). However, when appropriate levels of SCMs were used, PLC containing up to 15% limestone performed as well as Portland cement made from the same

clinker in long-term sulfate exposure of concrete at low temperatures (Hooton and Thomas 2016).
Dolomite is a common carbonate rock that often coexists with limestone. Recently, the use of dolomite to produce Portland-dolomite cement (PDC) has received interest as a promising modification of low-carbon portland-limestone cement. Previous studies (Zajac 2014, Xu 2022) have shown that the addition of dolomite may accelerate the hydration of cement and improve early strength, and also result in the formation of carboaluminates and, as a result, ettringite stabilization, which is similar to the behaviour of limestone. Magnesium from dolomite can react to produce increased amounts of hydrotalcite and brucite, potentially increasing the compressive strength of mortar and improving volume stability. In addition, several studies demonstrated that PDC exhibited comparable durability to PLC in terms of chloride penetration and carbonation (Zhang 2022). However, there is little research on the sulfate resistance of PDC, particularly with respect to TSA, which may be favored by the carbonate ions from dolomite. Besides, a field case of TSA occurred in concrete made using dolomite aggregates (Mittermayr 2017).
In this study, the sulfate resistance of portland-dolomite cement with various dolomite contents was evaluated both at 5℃and 23℃, with portland-limestone cement as a comparison. Also, hydration products formed after the sulfate attack on the samples were examined using X-ray diffraction (XRD).

2. Materials and methods

Canadian CSA A3000 Type GU cement, dolomite and limestone were used in this study. The chemical compositions of the raw materials are given in Table 1. The mineralogical composition of the cement by Bogue formula is 53%C_3S, 17%C_2S, 10%C_3A and 8%C_4AF, and so this cement would not be sulfate resistant. The dolomite and limestone powders contained about 93% $CaMg(CO_3)_2$ and 92% $CaCO_3$, and their median particle sizes are about 6 μm and 8 μm, respectively (data provided by supplier). ASTM standard graded Ottawa sand was used for casting mortar samples.

Table 1 Chemical composition of raw materials (wt%)

Materials	CaO	SiO_2	Al_2O_3	Fe_2O_3	MgO	SO_3	K_2O	Na_2O	LOI
Cement	62.20	19.70	5.30	2.60	2.40	2.90	0.62	0.12	2.10
Dolomite	31.45	1.36	0.34	0.10	21.23		0.03		45.06
Limestone	54.48	0.26	0.17	0.03	1.38		0.02	0.06	43.62

Dolomite and limestone replaced cement at 0%, 5%, 15% and 30% by mass, respectively. For all mixtures, mortars with a water/binder/sand ratio of 0.485:1:2.75 were cast into 25×25×285mm prism (for length change) and 50mm cube (for compressive strength) moulds. Paste samples with a water/binder ratio of 0.50 were cast into 12 mm diameter plastic cylinders. After 24 hours, all samples were demolded and stored in tap water at room temperature. These samples were divided into two groups. The first group was immersed in 50g/L Na_2SO_4 solution at 23℃ after the mortars attained a strength of 20MPa (as per ASTM C1012), and the second group was immersed in the same solution at 5℃ after being pre-cured at room temperature for 28 days. The length change of the samples was recorded periodically, and the sulfate solution was renewed every month.
The hydration products of cement pastes were examined by X-ray diffraction. At the selected age, the pastes were crushed and stored in excess ethanol for 24 hours to arrest hydration, and then dried in a desiccator at 40℃ for 24 hours. X-ray diffraction was performed on SmartLabTM 3Kw Powder Diffractometer (Cu Kα1, λ=1.5406 Å) with operation conditions of 40kV and 30mA. The scan speed was set to 5 º/min with a step size of 0.02 °.

3. Results and discussion

3.1 Expansion and visual observations after sulfate exposure at 23 ℃ and 5℃

Fig. 1 show the average length change for mortar bars exposed to 5% Na_2SO_4 solution at 23 ℃ (Fig. 1a) and 5℃ (Fig. 1b). As shown in Fig. 1a, as expected, all of the mortar bars exposed to sulfates at 23℃ exceeded the 0.10% expansion limit before 6 months, due to the high C_3A content of the cement used. After 90 days of exposure, the incorporation of dolomite and limestone in cement significantly reduced the onset time of expansion and increased expansion of the mortars, with higher carbonate content resulting in greater expansions. In comparison to the PLC samples, the PDC mortar bars expanded less. After 210 days, the expansion of PDC5, PDC15 and PDC30 were 0.23%, 0.39% and 0.72%, respectively, whereas the respective expansions of PLC5, PLC15 and PLC30 were 0.29%, 0.60% and 1.06%. For

sulfate attack at 5°C (Fig. 1b), all samples had fractured and disintegrated after 150 days of exposure, exhibiting a more severe attack at lower temperature than at room temperature. It is obvious that a higher carbonate content caused the mortar to fracture sooner. PDC30 and PLC30 began to fracture as early as after 90 days of exposure, PDC15 and PLC15 fractured at 120 days, and GU, PDC5 and PLC5 fractured at 150 days. The expansions of the PDC samples were smaller than those of the PLC samples, although having an equivalent failure time. Moreover, PDC exhibited less visual degeneration than PLC, where mush appeared (Fig. 2). While all mixtures failed, both dolomite and limestone additions further reduced the sulfate resistance of mortar, especially at low temperatures, but dolomite had a less adverse effect on the sulfate attack than limestone.

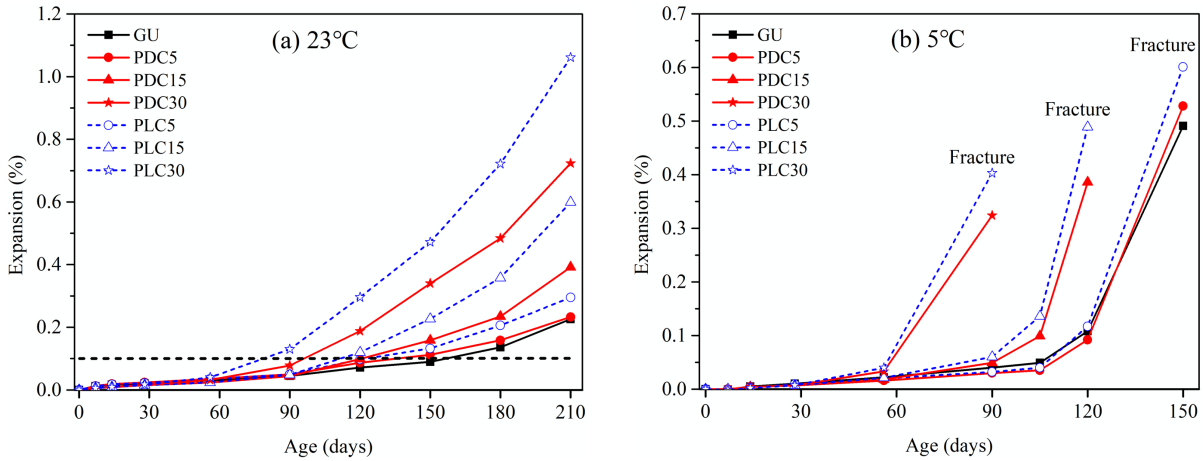

Fig. 1 Length changes for mortar bars exposed to 5% Na_2SO_4 solution at (a) 23 °C and (b) 5°C

Fig. 2 Visual condition of mortar bars immersed in 5% Na_2SO_4 solution at 5°C for 150 days

3.2 Hydration products after sulfate attack at 23 °C and 5°C

Fig. 3a and b show the XRD patterns of paste samples exposed to 5% Na_2SO_4 solution at 23 °C and 5°C, respectively. Ettringite, gypsum, and portlandite were the primary hydration products that formed after 28 days and 180 days of exposure at 23°C (Fig. 3a). The intensities of ettringite and gypsum peaks clearly increased with increasing exposure time, and the PDC and PLC samples, notably the PLC samples, had higher peaks of ettringite and gypsum than the reference GU cement. For the samples exposed at 5 °C (Fig. 3b), ettringite and gypsum were also observed after 28 days of exposure, which is similar to the observation at 23 °C. At 150 days, however, thaumasite was formed in addition to the increase in ettringite and gypsum peaks, and its peaks were significantly increased with the addition of both types of carbonate powders. The formation of thaumasite was more pronounced in the PLC samples when compared to the PDC samples. Furthermore, a significant decrease in portlandite was observed in both the PDC and PLC samples, which can be associated with the enhanced gypsum formation. This demonstrates that, similar to PLC, PDC can suffer from conventional ettringite sulfate attack at room temperature, and initial ettringite attack with late formation of thaumasite at the lower temperature. The lower expansions

of PDC bars compared to PLC are attributable to the lower amounts of corrosion products formed in the cement matrix.

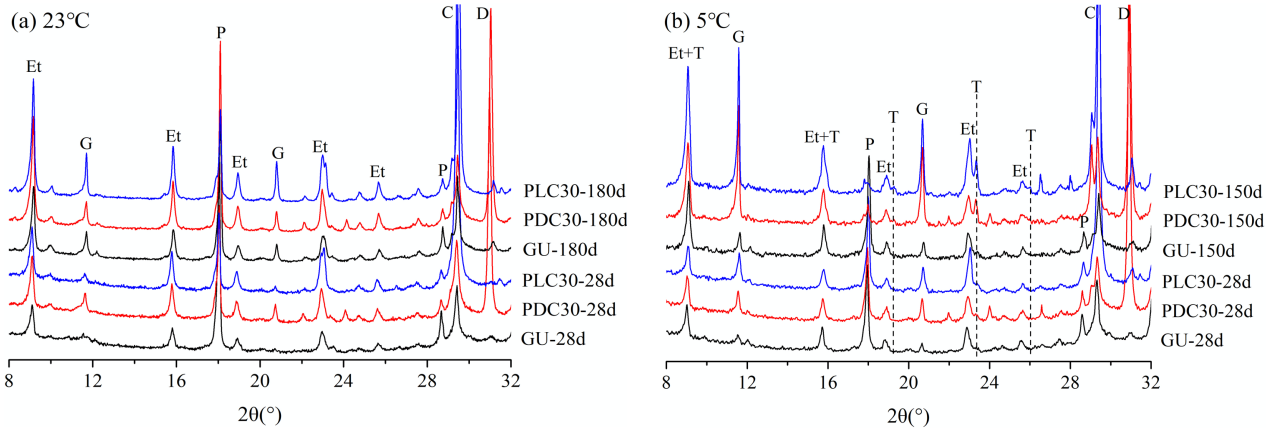

Fig. 3 XRD patterns of paste samples exposed to 5% Na_2SO_4 solution at (a) 23 °C and (b) 5°C

3. Conclusions

This study investigated the influence of dolomite additions to portland cement on the sulfate attack of mortars exposed at 5°C and 23°C, with limestone additions used for comparison. All mortar samples degraded more severely at lower temperature than at room temperature. At both exposure temperatures, the sulfate resistance of mortar was reduced as a result of dolomite incorporation into cement, with higher dolomite contents resulting in poorer sulfate resistance. However, dolomite additions had less adverse effect on sulfate resistance than limestone additions, which was related to smaller amounts of corrosion products formation in PDC. Similar to PLC, the type of destruction of PDC is conventional sulfate attack at room temperature, and at low temperatures, initial ettringite attack followed by thaumasite sulfate attack.

Acknowledgements

This work was supported by the National Science Fund for Distinguished Young Scholars of China (52102025), and the Priority Academic Program Development (PAPD) of Jiangsu Higher Education Institutions.

References

Hooton, R. D., Nokken, M., and Thomas, M.D.A. (2007) "Portland-limestone cement: state-of-the-art report and gap analysis for CSA A 3000", *report prepared for St. Lawrence Cement*.

Hooton, R.D. and Thomas, M.D.A., (2016) "Sulfate Resistance of Mortar and Concrete Produced with Portland-Limestone Cement and Supplementary Cementing Materials", Portland Cement Association Research Report SN3285, 2016, 25pp.

Mittermayr, F., et al. (2017) "Environmental controls and reaction pathways of coupled de-dolomitization and thaumasite formation", *Cement and Concrete Research*, 95: 282-293.

Rahman, M.M., and Bassuoni, M.T. (2014) "Thaumasite sulfate attack on concrete: Mechanisms, influential factors and mitigation", *Construction and Building Materials*, 73: 652-662.

Ramezanianpour, A.M. and Hooton, R.D. (2013) "Thaumasite sulfate attack in Portland and Portland-limestone cement mortars exposed to sulfate solution", *Construction and Building Materials*, 40: 162-173.

Shi, C., Wang, D. and Behnood, A. (2012) "Review of thaumasite sulfate attack on cement mortar and concrete", *Journal of materials in civil engineering*, 12: 1450-1460.

Wang, De., et al. (2018) "A review on use of limestone powder in cement-based materials: Mechanism, hydration and microstructures", *Construction and Building Materials*, 181: 659-672.

Xu, J., et al. (2022) "Volume stability of Portland-dolomite cement pastes cured in different conditions", *Journal of Sustainable Cement-Based Materials*, 1-13.

Zajac, M., et al. (2014) "Effect of CaMg $(CO_3)_2$ on hydrate assemblages and mechanical properties of hydrated cement pastes at 40 C and 60 C", *Cement and concrete research*, 65: 21-29.

Zhang X., Yu L., and Wu Y. (2022) "Research on the carbonation resistance of concretes containing dolomite powder", *Fullerenes, Nanotubes and Carbon Nanostructures*, 1-12.

The 16th International Congress on the Chemistry of Cement 2023 (ICCC2023)
"Further Reduction of CO_2 -Emissions and Circularity in the Cement and Concrete Industry"
September 18–22, 2023, Bangkok, Thailand

Contribution of the thermochemical conversion kinetics to predict the mass transfer of hydraulic binders panels submitted to fire

E. Huby[1], A. Rojo[2], D. Giovannacci[1], J-D. Mertz[1], and Y. Mélinge[1*]

[1] *Laboratoire de Recherche des Monuments Historiques (LRMH), CRC – MNHN, CNRS, Ministère de la Culture – UAR 3224, Champs sur Marne, France*

Email: emilie.huby@culture.gouv.fr, david.giovannacci@culture.gouv.fr, jean-didier.mertz@culture.gouv.fr, yannick.melinge@culture.gouv.fr

[2] *Université de Reims Champagne-Ardennes, Reims, France*

Email: amandine.rojo@univ-reims.fr

ABSTRACT

Better understanding of the fire resistance is the aim with the proposed research works and, more specifically, the mass transfer identification when building materials are submitted to fire. The experimental methodology has been developed by the combination of the data recorded during a fire test at reduced scale and thermo-chemical characterization of a considered recipe. On the one hand, squared panels (550x550 mm^2) with constant thickness are heated on one face using the standard fire ISO834 in order to identify the fire resistance properties and the mass change. On the other hand, chemical conversion kinetics of the studied recipe are modeled by means of iso-conversional methodologies at the micro scale. The model combines different parameters such as the temperature, the chemical state and the heat rate. Classically, the combination of the Arrhenius law and the extended Prout-Tompkins model have been used to assess the chemical conversion kinetics. The mass transfer (from exposed side to non-exposed side of the panel) is modelled and compared to the direct measurements. In order to reduce the risk with concrete characterization, such methodology has first been tested using gypsum based material often used as passive fire protection. Obtained results are well correlated with those obtained by direct mass measurement of the panel.

KEYWORDS: *Mass transfer, Fire resistance, Thermo-chemical conversion kinetics, Gypsum-based materials*

1. Introduction

A good understanding of building materials and structures behaviors submitted to fire remains today a real challenge in order to develop new materials able to resist or to increase the performances of the fire protection materials. Furthermore, the improvement of the efficiency of the characterization methodologies is also a big challenge. The present paper is a contribution to better identify experimentally the thermo-hydro-chemical and mechanical (THCM) behavior of building materials at the macro scale. A focus is devoted to the mass transfer identification and its analysis. In fact, when building material is submitted to fire, mass transfer is induced by the thermo-chemical changes. If the porous media is not well adapted, impeded mass transfer can lead to severe mechanical damages as it can be seen in concrete structure (cracks appearance, spalling, explosion…). In order to better understand the fire resistance at reduced scale, an experimental protocol has been developed to test technical solutions (macro scale) as board with constant thickness submitted to fire on one face. In the present paper a first step of the protocol is presented by taking into account of the thermo-chemical changes of the tested material and its characterization. The deduced thermo-chemical model is then used to predict the mass evolution of the board. To prevent the risk of the apparatus being destroyed during the fire test, concrete samples are replaced by gypsum based material for the present study. Such material is generally used for passive fire protection. Finally, the mass transfer is a

combination of the water departure during the dehydration period and the CO_2 departure during the decarbonation period (natural impurity in the gypsum careers). Isoconversionnal methodologies have been applied to characterize and to model the thermo-chemical conversion kinetics of the recipe.

2. Experimental protocols, materials and data treatment

2.1 Fire resistance analysis, studied material and samples

Equivalent one dimensional fire tests have been carried out by means of squared panels laid to close an horizontal electrical furnace, Mélinge et al. (2010). Standard ISO834 thermal fire is fixed on the inner side while the other side remains at the ambient conditions of the test room. Radiative flux is dominant near the exposed side of the board. Conduction regime inside the board is highlighted using thin thermocouples positioned all along the thickness. Radiative thermal flux and strains at the non exposed side are respectively recorded by an IR thermal camera and a lidar. Global damages and mass evolution are characterised after testing for fixed duration. After a cooling period, the residual properties of the panels can then be studied from the exposed to the non-exposed side, Rojo (2013). For the present study, thirty panels (550x550x40 mm) have been made by mixing a β natural hemihydrate of calcium sulfate with water (W/P = 0.65). After a curing period, the main properties of the gypsum panels can be seen in the table 1.

Table 1: Main properties of the studied material. Mix of plaster and water (W/P = 0.65).

Density ($kg.m^{-3}$)	1095	Thermal conductivity ($W.m^{-1}.K^{-1}$)	0.41
Average porosity (-)	0.52	Specific heat ($J.K^{-1}.g^{-1}$)	1.24

Four thermo chemical conversions characterise gypsum material from room temperature to 1000°C, Abriel (1983), Kirfel et al. (1980). The dehydration is well characterised by two combined endothermic reactions between 80 to 200 °C. Then, anhydrite III to anhydrite II exothermic phase transition is observed between 350 and 400°C. The last reaction usually takes place between 600 and 750°C and is due to decarbonation of $CaCO_3$ impurities. Other reactions above 1000°C are not studied in the present works. At the panel scale, previous works helped us to better understand the thermo chemical changes effect along the thickness in fire condition Mélinge et al. (2011) and to describe and model the porosity kinetics, Rojo et al. (2013).

2.2 Thermo chemical changes analyses

Thermo chemical changes are analysed and modelled using thermal analyses (TG/DSC) through non isothermal protocol and for an important spectrum of heat rates which are in good accordance of the fire conditions (1 to 100 $K.min^{-1}$). Endothermic, exothermic reactions with and without mass variation can be then characterised. Adimensional parameter, $0 \leq \alpha \leq 1$, allows to highlight the chemical state of the recipe and its evolution is introduced. $\alpha = 0$ characterises the non chemically damaged compounds and $\alpha = 1$ characterises the total achievement of the chemical conversion. Then, the thermo-chemical kinetics are classically modelled by the equation 1 which combines the effect of the temperature and the chemical conversion mechanism.

$$\frac{d\alpha}{dt} = f(\alpha).g(T) = \alpha^m(1-\alpha)^n.kexp^{\frac{-E_a}{RT}} \quad (1)$$

The temperature effect is well described by the Arrhenius law and the Prout Tompkins model ($B1_{m,n}$) generally used to characterise nucleation processes is well adapted to describe the chemical conversion. Friedman and Flynn-Owaza-Wall (FOW) methodologies combined to non-linear regression analysis have been performed to identify first the activation energy and then the three other parameters of each of gypsum chemical changes, table 2, Rojo (2013).

2.4 Data treatment methodology

When the gypsum panel is thermally loaded by the standard ISO 834, the thermal transfer is presented in the figure 1 from the exposed side to non-exposed side. Significant numbers of thermocouples are implemented along the thickness. This local instrumentation helps to better increase the accuracy of the

mesh in order to interpolate the temperature for each position along the thickness. A high correlation level between the signals helps to ensure the measurement quality and to prevent against a cell damage or the interaction of the thermocouples with cracks development during the test. Such detection during the treatment helps to reject the wrong data. Illustration of a damaged thermocouple is clearly noticed at the 25 mm position referenced from the non exposed side (important noise detection around 6000s). Thus, illustration of two thermocouples closed to a crack development can be seen at the 15 and 20 mm position; Signal deviation from the others is detected from 8000 s. After data validation, the recorded signal is well in accordance with a latent heat material thermally loaded. For a local temperature ranged from 75 to 80 C, a large thermal plateau is reached and the temperature remains constant until the dehydration front reaches the considered thermocouple. This plateau illustrates the effect of the thermal barrier induced by latent heat.

Table 2: Identification of the thermo chemical kinetics of the dihydrated of hemihydrate of calcium sulfate.

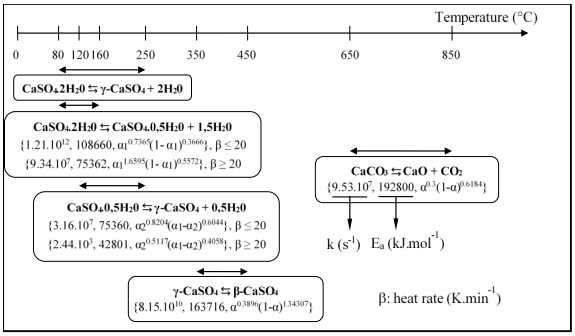

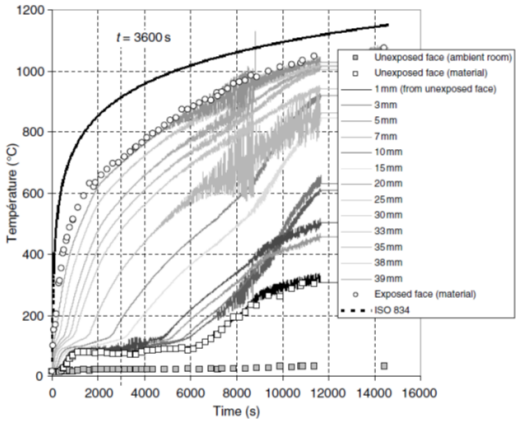

Figure 1: Thermal transfer through a gypsum board (W/P = 0.65) of 40 mm thick heated on one face using the standard ISO 834.

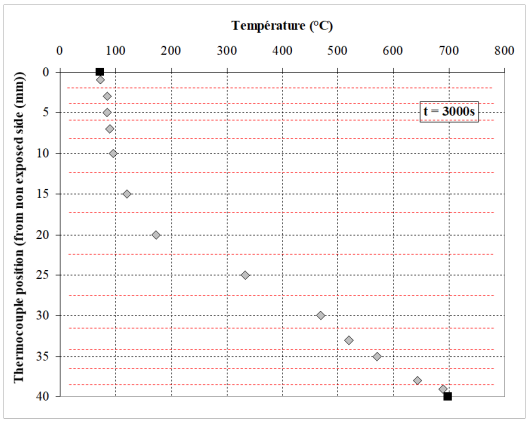

Figure 2: Illustration of the temperature evolution along the thickness at a fixed time. The red line illustrate the mesh of the mass balance.

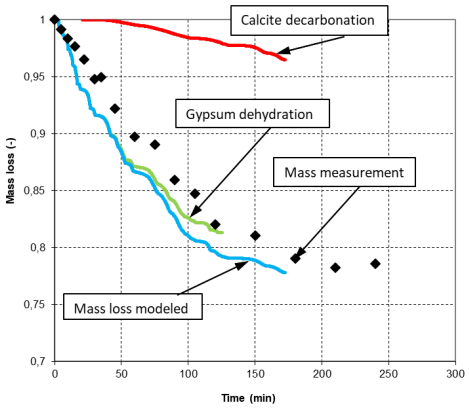

Figure 3: Gypsum board mass evolution versus time during the fire test. Comparison of the direct mass measurement and the modeled one.

From the thermal map, figure 1, temperature evolution along the board thickness can be deduced for a fixed time, figure 2. The used mesh for the mass balance is illustrated in this figure. Local mass evolution can be modeled from the thermo-chemical kinetics and the evaluation of dα/dt for the considered time, equation 2. The mass of the panel is then deduced by means of an integral calculation along the thickness and finally generalised all along the fire test.

$$\left.\frac{d\alpha}{dt}\right|_t \approx \frac{(\alpha_{t+1}-\alpha_{t-1})}{2.\Delta t} \quad (2)$$

3. Results and discussion

The obtained results combining the gypsum dehydration process, the calcite decarbonation and the direct mass measurement are presented in the figure 3. Tendency showed by the calculus versus time is in good agreement with the direct measurements even if, and logically, the mass decreasing seems to be faster by the proposed calculus. This expected result helps us highlight the capability of the restricted hypothesis to only consider the chemical changes of the material to accurately reproduce the mass transfer induced by the water and CO2 disappearance. After this first step of the works, the addition of a transport equation through the porous media could improve the quality of the numerical prediction.

4. Conclusions

Dehydration and decarbonation thermo-chemical conversion models have been used to identify the mass transfer of gypsum board submitted to standard fire on one side. The obtained results are in good agreement with the direct mass measurement of the panels. Because of the present works assume the disappearance of the water vapour and the CO_2 just after the chemical conversion, transport regime of the fluid through the porous media seems to be well adapted to characterise the fluid flow regime with permeable porous media. Nevertheless, better prediction of the mass transfer should be obtained by taking into account the direct momentum equation. Such consideration is under way but a permeability level versus mechanical damages advances is needed to really consider this incorporation. Finally, such results represent a new step to better understand the THCM behaviour of building material submitted to fire including the concrete materials.

References

Mélinge, Y., Nguyen, K.S., Lanos C. (2010) "Experimental study of thermo-chemical behaviour of gypsum based material under standard ISO 834 fire condition", *European Journal of Environmental an Civil Engineering (EJECE)*, 14(5): 561-577

Mélinge, Y., Nguyen, K.S., Daiguebonne, C., Guillou, O., Freslon, S., Lanos, C. (2011) "One-Dimensional-Time Study of the Dehydration of Plasterboards Under Standard Fire Condition (ISO 834): Thermo-Chemical Analysis", *Journal of Fire Sciences,* 29(4): 299 – 316

Rojo, A., Mélinge, Y., Guillou, O. (2013) "Kinetics of internal structure evolution in gypsum board exposed to standard fire", *Journal of Fire Sciences*, 31(5): 395-409

Rojo, A. (2013) "Etude de la structuration et du comportement du gypse sous condition incendie" (2013) *PhD thesis INSA Rennes*

Abriel, VW. (1983) "Calcium Sulphate Subhydrate, CaSO4_0.8H2O", *Acta Crystallographica*; C39: 956–958.

Kirfel, A., Will, G. (1980) "Charge Density in Anhydrite CaSO4 from X-ray and Neutron Diffraction measurements", *Acta Crystallographica*; B36: 2881–2890

The 16th International Congress on the Chemistry of Cement 2023 (ICCC2023)
"Further Reduction of CO_2 -Emissions and Circularity in the Cement and Concrete Industry"
September 18–22, 2023, Bangkok, Thailand

SURFACE EFFECT ON CHLORIDE DIFFUSION IN CALCIUM SILICATE HYDRATE

L. Xiong[1] and G. Geng[1*]

1 Department of Civil and Environmental Engineering, National University of Singapore, 117576, Singapore
** ceegg@nus.edu.sg*

ABSTRACT

The diffusivity of chloride ion in calcium silicate hydrate (C-S-H) has been intensively discussed via modelling or theoretical methods due to experimental challenges caused by preparing a bulk volume of pure C-S-H with certain pore structure. The surface effect of C-S-H on chloride ion transport is lumped into a hypothetical parameter called constrictivity which again requires investigation from experimental aspects. In this study, C-S-H with nominal Ca/Si 1.3 was synthesized using hydrothermal method. The synthetic C-S-H powder was pressed into solid platelets with different compactness and chloride ingress tests in concentration-driven and voltage-driven migration setup were directly conducted on these pure porous C-S-H platelets. The effective diffusivities of C-S-H samples were calculated from the through-diffusion test results, based on which the surface effect on chloride transport were discussed. The effect of change of pH in pore solution during migration test on chloride diffusion was captured by two-segment behavior of downstream chloride content evolution. The difference in effective diffusivities obtained from diffusion and migration tests showed that the surface effect played an important role in determining Cl^- transport rate within C-S-H. This work provides a novel insight into the transport of Cl^- in C-S-H pore structure.

KEYWORDS: *Calcium silicate hydrate, Through-diffusion tests, Effective chloride diffusivity, pH, Surface effect*

1. Introduction

Chloride-related durability issues are widely discussed and studied since its' universal existence in the steel reinforced concrete infrastructure serving under chloride environment. The measurement of chloride ion penetration into concrete, commonly referred to as chloride diffusivity, holds significant importance as an essential factor in predicting the service life of steel-reinforced concrete structures described in Alexander et al (2015). The process of chloride diffusion within saturated concrete, characterized as the movement of ions driven by concentration, occurs through accessible pathways including pre-existing cracks, capillary pores, and the diffusive porous structure of the hydration product known as Calcium silicate hydrate (C-S-H). Cl^- transport within C-S-H phase, the main diffusive solid when porosity is smaller than certain threshold value demonstrated in Patel et al (2018), is thought to be subjected to the effect from C-S-H pore wall. The effect of electric double layer on ion diffusion in cement paste was modeled or analytical solution from simplified ideal Poisson-Boltzmann equation described in Yang et al (2019) and Zhang et al (2023). The surface effect is yet to be explored from the experiment aspect.
This paper examines the transport behavior of Cl^- in C-S-H by quantifying the effective diffusivity from through-diffusion tests conducted on pure C-S-H solids for the first time. Samples with varying pore structures were tested to identify the role of pore size information on Cl^- transport rate and possible relation to the surface effect, as indicated by the obtained diffusivity values. Furthermore, the impact of

pH variations in the pore solution on transport was assessed by comparing the diffusivity values obtained from natural diffusion tests and migration experiment results.

2. Methodology

C-S-H sample with nominal Ca/Si of 1.3 was synthesized via hydrothermal method and the procedure was detailed in the previous study of Geng et al (2022). C-S-H solid pellets with a specific pore structure were obtained through the application of mechanical compression on synthetic C-S-H powders. To compare the impact of pore structure on chloride ion transport, stress levels of 200 MPa and 800 MPa were employed in this study. Afterwards, the solid pellets were submerged in epoxy and subsequently polished to achieve an approximate height of 10 mm, allowing both ends to be exposed once the epoxy had hardened. This preparation was done to facilitate the ingress of chloride ions. The polished samples underwent an additional step wherein they were individually immersed in an equilibrium solution of C-S-H within a desiccator that was slightly vacuumed to account for any water loss that occurred during the polishing process. Once their mass reached a stable state, the samples were mounted to diffusion cells specifically designed for accommodating such small sample sizes, as shown in Figure 1. The study aimed to examine the transport of chloride ions in C-S-H pellets, driven by the ion concentration gradient, using a natural diffusion setup as illustrated in Figure 1(a). The diffusion cell employed had a volume of approximately 113 mL in the upstream part (containing the chloride ion source) and 23 mL in the downstream part (without chloride addition). For each sampling interval, the solution in the downstream cell was completely replaced to maintain a relatively constant chloride concentration difference between the upstream and downstream regions. Moreover, the diffusion test employed a solution prepared from the filtered solution of C-S-H powder that had reached equilibrium. To account for the potential influence of different hydroxide ion (OH^-) concentrations on chloride ion transport rate, the pH of the filtered solution was adjusted by adding solid NaOH. To compare the steady-state diffusivity obtained from the natural diffusion test, another commonly employed method, namely the external electric field accelerated migration test, was conducted. In this test, the electrolyte cell volume was approximately 113 mL to facilitate frequent sampling, as depicted in Figure 1(b). To expedite the experiment, a constant voltage output of 5 V for the 200 MPa-compressed sample and 10 V for the 800 MPa-compressed sample was applied to the stainless-steel mesh, which functioned as the two electrodes in the setup. During the test, the voltage across the specimen was also recorded to account for any polarization effects of the electrodes. The catholyte consisted of a 0.5 M NaCl and 0.01 M NaOH (or 0.3 M NaOH) solution and a 0.3 M NaOH solution was chosen as the anolyte. The pore structure information was investigated from nitrogen sorption tests on samples after through-diffusion tests via density functional theory (DFT).

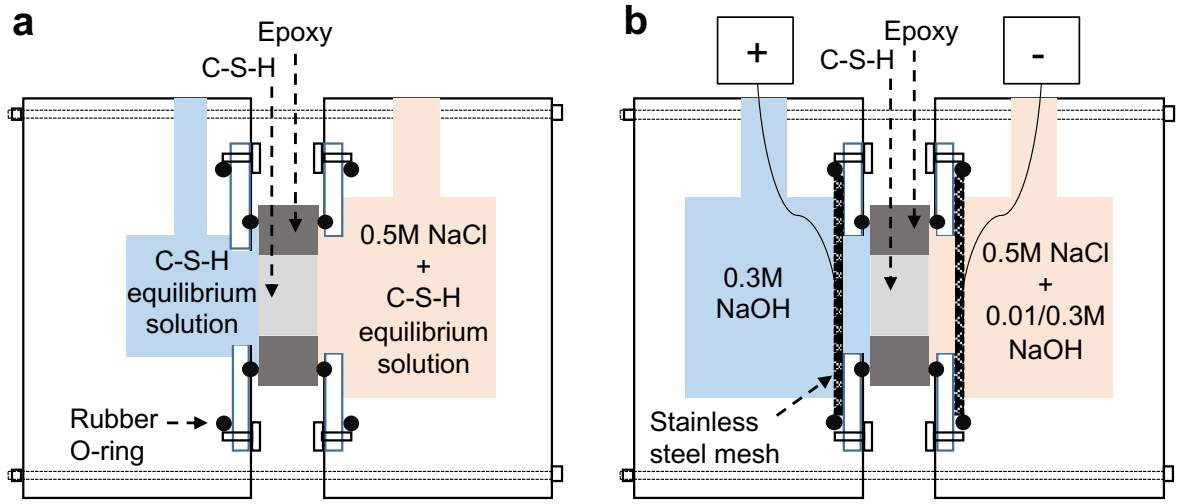

Figure 1 Schematics of through-diffusion experiment setup, (a) concentration-driven natural diffusion test, and (b) external electric field accelerated migration test.

3. Results and discussion

Pore structure of compacted platelets from 200 MPa and 800 MPa treatment by DFT analysis is shown in Figure 2 (a). Total porosity of samples prepared from 800 MPa (27.0%) is smaller than that of samples compressed under 200 MPa (41.3%) which is quite intuitive since the higher compaction load made sample denser. More fine pores can also be noticed in 800 MPa-compacted samples.

Typical chloride content evolution results in the downstream cell from diffusion and migration tests are shown in Figure 2 (b) and (c). Corresponding effective diffusivity was calculated based on Fick's 1st law and simplified Nernst-Planck equation, respectively. Obtained diffusion coefficients are listed in Table 1 and Table 2.

Based on diffusion test results, D_e was smaller for sample of same Ca/Si prepared from 800 MPa-compression compared with 200 MPa sample due to smaller total porosity which can also be noticed in migration tests. However, the diffusivity was not only influenced by the total porosity but the pore size distribution and different degree of interaction between C-S-H substrate and Cl^-. A clear shift towards smaller size regarding the most probable pores of 800 MPa compaction group compared with these of 200 MPa group can be noticed, indicating the higher chances that these diffusive pathways are interconnected via these critical pores. As a result, more pronounced constrictive effect in these small pores would also contribute to the reduction of Cl^- transport rate. When change pH of the equilibrium solution, the obtained effective diffusivities varied and is dependent on the concentration of source chloride. As shown in 800 MPa diffusion test with different upstream chloride concentration and equilibrium solution pH, When the upstream Cl^- concentration is 0.5 M, adjusting the equilibrium solution pH to 0.005 M would double the ion transport rate. However, the effective diffusivity decreased around 20% for the group with source chloride concentration of 0.01 M. And the diffusivity for 0.01 M group without pH adjust to equilibrium solution was relatively smaller than that of 0.5 M group. Thus, when the steady state diffusion was achieved, the ionic strength of the pore solution would affect the charged C-S-H pore wall's interaction with Cl^- and the role of OH^- would also change since the introduction of extra screening Na^+ to charged C-S-H surface would compete with the effect of C-S-H silanol group deprotonation caused by OH^- causing the different Cl^- transport rate.

Regarding the migration test results, two-segment linear evolution of chloride content in downstream cell can be observed. This behaviour was thought be related to the continue increase of OH^- concentration in the upstream due to the electrolysis of water during migration process. Effective diffusivity D_{e1} calculated from the first linear part was of the same magnitude to that from natural diffusion test D_e while this coefficient decreased sharply when using the second linear part to compute D_{e2}. Similar results were also obtained when change the upstream OH^- concentration from 0.01 M to 0.3 M. One of possible reasons could be the competition of current carrier for OH^- and Cl^-. However, it is not suitable to account for the reduction degree between 200 MPa and 800 MPa group since the concentration ratio of OH^- to Cl^- was similar when the chloride content began to slow down. As a result, the external electric should change the interaction between the charged C-S-H surface and Cl^- during migration and this interaction should be pore size dependant. In addition, the choice of OH^- in the chloride source part should also be careful based on the difference between diffusion and migration test results.

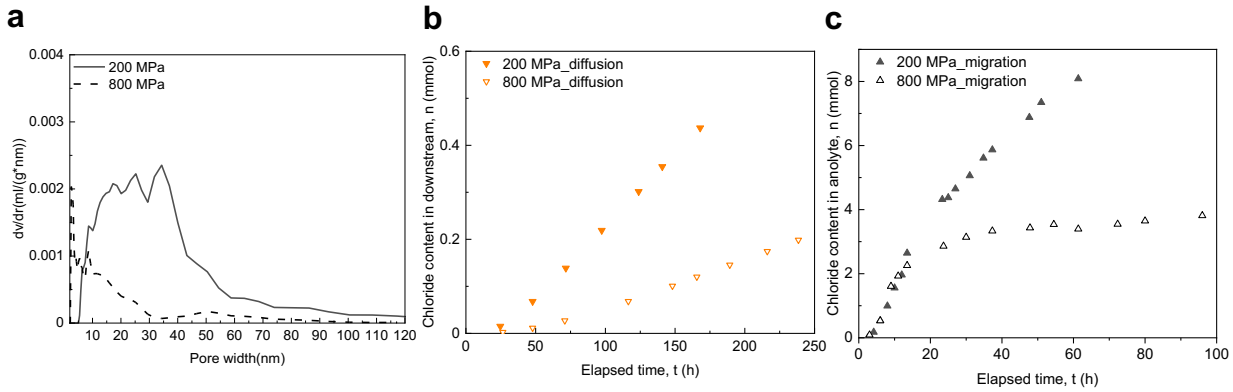

Figure 2 a) pore size distribution of 200 MPa and 800 MPa-compacted C-S-H platelets from nitrogen sorption test via DFT; typical chloride ion content evolution in downstream cell during b) diffusion test and c) migration test without pH adjustment showing two linear-segment behavior where De_1 and De_2 are calculated

Table 1 Effective diffusivity calculated from diffusion test with different pH and Cl^- concentration

	Diffusion				
upstream chloride concentration (M)	0.5	0.5	0.5	0.01	
Compaction load (MPa)	200	800	800	800	800
pH adjustment	equilibrium solution	equilibrium solution	equilibrium solution with 0.005M NaOH	equilibrium solution	equilibrium solution with 0.005M NaOH
D_e (10^{-11} m^2/s)	4.09	1.28	2.68	1.11	0.90

Table 2 Effective diffusivity calculated from migration test with different pH

	Migration			
upstream chloride concnetration (M)	0.5		0.5	
Compaction load (MPa)	200		800	
pH adjustment	0.01 M NaOH	0.3 M NaOH	0.01 M NaOH	0.3 M NaOH
D_{e1} (10^{-11} m^2/s)	4.16 ± 0.14	1.58	1.64	0.056
D_{e2} (10^{-12} m^2/s)	14.5 ± 2.23		0.57	

4. Conclusion

To sum up, the effect of charged C-S-H surface on chloride ion transport within C-S-H was investigated from the obtained macro diffusivities via diffusion and migration tests on pure C-S-H platelets. The OH^- played a different role in Cl^- ingress process considering the competition of effect from silanol group deprotonation caused by OH^- and the screening cations (Na^+ in this study) to the charged pore wall in diffusion test setup. On the other hand, the increase of OH^- concentration in the upstream during migration test would hinder chloride transport and the reduction extent was related to C-S-H pore structure, providing information on the choice of OH^- in the migration test to make the accelerated test results comparable to that from diffusion test. And these results demonstrated the importance role of charged C-S-H surface on chloride ion transport.

References

Alexander, M. and Thomas, M. (2015). "Service life prediction and performance testing—Current developments and practical applications", *Cement and Concrete Research*, 78, 155-164

Liu, C. and Zhang, M. (2023). Microstructure-based modelling of chloride diffusivity in non-saturated cement paste accounting for capillary and gel pores. *Cement and Concrete Research*, 168, 107153

Patel, R. A., Perko, J., Jacques, D., De Schutter, G., Ye, G. and Van Bruegel, K. (2018). Effective diffusivity of cement pastes from virtual microstructures: Role of gel porosity and capillary pore percolation. *Construction and Building Materials*, 165, 833-845

Yang, Y., Patel, R. A., Churakov, S. V., Prasianakis, N. I., Kosakowski, G. and Wang, M. (2019). Multiscale modeling of ion diffusion in cement paste: electrical double layer effects. *Cement and Concrete Composites*, 96, 55-65

Zhang, Z., Yan, Y., Qu, Z. and Geng, G. (2022). Endowing strength to calcium silicate hydrate (CSH) powder by high pressure mechanical compaction. Cement and Concrete Research, 159, 106858

The 16th International Congress on the Chemistry of Cement 2023 (ICCC2023)
"Further Reduction of CO_2 -Emissions and Circularity in the Cement and Concrete Industry"
September 18–22, 2023, Bangkok, Thailand

Increasing circularity and material efficiency using ore sand in concrete - A Brazilian case study

L. Bento[1], M. F. L. Menezes[2]*, A. C. L. Alves[3], M. F. Araújo[4], G. Reis[5] and R. J. P. Reis[6]

[1] *Co-log, Belo Horizonte, Brazil*
Email: luciano.bento@cologcoprodutos.com
[2] *Co-log, Belo Horizonte, Brazil*
Email: mariana.menezes@cologcoprodutos.com
[3] *Consultare Labcon, Belo Horizonte, Brazil*
Email: qualidade@consultarelabcon.com.br
[4] *Consultare Labcon, Belo Horizonte, Brazil*
Email: marcelo@consultarelabcon.com.br
[5] *Consultare Labcon, Belo Horizonte, Brazil*
Email: guilherme@consultarelabcon.com.br
[6] *Consultare Labcon, Belo Horizonte, Brazil*
Email: rubens@consultarelabcon.com.br

ABSTRACT

The most common types of fine aggregates for concrete are natural sands and crushed rocks. The ore sand comes from a new source: the iron ore mining sites. The ore is mainly constituted from hematite and quartz and the beneficiation process aims to separate them. The quartz part, that used to be the tailings, can be used as ore sand for concrete. Since this material is already mined and would otherwise goes to dams or dry stacking, using it reduces exploration from the conventional sources of aggregates. Therefore, the ore sand presents a low environmental impact and enables civil construction to become more sustainable. So, this work aims to evaluate the ore sand application in concrete comparing it with the other three most used sands in Belo Horizonte region. This work shows the characterization of this new fine aggregate and compares a range of concrete mixes using ore sand with the ones using natural sand and crushed rocks from local sources in Belo Horizonte, Brazil. It was found that using 30% of ore sand and 70% gneiss crushed rock was the best sand mix in concrete, increasing material efficiency in the whole compressive strength range evaluated and achieving up to 25% reduction on the cement consumption. It can be explained by ore sand morphology plus the improvement of particle packing that allows the concrete optimization.

KEYWORDS: *Ore sand, co-products, concrete, iron ore, tailings*

1. Introduction

Sand is a key raw material for construction, paving, land reclamation and other applications, so UNEP recommends sand should be recognized as a strategic resource. Its extraction, especially in active sand bodies as rivers, when outpaces the natural supply, causes erosion that extends its effect beyond the deposit to the communities downstream the river system, impacting on land-use changes, air pollution, salinisation, fisheries and biodiversity (UNEP (2022), Golev et al (2022), Hackney et al. (2021)).
In Brazil, approximately 500 million tons of aggregates are used (ANEPAC (2020)). On the other hand, only in the state of Minas Gerais, 290 million tons of tailings and overburdens are generated from the mining activity (FEAM (2018)). The use of these tailings as aggregates can increase the circularity of the local concrete and mortar, as recommended by UNEP to search for diversity material and focus on local solutions (UNEP (2022), Golev et al (2022), Vilaça et al. (2022)). In this context, iron ore beneficiation, which consists of grinding, milling and iron concentrating, generates a sandy tailing. This material

characteristics fit well as a fine construction sand (Faria and Menezes (2022), Almada et al (2022), Kuranchie1 et al (2015), Protasio et al (2021), Shettima et al (2016)). This work aims to compare the ore sand use in concrete with the other three most used sands in Belo Horizonte region.

2. Materials and Methods

The characteristics of the aggregates are presented in Table 1 and the iron ore sand typical chemical characterization in Table 2. It is important to mention that ore sand is potentially innocuous for alkali-aggregate reaction (ABNT NBR 15577:2018). It can be noted that the ore sand is finer than the other sands generally used in concrete. Also, its sphericity is greater than the other sands, although the roundness is the lowest one. The cement used was a CP-V-ARI-RS (high initial strength and sulphate resistant) from Holcim. The admixture was a lignosulfonate *Clarena* from GCP.

Table 1 – Characteristics of the aggregates used on the study

Characteristic		Ore Sand	Natural Sand	Gneiss Sand	Limestone Sand	12,5mm Gneiss Gravel	25mm Gneiss Gravel
Particle Size Distribuition – ABNT NM 248:2003. Accumulated retained material in each sieve (%)	19 mm	X	X	x	x	X	11
	12.5 mm	X	X	x	x	X	80
	9.5 mm	X	X	x	x	26	97
	6.3 mm	X	X	x	x	76	100
	4.8 mm	X	1	x	1	90	100
	2.4 mm	X	3	14	25	98	100
	1.2 mm	1	10	37	44	99	100
	0.6 mm	4	36	54	53	99	100
	0.3 mm	8	74	65	56	99	100
	0.15 mm	33	94	77	60	99	100
	Bottom	100	100	100	100	100	100
Maximum Dimension (mm) - NM 248:2003		0.6	2.4	4.8	4.8	12.5	25.0
Fineness Modulus - NM 248:2003		0.46	2.18	2.47	2.90	6.10	7.08
Powdery Material (passing on 75µm) (%) – ABNT NBR 16973:2021		26.4	0.8	13.2	29.0	1.0	0.2
Real Density (kg/dm³) – NBR 16916:2021		2.78	2.73	2.66	2.74	2.66	2.68
Typical Roundness – ISO 13503-1		0.21	0.44	0.25	0.25	x	x
Typical Sphericity - ISO 13503-1		0.74	0.72	0.68	0.70	x	x

Table 2 – Ore sand typical chemical analysis (X-Ray Fluorescence) and Soluble ions (ABNT NBR 9917:2022)

SiO_2	Fe	Al_2O_3	P	Mn	CaO	MgO	TiO_2	Soluble chloride	Soluble sulfate
84%	10.1%	0.36%	0.01%	0.03%	0.01%	0.02%	0.02%	0.01%	<0.01%

The study goal was comparing the main possibilities for fine aggregates mixes for concrete in Belo Horizonte region through particle packing and Abrams' curves evaluation. So, five concrete series with distinct sand blends were tested: 70 % Natural Sand + 30 % Ore Sand (70NS_30OS); 70 % Gneiss Sand + 30 % Natural Sand (70GS_30NS); 70% Gneiss Sand + 30% Ore Sand (70GS_30OS); 70% Gneiss Sand + 30% Limestone Sand (70GS_30LS) and 70% Natural Sand + 30% Gneiss Sand (70NS_30GS). Each serie was composed by four concrete mixes with 0.45, 0.60, 0.75, 0.90 water/cement (w/c) ratio. In order to carry on the study, the basic concrete mix with 0.60 w/c ratio of each serie was calculated, executed and had it water consumption and mortar content adjusted by ACI Method. With the basic concrete mix defined, the other w/c ratio concrete were calculated and executed. The basic mix (w/c approximatly

0.60) for each sand blend is presented in Table 3. For the 20 concrete, the workability was fixed on 120 ± 20 mm slump test result and compressive strength was evaluated for 3, 7 and 28 day.
With these results, Abrams' curves (compressive strenght vs w/c ratio) were adjusted by least squares method for each sand blend concrete serie. In order to understand the material efficency, the cement consumption for the main concrete types demanded by construction market in Brazil (f_{ck} 15, 18, 20, 25, 30, 35, 40MPa) were calculated based on the Abrams' curve.

Table 3 – Basic concrete mix (w/c ratio approximatly 0,60) for each sand blend serie

Concrete Parameter	70NS_30OS	70GS_30NS	70GS_30OS	70GS_30LS	70NS_30GS
Cement (kg/m^3)	324	341	318	355	326
Natural Sand (kg/m^3)	581	259	-	-	-
Ore Sand (kg/m^3)	261	-	-	-	606
Gneiss Sand (kg/m^3)	-	608	556	606	261
Limestone Sand	-	-	250	272	-
9,5mm Gravel (kg/m^3)	306	283	307	286	281
19mm Gravel (kg/m^3)	713	660	715	667	654
Water (l/m^3)	198	196	201	196	189
Aditional water (l/m^3)	+3.0	-3.0	+6.0	-4.0	-3.0
Admixture (l/m^3)	2.59	2.72	2.86	2.84	2.61
Slump (mm)	12.5	12.0	11.0	11.0	12.0

3. Results

The combined sand particle size distribuition for each concrete serie is presented in Figure 1. In order to analise the particle packing, the ideal distribuition for Andreasen (1930), considering 2,4mm maximum dimension and Q as 0.37, is also plotted. It can be noted that the Ore Sand and the Limestone Sand bring the fines below 0,3mm for ideal packing according to Adreasen that lacks when using only gnaisse and natural sand. Since the gnaisse sand has an important ammount of coarser material above 1,2mm, its blend with Ore Sand and Limestone Sand achieves a distribuition close to Adreasen ideal packing.

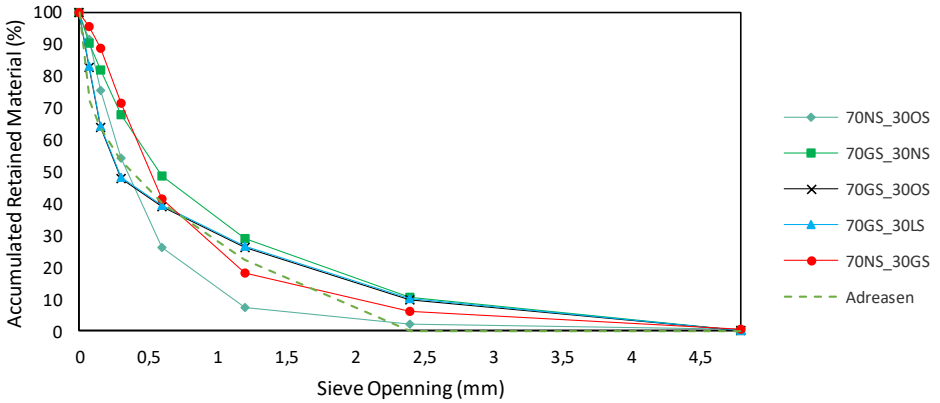

Figure 1 – Sand combined particle size distribuiton for each concrete series and Adreasen distribuition

The concrete results for the 28-day compressive strength and the adjusted Abrams curve for each family is presented on Figure 2. It can be noticed that the R^2 of every serie, is above 0.87, showing a good fit. Comparing the series for each blend, the blend 70% Gneiss Sand + 30% Ore Sand is the one presenting the highest compressive strength in the whole w/c ratio range. Besides this serie, the 70% Natural Sand + 30% Ore Sand is the second best blend on the 0.40 to 0.70 w/c ratio range and on the higher w/c ratio the 70% Gneiss Sand + 30% Natural Sand is the second best pick. The Gnaisse and Ore Sand results can be justified by the particle packing close to ideal Adreasen distribuition, and by the high sphericity of ore

sand and favourable morphology of gnaisse sand, as well. The second best blend being Natural Sand and Ore Sand probably was driven by morphology, since both sands have with high sphericity and high roundness for natural sand, because the combined particle size distribuition was too fine according to ideal Adreasen packing.

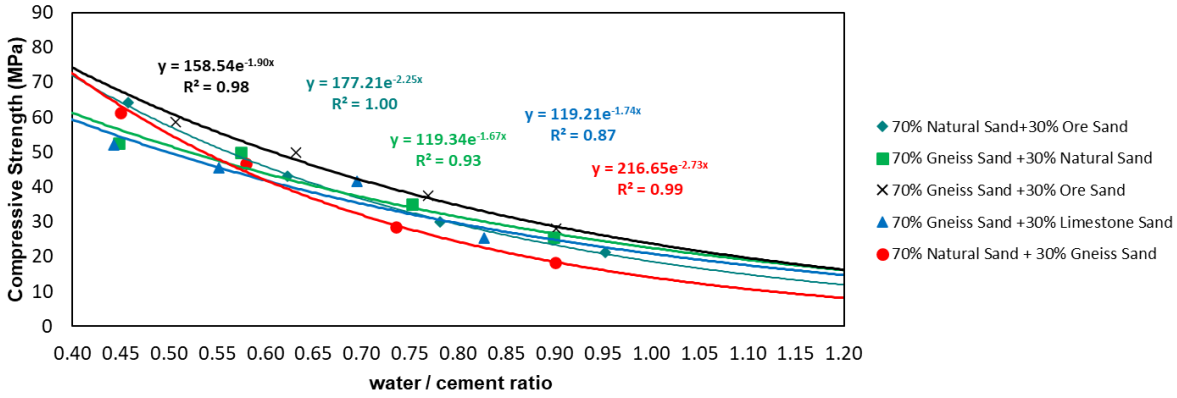

Figure 2 – Abrams' Curves: 28-day compressive strength vs w/c ratio for each sand blend serie

Based on the Abrams's Curves adjustment, the estimated cement consumption for the main market concrete is shown in Figure 3. From the graph, it can be seen that the 70% Gneiss Sand + 30% Ore Sand can diminish cement consumption on the concrete from 10 to 45MPa, reducing up to 25% consumption comparing to the other series. This increase on material efficiency by using the ore sand lowers CO_2 emissions and reduces costs of concrete.

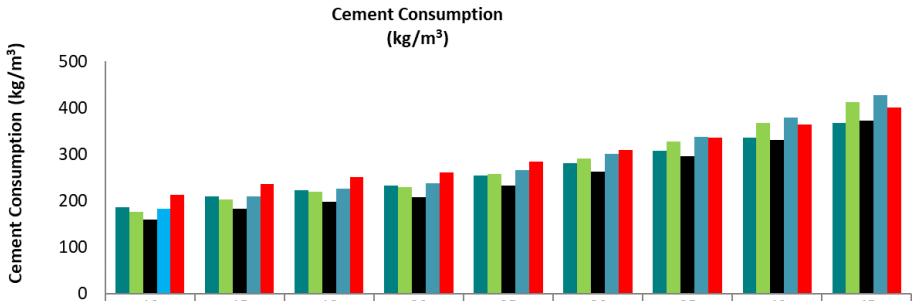

	10	15	18	20	25	30	35	40	45
70% Natural Sand+30% Ore Sand	186	209	222	232	255	281	308	336	368
70% Gneiss Sand +30% Natural Sand	176	202	218	229	258	291	327	367	413
70% Gneiss Sand +30% Ore Sand	159	183	197	207	233	263	295	331	372
70% Gneiss Sand +30% Limestone Sand	183	209	226	237	266	300	337	379	426
70% Natural Sand + 30% Gneiss Sand	212	236	250	260	283	309	336	363	401

Figure 3 – Cement consumption from f_{ck} 10 to 45MPa concrete for each sand blend

3. Conclusions

The study goal was comparing the available sands mixes for concrete in Belo Horizonte region through Abrams' curves, specially evaluating the ore sand use. The results were consistent that the highest compressive strength in the whole w/c ratio range was the blend 70% Gneiss Sand + 30% Ore Sand. It can be explained by a good particle packing and also by morphology of both sands. This blend allowed to reduce up to 25% cement consumption on concrete, compared to the other sand blends. The second best blend on the 0.40 to 0.70 w/c ratio range is the 70% Natural Sand + 30% Ore Sand. So, besides the circularity gains, using the ore sand enhances the concrete efficency in Belo Horizonte region and contributes to reduce CO_2 emissions of these concrete.

References

Andreasen, A.H.M. and Andersen, J. (1930). "Über die Beziehung zwischen Kornabstufung und Zwischenraum in Produkten aus losen Körnern (mit einigen Experimenten)." *Colloid & Polymer Science*, 50 (3), 217-228.

Almada, B. S., Melo, H. S. S., Duarte, M. S., Aguilar, M. T. P., Garcia, D. C. S, Silva, G. B., Santos, W. S. (2022) "Study of mechanical, durability and microstructural properties of cementitious composite with addition of different iron ore tailings from Brazil." *Journal of Materials Research and Technology*, 18, 1947-1962.

Associação nacional das entidades de produtores de agregados para construção – ANEPAC (2020) *"*Panorama ambiental da mineração*". Final Report.*

Faria, S. F., Menezes, M. F. L., (2022) "Reduction in cement consumption of concrete by using mining sand" *63rd Congresso Brasileiro do Concreto.*

Fundação estadual do meio ambiente – FEAM (2020) "Dados econômicos." *Final Report*.

Golev, A., Gallagher, L., Vander Velpen, A., Lynggaard, J.R., Friot, D., Stringer, M., Chuah, S., Arbelaez-Ruiz, D., Mazzinghy, D., Moura, L., Peduzzi, P., Franks, D.M. (2022) "Ore-sand: A potential new solution to the mine tailings and global sand sustainability crises" *Final Report*. Version 1.4. The University of Queensland & University of Geneva

Hackney, C.R., Vasilopoulos, G., Heng, S., Darbari, V., Walker, S. and Parsons, D.R. (2021). Sand mining far outpaces natural supply in a large alluvial river. *Earth Surface Dynamics*, 9(5), 1323–1334.

Kuranchie1, F. A., Shukla1, S. k., Habibi1, D. and Mohyeddin, A. (2015) "Utilization of iron ore tailings as aggregates in concrete" *Cogent Engineering*, 2: 1083137

Protasio, F. N. M., Avillez, R.R., Letichevsky, S., Silva, F. A. (2021) "The use of iron ore tailings obtained from the Germano dam in the production of a sustainable concrete" *Journal of Cleaner Production*, 278, 123929.

Shettima, A. U., Hussin, M. W., Ahmada, Y., Mirza, J. (2016) "Evaluation of iron ore tailings as replacement for fine aggregate in concrete." *Construction and Building Materials*, 120: 72–79

UNEP (2022) "Sand and Sustainability: 10 strategic recommendations to avert a crisis", GRID-Geneva, United Nations Environment Programme, Geneva, Switzerland.

Vilaça, A.S.I., Simão, L., Montedo, O.R.K., Novaes de Oliveira, A.P., Raupp-Pereira, F. (2022) "Waste valorization of iron ore tailings in Brazil: Assessment metrics from a circular economy perspective.", *Resources Policy*, 75, 102477.

The 16th International Congress on the Chemistry of Cement 2023 (ICCC2023)
"Further Reduction of CO_2 -Emissions and Circularity in the Cement and Concrete Industry"
September 18–22, 2023, Bangkok, Thailand

Effect of Mix Proportion as W/C and Amount of GGBS Contents on CO_2 Adsorption

R. Yahiro[1*], M. Kojima[2], and T. Iyoda[3]

[1] *Shibaura Institute of Technology, Tokyo, Japan*
Email: mh22020@shibaura-it.ac.jp
[2] *Takenaka Corp., Chiba, Japan*
Email: kojima.masarou@takenaka.co.jp
[3] *Shibaura Institute of Technology, Tokyo, Japan*
Email: iyoda@shibauta-it.ac.jp

ABSTRACT

In recent years, there has been a growing movement in the world toward the realization of a carbon neutral society as a measure against global warming. There are also a number of efforts in the construction industry. Types of cement with a high percentage of admixture replacement are becoming widely used to reduce CO_2 emissions during cement production. In addition, technology that uses the carbonation reaction of concrete to adsorb CO_2 into concrete is attracting attention. At higher W/C, CO_2 penetrates deeper into the concrete because of the larger pores, resulting in a greater depth of carbonation. In this study, we examined the effect of different mix proportions on the amount of CO_2 adsorption. Cement pastes with different W/C and blast furnace slag fine powder substitution rates were carbonated in a high concentration CO_2 chamber and measured the amount of adsorption, considering the ease of CO_2 penetration. As a result, a tendency was observed that the CO_2 penetrates more deeply, and the amount of CO_2 adsorption is higher in mix proportion with high blast furnace slag fine powder content or high W/C. Also, it shows a trend that the potential to adsorb CO_2 is greater as the CaO percentage that the sample has is increased.

KEYWORDS: *CO_2 adsorption, ground granulated blast furnace slag, carbonation reaction, CO_2 penetration*

1. Introduction

In recent years, rising seas, droughts, floods, and extreme weather conditions caused by global warming have occurred in the world. Therefore, as a measure against global warming, there is a growing movement toward the realization of a carbon-neutral society, in which the sum of emissions and absorption of the greenhouse gases that cause the problem is substantially zero. There are also a number of initiatives being undertaken in the construction industry. It is a problem of CO_2 emissions during cement production. In an effort to reduce CO_2 emissions from the cement production process, cement with high replacement of admixtures such as ground granulated blast furnace slag or fly ash is being used. In addition, there has been a growing interest in technologies that use the carbonation reaction of concrete in order to absorb CO_2 into the concrete. Considering the carbonation reaction, even if the concrete is carbonated in the same period of time and in the same environmental place, the ease of CO_2 penetration is different depending on the types of cement and W/C. Therefore, the carbonation depth is different. CO_2 absorption cannot be determined by only the carbonation depth because different types of W/C and cement absorb different amounts of CO_2 when carbonated.

In this study, we prepared specimens of cement paste with different types of cement and W/C. Accelerated carbonation was applied. The sample was divided, and the CO_2 absorption was calculated for each part of the sample. This allowed us to study the quantification of CO_2 absorption considering the ease of CO_2 penetration and the CO_2 absorption potential of different types of cement.

2. Materials and outline of experiments

2.1 Materials and mix proportions

In this study, cement paste samples were used to eliminate the influence of aggregate as a fundamental study. The mix proportion is shown in Table 1. The experiment was conducted with four mix proportions, different types of cement and different W/C. As cement, Ordinary Portland Cement (OPC) and Blast Furnace Cement, which is made by replacing ground granulated blast-furnace slag (GGBS) with OPC, were used in the test. The blast furnace slag cement was set as BB with 50% replacement of GGBS and BC with 70% replacement of GGBS. Table 2 also shows the chemical composition of OPC and GGBS. The amount of CaO in the cement was changed by changing the percentage of GGBS.

Table 1 Mix proportion of cement paste

No.	Type of cement	W/C (%)	Unit weight (kg/m^3)		
			W	OPC	GGBS
N30	OPC	30	487	1622	-
N50	OPC	50	612	1225	-
BB50	BB	50	602	602	602
BC70	BC	70	675	289	675

Table 2 Chemical Compositions of OPC and GGBS

	Chemical composition (%)											
	SiO_2	Al_2O_3	FeO	Fe_2O_3	CaO	MgO	TiO_2	MnO	SO_3	Na_2O	K_2O	P_2O_5
OPC	20.19	5.18	-	2.78	65.01	1.18	0.25	0.15	2.10	0.31	0.36	0.16
GGBS	33.27	13.94	0.31	-	40.00	5.47	0.57	0.15	1.99	0.26	0.26	0.02

2.2 Calculation of CO_2 absorption

Figure 1 shows the outline of the experiment. Rectangular specimens of 40×40×160mm were casted, demolded the day after placing, and sealing cured for 7 days. After curing was completed, the sides were sealed with aluminium tape and one 40×40mm surface was released. The specimens were placed in an accelerated carbonation chamber (20°C, 60% RH, 5% CO_2 concentration) for 28 days of accelerated carbonation. After carbonation, they were sliced at 10 mm intervals from the release surface and treated with acetone to stop the hydration reaction. The measurement of TG-DTA was performed under N_2 flow environment with a temperature increase rate of 20°C/min from room temperature to 1000°C. The $CaCO_3$ content ratio was calculated by using the inflection point of the peak in the DTA curve to estimate the amount of decarbonation. Amount of CO_2 absorption was calculated using difference in $CaCO_3$ content ratio between carbonated and uncarbonated. In addition, specimens made under the same conditions were saturated with water under vacuum conditions, and the saturated mass and mass in water were measured. After that, the specimens were placed at 40°C, 30% RH until the mass loss became constant, and then the dry mass was measured. Porosity was calculated by Archimedes' method using saturated mass, mass in water, and dry mass.

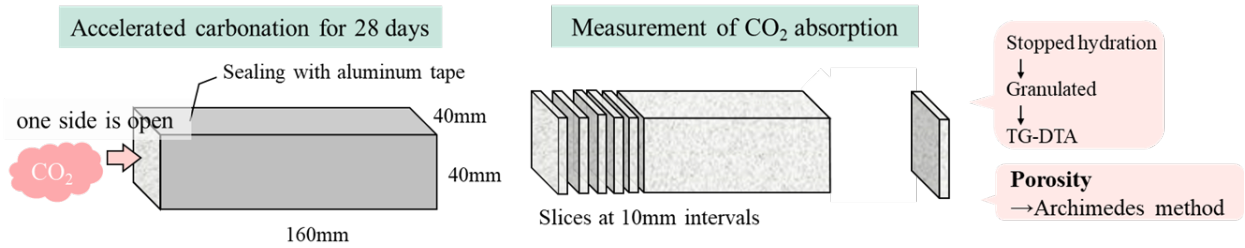

Figure 1 Outline of the experiment

The amount of CO_2 absorption per sliced 40×40×10mm sample which volume is 16 cm^3, with porosity taken into account, was calculated using Equation (1).

$$CO_2 \text{ absorption[g]} = \text{density}\left[\text{g/cm}^3\right] \times \text{Volume}(16\text{cm}^3) \times (1\text{-Porosity}) \times A[\%] \times \frac{44}{100} \quad (1)$$

where, A: difference in $CaCO_3$ content ratio between carbonated and uncarbonated

3. Results and discussion

3.1 CO_2 absorption as hardened cement

Figure 2 shows the amount of CO_2 absorption in each mix proportion for each sliced sample. The horizontal shows the distance from the surface in contact with the CO_2. N30 and N50 were not completely carbonated even at 10 mm from the surface. On the other hand, carbonation reached 20 mm in BB50 and 40 mm in BC70. It is clear that the depth of CO_2 absorption is different depending on the types of cement and W/C as well as the carbonation depth. It was found that in the order of BC70, BB50, N50, and N30, CO_2 was absorbed more deeply into the specimen. In BC70, CO_2 absorption from 0~10 mm, 10~20 mm, and 20~30 mm was about the same in each layer.

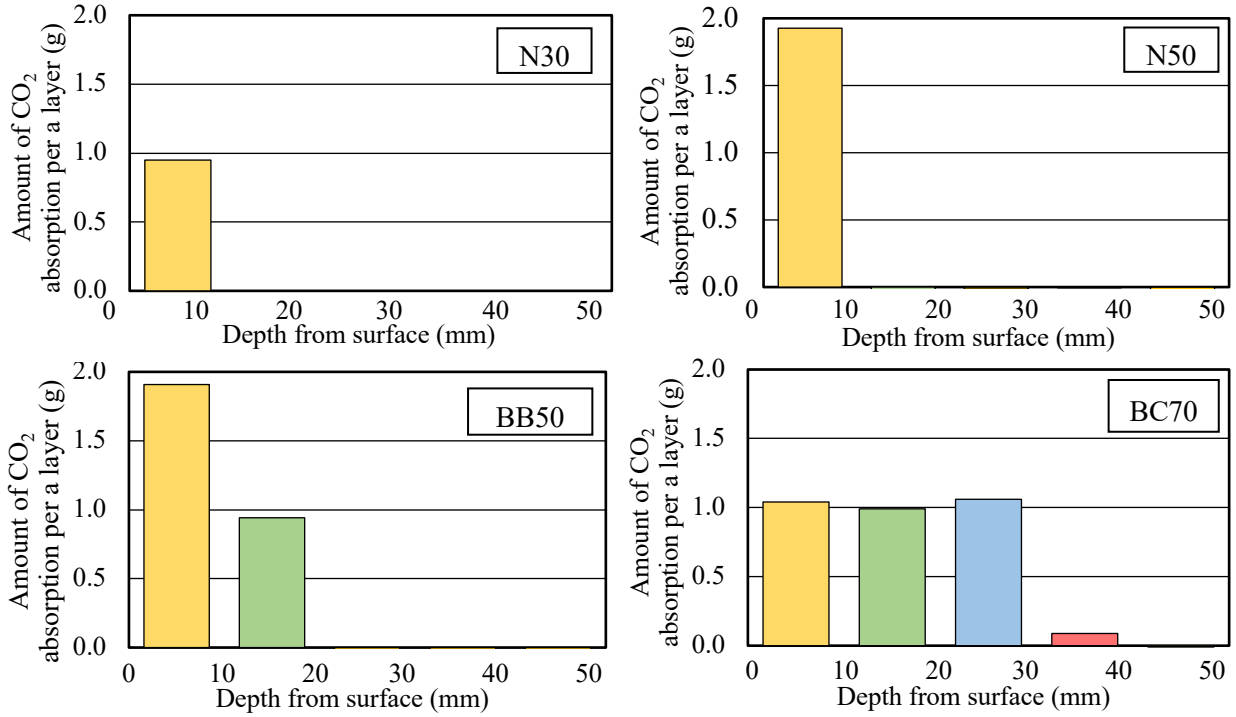

Figure 2 The amount of CO_2 absorption

Figure 3 shows the amount of CO_2 absorption by the total of 40×40×160mm specimen. CO_2 absorption was high in the order of BC70, BB50, N50, and N30. It was found that CO_2 absorption is greater in total as it absorbs CO_2 to a more internal level by carbonating at 5% CO_2 concentration for 28 days.

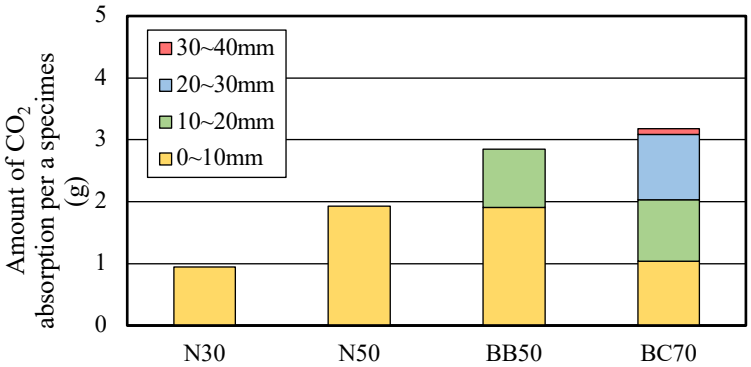

Figure 3 Amount of CO_2 absorption by the total of 40×40×160mm specimen

3.2 CO_2 absorption potential of each mix proportion

We focused on the amount of CO_2 absorbed per layer shown in Figure 3. It can be seen that the amount of CO_2 absorption in one layer is different depending on the mix proportion. Though the largest total absorption was BC70, amount of CO_2 absorption of the first layer was smaller in BC70 than in BB50.In addition, the CO_2 absorption of N30 and N50 did not reach the second layer, and the first layer is not considered to be fully carbonated either, but the CO_2 absorption of the first layer was equal to or higher than that of B70. Therefore, we considered there was potential for the amount of CO_2 that could be absorbed by each mix proportion.
CO_2 absorption was measured using powder samples in which the effect of porosity was eliminated so that carbonation proceeds in the same regardless of mix proportion. Samples of 48×40×2 mm were made and sealing cured for 7 days. And hydration was stopped and the specimens were granulated. Based on previous studies, accelerated carbonation was performed for 7 days after adding 70% water to the sample mass to eliminate the effect of sample drying. After carbonation, CO_2 absorption was measured by TG-DTA.
The results of the CO_2 absorption per $1m^3$ of cement paste are shown in Figure 4 Amount of CO_2 absorption was high in the order of N30, N50, BB50, and BC70 and smaller for higher GGBS content. Figure 5 shows the relationship between the amount of CaO content per $1m^3$ of cement and the amount of CO_2 absorption. The larger the CaO content, the greater the CO_2 absorption potential. BC70, which has a smaller CO_2 absorption potential, has a smaller CaO content, indicating that the potential for CO_2 absorption is affected by the CaO content. It is thought that this difference in potential affected the amount of CO_2 absorption in each layer.

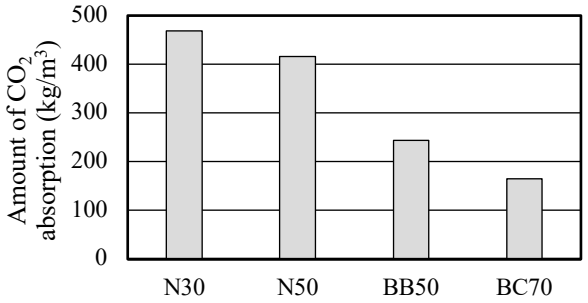

Figure 4 Amount of CO_2 absorption

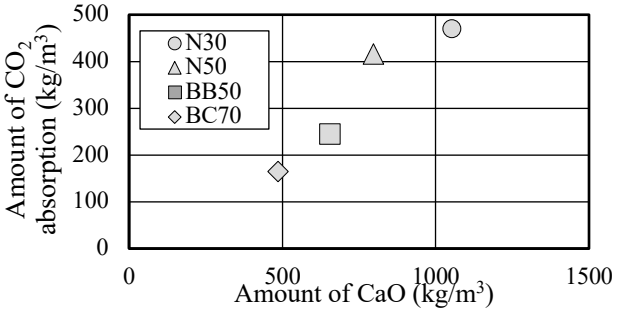

Figure 5 Relationship between the amount of CaO

4. Conclusions

1) By carbonating the hardened cement pastes and measuring the amount of CO_2 absorbed by separating it at each distance from the surface, it was found that the deeper the CO_2 absorption, the more CO_2 was absorbed.
2) Carbonation with powder samples without considering the ease of CO_2 absorption, such as porosity, is thought to provide the potential for CO_2 absorption of cement paste, and the higher the amount of CaO in the mix proportion, the greater the potential for CO_2 absorption.

Acknowledgements

This paper is based on results of "Development of Materials, Manufacturing Methods and Quality Control System on Innovative Carbon Negative Concrete", JPNP21014, commissioned by the New Energy and Industrial Technology Development Organization (NEDO).

References

Iyoda, T., Ishikawa, E.and Ikeo, Y. (2023) "Experimental study on quantification of carbon dioxide adsorption by different cement types and mix proportions", *Eighth International Symposium on Life-Cycle Civil Engineering (IALCCE 2023)* (Printing)

Kuroda, Y. and Kikuchi, T. (2009) "Uptake of Carbon Dioxide in the Demolished and Crushed Concrete", *Concrete Research and Technology*, Vol.20, No.1, :15-22

The 16th International Congress on the Chemistry of Cement 2023 (ICCC2023)
"Further Reduction of CO_2 -Emissions and Circularity in the Cement and Concrete Industry"
September 18–22, 2023, Bangkok, Thailand

Formation of closed pore structure porous glass-ceramics for thermal insulation

Kefeng. Jiang[1] and Wei. Chen[2*]

[1] *State Key Laboratory of Silicate Materials for Architectures, Wuhan University of Technology, Wuhan, China*
Email: jiangkefeng@whut.edu.cn
[2] *State Key Laboratory of Silicate Materials for Architectures, Wuhan University of Technology, Wuhan, China*
Email: chen.wei@whut.edu.cn

ABSTRACT

Due to the low density, low thermal conductivity and low water absorption, porous glass-ceramics have demonstrated excellent performance for thermal insulation. Closed pore structure can greatly reduce the thermal conductivity and convection as well as achieve high mechanical strength. Here we use Fe_2O_3, which is the by-product of copper tailings, to optimize the pore structures of the porous glass-ceramics and facilitate the formation of uniform closed pore structure. The porous glass-ceramics were prepared by melting-quenching method, followed by sufficiently foaming through powder sintering route with SiC powders as foaming agent. The micro structure, pore structure and thermal insulation performance were directly observed by X-ray computed tomography and infrared thermal imager. The results show that the addition of Fe_2O_3 modified the depolymerization degree of the glass network and increased the numbers of non-bridged oxygen. The resultant closed pore structure showed a better thermal insulating performance than open pore structure.

KEYWORDS: *Porous-glass ceramics; Pore structure control; Closed pores; Fe_2O_3; Foaming process*

1. Introduction

Porous glass-ceramic is a kind of porous material, which generally composed by glass phase and crystalline phase with gas inside[1,2]. Due to the unique properties, such as low density, low thermal and acoustic conductivity, low water absorption and excellent chemical resistance[3,4], porous glass-ceramics have been used in thermal insulation, acoustic insulation, catalyst support, water treatment and so on. Pore structure is a key factor to the performance of the porous glass-ceramics. As the air possesses a much lower thermal conductivity (0.0257 $W \cdot m^{-1} \cdot K^{-1}$ at 20 ℃) than Al_2O_3 ceramics (25 $W \cdot m^{-1} \cdot K^{-1}$) or multicomponent glass (0.771 $W \cdot m^{-1} \cdot K^{-1}$ to 0.971 $W \cdot m^{-1} \cdot K^{-1}$)[5,6], pores foamed in glass-ceramics can greatly reduce the thermal conductivity of materials. Furthermore, when the pores are disconnected, the closed pores can further reduce the thermal radiation and convection. Therefore, the closed pore structure has the lowest effective thermal conductivity in non-vacuum conditions. In addition, closed pores can also increase mechanical strength and lower water absorption. In this work, the influences of Fe_2O_3 on the foaming process and properties of porous glass ceramics was investigated. We use Fe_2O_3 to optimize the pore structures of porous glass-ceramics and to facilitate the formation of closed pores. We investigated influences of Fe_2O_3 on the glass network in the porous glass-ceramics and analyze the pore structures and thermal insulation performance of the porous glass-ceramics.

2. Materials and methods

The starting materials used in this work are analytical reagents supplied by Sinopharm Chemical Reagent Co. including SiO_2 (≥99.0%), CaO (≥98.0%), Al_2O_3 (≥99.0%), MgO (≥98.5%), Fe_2O_3 (≥99.0%), P_2O_5 (≥98.0%), K_2CO_3 (≥99.0%) and SiC (≥99.9%). SiC is used as foaming agent and grinded below 75 μm. The composition of the designed glass sample is $52SiO_2$-15.6CaO-$12Al_2O_3$-11MgO-$3P_2O_5$-$4K_2O$ (in wt.%) with additional 0 wt.%, 2.4 wt.%, 4.4 wt.%, 6.4 wt.% and 8.4 wt.% Fe_2O_3 (named as G0, G1, G2, G3, and G4), respectively. The composition of the basic glass is designed by the phase region of diopside

in the phase diagram (Fig. S1) and the normal components of copper tailings and phosphorus tailings. A bunch of 150 g mixed raw material powders were ball-milled in agate ball mills with 20 mm balls for 2h using a rotation speed of 300 rpm and powder/ball ratio of 1:1 before being melted in a corundum crucible at 1450 ℃ for 2h in a furnace. Then the melt was water quenched and obtained basic glass were dried at 105 ℃ for 12 h in an oven. The glass was broken into powders in a vibration mill for 3 min and then sieved through 160 screen(97μm). The sieved glass powders were mixed with 0.3 wt.% SiC powders in deionized water for 2 h for uniform dispersion. The slurry was dried at 105 ℃ for 12 h in an oven and then 7 g dried powder was pressed into green bodies with diameter of 2 cm under the pressure of 15 MPa for 1 min. The samples were heated to 1150 ℃, respectively, with a heating rate of 10 ℃ min^{-1} and kept for 30 min for sufficiently foaming.

3. Results and discussion

As shown in Fig. 1, the broad band of [SiO_4] shifts to smaller wavenumbers with the amount of Fe_2O_3, indicating Si–O tetrahedron linkage becomes relatively loose. The content ratio of the characteristic structural units is related to the area ratio of its characteristic peak. Fig.1 also shows the Gaussian fitting results of Raman spectra and the corresponding Q^n in each basic glass. No obvious Q^1 and Q^4 structural units were observed and the similar phenomenon had also been reported before[7]. The area fraction of Q^0, Q^2 and Q^3 is summarized in Table. 1. With the increase amount of Fe_2O_3 from 0 to 8.4 wt.%, the relative content of $[Si_2O_5]^{2-}$ structural units decreases from 44 % to 23 %, while the content of $[SiO_4]^{4-}$ and $[Si_2O_6]^{4-}$ increase. This reveals that addition of Fe_2O_3 destroys the glass network and leads to the overall shift of the broad band. The addition of Fe_2O_3 modifies the depolymerization degree of the glass network and increases the numbers of non-bridged oxygen. As depolymerization degree decreases, the viscosity of the molten glass decreases which helped the pore formation of porous glass ceramics. Therefore, during the preparation of porous glass-ceramics from solid wastes, viscosity of molten glass and pore structures of porous glass ceramics can be controlled by optimizing the amount of solid wastes contain Fe_2O_3.

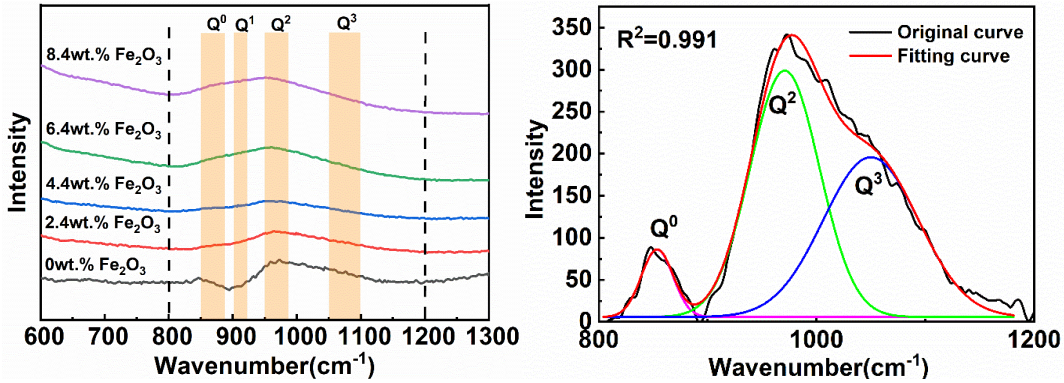

Fig. 1 Raman spectra and peakfit of samples.

Table.1 Area fraction of Q^n.

Content of Fe_2O_3/wt.%	Q^0/%	Q^2/%	Q^3/%
0	6	50	44
2.4	4	54	42
4.4	8	63	29
6.4	6	65	29
8.4	11	66	23

Fig. 2a-c show the 3D and 2D X-CT images of porous glass-ceramics sintered at 1150 ℃ for 30 min. The images show the pore structures adjusted by different amount of Fe_2O_3. From the 3D images, we found that without the addition of Fe_2O_3, the sample could not form complete and uniform pores. With the increase of Fe_2O_3, the pores of samples became bigger and more uniform. The ratio of the closed porosity to open porosity also changed along with the change of Fe_2O_3 amount. In the 2D X-CT images, red parts

represented the connected pores and blue parts represented the closed pores. It is obvious samples with 2.4 wt.% Fe_2O_3 had the highest closed porosity. It is reasonable to deduce the sample with 2.4 wt.% Fe_2O_3 possessed a totally closed pore structure. As the amount of Fe_2O_3 increased to 4.4 wt.%, all the pores were in red which meant the sample had almost all open pores. When further increasing the amount of Fe_2O_3, the porosity and pore sizes increased and almost all pores were connected. It can be concluded that appropriate doping amount of Fe_2O_3 and suitable sintering temperature is beneficial to the formation of closed pore structure.

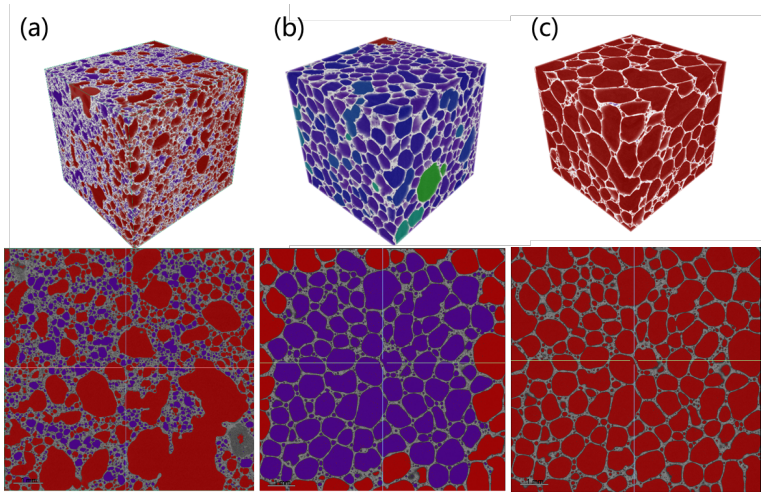

Figure 2 X-CT images of samples with different content of Fe_2O_3 sintered at 1150 ℃: (a) G0 sample, (b) G1 sample, (c) G2 sample.

To investigate the thermal insulating performance of the porous glass-ceramics, infrared thermogram of G1 sample (closed pore structure) and G3 sample (open pore structure) heating at 60 ℃ are recorded, as shown in Fig. 3. The samples were cut into 25 mm×25 mm×15mm. The corresponding maximum temperature, minimum temperature and average temperature were read out along with the heating duration. G1 sample showed more homogeneous temperature distribution than G3 sample because of the uniform closed pore structure, blocking the heat conduction homogeneously. G3 sample exhibited continuous temperature rising and exceeds G1 sample after heating for 10 min, demonstrating the closed pore structure facilitating better insulation effect.

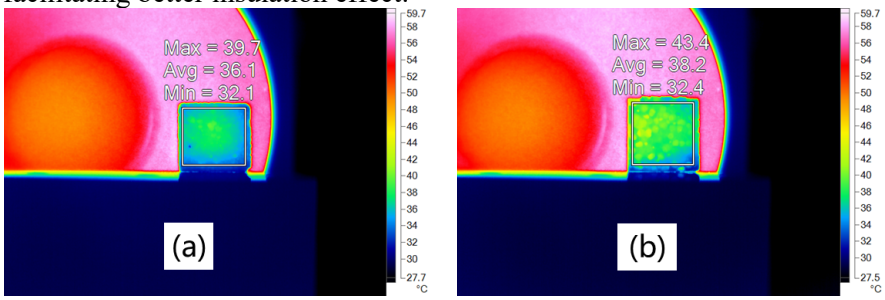

Figure 3 Infrared thermogram of G1 sample and G3 sample heating continuously at 60 ℃ for10 min: (a) G1 sample, (b) G3 sample.

4. Conclusions

In summary, we used Fe_2O_3 to optimize the pore structures of the porous glass-ceramics and facilitated the formation of uniform closed pore structure. The effect of Fe_2O_3 on the glass network, pore structure and thermal insulation performances of porous glass-ceramics was studied in details. The addition of Fe_2O_3 modified the depolymerization degree of the glass network and increased the numbers of non-bridged oxygen, decreasing the viscosity and the foaming temperature. 2.4 wt.% Fe_2O_3 doping optimized the pore structure into closed pore structure. The closed pore structure porous glass-ceramics exhibited better thermal insulation performance than open pore structure porous glass-ceramics.

Acknowledgements

This work is financially supported by the National Key Research and Development Program of China (No. 2019YFC1904900).

References

[1] H. Wang, K. Feng, Q. Sun, Effect of calcium carbonate on the preparation of glass ceramic foams from water-quenched titanium-bearing blast furnace slag and waste glass, Adv. Appl. Ceram. 117 (2018) 312–318. https://doi.org/10.1080/17436753.2017.1412120.

[2] Z. Luo, H. Liang, C. Qin, J. Zhang, T. Liu, A. Lu, Sintering behavior, microstructures and mechanical properties of porous CaO-Al2O3-SiO2-Si3N4 glass-ceramics, J. Alloys Compd. 773 (2019) 71–77. https://doi.org/10.1016/j.jallcom.2018.09.231.

[3] H. Cengizler, M. Koç, O. Şan, Production of ceramic glass foam of low thermal conductivity by a simple method entirely from fly ash, Ceram. Int. 47 (2021) 28460–28470. https://doi.org/10.1016/j.ceramint.2021.06.265.

[4] C. Xi, F. Zheng, J. Xu, W. Yang, Y. Peng, Y. Li, P. Li, Q. Zhen, S. Bashir, J.L. Liu, Preparation of glass-ceramic foams using extracted titanium tailing and glass waste as raw materials, Constr. Build. Mater. 190 (2018) 896–909. https://doi.org/10.1016/j.conbuildmat.2018.09.170.

[5] S.M. Salman, S. Gharib, Thermal conductivity of some multicomponent silicate glasses, Thermochim. Acta. 77 (1984) 227–239. https://doi.org/10.1016/0040-6031(84)87062-8.

[6] C. Vakifahmetoglu, T. Semerci, G.D. Soraru, Closed porosity ceramics and glasses, J. Am. Ceram. Soc. 103 (2020) 2941–2969. https://doi.org/10.1111/jace.16934.

[7] S. Zhang, Y. Zhang, Z. Qu, Effect of soluble Cr 2 O 3 on the silicate network, crystallization kinetics, mineral phase, microstructure of CaO-MgO-SiO 2 -(Na 2 O) glass ceramics with different CaO/MgO ratio, Ceram. Int. 45 (2019) 11216–11225. https://doi.org/10.1016/j.ceramint.2019.02.106.

The 16th International Congress on the Chemistry of Cement 2023 (ICCC2023)
"Further Reduction of CO_2 -Emissions and Circularity in the Cement and Concrete Industry"
September 18–22, 2023, Bangkok, Thailand

Carbonation effects on mechanical performance and microstructure of LWAs produced with hydrated cement paste powder

Y.J. Tang[1], K. Schollbach[2], W. Chen[3*], and H.J.H. Brouwers[4]

[1] *State Key Laboratory of Silicate Materials for Architectures, Wuhan University of Technology, Wuhan 430070, China*

Department of the Built Environment, Eindhoven University of Technology, 5612 AP Eindhoven, The Netherlands

Email: y.tang3@tue.nl

[2] *Department of the Built Environment, Eindhoven University of Technology, 5612 AP Eindhoven, The Netherlands*

Email: k.schollbach@tue.nl

[3] *State Key Laboratory of Silicate Materials for Architectures, Wuhan University of Technology, Wuhan 430070, China*

Email: chen.wei@whut.edu.cn

[4] *State Key Laboratory of Silicate Materials for Architectures, Wuhan University of Technology, Wuhan 430070, China*

Department of the Built Environment, Eindhoven University of Technology, 5612 AP Eindhoven, The Netherlands

Email: jos.brouwers@tue.nl

ABSTRACT

This paper aims to evaluate lightweight aggregates produced with hydrated cement paste powder (HCP) using carbonation. The mechanical properties, reaction products and microstructure were analysed and the results show that the optimal carbonation period for HCP I- and HCP III-type aggregates are different due to different amounts of portlandite. HCP I-type aggregates can gain 3.14 MPa after 7-day carbonation and contain 35.60 wt.% calcium carbonates. The remaining 13.95 wt.% portlandite shows the enormous potential in elevating the strength and CO_2 capture capacity jointly via the optimized carbonation curing method. On the contrary, HCP III-type aggregates gained 2.97 MPa after 1-day carbonation and further carbonation decomposed C-S-H and lead to the formation of calcite and amorphous silica gel with significantly elevated specific surface area (from 10.69 m^2/g to 42.96 m^2/g) (Tang et al., 2022). This study can provide some understanding in the performance prediction of carbonated LWAs originated from the real demolished cement and concrete materials.

KEYWORDS: *carbonation, decomposition, portlandite, C-S-H*

1. Introduction

As a newly developed building material, lightweight concrete shows some extraordinary properties such as extremely low density, excellent sound absorption, and thermal insulation (Chandra and Berntsson, 2002). The main ingredients for a lightweight concrete design are cement and lightweight aggregates (LWAs) (Spiesz et al., 2013). Generally, LWAs have a porous structure and low bulk density (less than 1200 kg/m^3) and thus reduce the density of concrete structure effectively. However, the commercial LWAs, for instance, expanded clay, expanded glass and perlite, consume huge amounts of energy, as well as natural resource due to the production at high temperatures (700 ℃ - 1400 ℃) (Tajra et al., 2019). Consequently, some studies started focusing on the development of a low-carbon footprint and sustainable LWAs.

Cold-bonding technology has been proposed and developed for the purpose of low energy consumption during LWAs manufacture with industrial wastes (Tang et al., 2020). Combined with a pelletizing process, pellets in different sizes with porous structure were produced and then applied as LWAs.

One industrial waste that has attracted much attention in recent years is aged concrete that can be recycled to recover most of the original high-quality fine and coarse aggregates and thus leave 10%-20% of fine concrete waste powder (Lu et al., 2018). The main components in waste powder are hydrated cement paste (HCP) but the exact composition can depend on the crushing and starting composition of the recycled concrete. The waste powder can have a high water demand due to the porous structure and high surface area, along with a very low reactivity when used as supplementary cementitious materials (SCMs) (Shi et al., 2016), causing difficulty in applying to normal concrete production without further treatment or activation (Spiesz et al., 2013).

The HCP contains mainly calcium silicate hydrate (C-S-H) gels, calcium hydroxide, AFt, AFm and some unreacted clinker phases. Gas-solid and aqueous carbonation were reported to be effective to utilize HCP powders as the SCMs. The workability and mechanical property of cement paste blended with carbonated HCP powder can be enhanced via the formation of calcium carbonates which can act as fillers and then optimize the pore structure (Mehdizadeh et al., 2022). Consequently, it is possible to produce HCP powder based cold-bonded LWAs by using carbonation instead of cement and alkali activator addition.

For the purpose of investigating the mechanism of the mechanical and microstructure development of the artificial aggregates under carbonation, this study used the laboratory-made cement paste instead of a real demolished concrete to obtain HCP powder and then produce LWAs, which allows to better control the chemical composition of the waste powder by eliminating the variability of its properties when recovered from demolished materials. Additionally, researchers prefer to investigate the properties of HCP powder from CEM I which contains few SCMs, whereas CEM III is also widely used and deserves more attention in the production of LWAs. Therefore, both CEM I 52.5 R and CEM III/A 52.5 N were chosen as the starting materials. The amount of hydration products from CEM I and CEM III is different, especially the amount of portlandite. A comparative study has been conducted to figure out the effects of portlandite amount in HCP I and HCP III on the aggregates production under carbonation curing. The mechanical properties, reaction products and microstructure were investigated via TGA, Nitrogen physisorption analysis and etc. to figure out the effects of carbonation on LWAs produced with HCP powder.

2. Experiments and methodology

2.1 Raw materials

The HCP powder was produced in the laboratory from the cement paste which was prepared by CEM I 52.5 R and CEM III/A 52.5 N provided by ENCI, the Netherlands. All cement pastes were prepared with a water to cement ratio of 0.5 and then demoulded until 24 hours after mixing, followed by the ambient curing in the resealable bags for at least 3 months.

The HCP was crushed manually and milled with a disc milling (Retsch, RS300XL) for 10 min to obtain the waste cement paste powder for the tests. The milled HCP powder originating from CEM I and CEM III was labelled as HCP I and HCP III, respectively. The chemical composition of HCP I and HCP III was analysed with X-ray fluorescence (XRF, Model Axios Advanced, PANalytical.B. V), as shown in Table 1. The mineral composition of HCP I and HCP III was determined using X-ray diffraction (XRD) analysis, which is shown in Fig. 1 (a) and (b), respectively. The D50 of HCP I and HCP III is 32.3μm and

38.3μm, respectively, analysed with a laser particle size analyser (Model Malvern Mastersizer 2000, Malvern PANalytical).

Table 1 The chemical composition of raw materials for preparation of aggregates (milled hydrated cement paste powder I (HCP I) and milled hydrated cement paste powder III (HCP III))

Materials (wt. %)	CaO	SiO_2	Al_2O_3	Fe_2O_3	SO_3	MgO	MnO	TiO_2	Others
HCP I	65.96	17.42	7.57	3.51	3.08	1.43	0.08	0.44	0.51
HCP III	49.32	27.10	12.02	1.24	4.83	4.24	0.17	0.55	0.53

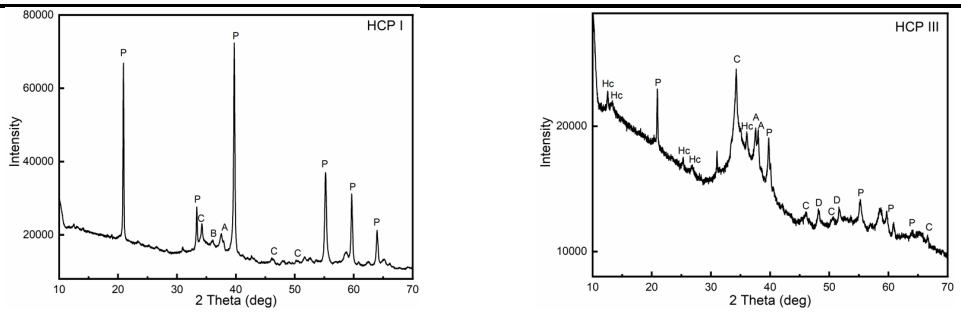

(a) (b)

Fig. 1 XRD patterns of HCP I (a) and HCP III (b) (P=portlandite, A=alite, B=belite, C=calcite, Hc=hemicarbonate, D=dolomite)

2.2 Pelletizing procedure

The disc pelletizer was used to produce the artificial aggregates. The model was D-7736, Maschinenfabrik Gustav Eirich, Germany. The size of the pelletizer was 40 cm in diameter and 10 cm in collar height. The vertical angle of the pan is 75° and the rotating speed was set as 60 rpm during the production process. 500 grams of HCP were placed on the rotating pan. After about 3 min of rotating, 50 grams of distilled water was sprayed slowly onto the mixed powder in the pan using a spray bottle over 10 min. After the aggregation was observed, the pan continued running for 5 min to form the pellets. The as-prepared aggregates fell out of the pan automatically once they reached sufficient size and were collected. The freshly prepared LWAs were placed in a CO_2 chamber with a CO_2 concentration of 5% and a relative humidity of 75% and carbonated for 1, 3 and 7 days, respectively for carbonation curing. The temperature during curing was constant, around 20 °C. The prepared aggregates, which were originated from HCP I and HCP III, carbonated for 1, 3 and 7 days were labelled as C1A I, C3A I, C7A I, C1A III, C3A III and C7A III, respectively.

2.3 Mechanical property of prepared LWAs

The mechanical properties of the individual pellets with different diameters were tested in an MTS Criterion equipped with a load cell of 100 kN at a speed of 0.6 mm/min until collapse. The maximum compression load was used to calculate the individual crushing strength with Eq. (1). 20 pellets were chosen as representatives for each group of prepared LWAs.

$$\sigma = 2.8P/\pi h^2 \quad (1)$$

Where σ (MPa) is the crushing strength of each pellets tested, P (N) is the maximum compression load each pellet can withstand, h (mm) is the diameter of the round pellet produced.

2.4 Characterization of reaction products and microstructure

The loose bulk density test was carried out according to EN 1097-3. Different artificial aggregates were crushed manually and ground finely to pass a sieve of 68 μm. Afterwards, samples were immersed in isopropanol for 30 min to eliminate hydration according to literature (Scrivener et al., 2018) and then dried in an oven at 40 °C until a constant mass. All samples were stored in desiccators, using a drying agent ($CaCl_2$ pellets) and sodium hydroxide pellets as a CO_2 trap until further different tests.

3. Results and discussion

It can be seen that all the samples have a loose bulk density of around 576.0-753.6 kg/m^3, which is below 1200 kg/m^3 and thus satisfies the density requirement of lightweight aggregates according to EN 13055-1 (2002). The individual strength of the carbonated aggregates originated from HCP I increases from 1.60

MPa to 3.14 MPa after 7-day carbonation (Fig. 2(a)), in line with the re-cementation effects of carbonation. Without carbonation, the reference aggregates only reach 0.83 MPa (Tang et al., 2022), indicating that carbonation can benefit the strength development. A reduction of porosity is observed most likely because the volume of the carbonates formed is 11–12% greater than the volume of portlandite as reported in (Šavija and Luković, 2016), which can optimize the pore structure and then enhance the mechanical property. However, the HCP III system shows the opposite results, where the individual strength of the carbonated aggregates decreases from 2.97 MPa to 0.57 MPa (Fig. 2(b)).

Table 2 Bulk density of the produced LWAs

Bulk density (kg/m^3)	C1A I	C3A I	C7A I	C1A III	C3A III	C7A III
	614.6±2.0	668.6±3.0	738.4±1.8	753.6±4.5	715.8±3.6	605.3±2.2

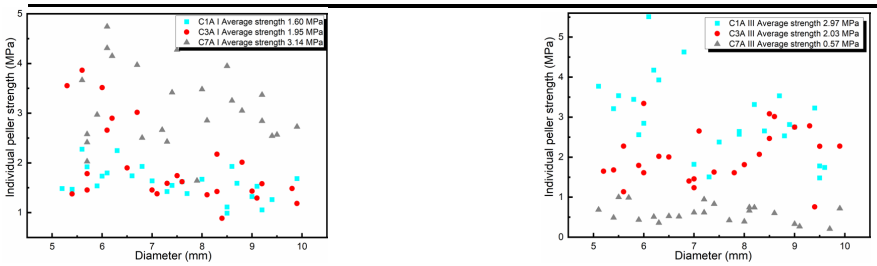

(a) (b)

Fig. 2 Individual pellet strength of the produced aggregates

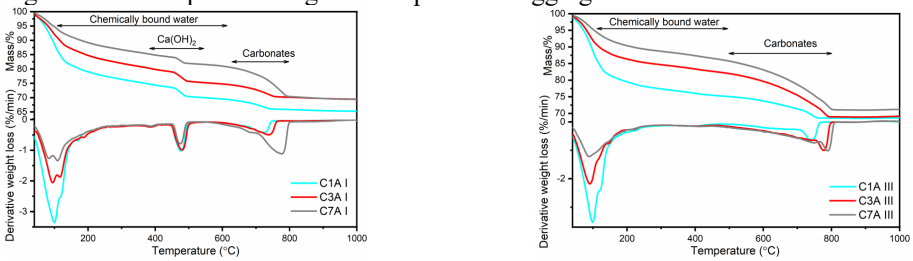

(a) (b)

Fig. 3 Weight loss determined with thermogravimetric analysis (TGA) and the first derivative of TGA (DTG) of the produced aggregates

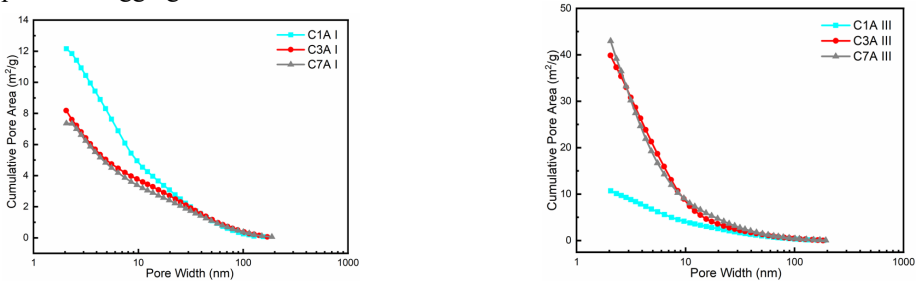

(a) (b)

Fig. 4 Cumulative pore area of the produced aggregates

It is suggested that carbonation of C-S-H is accompanied with a decalcification process. The decomposition of C-S-H gel can happen when the Ca/Si ratio is below around 0.66, followed by the severe carbonation shrinkage and cracking. The existence of portlandite can protect the other hydration products from becoming the main carbonated subjects and thus maintain the Ca/Si ratio of C-S-H gel at a high level (Šavija and Luković, 2016). From thermogravimetric analysis (Fig. 3), HCP I shows an initial amount of portlandite of 24.17 wt. % and after 7-day carbonation the amount of portlandite remains 13.95 wt.% while HCP III starts with only 2.55 wt.% portlandite and after 1-day carbonation, portlandite cannot be detected in TGA. XRD and FTIR analysis confirm these results (not shown in this paper). The sufficient portlandite in HCP I system acted like a buffer and prevented the decomposition of other phases like C-S-H gel during the carbonation curing even though C-S-H gel and other phases underwent the carbonation simultaneously (Borges et al., 2010; Šavija and Luković, 2016). The absence of portlandite is detected in HCP III system after 1-day carbonation. Therefore, C-S-H gel, ettringite etc. suffered the strong CO_2 attack, leading to the serious decomposition of C-S-H gel which usually plays a cementitious

role. The peak shift from 958 cm^{-1} to 1026 cm^{-1} in FTIR and the significantly elevated specific surface area from 10.69 m^2/g to 42.96 m^2/g (Fig. 4(b)) after carbonation treatment evidences the decomposition of C-S-H and formation of amorphous silica gel containing abundant evaporation water that can cause dry shrinkage and produce macro pores (Skocek et al., 2020). On all account, the aggregates obtained from HCP III suffered carbonation shrinkage and internal cracking during carbonation process, leading to the reduction of individual strength and increasing water absorption (Borges et al., 2010).

4. Conclusions

The comparative study was conducted to figure out the effects of portlandite amount in HCP I and HCP III on the aggregates production under carbonation curing. Based on the findings from this study, the following conclusions can be drawn.

Carbonation reaction benefits the fast strength development because the formation of calcium carbonates decreases the porosity, optimizing the pore structure and then benefiting the mechanical property. However, carbonation curing is more appropriate for HCP I-type aggregates than HCP III-type aggregates due to the different amount of portlandite. HCP I-type aggregates show the enormous potential in elevating the strength along with CO_2 capture capacity via the extended carbonation curing until the optimal curing period is reached. The optimal curing period for HCP III-type aggregates is short so that the individual strength and CO_2 uptake are undoubtedly limited.

The sufficiently available portlandite acts like a buffer to prevent decomposition in C-S-H and other phases caused by carbonation. The lack of available portlandite makes C-S-H the dominant phase subjected to carbonation, accompanying with the decomposition of C-S-H at the extensive carbonation calcification. Consequently, shrinkage and internal cracking during carbonation can occur, leading to a significant reduction of individual strength.

References

Borges, P.H.R., Costa, J.O., Milestone, N.B., Lynsdale, C.J., Streatfield, R.E., 2010. Carbonation of CH and C-S-H in composite cement pastes containing high amounts of BFS. Cem. Concr. Res. 40, 284–292. https://doi.org/10.1016/j.cemconres.2009.10.020

Chandra, S., Berntsson, L., 2002. Introduction, in: Chandra, S., Berntsson, L.B.T.-L.A.C. (Eds.), Lightweight Aggregate Concrete. William Andrew Publishing, Norwich, NY, pp. 1–3. https://doi.org/https://doi.org/10.1016/B978-081551486-2.50003-1

Lu, B., Shi, C., Zhang, J., Wang, J., 2018. Effects of carbonated hardened cement paste powder on hydration and microstructure of Portland cement. Constr. Build. Mater. 186, 699–708. https://doi.org/10.1016/j.conbuildmat.2018.07.159

Mehdizadeh, H., Cheng, X., Mo, K.H., Ling, T.C., 2022. Upcycling of waste hydrated cement paste containing high-volume supplementary cementitious materials via CO2 pre-treatment. J. Build. Eng. 52, 104396. https://doi.org/10.1016/j.jobe.2022.104396

Šavija, B., Luković, M., 2016. Carbonation of cement paste: Understanding, challenges, and opportunities. Constr. Build. Mater. 117, 285–301. https://doi.org/10.1016/j.conbuildmat.2016.04.138

Scrivener, K., Snellings, R., Lothenbach, B., Group, F., 2018. A Practical Guide to Microstructural Analysis of Cementitious Materials, CRC Press. https://doi.org/10.1201/b19074

Shi, C., Cao, Z., Xie, Z., 2016. Research Progress in the Mechanical Properties of Recycled Aggregate Concrete. Mater. Rev. 30, 96–102.

Skocek, J., Zajac, M., Ben Haha, M., 2020. Carbon Capture and Utilization by mineralization of cement pastes derived from recycled concrete. Sci. Rep. 10, 1–12. https://doi.org/10.1038/s41598-020-62503-z

Spiesz, P., Yu, Q.L., Brouwers, H.J.H., 2013. Development of cement-based lightweight composites - Part 2: Durability-related properties. Cem. Concr. Compos. 44, 30–40. https://doi.org/10.1016/j.cemconcomp.2013.03.029

Tajra, F., Elrahman, M.A., Stephan, D., 2019. The production and properties of cold-bonded aggregate and its applications in concrete: A review. Constr. Build. Mater. 225, 29–43. https://doi.org/10.1016/j.conbuildmat.2019.07.219

Tang, P., Xuan, D., Li, J., Cheng, H.W., Poon, C.S., Tsang, D.C.W., 2020. Investigation of cold bonded lightweight aggregates produced with incineration sewage sludge ash (ISSA) and cementitious waste. J. Clean. Prod. 251, 119709. https://doi.org/10.1016/j.jclepro.2019.119709

Tang, Y., Liu, G., Schollbach, K., Chen, Y., Chen, W., Brouwers, H.J.H., 2022. Re-cementation effects by carbonation and the pozzolanic reaction on LWAs produced by hydrated cement paste powder. J. Clean. Prod. 377, 134529. https://doi.org/10.1016/j.jclepro.2022.134529

The 16th International Congress on the Chemistry of Cement 2023 (ICCC2023)
"Further Reduction of CO_2 -Emissions and Circularity in the Cement and Concrete Industry"
September 18–22, 2023, Bangkok, Thailand

Cement types and seawater exposure in Europe – implications for infrastructure and its integration into marine habitats

S.N. Lørup[1,2], W.B. Feldthus[1], N.R. Padró[1], L.M Ottosen[1,4], W. Kunther[1,3,*]

[1] *Technical University of Denmark, 2800 Kgs.Lyngby, Denmark*

[2]*E-mail: sinl@dtu.dk*
[3]*E-mail: wolku@dtu.dk*
[4]*E-mail: limo@dtu.dk*

ABSTRACT

In addition to the carbon footprint of construction materials, infrastructure in marine exposure has an environmental impact from construction processes and hardened waterfronts (ocean sprawl), which may amplify the biodiversity crisis. For artificial reef structures, different design approaches have been used and may also improve the integration of infrastructure into marine habitats to breathe life into ecosystems that are heavily influenced by human activity. Downsides of human activity are e.g., contaminants, noise, geometry, and textures that may be suboptimal for biogenic colonization and balanced ecosystems. One of the most reported materials for artificial reef structures is concrete due to its durability, the possibility to control its chemistry, and flexible use when it comes to geometry and surface textures. Hence, different cement types have been used and may yield somewhat different biological results, given equal biological conditions. At the same time, the regulations for the use of cement types for concrete in these exposure conditions differ between European countries, as concrete standard EN 206 is not harmonized. This article reviews the different cement types allowed in European standards for use in seawater exposure in selected European countries together with concrete design strategies of artificial reefs to highlight possibilities and limitations for the integration of infrastructure projects into existing habitats.

KEYWORDS: *Seawater, cement, standardization, EN 206, artificial reefs*

1. Introduction

Even though the distance between the different countries in Europe is relatively short, a significant national variation in concrete standards can be observed. These standards conform with the harmonized standard, EN 197-1 (European Commission (2011)), which defines cement types, but differ in their national application of EN 206 (European Commission, (2021)) which defines the use of concrete in each country as this standard is not harmonized. The intention of standardization was to facilitate trade through product specifications. The differences in national concrete standards, based on the same overall cement standard for Europe have been partially explained by differences in climate, building traditions, products, and market structure (Müller (2012)). Analyzing the differences between national standards and putting them in the context of marine structures that connect many of the chosen countries together with publications on ecosystem rehabilitation, provides insight into the potential of infrastructure projects to support ecosystems. Ultimately, the high environmental impact associated with cement production and infrastructure projects might be offset somewhat by implementing restoration efforts into the projects, while still maintaining the structural and durability requirements for the concrete/structure in question. Possible benefits include resource optimization, decreasing the environmental impact, enhancing biodiversity, and reducing potential damages to the concrete caused by marine exposure (Huang et al. (2016)). The environment of concrete is considered in the design (Eurocode 2) and its severity is defined by their exposure classes. Relevant for the integration of infrastructure into marine habitats are XS2 and 3, and XA3. Here we focus on XS2 and XA3, which is defined as the threat of reinforcement corrosion caused by chloride ions in permanently submerged conditions and an aggressive environment for the cement past in concrete with a special focus on sulfate attack, respectively.

Currently, no systematic studies have been found that link commonly used cement types in European countries in marine environments with infrastructure and ecosystems purposes (e.g., artificial reef), hence we started with a comparison of standards for engineering purposes as these should at least ensure the durability of the materials for 50 years; the design age in many national annexes (NA) to EN 206.

2. Method

A literature study was conducted on different concrete standards in European countries and concrete as a substrate in artificial reefs to potentially enhance biodiversity and maritime ecosystems. The state of technology for cement types used in marine constructions was analyzed by comparison of several NA of the EN 206 concrete standard, which typically refers to the harmonized standard EN 197-1 concerning cement types. During the analysis, we came across DS/CEN/TR 15868:2018 which has been used as a starting point for comparison of the permitted cement types in exposure class XS2 and XA3. The focus here is on permanently submerged structures.

The main results for XS2 and XA3 are based on 14 and 18 countries respectively and 27 cement types in compliance with EN 197-1. The data obtained in DS/CEN/TR 15868:2018 has been compared with 6 individual national standards (Denmark, Norway, Germany, Spain, Sweden, and France) as the reported data of DS/CEN/TR 15868:2018 differed in several aspects from the cited NA for Denmark. Hence it is possible that the listed cements might deviate from other countries as well as we could not get access to all NA. Please contact the authors if you want to share some of these details for other countries than the six listed above.

3. Results and discussion

Tables 1 and 2 summarize the allowed cement types regarding exposure class XS2 and XA3, respectively, for the selected 6 countries. Note that the overall trends for these countries are the same when including the remaining 8 and 12 countries, respectively for XS2 and XA3.

We focus on the cement types first as this parameter is typically provided in biological articles that focus on biofouling, not all desired material parameters such as cement quantity, strength requirement, w/b ratio or aggregate types etc. are included in biology-oriented articles. Nevertheless, the cement type provides an insight into basic design considerations that are applied in the standardization committees and restoration efforts of ecosystems as the minimal denominator.

3.1 Exposure class XS2 – Permanently submerged in seawater.

The cement types permitted for exposure class XS2 in the selected 6 European countries are stated in Table 1, for which some types are permitted under conditional constrains.

CEM I and CEMII/A-V are the only types that are permitted in all selected countries. However, when summarizing the cement types across countries, slag cements (CEM II/S, CEM II/M, CEM III) are permitted significantly more than fly ash cement (CEM II/V, CEM II/W, CEM II/M) with 28 against 16 counts respectively (76 against 56 respectively when all 14 countries are included). Please note that not all footnotes/nuances were implemented in this overview for the sake of clarity and space.

Tabel 1. Permitted cement types for exposure class XS2 for selected relevant countries. Summarized values are stated for cement types permitted in each country, and amount of cement types in each country. Cells marked with √ indicate permitted cement types. Cells marked with (√) indicate conditional use and blank cells indicate no guidance provided in the national standards.

Country		CEMI	CEM II																			CEM III			CEM IV		CEM V		
			S		D	P		Q		V		W		T		L		LL		M									
			A	B	A	A	B	A	B	A	B	A	B	A	B	A	B	A	B	A	B	A	B	C	A	B	A	B	SUM
EN 206-1		√																											*1*
Denmark	DK	√								√																			*2*
France	FR	(√)	(√)	(√)	(√)	(√)				(√)						(√)		(√)		(√)	(√)	(√)	√	√			√	√	*15*
Germany	DE	√	√	√	√	√	√	√	√	√	√			√	√	√		√				√	√	√					*17*
Norway	NO	(√)	(√)	√						(√)	√					(√)		(√)		(√)	(√)	√	√						*11*
Sweden	SE	√	√	√	√					√	√							√		√	√	√							*10*
Spain	ES	√	√	√	√	√	√			√	√											√	√	√	√	√	√		*14*
SUM	-	6	5	5	4	3	2	1	1	6	4	0	0	1	1	3	0	4	0	3	3	5	4	3	1	1	2	1	-

None of the 6 countries permits calcareous fly ash cement while the different slag cement types (CEM II/S and CEM III/B) have similar counts, except for CEM III/C.

France and Germany are the countries that permit the most with 15 and 17 respectively. However, countries such as Belgium, Greece, and Italy permit more than 23 cement types (Danish Standard Association (2019)). Denmark permits 2 types, and as such is the most restrictive country included.

2.2 Exposure class XA3 – Highly aggressive chemical environment

From the summarized values of XA3 for each cement type across the countries (Table 2), CEM I and CEMII/A-V are observed to be the most permitted types, closely followed by CEM II/S and CEM III/A and B. As with XS2 slag cement dominates the overall permitted type with 28 cases compared to 15 for fly ash. CEM III is again the decisive factor for slag cement to be the most permitted type. None of the 6 countries permits CEM II/W, CEM II/B-L or CEM II/B-LL.

A trend that does not appear in table 2, is the high amount of cement types that require additional conditions ((√)) for XA3. In table 2, 29% are conditional, while for the 18 countries it is 79%, which might be explained by the cultural, climatic and market structure described in Müller (2012).

Denmark is again the country permitting the fewest cement types with only 2 which both additional requirements. The specific additional requirements vary depending on the country, especially Germany specify multiple conditions for XA3 which are described in Danish Standard Association (2019) and NABau (2022).

Tabel 2. Permitted cement types for exposure class XA3 for selected relevant countries. Summarized values are stated for cement types permitted in each country, and amount of cement types in each country. Cells marked with √ indicate permitted cement types. Cells marked with (√) indicate conditional use and blank cells indicate no guidance provided in the national standards.

Country		CEM I	CEM II																		CEM III			CEM IV		CEM V		
			S		D	P		Q		V		W		T		L		LL		M								
			A	B	A	A	B	A	B	A	B	A	B	A	B	A	B	A	B	A	B	A	B	C	A	B	A	B	SUM
EN 206-1		(√)																										1
Denmark	DK	√								√																		2
France	FR	(√)	(√)	(√)		(√)				(√)										(√)		(√)	√	√			√	√	11
Germany	DE	(√)	√	√	√	√	√	√	√	√	√			√	√	√		√				√	√	√					17
Norway	NO	(√)	(√)	(√)	√					(√)	(√)					(√)		(√)		(√)	(√)	(√)	(√)						12
Sweden	SE	√	√	√	√					√	√							√		√	√	√	√						11
Spain	ES	√	√	√	√	√	√			√	√											√	√	√	√	√	√		14
SUM	-	6	5	5	4	3	2	1	1	6	4	0	0	1	1	2	0	3	0	3	2	5	5	3	1	1	2	1	-

3. Ecosystems restauration

Slag cement is the most permitted standard across the two analyzed exposure classes. It also happens that slag-based cement types are amongst the most utilized cement types in the context of artificial reefs and ecosystems restauration (Padró (2023)), which is maybe somewhat surprising as it is an industrial by-product. Slag cement has shown to outperform fly ash cement and Portland cement on additional parameters such as biodiversity, ecological performance, and durability (Hayek et al. (2021), Perkol-Finkel et al. (2018)), which has been suggested to depend on the pH of the material (Ido and Perkol-Finkel (2015)). Thus, slag cements appear to enhance biological colonization, making it more suitable for ecosystem restoration (Padró (2023)). Furthermore, biofouling depends on the region, for which physical parameters such as pH, salinity and chemical composition are variables, all influencing biomass and colonization (Boukhelf et al. (2022)). On the engineering side, investigations have shown that CEM III/B can display beneficial mechanical properties, particularly for marine environments due to a denser microstructure and resistance towards sulfate attack after hydration (Boukhelf et al. (2022), Ly et al. (2021)).

This insight might provide initiatives toward more balanced standardization in which eco-efficiency and durability are achievable through appropriate monitoring and relevant tests. Implementation of more binder types increases the flexibility to adapt to the increasing CO_2 emissions and the circularity agenda of the future.

4. Conclusions

Even though the cement standard in Europe, EN 197-1, is harmonized, the national standards for concrete create a wide range of possible options. This may lead to significantly different material choices even for countries that share common bodies of water. The reasoning is not necessarily transparent and may lay in traditions, market structure and experiences with different climatic conditions.

Related to constructions in marine environments, slag cements appear to provide biological, physical, and ecological advantages over e.g., Portland cements. The cement type used in marine constructions influences at least the early biological succession and thereby ecological restoration and should thus be considered for marine infrastructures. However, not all cement types which are beneficial for habitat creation/restoration are permitted in marine environments for all national standards. There might be potentials for ecological restoration and the green transition that are therefore not utilized (Scrivener et al. (2018), Sella and Perkol Finkel (2015)).

Acknowledgements

This project has received funding from European Union's Horizon 2020 research and innovation programme under grant agreement No GA 970972 and VELUX FONDEN through the project "Køge Bugt Marine Park".

References

Boukhelf, F., Sebaibi, N., Boutouil, M., Yoris-Nobile, A. I., Blanco-Fernandez, E., Castro-Fresno, D., Real-Gutierrez, C., Herbert, R. J. H., Greenhill, S., Reis, B., Franco, J. N., Borges, M. T., Sousa-Pinto, I., van der Linden, P., Gómez, O. B., Meyer, H. S., Almada, E., Stafford, R., Danet, V., … E. Hall, A. (2022). On the Properties Evolution of Eco-Material Dedicated to Manufacturing Artificial Reef via 3D Printing: Long-Term Interactions of Cementitious Materials in the Marine Environment. *Sustainability (Switzerland)*, *14*(15). https://doi.org/10.3390/su14159353

Danish Standard Association. (2019). DS/CEN/TR 15868:2018 Survey on provisions valid in the place of use used in conjuction with the European concrete standard and developing practice. Em *Dansk Standard*. www.ds.dk

European Commission. (2021). EN 206:2013+A2:2021 Concrete-Specification, performance, production and conformity.

European Commission (2011). EN 197-1:2011 Cement - Part 1: Composition, specifications and conformity criteria for common cements.

Hayek, M., Salgues, M., Souche, J. C., Cunge, E., Giraudel, C., & Paireau, O. (2021). Influence of the intrinsic characteristics of cementitious materials on biofouling in the marine environment. *Sustainability (Switzerland)*, *13*(5), 1–24. https://doi.org/10.3390/su13052625

Huang, X., Wang, Z., Liu, Y., Hu, W., & Ni, W. (2016). On the use of blast furnace slag and steel slag in the preparation of green artificial reef concrete. *Construction and Building Materials*, *112*, 241–246. https://doi.org/10.1016/j.conbuildmat.2016.02.088

Ly, O., Yoris-Nobile, A. I., Sebaibi, N., Blanco-Fernandez, E., Boutouil, M., Castro-Fresno, D., Hall, A. E., Herbert, R. J. H., Deboucha, W., Reis, B., Franco, J. N., Teresa Borges, M., Sousa-Pinto, I., van der Linden, P., & Stafford, R. (2021). Optimisation of 3D printed concrete for artificial reefs: Biofouling and mechanical analysis. *Construction and Building Materials*, *272*. https://doi.org/10.1016/j.conbuildmat.2020.121649

Müller, C. (2012a). Use of cement in concrete according to European standard EN 206-1. *HBRC Journal*, *8*(1), 1–7. https://doi.org/10.1016/j.hbrcj.2012.08.001

Müller, C. (2012b). Use of cement in concrete according to European standard EN 206-1. *HBRC Journal*, *8*(1), 1–7. https://doi.org/10.1016/j.hbrcj.2012.08.001

NABau. (2022). *DIN 1045-2 Tragwerke aus Beton, Stahlbeton und Spannbeton - Teail 2:Beton*.

Padró, N. R. (2023). *DESIGN OF CONCRETE REEF UNITS FOR DANISH MARINE HABITATS*. www.sustain.dtu.dk/english

Perkol-Finkel, S., Hadary, T., Rella, A., Shirazi, R., & Sella, I. (2018). Seascape architecture – incorporating ecological considerations in design of coastal and marine infrastructure. *Ecological Engineering*, *120*, 645–654. https://doi.org/10.1016/j.ecoleng.2017.06.051

Scrivener, K. L., John, V. M., & Gartner, E. M. (2018). Eco-efficient cements: Potential economically viable solutions for a low-CO2 cement-based materials industry. *Cement and Concrete Research*, *114*, 2–26. https://doi.org/10.1016/j.cemconres.2018.03.015

Sella, I., & Perkol Finkel, S. (2015). Blue is the new green - Ecological enhancement of concrete based coastal and marine infrastructure. *Ecological Engineering*, *84*, 260–272. https://doi.org/10.1016/j.ecoleng.2015.09.016

The 16th International Congress on the Chemistry of Cement 2023 (ICCC2023)
"Further Reduction of CO_2 -Emissions and Circularity in the Cement and Concrete Industry"
September 18–22, 2023, Bangkok, Thailand

A micromechanical modelling approach to study the effect of shape of hydrates on creep properties of cement pastes

Amit Kumar[1*], Shashank Bishnoi[1]

[1] *Indian Institute of Technology, New Delhi, India*

Email: iitd.amitkr@gmail.com, Bishnoi@iitd.ac.in

ABSTRACT

Creep has been one of the major causes of the long-term deterioration of concrete structures. Despite extensive research in this area, it is still not predictable accurately. The most fundamental reason for the same is that the origin of this phenomenon is at the micro-level of cement paste. If the microstructure and its response to an applied load are understood, a better prediction of creep is possible. With recent advancements in the field of characterization techniques, the microstructure of cement pastes is now better understood. Models that can precisely simulate the microstructures and their constitutive behavior are promising techniques to estimate creep at the macro level. Analytical methods based on physics are popular amongst such techniques for simulating this micro-level phenomenon. Besides modeling their interactions fairly, they can account for various shapes of the cement hydrates and their pore structures at micro and nano levels. This work uses a MATLAB model with Eshelby's theory and the homogenization approaches of continuum micromechanics to account for hydrates' shapes and volume fractions and their mutual interaction. The model predicts that with the increase in aspect ratios of the shape of hydrates, the macroscopic creep of cement paste reduces.

KEYWORDS: *Cement, creep, multiscale modeling, continuum micromechanics*

1. Introduction

Creep in concrete is one of the major concerns when it comes to long-term performance of concrete. The reason is that it cannot be precisely predicted and hence its effects cannot be accounted a priory. However, it is known that creep in concrete is mainly in cement paste, as the aggregates are almost elastic when compared to cement paste. Further, the macrostructural behavior of creep of cement paste and hence concrete has its roots at the micro/nano level of cement paste. Therefore, the microstructure of cement paste and the physics of the interaction of the microstructural hydrates (hydration products of cement) of cement becomes essential to be understood and appropriately incorporated while developing the methods of estimation of creep in any structure. Models accounting for the microstructural behaviour of cement paste are therefore powerful techniques for predicting its macrostructure behaviour like creep.
The method of using microstructural creep models of concrete have three stages. Firstly, the microstructure of cement paste (sizes of hydrates and their spatial arrangement), secondly, their individual constitutive property and lastly physics of interaction between them.
This paper will first discuss a brief summary about first two stages and then a detailed discussion of the third stage which involves micromechanical modelling of the intrinsic properties and their upscaling.

2. Cement Paste Microstructure

Knowing the exact shapes, sizes, orientation and spatial arrangement of hydrates is very difficult. It keeps changing with time due to ongoing hydration. Therefore, a cement paste can be classified into an ageing one (whose microstructure is still developing, due to ongoing hydration) and a non-ageing one (whose hydration can be assumed to be almost complete and hence microstructure is stable).
Experimental techniques like Scanning Electron Microscopy (SEM), Transmission electron microscopy (TEM), X-ray diffraction (XRD), Nuclear Magnetic Resonance (NMR), etc. are very much sensitive to the

sample and many of such experiments are required to statistically represent the cement paste. Moreover, the microstructure of even a completely hydrated paste cannot be idealized and used for another hydrated paste, because, it depends upon several factors like, composition of the cement, water-cement ratio, quality of water, curing conditions like temperature and relative humidity, etc.

Microstructural models have the advantage of modelling only the aspects required such as porosity, permeability or say other mechanical properties. They are relatively easy and faster to have a quick and precise representation of the microstructure. One of the most widely used model is the two-phase model: the solid phase consisting of hydrated cement particles and other mineral phases and the other is the pore phase. Other models include multi-phase model, which considers additional phases such as unhydrated clinker too. A detailed review of microstructural models' importance, utility, and current limitations may be found in Bishnoi and Bullard (2022).

3. Intrinsic properties of hydrates

Constitutive properties of hydrates of cement as well as unhydrated clinker particles may be taken as intrinsic in nature. It is the variation in the volume of these constituents, which changes the overall response in different cement pastes. Several works in this area may be found in literature which either used nano/micro indentation tests or have downscaled a macroscopic response of cement paste. A summary of intrinsic properties of different constituents of a cement paste is shown in **Error! Reference source not found.**1.

Table 1 Intrinsic elastic properties of constituents of a cement paste

Phase	Young's modulus [GPa]	Poisson's ratio	References
C_3S	128-142,142-152	0.3	Acker (2004),Velez et al. (2001)
C_2S	130-150,110-150	0.3	Acker (2004), Velez et al. (2001)
C_3A	150-170,135-155	0.3	Acker (2004), Velez et al. (2001)
C_4AF	100-150	-	Velez et al. (2001)
Portlandite	33-39,33-43, 39.77-44.22	0.305-0.325	Acker (2004),Constantinides and Ulm (2004),Monteiro and Chang (1995)
LD C-S-H	18-22,19.5-23.9	0.24	Acker (2004), Constantinides and Ulm (2004)
HD C-S-H	27-35,27.0-31.8	0.24	Acker (2004), Constantinides and Ulm (2004)

3. Multiscale Models of creep

Multiscale analytical models involve the concept of viewing concrete as a multiscale composite. A concrete which appears homogenous at a macroscale can be viewed as a heterogenous material composed of aggregates and a homogenous cement paste at an observation scale of say millimetres. Similarly, the "homogenous" cement paste at a millimetre scale is a heterogenous material composed of hydrates and pores at few micrometres. Similarly various multiscale thought models have been used for modelling cement pastes Constantinides and Ulm (2004); Honorio, Bary, and Benboudjema (2016).

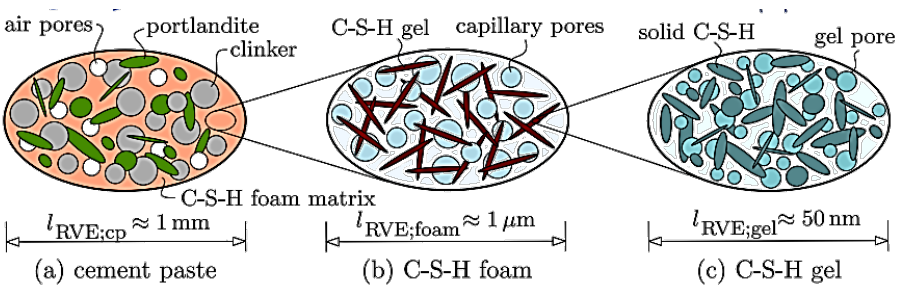

Figure 1 A sample Multiscale micromechanical model

For accounting the response of an individual constituents to an applied stress/strain on the boundary of the RVE, the approach of stress and strain concentration tensors are used which are based upon the Eshelby theory, Eshelby (1957). It gave solution for strain distribution due to an ellipsoidal inclusion inside an infinite homogemous medium (Figure 2).

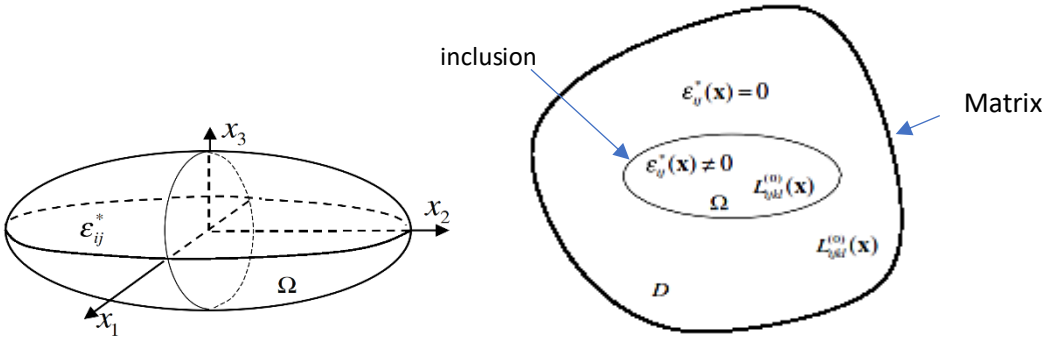

Figure 2 an Ellipsoidal inclusion inside a homogenous matrix

Total strain inside the inclusion $\varepsilon(\boldsymbol{x})$ due an eigen strain ε^* inside it is given as

$$\varepsilon_{ij}(\boldsymbol{x}) = S_{ijkl}\varepsilon_{kl}^* \tag{1}$$

Where **S** is called the Eshelby's concentration tensor and is independent of the eigen strain and size of the inclusion. It only depends on shape of the inclusion and the stiffness of the matrix. Hydrates of cement paste can be modelled as idealized shapes like spheres, ellipsoids, prolates, oblates, etc. Combining Eshelby's theory with the average stress theorem, various homogenization techniques, for example, the Mori and Tanaka (1973), the Self-Consistent scheme Hill (1965), can be applied to get equivalent properties of the material at a particular scale by accounting the interaction of the constituents of that level. Thereafter, the equivalent stiffness of the heterogenous RVE can be found from expression like

$$\bar{\boldsymbol{L}} = \boldsymbol{L}_0 + \sum_{r=1}^{N} c_r(\boldsymbol{L_r} - \boldsymbol{L}_0)\,\boldsymbol{A}_r \tag{2}$$

Where c_r is the volume fraction of r^{th} inhomogeneity. The strain concentration tensor $\boldsymbol{A}_r$ is then

$$\boldsymbol{A}_r = [\boldsymbol{I} + \boldsymbol{S}_r\boldsymbol{L_0^{-1}}(\boldsymbol{L}_r - \boldsymbol{L}_0)\,]^{-1} \tag{3}$$

Though exact equations for calculating Eshelby's tensors exist, but they are complex and involve a lot of calculative efforts. Therefore, for modelling, equations by Mura (1987) are used. A relationship between the Eshelby's concentration tensor and aspect ratio of a prolate shaped hydrate is shown by the output of the model in MATLAB in Figure 3 below. The inverse relation between the Eshelby's tensor and stiffness tensor from equation (2) and (3) means a direct relation with the creep compliance. The homogenization techniques mentioned were developed for elastic behavior and can be applied to obtain the equivalent strain response of a heterogenous viscoelastic material using the correspondence principle.

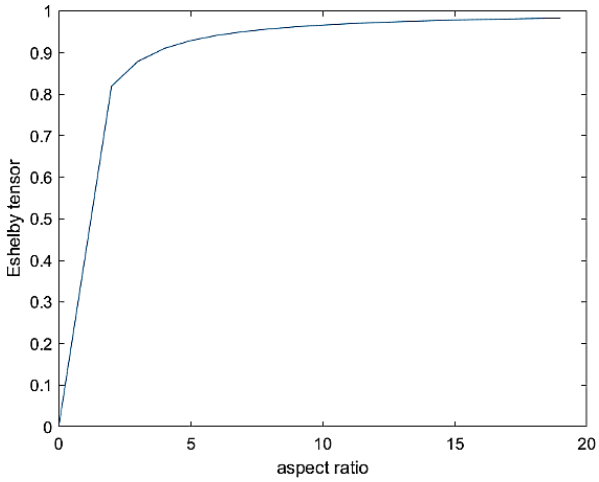

Figure 3 Dependence of strain concentration tensor on aspect ratio

3. Methodology

For the aging case, the material parameters change which change the compliance function $J(t,\tau)$ over time. It means that J is a function of both the time "τ" at which the sample was loaded and "t" the sample age. Whereas for non-aging cases, the compliance function is not modified with time, only its value increases. Therefore, it only depends upon the time elapsed since loading and can be represented as $J(t-\tau)$. Expression for strain (Figure-2) becomes a convolution integral in this case and Laplace Carson (LC) transformation of the integral gives an expression like elastic material in LC domain. Homogenization techniques can then be employed in the Laplace-Carson (LC) domain using the correspondence principle. After homogenization, the final compliance is converted back to the time domain to get the overall compliance of the material. Figure-2 illustrates the same.

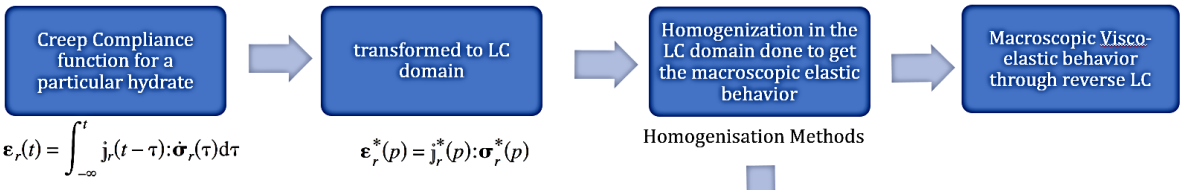

Figure 4 Flowchart for micromechanical analytical models of creep: non-Aging case

The third step in Figure 4 above involves finding an equivalent material for a heterogenous RVE and homogenisation techniques as listed above are used for it.

4. Conclusions

Eshelby Tensor and hence creep modulus of cement paste is found to increase with the aspect ratio of assumed prolate shape of the hydrates of cement pastes. This may be explained due to the possible mechanism of a more direct interaction between the isotropically arranged hydrates due to their longer shape.

References

Acker, P. (2004). "Swelling, Shrinkage and Creep: A Mechanical Approach to Cement Hydration." *Materials and Structures* 37:7.

Bishnoi, Shashank, and Jeffrey W. Bullard. (2022). "Microstructure Models of Cement: Their Importance, Utility, and Current Limitations." *RILEM Technical Letters* 6:188–95. doi: 10.21809/rilemtechlett.2021.135.

Constantinides, Georgios, and Franz-Josef Ulm. (2004). "The Effect of Two Types of C-S-H on the Elasticity of Cement-Based Materials: Results from Nanoindentation and Micromechanical Modeling." *Cement and Concrete Research* 34(1):67–80. doi: 10.1016/S0008-8846(03)00230-8.

Eshelby, J. D. (1957). "The Determination of the Elastic Field of an Ellipsoidal Inclusion, and Related Problems." *Royal Society*.

Hill, R. (1965). “A Self-Consistent Mechanics of Composite Materials.” *Journal of the Mechanics and Physics of Solids* 13(4):213–22. doi: 10.1016/0022-5096(65)90010-4.

Honorio, Tulio, Benoit Bary, and Farid Benboudjema. (2016) “Multiscale Estimation of Ageing Viscoelastic Properties of Cement-Based Materials: A Combined Analytical and Numerical Approach to Estimate the Behaviour at Early Age.” *Cement and Concrete Research* 85:137–55. doi: 10.1016/j.cemconres.2016.03.010.

Königsberger, Markus, Bernhard Pichler, and Christian Hellmich. (2020). “Multiscale Poro-Elasticity of Densifying Calcium-Silicate Hydrates in Cement Paste: An Experimentally Validated Continuum Micromechanics Approach.” *International Journal of Engineering Science* 147:103196. doi: 10.1016/j.ijengsci.2019.103196.

Monteiro, Paulo J. M., and C. T. Chang. (1995). “The Elastic Moduli of Calcium Hydroxide.” *Cement and Concrete Research* 25(8):1605–9. doi: 10.1016/0008-8846(95)00154-9.

Mori, T., and K. Tanaka. (1973). “Average Stress in Matrix and Average Elastic Energy of Materials with Misfitting Inclusions.” *Acta Metallurgica* 21(5):571–74. doi: 10.1016/0001-6160(73)90064-3.

Mura, Toshio. (1987). *Micromechanics of Defects in Solids*. 2nd, rev. ed ed. Dordrecht, Netherlands ; Boston : Hingham, MA, USA: M. Nijhoff ; Distributors for the U.S. and Canada, Kluwer Academic Publishers.

Velez, Karine, Sandrine Maximilien, Denis Damidot, Gilbert Fantozzi, and Fransois Sorrentino. (2001). “Determination by Nanoindentation of Elastic Modulus and Hardness of Pure Constituents of Portland Cement Clinker.” *Cement and Concrete Research* 31(4):555–61. doi: 10.1016/S0008-8846(00)00505-6.